UWTOR-M - A Conceptual Modular Stellarator Power Reactor

B. Badger, I.N. Sviatoslavksy, S.W. Van Sciver,
G.L. Kulcinski, G.A. Emmert, D.T. Anderson, A.W. Bailey,
J.D. Callen, J.A. Derr, L. El-Guebaly, K.J. Lee, J.L. Shohet,
D.K. Sze, R.C. Sanders, J . Tataronis, and K.Y. Yuan

October 1982

UWFDM-550

FUSION TECHNOLOGY INSTITUTE

UNIVERSITY OF WISCONSIN

MADISON WISCONSIN

UWTOR-M - A Conceptual Modular Stellarator Power Reactor

B. Badger, I.N. Sviatoslavksy, S.W. Van Sciver, G.L. Kulcinski, G.A. Emmert, D.T. Anderson, A.W. Bailey, J.D. Callen, J.A. Derr, L. El-Guebaly, K.J. Lee, J.L. Shohet, D.K. Sze, R.C. Sanders, J. Tataronis, and K.Y. Yuan

Fusion Technology Institute
University of Wisconsin
1500 Engineering Drive
Madison, WI 53706

http://fti.neep.wisc.edu

October 1982

UWFDM-550

UWTOR-M

A CONCEPTUAL MODULAR STELLARATOR POWER REACTOR

B. Badger, I.N. Sviatoslavsky, S.W. Van Sciver,
G.L. Kulcinski, G.A. Emmert, D.T. Anderson, A.W. Bailey,
J.D. Callen, J.A. Derr, L. El-Guebaly, K.J. Lee, K. Plute,
J.L. Shohet, D.K. Sze, R.C. Sanders, J. Tataronis, K.Y. Yuan

Fusion Engineering Program
Nuclear Engineering Department

and

Torsatron/Stellarator Laboratory
Electrical and Computer Engineering Department

University of Wisconsin
Madison, Wisconsin U.S.A.

October 1982

UWFDM-550

Acknowledgment

The work on this study was completed on October 1, 1982 and a draft of the report submitted to DOE for review at that time. The authors of this report wish to acknowledge the support of the project by the Department of Energy, Division of Magnetic Fusion Energy under contracts DE-AS02-78ET52048 and DE-AC02-78ET53082. Publication funds have come from the later contract.

We wish to thank our colleagues at Los Alamos National Laboratory, New York University, Princeton Plasma Physics Laboratory, Massachusetts Institute of Technology, and Oak Ridge National Laboratory for productive technical interactions. Special thanks go to Dr. Ron Miller of Los Alamos for his interest and cooperation. Discussions with Prof. G. Grieger of Max-Planck-Institut für Plasmaphysik, Dr. I. Motogima and Prof. K. Uo of Kyoto University, and Prof. K. Miyamoto of the University of Tokyo are gratefully acknowledged.

The efforts of Ms. Beth Brown and Ms. Gail Herrington in typing the report are also gratefully acknowledged.

Finally, a special debt of gratitude is due to Mr. Dennis Bruggink for the proofreading, coordinating, printing and assembling of this report with great patience and professionalism.

UWTOR-M REPORT TABLE OF CONTENTS

Executive Summary

The UWTOR-M conceptual modular stellarator power reactor study was initiated in October 1980 in an attempt to evaluate the feasibility and competitiveness of stellarator reactors with modular coils.

The stellarator offers a distinct alternative to the mainline approaches to magnetic fusion by being the only magnetic confinement concept that can maintain an ignited steady-state fusion plasma without external power input. The primary advantages of stellarators are steady state magnetic fields and continuous plasma operation. This removes complications associated with pulsed fields such as pulsed power storage and switching, enormous pulsed loads and fatigue problems on magnet structures, eddy currents in superconductors, thermal fatigue on blanket components and finally, it obviates the need for a thermal flywheel to even out the load on the power cycle. Since plasma heating is only required at startup, there is no recirculating power and because startup is on existing magnetic surfaces, plasma control is vastly simplified. Further, the stellarator has a natural divertor, thus offering a demonstrated impurity control mechanism. Finally, since there is no net current in the plasma there are no identified plasma disruptions.

Experiments with net current free operation which has been achieved with neutral beam injection and with RF heating have shown no MHD activity, no major disruptions, an extremely low level of small-scale turbulence and transport losses which are smaller than in ohmically heated discharges of similar plasma conditions.

The modular coil approach to stellarators has removed the main objection to the feasibility of extrapolating this concept to a power reactor, namely maintainability of the coils.

The initial constraints on the study were coil modularity and a magnetic divertor topology. Modularity seems to be essential for the reactor to be maintainable. A magnetic divertor, giving a demonstrated impurity control mechanism, would be a definite advantage.

It was decided to assume a β of 6% for the UWTOR-M study. Although this assumption is not quantitatively coupled to any stability/equilibrium model, the design goal was to maximize rotational transform and shear, avoid island formation and provide an adequate magnetic volume within a practical coil system.

A nominal power output of ~ 5000 MWth was selected. Magnetic field line calculations using a winding law for modular ℓ=3 stellarator coils were performed to generate the magnetic surfaces and determine the rotational transform. Many iterations were performed before a self consistent set of parameters evolved and was adopted for the base case. The performance of the plasma with these parameters was calculated by using a transport code which solves a set of fluid equations for the density and temperature profiles. The transport coefficients are an input to this code. The DT power is then determined by specifying the volume averaged β, the average density and the pellet injection velocity. Ignition can be achieved with ICRF heating at a level of 80-100 MW for about 5 seconds. Plasma control is achieved with two small poloidal field coils located on the outer radius of the device. Table I lists the primary parameters for UWTOR-M.

The reactor has 18 modular twisted coils arranged in a toroidal configuration as shown in Fig. I. It should be noticed that there are only two different coil geometries in the coil set. The reactor is housed in a toroidal reactor building as shown in Fig. II, which is a cross section through one of

Table I Important Parameters for UWTOR-M

DT fusion power - MWth	4300
Major radius - m	24.09
Minor coil radius - m	4.77
Plasma aspect ratio	14
Assumed avg. β-%	6
Rotational transform on edge	1.13
No. of field periods	6
No. of coils	18
Field on axis - T	4.5
Max. field on the cond. - T	11.6
Avg. ion density - m^{-3}	1.46×10^{20}
Avg. ion temp. - keV	9.8
Ion energy conf. time - s	3.7
$n\tau$ avg. through plasma - sm^{-3}	5.4×10^{20}
Centerline Z_{eff}	1.28
Ave. neutron wall flux - MW/m^2	1.41
Global breeding ratio	1.08
Blanket energy multiplication	1.15
Total thermal power MWth	4820
Gross electric power MWe	1898
Net electric power MWe	1836

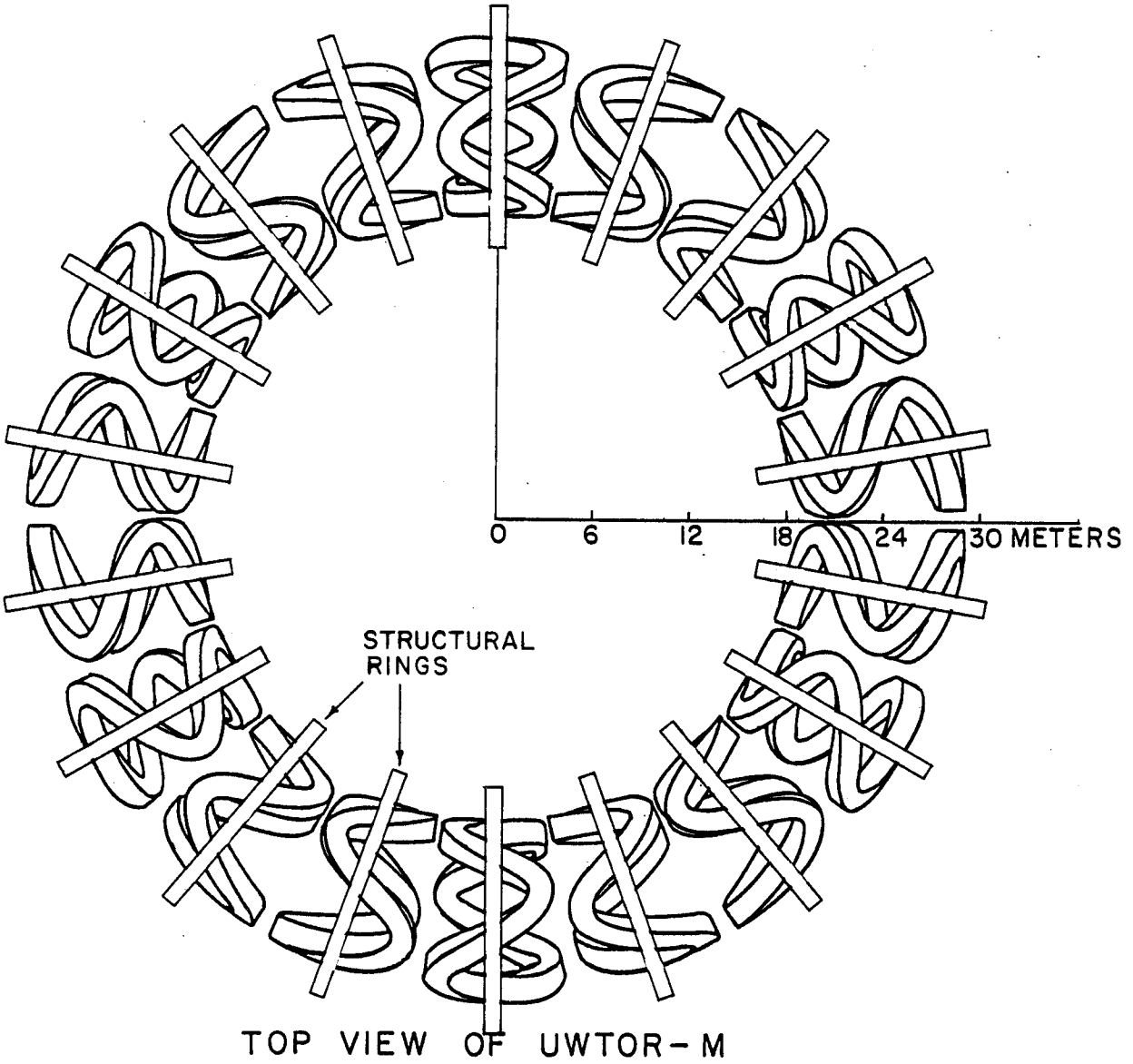

Figure I Top view of UWTOR-M coil set.

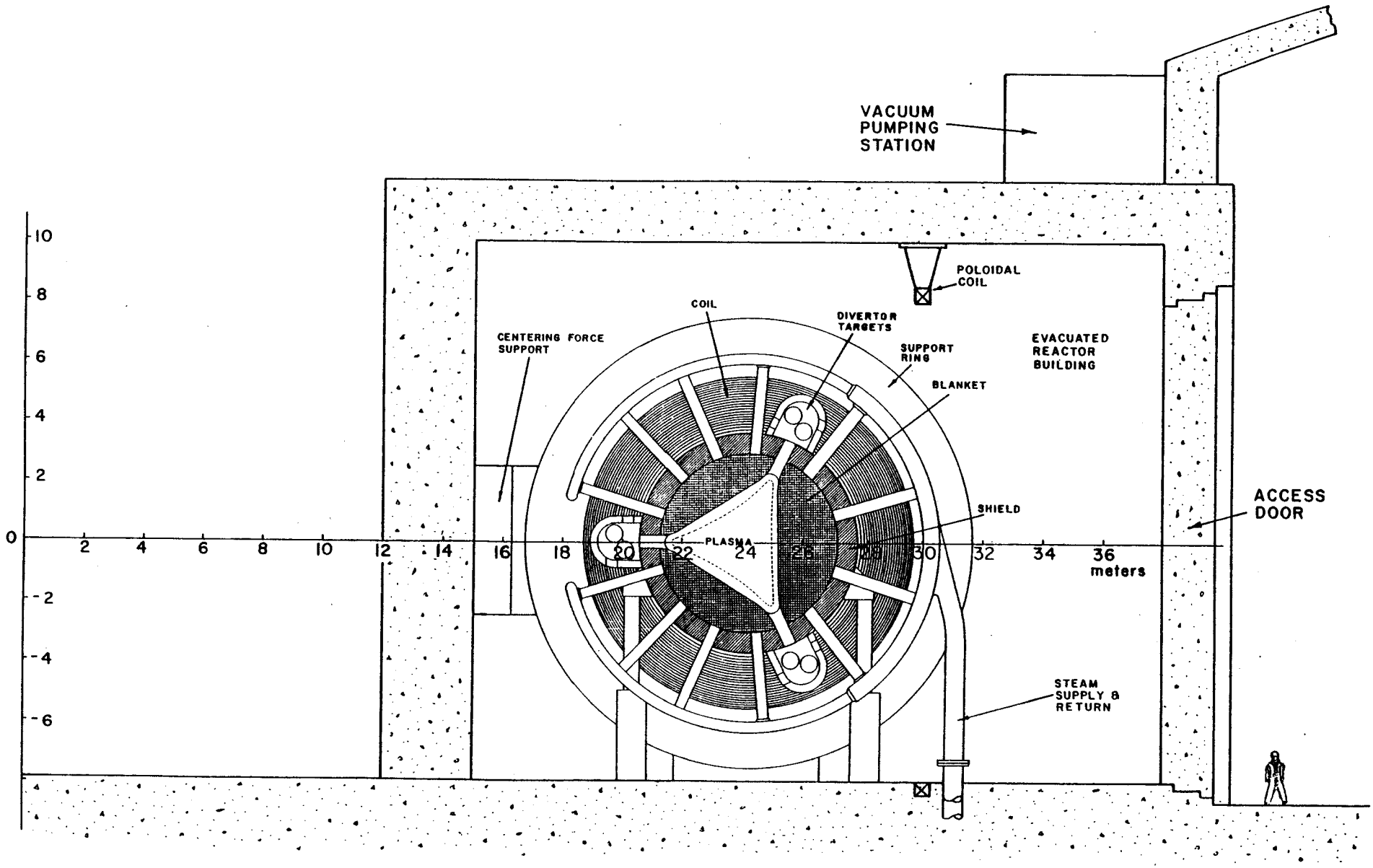

Figure II Cross section of reactor in evacuated building.

the modular coils. All the components of the reactor are shown in this figure. The reactor building is evacuated by pumping stations appropriately located around the toroidal enclosure. It is capable of evacuation down to 10^{-6} torr which is consistent with space simulation chambers much larger in size. Thus, it is steel lined and reinforced to withstand 1.5 atm. of over-pressure.

The magnets constituted a major challenge in the design of the reactor. It should be mentioned at the outset that the choice of an ℓ=3 magnet set with a large lateral deformation was prompted by a desire to maximize the rotational transform. In many ways, this choice has placed a great burden on the magnet group. One might say that we have chosen perhaps the most difficult case as far as modular stellarator coils are concerned, and have come up with a design which at least on paper seems credible and feasibile with minor extrapolation of present day technology.

The construction difficulty derives from the fact that the coils will be large (11 m in OD) and heavy (~ 960 tonnes). Once the technology of handling such coils is secured, the actual winding will be similar to that of yin yang coils and in some ways may be easier, since the poloidal bore of the coils is circular.

The forces on the coils during operation come from two sources, the self force due to their own field and the mutual attractive force between adjacent coils. In the regions where the coils come close together (at the twist extremities) the mutual attractive forces dominate causing large toroidal forces. The poloidal components of these forces when integrated around the coil produce a net centering force. The self field produces radial forces which attempt to expand the coil radially.

Calculations of the magnetic field and the forces were performed with the EFFI code. Extensive finite element stress analysis was performed using the SAP-4 code. It was found that the best way to react the radial forces was with an external structural ring circumventing the coil at the midplane. The ring will be welded to the coil frame at the points of intersection and will be enclosed within its own dewar. The coil is operated at 1.8 K with HeII and has NbTiTa in the high field region (11.6 T). This superconductor has properties similar to NbTi but has a higher critical field at 1.8 K. Results of the stress analysis show that the stresses can be kept below 2/3 of the yield limit for 304 LN SS in both the coil case and the structural ring.

The centering force on the coils is reacted by the structural ring bearing against a central support structure. Toroidal forces are reacted by allowing the coils to make contact with each other at the twist extremities.

The helical shape of the flux surfaces can be tracked by the reaction chamber with stepwise poloidal rotation of adjacent blanket segments. This simplifies the geometry of the blanket.

The blanket in UWTOR-M is made of ferritic steel HT-9 and the breeding material is $Li_{17}Pb_{83}$ (35% enriched ^{6}Li). The breeding material is static and has steam cooled tubes immersed in it. Adjacent blanket modules are not sealed to each other. This is made possible by the fact that the reactor building is evacuated. The steam enters at 330°C and exits at 500°C. Figure III shows the steam distribution manifolds and the headers connecting them to the blanket. Tritium is allowed to diffuse into the steam and then is removed in the same way as heavy water is extracted. The resulting T_2 inventory in the blanket is only 180 g.

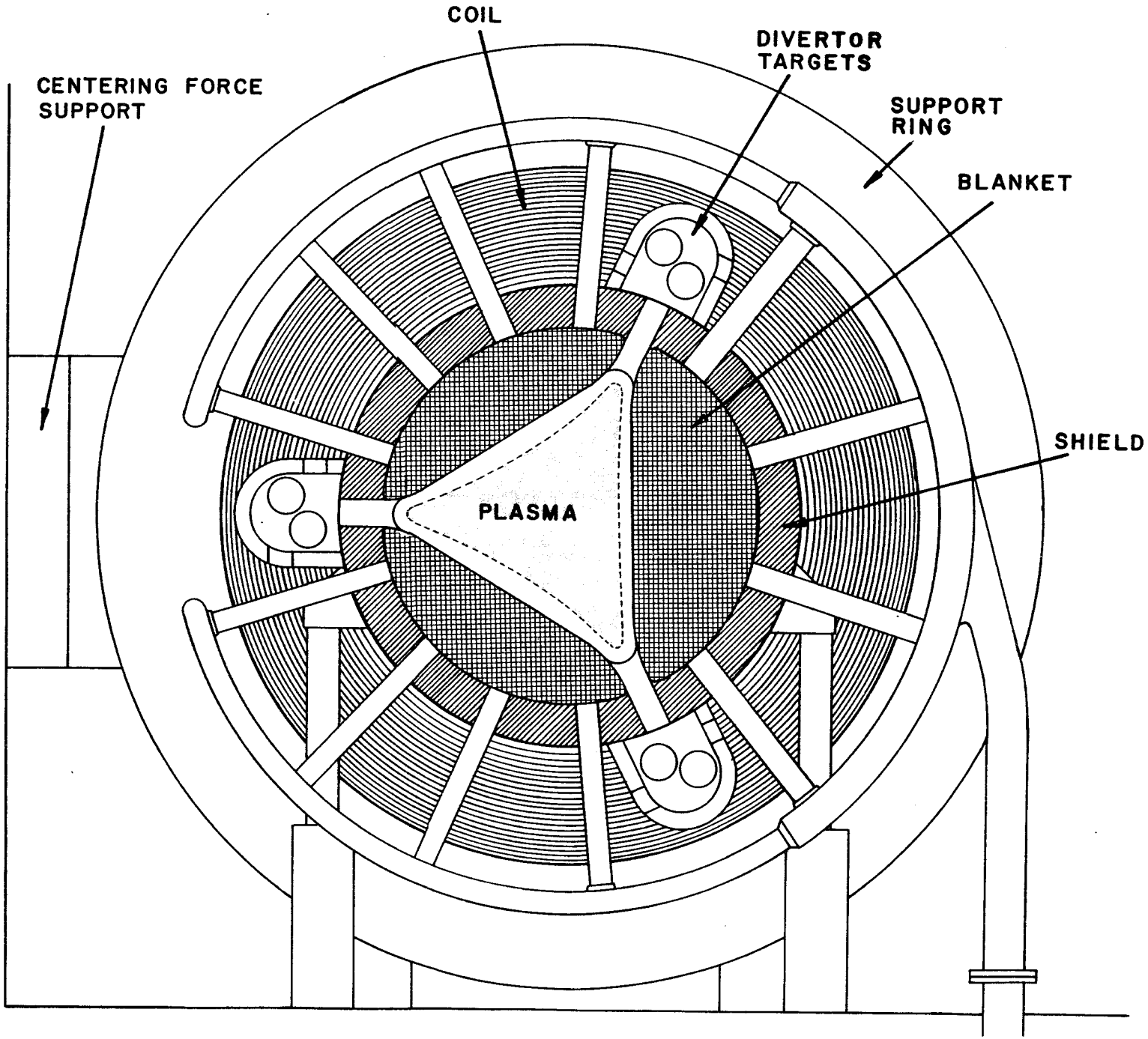

Figure III Cross section of the reactor between modular coils.

Impurity control is achieved with the magnetic divertor. The natural divertor in the stellarator occurs as a consequence of the magnetic separatrix bounding regions of closed nested flux surfaces. Inside the separatrix, magnetic flux links all the coils, but outside it, the flux links only some of the coils. Thus, some of the flux must emerge between magnets, but for flux conservation must reenter the toroid at some location. This divertor is modular in a modular stellarator. Flux bundles are discrete and well focused.

Divertor targets are used to recover the energy at a high temperature and to prevent neutron streaming through the divertor slots. This is achieved with cylindrical actively cooled shields surrounded with a rotating (100 RPM) cylindrical graphite surface. The neutralized exhaust is vented into the reactor building and is recovered by the vacuum pumps. Energy from the graphite is radiated to cooled surfaces in the divertor target housings and is converted at a high efficiency in the power cycle. The space for bearings and drives is made possible by the discreteness of the flux bundles. It would be impossible to use such a scheme on any other magnetic fusion system.

The neutronics and photonics analysis was carried out by one and three dimensional calculations. The thickness of the blanket, reflector and shield was optimized for adequate breeding (1.08), high energy multiplication (1.15) and protection of the superconducting coils where the peak dpa indicates that the coils will not have to be annealed during the lifetime of the reactor.

Neutron streaming through the divertor slots was accomplished with Monte Carlo calculations as was the radiation streaming through the pumpout ports. A 3.1 m thick biological shield was found to result in an acceptable dose of 2.4 mrem/hr in the toroidal service hall during reactor operation.

As was mentioned earlier, the T_2 from the blanket is recovered from the primary cooling steam. The reactor is fuelled with DT pellets and the unburned fraction, including the He ash which goes through the divertor system, is exhausted into the reactor building and is pumped out by cryopumps. The impurities are separated by a fuel cleanup unit and the hydrogen species then go to an isotope separation system. Total T_2 inventory in the plant, including a day's supply of fuel (14.9 kg), is 16.7 kg.

The power cycle depends on a steam to steam heat exchanger in which steam from the blanket exchanges heat with the steam which drives the turbine. In this way, T_2 is confined to the primary steam side. The secondary steam has a temperature of 454°C and a pressure of 13.8 MPa. This gives a gross thermal efficiency of 40% and a gross electric output of 1898 MWe. Pumping power for the stream is estimated at ~ 80 MW and is taken off the steam turbine shaft. Additional household requirements are estimated at 62 MWe, giving a net electric power output of 1836 MWe.

The blanket in UWTOR-M is estimated to have a life of three full power years, which at 75% availability, is four actual years. It is expected that 1/3 of the blanket segments would be changed out every 16 months.

Blanket changeout will require radial extraction of every other coil from the reactor building. Thus, the reactor building is designed with an access door spaced every other coil. Radial extraction of a coil makes it possible to remove blanket segments from either side, both from the extracted coil and the remaining one. Figure IV is a perspective view of a removed blanket segment. Removing 1/3 of the blanket will necessitate the extraction of only three coils. A downtime of four weeks is designated for this operation. Divertor targets are maintained at the same time.

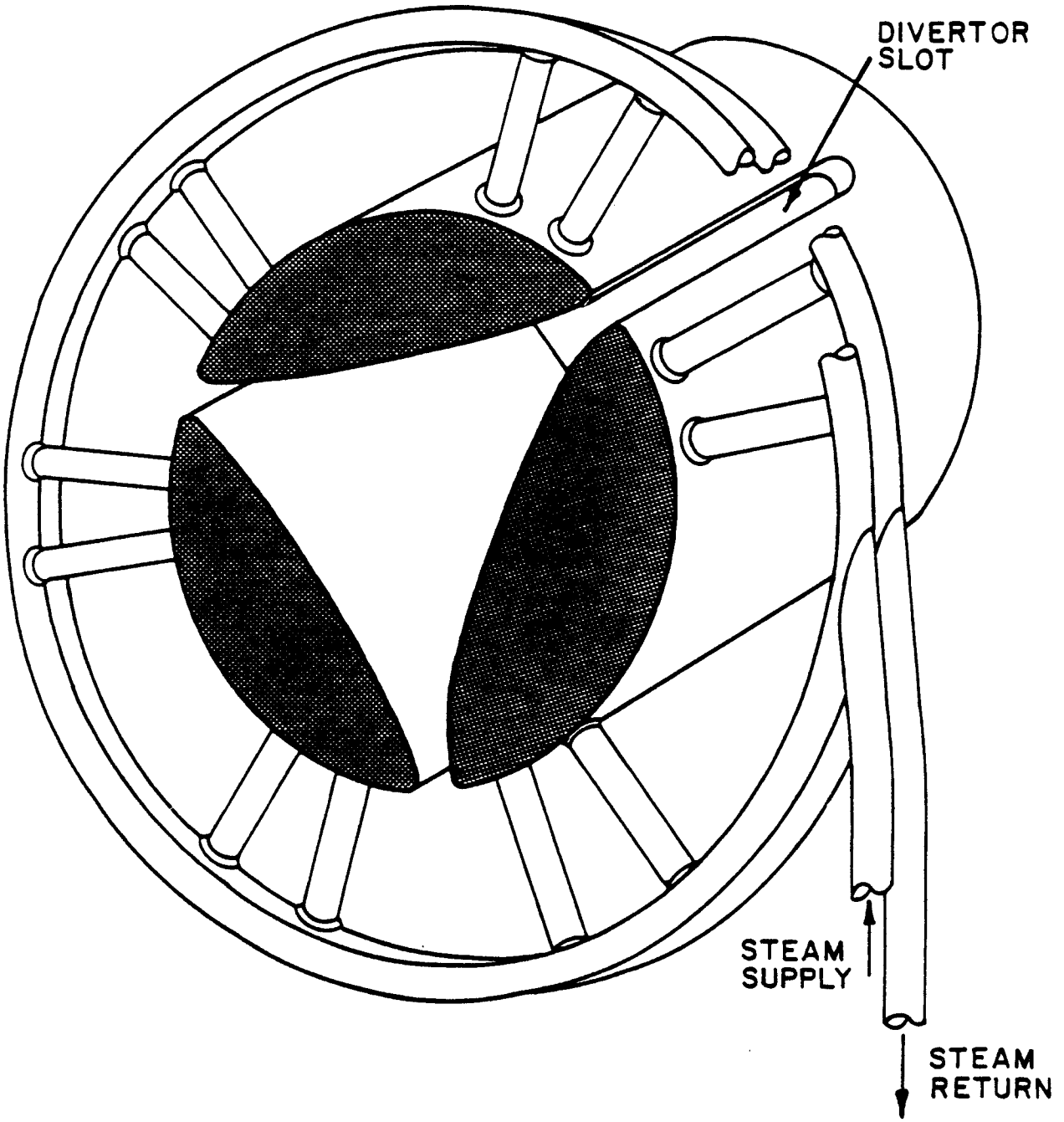

Figure IV Perspective view of a blanket segment.

This maintenance scheme automatically provides for the servicing of the coils. It is assumed that spares will be available should a failure occur in one of the coils.

Economic analysis of UWTOR-M was performed using DOE guidelines. The magnets account for 52.4% of the reactor plant equipment cost. Furthermore, the reactor plant equipment comprises 67.4% of the total direct costs.

The unit plant cost for UWTOR-M is found to be $2034/kWe in 1982 dollars. This compares favorably with STARFIRE, which had a plant cost of $2000/kWe in 1980 dollars. Busbar costs for UWTOR-M are 36 mills/kWh as compared with 35.1 mills/kWh for STARFIRE. This indicates that modular stellarators with β of 6% are competitive with other magnetic confinement fusion reactors.

Major Conclusions

- The most critical engineering issue of modular stellarators are the coils. Apart from being physically large and heavy, we have not identified any fundamental problems that cannot be solved with minor extrapolations of present technology.
- The need for a high rotational transform drive modular stellarators to a large number of periods and a high aspect ratio resulting in rather large devices.
- A modular divertor can be well integrated into a modular stellarator at the expense of a minor complication in the blanket geometry.
- The magnetic volume utilization in a modular stellarator is similar to tokamaks with poloidal divertors and slightly lower than tokamaks without poloidal divertors. However, the low recirculating power fraction in stellarators seems to make up for this deficiency from the economic standpoint.

- Maintainability for the whole reactor can be achieved with radial extraction of modular coils.
- Modular stellarators of $\beta \approx 6\%$ and power output in the range of 4000-5000 MWth are economically competitive with tokamaks and other magnetic fusion reactor concepts.

I. Design Philosophy

I.1 Introduction

In the last ten years, there have been numerous conceptual fusion reactor design studies, primarily in the area of tokamaks and more recently in tandem mirrors, bumpy tori and various kinds of pinches. Although the stellarator concept is the oldest of all these devices, reactor studies based on it have been limited to minor efforts of a scoping nature, many of which were performed outside the USA.

Recent encouraging experimental results and new developments in modular coils have renewed interest in the stellarator. The modular coil approach to the stellarator is studied in two places, one at the University of Wisconsin and the other at Los Alamos. In this chapter we will set forth the guidelines and constraints under which the UWTOR-M study has been conducted.

I.2 Scope of the Study

The UWTOR-M study is a self-consistent stellarator reactor design with special emphasis on the engineering problems, in particular:

- A credible coil configuration.
- Maintainable system components.
- A workable divertor.

The study does not include a balance of plant design. Instead the BOP was scoped out only to the extent of obtaining a reasonable cost estimate.

I.3 Design Evolution

The initial phase of the study involved the investigation and selection of a coil configuration. Coil configurations considered were the following:

1. Continuous Helices.
2. Modular Torsatron Coils.
3. Twisted (Rehker-Wobig) Coils.

Since a main objective of the study was to have a maintainable system, it was decided to forego continuous helices on the premise that they would be difficult if not impossible to maintain. Although attempts have been made[1] and continue to be made at making demountable joints in large superconducting magnets, it was felt that for the present, questions about the credibility of such joints are still prevalent.

Modular torsatron coils[1] with windbacks were also considered. At the initiation of the study, available designs of modular torsatron coils were extremely large and had a very low magnetic volume utilization. Furthermore, there were some serious questions as to the quality of the flux surfaces produced. Since then, some new ideas with respect to modular torsatron coils have emerged.[2] These coils are much smaller, simpler, have good magnetic volume utilization and appear to generate good flux surfaces. There may be good justification for basing a reactor design on these new modular torsatron coils.

As the study focused on twisted stellarator coils the question arose whether to pursue an $\ell = 2$ configuration such as proposed by Rehker-Wobig[3] or the $\ell = 3$ design with a larger lateral deformation proposed by J. Derr[4] at the UW. Since the $\ell = 2$ configuration was already being investigated at Garching (FRG) and at Los Alamos, it seemed reasonable that an alternate approach would be appropriate. Furthermore, the $\ell = 3$ Proto Cleo continuous coil stellarator at the UW was in the process of being outfitted with a modular coil set (IMS)[4] based on the Derr configuration. Experience gained in

investigating the best configuration available could be directly applied to the UWTOR-M design. This reasoning led to the adoption of the coil configuration used in this design study.

One of the main advantages of the stellarator is that it has a built-in divertor as a natural consequence of its magnetic topology. Tokamak designers have been struggling for years to incorporate divertors without unduly complicating the design and reducing the magnetic volume utilization. Driving a null at certain points in the plasma necessitates close placement of poloidal field coils which often leads to the so-called Gordian Knot, where a set of coils is trapped within another set. In fact, the pumped limiter method for impurity control was invented to circumvent some of these difficulties. Thus a major design goal was to determine if system integration would allow the use of the divertor for impurity control.

Additional design goals which have an impact on the credibility of the assumed 6% β were:

- A high rotational transform.
- An effective magnetic volume utilization.
- High shear on the plasma edge.
- No magnetic islands.

I.4 General Guidelines

Other general design guidelines assumed for the UWTOR-M study are:

1. It is a "near term" commercial DT fusion power reactor which will operate in the 2020-2030 time frame.
2. It is a tenth of a kind and thus draws from a well-established and experienced fusion economy.

3. It should have a power output in the 1200-1800 MWe range.

4. The economic analysis will follow recommended DOE guidelines.

References for Chapter I

1. L.M. Lidsky et al., "The T-1 Self-Consistent Point Design," Stellarators - Status and Future Directions, Joint US-Euratom Report, July 1981.

2. J.F. Lyon et al. "Stellarator Physics Evaluation Studies," 9th Int. Conf. on Plasma Physics and Controlled Nuclear Fusion Research, IAEA-CN-41/Q-3, Baltimore, USA, September 1982.

3. S. Rehker and H. Wobig, Proc. of the Symp. on Fusion Technology, Grenoble, 1972.

4. D.T. Anderson, J.A. Derr and J.L. Shohet, "The Interchangeable Modular Stellarator," IEEE Trans. on Plasma Science, Vol. PS-9, No. 4, 1981.

II. Overview

II.1 Parametric Considerations

Magnetic field line calculations using a particular winding law for the modular coils were performed to generate the magnetic surfaces and determine the rotational transform. This was done for various coil aspect ratios using a filamentary model for the windings. This winding law produces a magnetic separatrix with what is effectively a helical bundle divertor outside the separatrix. Thus the hot, confined plasma is assumed to be bounded by a magnetic separatrix. The divertor is utilized in the UWTOR-M design for impurity control.

Figure II.1-1 shows the rotational transform at the separatrix and magnetic volume utilization (fraction of the volume inside the coils which is also inside the separatrix) as a function of the coil aspect ratio for 5, 6, and 7 field periods. Configurations near the peak of the rotational transform curve generally have good magnetic surfaces and good magnetic field line behavior in the divertor region. One also needs space, however, between the outside of the divertor scrape-off zone and the coils for the blanket and shield. Figure II.1-2 shows the plasma aspect ratio and the minimum plasma size such that there is adequate space between the plasma and the coils for the blanket and shield. Generally, one wants the plasma volume not too large so that the thermal power output of the plant is not excessively large. Based on these considerations, a design point with the parameters given in Table II.1-1 was chosen.

Fig. II.1-1 Rotational transform at the separatrix and magnetic volume versus coil aspect ratio for 5, 6, and 7 field positions.

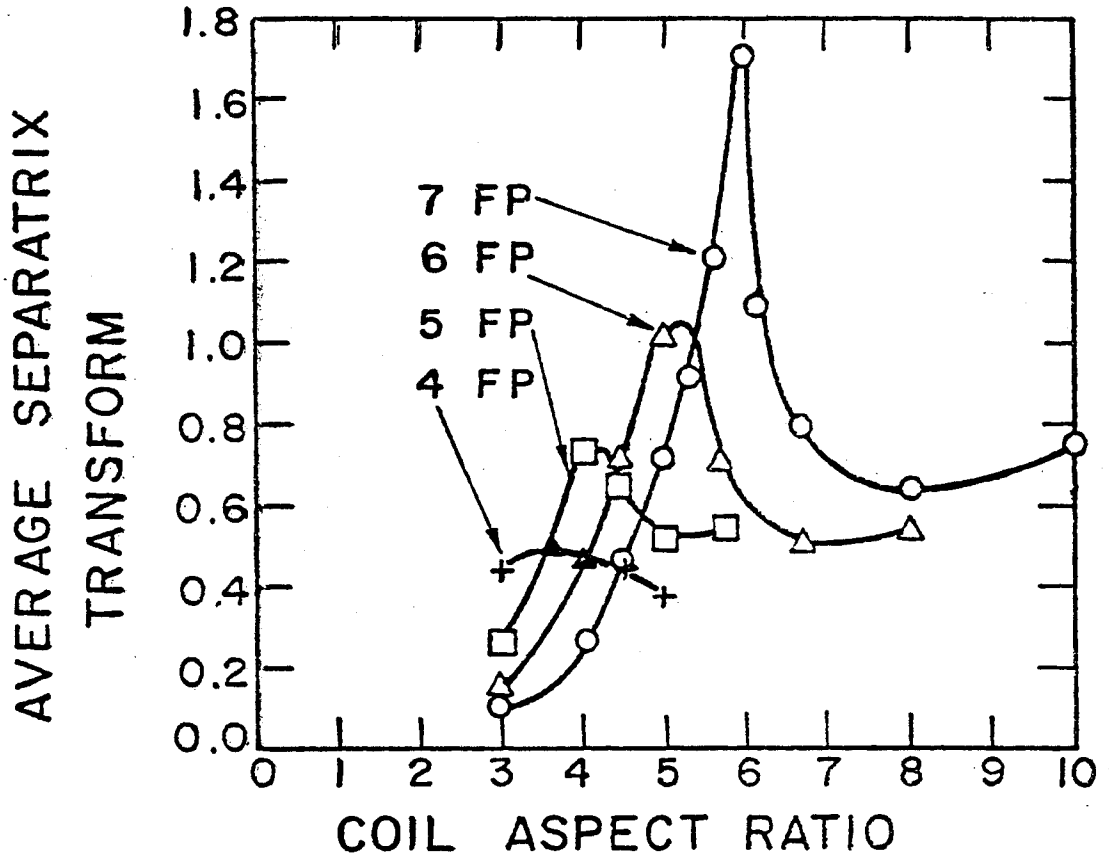

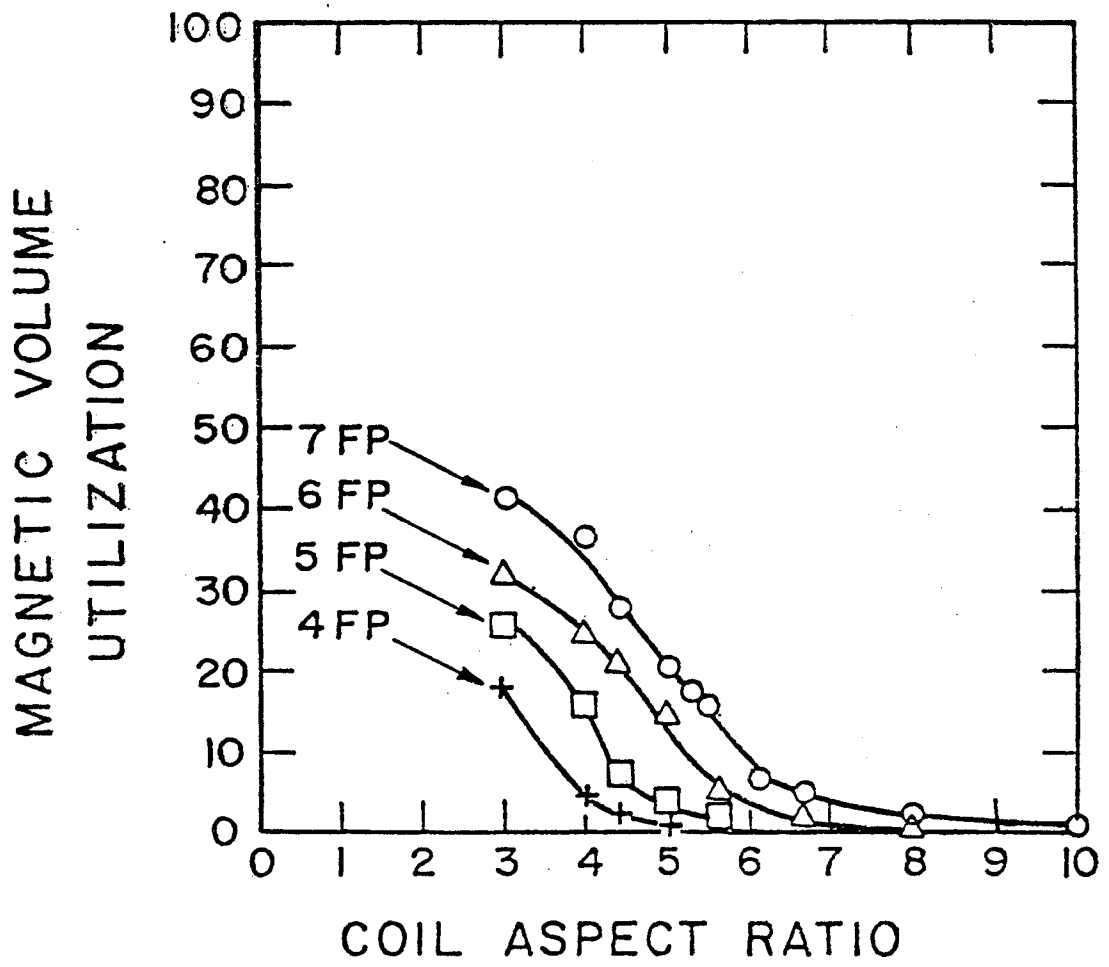

Fig. II.1-2. Plasma aspect ratio and minimum plasma volume versus coil aspect ratio for 5, 6, and 7 field periods.

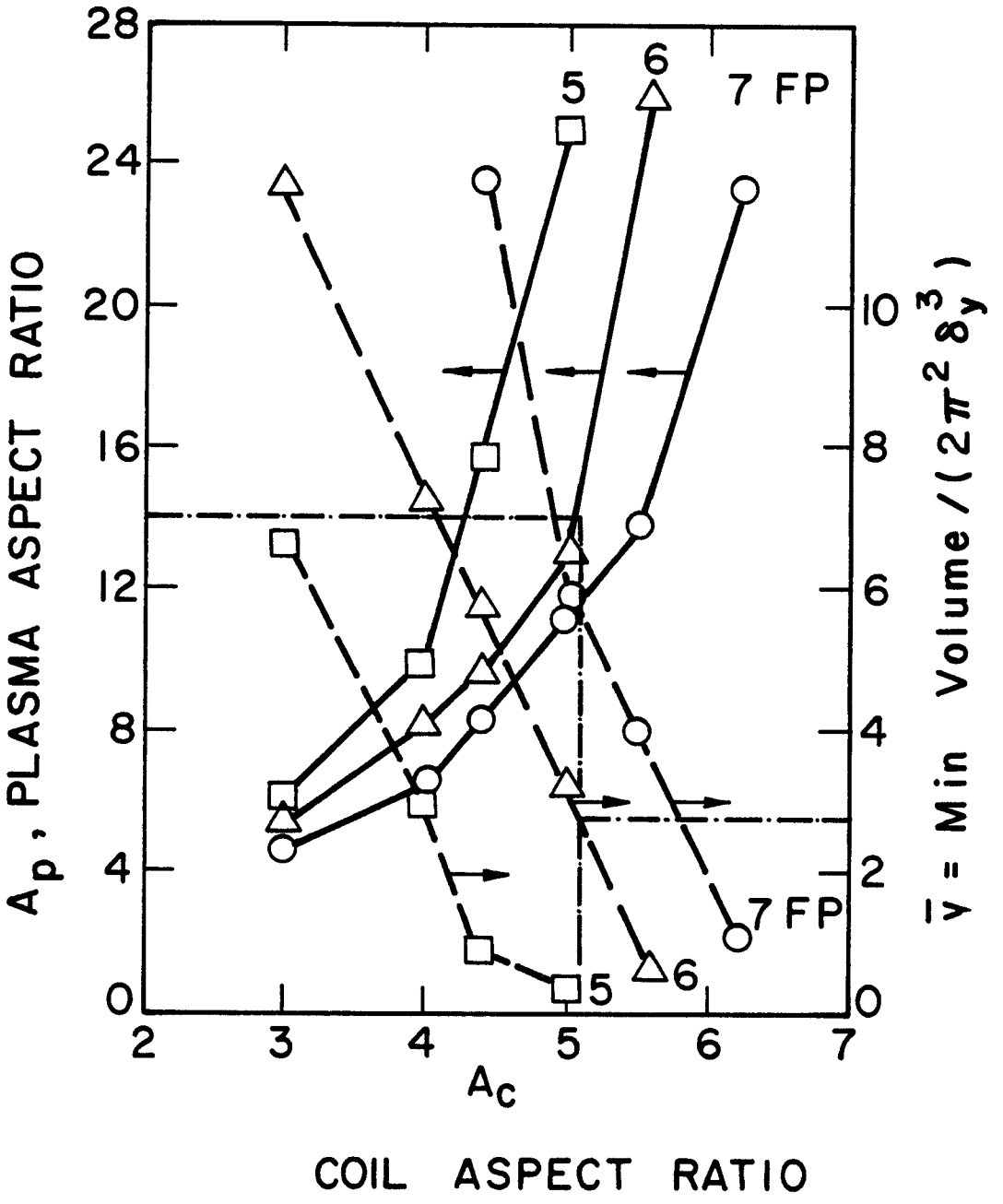

Table II.1-1

Major radius, m	24.10
Coil aspect ratio	5.05
Plasma aspect ratio	14
Multipolarity	3
Number of field periods	6
Rotational transform at edge	1.13
Rotational transform at center	0.16
Plasma volume, m^3	1400

II.2 Plasma Analysis

The performance of the plasma using the design parameters given in Table II.1-1 was calculated using a plasma transport code. This code solves a set of fluid equations for the density and temperature profiles. The transport coefficients are an input to this code; it is described further in Chapter VI. In order to determine the DT power output, one has to specify the volume-averaged beta, the average density and the pellet injection velocity. The volume-averaged beta was taken to be 6% for this study; this is considered to be reasonable, but it has not been checked by three-dimensional MHD calculations. The average density and pellet velocity were varied to determine the conditions for maximum power output without excessive peaking of the profiles and the beta at the magnetic axis. From this study, the plasma parameters given in Table II.2-1 were obtained. The DT fusion power output is 4300 MW. The steady-state density and temperature profiles are shown in Fig. II.2-1. The "flat" ion temperature profile results from the high ion thermal conduct-

Fig. II.2-1. Plasma temperature and density profiles versus minor radius.

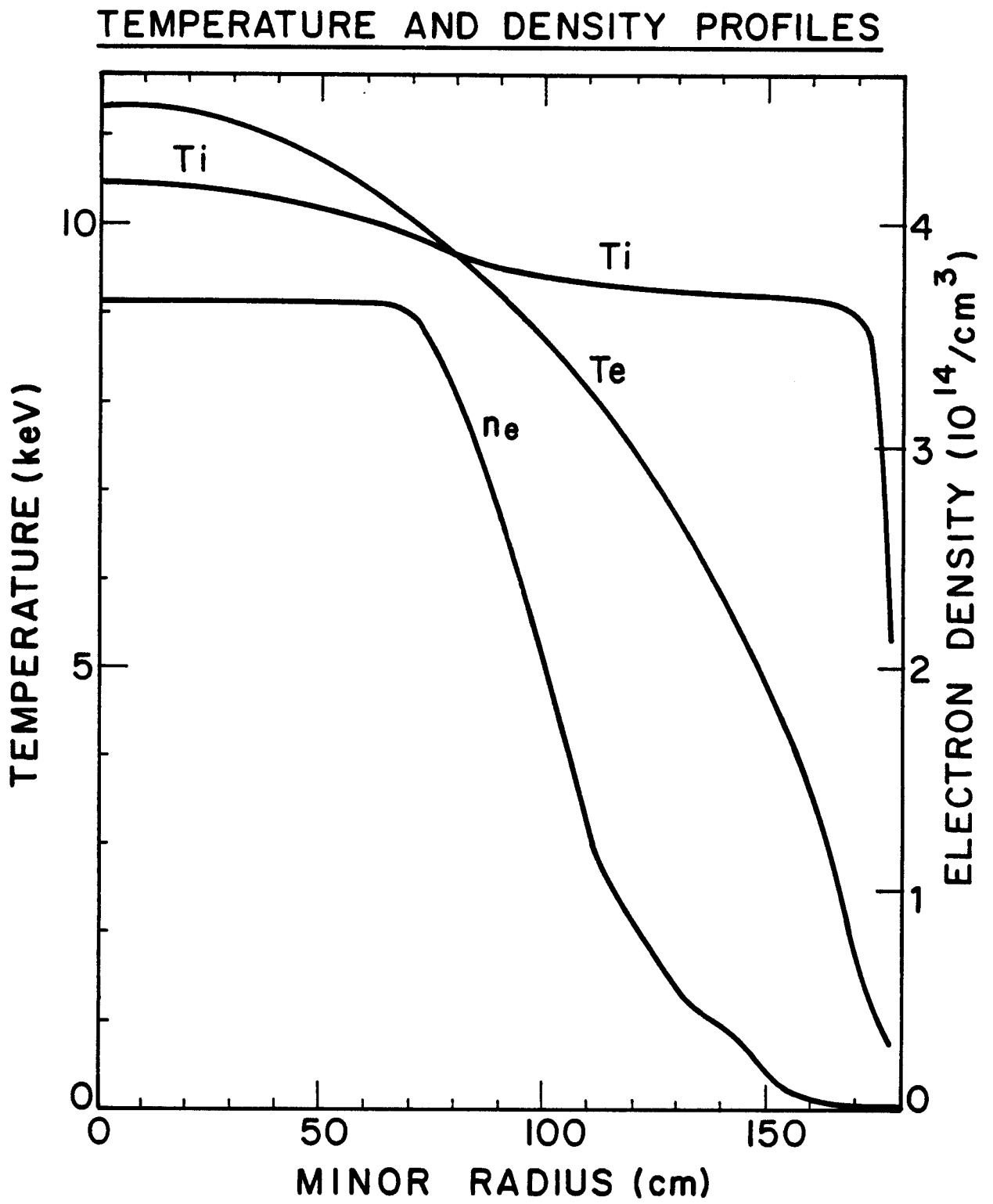

Fig. II.2-2. Central temperature during startup.

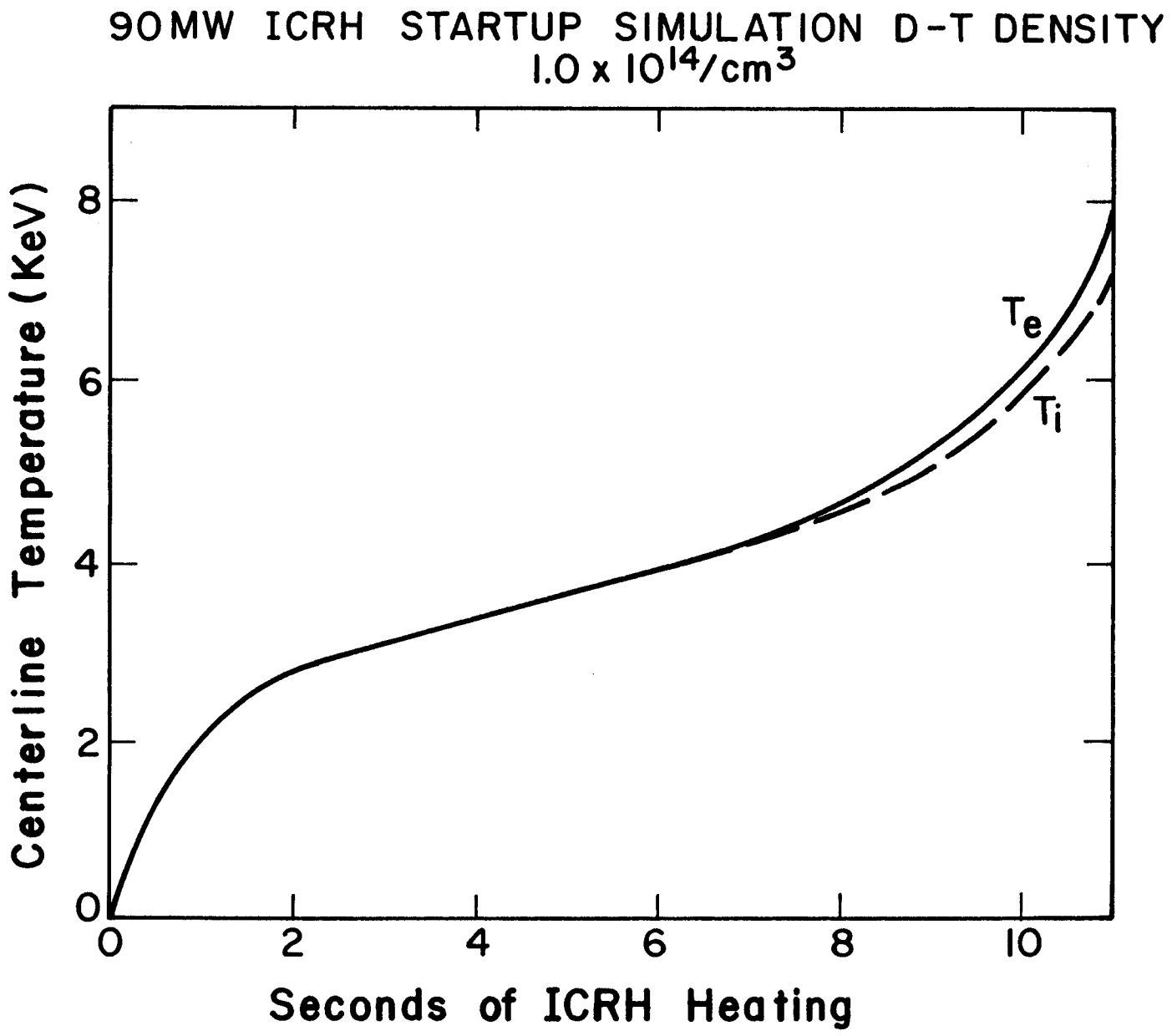

Table II.2-1. Steady State Plasma Parameters for the UWTOR-M Design Point

• Average Electron Density	$1.52 \times 10^{14}/cm^3$
• Average Electron Temperature	9.5 keV
• Average Ion Temperature	9.8 keV
• Average Toroidal Beta	6.0%
• Xenon Concentration (deliberately introduced to lower the electron temperature)	$3.3 \times 10^{10}/cm^3$
• Particle Confinement Time	4.0 sec
• Energy Confinement Time	1.5 sec
• Fractional Tritium Burnup	4.4%
• Net Toroidal Current	0
• D-T Fusion Power	4300 MW
• Edge Field Ripple	23%
• Power Radiated to First Wall	~ 470 MW
• CX Power to First Wall	~ 70 MW
• Power to the Divertor	~ 320 MW

ivity at the edge due to magnetic ripple; this is the dominant transport mechanism at the edge.

Startup of UWTOR-M is accomplished by ICRF heating at the second harmonic of deuterium. Approximately 90-100 MW of ICRF power is required to ignite the plasma. Figure II.2-2 shows the increase in the ion and electron temperature during startup.

II.3 Magnets

The reactor has 18 modular twisted coils arranged in a toroidal configuration as shown in Fig. II.3-1. It will be noticed that the coils have a rather large lateral deformation. The main reason for this is a desire to maximize the rotational transform in order to better justify the assumed 6% β.

Fig. II.3-1. Top view of UWTOR-M coil system.

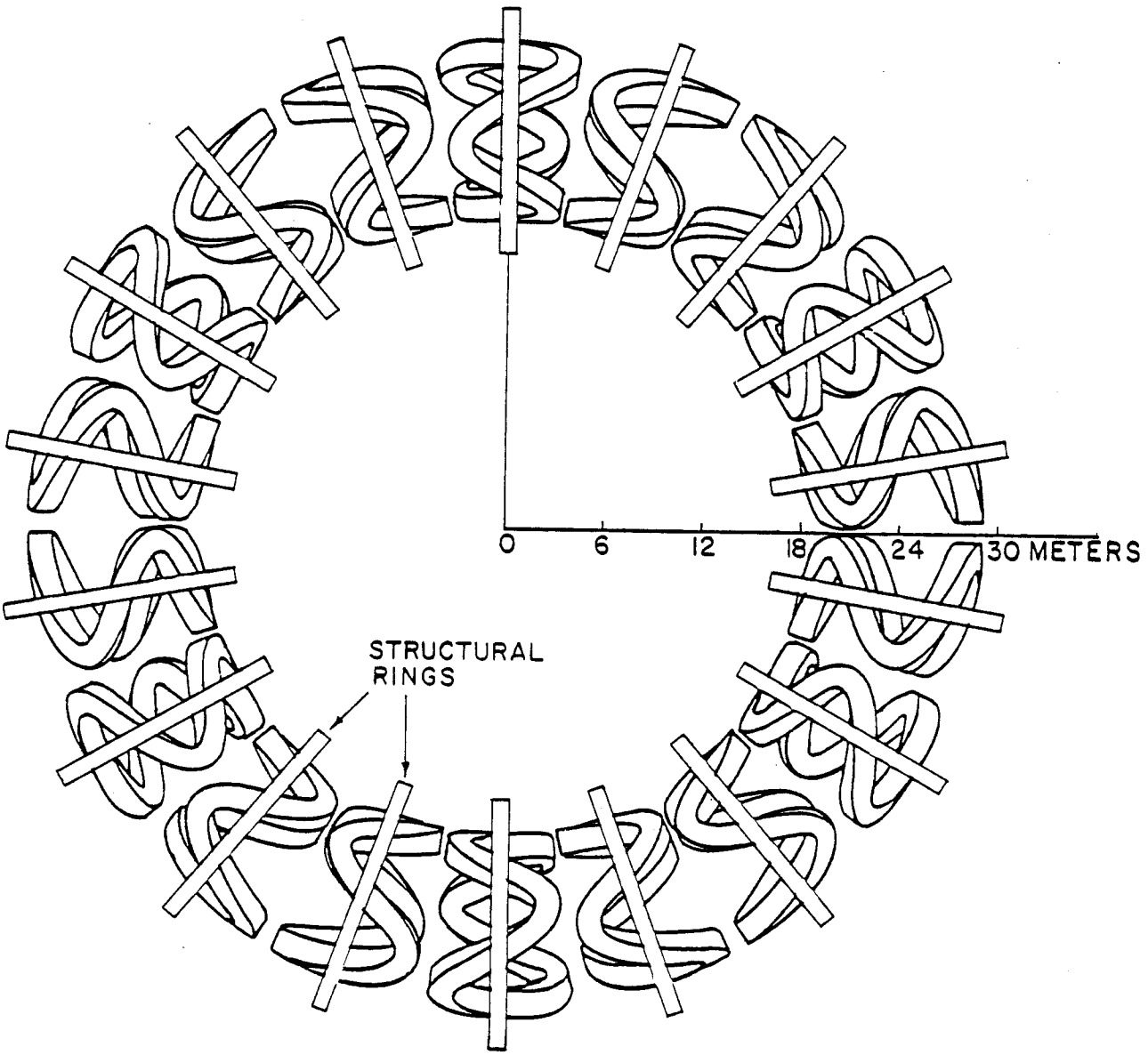

This decision has led to some difficulty with respect to the design of the structure needed to react the radial forces in the coils. The coil set produces a field of 4.5 tesla on axis and gives a respectable rotational transform on the plasma edge of 1.13.

The reactor parameters which impact the magnet design are listed in Table II.3-1. There are three coils per field period, two of which are identical, only rotated 180° about the radial axis. Thus, the entire reactor gains simplicity by having two coil types (12 of one and 6 of the other). The magnets are discrete superconducting coils operated in the steady-state mode. No pulsed coils are evident. These considerations allow for a rather traditional coil design with the one requirement that the operating temperature of the coils be reduced to 1.8 K, utilizing superfluid helium cooling. This latter requirement is dictated by the maximum field at the conductor which is 11.6 T.

The modular coils are designed with superconductor composite windings which are supported by the coil case structure. Under normal operating conditions, the interaction of the coil current with the field results in steady-state magnetic forces which must be resisted by the coil structure. The calculations of magnetic field and forces are carried out using the MFE network EFFI code. Each coil is approximated by 89 straight segments at equal poloidal angles.

The magnetic forces on the coil can be thought of as being comprised of two principal components, the self force due to its own field and the mutual attractive force between adjacent coils due to the interactive fields. In the regions where the coils come close together, the mutual attractive forces dominate, causing large toroidal forces. The radial force component is about 560 MN/m, while the total force has a maximum around 150 MN/m.

Table II.3-1. Reactor Coil Design Parameters

Number of coils	18
Number of field periods	6
Number of coil types	2
Central field (B_o)	4.5 T
Peak field (B_{max})	11.6 T
Major radius (R_m)	24.1 m
Coil minor radius (A_c)	4.77 m
Total coil current (NI)	31.2 MA-turns
Structural material	304-LN-SS
Maximum design stress	533 MPa (80 ksi)
Conductor	NbTi in copper
Operating temperature	1.8 K
Overall current density	11.6 MA/m^2

The coil support scheme employs a 304 LN-SS reinforcing ring outside the coil case to resist the expansion due to the radial component of the force. The ring is welded directly to the outer surface of the coil case forming a coil-ring assemblage and both are surrounded with an insulating vacuum. The coil case and structural ring are both maintained at liquid helium temperatures. To maintain the cryogenic independency, separate dewars are required for each coil and ring assemblage.

The stress distribution over each cross section of the coil case and ring is obtained from the SAP4 finite element stress analysis code. The effective stresses at twelve critical points are calculated and checked against the yield stress and allowable design value. The maximum effective stresses in the coil case and the ring are shown in Fig. II.3-2. It can be seen that the 2/3 yield limit value of 550 MPa for 304 SS at 4.2 K is exceeded only at the

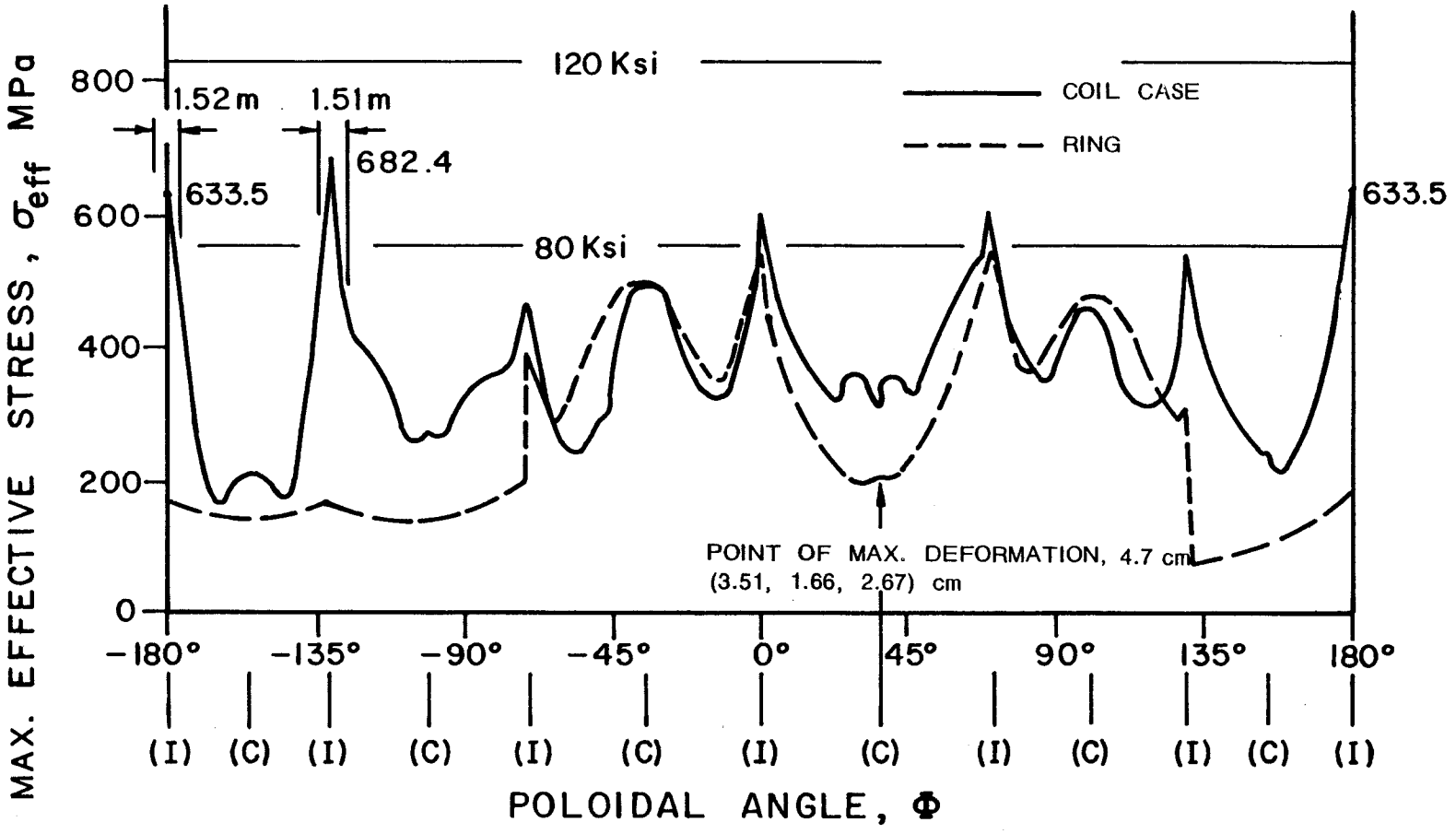

MAX. EFFECTIVE STRESSES IN COIL CASE & RING

Fig. II.3-2. Maximum effective stresses on each cross section for reinforcing ring and coil case.

connection points between the coil case and the ring. This is simply an artifact of the code which assumed a point contact between the two components. In the actual fact, the coil case and ring contact is made over a large area and thus the stresses will be considerably lower. Everywhere else the stresses are well below this limit.

II.4 Divertor

The stellarator family of toroidal confinement systems possesses a natural helical divertor. This divertor is characterized by a magnetic limiter or separatrix, which isolates the confinement region of closed nested toroidal flux surfaces from the surrounding divertor region and the wall of the reaction chamber. Inside the separatrix the enclosed magnetic flux links all of the coils, but outside the separatrix, the flux links only some of the coils. Thus some of the flux must emerge from the spaces between magnets, but to conserve flux, it must reenter the device at some other location as shown in Fig. II.4-1. It is this property of the magnetic flux external to the separatrix which forms the basis for the magnetic divertor and is typical of any toroidal magnetic confinement system characterized by a magnetic separatrix. The difference between the stellarator family and the other toroidal magnetic systems is that the null, and therefore the separatrix, occur naturally in the stellarator, while other systems such as the tokamak have to drive the null artificially by special placement of poloidal field coils.

There are only two impurity control mechanisms under serious consideration for magnetic fusion reactors, namely magnetic divertors and pumped limiters. The effectiveness of magnetic divertors has been demonstrated on several experimental devices.

Fig. II.4-1

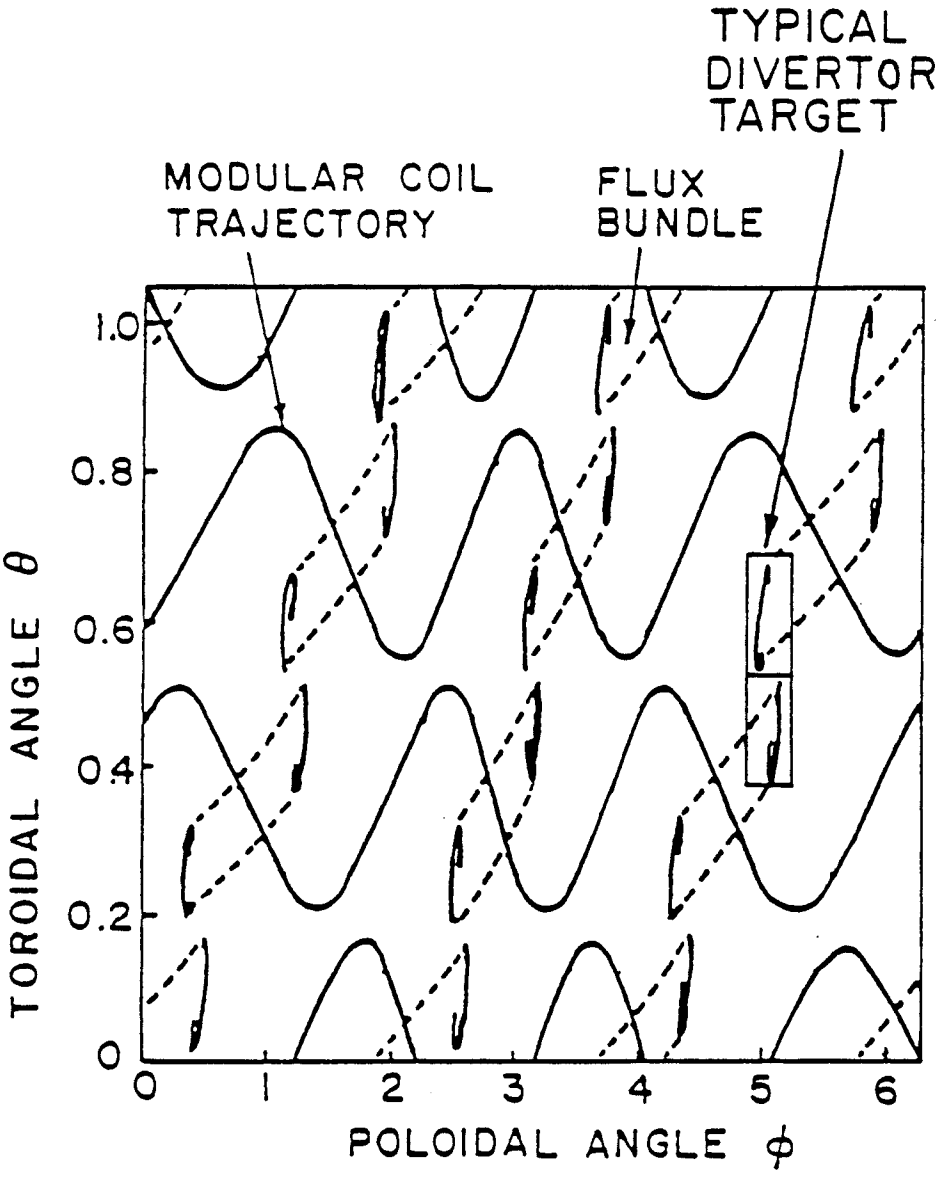

EMERGING FLUX BUNDLES THROUGH TOROID AT $R_{min.}$ MAPPED ONTO ONE FIELD PERIOD

Early in the UWTOR-M study it was decided that an attempt should be made to utilize the magnetic divertor for impurity control. It was recognized that this decision may mean a somewhat more complicated reaction chamber geometry, necessitated by the need to provide slots for the emerging flux bundles. As the study progressed, it became obvious that the nature of the modular divertor was such that the complication of the reaction chamber geometry was not that severe. Tracking of the helical flux surfaces could be accomplished by stepwise rotation of the adjacent blanket segments. Furthermore, the divertor slots are toroidally oriented and discrete.

The uncertainty for stellarators with respect to impurity control is the contention by some scientists that confinement near the axis of the device is so good as to prevent impurities from migrating to the plasma edge where divertor action will remove them from the reaction chamber. This is in contrast to the tokamak which apparently has demonstrated an anomalous diffusion of impurities to the edge of the plasma. If this contention is true, then neither magnetic divertors nor pumped limiters would be useful in removing the impurities. Some mechanism, which would promote radial transport of impurities without affecting confinement of the fuel species, will have to be incorporated into the system. This may take the form of RF waves which would excite the fundamental or some harmonic frequency of the impurities. It is hoped future stellarator experiments may be able to test impurity transport and determine the auxiliary means for promoting radial transport of impurities. Table II.4-1 gives the advantages of the UWTOR-M divertor.

The modular divertor is the adopted impurity control mechanism in UWTOR-M. There are 18 coils and 108 divertor slots. Each divertor slot has two cylindrical divertor targets designed to recover the energy in the divertor

Table II.4-1. Advantages of the UWTOR-M Divertor

1. No additional coils required
2. Compatible with the blanket and shield
3. Modular, localized collection regions
4. Effective for trapped particles
5. Well defined scrape-off zone
6. Low stray fields
7. Compatible with desired large rotational transform
8. Compatible with a practical coil configuration

region at a high temperature so that it can be converted at a high efficiency in the power cycle. The stationary cylinders are made of actively cooled shield material which prevents neutron streaming though the slots. A graphite surface cylinder rotates about the stationary cylinders at a nominal speed of 100 RPM. The particles striking the rotating surface are neutralized and pumped out. The surface energy is radiated to the cooled surrounding housing and the cooled stationary shield cylinders. Figure II.4-2 is a cross section of the reactor showing the locations of the divertor targets and the surrounding housings. These housings are self-contained units which can be removed as a whole for maintenance purposes. They include apertures for venting neutral gas into the containment building and steam lines for cooling the surfaces which almost completely surround the two targets.

All of the divertor targets are cylindrical with an outside diameter of 60 cm, and are about 2.5 m long. The central core, which has an outside diameter of 55.6 cm, does the bulk of the neutron shielding and is actively cooled by steam. The rotating shell is separated from the core by a 1 cm

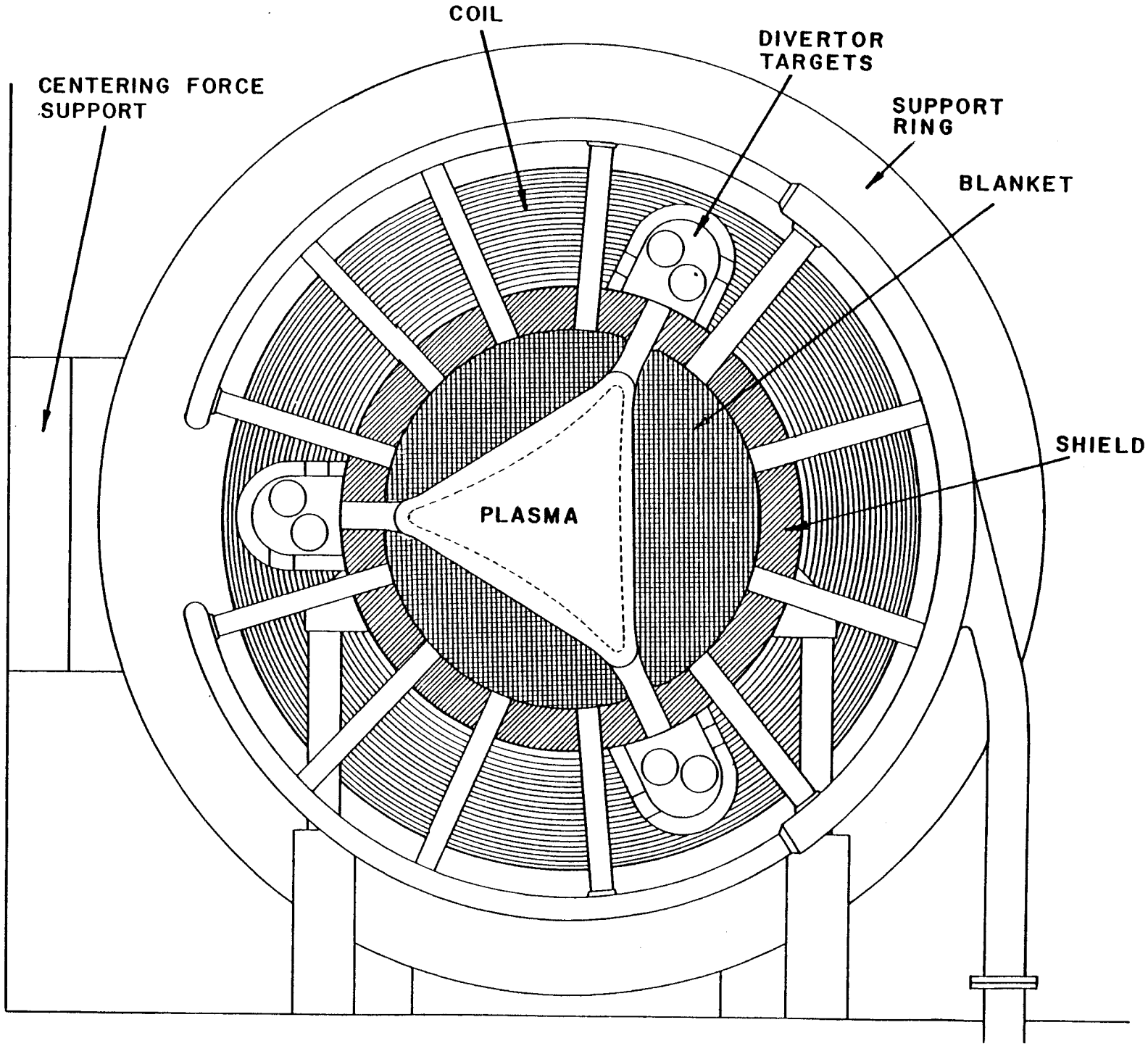

Fig. II.4-2. Cross section of reactor showing location of divertor targets.

vacuum gap and is supported by bearings at both ends. The shell receives the full brunt of the particle flux along with a small amount of neutron heating. At a nominal rotational speed of 100 RPM the concentrated surface heat load is spread over the shell's external surface to give an average heat flux of 30 W/cm^2. The surface temperature of the graphite will be between 1500-1600°C and will fluctuate 30-300°C with each revolution. The fluctuation depends on the conductivity of the graphite and can be controlled by judicious choice of materials and directional orientation. Figure II.4-3 is the model used in the heat transfer calculation.

Surface sputtering of about 2 mm per full power year is estimated. Thus a graphite layer of 1-2 cm would be more than adequate to last between scheduled blanket changeouts when the graphite layer will be replaced as well.

The reactor is contained within an evacuated building. Neutral gas from the divertor targets is exhausted into the building through ports in the divertor housings and then is pumped out by 12 pumping stations uniformly distributed along the toroidal building. Table II.4-2 gives the vacuum system design specifications.

Fig. II.4-3. Model used in heat transfer calculations for the divertor targets.

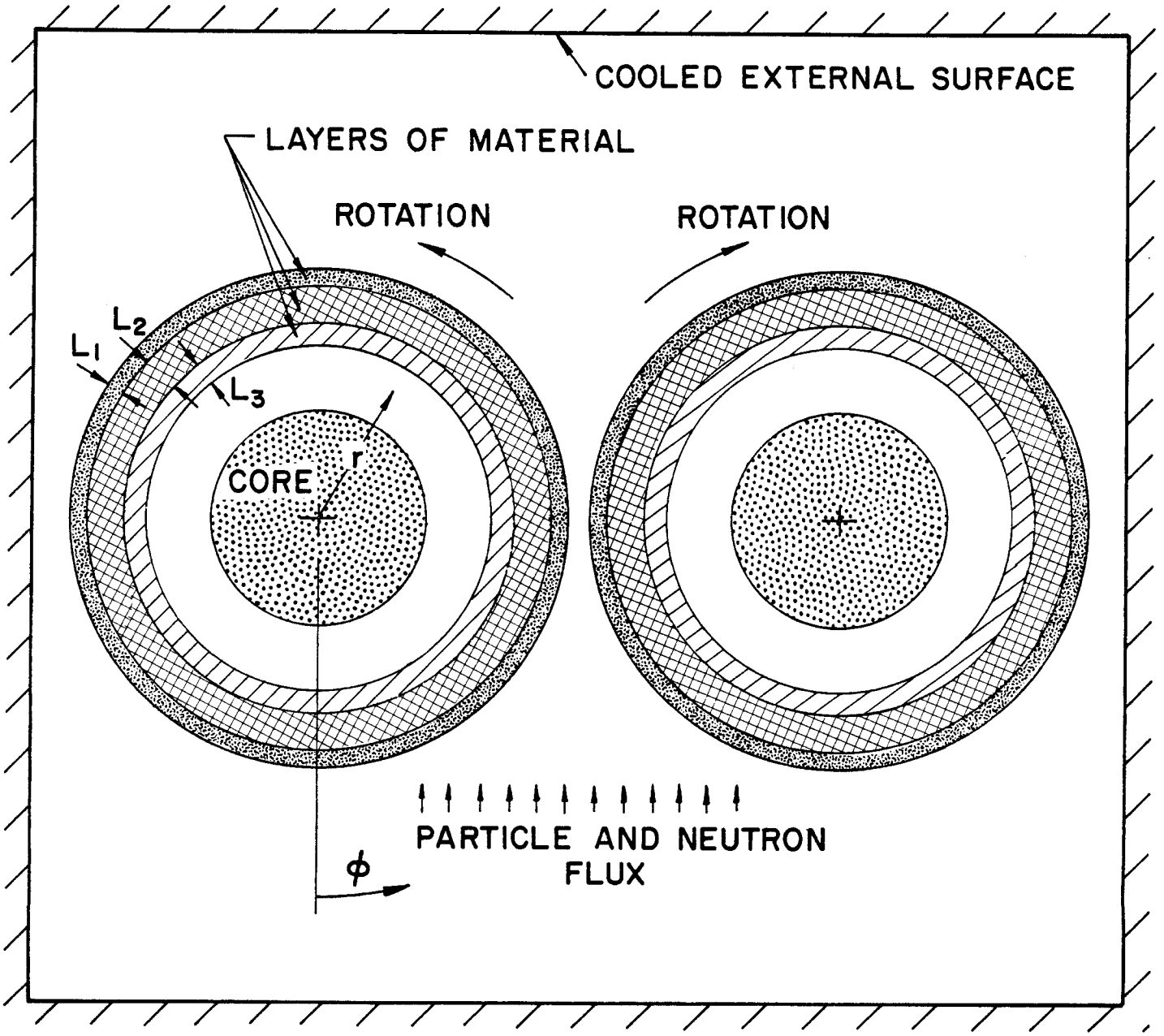

Table II.4-2. Vacuum System Design Specifications

Number of pumping stations	12
Active cryopanel area per station (m^2)	35
Total cryopanel area per station (m^2)	70
D_2, T_2, DT throughput (torr-ℓ/s)	1007
He throughput (torr-ℓ/s)	47
D_2, T_2, DT pumping speed (ℓ/s)	2.5×10^7
He pumping speed (ℓ/s)	8.3×10^6
Equilibrium D_2, T_2 pressure (torr)	4×10^{-5}
Equilibrium He pressure (torr)	6×10^{-6}
Liquid He consumption (liters/day)	110×10^3
Liquid N_2 consumption (liters/day)	750×10^3

II.5 Blanket Design

The UWTOR-M blanket concept is relatively new. The blanket contains static molten $Li_{17}Pb_{83}$ as the breeding material within a structure of HT-9 martensitic stainless steel. It is cooled with steam going through HT-9 tubes immersed in the $Li_{17}Pb_{83}$.

$Li_{17}Pb_{83}$ is an attractive candidate for the breeding material due to its low tritium solubility, good neutronic properties and relative inertness to water and air. The structural material HT-9 is chosen for its greater resistance to radiation damage and good thermal characteristics. It is anticipated that it will also be more compatible with $Li_{17}Pb_{83}$ than austenitic steels because of its lower Ni content. High pressure steam is proposed instead of helium gas for its larger volumetric density (ρc_p), such that the required pumping power will be one half that of helium.

$Li_{17}Pb_{83}$ has been proposed for use both as coolant and the breeding material for several fusion reactors. The main advantage of such a blanket design is implicit since it does not require a heat exchanger inside the blanket. The problems, however, are corrosion, corrosion product transport, MHD pressure drops and tritium confinement. For UWTOR-M, the MHD pressure drop problems can be very severe, due to the irregular blanket geometry. Fluid distribution will be very difficult and hot spots will form at the stagnation points. For this reason, a static $Li_{17}Pb_{83}$ blanket with active cooling has been considered to eliminate the problems associated with a flowing $Li_{17}Pb_{83}$ blanket. To take advantage of the low tritium solubility and, consequently, high tritium partial pressure, we propose that the tritium permeate the primary coolant from which it can be recovered. Steam is a good sink for tritium which forms HTO. Furthermore, the H_2O inventory in the primary

loop is moderate, such that tritium recovery is feasible with only a moderate tritium inventory in the primary loop.

The primary steam temperature range is 330-500°C. This steam exchanges heat in a steam generator to obtain secondary steam at 450°C and 13.8 MPa which drives the turbine. A gross efficiency of 40% is achievable. To improve the power cycle, pumping power is taken as MW_{th} from the steam turbines.

The tritium is recovered by using a liquid phase catalytic exchange (LPCE) and cryogenic distillation process. This process is expected to be simpler than the vapor phase catalytic exchange (VPCE). The process is being developed in a pilot plant in the Chalk River Nuclear Facility in Canada. Table II.5-1 gives the thermal hydraulics parameters and Table II.5-2 the power cycle parameters for the UWTOR-M blanket.

Figure II.5-1 is a cross section through a modular coil showing the triangular plasma characteristic of an $\ell = 3$ stellarator. The blanket segment is divided into three regions filling out the space between the plasma and the inner surface of the reflector and separated by the divertor slots. The outer perimeter of the blanket segment is circular. The three blanket regions within a segment are interconnected to allow draining of breeding material through a line attached to the lowest point in the segment. Thus, the blanket segments are always empty of breeding material prior to initiation of any maintenance procedure. For protection against steam line leaks into the blanket, a rupture disk will also be provided which will permit a quick routing of breeding material into a dump tank.

Each blanket region will have two supply and two return steam headers connected to common distribution manifolds. These manifolds are shown in Fig. II.5-1 as circular with the headers radiating inwards to the blanket,

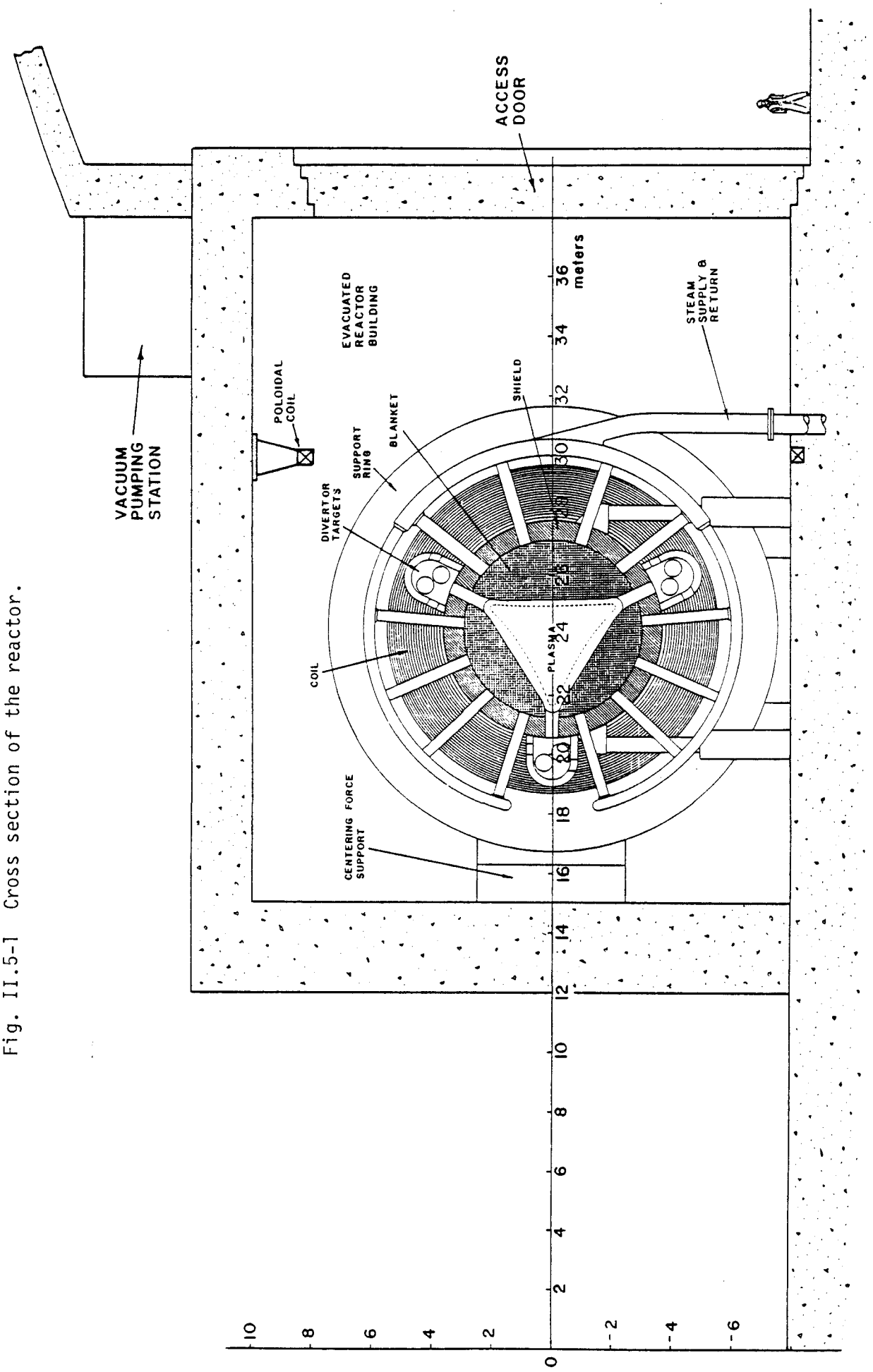

Fig. II.5-1 Cross section of the reactor.

Table II.5-1. UWTOR-M Thermal Hydraulic Parameters

Blanket power	4340 MW
Divertor zone power	480 MW
Total thermal power	4820 MW
Coolant inlet temperature	330°C
Coolant outlet temperature	500°C
Coolant pressure	5 MPa
Coolant velocity in pipe	35 m/sec
Coolant heat transfer coefficient	0.23 W/cm^2-°C
Coolant flow length	5 m
Coolant pressure drop in pipe	0.07 MPa
Maximum structural temperature	530°C
Coolant tube arrangement	Triangular pitch
Minimum distance between tubes (center to center)	1.40 cm
Coolant tube O.D.	1 cm
Coolant tube wall thickness	1 mm
Maximum $Li_{17}Pb_{83}$ temperature	570°C
Coolant flow rate	4.8×10^7 kg/hr
Coolant pumping power	75 MW

Table II.5-2. Power Conversion System

A single wall, once through steam to steam generator

Gross thermal power	4820 MW
Primary coolant inlet temperature	500°C
Primary coolant outlet temperature	330°C
Steam temperature	454°C
Steam pressure	13.8 MPa
Reheat temperature	454°C
Feedwater temperature	280°C
Pumping power requirement	75 MW
Net thermal power	4725 MW
Cycle efficiency	40%
Power output	1898 MW

resembling the spokes of a wagon wheel. The headers in turn supply manifolds within the segments to which the cooling tubes are attached.

Figure II.5-2 shows a plan view and a cross section of a blanket segment. The tubes are shown traversing the segment from supply to return mainfolds and are spaced proportionately to the amount of nuclear heating. The first wall and other areas exposed to surface heating are covered with close packed arrays of tubes supplied by the same manifolds.

Figure II.5-3 is a perspective view of a blanket segment where the shaded area indicates the end plates of the three blanket regions. Note that the divertor slot is toroidal and that the inter-region connections are on the opposite side from the header penetrations. The inter-region connections actually fall in the middle of a modular coil, where there is no divertor

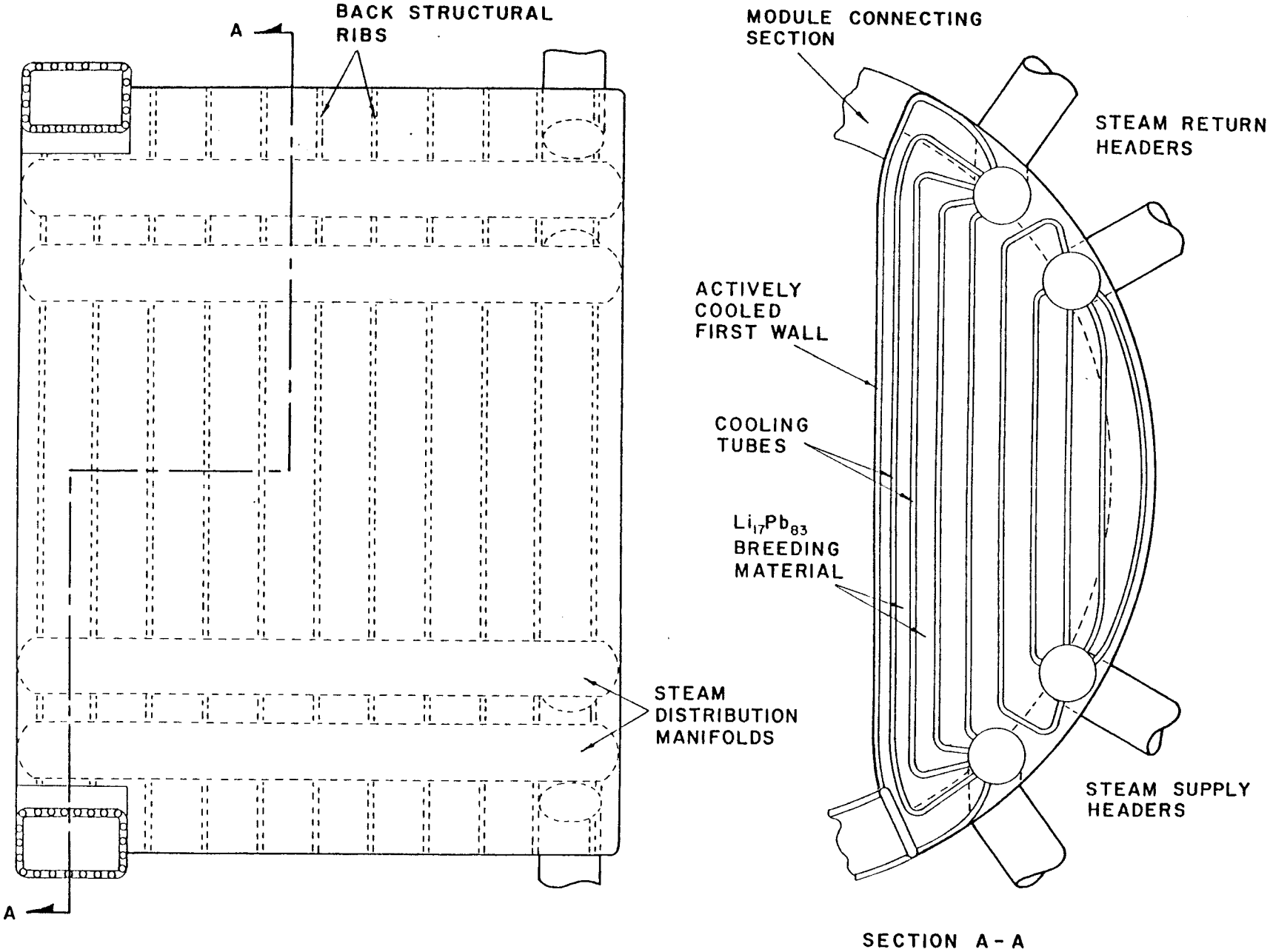

Fig. II.5-2 Plan view and a cross section of a part of a blanket segment.

Fig. II.5-3. Perspective view of a blanket segment.

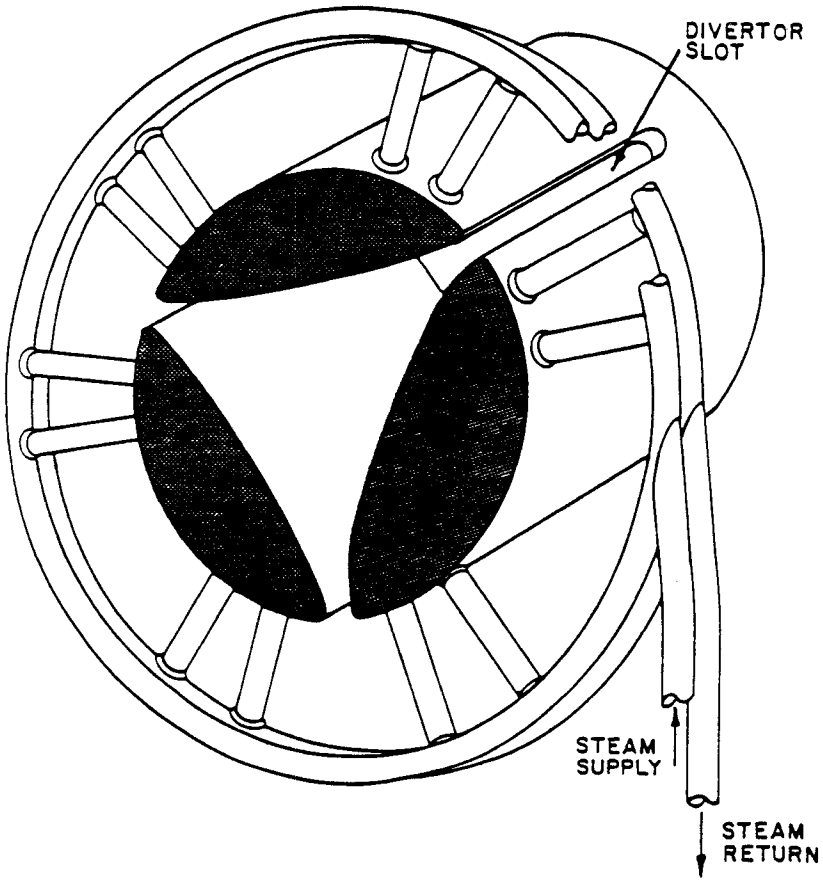

action. The headers are thus connected on the opposite side to avoid making large slots in the reflector/shield. The second segment in the coil module will be a mirror image of the one shown but with the triangular shape of the reaction chamber and divertor slots rotated poloidally.

One of the most difficult problems in any blanket design is that of making seals between adjacent segments. Plasma experiments operating at base pressures on the order of 10^{-6}-10^{-7} torr have no choice but to provide vacuum tight first walls. Reactor grade plasmas, however, can operate at higher pressures, perhaps as high as 10^{-4} torr. This relaxation in pressure opens up design possibilities which are not available in current plasma experiments. Thus, recent designs have considered placing the vacuum barrier at the back of the shield where it is both accessible and protected from radiation damage. In principle such a design would be possible in UWTOR-M, but it would entail the use of large omega bellows at the shield interface between modules.

To avoid the complication of using bellows and mechanical or welded seals, we have decided to enclose the whole reactor in an evacuated building, thus avoiding seals between blanket segments altogether. This decision has enormous significance in the maintainability of the reactor. Making a vacuum tight building, however, is not easy, especially since it would have large access ports. Experience with space simulation chambers, however, has shown that it is possible. Table II.5-3 gives the general blanket parameters.

Table II.5-3. UWTOR-M Blanket Parameters

Fusion power	4300 MW
Blanket power	4340 MW
First wall area	2318 m^2
Neutron wall loading	1.41 MW/m^2
First wall surface heating	23 W/cm^2
Maximum nuclear heating	22.5 W/cm^3
Total heat transfer surface area	5.5×10^4 m^2
Nominal flux to coolant tube	8 W/cm^2
Structural material	HT-9
Breeding material	$Li_{17}Pb_{83}$
Coolant	Steam
Tritium breeding ratio	1.08
Tritium breeding rate	8.3×10^{-3} g/sec

II.6 Neutronics

The neutronics and photonics analysis of UWTOR-M was carried out using one and three-dimensional calculations. The breeding blanket consists of three segments having different cross-sectional areas as shown in Fig. II.6-1. The radial neutron source density distribution peaks at the center of the triangular plasma zone. Some of the source neutrons will stream through the divertor slots which occupy ~ 5% of the solid angle. A significant number of lower energy secondary neutrons that have been moderated in the blanket and reflector will also stream out from the slots along with some gamma photons that are produced in neutron interactions with different materials. Therefore shielding materials are used in the divertor regions to protect vital components in the toroidal hall against streaming radiation.

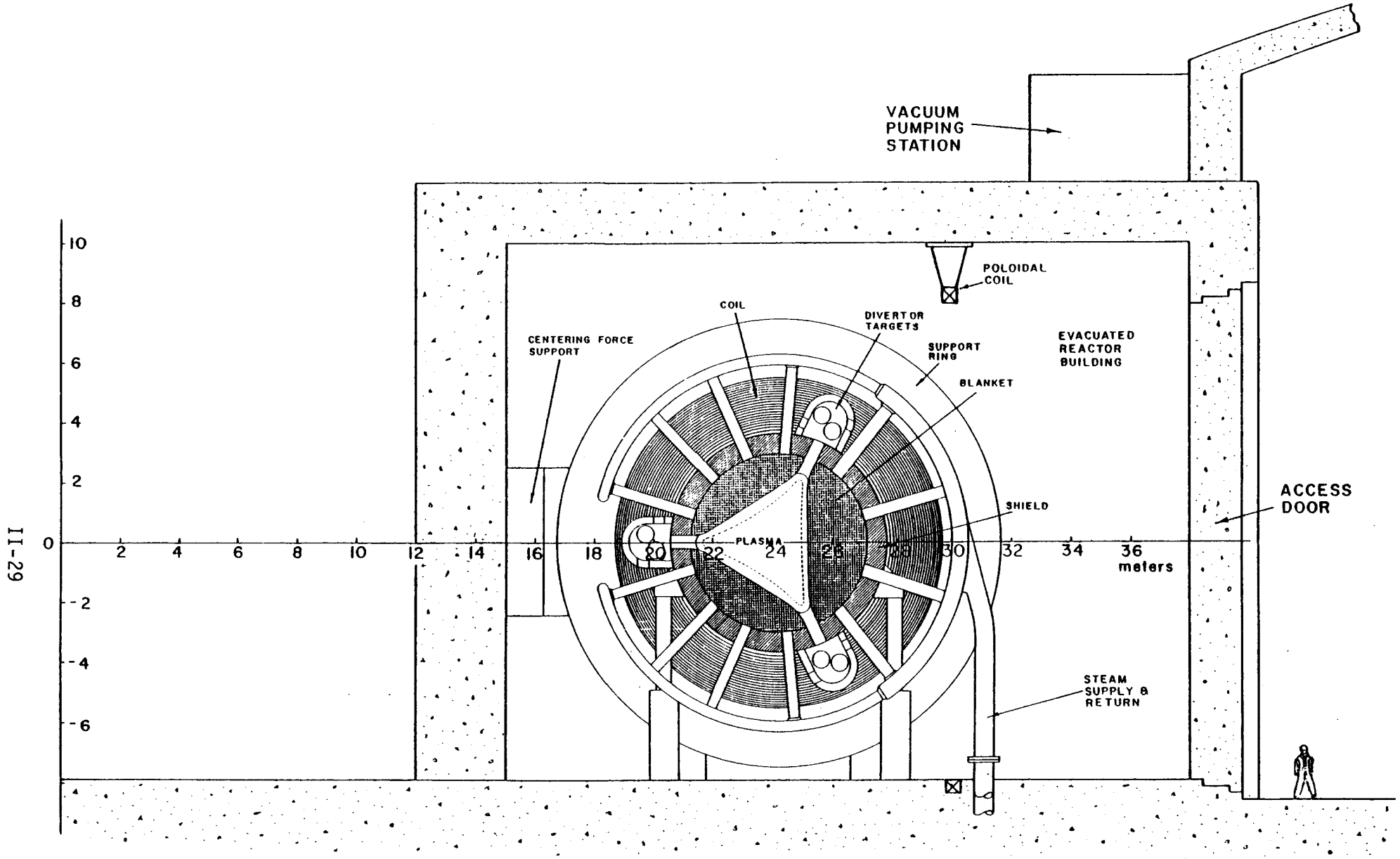

Fig. II.6-1 Vertical cross section of blanket and coil within evacuated reactor containment.

The lithium enrichment in the $Li_{17}Pb_{83}$ breeder and the material structure of the reflector and its thickness were varied to achieve an overall tritium breeding ratio greater than one with the largest energy muliplication. The results show that the only way to increase the energy multiplication without having a drastic reduction in the breeding ratio is to lower the enrichment and keep the structural content in the blanket to its minimal value while meeting structural demand. In order to increase the fraction of energy recovered from the reflector, the Fe 1422 steel was used as structural material and its thickness was increased up to 40 cm to intercept most of the neutron and gamma energies before leaking into the shield. The three-dimensional results show that an enrichment of 35% gives an adequate overall tritium breeding ratio of 1.08 and an energy multiplication of 1.15. More than 98% of the breeding is contributed from ^{6}Li and about 54% of the total nuclear heating results from gamma heating.

The bulk shield composition was optimized to provide adequate protection for the superconducting magnet. The radiation dose in the magnet was found to be the design driver for the shield as other magnet components are further protected by the 25 cm structural case. An attempt was made to heterogenize the shield to efficiently utilize the shielding capability of the materials. A series of one-dimensional calculations was carried out in which the thicknesses of the steel, B_4C, and lead shield layers were varied one at a time to determine the optimum shield configuration. The optimization study reveals that a substantial amount of B_4C is required to minimize the dose in mylar. The optimized shield configuration results in an acceptable dose in mylar and epoxy insulators after the estimated 24 FPY reactor lifetime. In addition,

the peak dpa rate in the Cu stabilizer implies that no magnet annealing is required during the whole reactor lifetime.

The effectiveness of the bulk shield is reduced by the streaming of radiation through the divertor slots. The calculational procedure for the radiation streaming calculations was divided into two parts by modeling the geometrical configuration of the reactor in two separate problems. The blanket, reflector, and shield are considered as one problem and the divertor targets and associated shield are the other. Trapping surfaces were located at the entrance of the three divertor regions where all particles crossing the surfaces are counted according to angle and energy bins. This information was then stored to serve as surface sources in later modeling of the divertor region itself.

For each D-T fusion event, the total neutrons and gamma photons streaming through the divertor slots are 0.214 and 0.024, respectively, carrying a total power of 176 MW which represents 5% of the neutron fusion power; fortunately most of it is recovered by the divertor targets. About 20% of the streaming neutrons are primary neutrons, and they carry 83% of the streaming energy.

Radiation streaming through the pumpout ports of the divertor regions has a large impact on the operation and maintenance of the reactor and its sensitive equipment. The divertor region was modeled to obtain information about radiation exiting each pumpout port through the use of trapping surfaces and also to estimate the amount of energy recovered by the divertor targets. The pumpout ports are located appreciably off the direct line of sight of the flowing particles from the divertor entrance. This is of importance in reducing radiation streaming through the ports. The results indicate that considerable attenuation and spectrum softening result from neutron interactions

with divertor targets which, as a result, recover 91% of the energy streaming into the divertor region. The total power carried by radiation streaming through all ports of the divertor regions is 6.12 MW representing only 0.18% of the neutron fusion power.

Due to the necessity of penetrations in the shield, radiation streaming raises the biological dose level outside the reactor. A 3.1 m thick biological shield was found to result in an acceptable dose of 2.35 mrem/hr in the toroidal service hall during reactor operation.

II.7 Materials

There are 5 classes of materials in UWTOR-M that must be considered with respect to radiation damage from neutrons. They are:

1. Blanket structure (HT-9)
2. Reflector structure (Fe 1422)
3. Shield (Fe 1422, Pb, B_4C)
4. Divertor liners (C)
5. Superconducting magnets (Cu, NbTi, Polyimide).

Figure II.7-1 shows the damage-temperature relationship for these materials. In general it can be concluded that

1. The maximum dpa rate in the first wall is 53 dpa/FPY which corresponds to $\sim$ 5 MW-y/m^2 per FPY.
2. The damage rate quickly falls to 0.02 dpa/FPY at the front of Blanket II region and to 0.004 dpa/FPY at the start of the reflector.
3. The maximum damage in the shield is 10^{-4} dpa/FPY.
4. The maximum damage in the carbon liner of the divertor targets is 1.4-2.1 dpa/FPY depending on location.

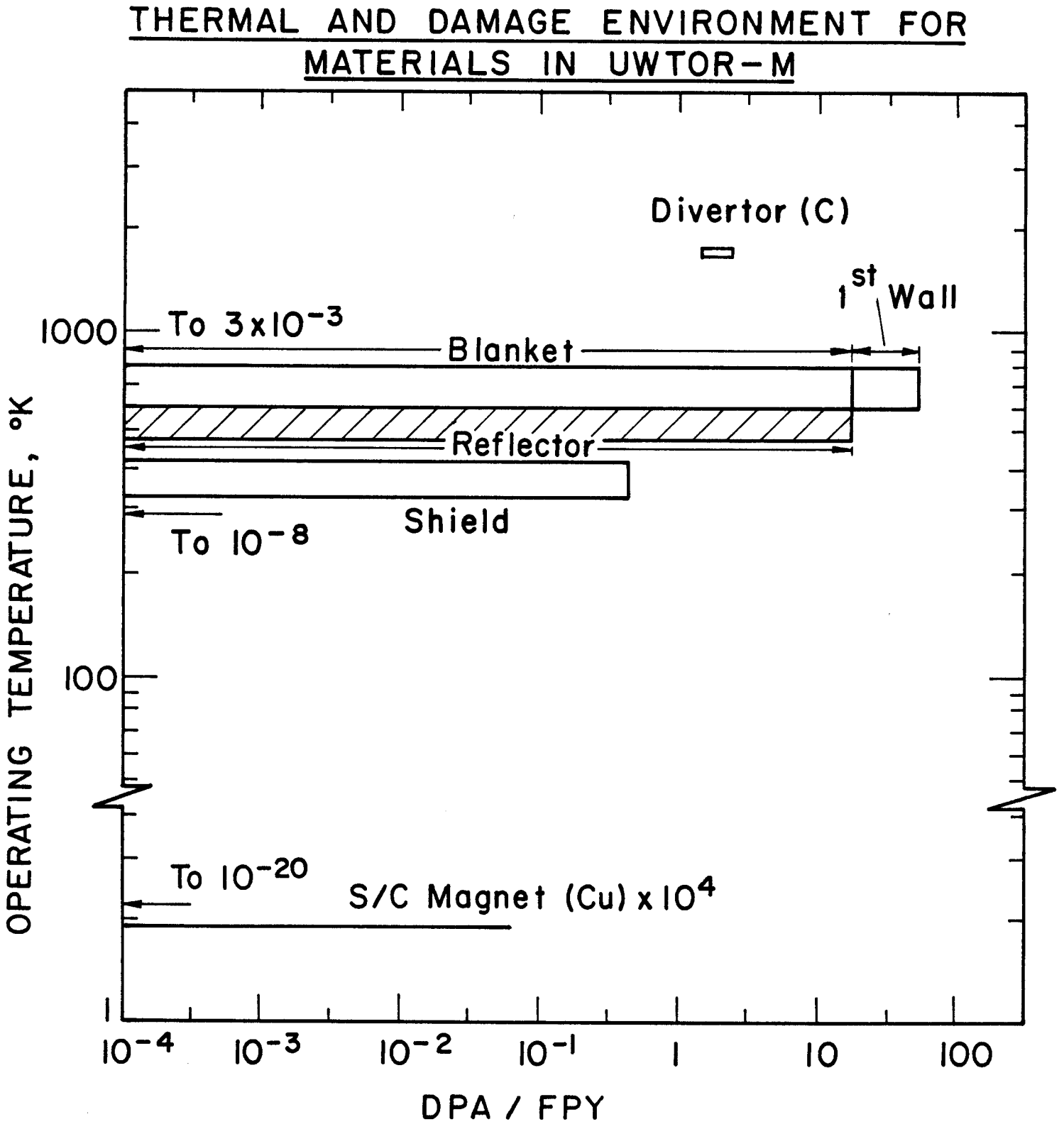
THERMAL AND DAMAGE ENVIRONMENT FOR MATERIALS IN UWTOR-M
Divertor (C)
1st Wall
To 3x10-3
Blanket
Reflector
Shield
To 10-8
To 10-20
S/C Magnet (Cu) x 10^4
OPERATING TEMPERATURE, °K
1000
100
1
10-4
10-3
10-2
10-1
1
10
100
DPA / FPY

Fig. II.7-1

5. The maximum damage rate in the Cu stabilizer is 6.5×10^{-6} dpa/FPY and about the same in the NbTi. The peak dose in the epoxy is 8×10^{6} Rads/FPY.

II.8 Tritium System

The tritium systems in UWTOR-M are designed to purify and recycle the tritium and deuterium fuel for the reactor. Tritium production and recovery from the blanket are discussed in Chapter IX. The tritium systems are patterned after information available from the Tritium Systems Test Assembly at Los Alamos National Laboratory.

The UWTOR-M reactor is fueled by injection of 14.9 kg-T/d and 9.71 kg-D/d as cryogenic DT pellets. The inventory in the pellet injection system is 23 g. The reactor produces 4300 MW of fusion power by burning 0.656 kg-T/d and 0.437 kg-D/d which corresponds to a tritium and deuterium burn fraction of 4.40% and 4.50%, respectively. The exhaust gases exit through divertor slots, strike rotating graphite targets and scatter into the evacuated reactor building. The exhaust and impurity gases are pumped by cryopumps and the tritium inventory in the pumps is 1.2 kg for a 2 hr on-line time. Helium ash (0.875 kg/d) is separated from the fuel during regeneration of the cryopumps.

The graphite divertor targets are operated under conditions where hydrocarbon production is minimal, although physical sputtering of graphite is anticipated. Other impurities in the exhaust will include hydrogen, which permeates from the steam cooling tubes, xenon, which is added to the plasma, and oxygen and nitrogen, which outgas at low levels from construction materials. These impurities are separated from the hydrogen isotope stream by the fuel cleanup unit (FCU). This unit consists of molecular sieve beds at 75°K which condense impurities. The inventory on the sieve beds is estimated as

120 g for a 12 hr operation cycle. The beds are regenerated by heating and the impurities then pass through an oxidizing unit which forms HTO and tritium free compounds. The HTO is electrolyzed and the hydrogen isotopes are sent to the Isotopic Separation System (ISS).

The ISS consists of a 2 column unit with one equilibration cell. It produces a waste hydrogen stream with less than 1 Ci/d vented to the atmosphere and a purified DT fuel stream. The tritium inventory in the columns is estimated as 270 g.

The total estimated inventory in the fuel recycling system is 1.6 kg of tritium. There is also a 1 day fuel supply of 14.9 kg of tritium kept in storage on uranium beds.

The reactor building serves as a primary containment vessel and must be designed to maintain a tritium release rate of $\lesssim$ 10 Ci/d.

Table II.8-1 gives the T_2 inventory in the primary loop and Table II.8-2, in the fuel processing system.

Table II.8-1. Primary Loop Tritium Summaries

Tritium inventory in $Li_{17}Pb_{83}$	72 g
Tritium partial pressure	2×10^{-2} torr
Tritium inventory in coolant	100 g
Tritium dissolved in blanket structure	4 g
Tritium concentration in blanket	6 wppb
Tritium concentration in coolant	50 wppm
Tritium loss from primary coolant loop	< 10 curies/day
Total blanket system tritium inventory	176 h

Table II.8-2. Summary of Tritium Inventories in Fuel Processing Systems for UWTOR-M

Subtotals (kg):	
Pellet Injector	0.023
Cryopumps	1.2
Fuel Cleanup	0.120
Distillation Columns	0.270
Fuel and Exhaust Systems Total (kg):	1.6
Storage (1 Day Fuel Supply) (kg):	14.9

II.9 Maintenance

The philosophy for maintaining the blanket in UWTOR-M entails the radial extraction of nine of the eighteen modular coils. This has been necessitated by two aspects of the design:

1. The use of grossly twisted modular coils for maximizing rotational transform, thus requiring external support structure.
2. The decision to utilize the magnetic divertor for impurity control.

The reasons for adopting these design aspects have been elaborated on earlier in the chapter. The consequences are a somewhat more difficult maintenance requirement entailing the moving of heavy and rather cumbersome modules.

One major advantage of this maintenance scheme is that it automatically provides for the capability of servicing the magnets. There is a danger that coil maintainability can be compromised on the theory that nothing will ever go wrong with them.

In UWTOR-M, radial extraction of the coil modules is, therefore, central to the maintenance scheme. It provides for:

1. Maintenance of the blanket segments with the extraction of one-half of the coil modules.
2. Maintenance of the coils by either straight radial extraction or initial circumferential, then radial extraction (in the case of coils not moved for blanket maintenance).
3. Maintenance of divertor targets in the same way as the blanket.

Figure II.9-1 is a top view of the reactor inside the reactor hall, showing access doors located behind every other coil. A complete coil module, as viewed from the back, is shown in Fig. II.9-2 without the transporters and rails. Blanket segments with the steam manifolds attached come out of each side of the module. Such a blanket segment, shown in Fig. II.5-3, weighs ~ 45 tonnes and can be easily handled with an overhead crane.

Specially designed carriages will enter the space vacated by a coil module. They will have the capability of removing the blanket segments within the stationary modules. In this way, only 50% of the modules need to be moved for routine blanket and divertor target maintenance. Table II.9-1 gives a breakdown of the masses in a single coil module.

In summary, the following points can be made about the maintenance of UWTOR-M:

- The reactor is enclosed within an evacuated reactor hall.
- No seals are employed between blanket segments.
- Coolant connections are minimized.

Fig. II.9-1

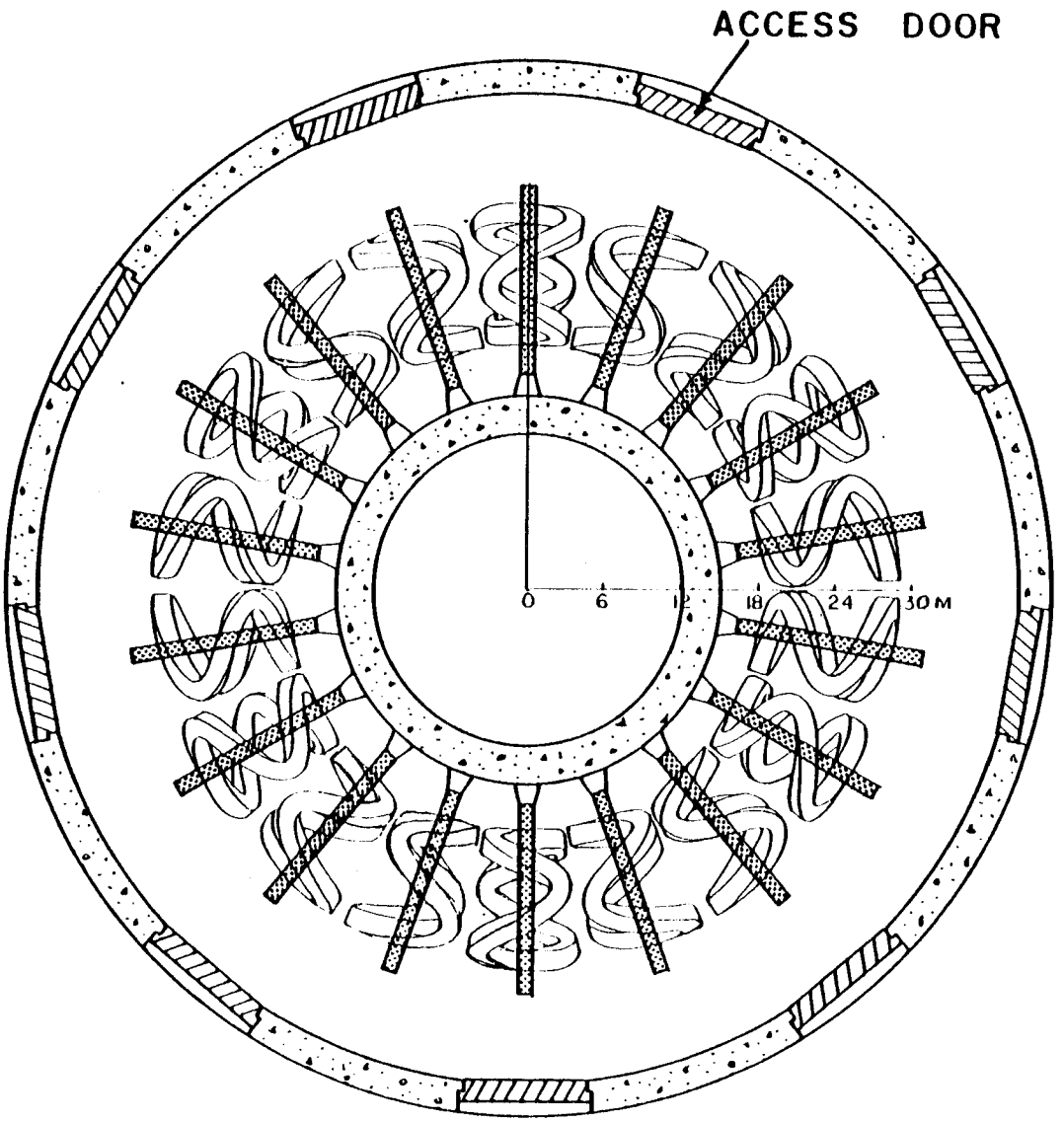

TOP VIEW OF UWTOR-M WITHIN EVACUATED REACTOR BUILDING

Fig. II.9-2

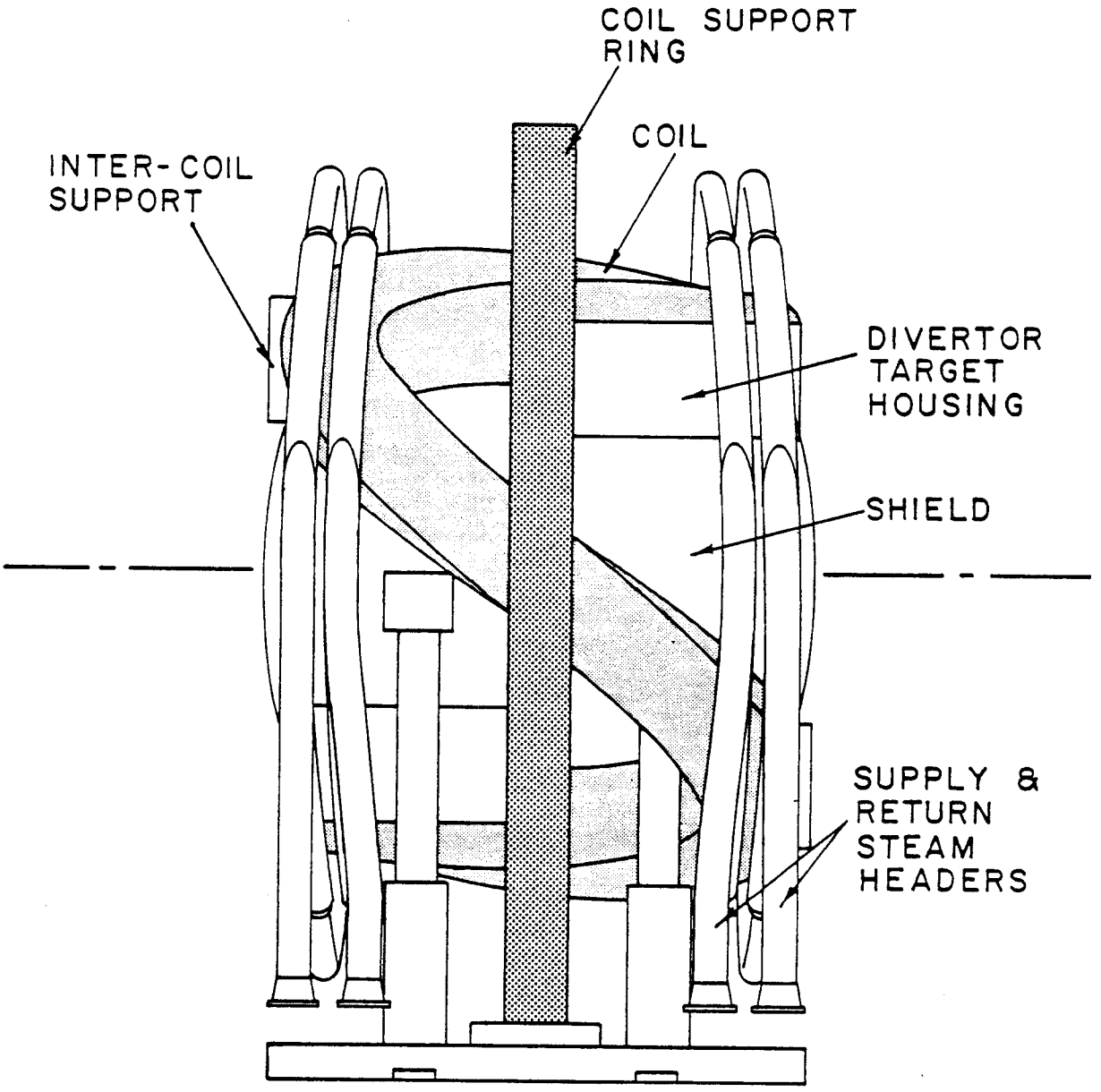

REACTOR MODULE AS VIEWED FROM THE BACK

Table II.9-1. Breakdown of Masses in a Single Coil Module

	Tonnes
Coil and support ring	1175
Blanket structure	90.5
Reflector	451
Shield	254
Divertor targets (6 sets)	52
Steam manifolds	3.5
Support structure	19
Total	2045

- One-half of the coil set (9 coils) can be extracted radially out of the reactor hall providing access for maintaining all the blanket segments and divertor targets.
- In the event of a coil failure, the remaining coils can be extracted by initial circumferential, then radial movement.

II.10 System Economics

The economic analysis for UWTOR-M conforms to the guidelines provided in the DOE "Fusion Reactor Design Studies - Standard Accounts for Cost Estimates."

The two modes of analysis used are the constant dollar and the current dollar. The constant dollar mode defines general inflation rates and component escalation rates equal to zero. All costs, regardless of the time of incurrence, will be reported in present year price levels. In the current dollar mode, cost escalation on the estimated capital is assumed to exist and is taken as a single escalation during construction account.

Figure II.10-1 shows the percentage breakdown of the reactor plant equipment costs. The cost of the magnets exceeds all the other reactor equipment put together.

Construction facilities, equipment and services were taken as 10% of direct costs, engineering and construction management as 8% of direct costs and other costs were taken as 5% of the direct costs. The direct and indirect costs are listed in Table II.10-1.

For the constant dollar mode, interest on capital was taken as 5% and escalation was zero. In the current dollar mode, interest was 10% and escalation 5%. An eight year construction period was assumed. Table II.10-2 gives the total capital cost summary.

The busbar energy cost in mills/kWh is the expense which a utility incurs in generating a kilowatt-hour of electricity. When the utility sells this electricity to the customer it adds a quantity to account for profit.

The expenses which make up the busbar energy costs are:

1. Fixed charge rate.
2. Annual operating and maintenance.
3. Scheduled component replacement.
4. Annual fuel costs.

Other elements needed to determine busbar costs are plant capacity and plant availability. Plant capacity at 75% availability is 1.206×10^{10} kWh/year.

Table II.10-3 gives the plant costs and busbar costs for UWTOR-M and compares them with STARFIRE in 1980 dollars. It can be seen that UWTOR-M is quite similar to STARFIRE both in plant as well as busbar costs.

Fig. II.10-1. Percentage breakdown of reactor plant equipment costs.

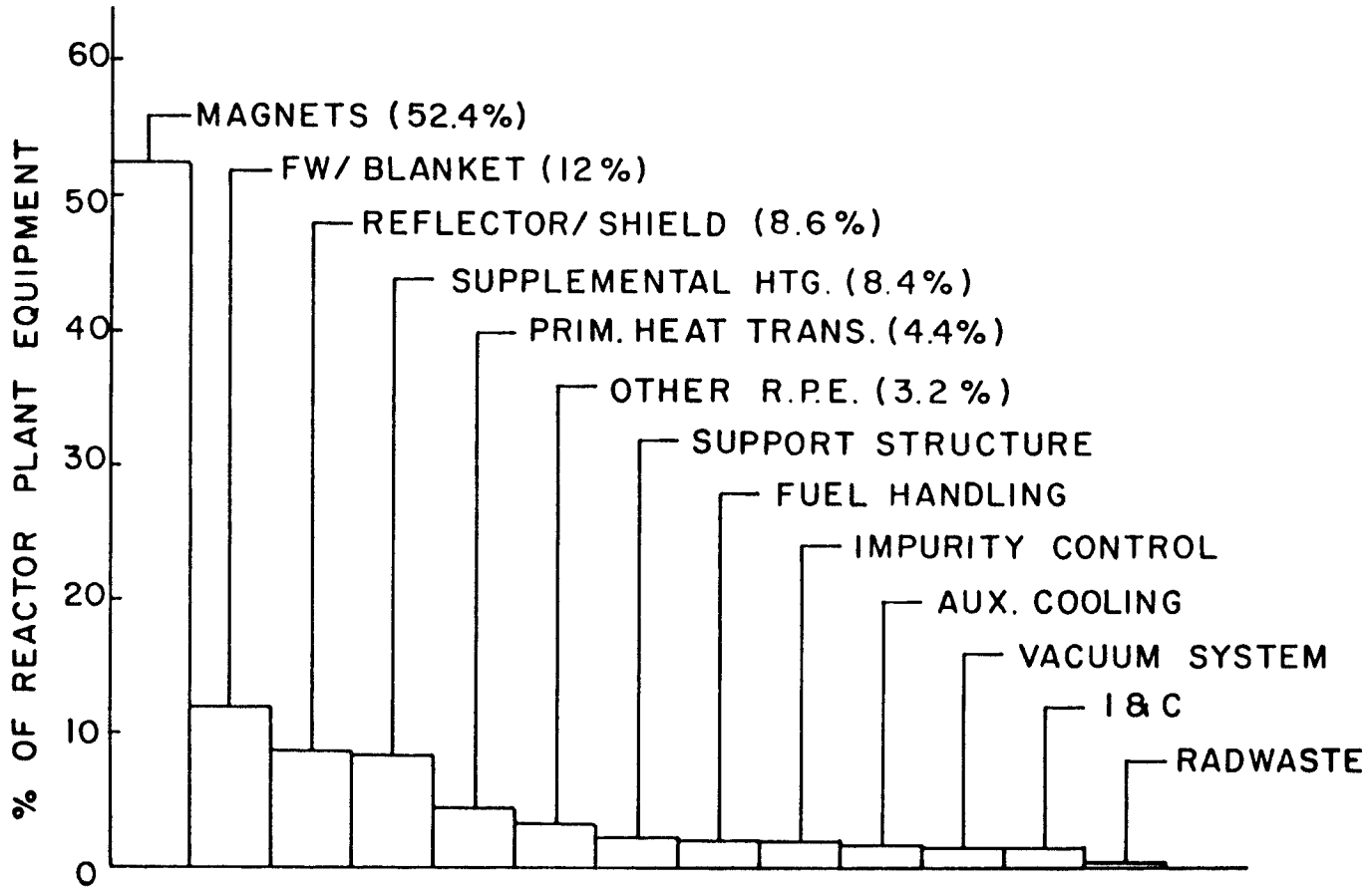

Table II.10-1. Total Capital Cost Summary

Acct. No.	Description	Cost ($ x 10^6)	
20	Land and land rights	3.30	
21	Structures and site facilities	355.36	
22	Reactor plant equipment	1764.99	
23	Turbine plant equipment	301.62	
24	Electric plant equipment	137.03	
25	Miscellaneous plant equipment	45.48	
26	Special materials	3.50	
	TOTAL DIRECT COSTS		2611.28
91	Construction facilities	261.13	
92	Engineering and construction management	208.90	
93	Other costs	130.56	
	TOTAL INDIRECT COSTS		600.59
TOTAL DIRECT AND INDIRECT COSTS			3211.87

Table II.10-2. Total Capital Cost Summary

Acct. No.	Description	Constant Dollar	Current Dollar
94	Interest during construction		
	F_{IDC} (constant dollar) = 0.170	546.02	
	F_{IDC} (current dollar) = 0.466		1496.73
95	Escalation during construction		
	F_{EDC} (constant dollar) = 0	0.00	
	F_{EDC} (current dollar) = 0.261		838.30
	TOTAL CAPITAL COSTS	3757.89	5546.90

Table II.10-3. Comparison of Plant Costs and Busbar Costs Between UWTOR-M and STARFIRE

	Constant Dollars	Current Dollars
Plant Costs		
UWTOR-M ($/kWe)	2034 (1982)	3001 (1990)
STARFIRE ($/kWe)	2000 (1980)	2665 (1986)
Busbar Costs		
UWTOR-M (mills/kWh)	36 (1982)	76 (1990)
STARFIRE (mills/kWh)	35.1 (1980)	67.1 (1986)

The following conclusions can be drawn from the cost estimate:

- A reasonably detailed cost analysis indicates that modular stellarators are competitive with other magnetic fusion systems.
- To be competitive, indications are that modular stellarators must be in the 4000-5000 MW_{th} range.
- Risks associated with the magnets are higher for modular stellarators because they comprise a higher fraction of the reactor plant equipment.

III. Historical Background

A chart of stellarators in the world today is shown in Table III.1-1.

An historical perspective of stellarator devices can, in many ways, be likened to a novel. First invented in the United States by Lyman Spitzer of Princeton University in the 1950's, the then Atomic Energy Commission in the United States abandoned stellarators in 1969 after converting the last stellarator, Model C, into a tokamak.

It remained for the National Science Foundation to begin the experimental program in stellarators, five years later in 1974, with the purchase and moving of the Proto-Cleo Stellarator from the United Kingdom to the University of Wisconsin. After 1976, when the large stellarator experiments, Wendlestein VII A at Garching, Cleo at Culham, and L-2 at the Lebedev Institute began giving dramatic results with confinement parameters comparable to tokamaks, some renewed interest on the part of the U.S. Department of Energy appeared.

Since that time interest in stellarators has mushroomed. Groups advocating such devices have appeared at MIT, Princeton, Oak Ridge, Los Alamos as well as at Wisconsin, with the competition for eventual devices being very fierce. As of this writing, no new large device has been commissioned, but the University of Wisconsin is constructing a modular stellarator, IMS, which is the same size as the Proto-Cleo stellarator, but built in modular form to test the operation of such a device.

The earliest reactor studies in the United States in stellarators began with the proposal for the Model D stellarator, which was to be a reactor if the Model C device had worked properly. Subsequently, studies have taken place at MIT and are now being examined at Los Alamos in addition to the present study at Wisconsin.

Table III-1. Present Stellarator Devices

The following is a list of stellarators, operating or under construction as per end of 1980.

NAME	LOCATION	COMMENTS R = major radius; r = radius of last closed magnetic surface; B_ϕ = toroidal magnetic field; ℓ = number of poloidal field periods.
Wendelstein II-A	Bochum, FRG	R = 50 cm, r = 5 cm, $B_\phi \sim 8$ kG, $\ell = 2$. RF plasma.
Wendelstein II-B	Garching, FRG	R = 50 cm, r = 5 cm, $B_\phi \sim 7.5$ kG steady state, 15 kG, pulsed mode, $\ell = 2$.
Wendelstein VII-A	Garching, FRG	R = 200 cm, r = 10 cm, $B_\phi \sim 40$ kG, $\ell = 2$.
Heliotron DM	Kyoto, Japan	R = 50 cm, r = 5 cm, $B_\phi \sim 10$ kG.
Heliotron D	Kyoto, Japan	R = 105 cm, r = 10 cm, $B_\phi \sim 5$ kG.
Heliotron E	Kyoto, Japan	R = 220 cm, r ≅ 21-40 cm, $B_\phi \sim 20$ kG, $\ell = 2$.
JIPP-I	Nagoya, Japan	R = 50 cm, r = 7 cm, $B_\phi \sim 4$ kG, $\ell = 2$ and 3.
JIPPT-II	Nagoya, Japan	R = 91 cm, r = 17 cm, $B_\phi \sim 30$ kG, $\ell = 2$.
Cleo	Culham, UK	R = 90 cm, r = 13.5 cm, $B_\phi \sim 20$ kG, $\ell = 3$.
IMS	Madison, USA	R = 40 cm, r = 5 cm, $B_{\phi\ max} = 6$ kG, $\ell = 3$. Modular stellarator, under construction.
Proto-Cleo	Madison, USA	R = 40 cm, r = 5 cm, $B_\phi \sim 5$ kG, $\ell = 2$ and 3, $\ell = 3$ torsatron.
Chrystall-2	Kharkov, USSR	R = 36 cm, r = 8.7 cm, $B_\phi = 25$ kG, $\ell = 3$. Torsatron, superconducting, under construction.
Uragan-II	Kharkov, USSR	Race track of length 1035 cm, r = 10 cm, $B_\phi = 20$ kG.
Uragan-III	Kharkov, USSR	R = 100 cm, r = 17 cm, $B_\phi = 30$-45 kG, $\ell = 3$. Torsatron, under construction.
Sirius	Kharkov, USSR	Race track of length 600 cm, r = 10 cm, $B_\phi = 20$ kG.
Saturn-1	Kharkov, USSR	R = 36 cm, r = 8.7 cm, $B_\phi = 10$ kg.
VINT-20	Kharkov, USSR	R = 31.5 cm, r = 7.2 cm, $B_\phi = 20$ kG torsatron, $\ell = 1$.
M-8	Kurchatov, USSR	Figure-8 device, r ≅ 8 cm.
L-2	Lebedev, USSR	R = 100 cm, r = 11 cm, $B_\phi = 20$ kG, $\ell = 2$.
R-O	Sukhumi, USSR	R = 50 cm, r = 5 cm, $B_{\phi\ max} \sim 8$ kG, $\ell = 3$.
RT-2	Sukhumi, USSR	R = 65 cm, r = 4 cm, $B_{\phi\ max} \sim 20$ kG, $\ell = 2$.

IV. Magnetic Topology

IV.1 Introduction

In order to generate closed magnetic surfaces in a torus to compensate outward drifts and to provide MHD equilibrium, it is necessary to keep the magnetic field lines from closing on themselves after one pass around the torus by introducing a twist in the poloidal direction. Figure IV.1-1 shows a coordinate system useful for describing these configurations. We call the angle theta the toroidal angle and the angle phi the poloidal angle.

Tokamaks provide the necessary twisting of the magnetic field lines by passing a current in the toroidal direction through the plasma. Stellarators provide the twisting by means of either deformation of the torus itself, e.g., twisting the torus into a figure 8, or by utilizing a set of twisted helical coils. Figure IV.1-2 shows an artist's view of the similarities and differences between a stellarator and a tokamak.[3]

Examination of Fig. IV.1-2 shows that stellarators will require toroidal field coils. This can be seen physically as follows. In the stellarator shown in Fig. IV.1-2 the currents in adjacent helical windings flow in opposite directions. A qualitative picture of the magnetic fields generated by these helical windings can be obtained by noting that a helical winding is really a loosely wrapped solenoidal winding. That is, a single helical winding generates a toroidal field and vertical field of its own as well as a poloidal field. The vertical field appears because the helix is not only a loosely wrapped solenoid, but a loosely wrapped vertical field coil as well, as can be seen by looking down on the torus. Therefore, currents flow-ing in opposite directions in adjacent helices (of the same pitch) cancel out each other's vertical fields and toroidal fields on the average. Thus, the need

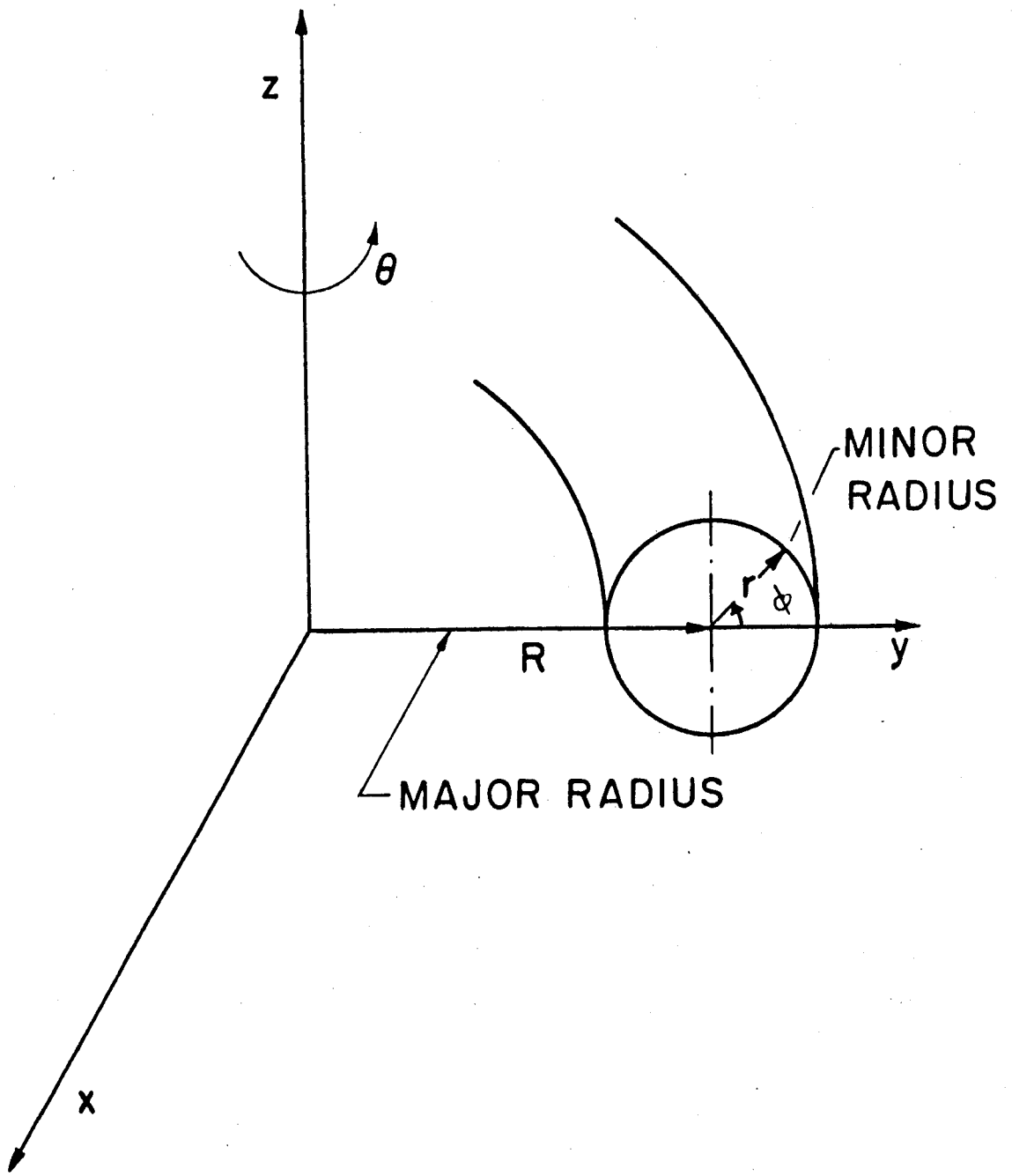

Figure IV.1-1 Toroidal coordinate system.

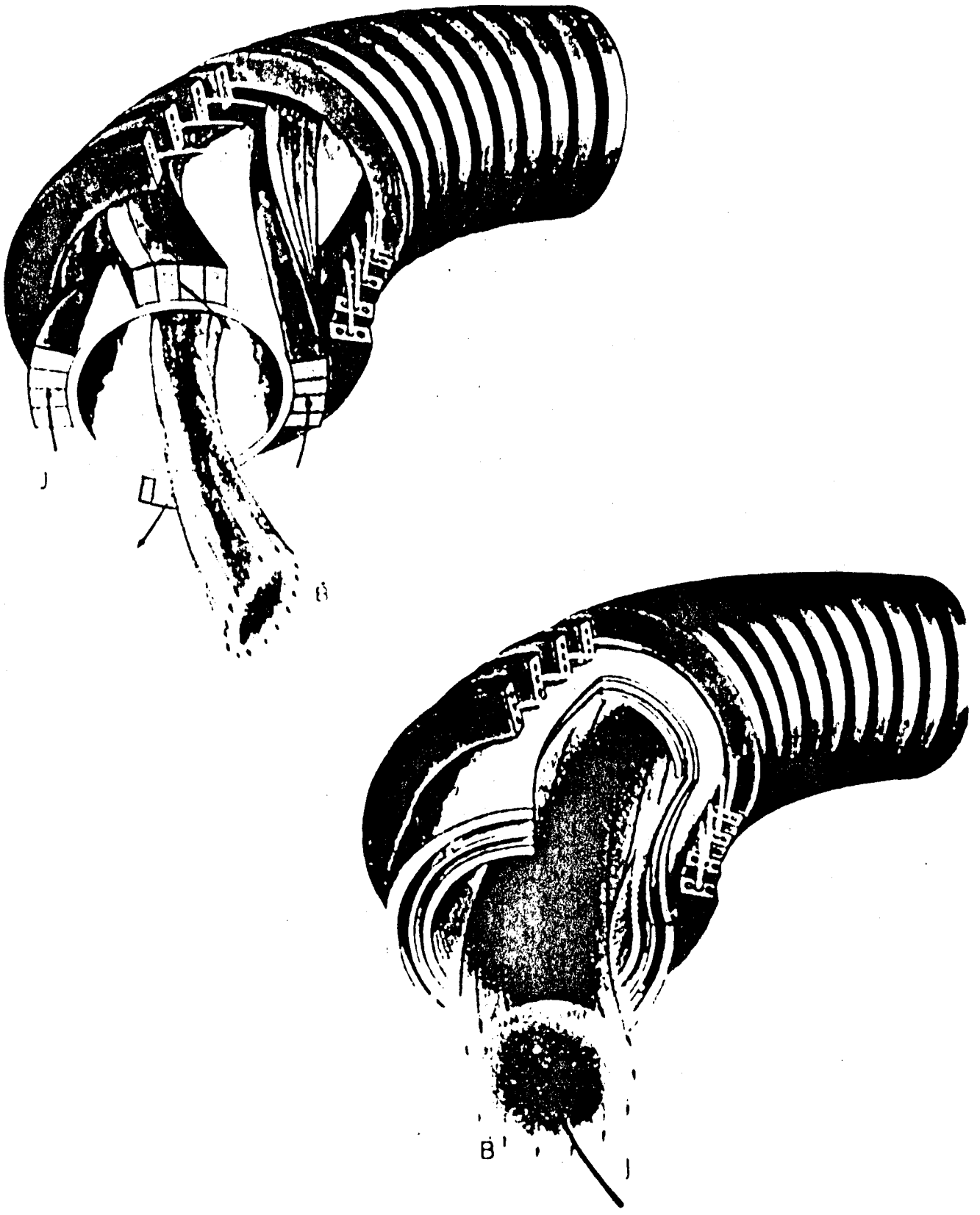

Figure IV.1-2 Artist's sketch of a stellarator and a tokamak.

for a separate set of toroidal field coils exists. The toroidal field is needed to provide a magnetic "connection" between adjacent sections of the torus and to provide the basis for generating the toroidal magnetic surfaces.

What is not cancelled from the helical windings are the poloidal fields and fluxes. The combination of the poloidal fields from the helical windings and the toroidal fields from the separate set of toroidal field coils results in a net flux which twists the magnetic field lines as they pass around the torus. Figure IV.1-3 shows a trajectory of a field line as it passes around the torus, projected on a fixed poloidal plane.[4] Figure IV.1-4 shows the same trajectory looking at the side of the torus. Each time the line moves downward it is passing near a helical coil carrying current in the "+" direction, but there is a net drift of the line in the poloidal direction in the direction of the "wrapping" of the helical windings. The net drift occurs because the toroidal field of the helical coils alternately adds to or subtracts from the external toroidal field without affecting the poloidal field, thus changing the direction of the field line as shown in Fig. IV.1-4. If the stellarator windings are designed properly, the magnetic field line can pass many times around the torus before it closes upon itself and can thus generate a toroidal closed surface, which is called a magnetic surface. Figure IV.1-5 shows the intersection (not the projection) of the particular field line of Fig. IV.1-3 with a fixed plane. This intersection is what the magnetic surface looks like at that plane. This surface rotates as the field line moves around the torus as seen in Fig. IV.1-2. The trajectory of the line always lies between two circles; the inscribed and circumscribed circles of the magnetic surface shown in the figure. Due to toroidal effects these

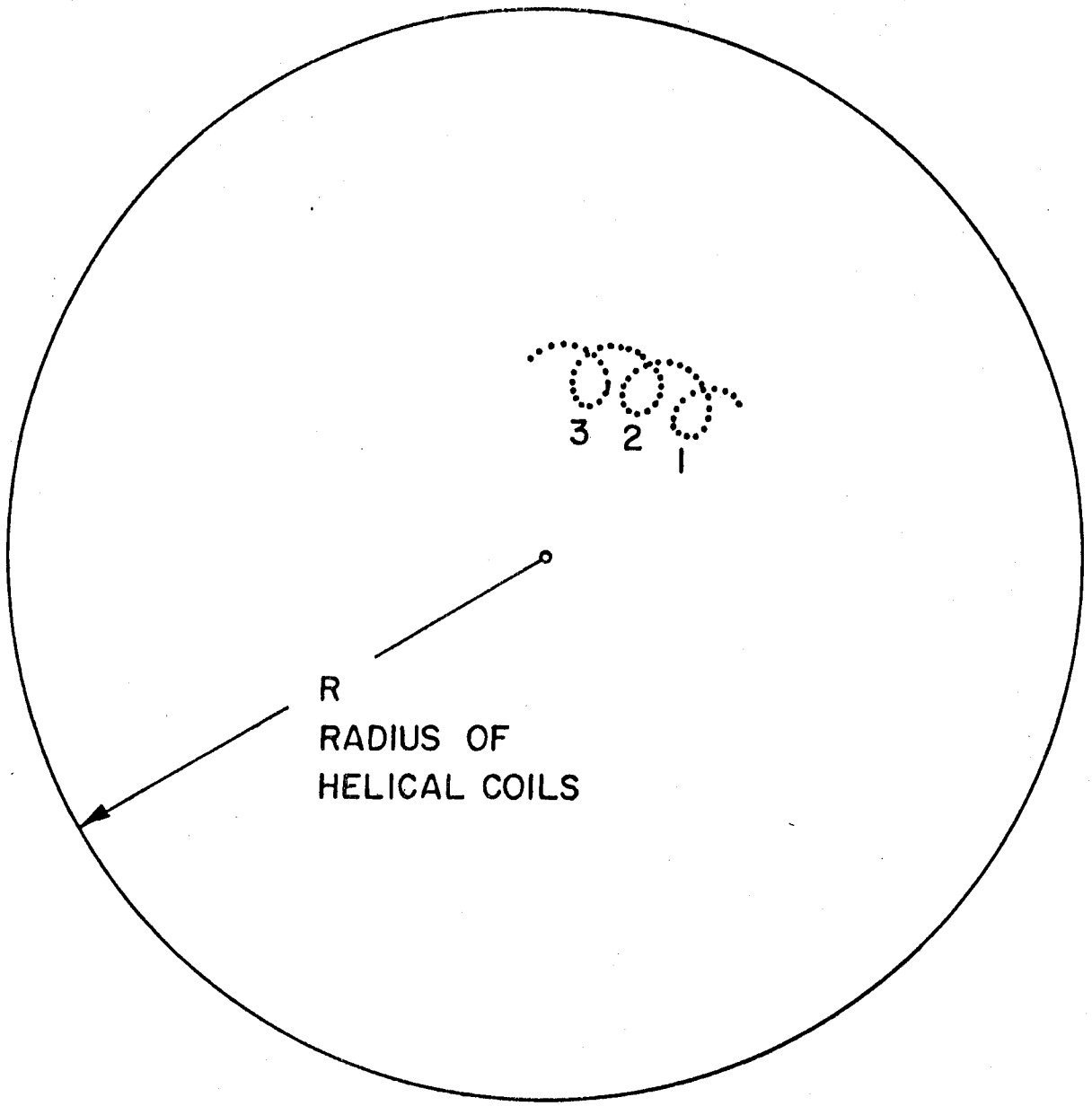

Figure IV.1-3 Trajectory of field line projected to a poloidal plane. The numbers 1, 2, 3 in the figure are the same as those numbered locations in Fig IV.1-4.

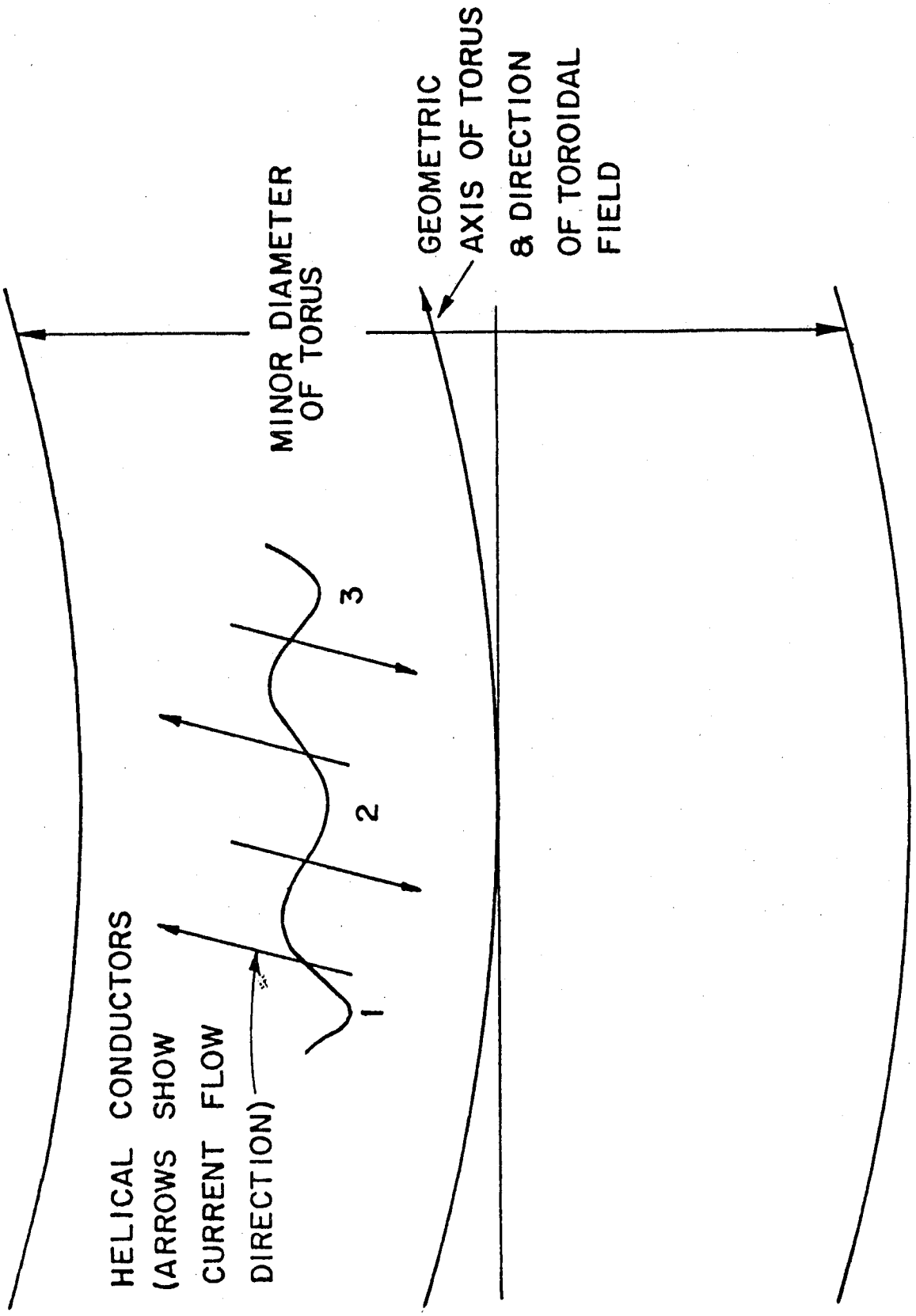

Figure IV.1-4 The same trajectory viewed from the outside of the torus. The lines with arrows refer to the passage of the helical conductors past the field line and the direction of the current is indicated by the direction of the arrows.

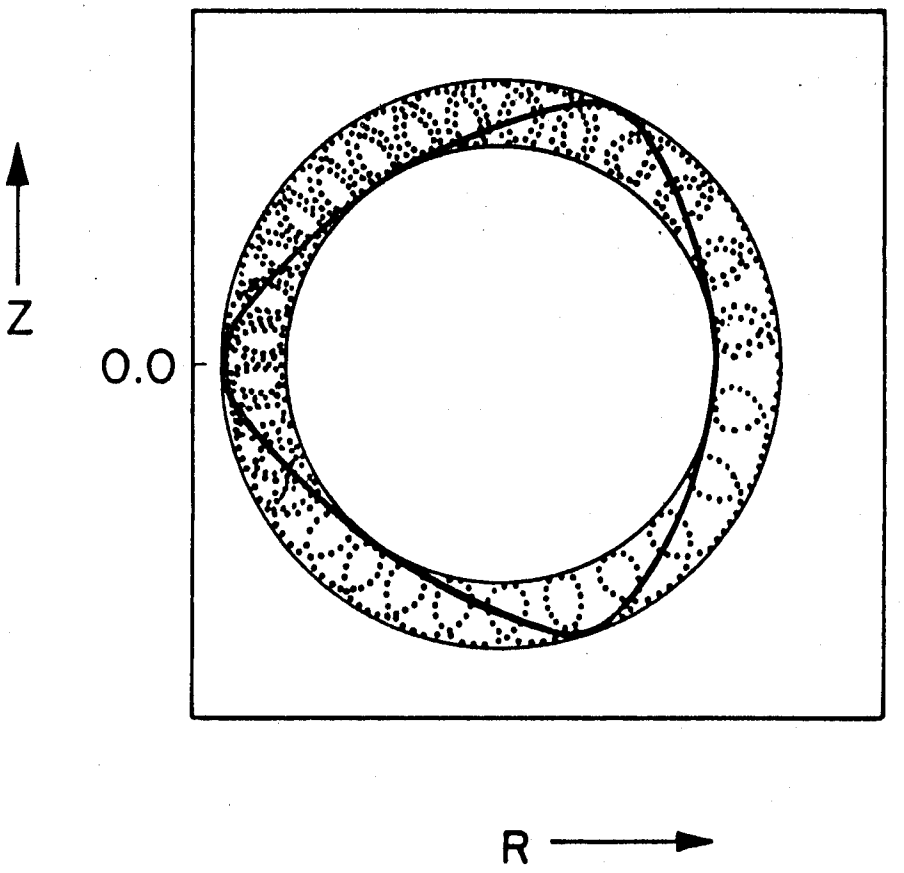

Figure IV.1-5 A magnetic surface (the triangular shaped structure) generated by the field line shown.

circles are not concentric, however. Figure IV.1-6 is a 3-dimensional plot of the magnetic surface.

Each magnetic surface is generated by a different magnetic field line. Often the amount of twist of each field line is different from that of other field lines. Optimization of the magnetic configuration will result in a set of nested toroidal magnetic surfaces. Figure IV.1-7 shows several types of magnetic surfaces that can be generated by stellarator windings.

The four different surfaces in Fig. IV.1-7 are labelled $\ell = 1$, $\ell = 2$, $\ell = 3$, and $\ell = 4$ surfaces, respectively. The ℓ numbers refer to the apparent symmetry of the magnetic surfaces in the minor cross section. For example, an $\ell = 2$ magnetic surface exhibits 2-fold symmetry in the minor cross section. It can be seen from Fig. IV.1-7 that for a stellarator configuration, the number of helical windings passing through the poloidal plane is exactly equal to twice the ℓ number. The shaded areas in Fig. IV.1-7 are the regions in which closed magnetic surfaces are generated and presumably inside of which plasma is confined. At the corner of the last closed magnetic surfaces, a magnetic "stagnation point" is reached (the twisting of the magnetic field line at this point matches the pitch of the helix), and "divertor action" may occur. This means that particles passing through this region may suddenly find themselves outside the last closed magnetic surface and on the surfaces that wrap around the helical conductors, where they may be collected. Outside of the last closed magnetic surface, the field lines wrap around the individual conductors.

Often, the last closed magnetic surface is called a separatrix. Strictly speaking, however, this only can exist in the limit of infinite toroidal aspect ratio because toroidal effects tend to spread the last closed magnetic

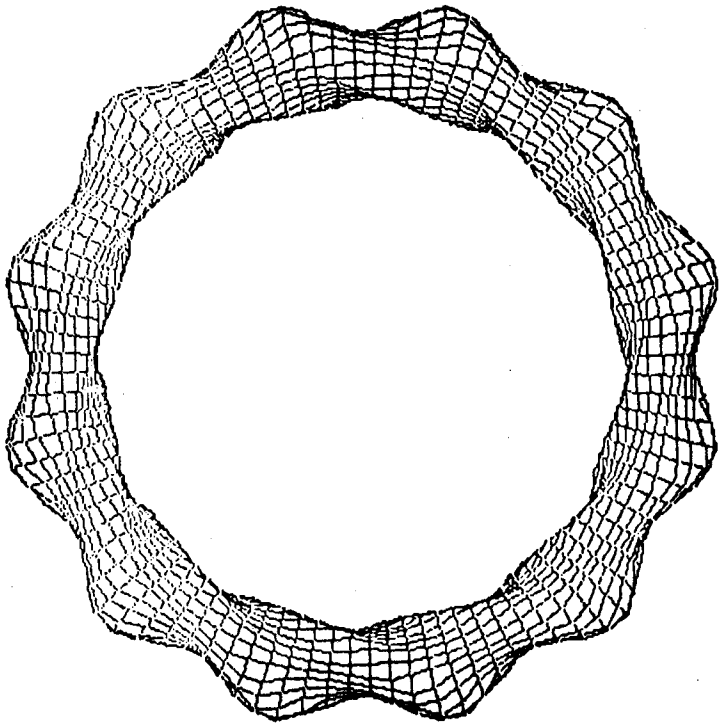

Figure IV.1-6. A top view of a complete magnetic surface.

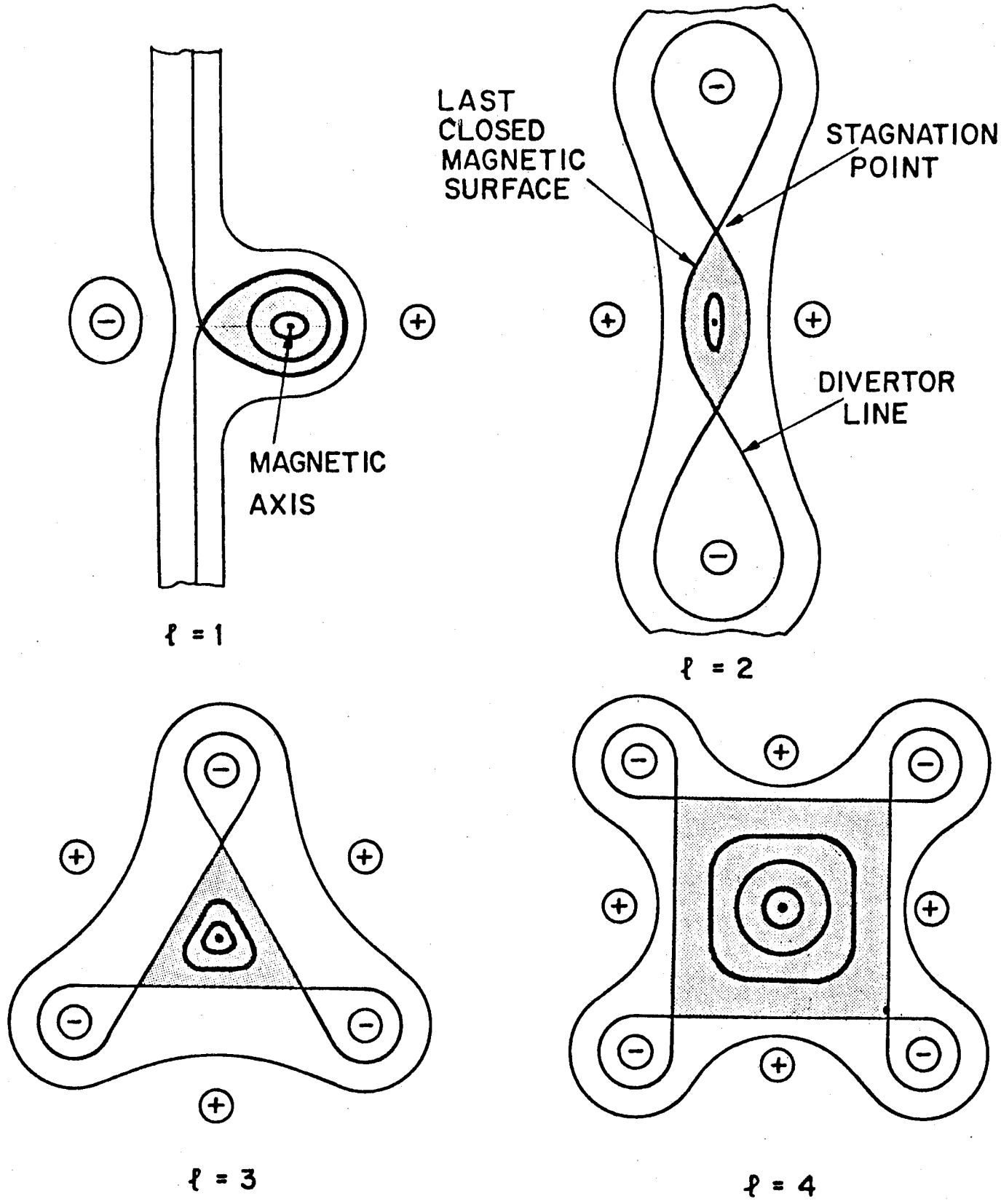

Figure IV.1-7 Four sets of magnetic surfaces. In each figure the magnetic field is directed out of the paper and the helical coils are wrapped over the top of the torus from the outside and along the direction of the field line. "+" means the current flows into the paper.

surface into a broader region of "ergodic" (not well behaved) magnetic field lines. In Fig. IV.1-7, the toroidal field is assumed to point out of the paper, and the helical windings wrap from the outside to the inside of the torus over the top of the torus. The signs of the currents refer to their direction with respect to the toroidal field. The net twisting of the magnetic field lines always occurs in the same direction as the wrapping of the helical windings regardless of the direction of the toroidal field. In the case of Fig. IV.1-7 the stagnation points occur beneath the conductors carrying currents out of the paper ("-" sign).

If the magnetic surfaces are nested as shown in Fig. IV.1-7, there is often a single line around which all of the magnetic surfaces appear to be nested. Such a line is called the magnetic axis. The average angular rotation in the poloidal direction made by a field line in traversing once around the toroidal direction is called the rotational transform, the angle of which is measured with respect to the magnetic axis. Typical plots of the average rotational transform angle for the four magnetic surface configurations shown in Fig. IV.1-7 are shown in Fig. IV.1-8. The transform profiles of the $\ell = 3$ and $\ell = 2$ devices begin at zero transform on the magnetic axis, whereas $\ell = 1$ and $\ell = 2$ begin at non-zero values.[5] In all cases, the transform increases monotonically out to the last closed magnetic surface. Since the $\ell = 1$ and $\ell = 2$ configurations have non-zero transform on the magnetic axis, it is possible to design a device in which the transform is constant out to a very large value of minor radius. Such a configuration is said to have no shear. A convenient definition of the shear parameter is

$$L_s = \frac{R}{2\pi r} \frac{d\iota}{dr}^{-1} \qquad (1)$$

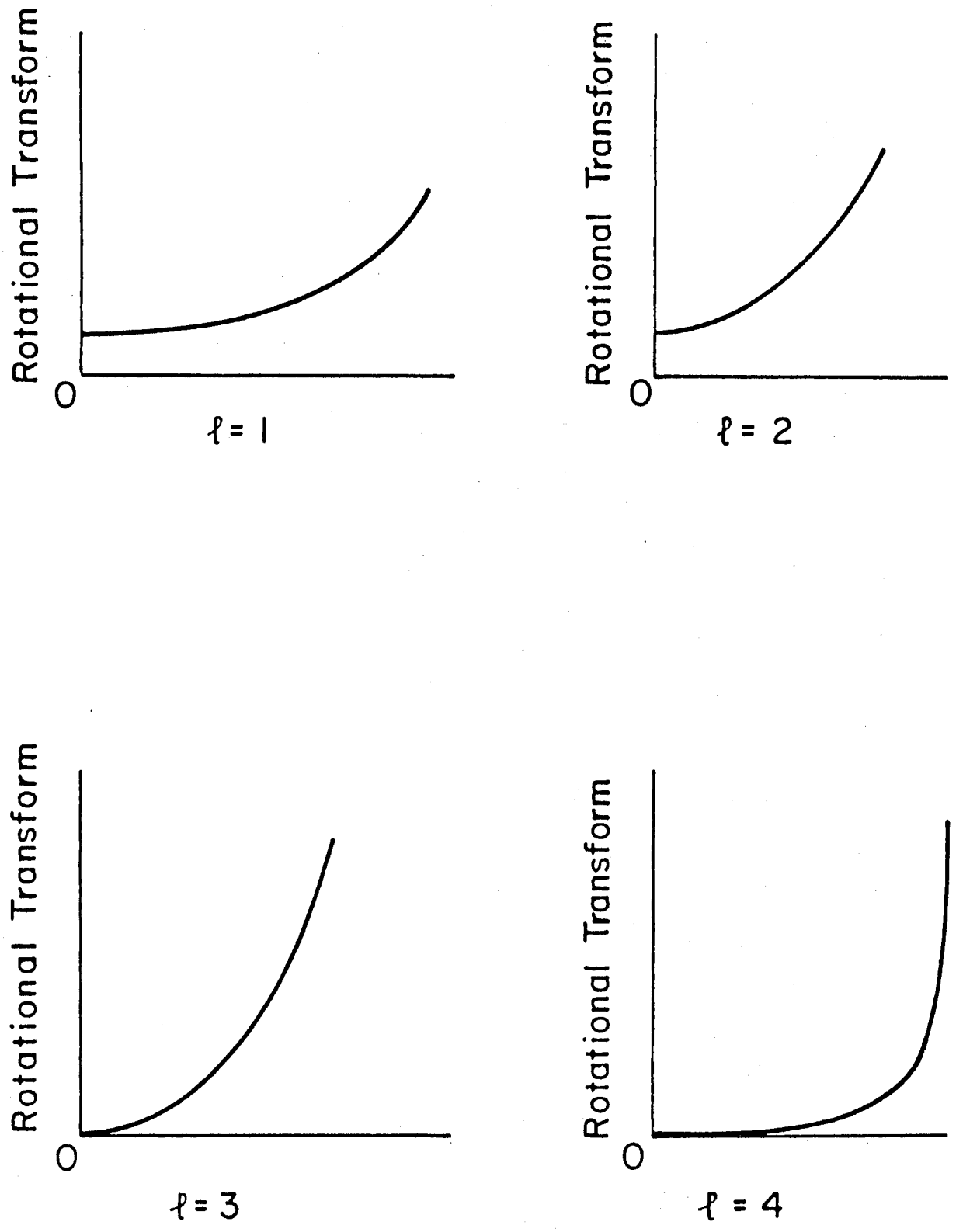

Figure IV.1-8 Transform profiles for the four configurations shown in Figure IV.1-7. Note that the $\ell = 1$ and $\ell = 2$ configurations have non-zero transform on the magnetic axis.

In Eq. (1) ι is the rotational transform value in radians. Often ι is normalized with respect to 2π and then written as $\iota\!\!\!/$. When ι is unity, the transform is 2π and the field line should close upon itself after 1 pass around the torus the long way, provided that the minor radius of the field line does not change when it completes the pass around the torus. Whenever $\iota\!\!\!/$ is a rational number, the magnetic field line closes upon itself after a finite number of passes and generates a closed line configuration (not a closed magnetic surface). Often confinement is poor if there is no shear and $\iota\!\!\!/$ is rational, especially if $\iota\!\!\!/$ is an integer near unity. With shear, both rational and irrational values of $\iota\!\!\!/$ appear and confinement tends to be improved.

In contrast to tokamaks, $\iota\!\!\!/$ increases as minor radius increases. If it is recalled that $q = 1/\iota\!\!\!/$ then it can be seen that the q profile for stellarators tends to decrease as minor radius increases. This means that the lowest value of q tends to be on the outside of the plasma, and thus it is fairly easy to avoid $q = 1$ surfaces appearing inside the plasma, which can lead to instabilities and possible loss of confinement. However, if ohmic heating is added, the transform profile gradually becomes more tokamak-like with increasing ohmic heating current and eventually begins to decrease with minor radius as shown for an $\ell = 3$ stellarator in Fig. IV.1-9. If the ohmic and helical transforms are made to oppose each other, it is likely that the point $\iota\!\!\!/ = 0$ will appear inside the plasma away from the magnetic axis. This will tend to produce magnetic islands, secondary magnetic axes, instabilities, and possible loss of confinement. A variation of this situation, presently called a reversed field ohmically heated stellarator,[6] attempts to reverse the transform by passing through the point $\iota\!\!\!/ =$ infinity, rather than $\iota\!\!\!/ = 0$.

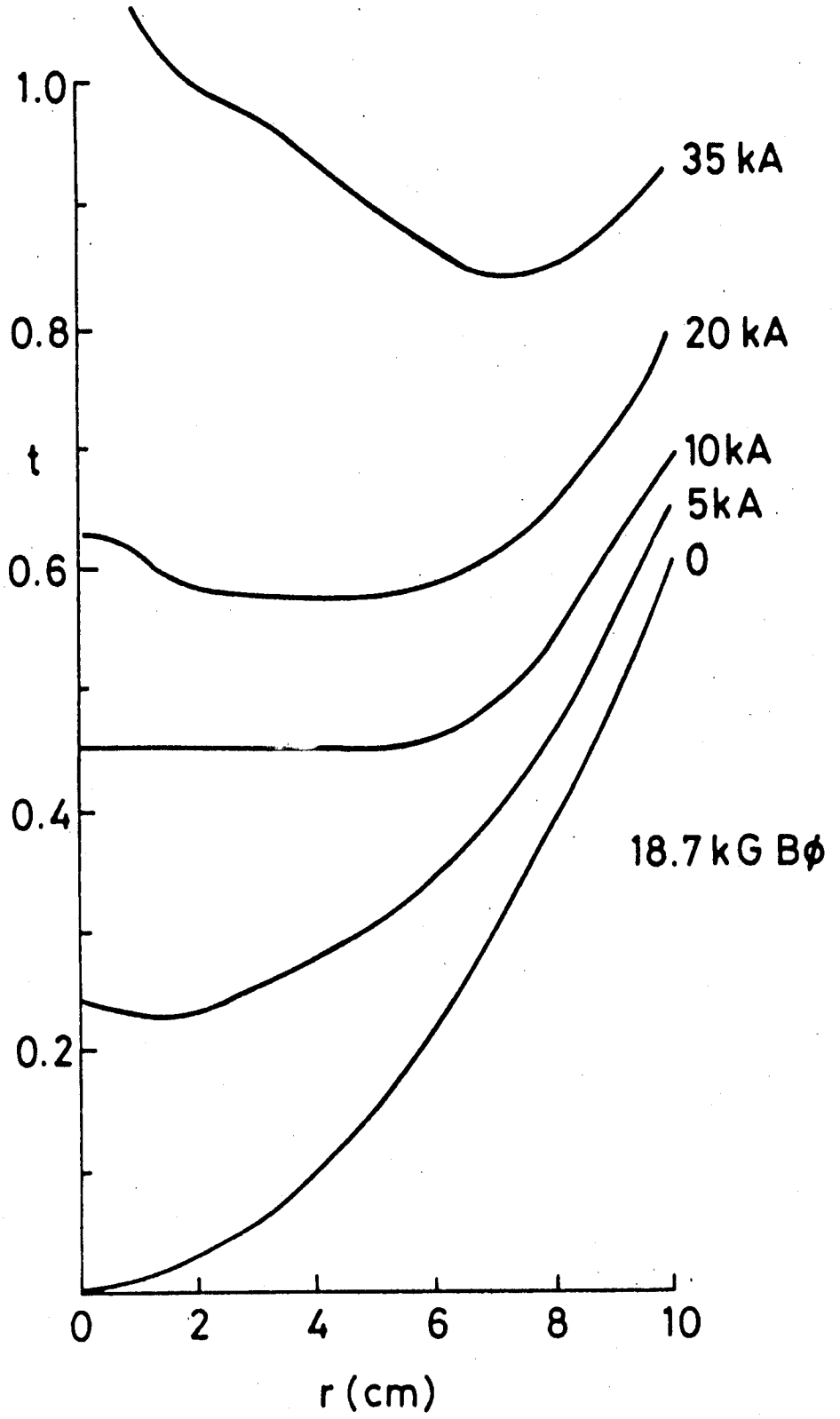

Figure IV.1-9 Rotational transform versus minor radius as a function of ohmic heating current. As the current increases, the profile begins to decrease with minor radius.

Figure IV.1-10 shows the magnetic surfaces and the helical conductors for a device called a torsatron.[7,8] This configuration is a very similar type of confinement system to a stellarator, but is simpler to construct. Both devices have helical widings, but in a torsatron the currents in adjacent helical windings flow in the same direction. This means that the helical coils will now produce a net toroidal field (along with a net vertical field). Hence, if a torsatron is designed properly, no auxiliary toroidal field coils are required. The net vertical field, however, presents a different problem. This field must be cancelled out by an auxiliary vertical field which points in the opposite direction from the self-generated vertical field of the helical coils. Typically, this is done by adding a separate vertical field coil or coils. The location at which the average vertical field is cancelled defines the magnetic axis. If the vertical field could not be cancelled at this point, the line defining the magnetic axis would not be able to close upon itself after one pass around the torus. If the vertical field coils are located outside of the helical coils and have a radius larger than the maximum major radial position of the helical coils, then the current flowing in the vertical field coils should be oppositely directed to that flowing in the helical coils. If the vertical field coils are located towards the major axis of the torus, then the current must go in the same direction as that in the helical coils. It is also obvious that the currents in the vertical field coils must be comparable to the currents flowing in the helical coils.

In the stellarator configuration, it is possible to adjust the ratio of the poloidal and toroidal magnetic fields by varying the ratio of the currents in the helical and toroidal field coils, respectively. As the helical coil current is increased relative to the toroidal field coil current, the location

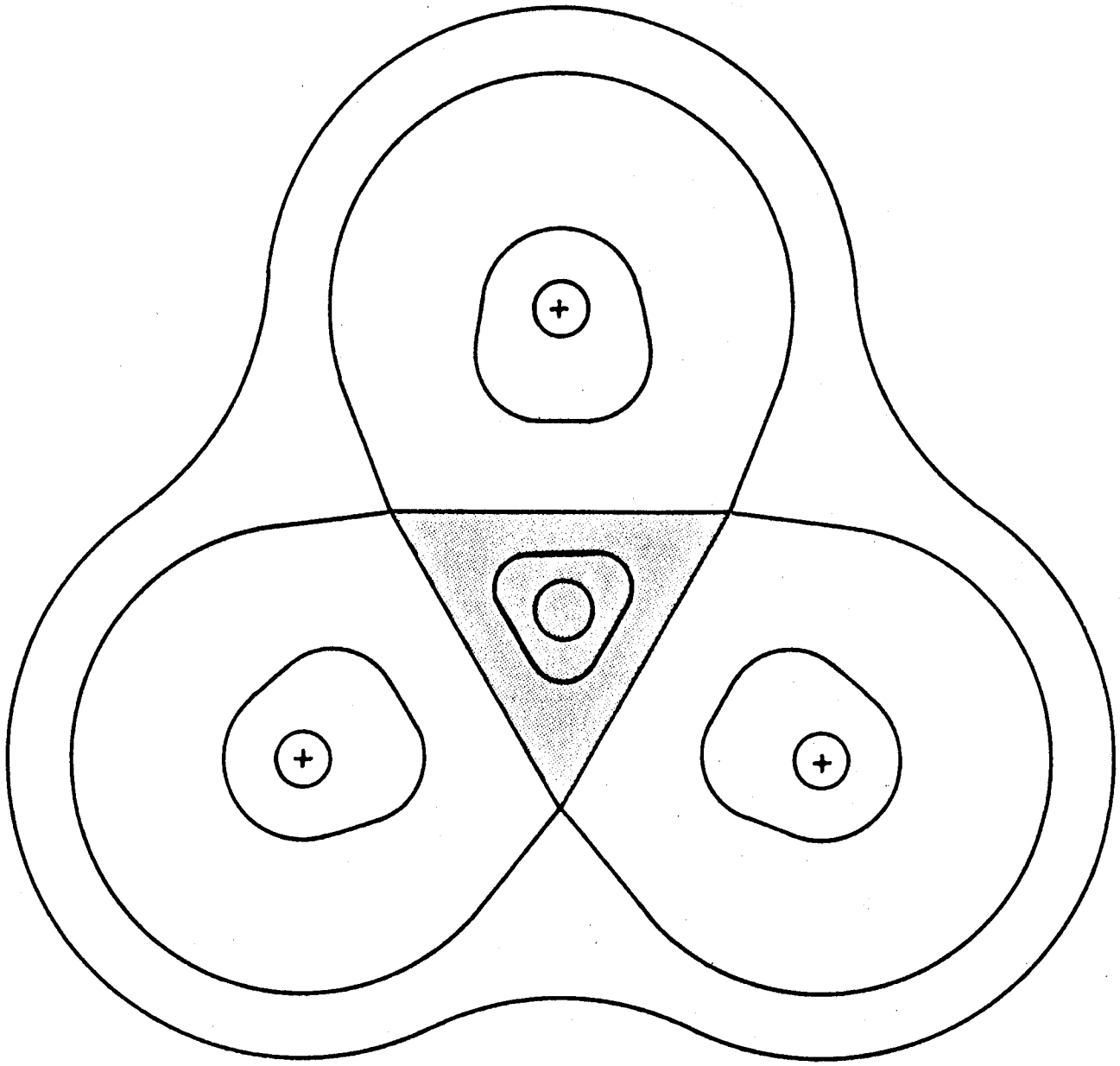

Figure IV.1-10. A torsatron magnetic surface configuration ($\ell = 3$). The wrapping is in the same direction as the sense of the helices in Fig. IV.1-7, and in this case the toroidal field is out of the paper. The reader should be able to verify this easily. "+" means into the paper.

of the last closed magnetic surface shrinks and often a corresponding decrease in the value of the rotational transform at the last closed magnetic surface also takes place. Thus, it is possible to vary the value of the transform along with plasma radius in this way.

In examining the magnetic surfaces of toroidal stellarators and torsatrons, it is obvious that the poloidal symmetry of these surfaces is not strictly defined by poloidal harmonic number (ℓ - number). Spatial Fourier decomposition of the minor radius of the last closed magnetic surface,[9] for example, yields several harmonics, many of which have comparable magnitude to that of the "main" harmonic number. If one can vary the values of the currents in the helical windings with respect to each other, then the harmonic content of the magnetic surfaces can change. In addition, variation of the magnitude of the compensating vertical field can shift the position of the magnetic axis, change the harmonic content of the magnetic surfaces, and vary the transform profile. Figure IV.1-11 shows the Fourier components of the last closed magnetic surface of an $\ell = 3$ stellarator.

In addition to the absence of a separate set of toroidal field coils, torsatrons also require only half the number of helical coils for the same ℓ number as do stellarators. In fact, it is possible to create a torsatron with only a single helical coil. Typically, a winding law for helical coils is of the form:

$$\phi = m\Theta \ . \qquad (2)$$

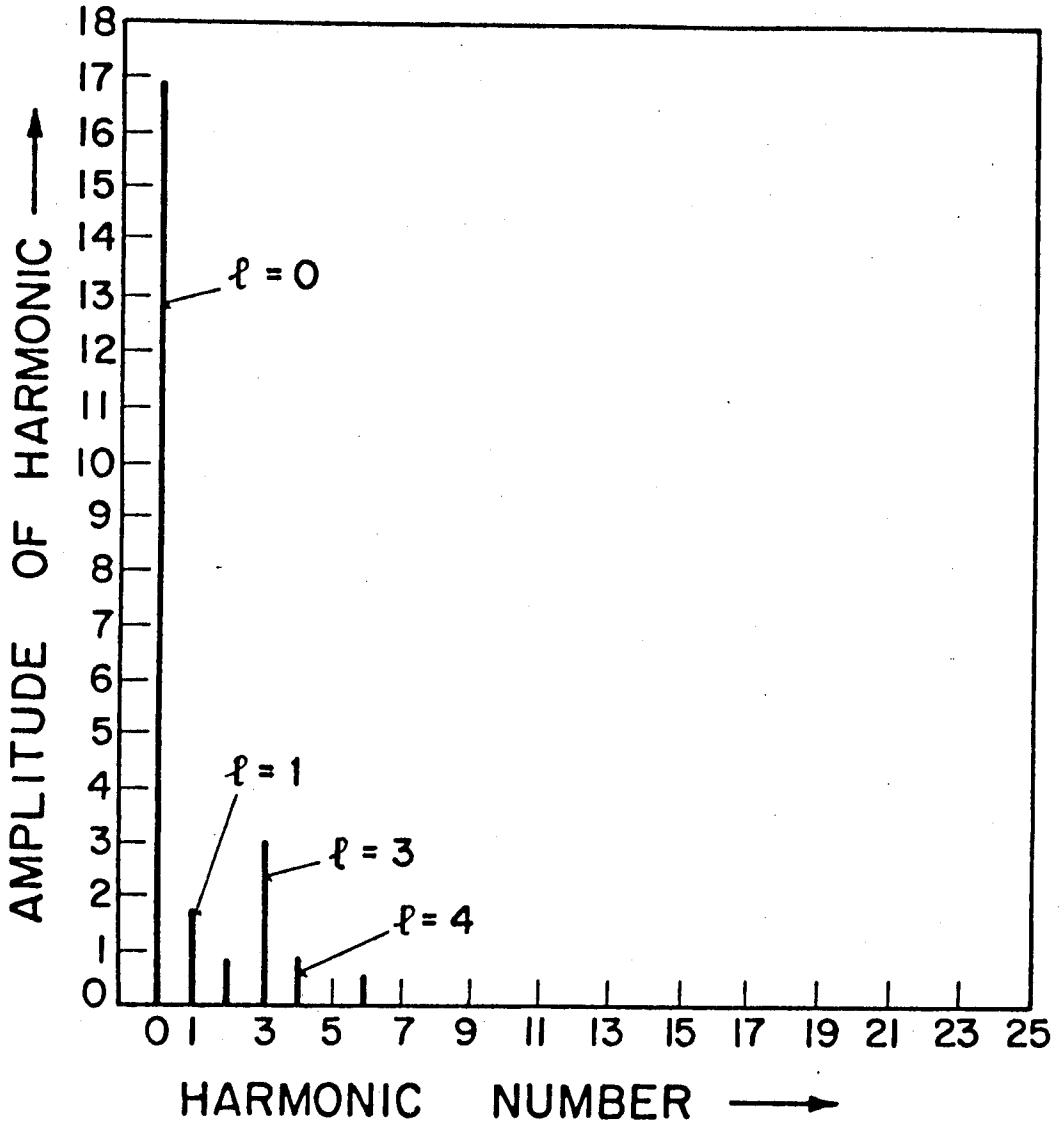

Figure IV.1-11 Fourier decomposition of the last closed magnetic surface of an $\ell = 3$ stellarator. Note the very strong presence of an $\ell = 0$ component.

m is always a rational number, but not necessarily an integer. For example, Table IV.1-1 lists several possible and one impossible set of winding laws for helical coils.

The column labelled # cond refers to the number of separate helical conductors needed to generate a complete set of windings. The column #FP refers to the number of field periods, that is, the number of times the magnetic surfaces repeat in going around the major axis of the torus. One field period is not, in general, a 360 degree rotation of the surface, but rather only a poloidal rotation sufficient to have the shape of the surfaces repeat. Figure IV.1-12 shows such a set of surfaces in perspective, together with a set of torsatron helical windings. The number of field periods is exactly the product of ℓ and m. Any of the stellarator configurations may be turned into a torsatron configuration of the same ℓ number provided that the currents in the adjacent coils are shut off and, of course the toroidal field coils are also shut off and a vertical field is added. (Otherwise the ℓ number would be doubled, if the currents all flow in the same direction.) Only a torsatron

Table IV.1-1

Configuration	ℓ	m	# cond	#FP	possible?
Stellarator	2	3	4	6	yes
Stellarator	3	7/3	2	7	yes
Torsatron	3	4	3	12	yes
Torsatron	2	13/3	-	-	no
Torsatron	3	13/3	1	13	yes
Torsatron	1	12	1	12	yes

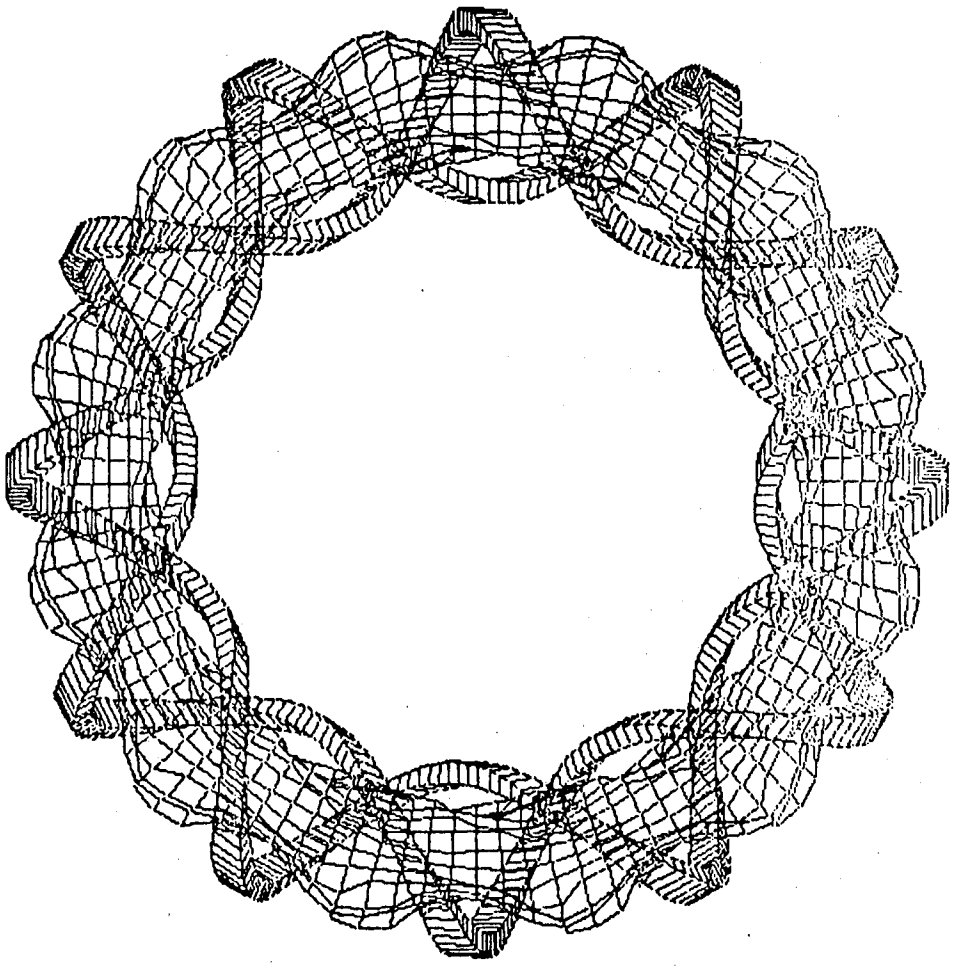

Figure IV.1-12 A torsatron magnetic surface inside the helical windings which generate the surface.

configuration, therefore, may be wound from a single conductor. Other winding laws, such as constant pitch or other toroidal geodesics are also used, but the basic relationship between the ℓ number and the number of field periods remains the same. If a separate set of toroidal field coils is added to a torsatron such a configuration is called a heliotron.[10-13]

A further interesting simplification of the torsatron configuration is called the "ultimate" torsatron.[14] The winding law for the helices in the ultimate torsatron differs from that shown in Eq. (2) in that the pitch is modulated as per the following, but non-unique, relation

$$\phi = m\theta + \alpha \sin \theta \tag{3}$$

The purpose of the modulation of the winding law is to produce a net compensating vertical field directly from the helical winding itself. Figure IV.1-13 shows the comparison between an ultimate and a conventional torsatron winding. It is clear that the modulation results in a winding that is more like a toroidal field coil on the outside and more like a vertical field coil on the inside of the torus than a conventional torsatron winding. Laying out both of these windings on a graph (Fig. IV.1-14) in which the horizontal axis is proportional to toroidal angle and whose vertical axis is proportional to poloidal angle, the conventional torsatron winding is a straight line. The ultimate torsatron winding is the sinusoidal waveform shown in the figure. The top, bottom, inside, and outside of the torus are marked. It can be seen that at the top and bottom of the torus, the direction of the current in the conventional winding is identical to the direction of the current in the ultimate winding. However, at the inside and outside of the torus, the direction of

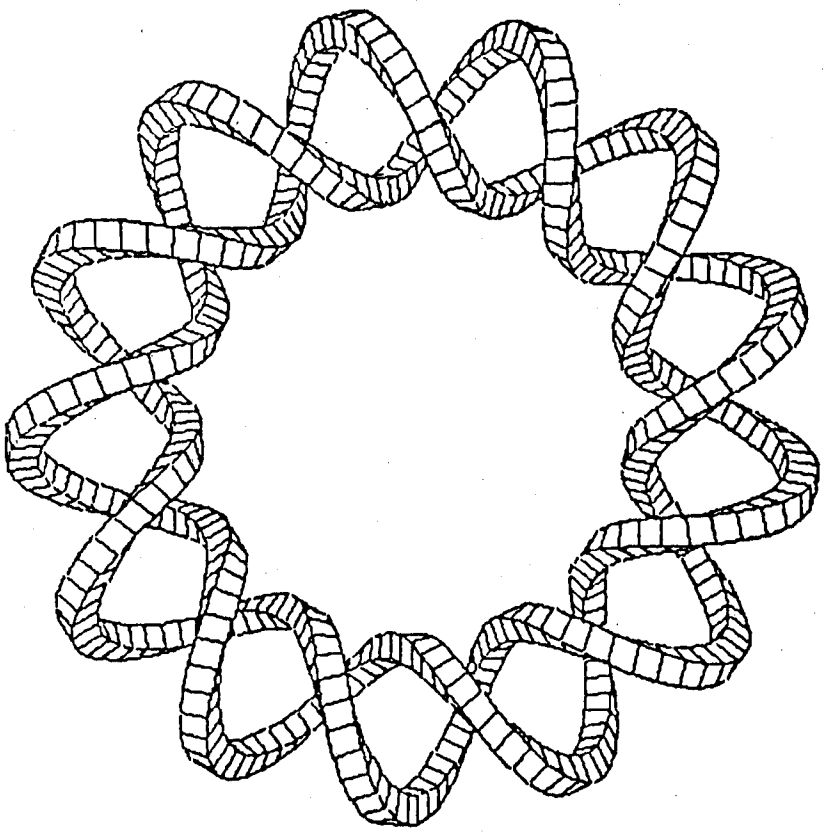

CLASSICAL

$$\theta = \frac{\ell}{N}\phi$$

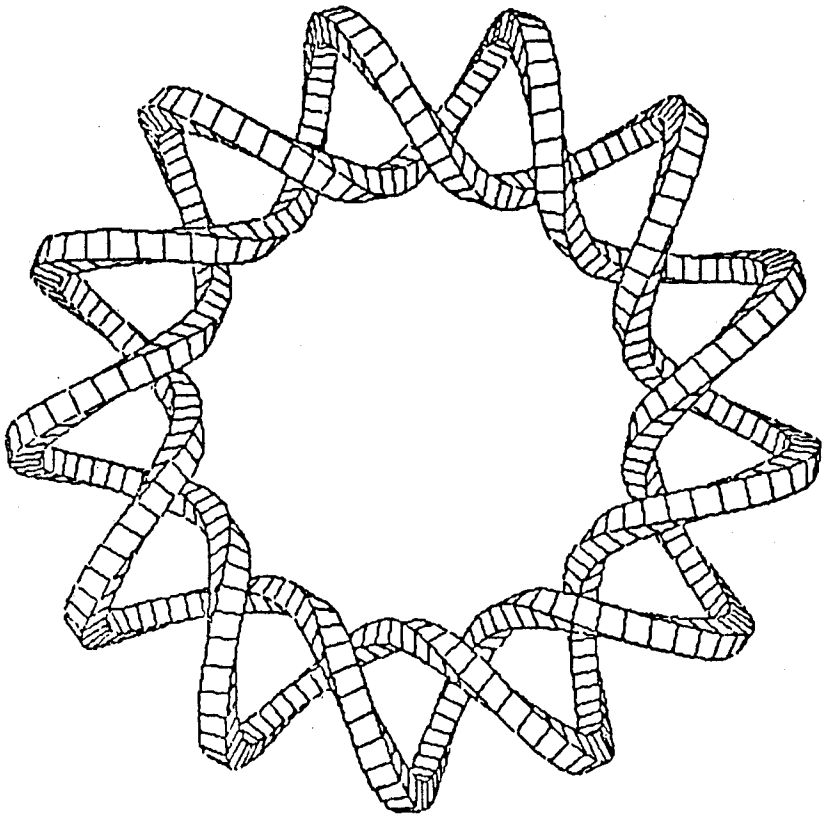

"ULTIMATE"

$$\theta = \frac{\ell}{N}(\phi - \alpha \sin\phi)$$

Figure IV.1-13 Comparison between a conventional and an ultimate torsatron winding.

Figure IV.1-14 Drawing used to show how the compensating vertical field is generated in the case of an ultimate torsatron.

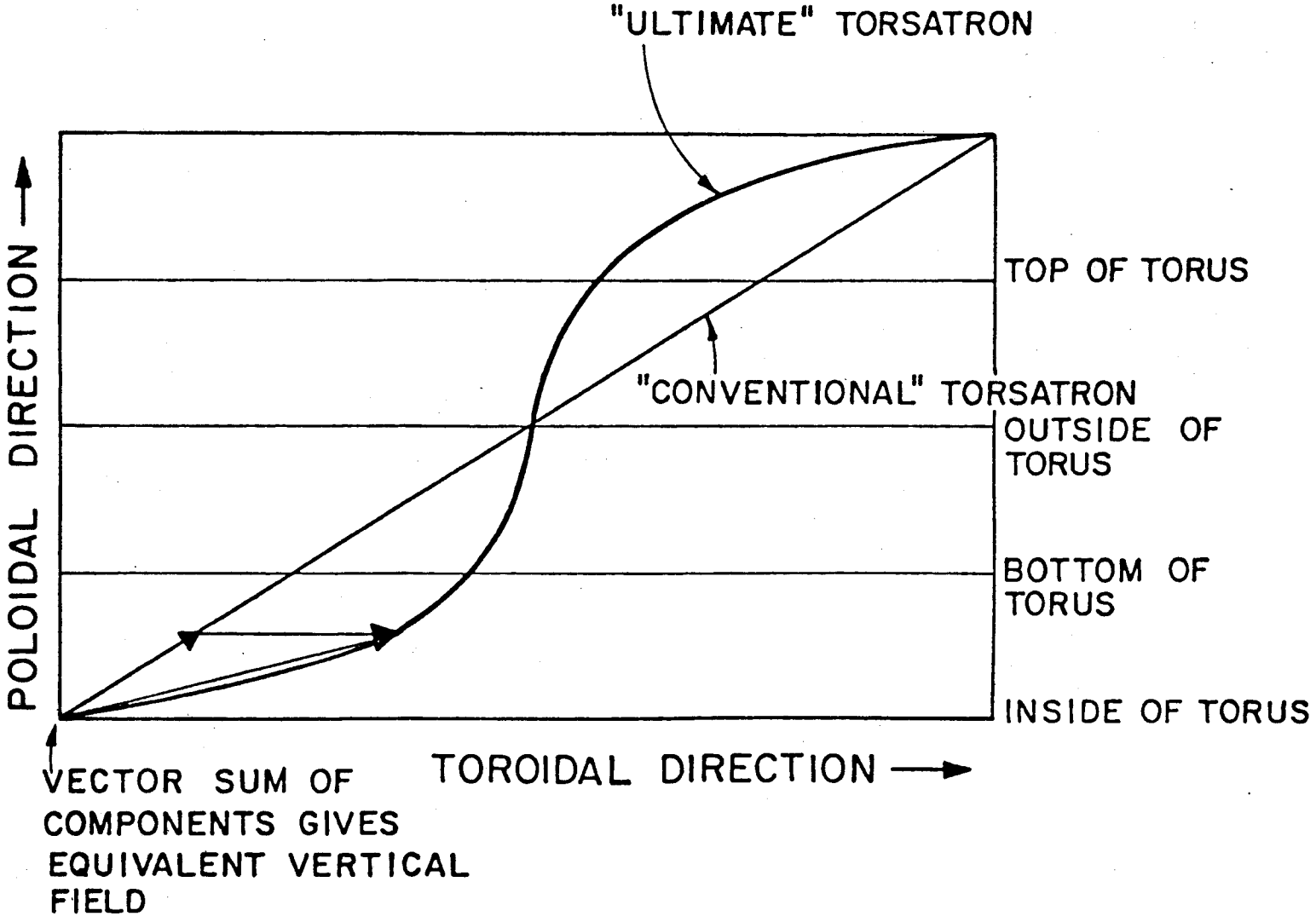

the current in the ultimate torsatron winding differs from the conventional winding in just such a way as to produce a component of current in the same direction as that of an appropriate compensating vertical field coil. This is the case on both the inside and outside, since the net vertical field from both deformed parts is in the same direction. An ultimate torsatron only needs a small vertical field trim coil to be used to vary the transform profile, etc., if desired.

Another method used to produce stellarator configurations is the "twisted-coil" stellarator.[15-19] Figure IV.1-15 shows a plan view of a sketch of such a device. Basically, a twisted coil stellarator is made of a set of deformed toroidal field coils, that are bent in such a way as to simulate a section of a continuous helix. The heavy line in the figure corresponds to the trace of a single effective helix.[20] A potential reactor advantage of this configuration is that the coils may be made in individual modules, rather than in continuous helices as in the more traditional stellarator/torsatron configurations.

Figure 8 stellarators generate rotational transforms by deformation of the torus into a "pretzel" or 3-dimensional figure 8 configuration.[21] These devices tend to have low shear. The transform is proportional to the deformation of the torus. A sketch is shown in Fig. IV.1-16. Extensions of this concept have resulted in stellarators whose magnetic axis varies spatially around a torus (Heliac).[22,23]

In addition to the magnetic surfaces shown in Figs. IV.1-6 and IV.1-10, it is also important to determine the surfaces of constant magnetic field (mod-B surfaces). Figure IV.1-17 shows the mod-B surfaces for a stellarator and a torsatron. A distinct difference between them appears. Stellarators

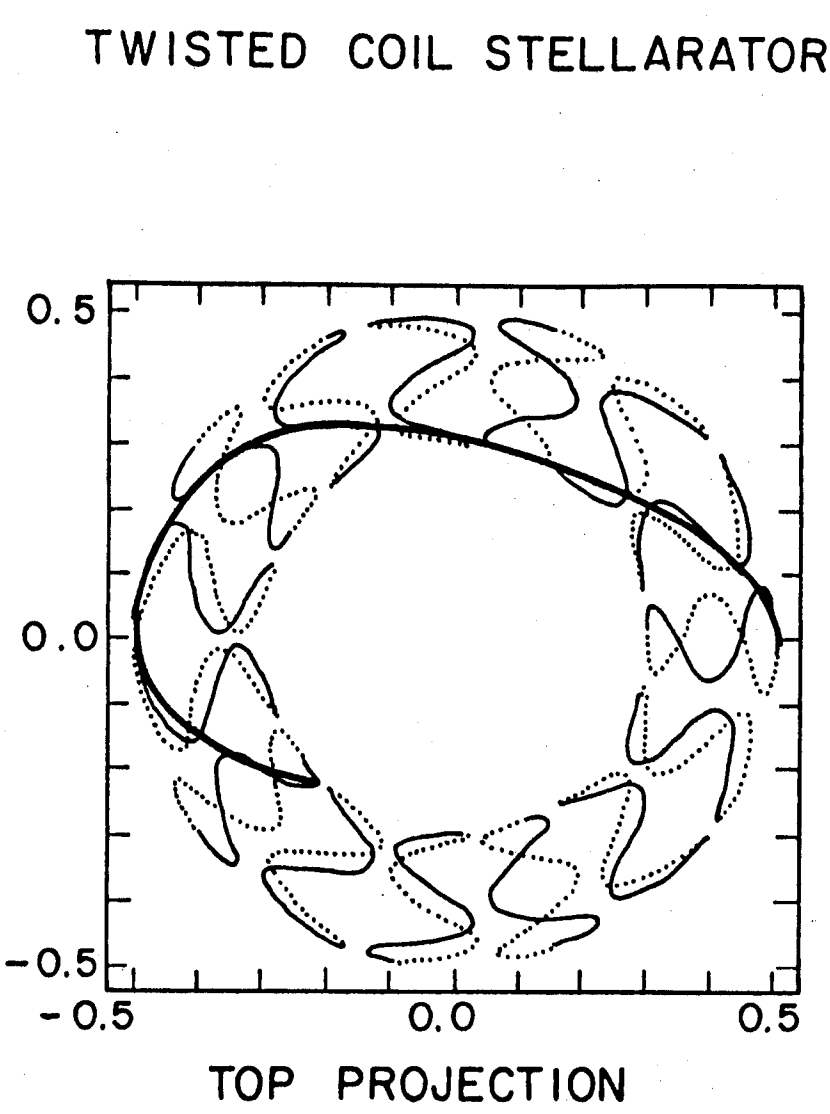

Figure IV.1-15 A twisted coil stellarator. The heavy line traces out an effective helix.

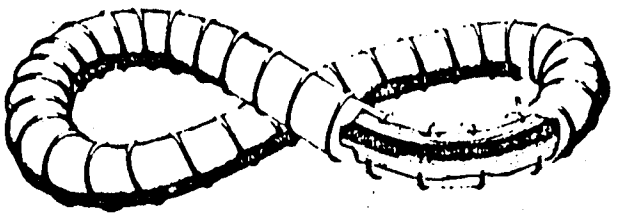

Figure IV.1-16 A figure 8 stellarator.

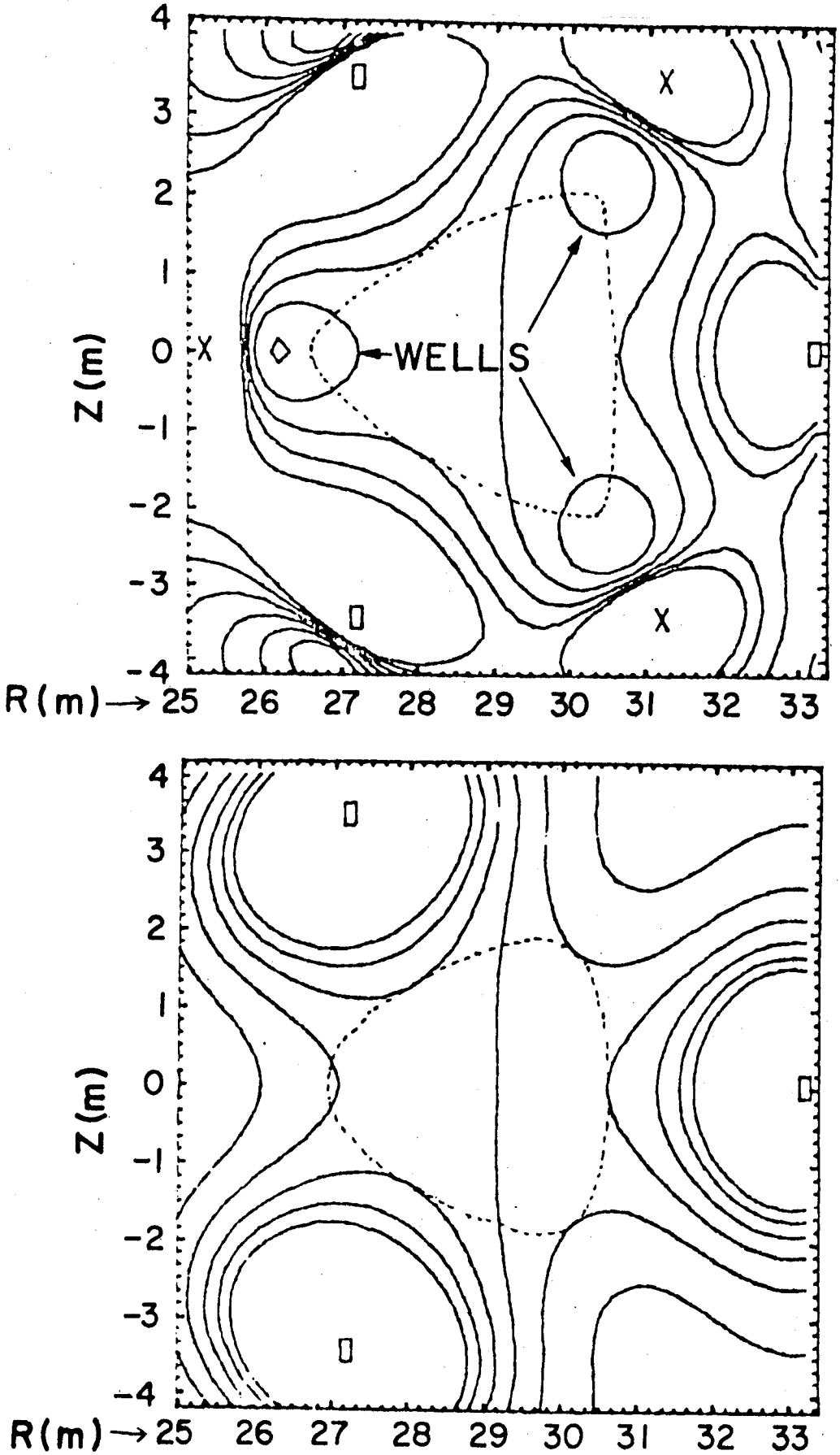

Figure IV.1-17 Mod-B surfaces of a stellarator (top) and a torsatron (bottom). Note the presence of the magnetic wells in the case of the stellarator. The dotted lines are the last closed magnetic surfaces, respectively.

tend to have local magnetic wells, while torsatrons have no such wells. These wells are distinguished from the "flux-averaged wells" defined as the derivative of the function V' (V")

$$V' = \lim_{L\to\infty} \frac{1}{L} \int \frac{d\ell}{B} \quad \text{where } L = \int d\ell \text{ the distance along the field line}$$

which exists in both stellarators and torsatrons. These flux wells also can be changed into anti-wells (hills) by adjusting the currents in vertical field coils in both the stellarator and torsatron configuration.

A maximum-B stellarator[24] not only has local wells as shown in the figure, but will also have a global mod-B surface that is also closed, of roughly the same area as the last closed magnetic surface. This is shown in Fig. IV.1-18.

A final property of stellarators/torsatrons is observed in examining the value of the magnitude of the magnetic field as a magnetic field line is followed around the torus. Figure IV.1-19 shows a comparison between a tokamak, a stellarator and a torsatron.[25] One can see that a toroidal magnetic mirror appears in all three devices, but the latter two configurations have both toroidal and local mirrors (helical mirrors). Although a tokamak may have ripple that looks like the ripple of a stellarator or torsatron due to the fact that all tokamaks generate their toroidal field from spaced coils, the ripple is really quite different, since only in the case of a stellarator/torsatron is the ripple truly helical.[26] Table IV.1-2 shows a summary of the various stellarator/torsatron configurations discussed in this section, grouped into two categories - stellarators, characterized by no net dipole moment and torsatrons, having a net dipole moment.

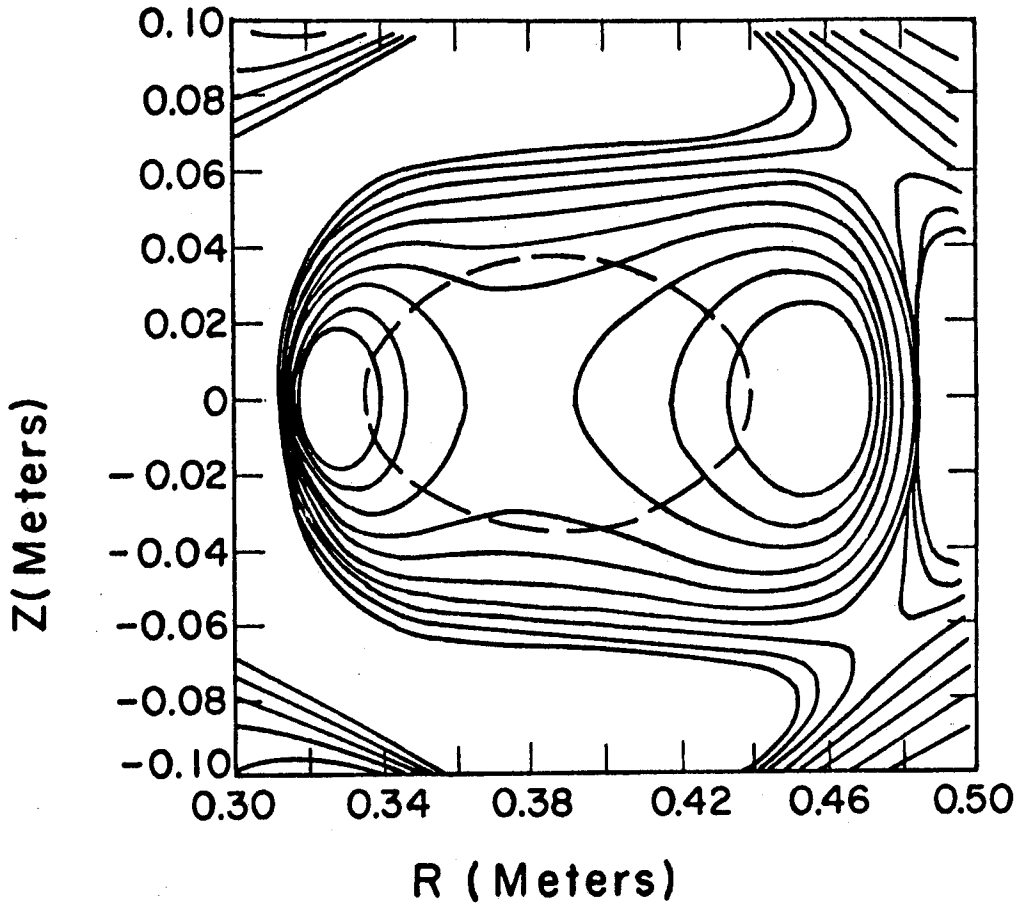

Figure IV.1-18 A maximum-B $\ell = 2$ stellarator.

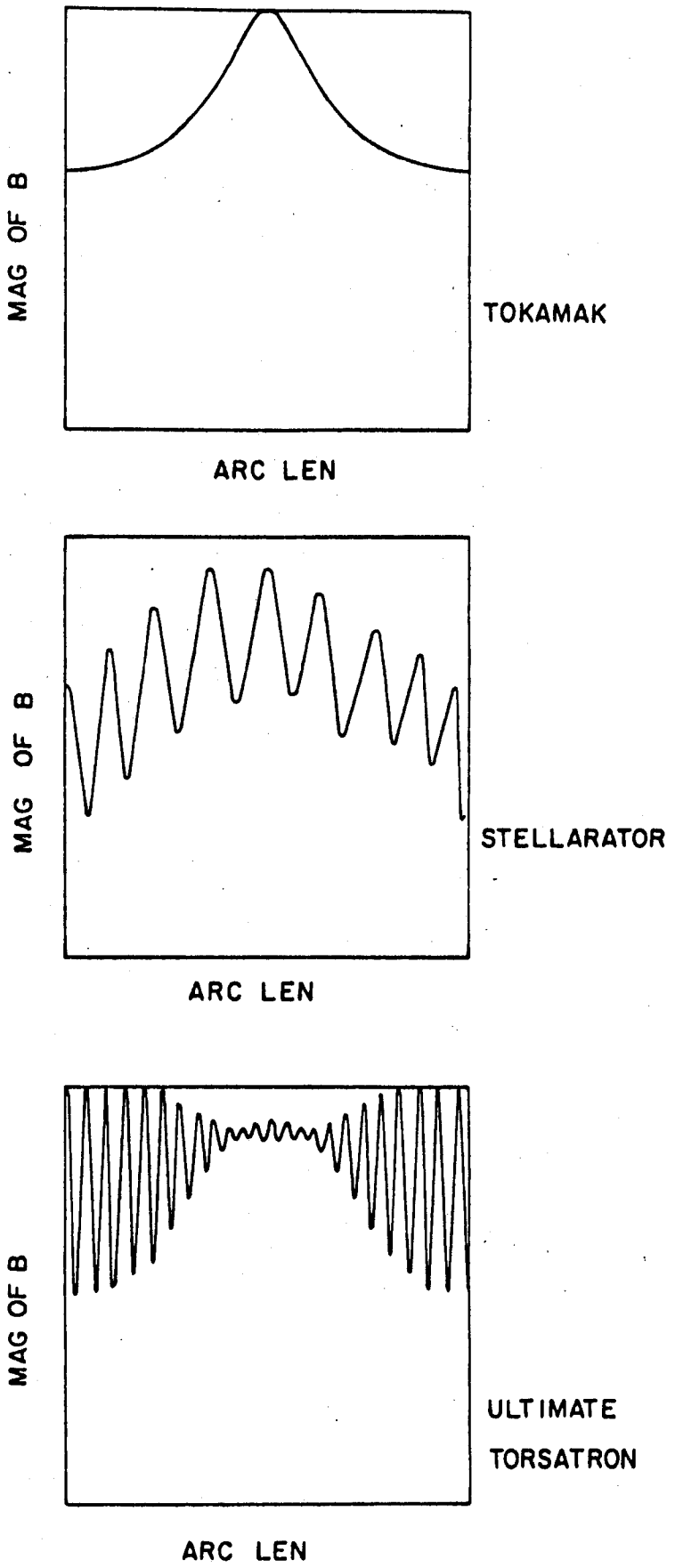

Figure IV.1-19 Mod-B versus distance along a magnetic field line for a tokamak, stellarator and a torsatron.

Table IV.1-2: Categories of Stellarator-Type Devices

Stellarators (Characterized by no net dipole moment)

A. Conventional stellarators: currents in adjacent helical windings go in opposite directions -- external toroidal field is required.

B. Modular stellarators: rotational transform is provided by a single set of non-planar toroidal field coils, or elliptical cross-section toroidal field coils, or a combination of both -- modular stellarator configurations can also be achieved by adding torsion to a toroidal magnetic field through geometry, as in a "figure 8" stellarator.

Torsatrons (characterized by a net dipole moment)

A. Conventional torsatrons: currents in adjacent helical windings go in the same direction, producing both toroidal and poloidal fields -- external vertical field coils are required for surface formation.

B. Ultimate torsatrons: modulation of the conventional torsatron winding law in such a fashion that the dipole field is removed in the region of plasma confinement -- no vertical field is required.

C. Heliotron: torsatron with an additional external toroidal field.

D. Modular torsatrons: use of the windback (as all helical currents flow in the same toroidal direction) to generate the required vertical field.

E. Heliac: planar toroidal field coils whose centers follow a helix, with a circular loop of current along the minor axis -- modular except for the possible linking of the toroidal field coils by the hardcore.

References for Chapter IV

1. L. Spitzer, Jr., Phys. Fluids 1, 253 (1958).

2. K. Miyamoto, Nuclear Fusion 18, 2 (1978).

3. G. Grieger, private communication.

4. A. Gibson, Phys. Fluids 10, 1553 (1967).

5. A. I. Morosov, and L. S. Solovev, Reviews of Plasma Physics, (M. A. Leontovich, Ed.) 2 (1966).

6. T. Ohkawa, Maxwell Prize Address, Annual Meeting, Division of Plasma Physics, American Physical Society, 1979.

7. C. Gourdon, D. Marty, E. K. Maschke and J. P. Dumont, Plasma Physics and Controlled Nuclear Fusion Research (Proc. 3rd Int. Conf. Novosibirsk, 1968) 1, IAEA, Vienna (1969) 845.

8. C. Gourdon, D. Marty, E. K. Maschke and J. Touche, Nuclear Fusion 11, 161 (1971).

9. J. A. Derr, private communication.

10. K. Uo, Plasma Physics 13, 243 (1971).

11. K. Uo, Nuclear Fusion 13, 661 (1973).

12. K. Uo, Phys. Soc. Japan 16, 1380 (1961).

13. K. Uo, A. Iiyoshi, Sh. Yoshioka, T. Ishida, Sh. Konoshima and M. Sato, in Plasma Physics and Controlled Nuclear Fusion Research (Proc. 4th Int. Conf. Madison, 1971) 3, IAEA, Vienna (1971) 3.

14. C. Gourdon et al., C. R. Acad. Sci. 271, Paris, 843 (1971).

15. Yu. N. Pentrenko and A. P. Popryadukhin, in Toroidal Confinement (Proc. 3rd Int. Symp. Garching, 1973), paper D8.

16. S. Rehker and H. Wobig, Fusion Technology (Proc. 7th Symp., Noordwijkerhout, 1974) 345.

17. S. Rehker and H. Wobig, Max Planck Institut für Plasmaphysik Report IPP 2/215 (Aug. 1973).

18. K. Ohasa and K. Miyamoto, Jap. J. Appl. Phys. 16, 813 (1977).

19. T. K. Chu, H. P. Furth and C. Ludescher, Bull. Am. Phys. Soc. 24, 956 (1979).

20. J. A. Derr, private communication.

21. L. Spitzer, Jr., Phys. Fluids 1, 253 (1958).

22. S. Nagao, K. Sugita, H. Watanabe, Y. Goto and Y. Kondo, J. Phys. Soc. Japan 27, 1082 (1969).

23. S. Nagao, H. Watanabe, K. Koyama, Pulsed High Beta Plasmas (D. E. Evans, Ed.), Pergamon Press, Oxford (1976) 369.

24. S. Fisher, H. Grad, Y. Sone and J. Staples, Plasma Physics and Controlled Nuclear Fusion Research (Proc. 3rd Int. Conf. Novosibirsk, 1968), IAEA, Vienna (1969) 899.

25. D. T. Anderson, private communication.

26. D. T. Anderson, J. A. Derr and J. L. Shohet, IEEE Transactions on Plasma Science PS-9, 212 (1981).

V. Parametric Considerations

The process of determining the plasma parameters began with the coil winding law and magnetic topology considerations discussed in Chapter IV. Initial constraints for this work were that we use modular coils and utilize the "natural" helical divertor associated with these coils. The choice of modular coils was based on considerations of maintainability and is discussed in Chapter XIII. The magnetic divertor property was utilized because it "comes for free" and has a better experimental data base for impurity control than the alternative of pumped limiters.

This decision, however, imposes a constraint on the coil system and the design of the reactor. This means that the plasma is bounded by the magnetic separatrix and cannot be bounded arbitrarily inside the separatrix surface, as is the case with pumped limiters. Between the separatrix and the first wall will be a scrape-off zone of about 20 cm in width. In addition, there must be adequate space for the blanket and shield between the first wall and the inner edge of the magnets. This drives the design to coil configurations for which the magnetic volume utilization η_V (the fraction of the volume inside the coil radius which is occupied by the plasma) is reasonably small, if the reactor size and power level is to be kept to a reasonable value.

The natural divertor in the stellarator family occurs as a consequence of the existence of the magnetic separatrix bounding the region of closed nested-flux surfaces. The existence of this separatrix can be proven for straight stellarators with perfect helical symmetry.[1] Inside the separatrix, the enclosed magnetic flux links all of the magnet coils. Outside the separatrix, however, the flux links some, but not all, of the coils. Thus some magnetic flux must emerge from the device between adjacent coils. To conserve flux, it

must re-enter the device at a different location. This property of the magnetic flux external to the separatrix is the basis for the magnetic divertor topology, which can be found in any toroidal system characterized by a magnetic separatrix.

Although nonaxisymmetric toroidal configurations do not have simple closed flux surfaces in terms of a rigorous mathematical existence, it can be shown that in many cases, closed surfaces may be described asymptotically in these devices.[2] Numerical tracing of magnetic field lines for such configurations shows that for divertor applications, an effective separatrix may be assumed to exist. Since modular stellarators can be shown to have such a separatrix, they also may have naturally occurring divertors.

We have studied the properties of $\ell = 3$ modular stellarators having coils with large deflections from the poloidal plane. The divertors in these configurations have been found to be highly localized and modular in nature, resembling small bundle divertors distributed over the surface of the torus.

The stellarators studied consist of discrete modular coils arranged into a torus having a number of field periods. The coils are very similar to Rehker-Wobig coils,[3] but follow a modified winding law[4] which produces surfaces having greater rotational transform and a magnetic axis which is shifted inward from the geometric axis of the torus. The coils are assumed to be composed of filaments which follow curves on the surface of a circular torus. The curves are defined by the expression

$$\theta^n(\phi) = \frac{-3\sqrt{3}}{2\pi m} \sin\left[\ell\phi - \frac{2\pi n}{3}\right] + \frac{2\pi n}{3m}, \qquad n = 1, 2, 3, \ldots, 3m .$$

$\theta^n(\phi)$ is the toroidal angle coordinate of the nth curve on the torus as a

function of the bipolar poloidal angle ϕ.[5] ℓ is the poloidal multipolarity of the coil, and m is the number of field periods; n is an index which labels each coil. Note that there are three coils composing each field period of the device.

Having defined the toroidal excursions of each coil as a function of the poloidal angle, we may obtain the cartesian components (x,y,z) of the coil filaments from the expressions

$$a = \sqrt{R^2_{major} - R^2_{minor}}$$

$$\cosh \eta = R_{major}/R_{minor}$$
$$\sinh \eta = a/R_{minor}$$

$$r = \frac{a \sinh \eta}{\cosh \eta - \cos \phi}$$

$$z = \frac{a \sin \phi}{\cosh \eta - \cos \phi}$$

$$x = r \cos \theta$$
$$y = r \sin \theta \ .$$

This winding law produces magnetic surfaces nested about an axis with a radius of approximately r = a, rather than r = R_{major}, as is the case for the Rehker-Wobig coils.

A systematic study of the winding law properties was made for ℓ = 3 configurations having 4, 5, 6, or 7 field periods. The coil aspect ratio was varied from three to ten, and the magnetic separatrix, its volume, and rota-

tional transform were computed numerically for each case using the TORFIELD[6] field line tracing code. Figure V-1 summarizes the results of the parametric study. The upper figure shows the average rotational transform at the magnetic separatrix plotted as a function of the coil aspect ratio. For each of the four configurations, the rotational transform is relatively low at low coil aspect ratios, reaches a peak value at an intermediate aspect ratio, and decreases at higher aspect ratios. Note that at a fixed-coil aspect ratio, increasing the number of field periods in the configuration can either increase or decrease the rotational transform at the separatrix.

The lower figure shows the magnetic volume utilization for each configuration also as a function of the coil aspect ratio. The volume utilization is the percentage of the total torus volume which is enclosed by the magnetic separatrix. For this winding law, magnetic volume utilizations approaching 50 percent were obtained at low coil aspect ratios. Note that at a fixed-coil aspect ratio, increasing the number of field periods increases the magnetic volume utilization for all four configurations.

The parametric study showed that a wide variety of different magnetic configurations could be obtained with the winding law. These different configurations are characterized by diverse separatrix shape, rotational transform, and suitability for divertor utilization.

The low aspect ratio regime has a separatrix which shows evidence of both $\ell = 3$ and $\ell = 6$ harmonic components in its structure. The rotational transform is very low, and the configuration appears to be unsuitable for effective utilization of the magnetic divertor, since the closed flux surfaces closely approach the coil system, leaving little room for a scrape-off zone, shielding, and coil support structure.

Figure V-1 Rotational transform at the separatrix and magnetic volume versus coil aspect ratio for 5, 6 and 7 field positions.

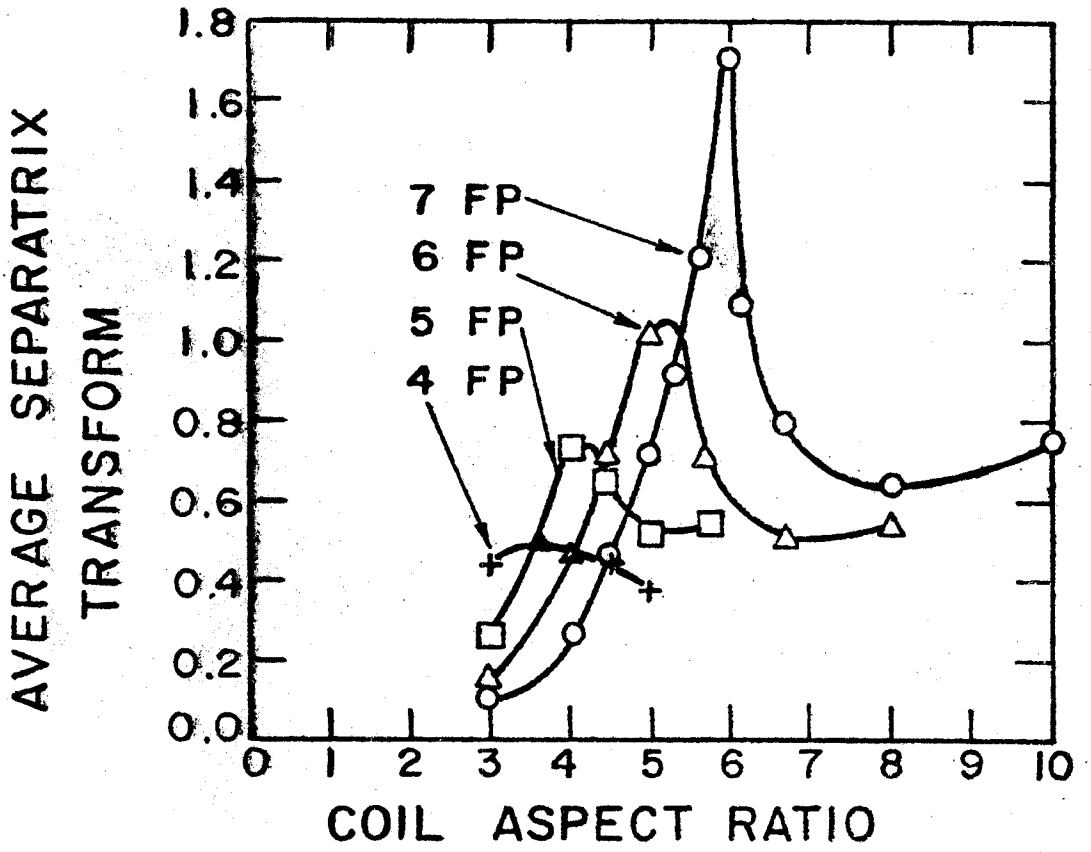

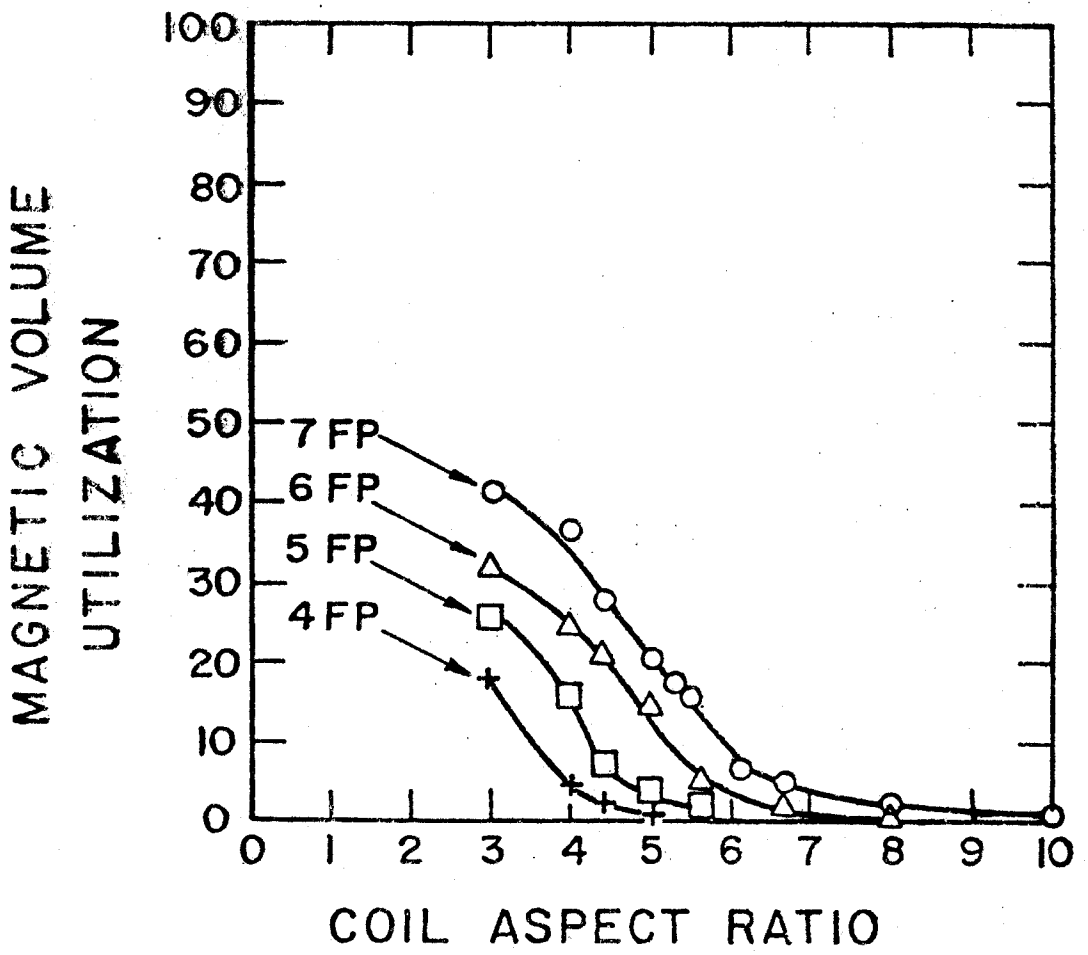

The intermediate aspect ratio regime is characterized by high values of rotational transform and cusp-like separatrix cross sections. It occurs at the peaks in the curves on the upper plot of Fig. V-1. This regime has been found to be quite suitable for utilization of the magnetic divertor, and has been adopted for this reactor design study.

The high aspect ratio regime is characterized by magnetic surfaces and rotational transform profiles which are very similar in shape to those obtained in classical stellarators and torsatrons. The divertors in this regime, though modular in nature, are also quite similar to those which occur in the continuous helical devices.[7,8] This regime may be unsuitable for reactor application due to the relatively high plasma aspect ratio; typically twenty or greater. Devices in this regime must be very large to obtain a sufficiently large plasma minor radius for confinement of a reactor-grade plasma.

Figure V-2 shows a schematic illustrating the coil radius r_c and the equivalent plasma radius r_p. The latter is defined such that the volume inside the torus of minor radius r_p and major radius R equals the actual volume inside the magnetic separatrix, i.e. the actual plasma volume. Then the magnetic volume utilization η_v is

$$\eta_v = \frac{\text{plasma volume}}{\text{coil volume}} = \left(\frac{r_p}{r_c}\right)^2 = \left(\frac{A_c}{A_p}\right)^2 , \qquad (V.1)$$

where A_c is the coil aspect ratio R/r_c, and A_p is the plasma aspect ratio R/r_p. We neglect for simplicity in this discussion the shift of the magnetic axis from the coil axis.

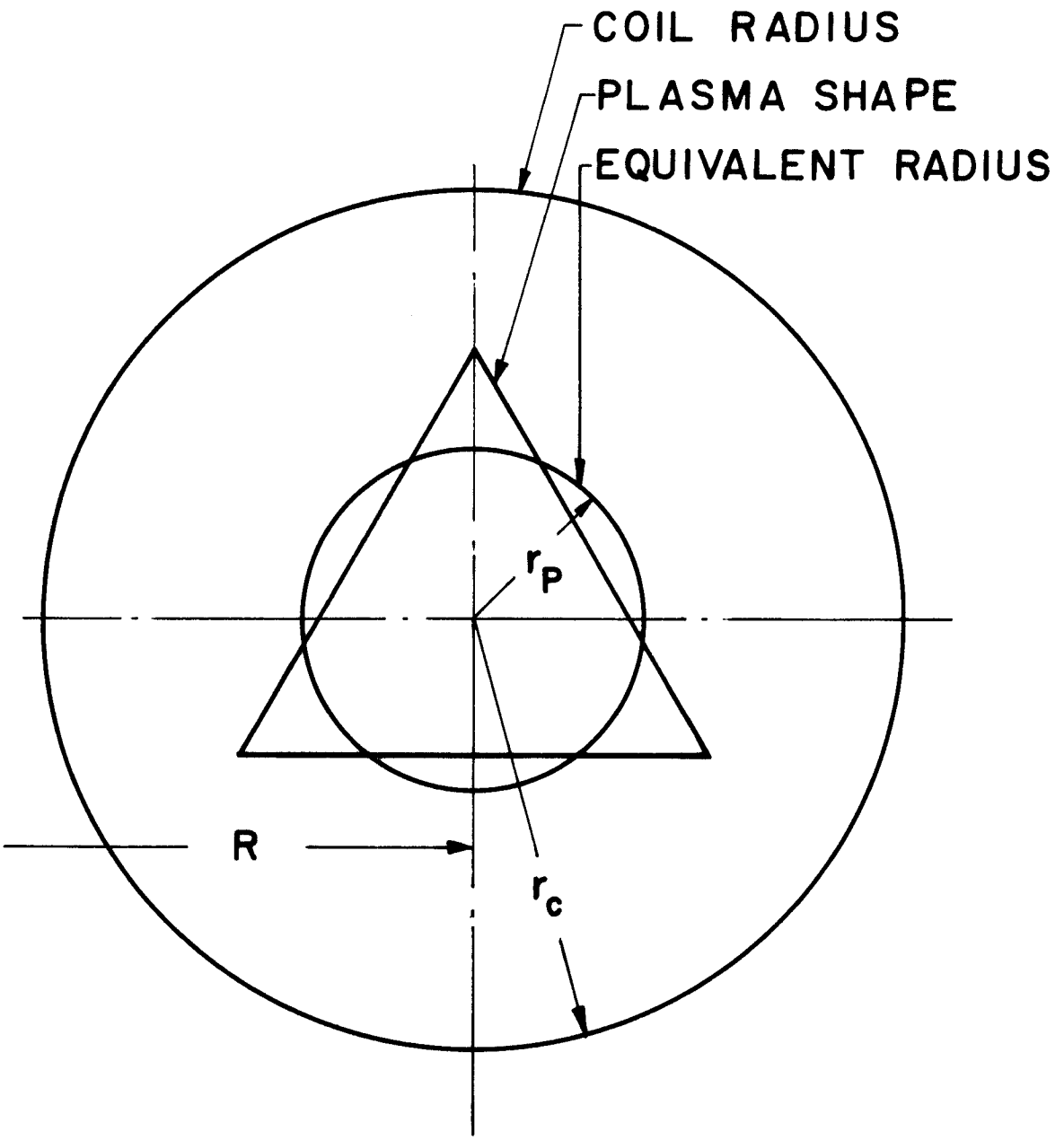

R = MAJOR RADIUS

A_c = COIL ASPECT RATIO = R / r_c

A_P = PLASMA ASPECT RATIO = R/r_P

Figure V-2 Schematic showing coil radius and equivalent plasma radius.

The plasma radius r_p is related to the coil radius r_c by

$$r_p = r_c\sqrt{\eta_v} \ . \tag{V.2}$$

Imposing the requirement of adequate space for the blanket and shield gives the relation

$$r_c \geq r_p + \delta_v \ , \tag{V.3}$$

where the separation δ_r is taken to be 3.05 m to allow for the blanket shield, scrape-off zone, half the coil thickness, and required thermal insulation. Equations (V.2) and (V.3) imply that, for a given η_v and δ_r, there is a minimum plasma volume, equal to

$$V_p = 2\pi^2 r_p^2 R = 2\pi^2 \delta_r^3 \frac{A_p A_c^3}{(A_p - A_c)^3} \ . \tag{V.4}$$

This is illustrated in Fig. V-3. Shown in Fig. V-4 is the plasma aspect ratio and minimum plasma volume for the winding law used in Fig. V-1. It can be seen that the minimum plasma volume decreases with increasing coil aspect ratio, which also corresponds to increasing coil aspect ratio, which also corresponds to increasing plasma aspect ratio. The normalization factor $(2\pi^2\delta_r^3)$ for the plasma volume equals 560 m^3 if δ_r = 3.05 m; consequently the plasma volume, and therefore the power output, can get rather large if a low plasma aspect ratio is required. At a normal (and moderate) power density of $\sim$ 3 W/cm^3 in the plasma, one needs to keep $\overline{V}$ $(= V_p/(2\pi^2\delta_r^3))$ less than or about three in order to keep the thermal power output $\lesssim$ 5000 MW. For the UWTOR-M

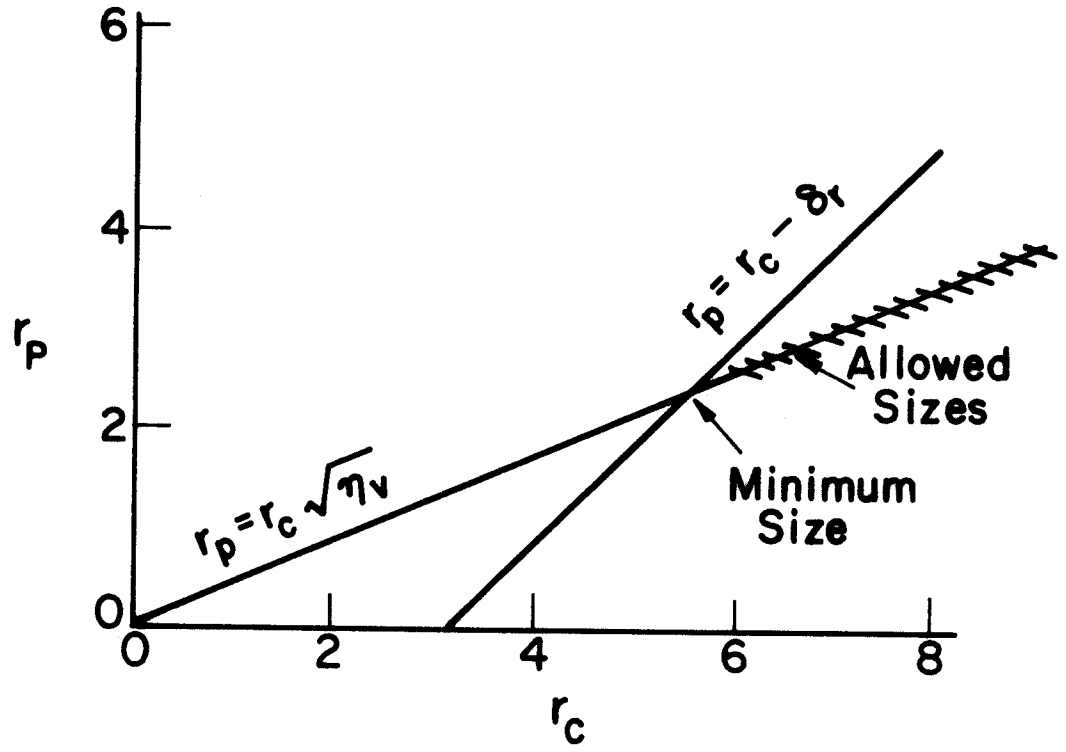

Figure V-3 Plasma radius versus coil radius and the range of allowable sizes which have adequate room for the blanket and shield.

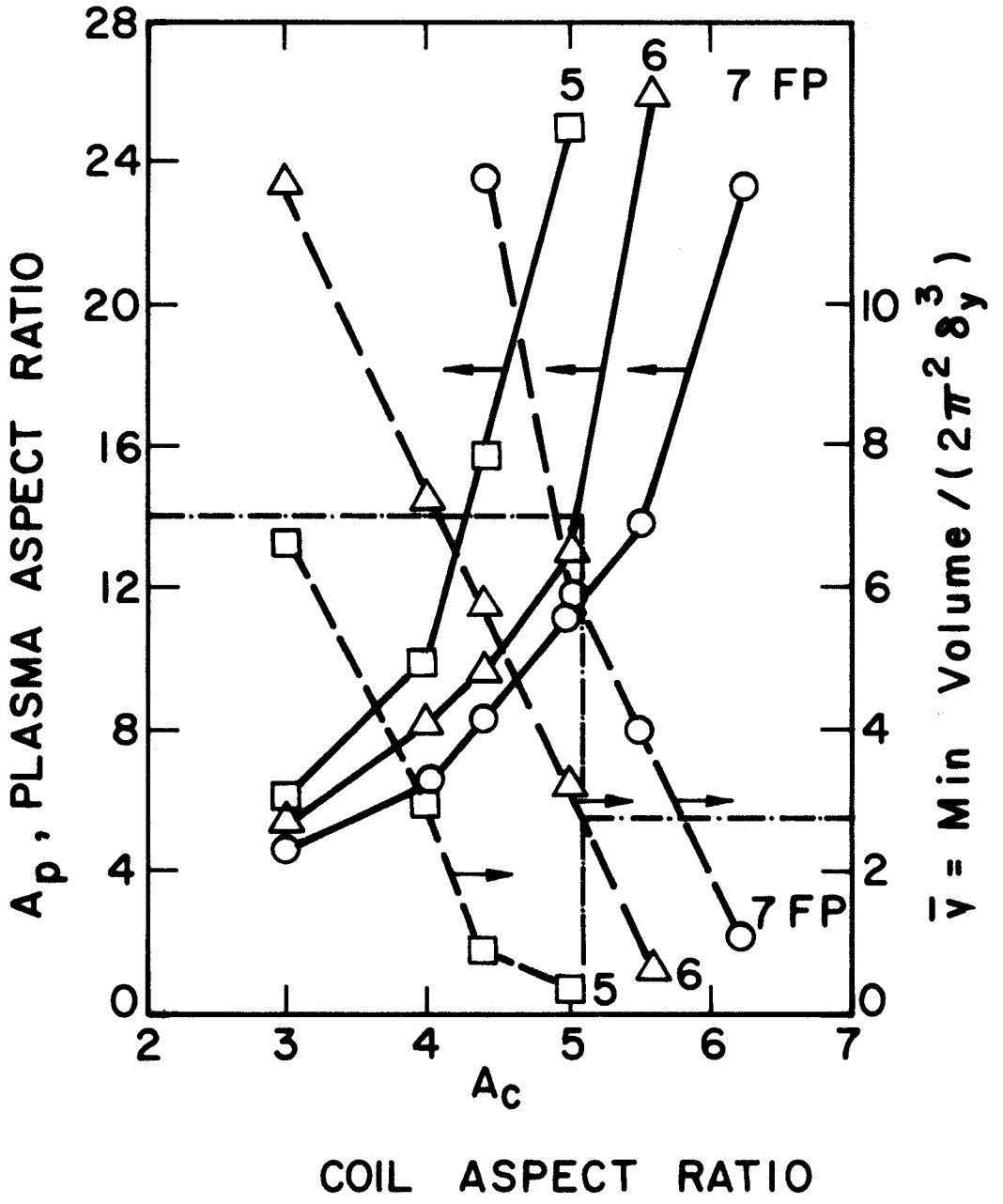

Figure V-4 Plasma aspect ratio and minimum plasma volume versus coil aspect ratio for 5, 6 and 7 field periods.

design, the point A_c = 5.05, A_p = 14, with 6 field periods, and a plasma volume of 1400 m^3 was chosen. This point is at the peak of the rotational transform curve, Fig. V-1, and therefore should have good MHD stability properties, at least according to simple arguments. This, however, needs to be checked by detailed MHD calculations. These are beyond the scope of this study and have not been done.

The transport calculations done for this configuration are presented in Chapter VI. Parametric studies of the power output versus mean density and density profile effects are given there. Ideally, one would want to couple those calculations with the considerations of this section through an iterative feedback loop to better optimize the entire system. An important ingredient in this optimization, however, are the magnet and support structure costs. Such an optimization study has not been done because it would be too costly and of limited value because some of the important physics aspects (MHD considerations, transport coefficients, etc.) are not sufficiently well established. The design point chosen appears reasonable, at least in terms of qualitative considerations.

References for Chapter V

1. A.I. Morozov and L.S. Solov'ev, Reviews of Plasma Physics, Consultants Bureau, New York, 1966, Vol. 2, p. 48.

2. K.J. Whiteman, Rep. Prog. Phys. 40, 1033 (1977).

3. S. Rehker and H. Wobig, Max Planck Institut für Plasmaphysik, IPP 2/215, 1973.

4. J.A. Derr, International Workshop on Stellarators (EPS Study Conf.), Schloss Ringberg (Lake Tegernsee (Bavaria)), FRG, Session B.3.5, 1980.

5. P. Moon and D. Spencer, Field Theory Handbook, Springer-Verlag, New York, (1971), p. 112.

6. T.J. Martin, private communication.

7. C. Gourdon, D. Marty, E.K. Maschke, and J. Touche, Nucl. Fusion 11, 161 (1971).

8. C. Gourdon, D. Marty, and J. Touche, "Fusion Technology," in Proc. 6th Symposium, Aachen, 1970, p. 485.

VI. Plasma Analysis

VI.1 Introduction

UWTOR-M is a six field period modular stellarator with a multipolarity of three. The strong twist of the modular coils gives a strongly sheared rotational transform profile with little transform on the magnetic axis of the machine and a transform of slightly greater than one at the separatrix (Fig. VI.1-1). This strong shear should allow a moderate value of beta to be achieved. In this design a volume average toroidal beta of 6% has been assumed, although this has not been substantiated by three-dimensional MHD calculations. The plasma is assumed to be bounded by the $\ell = 3$ magnetic separatrix. Outside the separatrix, the field lines map into the helical divertor and thus form a scrape-off layer. The magnetic topology, including the divertor, is described in detail in Chapter IV.

The machine has a large helical field ripple, strongly peaked near the edge of the plasma where it has a value of 23% (Fig. VI.1-2). This ripple is expected to produce an extremely high ion thermal conductivity near the plasma edge. The effect is to produce an ion temperature profile which is much flatter than is the case in tokamaks, with a high temperature at the plasma edge. The energy loss from the plasma due to this high edge temperature, while large, should not be excessive, being limited due to the fact that particle transport is not overly large. The ions lost by the plasma are hot, but the rate is moderate and so the energy loss is tolerable and ignited operation is possible.

Measurements on Wendelstein VIIA and Heliotron-E lead one to expect a low level of anomalous particle and electron energy transport in a zero net current stellarator.[1,2] In this study 1/5 of the Alcator scaling value has

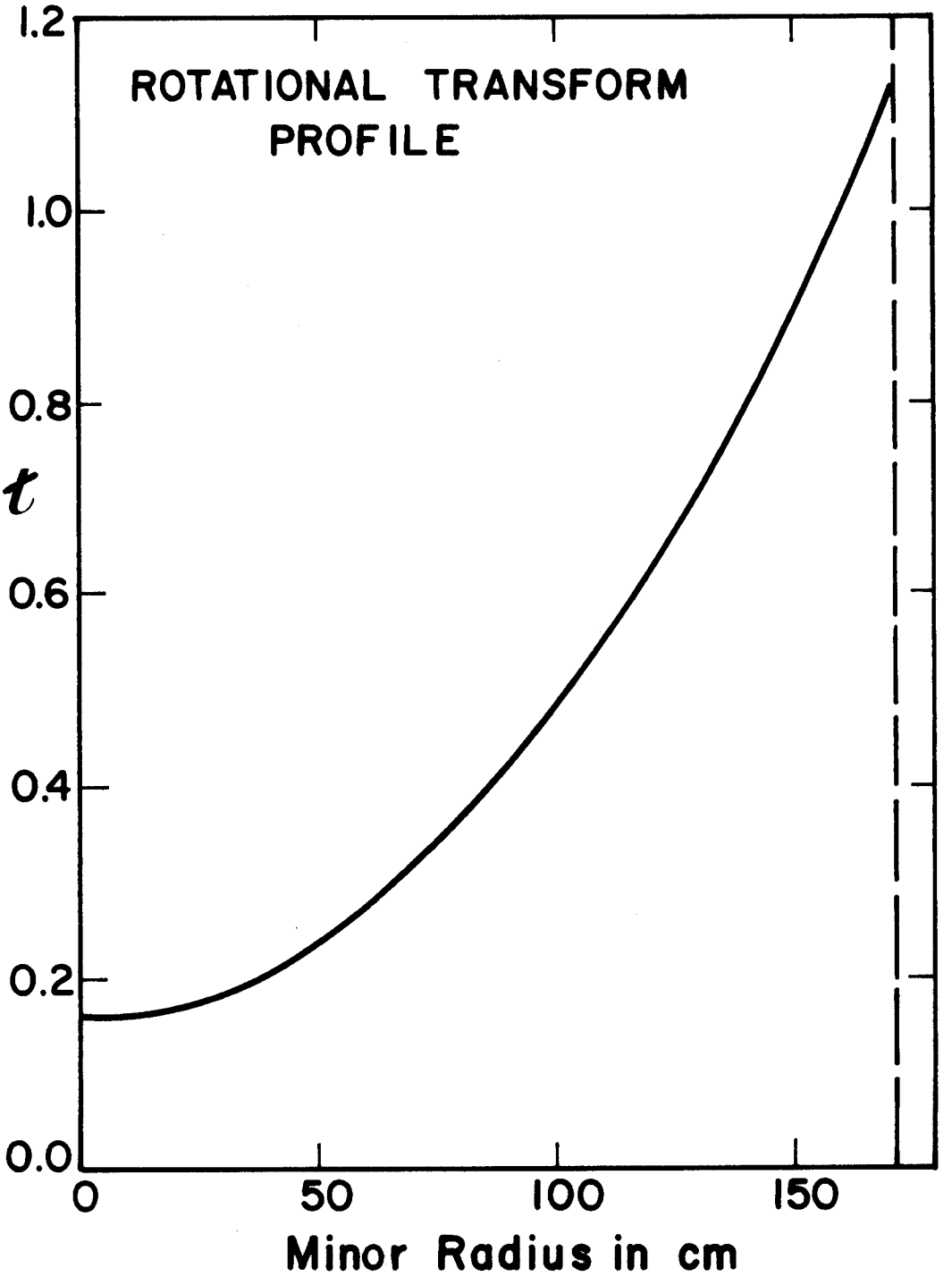

Figure VI.1-1 Rotational transform, ι, as a function of minor radius.

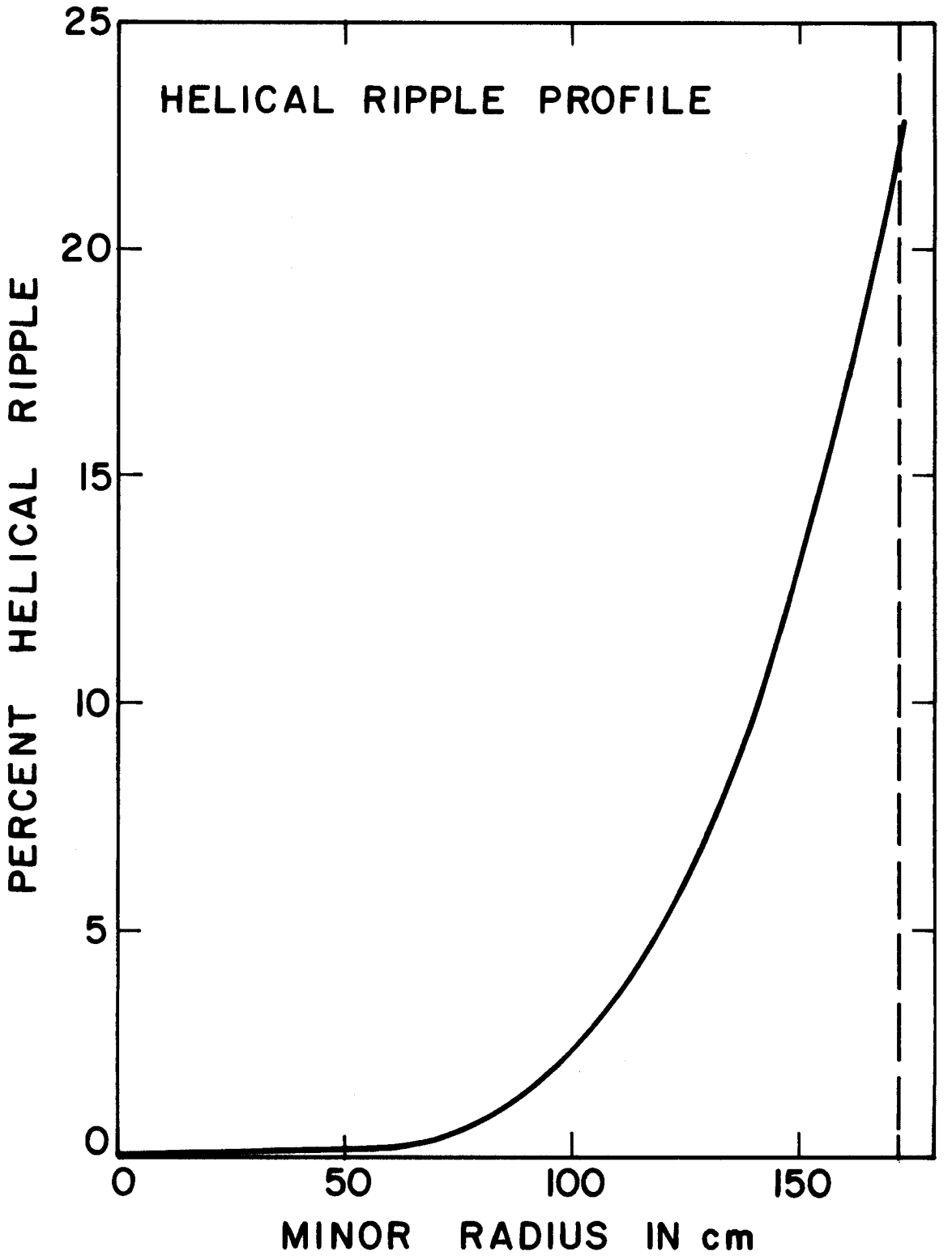

Figure VI.1-2 Helical magnetic ripple (in %) as a function of minor radius.

been used. This low level of electron energy loss coupled with the large ion energy losses tends to produce a plasma electron temperature much higher than the ion temperature. This is an undesirable situation inasmuch as excessively hot electrons will substantially increase the plasma pressure. Since the beta that the device can tolerate is fixed, this leads to a lower allowable plasma density, and thus to a lower power output.

To counteract this tendency, it is proposed that a small amount of a high-Z impurity, nominally xenon, be added to the plasma. This will produce large amounts of line radiation which will lower the electron temperature and will rather uniformly distribute the power of the plasma on the first wall of the device. This impurity injection also allows a means of burn control. In the transport calculations the machine is operated in what is apparently a thermally unstable regime; feedback on the impurity concentration and/or pellet injection in combination with gas puffing can provide control. Since the plasma energy confinement time is on the order of a second, the feedback can be on a leisurely time scale. In actuality, the chosen regime may not be thermally unstable; increased transport as the beta limit is approached (an effect not included in the transport code) might provide thermal stability.

The plasma is assumed to be pellet fueled. Simulation indicates that gas puff fueling is ineffective at reactor temperatures and densities. Pellet fueling and efficient divertors with low backstreaming also minimize the neutral gas density near the first wall. This is important, as the high ion temperature near the wall can cause excessive energy loss and wall damage if the neutral density is not kept low. By altering the pellet velocity, the desired density profile can be chosen.

UWTOR-M is optimally run at a somewhat low temperature compared to most reactor designs. The central ion temperature is only 10.4 keV. This low temperature reduces the effects of field ripple on the transport and for a given beta allows a denser plasma which reduces the alpha particle slowing down time and thus the pressure due to hot alphas.

Startup would be accomplished by ICRH heating. By slowly increasing the temperature until ignition is achieved and then slowly increasing the density, a gentle, steady power rise in the blanket may be maintained. The full power state may then be continued indefinitely without the need of beam or rf drivers. The machine would be shut down by reversing the startup procedure, decreasing the density and slowly reducing the temperature with ICRH-assist. In an emergency, faster shutdown could be achieved by stopping fueling, which would shut the reactor down within a period of seconds, or by injecting impurities, which would cause the energy of the plasma to be radiated immediately to the walls of the torus. Unlike in tokamaks, fast shutdown should not produce a disruption and its attendant wall damage.

VI.2 Transport Model

To model plasma transport in UWTOR-M, an adapted version of the ORNL WHIST tokamak transport code was used.[3,4] This code, called WHISTEL (WHIST for STELlarators), is a one-dimensional radial fluid space-time code.[5] Transport across flux surfaces is modeled by solution of one-dimensional particle and energy transport equations of the form

$$\frac{\partial n_j}{\partial t} = -\frac{1}{r}\frac{d}{dr}(r\Gamma_{\perp j}) + S_{FUS_j} + S_{BEAM_j} + S_{GAS_j} + S_{PEL_j} - \vec{\nabla}_{\parallel}\cdot\vec{\Gamma}_{\parallel j}$$

$$\frac{\partial}{\partial t}\left(\frac{3}{2} n_e T_e\right) = -\frac{1}{r}\frac{d}{dr}\left[r\left(Q_{\perp e} + \frac{3}{2} T_e \Gamma_{\perp e}\right)\right] - Q_{ei} + P_{FUS_e} - P_{RAD} + P_{OHM}$$

$$+ P_{RF_e} + P_{BEAM_e} - P_{NEUT_e} - \vec{\nabla}_{\parallel}\cdot\vec{Q}_{\parallel e}$$

$$\frac{\partial}{\partial t}\left(\frac{3}{2} n_i T_i\right) = -\frac{1}{r}\frac{d}{dr}\left[r\left(Q_{\perp i} + \sum_j \frac{3}{2} T_i \Gamma_{\perp j}\right)\right] + Q_{ei} + P_{FUS_i} + P_{RF_i}$$

$$+ P_{BEAM_i} - P_{NEUT_i} - \vec{\nabla}_{\parallel}\cdot\vec{Q}_{\parallel i}$$

where:

n_j = density of j^{th} ion species

n_i = total ion density

n_e = electron density

T_e, T_i = electron and ion temperatures

S_{FUS_j} = source or sink of ions of species j due to fusion

S_{BEAM_j} = source of ions of species j due to beam injection

S_{GAS_j} = source of ions of species j due to gas puffing

S_{PEL_j} = source of ions of species j from pellet fueling

Q_e, Q_i = electron and ion energy fluxes perpendicular to the magnetic flux surfaces

Q_{ei} = electron-ion re-thermalization

P_{FUS_e}, P_{FUS_i} = power to the electrons and ions due to fusion

P_{RAD} = power lost from the electrons due to radiation

P_{OHM} = power to the electrons from ohmic heating

P_{RF_e}, P_{RF_i} = power to the electrons and ions due to rf heating

P_{BEAM_e}, P_{BEAM_i} = power to the electrons and ions due to neutral beam heating

P_{NEUT_e}, P_{NEUT_i} = power lost from the electrons and ions due to ionization and charge exchange of neutrals

$\Gamma_{\perp j}$ = net flux of ion species j perpendicular to the magnetic flux surfaces

$\Gamma_{\parallel j}$ = net flux of ion species j along field lines in the divertor zone

$Q_{\perp e}, Q_{\perp i}$ = net electron and ion conduction energy fluxes perpendicular to the magnetic flux surfaces

$Q_{\parallel e}, Q_{\parallel i}$ = net electron and ion conduction energy fluxes along field lines in the divertor zone.

The electron density is computed as the ion density times the charge state of each ion, summed over all ion species. Electrons due to impurity species are included in the computation. The sources and sinks of particles and energy from fusion explicitly take account of all reaction paths (i.e., D-D and T-T fusion as well as D-T fusion are taken into account). The loss of hot fusion alpha particles born in unconfined orbits is included in the simulation. It is assumed that $\sqrt{2r/R_o}$ of the alphas are lost to the divertors. Alphas that do not escape are assumed to thermalize on the flux surface on

which they are born. The effects of beam-plasma fusion are also included. The energy and particle source of the beams is computed using an analytic pencil-beam routine which compares well with tokamak Monte-Carlo beam routines but is much faster.[6] The source due to gas puffing is computed using the fast one-dimensional slab neutral transport routine SPUDNUT.[7] A routine PELLET is included to model pellet ablation.[8] The power input form of rf heating is modeled as a Gaussian profile in a vertical slab with a linear dependence on electron density. For ICRH, a fraction $T_e(keV)/13.5$ of the energy is assumed to go to the electrons, the rest to go to the ions. The radiation loss term includes bremsstrahlung, synchrotron, and impurity radiation. The parallel particle and heat flux terms are taken from the bundle divertor model by Emmert,[9] and adapted to properly model the helical bundle divertors of this device.

The equations are discretized using finite differences to approximate the derivatives. The noncircular flux surfaces of stellarators are modeled as equivalent circles. The mapping is such as to preserve volume: the areas of the actual and equivalent tubes of flux are the same (Fig. VI.2-1). This produces some underestimate of the areas of the flux surfaces and of the total transport. The discretized equations are solved using a modified Crank-Nicolson scheme, made more implicit (future-weighted) than the usual time-centered formulation. Nonlinear effects can cause the time-centered Crank-Nicolson scheme to be numerically unstable; slightly increasing the implicitness makes the method stable while only slightly decreasing the numerical accuracy. Time steps are chosen so that the temperatures and densities do not alter excessively over a time step. A 60 mesh point radial grid was used having a smoothly varying grid spacing (grid spacing $\sim r^{-sdr}$, where sdr is a

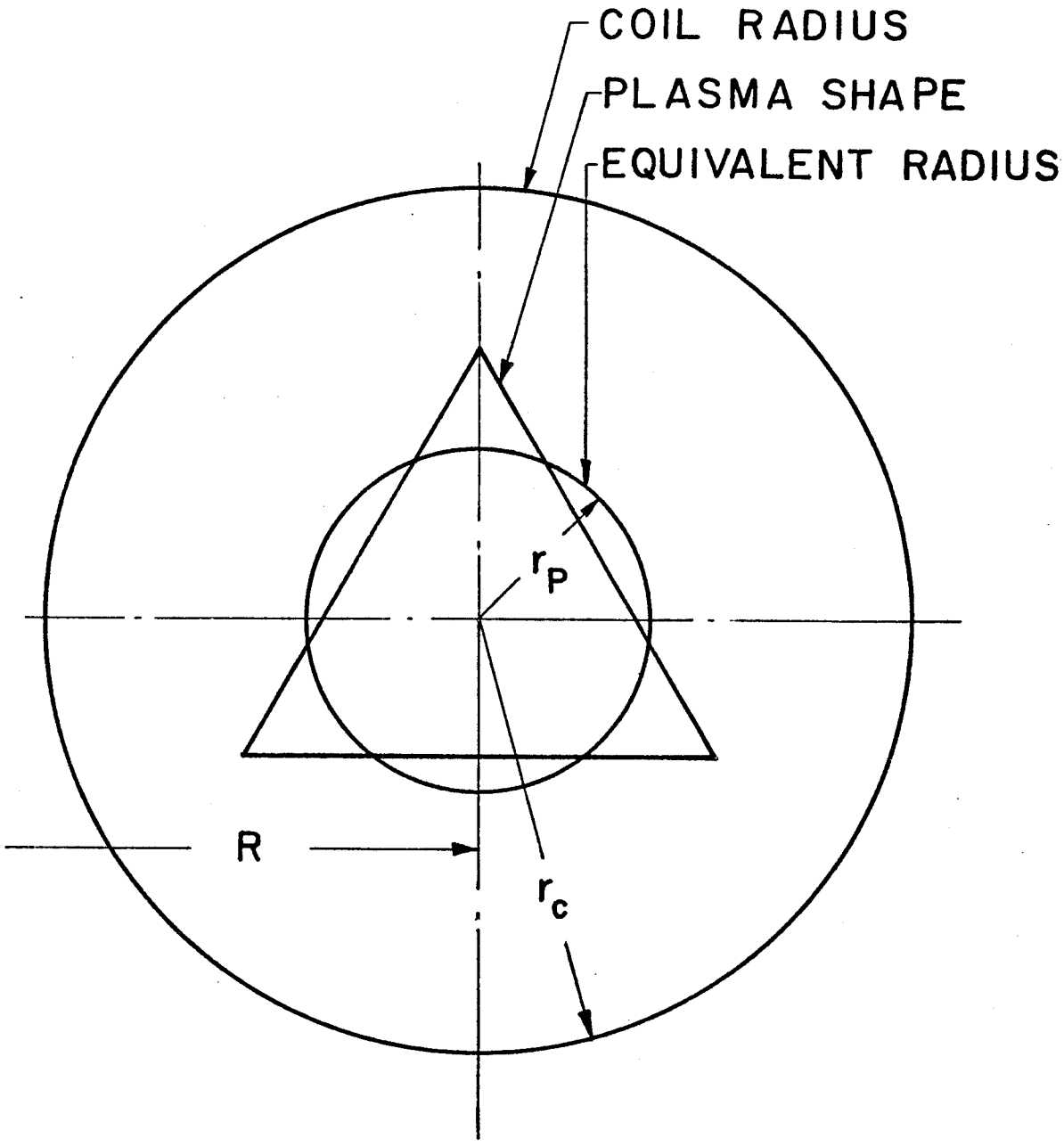

R = MAJOR RADIUS

A_c = COIL ASPECT RATIO = R / r_c

A_P = PLASMA ASPECT RATIO = R/r_P

Fig. VI.2-1. Idealized plasma shape and circular shape used in the transport code.

grid spacing parameter, typically 1-1.5) so that the grid was coarsest near the center of the plasma and finest near the separatrix where the gradients are sharpest. In the scrape-off zone the mesh was fine and uniform. Transport coefficients were computed at points intermediate to the grid points and at densities and temperatures extrapolated to a half a time step ahead so as to preserve the accuracy of the differencing method.

In addition to the transform due to a toroidal current, the code allows for an externally imposed rotational transform to be input. This transform is a factor in the computation of the transport coefficients. During startup the transform profile will vary due to the Shafranov shift of the flux surfaces. A routine producing a fit to $\ell = 2$ Chodura code results is included to allow the modeling of this effect.

The perpendicular loss terms are modeled such that

$$\Gamma_{\perp j} = -D_{jn} \frac{\partial n_j}{\partial r} - D_{ji} \frac{\partial T_i}{\partial r} - D_{je} \frac{\partial T_e}{\partial r}$$

$$Q_{\perp i} = -\sum_j k_{ji} \frac{\partial n_j}{\partial r} - k_{ii} \frac{\partial T_i}{\partial r} - k_{ie} \frac{\partial T_e}{\partial r}$$

$$Q_{\perp e} = -\sum_j k_{ej} \frac{\partial n_j}{\partial r} - k_{ei} \frac{\partial T_i}{\partial r} - k_{ee} \frac{\partial T_e}{\partial r}$$

where $D_{jn} = D$, $k_{ii} = \chi_i n_i$, and $k_{ee} = \chi_e n_e$. The transport coefficients D and χ are calculated so as to include the contributions of axisymmetric (tokamak-like) neoclassical transport, reduced anomalous transport, and ripple effects. Bohm diffusion is assumed in the scrape-off layer.

This axisymmetric neoclassical contribution to the transport is determined using a diagonal model[10] where

$$\chi_e = \varepsilon^{1/2} \nu_{ei} \rho_{e\theta}^2 K_{22}$$

$$\chi_i = \varepsilon^{1/2} \nu_{ii} \rho_{i\theta}^2 K_2$$

$$D = \varepsilon^{1/2} \nu_{ei} \rho_{e\theta}^2 K_{11} (1 + T_i/T_e)$$

$$\varepsilon = \frac{r}{R_o}$$

$$\rho_{e\theta}^2 = \frac{2 m_e T_e c^2}{e^2 B_{po}^2}$$

$$\rho_{i\theta}^2 = \frac{2 m_i T_i c^2}{Z_i^2 e^2 B_{po}^2}$$

R_o is the major radius, r is the local radius from the magnetic axis, B_o is the toroidal magnetic field, B_{po} is the poloidal magnetic field averaged over a flux surface, and K_{22}, K_2, and K_{11} are collisionality-dependent coefficients approximated by the expressions

$$K_{22} = \frac{2.55}{1 + 0.45 \nu_{*e}^{1/2} + 0.43 \nu_{*e} + \dfrac{0.43 \nu_{*e} \varepsilon^3}{1 + 0.43 \nu_{*e} \varepsilon^{3/2}}}$$

$$K_2 = \frac{0.66}{1 + 1.03 \nu_{*i}^{1/2} + 0.31 \nu_{*i} + \dfrac{1.77 \nu_{*e} \varepsilon^3}{1 + 0.74 \nu_{*i} \varepsilon^{3/2}}}$$

$$K_{11} = \frac{1.04}{1 + 2.01 \nu_{*e}^{1/2} + 1.53 \nu_{*e} + \dfrac{0.518 \nu_{*e} \varepsilon^2}{1 + 0.89 \nu_{*e} \varepsilon^{3/2}}}$$

where

$$\nu_{*e} = \frac{\sqrt{2}\, rB_o}{B_{po} V_{th_e} \tau_e \varepsilon^{3/2}}$$

$$\nu_{*i} = \frac{\sqrt{2}\, rB_o}{B_{po} V_{th_e} \tau_i \varepsilon^{3/2}}$$

$$\frac{1}{\tau_e} = \frac{\frac{4}{3}\sqrt{2\pi}\, n_i Z_i^2 e^4 \ln \Lambda}{m_e^{1/2} T_i^{3/2}}$$

$$\frac{1}{\tau_i} = \frac{\frac{4}{3}\sqrt{\pi}\, n_i Z_i^4 e^4 \ln \Lambda}{m_i^{1/2} T_i^{3/2}}$$

$$V_{th_e} = \sqrt{\frac{2T_e}{m_e}}$$

$$V_{th_i} = \sqrt{\frac{2T_i}{m_i}}$$

Anomalous transport during current-free operation is considered to be significantly reduced below the level found in tokamaks, as is indicated by measurements on Wendelstein VIIA and Heliotron-E.[1,2] One-fifth the Alcator scaling value is assumed. When an ohmic heating current is used, the anomalous transport is calculated such that the additional anomalous transport is proportional to the current and full Alcator scaling would result if all the rotational transform were due to the current. That is

$$\chi_e = \left(\frac{0.8\ J}{J_{TOK}} + 0.2\right) \frac{1.0 \times 10^{17}}{n_e(cm^{-3})} \frac{cm^2}{sec}$$

$$D = \left(\frac{0.8\ J}{J_{TOK}} + 0.2\right) \frac{2.0 \times 10^{16}}{n_e(cm^{-3})} \frac{cm^2}{sec}$$

where J is the toroidal current density and J_{TOK} is the current density that would be needed to produce the same rotational transform in a tokamak, i.e., if there were no externally applied transform.

The transport due to helical ripple effects is taken to be that derived by Conner and Hastie[11] and amended by Shaing and Callen.[12] The latter have found that as very low levels of collisionality are approached the transport ceases to rise and finally slowly falls. In the modeling a conservative approach is taken and the transport is considered to plateau for low levels of collisionality. The possible beneficial effects of collisionless detrapping are ignored. The algorithm used is

$$\chi_i = \frac{46.5\ \varepsilon_h^{3/2}}{\nu^*_{ii\ eff}} \left(\frac{T_i}{eBR_o}\right)^2$$

where ε_h is the peak to average helical ripple and $\nu^*_{ii\ eff}$ is the maximum of

$$\frac{4\sqrt{2\pi}\ n\ Z_i^4 e_i^4 \ln \Lambda}{3\ m_i^{1/2} T_i^{3/2}} \quad \text{and} \quad 88\ \varepsilon_h \left(\frac{T_i}{eBR_o}\right) \frac{1}{r}\ .$$

Also,

$$D_{jn} = 4.34\ \frac{\varepsilon_h^{3/2}}{\nu^*_{ei\ eff}} \left(\frac{T_e}{eBR_o}\right)^2 \left(1 + \frac{T_i}{T_e}\right)$$

$$D_{je} = 4.34\ \frac{\varepsilon_h^{3/2}}{\nu^*_{ei\ eff}} \left(\frac{T_e}{eBR_o}\right)^2\ 3.37\ \frac{n_e}{T_e}$$

$$D_{ji} = 4.34 \frac{\varepsilon_h^{3/2}}{\nu^*_{ei\ eff}} \left(\frac{T_e}{eBR_o}\right)^2 3.45 \frac{n_i}{T_i}$$

where $\nu^*_{ei\ eff}$ is the maximum of

$$\frac{4\sqrt{2\pi}\ n_e Z_i^2 e^4 \ln \Lambda}{3\ m_e^{1/2} T_e^{3/2}} \quad \text{and} \quad 32\ \varepsilon_h \left(\frac{T_e}{eBR_o}\right) \frac{1}{r} .$$

Bohm diffusion is assumed in the scrape-off layer, that is

$$\chi_e = \chi_i = D = \frac{T_e}{16\ eB} .$$

VI.3 Steady State Plasma Profiles

UWTOR-M is conceived as an ignited steady state device. Unlike tokamak designs in which there is a limit to the pulse length due to the finite induction possible in the ohmic heating coils, a stellarator can maintain a rotational transform without the need of a toroidal current and so can operate in a steady state mode for an indefinite period of time. While steady state tokamaks such as STARFIRE[13] have been proposed, stellarators have the advantage of requiring no external momentum sources with their attendant problems of complexity, reliability, and electrical consumption.

The basic machine parameters (magnetic field strength, rotational transform and magnetic topology, major and minor radius) were set by the magnetic coil limitations coupled with the parametric considerations described in Chapter V. In this section we attempt to optimize the fusion power output by varying the plasma parameters (e.g., density and temperature, pellet injection velocity) and determine a design operating point for the machine. The machine parameters used in this study are given in Table VI.3-1. Steady state plasma profiles for UWTOR-M were determined by starting the simulation with a hot, ignited plasma and running the code until the plasma relaxed to a steady state. The high ion heat conductivity due to the magnetic ripple and the low electron heat conduction from the expected low level of anomalous energy transport imply that the electron temperature tends to exceed the ion temperature by a considerable degree unless steps are taken to prevent this. Such an effect is undesirable since for a given allowable value of beta a high electron temperature, and thus a high electron pressure, reduces the density at which the device can be operated, and therefore reduces the power output. To counter this tendency, it is proposed that the radiation from the plasma be

Table VI.3-1. UWTOR-M Machine Parameters

Major Radius	24.1 m
Coil Radius	4.77 m
Plasma Minor Radius (Effective)	1.72 m
Coil Aspect Ratio	5.05
Plasma Aspect Ratio	14
Magnetic Field on Axis	4.5 T
Rotational Transform at Edge	1.125
Multipolarity	3
Number of Field Periods	6
Coils/Field Period	3
Plasma Volume	1400 m^3
Volume-Averaged Beta	6%

increased by the addition of a small amount of a high-Z impurity, as was done in the STARFIRE design study.[13] An impurity of high atomic number will not be fully stripped of its electrons even in the core of the plasma and can cause strong radiation losses at quite low densities, thus not contributing appreciably to the electron density, so high-Z impurities are preferable to low-Z impurities as deliberate contaminants. Xenon has been nominally chosen as the impurity to be used as it is high-Z (atomic number 54), is a noble gas and chemically inert, and data on its radiation is available.[14] Impurity injection also provides a means of burn control. The plasma appears to be thermally unstable and would run away without some kind of feedback mechanism. By varying the impurity injection rate this feedback can be easily accomplished. The feedback algorithm maintains constant volume averaged plasma beta. The feedback response speed need only be on the order of the energy confinement time, i.e. about a second, and so this is no difficulty. In actuality, stability may be provided by the increased transport experienced as the beta limit is approached. The xenon density profile is considered to be flat and has a density of $3.3 \times 10^{10}/cm^3$ in the chosen configuration, which is an average concentration of about 0.02%.

Table VI.3-2 gives the steady state power output at 6% average beta for various values of the pellet velocities and plasma density. Increasing the pellet velocity increases the penetration depth of the pellet and thereby affects the density and temperature profiles. Separate deuterium and tritium pellets are used in the simulation, though mixed species pellets could be used in an actual device. Actual pellet velocities would be less than the stated values due to geometrical effects (shoot through the flat side of the trefoil) and the Shafranov shift. Higher pellet velocities produce higher power output

Table VI.3-2. Effect of Density and Pellet Velocity on Power Output

Case Number	DT Density (10^{14}/cm^3)	Pellet Velocity (10^6 cm/sec) D	Pellet Velocity (10^6 cm/sec) T	DT Power (MW)	Central β (%)	Central T_i (keV)	Central T_e (keV)
23	1.2	1.9	1.5	4223	18.6	11.8	13.4
15	1.3	1.7	1.4	4191	17.8	11.1	12.4
6	1.4	1.5	1.1	4068	16.9	10.6	11.7
13	1.4	1.7	1.4	4203	17.8	10.5	11.4
8	1.4	1.9	1.5	4292	18.3	10.4	11.3
5	1.4	2.5	2.2	4674	21.3	10.3	11.0
14	1.6	1.7	1.4	4162	17.8	9.5	9.8
25	1.6	1.9	1.5	4122	18.0	9.2	9.7
28	1.6	2.5	2.2	4331	19.6	9.1	9.6
26	1.8	1.9	1.5	3961	18.0	8.3	8.6
27	2.0	1.9	1.5	3272	15.2	7.7	8.0
31	2.0	2.5	2.2	4447	27.8	7.3	7.5

but increase the maximum (central) beta due to peaking of the profiles. If the central beta is too large, the machine will likely be MHD unstable.

Different values of the density for a given pellet velocity also give different power outputs. For a given value of nT_i (i.e., beta), $n^2 \langle\sigma v\rangle_{FUS}$ for D-T has a maximum at around 14 keV; and so this might be assumed to be the optimum temperature at which to operate in order to maximize the power output for a given beta. However, due to the effects of field ripple transport and alpha particle pressure, it is found that a lower temperature, higher density regime gives the greatest power output. A D-T density of $1.4 \times 10^{14}/cm^3$ gives near-optimum performance. The lower ion temperature reduces ripple transport losses and the higher density decreases the slowing-down time of hot alphas, and so their contribution to the plasma pressure.

Case number 8 was chosen as the design point for UWTOR-M. This case gives adequate power output (4300 MW) with a tolerable value for the central beta (18.1%). The plasma parameters for this case are shown in Table VI.3-3. The density and temperature profiles for the chosen operating point are shown in Fig. VI.3-1. The pellets penetrate to within about 50 cm from the plasma axis, so the electron density is flat inward from that distance. The electron temperature is approximately parabolic, while the ion temperature is rather flat. A small decrease in the ion temperature is observed between 50-100 cm out, but beyond this radius the effects of field ripple prevent a significant decrease. Some decrease in the ion temperature takes place in the scrape-off zone, since the trapped particles which contribute to ripple heat conduction in the main plasma leave to the divertors in the scrape-off layer. The effect of recycling from the divertor was evaluated. For recycling up to ~ 50%, the

Table VI.3-3. Steady State Plasma Parameters for the UWTOR-M Design Point

• Average Electron Density	$1.52 \times 10^{14}/cm^3$
• Average Electron Temperature	9.5 keV
• Average Ion Temperature	9.8 keV
• Average Toroidal Beta	6.0%
• Xenon Concentration (deliberately introduced to lower the electron temperature)	$3.3 \times 10^{10}/cm^3$
• Particle Confinement Time	4.0 sec
• Energy Confinement Time	1.5 sec
• Fractional Tritium Burnup	4.4%
• Net Toroidal Current	0
• D-T Fusion Power	4300 MW
• Edge Field Ripple	23%
• Power Radiated to First Wall	~ 470 MW
• CX Power to First Wall	~ 70 MW
• Power to the Divertor	~ 320 MW

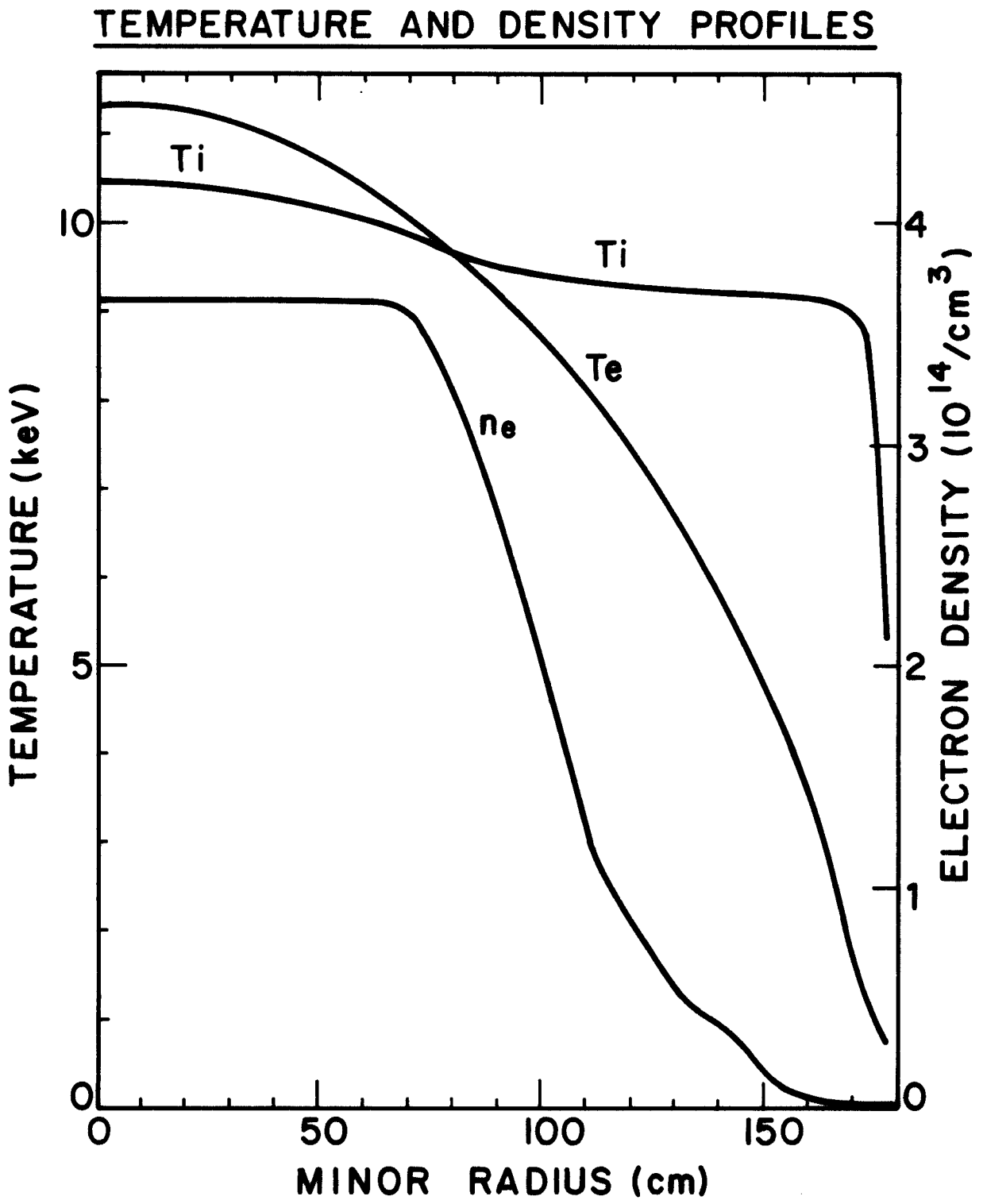

Figure VI.3-1 Plasma temperature and density profiles versus minor radius.

effect on the basic design point (beta, power output, required pellet fueling) was small.

The thermal conductivity and the diffusivity profiles are shown in Fig. VI.3-2. χ_i, χ_e, and D are all large near the axis due to the small rotational transform near the axis in an $\ell = 3$ stellarator. Further out, between 50 and 100 cm radially, they reach a minimum. χ_i increases beyond this point due to the effects of ripple transport. The plateauing of the effective collisionality can be observed in the smaller slope in the collisionality profile near the separatrix. χ_e increases near the outside of the plasma due to the density fall-off and the resultant anomalous transport. The diffusion coefficient shows all these effects as one moves outward, rising swiftly due to field ripple, plateauing, and then rising again due to anomalous transport.

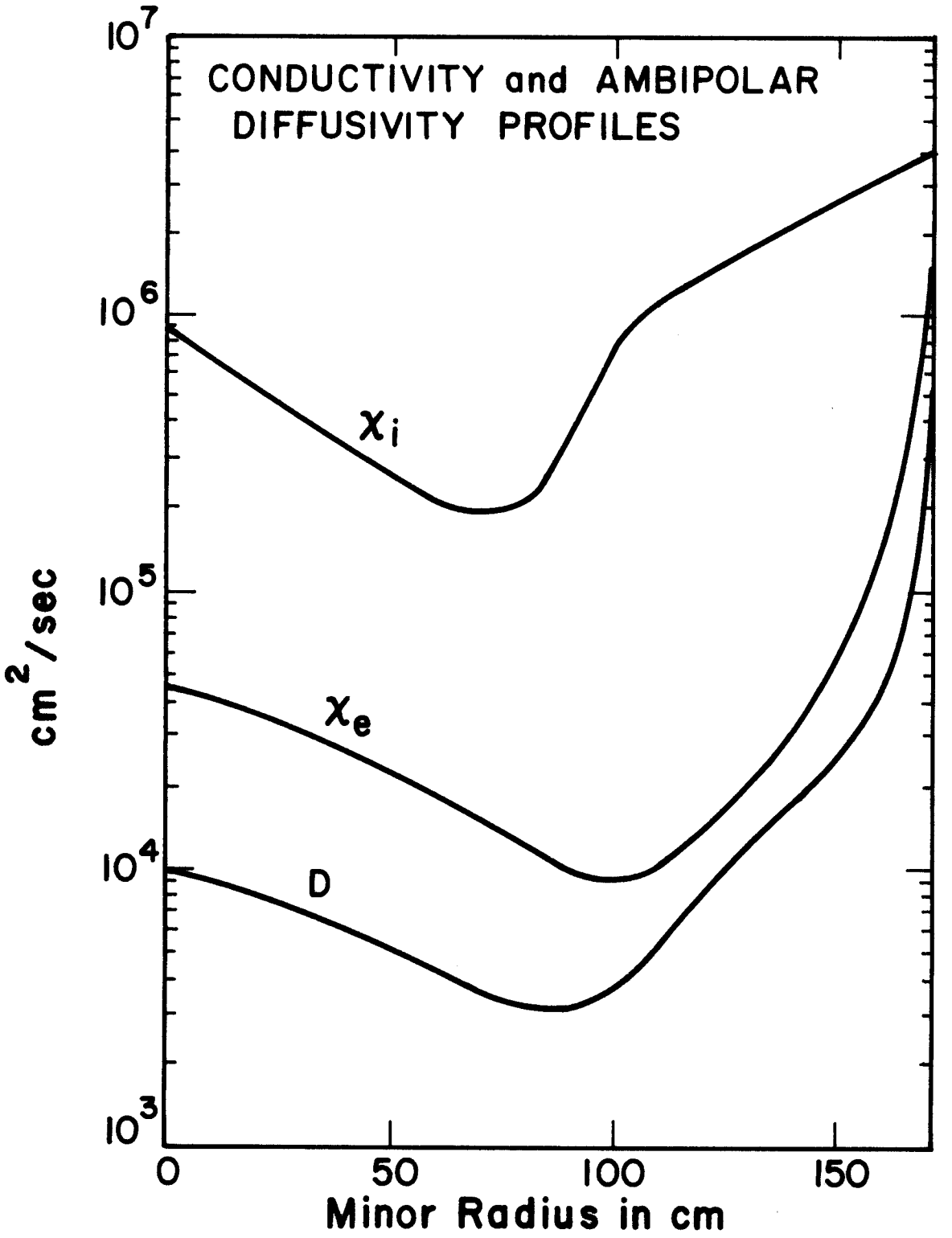

Figure VI.3-2 Plasma transport coefficients versus minor radius.

VI.4 Startup and Shutdown

Ion cyclotron resonance heating (ICRH) has been chosen as the startup heating mechanism for UWTOR-M. ICRH is the most well-developed of the radio-frequency heating techniques and should be less costly than lower hybrid or electron cyclotron resonance heating. The heating frequency chosen is the second ion cyclotron harmonic for deuterium, 69 MHz for the 4.5 tesla field in UWTOR-M.

For heating to take place it is necessary to have

External power	+	Fusion alpha power	>	Bremmsstrahlung radiation losses	+	Convective and conductive particle energy losses

The predominant mechanisms for particle energy transport during startup will be anomalous electron transport and regular ion ripple transport (scaling with the inverse of the collision frequency). In both of these loss mechanisms the confinement times scale as the density. Thus the particulate energy loss will be largely independent of the plasma density. There will be slightly less loss at lower densities due to neoclassical effects. Fusion power and bremsstrahlung both scale as the square of the density. In order for the fusion power to the plasma to exceed the bremsstrahlung losses, the temperature must be above about 4.5 keV. The mode for startup requiring the least power would therefore seem to be to heat a low density plasma to high temperature and then slowly raise the density. This way fusion power could always be available to aid in the heating of the plasma.

Simulations with the WHISTEL code indicate, however, that ICRH startup at very low density is unfeasible. At low electron temperatures ICRH predominantly heats ions, while at high electron temperatures it predominantly heats

electrons. (The code utilizes the simple approximation that a fraction $T_e(keV)/13.5$ of the ICRH power goes to the electrons.) As the plasma becomes hot, the ion-electron collisionality becomes small and thus so does the ion-electron rethermalization. Since stellarators have relatively low anomalous electron transport losses and large ion ripple losses, the energy loss is primarily through the ion channel, and thus energy flows from the electrons to the ions. At low densities, and thus low collisionality, the rethermalization can become small enough that the electron and ion temperatures decouple and the electron temperature runs away, the electrons absorbing a greater and greater share of the ICRH power and leaving behind a population of cooling ions (Fig. VI.4-1).

This problem does not arise with neutral beam heating, since beams continue to heat the ions even at high electron temperatures. Neutral beam heating has several disadvantages, however, which make it a less desirable heating technique than ICRH:

1) Except at near tangential injection angles, the ripple effects in stellarators can cause primary beam ions to enter helically trapped orbits and be lost from the machine.[15]
2) With tangential injection, as the plasma density increases the penetration of moderate energy (150 keV) beams becomes poor.
3) Neutral beam injection, particularly at tangential angles, greatly complicates the design of the magnets, blanket, and shield.
4) Neutral beams complicate the pumping and tritium processing.

The alternative is startup at a somewhat higher density with ICRH heating. A typical startup scenario would be as follows:

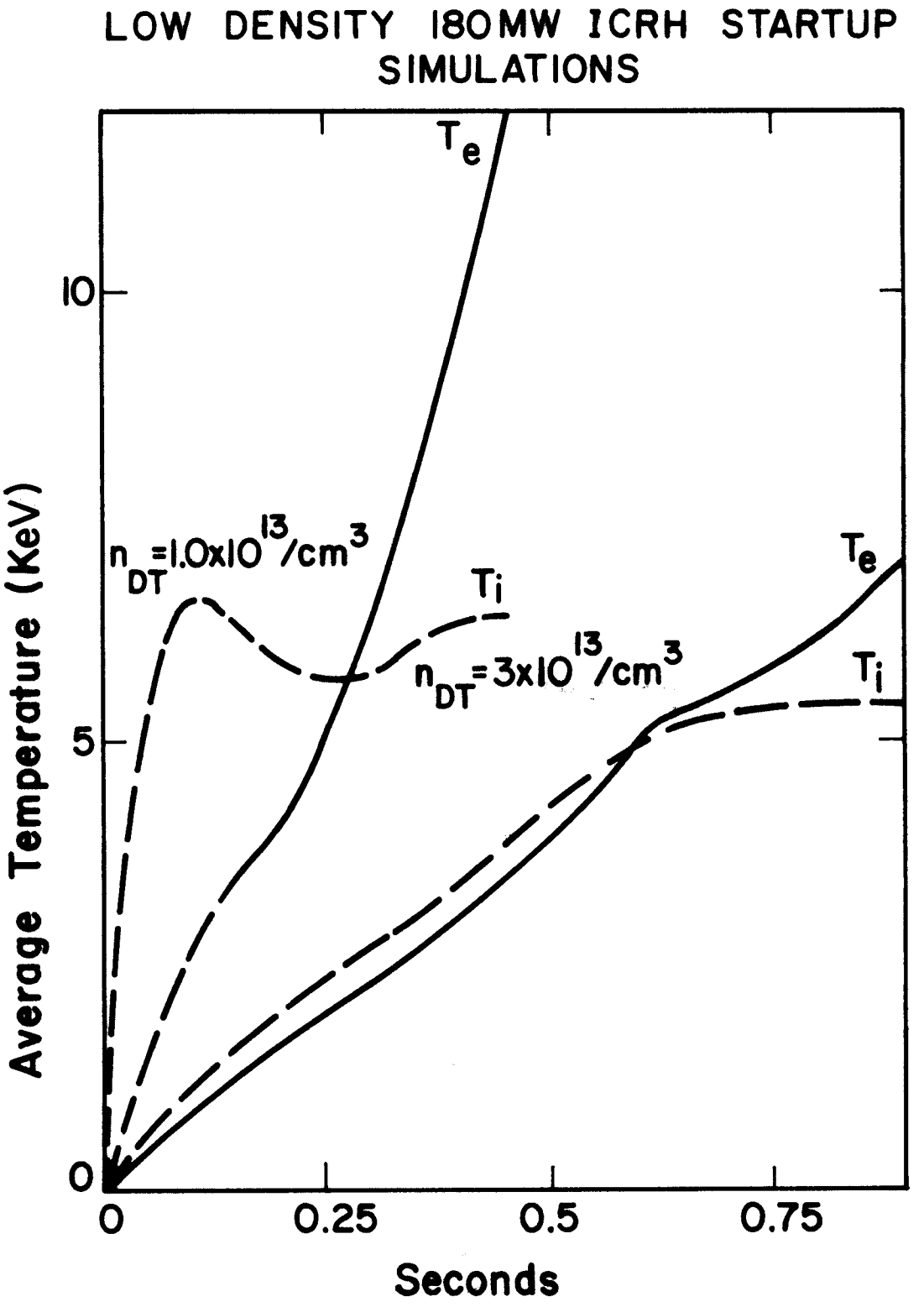
LOW DENSITY 180MW ICRH STARTUP SIMULATIONS
Average Temperature (KeV)
Seconds
0
5
10
0
0.25
0.5
0.75
T_e
T_i
$n_{DT}=1.0\times10^{13}/cm^3$
$n_{DT}=3\times10^{13}/cm^3$
T_e
T_i

Figure VI.4-1

1) An equal part D-T gas mixture of somewhat less than steady state density is introduced into the torus.
2) ICRH is used to break down the gas and heat it to ignition. By feedback regulation of the RF power, the fusion power output can be increased gradually over many minutes. This will prevent thermal shock of the blanket, heat exchangers, and turbines. The initial D-T ion density might be less than the approximately $1.0 \times 10^{14}/cm^3$ needed for ignition and then slowly increased to this value during the heating phase.
3) After ignition, the device is slowly brought to full power, the D-T density being increased to the steady state value of $1.4 \times 10^{14}/cm^3$. The power output is controlled by the addition of impurities during this phase of the startup.

Simulation of slow startup is unfeasible with the WHISTEL code, requiring excessive computer time. Quicker startup simulations suffice, however, to determine the power needed for startup, since all startup durations that are long compared to the energy confinement time require nearly the same power. Startup in 5 seconds proved possible with 150 MW of ICRH power and in about 11 seconds with 90 MW (Fig. VI.4-2 and Fig. VI.4-3). At 72 MW of ICRH power it did not ignite. Consequently one needs $\gtrsim$ 90 MW of ICRH power to start up the plasma. In this calculation 50% of the particles flowing to the divertors were assumed to recycle as neutrals. The pellet fueling velocity was adjusted so that the

$$\text{pellet velocity} = \text{steady state pellet velocity} \times \frac{\beta_{ave}(\%)}{6\%} ,$$

thus the pellet velocity gradually increased to the steady state value. This

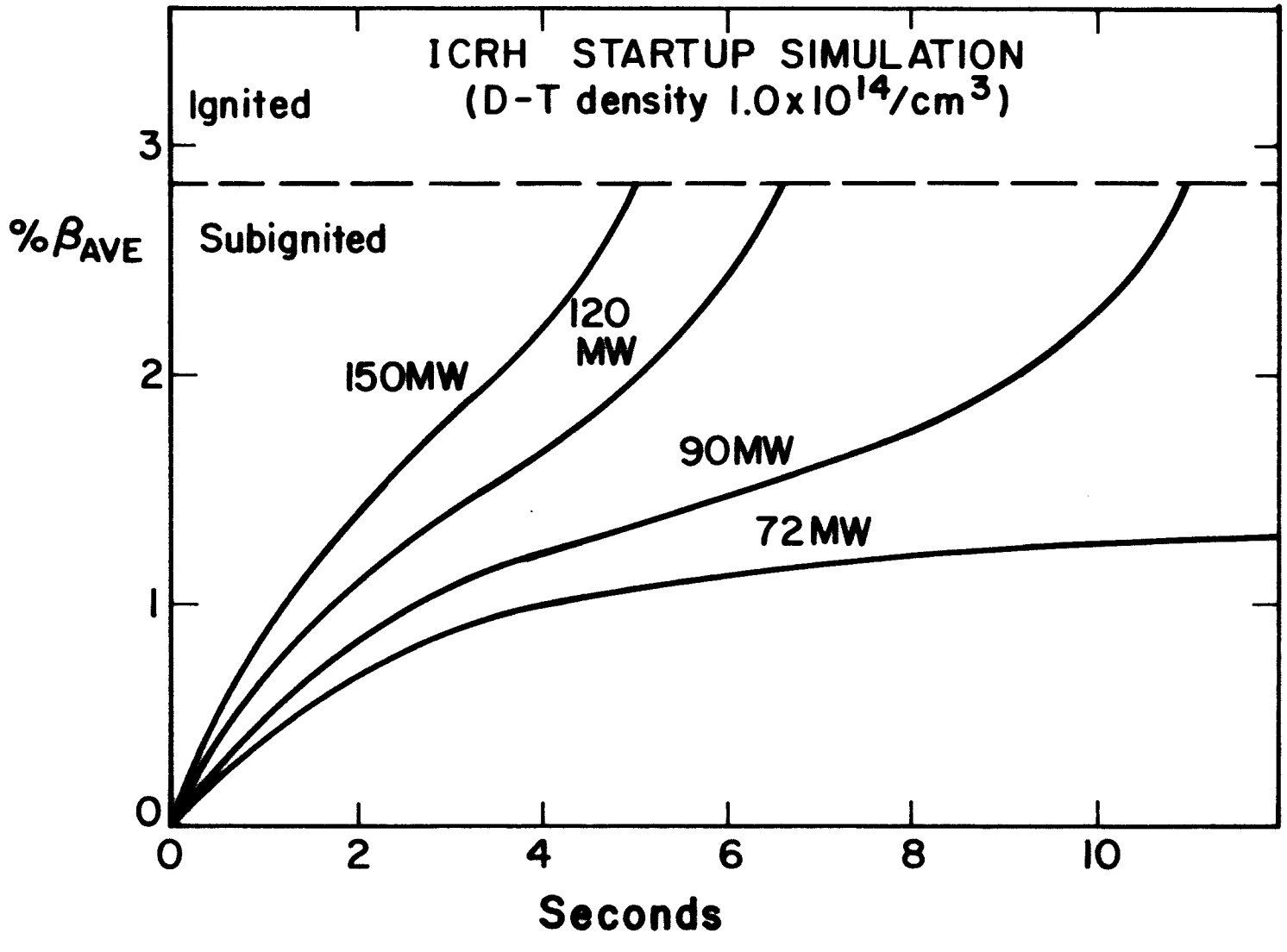
ICRH STARTUP SIMULATION
(D-T density 1.0x10^14/cm^3)
Ignited
Subignited
%β_AVE
150MW
120 MW
90MW
72MW
0
1
2
3
0
2
4
6
8
10
Seconds

Figure VI.4-2

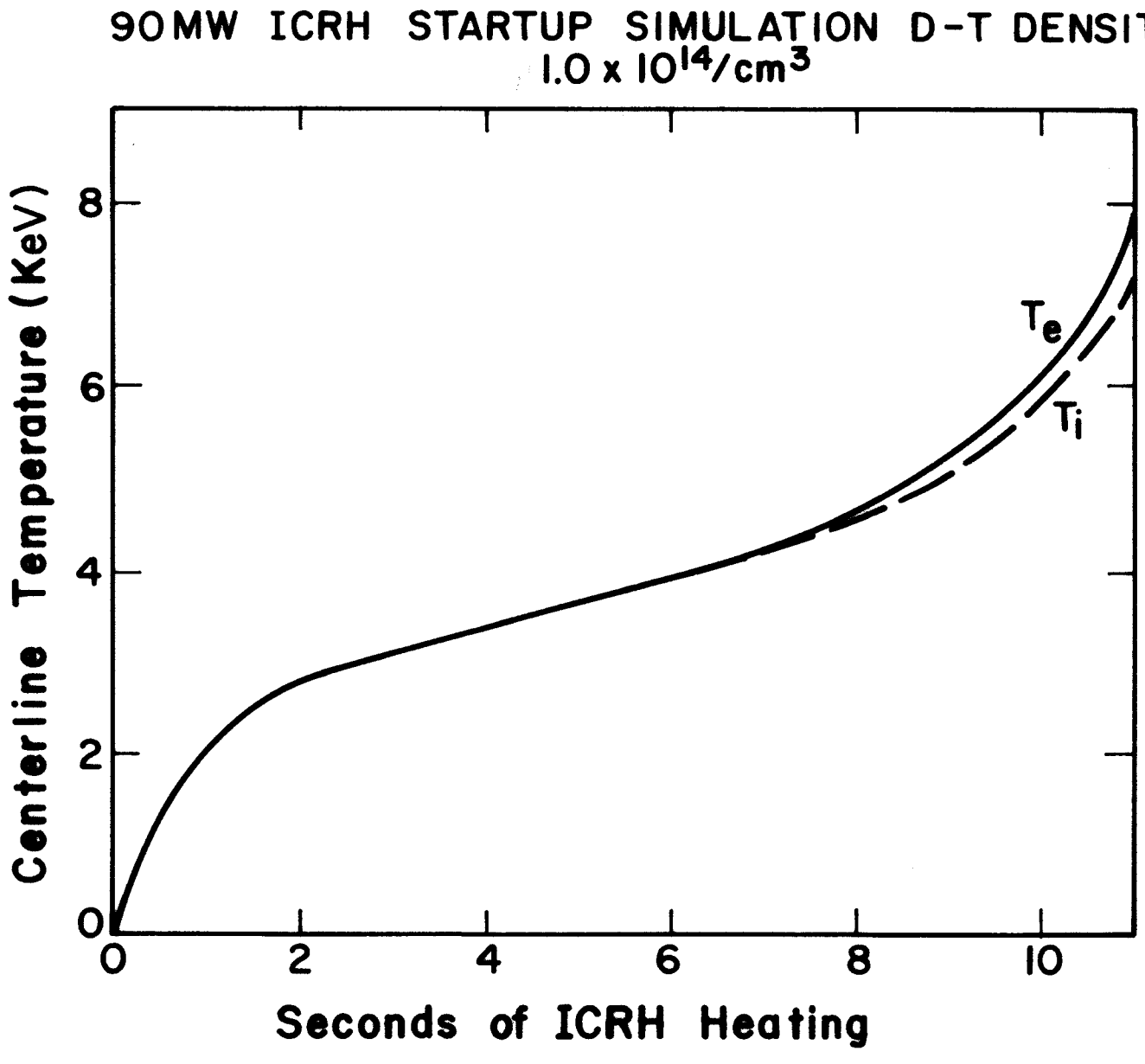

Figure VI.4-3 Central temperature during startup.

assured that the plasma pressure profile remained sensible during startup. If the pellet velocity was too high during startup, simulations could produce unphysically large density gradients. The pellets could even completely penetrate the plasma and hit the far wall of the torus. Too low a pellet velocity resulted in excessive energy being required for startup. The enhanced fusion power output and decreased transport of a peaked profile helped to ignite the plasma. An ICRH power of 180 MW was insufficient for ignition when the pellet velocity was kept low throughout startup.

A D-T density of $1.0 \times 10^{14}/cm^3$ was used during the startup simulations since this density is sufficient for ignition of the plasma. Startup might be possible with slightly less power by beginning with a somewhat lower density and slowly increasing it after the plasma is heated to fusion temperatures, but this is difficult to simulate in a short-time run due to the slow rate of particle diffusion. Therefore the conservative estimate of 100 MW of ICRH required for startup will be assumed in this study.

After startup is accomplished the machine should be able to run steady state for an indefinite period of time since no induced current is required. Shutdown would be effected by reversing the startup procedure. The power and density would be slowly reduced, ICRH-assist being used to maintain a gradual power decrease during the sub-ignited ramp-down phase. In an emergency situation a faster shutdown could be achieved simply by stopping fueling, which would shut the machine down within a few seconds. A still faster shutdown could be achieved by the injection of impurities, which would cause the plasma to immediately radiate its energy away to the walls of the machine. Unlike in tokamaks, a fast shutdown in a stellarator should not produce a wall-damaging disruption.

VI.5 Acknowledgment

The authors would like to thank Wayne Houlberg and Stan Attenberger of Oak Ridge National Laboratory for providing the WHIST code and for their frequent advice and suggestions in its conversion to a stellarator transport code.

References for Chapter VI

1. D.V. Bartlett et al., Proceedings of the Eighth International Conference on Plasma Physics and Controlled Nuclear Fusion Research, Brussels, 1-10 July 1980, IAEA, Vienna, (1981) p. 173.

2. K. Uo et al., in ibid., p. 217.

3. W.A. Houlberg and R.W. Conn, Nucl. Sci. Engr. 64 (1977) 141.

4. W.A. Houlberg, S.E. Attenberger, and A.T. Mense, Nucl. Fusion 20 (1980) 811.

5. A.W. Bailey, G.A. Emmert, and K.J. Lee, UWFDM-477 (1982).

6. R.M. Wieland, W.A. Houlberg, and A.T. Mense, ORNL/TM-6550 (1979).

7. K. Audenaerde, G.A. Emmert, and M. Gordinier, J. Comp. Phys. 343 (1980) 238.

8. W.A. Houlberg, M.A. Iskra, H.C. Howe, and S.E. Attenberger, ORNL/TM-6549 (1979).

9. G.A. Emmert, UWFDM-343 (1980).

10. F.L. Hinton and R.D. Hazeltine, Rev. of Mod. Phys. 48 (1976) 239.

11. J.W. Connor and R.J. Hastie, Nucl. Fusion 13 (1973) 221.

12. K.C. Shaing and J.D. Callen, UWFDM-416 (1981).

13. C.C. Baker et al., ANL/FPP-80-1 (1980).

14. D.E. Post, R.V. Jensen, C.B. Tarter, W.H. Grasberger, and W.A. Lokke, Atomic Data and Nuclear Tables 20 (1977) 397.

15. D.T. Anderson, J.L. Shohet, S. Rehker, and J.A. Tataronis, Nucl. Fusion 20 (1980) 197.

VII. Magnet Design

VII.1 Introduction

In the present chapter, the conceptual design of the magnet systems for UWTOR-M is summarized. Since the magnet system represents a major component of the reactor, it is imperative that the design be evaluated with sufficient care so that the critical areas can be identified. As part of this effort, the magnet design group has attempted to stay as close to state-of-the-art technology as possible. Where this goal has been difficult, an important mission has been to identify those aspects of the reactor that are considered to be extrapolations of technology and to minimize their impact on the feasibility of the entire reactor design.

The magnet configuration for UWTOR-M has evolved out of numerous iterations of design. Early in the study, it was deemed unattractive to consider continuous coils such as those utilized in classical stellarators and torsatrons because of their large size and difficult maintainability. The modular configuration, as adopted in the UWTOR-M design, is shown in Fig. VII.1-1. The goal of this configuration is to approximate a continuous set of stellarator-type windings with discrete coils. Numerous coil configurations[1-5] have been identified which approximate continuous stellarators and torsatrons. However, this particular configuration was adopted because of its economy of magnet windings, i.e., avoiding the need for large wind-back legs which only serve to cancel unneeded magnetic field components. Also, the configuration appears to provide some simplicity in that the coils are of only two types. The adopted configuration makes further contact with other fusion magnet systems through its similarity to mirror and tokamak designs. The modular stellarator device is toroidal and steady-state. Twisting of the coil case to

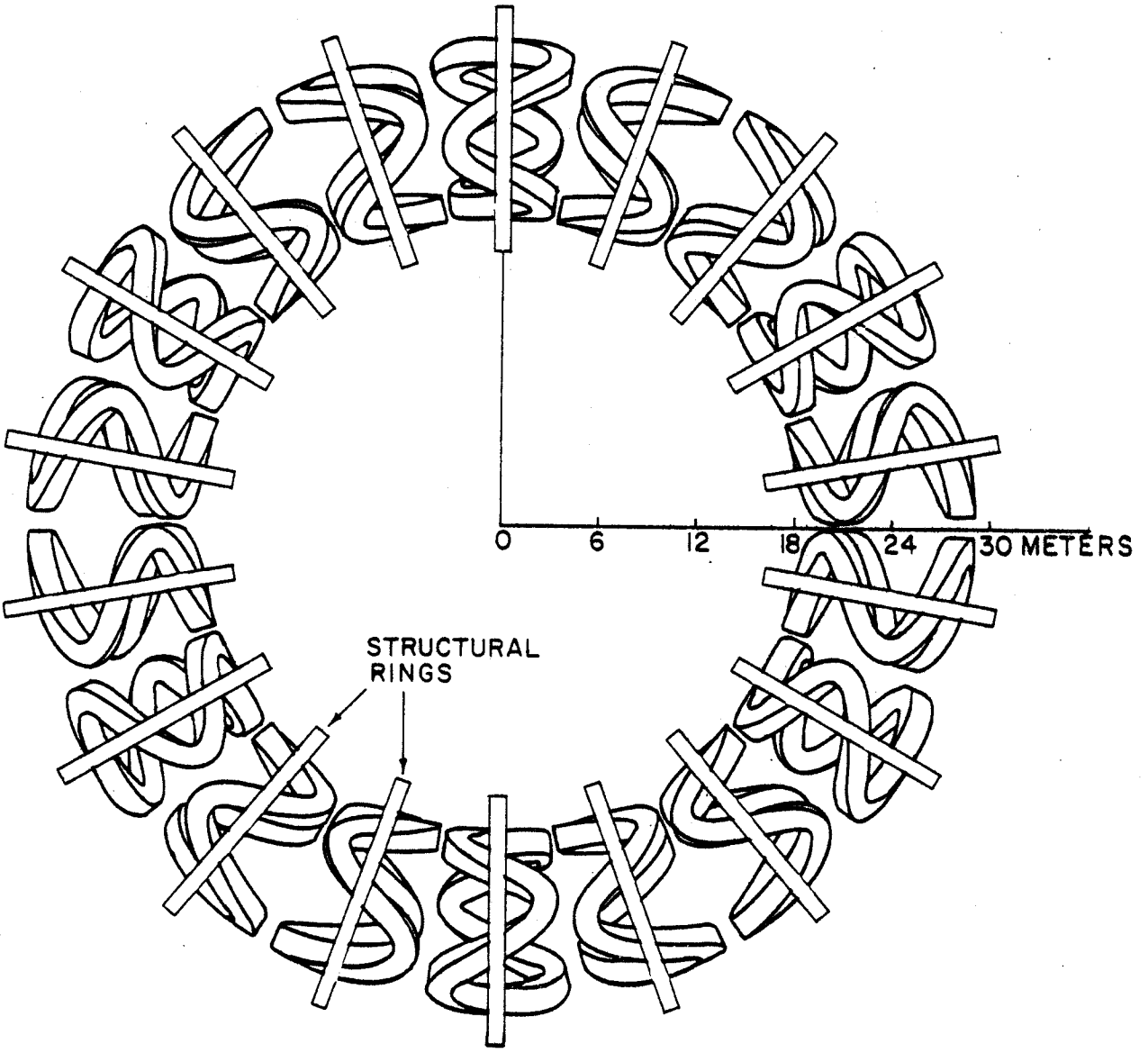

TOP VIEW OF UWTOR - M

FIGURE VII. 1-1 TOP VIEW OF UWTOR-M COIL SYSTEM

approximate helical windings is more complex than pure toroidal windings, yet it benefits from the inherent steady-state nature avoiding the need for pulsed ohmic heating coils. Because of the non-planar symmetry, the configuration of an individual coil appears more analogous to that of the end cell of a mirror reactor in size and winding difficulty. Therefore, regular contact has been made with the mirror reactor design efforts[6,7] so as to adopt useful innovations in UWTOR-M.

The parameters of the UWTOR-M reactor concept which impact the magnet design are listed in Table VII-1.1. There are three coils per field period, two of which are identical, only rotated 180° about the radial axis. Thus, the entire reactor gains simplicity by having two coil types (12 of one and 6 of the other). Although the major radius of UWTOR-M is rather large, each modular coil has a minor radius of only 4.77 m which makes its dimensions more comparable to the toroidal field coils for FED than those of a full scale reactor. One additional parameter to consider is that of the field on axis B_0. Although a B_0 = 4.5 T appears rather modest, because of the open nature of the coil configuration, the forces are relatively high and the peak fields at the coils are close to 12 T. These two facts restrict the possibility of increasing B_0 in the design, a desirable goal from the viewpoint of plasma physics. The magnets are discrete superconducting coils operated in the steady-state mode. No pulsed coils are evident. These considerations allow for rather traditional coil design with the one requirement that the operating temperature of the coils be reduced to 1.8 K, utilizing superfluid helium cooling.

Before addressing the details of the design, it is instructive to compare the magnets for UWTOR-M with present superconducting magnet technology. The

Table VII.1-1 Reactor Coil Design Parameters

Number of coils	18
Number of field periods	6
Number of coil types	2
Central field (B_o)	4.5 T
Major radius (R_m)	24.1 m
Coil minor radius (A_c)	4.77 m
Total coil current (NI)	31.2 MA-turns

features which make these coils challenging concern both their superconducting and structural aspects.

Each superconducting magnet for UWTOR-M is substantially larger in size than any existing fusion magnet. This fact most strongly impacts the structural design but it also must be taken into consideration when evaluating the magnet safety. The energy contained in the magnetic field of each coil is at least an order of magnitude greater than the largest superconducting magnet presently in operation. When considering magnets of this size, one must be concerned with safety under rapid discharge conditions. This problem, which surfaces in the form of potentially high discharge voltage, is germane to all reactor size magnets. It is required that a detailed design contain protection methods, possibly including inductive coupling, to avoid damaging the coil under extreme conditions.

The other superconducting aspect to these coils which are considered an extrapolation of technology is the limit to the peak field. Here the established limit of B_{max} is set to not exceed 12 T, to simplify conductor design and to allow options for superconducting material. The material selected was NbTi or NbTiTa operated at the reduced temperature of 1.8 K in superfluid helium. A backup option of pool boiling and Nb_3Sn conductor was also considered. A coil of this type is not beyond the capability of present day engineering although it has yet to be demonstrated.

The coil structural design is one of the major extrapolations of the present magnet technology in UWTOR-M. Since no pure tension configuration exists for the twisted configuration, the coils are subjected to large bending and torsion. Experience during the design study showed that no credible cross-sectional dimensions could be found for a self-supported modular coil.

Extra reinforcing structures in the form of a retaining ring are needed to withstand the magnetic forces. Even with such reinforcing structures, heavy cross sections are still required for the coil case and retaining ring design.

Structural features, such as those described above, impact the manufacture of the modular coils. Welding of thick stainless steel plates is needed to have the full strength in the coil case. Therefore, care must be exercised to protect the superconductor and insulator structure, and at the same time produce quality welds. The technology to do so and the design of the conductor pack to allow these necessary manufacturing features may require development. In the design of the support scheme discussed in Section VII.3, some concepts of the contact connection between neighboring coils are presented. Such contact connections require special insulation considerations to maintain cryogenic independency of the modular coils. Developments of these technologies would require careful engineering design but are not viewed as beyond the capability of present day engineering.

Finally, the coil fabrication scheme represents an area demanding innovative procedures. Since the coil has no axis about which pure tension can be applied, the winding procedure will require a method to hold the conductor in the coil case. One such scheme is presented in Section VII.6, although the methods are only conceptual at this time.

VII.2 Magnetic Loads

The modular coils of stellarator reactors are designed with superconductor composite windings supported by the coil case structure. Under normal operating conditions, the interaction of the coil current with the field results in steady-state magnetic forces which must be resisted by the coil structure. The design of coil case structure is discussed in Sections VII.3

and VII.4 based on the force calculation presented in this section. The design of coil winding is presented in Section VII.5.

The considerations of magnetic topology lead to the choice of a coil system with multipolarity ℓ=3 in each of the six field periods. The central lines of the coils are defined by the following equations describing the winding law:

$$x = r\cos\theta \tag{1a}$$

$$y = r\sin\theta \tag{1b}$$

$$z = R_{major}\sin\phi \tag{1c}$$

in which

$$r = R_{major} + R_{minor}\cos\phi \tag{2}$$

$$\theta = f(\phi) = c\alpha\sin[\ell(\psi-\psi_o)] + \theta_o \tag{3}$$

$$\psi = \tan^{-1}\left[\frac{\sqrt{R_{major}^2 - R_{minor}^2}\sin\phi}{R_{major}\cos\phi + R_{minor}}\right]$$

$$\alpha = \frac{3}{2M\pi}\left[\sin\frac{4\pi}{3} - \sin\frac{2\pi}{3}\right]$$

with

$$M = 6\ ,\ \ell = 1,2,3$$

$$\theta_o = \frac{2\pi n}{3M}\ ,\ \psi_o = \frac{2\pi n}{3\ell}\ ,\ n = 0,1,2\ .$$

The cartesian coordinates (x,y,z) have the origin at the center of the reactor. The constants ℓ, ψ_0, θ_0 specify the shape and orientation of each coil. The winding law $f(\phi)$ includes a gap factor c in Eq. (3). The gap factor provides space between the neighboring magnets for insulation and structure. A value of c = 0.95 is used in the present magnet design. The gap factor for the UWTOR-M coil system can be seen by the space between coils in Fig. VII.1-1. The design of UWTOR-M requires a spacing between windings of 60 cm to allow for structural support and vacuum insulation. This value for spacing is consistent with the gap factor of 0.95.

The calculations of magnetic field and forces are carried out using the MFE network EFFI code.[8] Each coil is approximated by 89 straight segments at equal poloidal angle. The calculated magnetic field lines over the radial mid-plane of the central coil in each period are shown in Fig. VII.2-1. The cross-section of the winding window is taken as 1.10 x 1.13 m^2 in the calculation. The maximum field strength on the conductor is found to be 11.6 T at a total coil current of 31.2 MA.

The magnetic force density for each coil is decomposed into radial, poloidal and toroidal components by F_R, F_p and F_T, respectively. Also, the vector sum of these individual force components is indicated as the force magnitude, F_M. All four components are calculated versus poloidal angle, ϕ. This convention is illustrated in Fig. VII.2-2 along with a schematic representation of the toroidal and radial force. Actual computed values of the magnetic force on the central coil in each field period are presented in Figs. VII.2-3 and VII.2-4. All values are given in terms of poloidal angle, ϕ. The magnetic forces on the coil can be thought to be comprised of two principal components, the self force due to its own field and the mutual attractive

MAGNETIC FIELD LINES

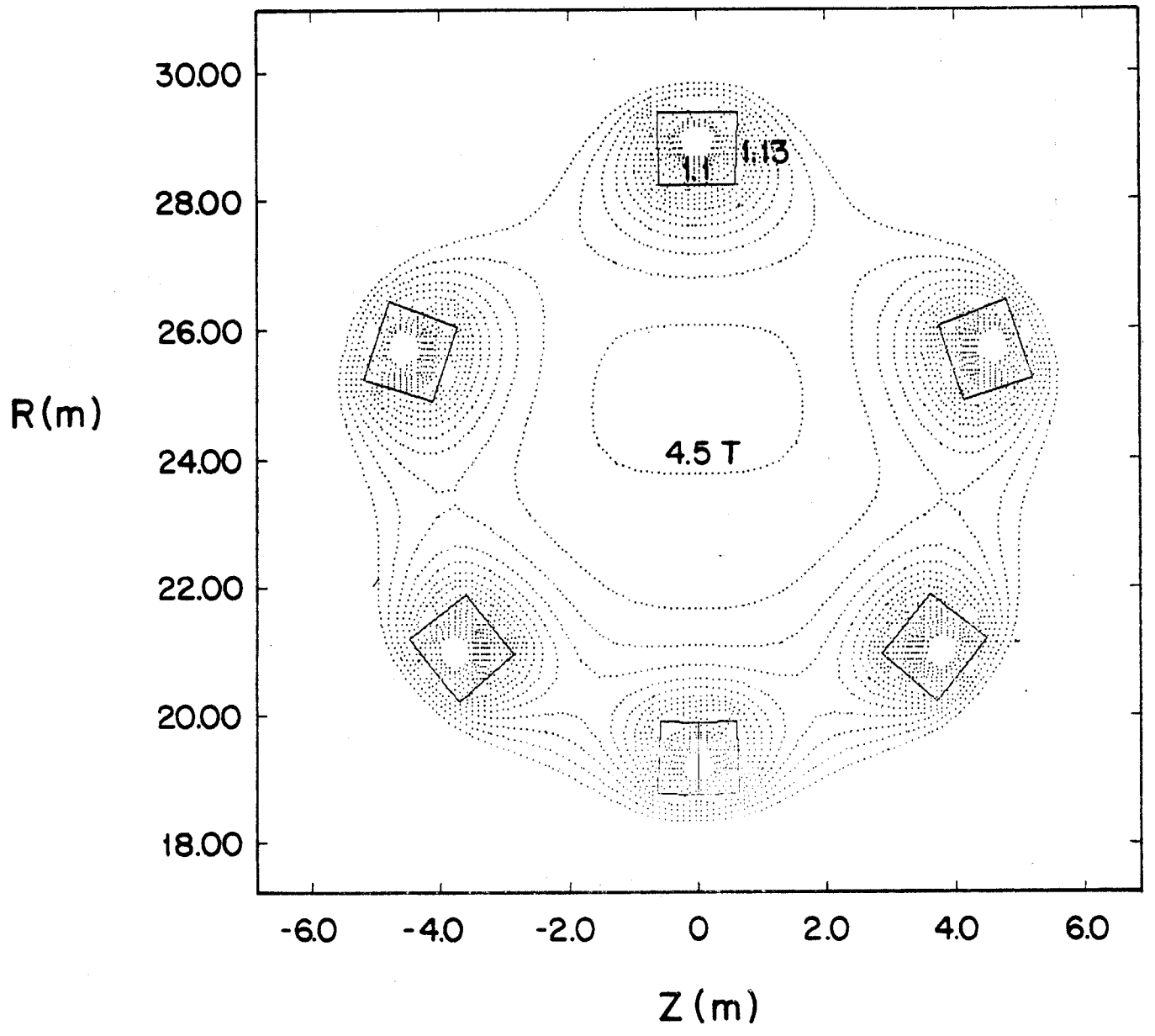

FIGURE VII. 2-1 MAGNETIC FIELD LINES ON RADIAL MID-PLANE

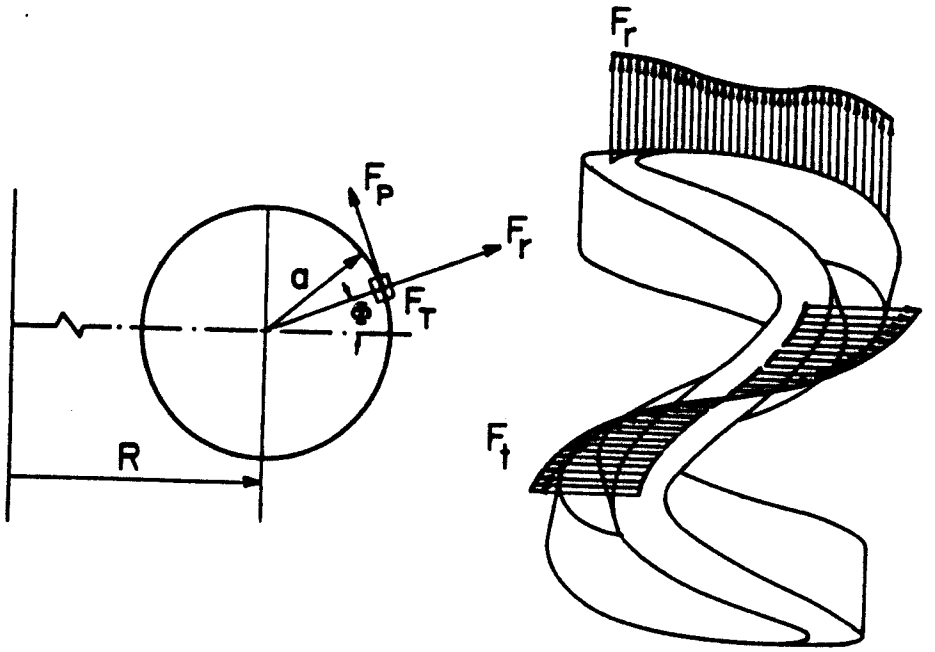

FIGURE VII . 2 - 2 NOTATION AND SIGN CONVENTIONS FOR THE MAGNETIC FORCES

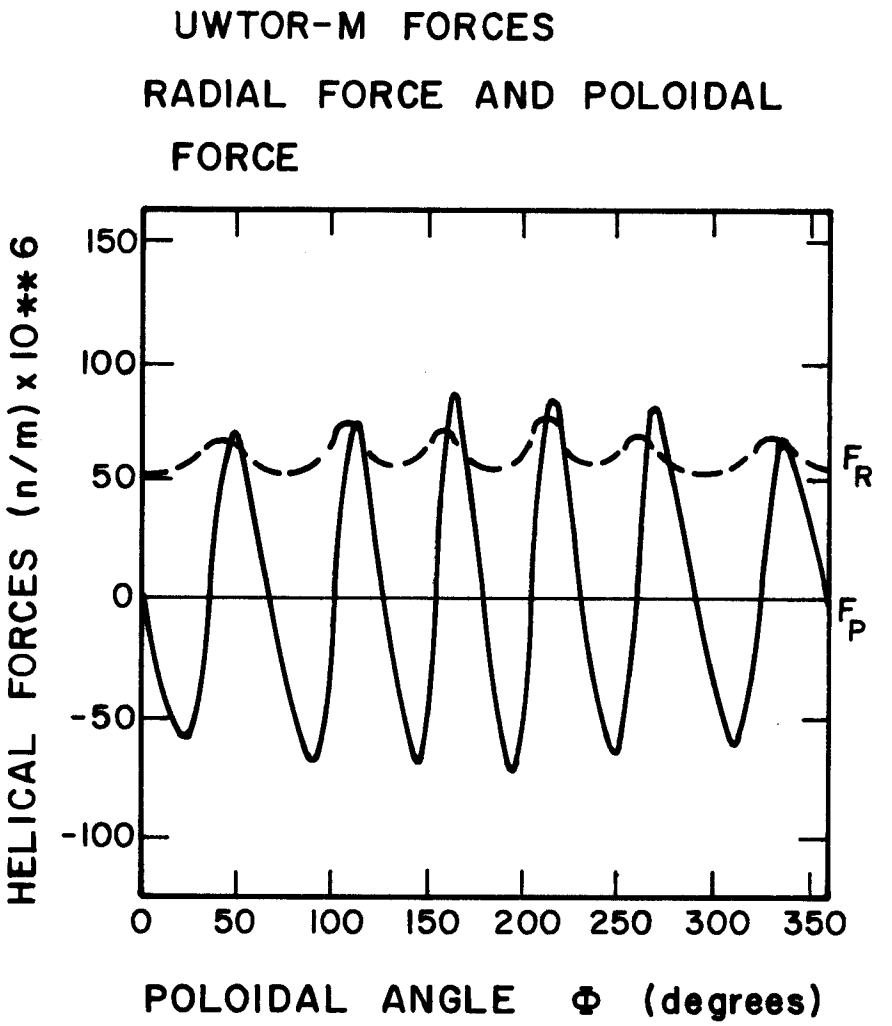

FIGURE VII. 2-3 RADIAL (F_R) AND POLOIDAL (F_P) COMPONENTS OF THE MAGNETIC FORCE

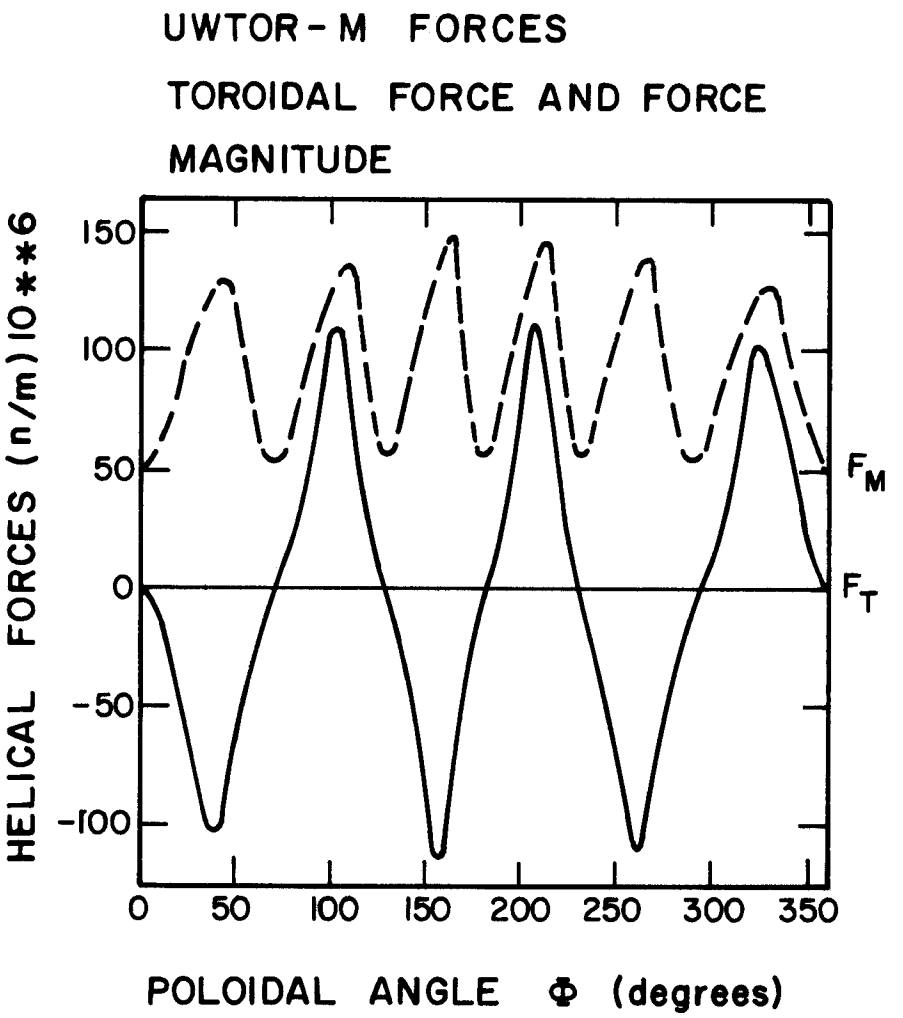

FIGURE VII. 2-4 TOROIDAL (F_T) AND TOTAL MAGNITUDE (F_M) OF THE MAGNETIC FORCE

force between adjacent coils due to the interactive fields. In the regions where the coils come in close proximity, the mutual attractive forces dominate, causing large toroidal forces. This effect can be seen in Fig. VII.2-4, where the large toroidal forces have six maxima associated with regions of proximity. In the in-between regions, the toroidal force is relatively small.

The net force on each coil is computed to equal 200 MN and is directed inward along the major radius. This force must be reacted against a central structure or bucking post as in most toroidal magnetic configurations. A unique aspect to the UWTOR-M centering load is that it must be reacted against a warm structure because of the large aspect ratio of the stellarator configuration. This requirement places some additional difficulty in terms of load transfer, but at the same time simplifies the design because of easier access on the inner bore and greater coil structural independence.

Typical force magnitudes on the UWTOR-M coil are in excess of 100 MN/m. Although this value appears high, it is in the range of that for most large superconducting fusion coils. The next section evaluates the support concept developed to withstand the magnetic loads. Since the reactor is truly a steady state device, including its magnetic field coils, it is not necessary to derate the structure because of cycle fatigue.

VII.3 Coil Support System

To study the feasibility of the reactor grade coils for the UWTOR-M stellarator, a proper coil support system must be determined first. A concrete definition of the coil support scheme is not only a prerequisite for the stress analysis of the magnet, but will also determine if a credible coil structure design can be achieved with respect to stress, strain and other operational criteria. This is particularly so for the modular coils in

UWTOR-M because of their three-dimensional curved configurations. The following considerations are essential in choosing a support system for the modular coils:

(1) The support structure for each coil must be separate and independent of each other to maintain the modularity and removability of each magnet. This consideration applies to both the structural and cryogenic requirements of the support scheme.

(2) The support scheme must be compatible with other reactor components for the ease of installation and maintenance. A complicated support system may not only hamper the elegance of the reactor design but also be technologically infeasible.

(3) Since no pure tension configuration exists for the modular UWTOR-M coils, the support system should be chosen such that the bending- and torsion-induced stresses are minimized. The transmission of the magnetic force to the supports should, therefore, take the shortest path possible.

Inspection of the magnetic force distributions in Figs. VII.2-3 and VII.2-4 shows that the radial component of the force varies little with respect to the position. The toroidal component of the force reverses direction six times over the angular position of the coil and is concentrated at the bend corner regions. The poloidal component of the force shows greater frequency of inversion and has zero value at the corner regions of the coil.

Study of the force distribution has led to the coil support concept shown in Figs. VII.3-1 and VII.3-2. A reinforcing ring outside the coil case is used to resist the expansion due to the radial component of the force. The ring is welded directly to the outer surface of the coil case forming a coil-ring assemblage. The coil case and structural ring are both maintained at

SUPPORT SCHEME

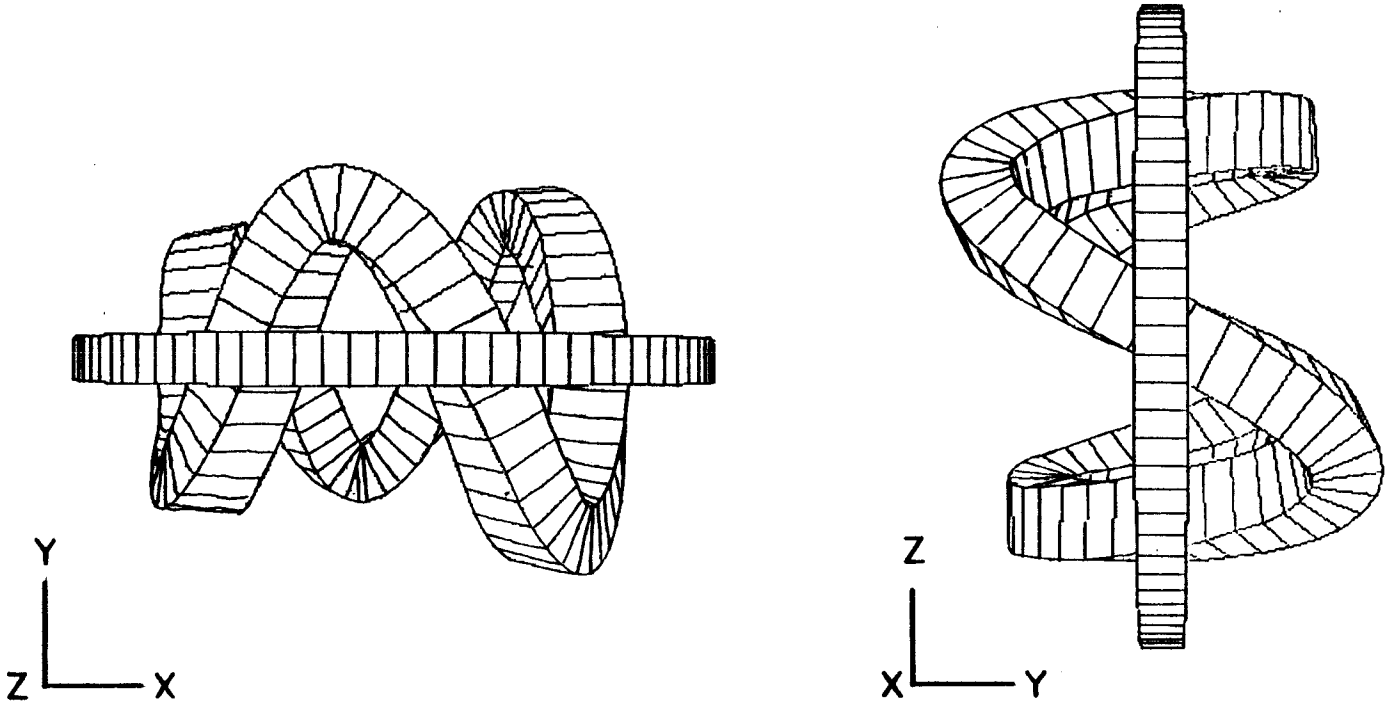

TOP VIEW

SIDE VIEW

Figure VII.3-1 Top and outside views of the ring-coil case assemblage.

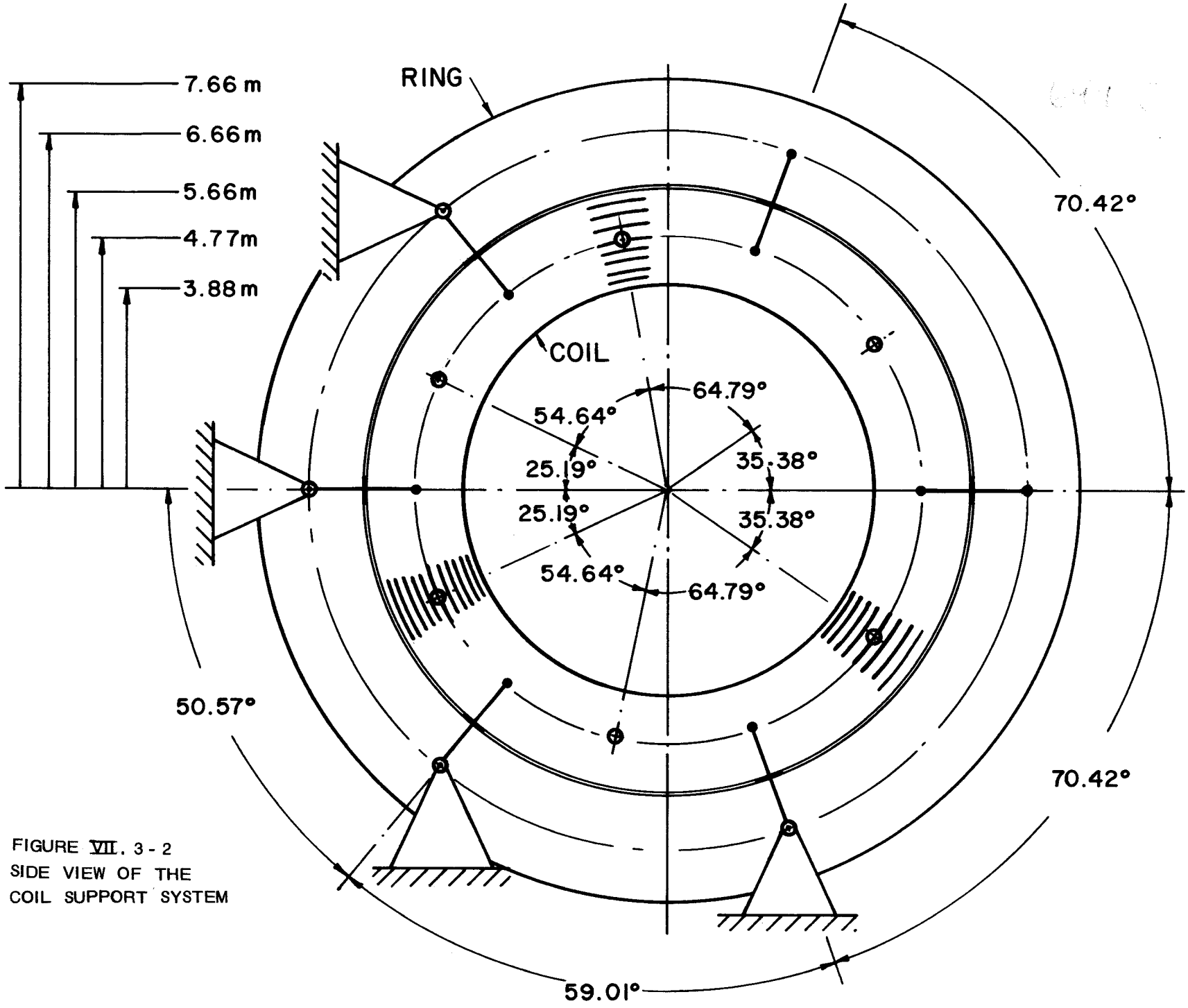

FIGURE VII. 3 - 2
SIDE VIEW OF THE
COIL SUPPORT SYSTEM

liquid helium temperatures, although the ring is only cooled by conduction. The coil-ring assemblage is mounted on the lower and central support and attached to the neighboring coils. In the present design four hinge supports situated at the ring-case connections are used to transmit the central force to the foundation and the central support structure as shown in Fig. VII.3-2. No additional support structure is needed on the top and outer regions of the reactor. Removal and maintenance of the reactor coil modules can be achieved without interfering with adjacent coil-ring assemblies.

To maintain the cryogenic independence, separate dewars are required for each coil and ring assemblage. At the bend corners of each coil, insulating structural material, NEMA-G-10CR or equivalent, is used to transmit the normal contact forces between the neighboring coils, Fig. VII.3-3. Six contact inter-coil connections are used for each coil to counteract these mutual attractive forces. Should maintenance of an individual coil be required, the coil system is deenergized. The mutual attractive loads are released allowing the contact regions to separate sufficiently to remove one coil without disturbing its neighbor. Thus, the coils maintain separate structural support and cryogenic environments. Such design fulfills the full modularization of the coil system.

The compatibility of the support system with other reactor components are demonstrated in the side view of the coil module, Fig. VII.3-4. The divertor targets are positioned in the gaps between coils and under the reinforcing rings. Coolant and breeding material connections can be accessed in the rear of the coil.

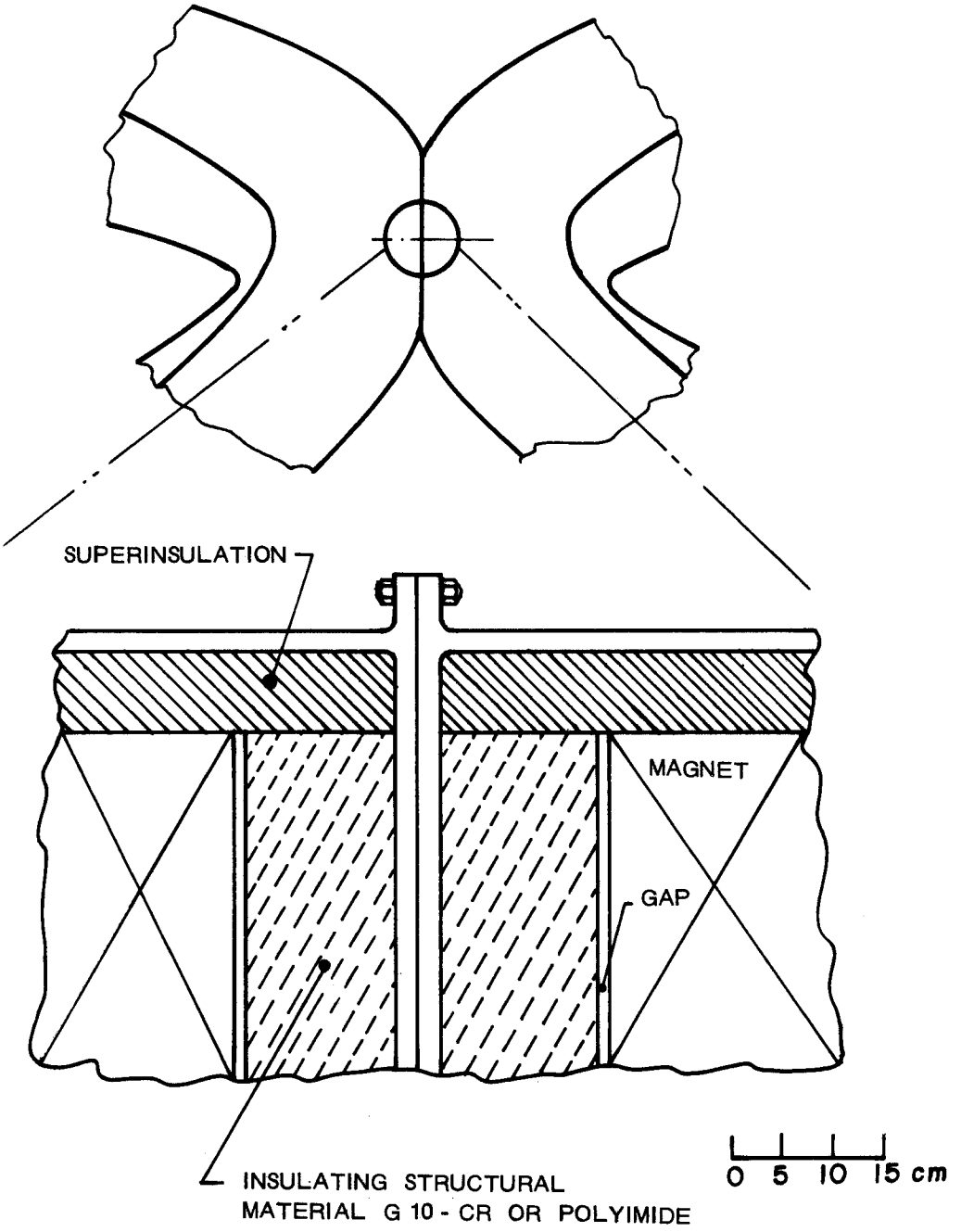

FIGURE VII. 3 - 3 CONCEPTUAL DESIGN OF CONTACT REGIONS BETWEEN NEIGHBORING COILS

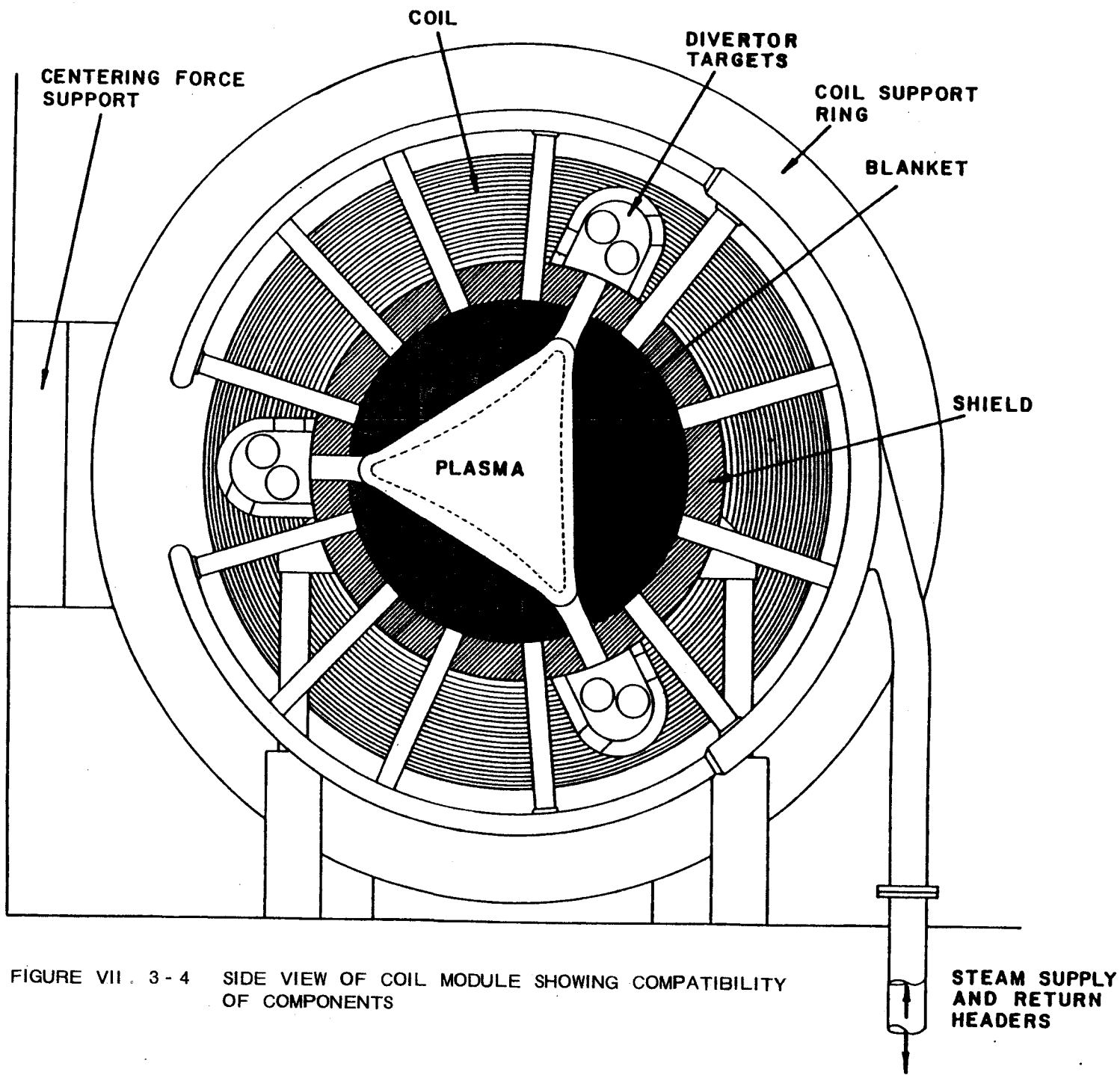

FIGURE VII . 3 - 4 SIDE VIEW OF COIL MODULE SHOWING COMPATIBILITY OF COMPONENTS

VII.4 Cross Sectional Design and Stress Analysis

The coil case and reinforcing ring are required to withstand the magnetic force, the thermal stresses due to cooling and the gravity force. The maximum induced stress in the coil should not exceed the maximum design stress of the material. To have the designed field topology for the plasma, the maximum deformation of the coil is limited to 5 cm, or 0.2% of the major radius of the reactor. This tolerance was established based on designs of smaller modular stellarator configurations.[9]

Emphasis in the initial design study of the UWTOR-M coils lies on determining if a credible magnet structure can be obtained to satisfy all its functional requirements. The credibility of the design is measured chiefly by the cross-sectional dimensions of the coil case and reinforcing ring needed to reach the design objectives of the magnet structure. Interest is also in determining the forces at the connections between coil case and ring, the interactions between neighboring coils and the reaction forces. Detailed connection and support designs are not included. In the present study the strength of the conductor coil is neglected as a simplifying assumption. The coil case, therefore, is assumed to take over all the forces. A complete modeling of the coil structure, taking account of the strength of the conductor, must include the effects of the initial non-linear behavior of the conductor and its relative displacement with respect to the coil case.[3] Such analysis is costly and can only be justified after the initial design has been solidified. This present approach leads to a conservative, over-estimated stress in the coil structure. The connections and supports are assumed to be rigid in the analysis. Since such components must be heavy in the final design, this assumption does not represent an overestimation of their stiffness.

However, higher local stresses in the connection and support regions are expected from the idealization of their sizes.

The design cycles lead to the cross sections of the coil case and reinforcing ring shown in Fig. VII.4-1. Stainless steel 304 LN-SS is chosen as the structural material for the coil. Its properties are listed in Table VII.4-1. A central web is added to the coil case to divide the conductor into two boxes. This serves to reduce the magnetic force accumulation in the conductor. A similar design is used for the cross section of the ring to stiffen the side walls. Dimensions of the cross sections chosen satisfy the stress and deformation requirements of the coil. The stress analysis of the coil structure is carried out using the MFE network SAP4 finite element code.[11] 100 three-dimensional beam elements are used for the coil case and ring each. The finite element model for the coil case is made consistent with the EFFI magnetic force calculation model. The calculated force results are input as distributed element forces into the SAP4 code. The beam elements simulate the effects of axial force, bending, torsion and shear deformations of the coil case and ring.

The connections between the coil case and ring are modeled as six beam elements with large values of elastic constants. The contact connections between neighboring coils are simulated by six boundary elements normal to the side wall of the coil case. The ring is supported by four rigid joints as shown in Fig. VII.3-2.

The stress distributions over each cross section of the coil case and ring are recovered from the SAP4 results. The effective stresses at twelve critical points are calculated and checked against the yield stress and allowable design value. The maximum values of the effective stresses over

Table VII.4-1. Mechanical Properties of Modular Coil Structural Metals

Material	304 LN-SS
Operating temperature	1.8°K
Young's modulus, E	200 GPa
Yield stress, σ_y	827 MPa (120 ksi)
Max. design stress, σ_a	533 MPa (80 ksi)
Specific weight	76.4 kN/m^3
Average thermal expansion coefficient, α	1.2×10^{-6}/°C

CROSS SECTIONS

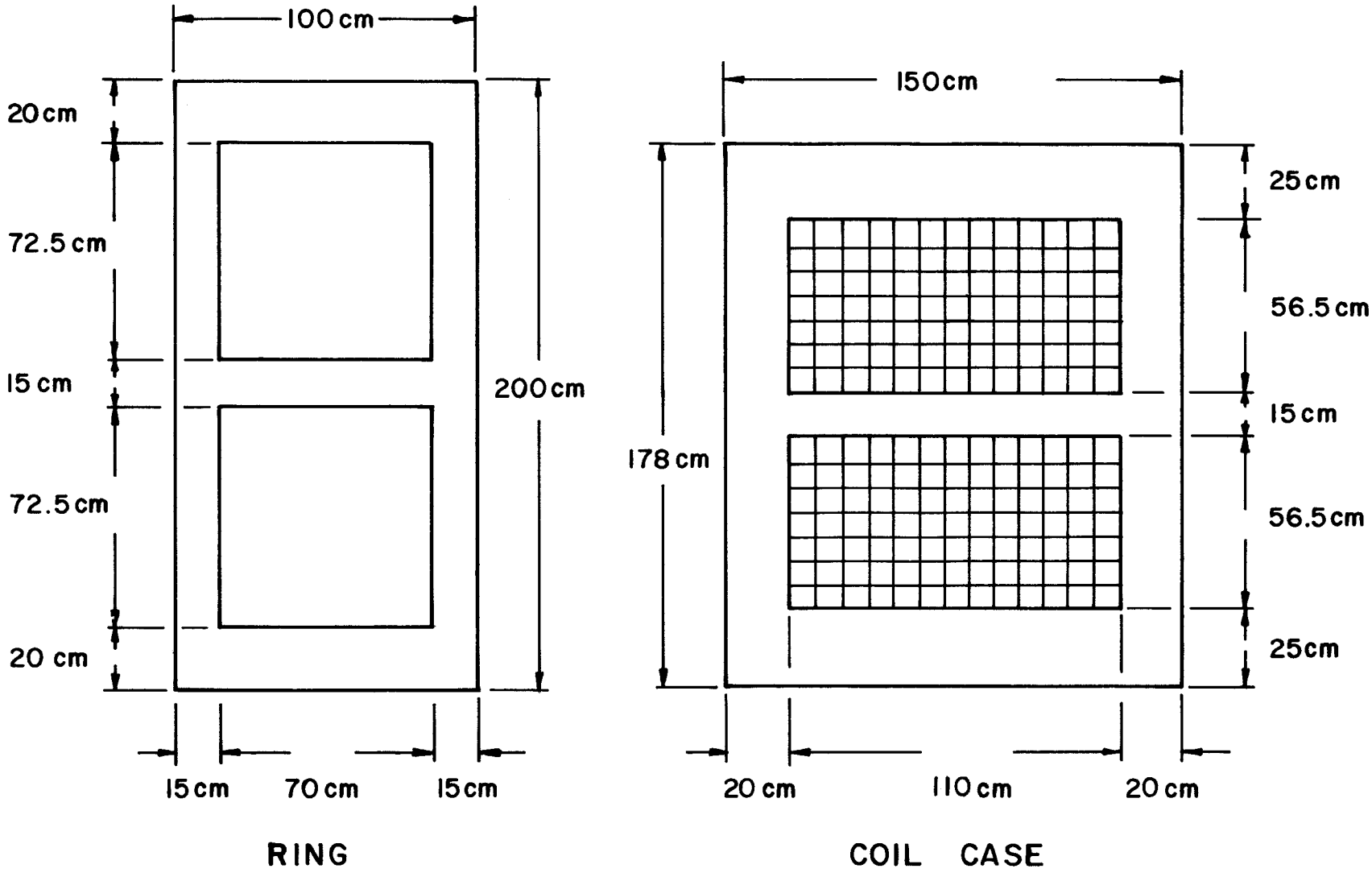

FIGURE VII. 4-1 CROSS SECTION DESIGNS FOR REINFORCING RING AND COIL CASE

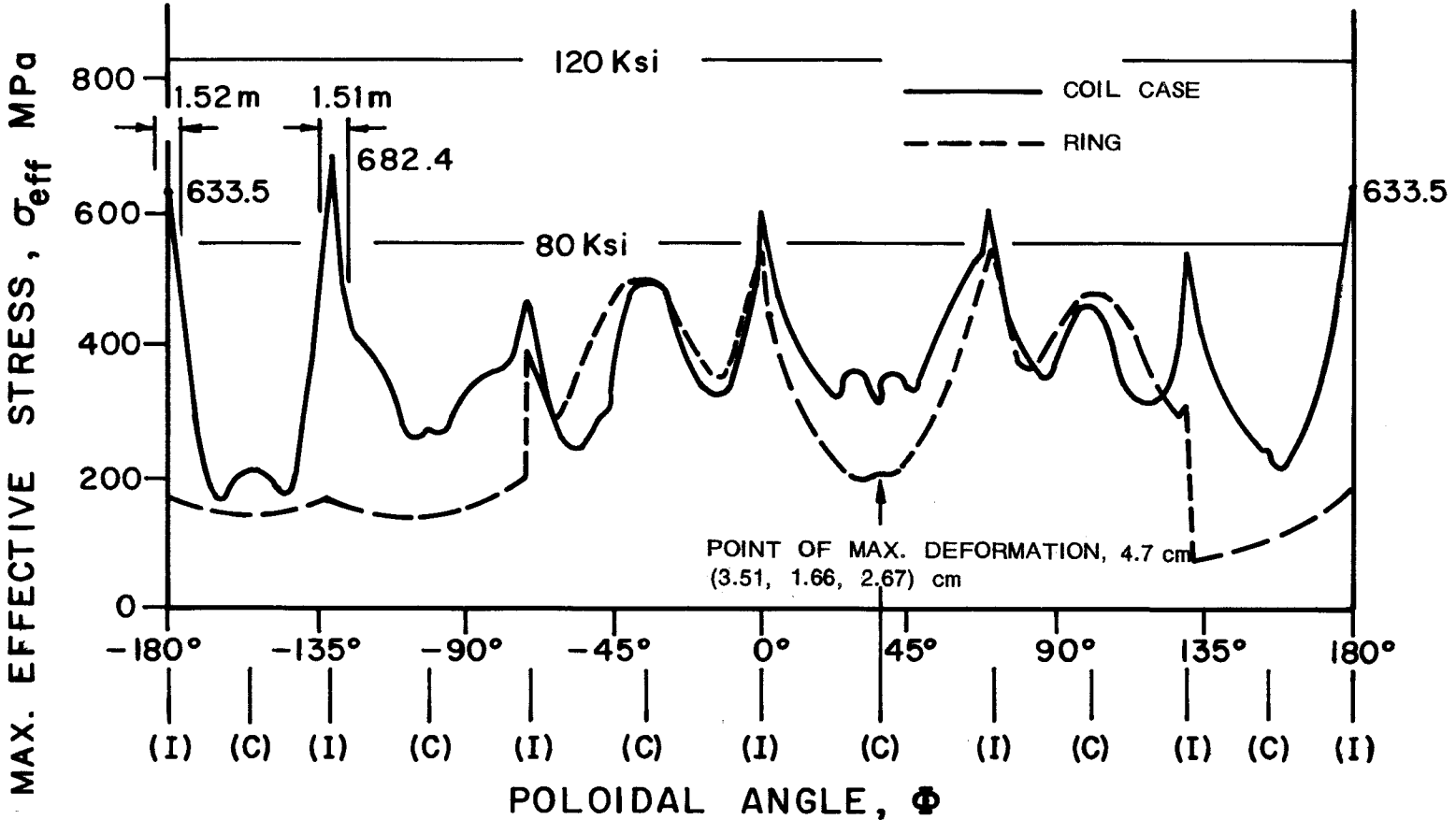

MAX. EFFECTIVE STRESSES IN COIL CASE & RING

Figure VII.4-2 Maximum effective stresses on each cross section for reinforcing ring and coil case.

each cross section are plotted in Fig. VII.4-2. Also indicted is the maximum deformation occurring at the bend corner located at $\phi = 35.4^0$.

The positions of the bend corners of the coil case and the case-ring intersections are indicated in Fig. VII.4-2 by (c) and (I), respectively. It is seen that except for the connection regions, the maximum stress levels are both below the allowable value. The narrow peaks in the connection regions, however, result from the idealization of the connections as rigid beams. Under such idealization, the three-dimensional nature of the stress field in the connection region is replaced by the linearly-varying stress field allowed by the beam element. The actual stress variations within the connection regions of 1.5 m should be much lower due to the stress redistribution. These local violations of allowable stress in the design may, therefore, be dismissed as caused by local boundary effect. For the more detailed connection design, a more refined three-dimensional stress analysis model needs to be built to study the stresses within these regions.

The reaction forces on the coil-ring assemblage are shown in Fig. VII.4-3 for the rigid joint support scheme. The forces and moments at the ring-coil case connections are presented in Fig. VII.4-4 in terms of local coordinate systems. The 1-2 planes of all the local coordinate systems lie on the radial midplane of the coil. The local 1-axis directs toward the center of the coil and the 2-axis normal to 1-axis as shown. The 3-axis is defined by the right-hand rule and is directed into the paper. The F_1 force components at all the connections are found to dominate. The ring, therefore, provides mainly a restraint to the radial expansion and some added flexural stiffness to the coil case.

REACTION FORCES

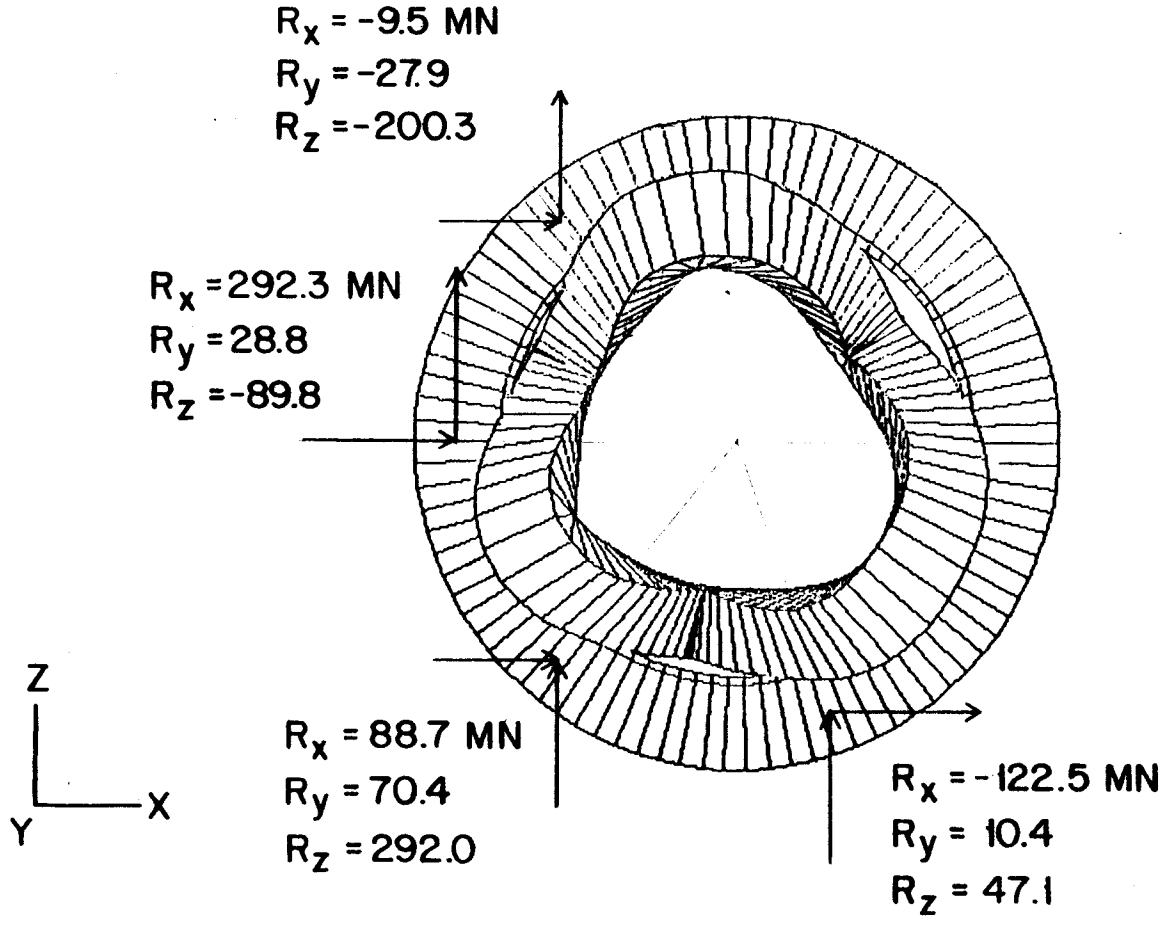

FIGURE VII 4-3 REACTION FORCES AT THE JOINT SUPPORTS FOR RING-COIL CASE ASSEMBLAGE

FORCES AND MOMENTS AT CONNECTIONS

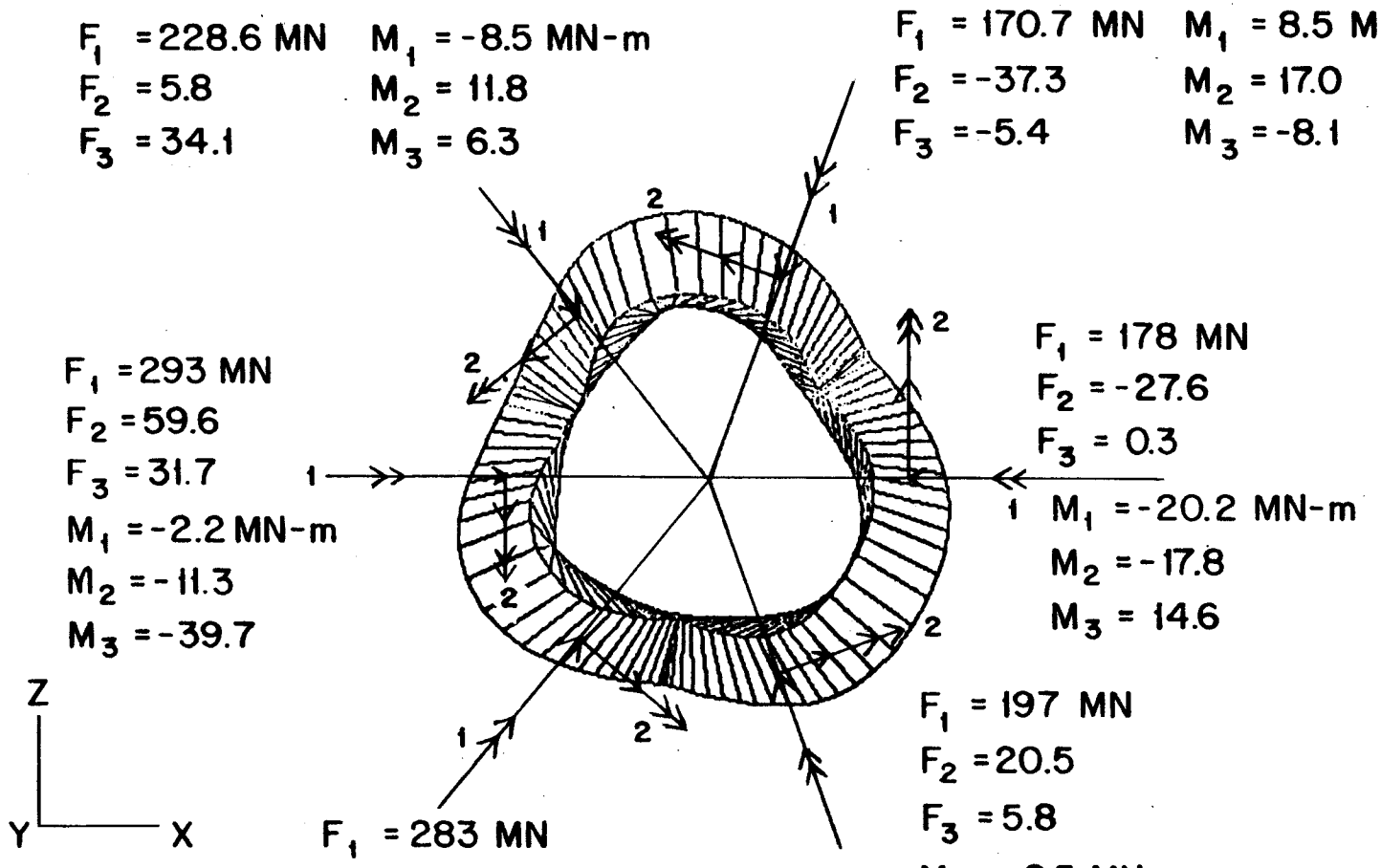

FIGURE VII. 4-4 FORCES AND MOMENTS AT RING - COIL CASE CONNECTIONS

FORCES BETWEEN COIL CASES

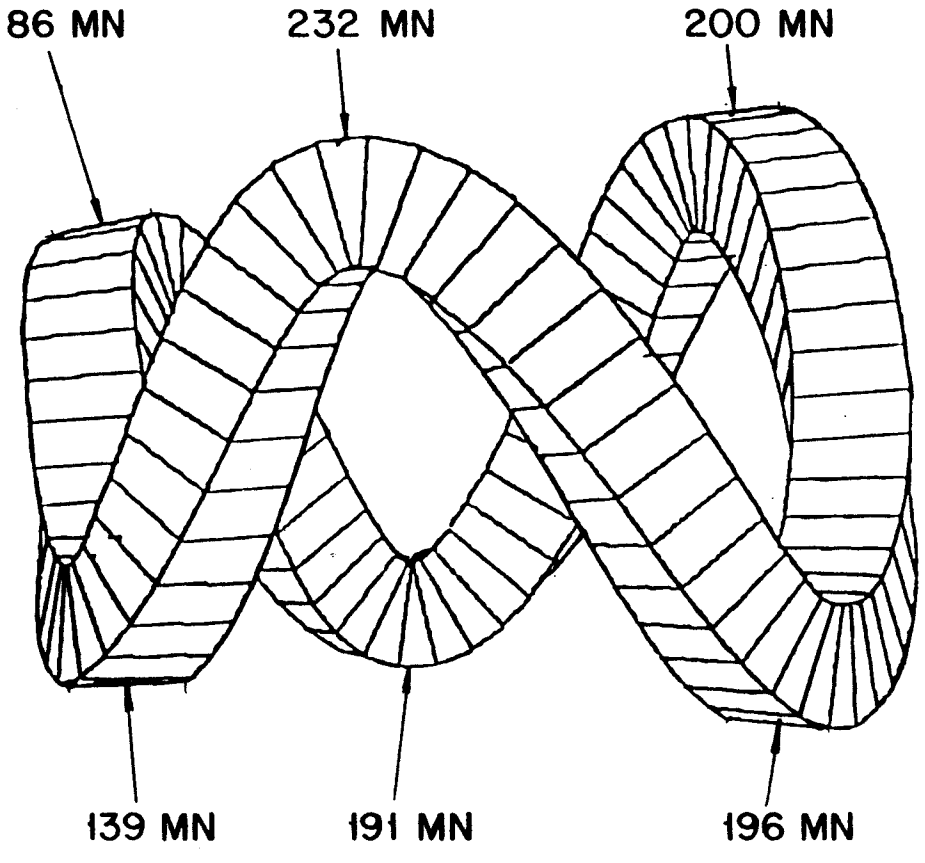

FIGURE VII . 4 - 5 CONTACT FORCES AT INTER - COIL CONNECTIONS

The contact forces between neighboring coils are shown in Fig. VII.4-5. The directions of these contact forces are determined by the twisting of the coil case. For the ease of assemblage, it would be more desirable to have the contact faces of the coil case parallel to the vertical radial planes passing through the contact connections. The contact forces would then serve some arch action and help reduce the net central force. Under normal operations these forces balance for each coil.

VII.5 Superconducting Coil Design

As with the other aspects of the UWTOR-M magnet system, the superconducting coil design has attempted to maximize credibility with as near to state-of-the-art technology as possible. The challenging aspects to achieving a high level of credibility are threefold:

(1) The coils are of the order of 10 GJ each, a figure roughly ten times that of the largest superconducting magnets in operation today. From the coil design viewpoint, this fact strongly affects safety considerations.

(2) The coils are of unusual configuration, lacking the symmetry of solenoids or even yin-yang coils for mirror end cells. The concern here is mostly one of fabrication to coil tolerances and winding procedure.

(3) The superconducting aspects to these coils are reasonably straightforward with the one exception that the field on the coils is high by today's standards for large coils. The established limit of $B_{max} \leq 12$ T was chosen to allow some flexibility in choice of superconducting material and cooling scheme. This limit has also been set for other large fusion magnet systems for tokamak and mirror reactor concepts.

The details of the coil design for UWTOR-M can be seen by reference to Fig. VII.4-1, which shows a multicomponent coil separated into two segments

and supported structurally by a stainless steel coil case. The coil itself is a composite of current carrying conductor, a NbTi or NbTiTa superconductor in a copper matrix, insulating structure and liquid helium. The general goal of the design is to achieve high current density while being fully stable from the superconductor viewpoint.

The reason for separation of the coil case into two segments is primarily structural. It was determined at the early stages of design that the conductor would not be able to carry tensile loads because of the complicated winding configuration. However, the individual conductors would need to transfer their load to the structural coil case and, therefore, must be designed to withstand accumulated loads. A coil structure in the form of a single winding window would have an excessively high accumulated load. By dividing the coil case into two segments, the load on the conductor is maintained below the yield of 3/4 hard copper.

The actual physical features of the coil design are listed in Table VII.5-1. The overall current density of 11.7 A/m^2 is the value determined by averaging over the entire winding cross section, including the coil case. As can be seen by the volume cross sections, this current density is determined by the large stainless steel cross section. Therefore, only small increases in the overall current density can be achieved by reducing the conductor cross section.

The current for the conductor is chosen at 20 kA. Reasons for this selection were to keep the coil inductance to a minimum for safety and discharge. Further, the conductor design utilizes a monolythic copper superconductor composite. Handling during fabrication of a conductor larger than that necessary to carry 20 kA is viewed to be difficult.

Table VII.5-1. Coil Design Configuration

Total current	31.2 MA
Overall current density	11.7 A/m^2
Number of turns	1560
Inductance/coil	48 H
Volume cross section	
Stainless steel (304 LN)	53%
Copper (3/4 hard)	33%
Superconductor	2%
Insulation	4%
Helium	8%

CONDUCTOR INSULATION SCHEME

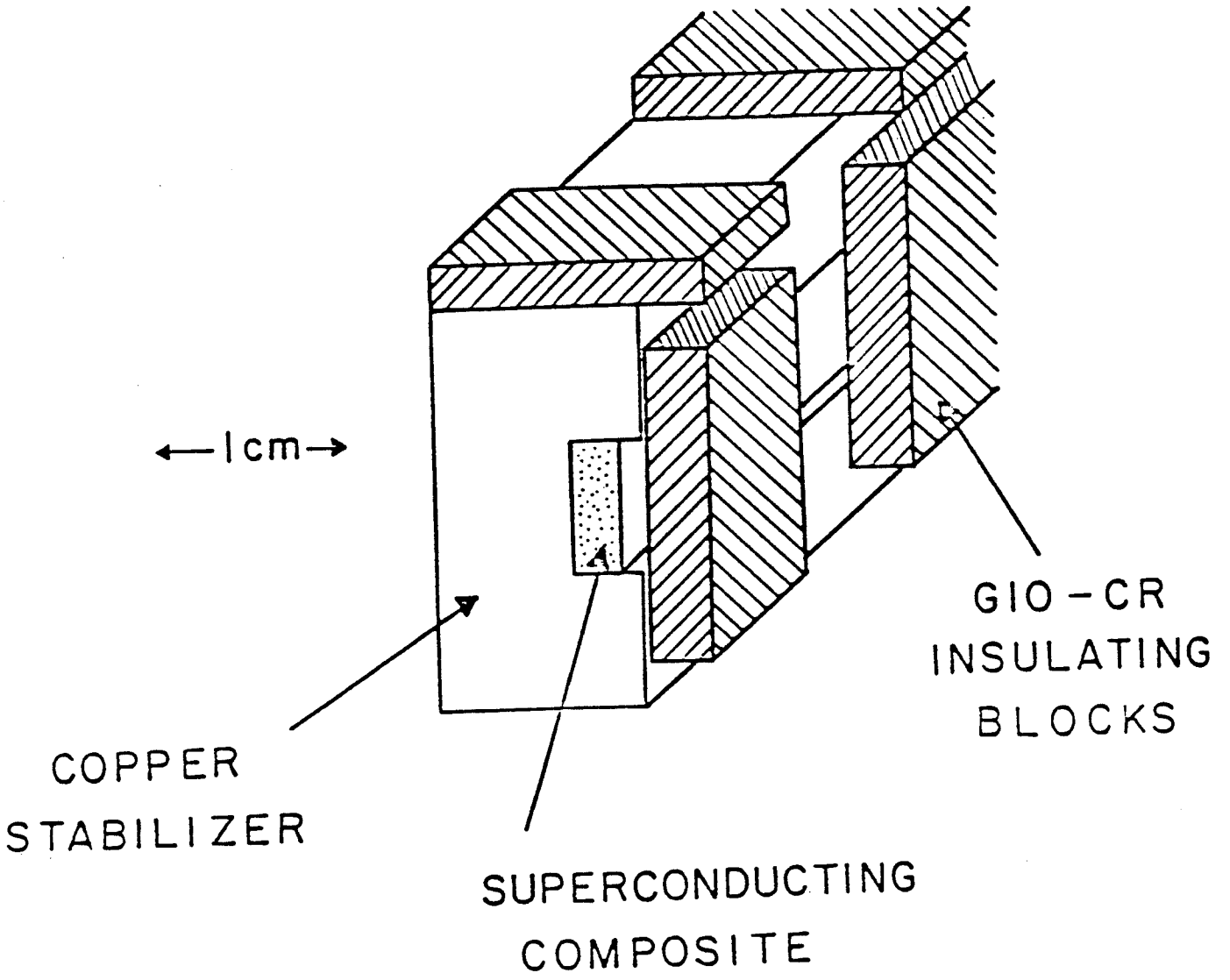

FIGURE VII. 5-1 CONDUCTOR INSULATION SCHEME

A schematic representation of the conductor configuration is shown in Fig. VII.5-1. The conductor is of a relatively simple design consisting of a composite of NbTi or NbTiTa in a monolythic 3/4 hard copper stabilizer. The conductor has a rectangular cross section with an aspect ratio of 2:1. Insulating blocks made of Nema G-10 or polyimide are positioned as shown to insure adequate surface cooling and proper load transfer. A monolythic conductor configuration was selected because of a need for good mechanical properties of the completed winding pack. Conductors of this type illustrated in Fig. VII.5-1 are in use in several large magnet systems presently in operation.

For a coolant scheme we have selected 1.8 K superfluid helium as a preferred choice for UWTOR-M coils. This decision was based on several factors:

(1) To reach a peak field of 11.6 T with NbTi superconductor one must operate at reduced temperatures. Otherwise Nb_3Sn conductor is required, with its associated poor mechanical properties.

(2) The use of superfluid helium cooling instead of normal pool boiling helium adds a higher degree of cryogenic stability for the conductor. Improved stability is perceived to be desirable for UWTOR-M because of the complex coil configuration and the need for moderately high current density.

The design parameters for the UWTOR-M conductor in the high field region are listed in Table VII.5-2. A conductor current density of 33.3 MA/m^2 at full field is possible mainly because of the improved stability in superfluid helium.

The superconductor current density of 800 MA/m^2 is based on a lower limit measured for NbTiTa at 12 T and 1.8 K.[12] The conductor would be graded in the low field region to minimize the quality of superconductor required. As a

Table VII.5-2 Conductor Design Parameters (high field region)

Conductor total current	20 kA
Cond. current density	33.3 MA/m^2
Stabilizer	3/4 Hard Cu
Superconductor	NbTi/NbTiTa
S/C current density	800 MA/m^2
Coolant	He II - 1.8 K, 1 bar
Heat generation (G/ℓ)	480 W/m
Maximum cooling (Q/ℓ)	560 W/m
Surface heat flux (q)	0.66 W/cm^2

backup position, Nb_3Sn superconductor may also be utilized in the high field region grading to NbTi in the low field regions. The use of Nb_3Sn would require greater care because of its brittle nature.

The stability of the UWTOR-M conductor was evaluated in terms of channel heat transport limits in the superfluid helium. With two-thirds of the conductor surface exposed to helium channels formed from the insulating blocks, the maximum heat transported by the helium should be 560 W/m of conductor length.[13] This value is nearly 20% higher than the peak heat generation rate in the high field region of 480 W/m, assuming the conductor is fully normal ($G=I^2R$). In terms of surface heat flux, the maximum heat transport converts to a value of 0.66 W/cm^2 of exposed conductor surface. This rate is a factor of two to three higher than would be possible if normal helium at 4.2 K was utilized.

One of the major considerations in the design of these coils is that of safety. Although the coils are not expected to have any problems, we must protect against the potential of a catastrophic event. Such an event may be a dewar rupturing and subsequently venting the magnetic coolant. Under circumstances such as this, the coil must be discharged rapidly to avoid damage.

To determine the safety of these coils, an adiabatic discharge analysis has been performed.[14] Here the assumptions are established that the coil is initially fully normal and a dump resistance is attached across the terminals of the leads. The energy is absorbed uniformly within the coil thereby raising its temperature. The maximum temperature is determined by equating the thermal energy with the magnetic energy.

The result of this analysis shows that the coil could be discharged in about 100 sec using a 0.5 Ω dump resistor and allowing the maximum terminal

voltage to reach 10 kV, a reasonable upper limit. Under these conditions, the adiabatic temperature rise would leave the coil at no higher than 55 K, a value which is quite acceptable in limiting thermally induced stress.

The above calculation is based on the assumption that the coils are powered separately and only one is discharged. This assumption is an over-simplification of the situation for the following reasons:

(1) There would be inductive coupling with adjacent coils driving the current up in these coils when one is discharged. If one wanted to maintain the other coils at full field under the discharge conditions, adjacent coils would have to be designed to carry the additional current.

(2) There would probably be considerable structural problems associated with discharging only one coil with the resultant asymmetry of field.

For the above reasons, the mode of operation for these coils should be that each operate individually with its own power supply. However, with this individual operation it would be necessary to slave all the power supplies to one master control so that they could be charged and discharged simultaneously.

VII.6 Fabrication Procedure

The difficulty with fabrication of the UWTOR-M coils lies mainly in their winding procedure. Since the coil configuration lacks an axis of symmetry, it is not possible to wind the conductor in tension. Rather, a method must be devised to mechanically hold the conductor in place against regions of negative curvature until the winding pack can be completed. Once the conductor pack is installed in the completed coil case, it is not required to carry tension and must only carry the accumulated loads to the structural case.

Two methods have been considered to support the coil in place during winding. The first consisted of a structural winding plate made most probably of stainless steel with grooves for each conductor turn. This method, which is analogous to that employed in the design of UWMAK-II,[15] has two major difficulties. Because of the asymmetric configuration of the UWTOR-M coils, these structural plates must be individually fabricated to rather tight tolerances. Additionally, there is concern about the insulation quality which must be maintained in order to prevent the coil from experiencing shorted turns. It was for the above two reasons that the preferred coil fabrication scheme does not include the winding plate described.

The alternative coil fabrication scheme involves the developmemt of a coil winding device. As envisioned, the coil would be wound in place and the insulation installed. Following this coil winding assembly, a conductor clamping mechanism would be necessary to insure the integrity of the winding pack until a subsequent turn could be installed. The clamping mechanisms would have to be attached to the coil case and consist of adjustable mechanical finger-like devices.

It is true that the fabrication of these coils represents a challenging aspect to the construction of UWTOR-M. However, certain credit should be given to the design because of its only requiring two different coil configurations.

VII.7 Control Coils

The only other coils required by the reactor are those needed to control the plasma center relative to the magnetic axis. These coils take the form of two solenoids located at a radius of 30 m and ±8 m in the vertical direction. The specifications for the coils are given in Table VII.7-1 where it is

Table VII.7-1. Control Coil Specifications

Major radius (m)	30
Vertical location (m)	±8
Current/coil (MA)	1.0
No. of turns	100
Radial shift $\Delta R/R$ (%)	45
Conductor winding pack (cm x cm)	20 x 20
Max. field at the conductor (T)	2.6
Field at plasma axis due to coils (T)	0.07
Coil case dimensions (cm x cm)	44 x 44
Dewar outside dimensions (cm x cm)	60 x 60
Stored energy/coil (MJ)	124
Mass of each coil (tonnes)	273

estimated that a current of 0.6 MA is needed in each coil to provide positioning $\Delta R/R \approx 45\%$. A safety factor of 65% is added to give a total current of 1.0 MA.

VII.8 Magnet Cryogenics

As the magnets for UWTOR-M must be maintained at their operating temperature of 1.8 K, an assessment of the helium refrigeration requirements is necessary to determine the recirculating power. The heat load at 1.8 K on the superconducting magnets is due mainly to four factors:

(1) Heat leak through structural supports, both for load transfer to the center post and for dead weight support: 2.4 kW.

(2) Heat leak through dewar structure which is mostly radiation loss through superinsulation: 1 kW.

(3) Nuclear heat absorbed in coil case and magnet windings: 0.5 kW.

(4) Conductor current lead heat leak. Helium gas is vented through leads and recovered at room temperatures: 1 kW.

Therefore, the total refrigeration power required at 1.8 K is 4.9 kW. Assuming a thermodynamic efficiency of 20% of Carnot indicates the room temperature power required is 833 W/W or a total power consumption of 4.1 MW. The reactor would have installed an excess of the minimum power required for cool down and fault operation. Still it is expected that 5 MW of refrigeration would be sufficient to operate the UWTOR-M magnets. The above calculation does not include that needed to operate the cryopumps, which is considered in another section of this report.

The liquid helium contained in each magnet is approximately 9.3 m^3 or 1350 kg based on the 8% helium volume fraction and the density of liquid helium at 1.8 K, $\rho = 145\ kg/m^3$. Since there are 18 magnets in the UWTOR-M

design, the system requires a minimum helium inventory of 167.7 m^3. Usually a safety factor of two is applied to a system design of this type in order to provide sufficient inventory for storage and distribution. It is, therefore, estimated that the UWTOR-M design would require about 335 m^3 of liquid helium or 48,600 kg. To convert from mass to volume at STP, the ratio is 200 ft^3/kg. In terms of standard volumes, the helium inventory turns out to be 9.7×10^6 ft^3. At the current price of \$35/1000 ft^3, the helium cost becomes $\$340 \times 10^3$, a small fraction of the entire UWTOR-M plant cost.

VII.9 Summary and Conclusions

Listed in Table VII.9-1 are summarizing features of the UWTOR-M magnet design. The total coil mass, although large, is not unreasonable from the viewpoint of fabrication and maintenance. It also appears reasonable for the mass per unit energy stored. The virial theorem sets a minimum required for each coil to be 127 tonnes, a factor which is rarely approached for an actual coil set.[16] The total coil mass of one UWTOR-M coil is 1175 tonnes, with the ratio of actual mass to that required by the virial theorem equal to 9.3. This value is reasonable considering a large fraction of the coil is assumed to carry no load. If we consider only the structural mass, a ratio of 6.2 is computed indicating a fairly efficient but conservative structural design.

VII.9.1 Magnet Summary

The parameters of the UWTOR-M reactor concept which impact the magnet design are listed in Table VII.9-2. There are three coils per field period, two of which are identical, only rotated 180° about the radial axis. Thus, the entire reactor gains simplicity by having two coil types (12 of one and 6 of the other). The magnets are discrete superconducting coils operated in the steady-state mode. No pulsed coils are evident. These considerations allow

Table VII.9-1. General Features of Coils for UWTOR-M

Total energy stored	171	GJ
Mass of each coil		
Stainless steel	481	tonnes
Copper	359	tonnes
Superconductor	18	tonnes
Insulation	7	tonnes
Helium	1.35	tonnes
	866	tonnes
Mass of support ring	309	tonnes
Virial theorem mass ($\rho E/\sigma$)	127	tonnes

for rather traditional coil design with the one requirement that the operating temperature of the coils be reduced to 1.8 K, utilizing superfluid helium cooling. This latter requirement is dictated by the maximum field at the conductor being 11.6 T.

The modular coils of stellarator reactors are designed with superconductor composite windings supported by the coil case structure. Under normal operating conditions, the interaction of the coil current with the field results in steady-state magnetic forces which must be resisted by the coil structure. The calculations of magnetic field and forces are carried out using the MFE network EFFI code.[8] Each coil is approximated by 89 straight segments at equal poloidal angle.

The magnetic forces on the coil can be thought to be comprised of two principal components, the self force due to its own field and the mutual attractive force between adjacent coils due to the interactive fields. In the regions where the coils come in close proximity, the mutual attractive forces dominate, causing large toroidal forces. The radial force component is about 560 MN/m, while the total force has a maximum around 150 MN/m.

The coil support scheme employs a reinforcing ring outside the coil case to resist the expansion due to the radial component of the force. The ring is welded directly to the outer surface of the coil case forming a coil-ring assemblage. The coil case and structural ring are both maintained at liquid helium temperatures. To maintain the cryogenic independency, separate dewars are required for each coil and ring assemblage.

The stress distribution over each cross section of the coil case and ring are recovered from the SAP4 results. The effective stresses at twelve critical points are calculated and checked against the yield stress and allowable

Table VII.9-2 Reactor Coil Design Parameters

Number of coils	18
Number of field periods	6
Number of coil types	2
Central field (B_o)	4.5 T
Peak field (B_{max})	11.6 T
Major radius (R_m)	24.1 m
Coil minor radius (A_c)	4.77 m
Total coil current (NI)	31.2 MA-turns
Structural material	304-LN-SS
Maximum design stress	533 MPa (80 ksi)
Conductor	NbTi in copper
Operating temperature	1.8 K
Overall current density	11.6 MA/m^2

design value. Stainless steel 304 LN is chosen as the structural material for these components. The maximum stress levels in both the ring and coil case are below the allowable value of 2/3 yield.

The coil is composed of composite conductors of NbTiTa and NbTi in copper. It is designed to be fully stable cooled by a bath of superfluid helium. The conductor current density is 33.3 MA/m^2 and the small current density including structure is 11.7 MA/m^2. Safety considerations dictate that the coils be operated in parallel and discharged together under fault conditions.

References for Chapter VII

1. D.T. Anderson, J.A. Derr and J.L. Shohet, "The Interchangeable Module Stellarator", IEEE Trans. on Plasma Science, Vol. PS-9, No. 4, pp. 212-220 (1981).

2. S. Rehker and H. Wobig, Proc. of the..Symp. on Fusion Technology, Grenoble, 1972, pp. 345; Max Planck Institut fur Plasmaphysik Rep. IPP 2/215, 1973.

3. R.L. Miller, R.A. Krakowski and C.G. Bathke, "Parametric Systems Analysis of the Modular Stellarator Reactor (MSR)", LANL Rep. LA-9344-MS (May 1982).

4. A.H. Boozer, et al., "Two High-Beta Toroidal Configurations: A Stellarator and a Tokamak-Torsatron Hybrid", 9th Int. Conf. on Plasma Physics and Controlled Nuclear Fusion Research, IAEA-CN-41/Q-4, Baltimore, U.S.A. (Sept. 1982).

5. J.F. Lyon, et al., "Stellarator Physics Evaluation Studies", 9th Int. Conf. on Plasma Physics and Controlled Nuclear Fusion Research, IAEA-CN-41/Q-3, Baltimore, U.S.A. (Sept. 1982).

6. B. Badger, et al., "WITAMIR-I: A University of Wisconsin Tandem Mirror Reactor Design", University of Wisconsin Fusion Engineering Report UWFDM-400 (Sept. 1980).

7. B. Badger, et al., "TASKA: A Tandem Mirror Fusion Engineering Facility", University of Wisconsin Fusion Engineering Report UWFDM-500, KfK-3311, FPA-82-1 (March 1982).

8. S.J. Sackett, "EFFI - A Code for Calculating the Electro-magnetic Field, Force and Inductance in Coil Systems of Arbitrary Geometry," UCRL-52402, Lawrence Livermore National Laboratory, March 29, 1978.

9. D.T. Anderson, et al., "Confinement and Heating in Modular and Continuous Coil Stellarators", 9th Int. Conf. on Plasma Physics and Controlled Nuclear Fusion Research, IAEA-CN-41/Q-2, Baltimore, U.S.A. (Sept. 1982).

10. J.A. Horath, "Mechanical Behavior of the Mirror Fusion Test Facility Superconducting Magnet Coils," Mechanics of Superconducting Structures, F.C. Moon (editor), AMD - Vol. 41, ASME, 1980.

11. S.J. Sackett, "User's Manual for SAP4 - A Modified and Extended Version of the U.C. Berkeley SAPIV Code," UCID-18226, Lawrence Livermore National Laboratory (May 1979).

12. D.C. Larbalestier, "Niobium-Titanium Superconducting Materials," from Superconductor Material Science, Ed., Simon Foner and Brian B. Schwartz, Plenum Press, 1981, Ch. 3.

13. S.W. Van Sciver, "Developments in HeII Heat Transfer and Applications to Superconducting Magnets", Advances in Cryogenic Engineering 27 (pp. 375) (1982).

14. B.J. Maddock and G.B. James, "Protection and Stabilization of Large Superconducting Coils", Proc. IEEE, Vol. 115, No. 4 (1968), pp. 543-547.

15. B. Badger, et al., "UWMAK-II, A Conceptual Tokamak Power Reactor Design", University of Wisconsin Fusion Engineering Program Report UWFDM-112 (Oct. 1975).

16. Y.M. Eyssa and R.W. Boom, "Considerations of a Large Force Balanced Magnetic Energy Storage System", IEEE Trans. on Magnetics, Mag 17, pp. 460 (1981).

VIII.1 Divertor

VIII.1.1 Introduction

The stellarator family of toroidal confinement systems possesses a natural helical divertor.[1,2,3] This divertor is characterized by a magnetic limiter or separatrix, which isolates the confinement region of closed nested toroidal flux surfaces from the surrounding divertor region and the wall of the reaction chamber. Such a configuration has been shown to be effective in guiding particles from the confinement region to localized collection areas well removed from the main plasma. These collection regions act to neutralize the particles and either trap them or have them pumped away by the vacuum system. Evidence for the effectiveness of the divertor is demonstrated by helical burn marks on the vacuum chamber walls of existing stellarators.[4] Monte Carlo particle simulations by Gourdon et al., have shown that the flux of particles through the separatrix occurs primarily at the apices of the magnetic separatrix cross section. The particle flux is then focussed into narrow streams which emerge between the spaces of adjacent helical windings. The computed topology is in good agreement with burn marks observed on the experimental devices.[4,5]

The natural divertor in the stellarator family of devices occurs as a consequence of the existence of the magnetic separatrix bounding the region of closed nested flux surfaces. Existence of this separatrix can be proved for straight stellarators with perfect helical symmetry.[6] Inside the separatrix the enclosed magnetic flux links all of the magnet coils. Outside the separatrix, however, the flux links some, but not all, of the coils. Thus, some of the flux must emerge from the spaces between magnets, but to conserve flux, it must reenter the device at some other location. It is this property of the

magnetic flux external to the separatrix which forms the basis for the magnetic divertor and is typical of any toroidal magnetic confinement system characterized by a magnetic separatrix. The difference between the stellarator family and the other toroidal magnetic systems is that the null, and therefore the separatrix, occur naturally in the stellarator, while other systems, such as the tokamak, have to drive the null artificially by special placement of poloidal field coils.

Although nonaxisymmetric toroidal configurations do not have simple closed flux surfaces in terms of a rigorous mathematical existence, it can be shown that in many cases, closed surfaces may be described asymptotically in these devices.[7] Numerical tracing of magnetic field lines for such configurations shows that for divertor applications, an effective separatrix may be assumed to exist. Since modular stellarators can be shown to have such a separatrix, they also have naturally occurring divertors.

A systematic study of the properties of ℓ=3 modular stellarators with coils which have large lateral deformation has been performed. The divertors in these configurations have been found to be highly localized and modular in nature, resembling small bundle divertors distributed over the surface of the torus.

Early in the UWTOR-M study it was decided that an attempt should be made to utilize the magnetic divertor for impurity control. It was recognized that this decision may mean a somewhat more complicated reaction chamber geometry, necessitated by the need to provide slots for the emerging flux bundles. As the study progressed, it becaomes obvious that the nature of the modular divertor was such that the complication of the reaction chamber geometry was not that severe. Tracking of the helical flux surfaces could be accomplished by

stepwise rotation of adjacent blanket segments. Furthermore, the divertor slots are toroidally oriented and discrete.

There are only two impurity control mechanisms under serious consideration for magnetic fusion reactors, namely magnetic divertors and pumped limiters. The effectiveness of magnetic divertors has been demonstrated on several experimental devices.[8,9,10] On the other hand, pumped limiters have yet to be tested experimentally and questions have been raised as to their survivability in a fusion reactor environment. Their proximity to the plasma may provide a source of impurities in itself. Such issues as sputtering, material deposition and the inaccessibility of pumped limiters for replacement are yet to be seriously considered. The main advantage of pumped limiters is that they allow a more effective utilization of the magnetic volume. This, of course, is a very important consideration which has economic implications.

The uncertainty for stellarators with respect to impurity control is the contention by some scientists that confinement near the axis of the device is so good as to prevent impurities from migrating to the plasma edge where divertor action will remove them from the reaction chamber. This is in contrast to the tokamak which apparently has demonstrated an anomalous diffusion of impurities to the edge of the plasma. If this contention is true, then neither magnetic divertors nor pumped limiters would be useful in removing the impurities. Some mechanism, which would promote radial transport of impurities without affecting confinement of the fuel species, will have to be incorporated into the system. This may take the form of RF waves which would excite the fundamental or some harmonic frequency of the impurities. It is hoped future stellarator experiments may be able to test impurity transport

and determine the auxiliary means for promoting radial transport of impurities.

The modular divertor is the adopted impurity control mechanism in UWTOR-M. There are 18 coils and 108 divertor slots. Each divertor slot has two cylindrical divertor targets designed to recover the energy in the divertor region at a high temperature so that it can be converted at a high efficiency in the power cycle. The stationary cylinders are made of actively cooled shield material which prevents neutron streaming through the slots. A graphite surface cylinder rotates about the stationary cylinders at a nominal speed of 100 RPM. The particles striking the rotating surface are neutralized and pumped out. The surface energy is radiated to the cooled surrounding housing and the cooled stationary shield cylinders. A comprehensive analysis of the divertor targets is presented in Section VIII.2.

VIII.1.2 Method of Computation

The magnetic structure of the modular divertor region was studied by the tracing of magnetic field lines which link the scrape-off region with the exterior of the torus. The field lines were traced from a layer just outside the computed magnetic separatrix and were followed until they emerged from the torus between adjacent magnet coils. By tracing a large number of field lines distributed uniformly over the scrape-off region, the properties of the divertor were investigated.

To launch the field lines uniformly over the scrape-off layer, a model for the magnetic separatrix was needed. The minor radius ρ of the separatrix was expressed as a function of the poloidal and toroidal angles, using a two-dimensional Fourier series which consists of terms having the form

$$\rho_{i,j} = \alpha_{i,j} \cos (i\theta + j\phi) + \beta_{i,j} \cos (i\theta - j\phi) .$$

This form takes advantage of the usual symmetry properties of stellarator configurations. Using these terms, the minor radius was expressed as a finite summation over the discrete harmonic components:

$$\rho(\theta,\phi) = \sum_{i=1}^{M} \sum_{j=1}^{N} \rho_{i,j} .$$

To fit the coefficients of the double series, the separatrix minor radius was found at equal intervals of poloidal and toroidal angles. This was accomplished by field line tracing with the TORFIELD[11] code, using the arc length of the field line as the independent variable of integration. Interpolation in the toroidal angle then yielded points at a number of poloidal planes equally spaced in toroidal angle. The field line was traced for 2N + 1 field periods around the torus with 2M + 1 interpolated points found within each field period. All of the points were then mapped onto a single field period, which was sectioned into 2M + 1 poloidal planes. The 2N + 1 points on each of these planes describe a closed curve in the plane. This curve is the intersection of the separatrix with the particular poloidal plane. A cubic interpolatory spline was fitted to each of the curves and was used to obtain 2N + 1 points in each plane, equally spaced in the poloidal angle and lying on the closed curve.

This technique thus produced a set of (2M + 1)(2N + 1) discrete sample points, equally spaced in the poloidal and toroidal angles. The coefficients of the two-dimensional discrete Fourier series were then fitted, using the expressions for an odd number of sample points.[12] From the Nyquist Sampling

Theorem, only those spatial frequencies less than the Mth and Nth toroidal and poloidal harmonics could be resolved by this method. If ergotic structures, rational field lines, or fine island chains were present in the surface being Fourier analyzed, they produced high spatial frequency components. By requiring a sufficiently large number of sample points and a band-limited Fourier spectrum, a test for the quality of the separatrix was obtained, allowing for an automatic calculation of the last closed magnetic surface. Experience has shown that this technique provides a good method for describing magnetic surfaces for numerical computation. In practice, values of M = 10, N = 25 are routinely used with good results.

After the Fourier series expansion of the separatrix was obtained, it was used as a basis for defining a scrape-off layer at the plasma boundary. The scrape-off layer is shown in Fig. VIII.1-1 as $\Delta\rho$. The outer boundary of the layer is

$$\rho_{outer} = \Delta\rho + \sum_{i=1}^{M} \sum_{j=1}^{N} \rho_{i,j}$$

where $\Delta\rho$ is taken as the constant width of the scrape-off layer. Field lines were traced from this outer boundary from initial points distributed uniformly over equal intervals in poloidal and toroidal angle, over one field period. Each line was followed in both the positive and negative directions with respect to the magnetic field vector. The lines were followed for a maximum distance or until they intersected the toroidal shell defined by a prescribed minor radius $\rho = r_{cutoff}$. These intersection points were then mapped onto a single field period to indicate concentrations of magnetic flux, or flux bundles, where the diverted flux passes between adjacent coils. The mapping

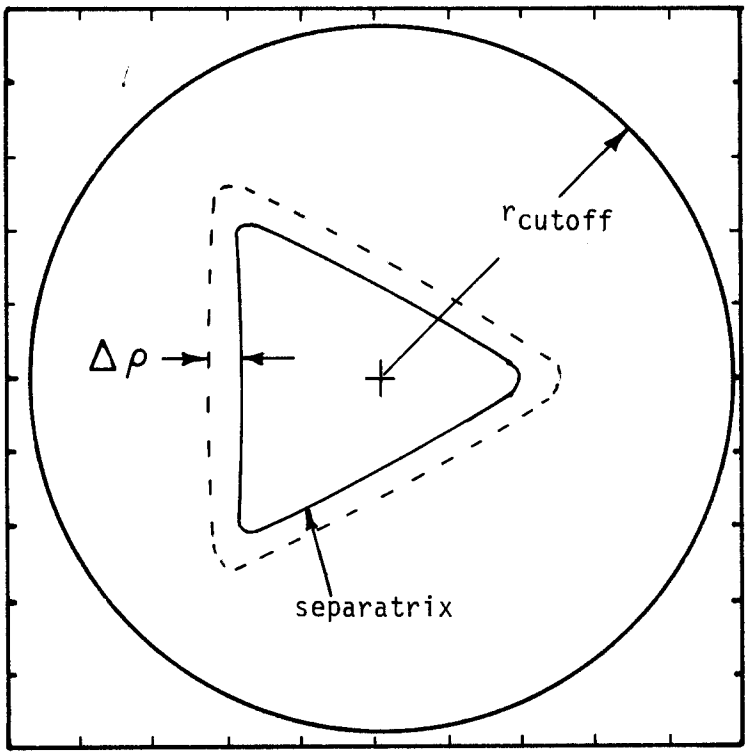

Figure VIII.1-1 Definition of terms in the computation.

thus indicates the regions on the toroidal shell where flux bundles emerge and reenter the torus. This indicates the size and location of the ports necessary to allow the diverted particles to stream freely across the shell.

Further details of the divertor structure were found through mapping of the divertor field lines onto poloidal planes. These mappings represent the intersection of the flux bundles with the poloidal angle, and give the position of the scrape-off layer with respect to the separatrix and the coil locations. They also define the boundary of the blanket and shield regions for the reactor. Such mappings were made for several poloidal sections within a field period to provide a detailed picture of the divertor configuration.

VIII.1.3 The Modular Divertor

The described method of analysis and computation was used to study divertor configurations for stellarators of intermediate and high coil aspect ratio. In these calculations a 60 x 60 grid of uniformly distributed starting points was established on the boundary layer and a pair of field lines was traced from each point to the cutoff radius, set to the minor radius of the torus which represents the centerline of the coils. The intersection of the divertor field lines with this toroidal shell is shown in Fig. VIII.1-2 which represents the poloidal and toroidal angle plane over one field period. The centerlines of the filamentary coils are shown in the figure as sinusoidal curves. The dark regions represent the signatures made by the intersection of the narrow flux bundles with the toroidal shell where they emerge and reenter the torus. The flux emerging from each signature circumvents the leg of a neighboring coil and then reenters through another signature. Each flux bundle and signature pair resembles a small bundle divertor.

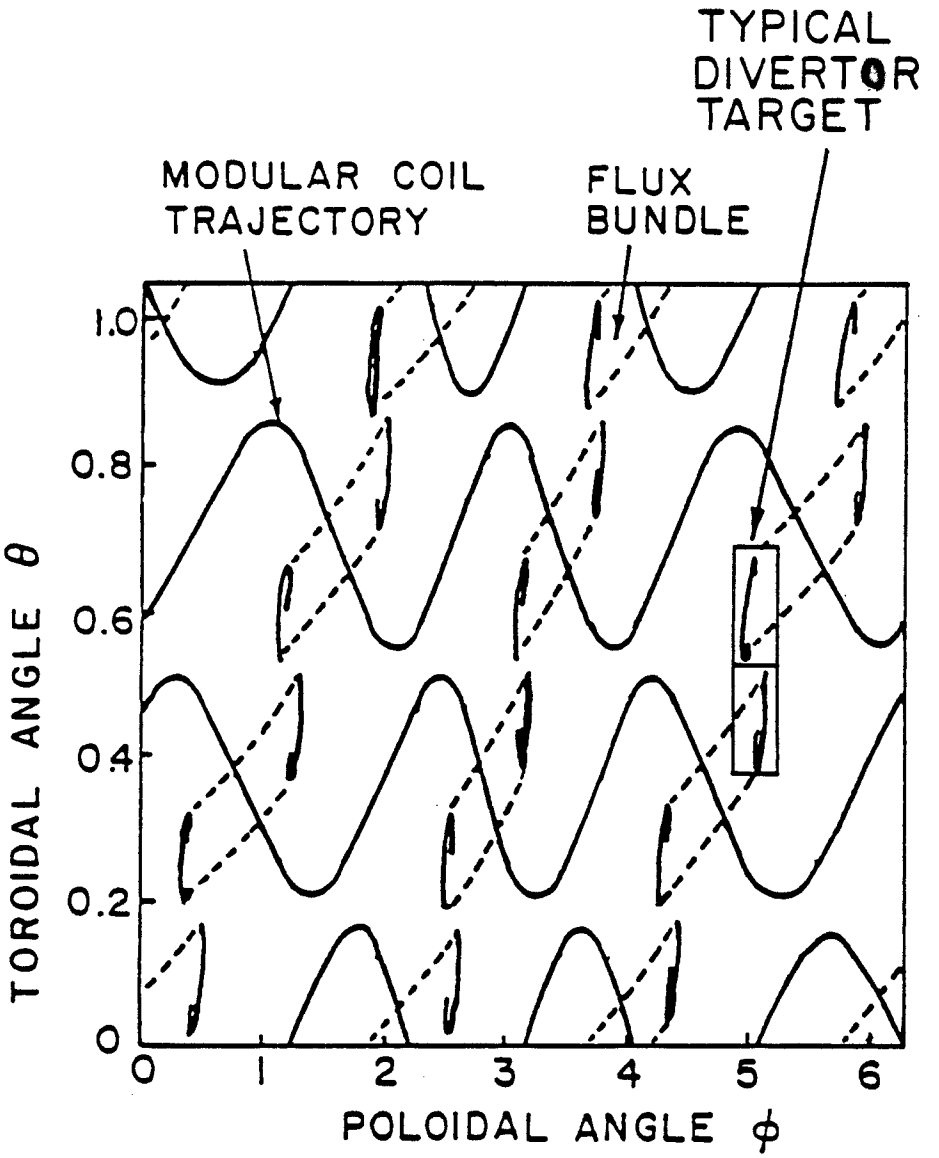

EMERGING FLUX BUNDLES THROUGH TOROID AT $R_{min.}$ MAPPED ONTO ONE FIELD PERIOD

Figure VIII.1-2

It can be seen from Fig. VIII.1-2 that each coil has three effective bundle divertors with two divertor slots associated with each. Thus, there are six divertor slots for each coil.

To demonstrate the degree to which the flux bundles are focussed while emerging through the slots, the signatures were recorded at several radial cutoffs. Figure VIII.1-3 shows six radial cutoffs where $r_{cutoff} = 0.04$ is at the plamsa edge and $r_{cutoff} = 0.08$ is at the coil centerline. If these two radial cutoff figures were superimposed, the flux bundle signatures fall on top of each other, indicating that the bundles are extremely well focussed.

To determine the impact of the divertor on the blanket geometry, additional mappings of the field lines onto many poloidal planes inside the torus are necessary. Figures VIII.1-4 - VIII.1-7 show the flux surface mapping for the UWTOR-M reactor at toroidal angles of 0, 15°, 30° and 45°, respectively. Figure VIII.1-4, where $\theta = 0^0$ shows the cross section of the plasma in the coil throat while Fig. VIII.1-6, where $\theta = 30^0$, is the cross section between coils. In the actual fact the plasma shape goes from that shown in Fig. VIII.1-4 to that shown in Fig. VIII.1-6 in only 10° of toroidal angle, namely the distance from the coil throat to the edge of the coil. It is obvious that the helical twist of the plasma in covering the distance is very small and indeed from Fig. VIII.1-2 and VIII.1-3, the orientation of the slots appears toroidal. This has a significant impact on the design of the blanket as is indicated in Section IX.3-1 of Chapter IX.

VIII.1.4 Conclusions

In conclusion, it appears that the modular divertor in UWTOR-M can be used for impurity control at the expense of a somewhat more complicated blanket geometry. We feel that the benefit of a demonstrated impurity control

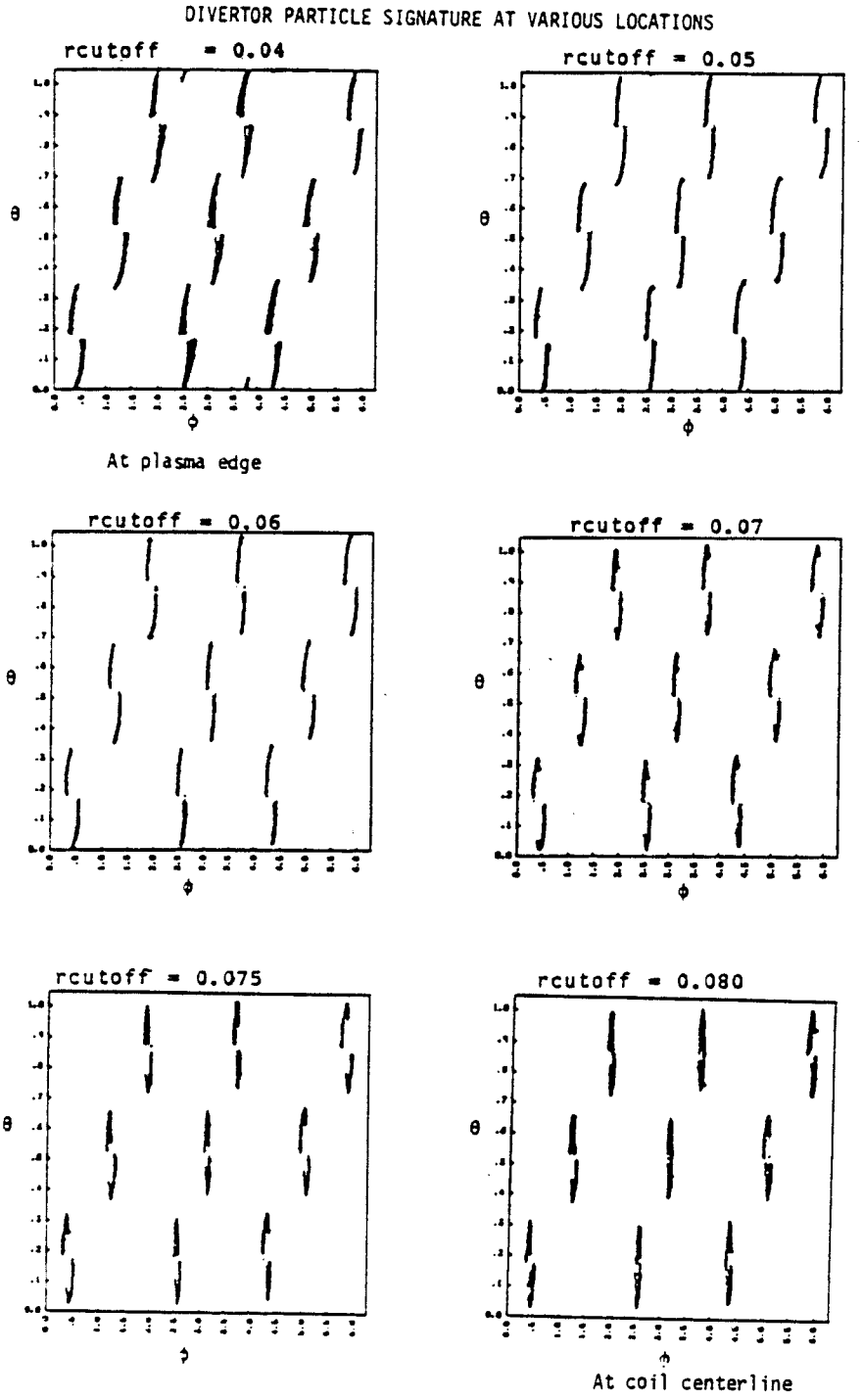

Figure VIII.1-3 Divertor particle signature at various cutoff: 0.04 at plasma edge, 0.08 at coil centerline.

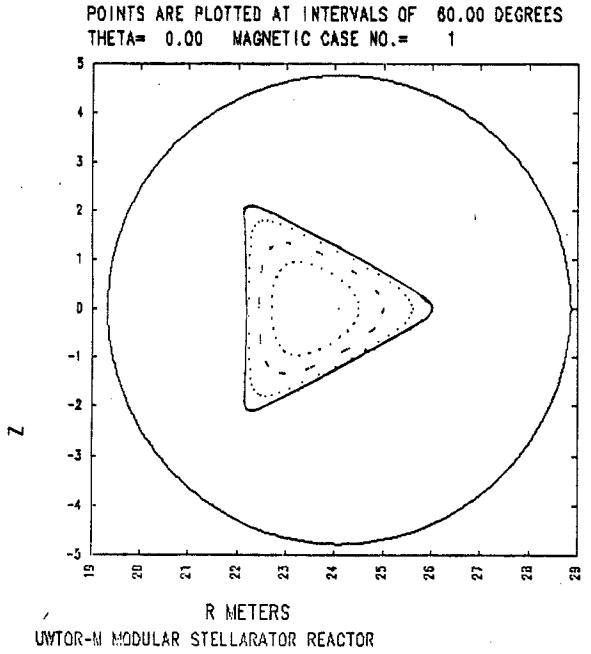

Figure VIII.1-4

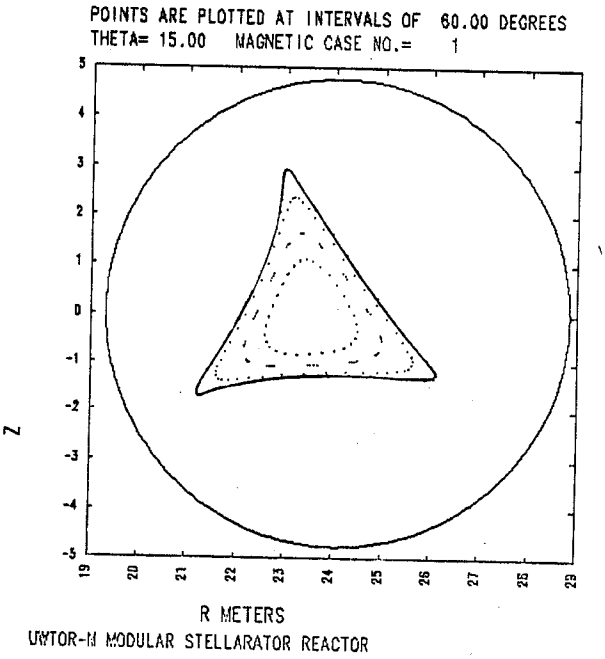

Figure VIII.1-5

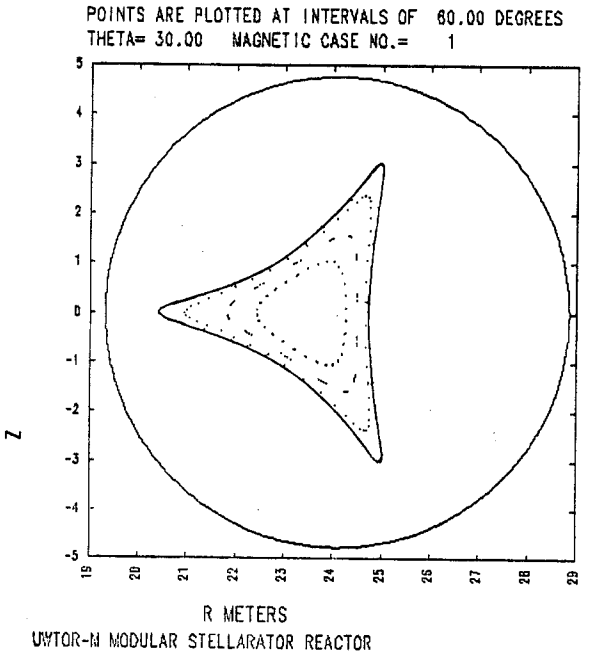

Figure VIII.1-6

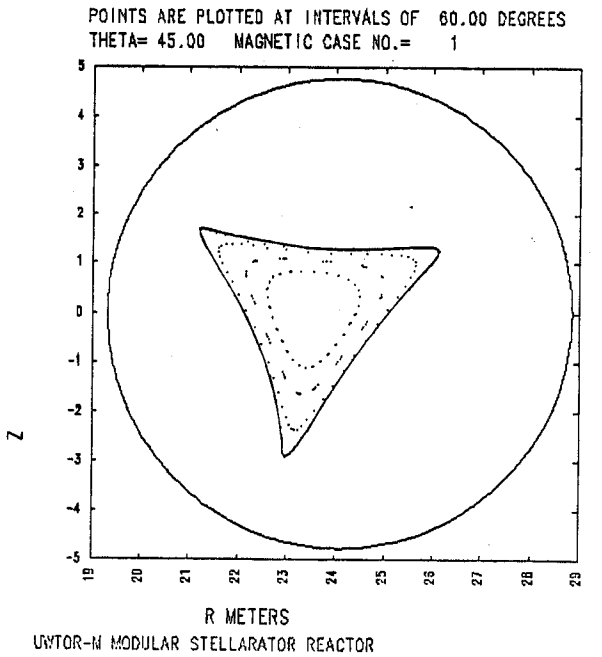

Figure VIII.1-7

Plasma shapes at different toroidal angles.
θ = 0 at coil throat; θ = 30 between coils.

is well worth this minor inconvenience. Table VIII.1-1 summarizes the advantages of the modular divertor.

Table VIII.1-1 Advantages of the UWTOR-M Divertor

1. No additional coils required
2. Compatible with the blanket and shield
3. Modular, localized collection regions
4. Effective for trapped particles
5. Well defined scrape-off zone
6. Low stray fields
7. Compatible with desired large rotational transform
8. Compatible with a practical coil configuration

References for Section VIII.1

1. C. Gourdon, D. Marty, E.K. Maschke and J. Touche, Nucl. Fusion, Vol. 11, p. 161, 1971.

2. C. Gourdon, D. Marty and J. Touche, "Fusion Technology", Proc. 6th Symposium, Aachen, 1970, p. 485.

3. A. Iiyoshi and K. Uo, "Plasma Physics and Controlled Nuclear Fusion Research", Proc. 5th Int. Conf., Tokyo, 1974, and 3rd IAEA Conf., Vienna, 1975, p. 619.

4. C.S. Voronow and M.S. Rabinovich, Invited Paper, 9th European Conf. on Cont. Fusion and Plasma Physics, Oxford, UK, 1979.

5. S.M. Hamberger, private communication.

6. A.I. Morozov and L.S. Solov'ev, Review of Plasma Physics, New York: Consultants Bureau, 1966, Vol. 2, p. 48.

7. K.J. Whiteman, Rep. Prog. Physics, 1977, Vol. 40, p. 1033.

8. S. Rehker and H. Wobig, Proc. 7th Symp. Fusion Tech., Grenoble, France, Oct. 1972.

9. J.A. Derr, Inter. Workshop on Stellarators, Schloss Ringberg, Lake Tegernsee, Bavaria, F.R.G., 1980.

10. P. Moon and D. Spencer, Field Theory Handbook, New York, Springer Verlag, 1971.

11. T.J. Martin, private communication.

12. F.S. Acton, "Numerical Methods That Usually Work," New York, Harper and Row, 1970.

VIII.2 Divertor Targets

VIII.2.1 General Description

The dual purpose of the divertor targets is to recover at a high temperature, the energy of the charged particles following magnetic field lines through the divertor slots and to shield the magnets from neutrons streaming. This high grade energy is then converted at a high efficiency in the power cycle. Each one of the 108 divertor slots in the UWTOR-M reactor is covered by a module (see Figs. VIII.2-1 and VIII.2-2) containing two divertor targets. These modules are self contained units which can be removed as a whole for maintenance purposes. They include apertures for venting neutral gas into the containment building and steam lines for cooling the surfaces which almost completely surround the two targets.

All of the divertor targets are cylindrical with an outside diameter of 60 cm, and about 2.5 m long. Figure VIII.2-3 is a lengthwise cross section of a single target showing its two basic components, a large stationary cylindrical core about which rotates a thin graphite shell. The central core, which has an outside diameter of 55.6 cm, does the bulk of the neutron shielding and is actively cooled by steam. The rotating shell is separated from the core by a 1 cm vacuum gap and is supported by bearings at both ends. The shell receives the full brunt of the particle flux along with a small amount of neutron heating. At a nominal rotational speed of 100 RPM the concentrated surface heat load is spread over the shell's external surface to give an average (ignoring neutron heating) heat flux of 30 W/cm^2.

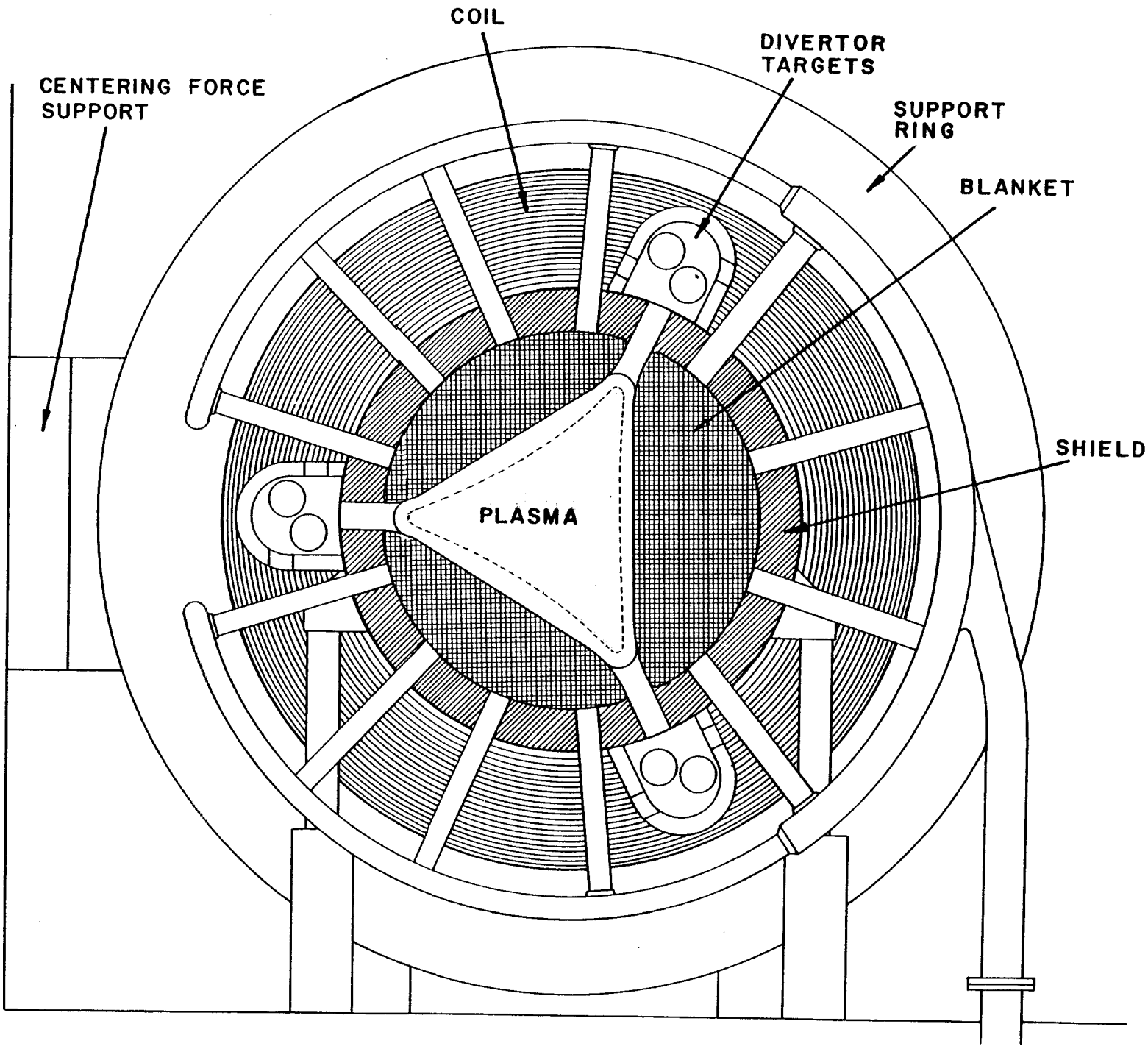

Figure VIII.2-1 Cross section of reactor showing location of divertor targets.

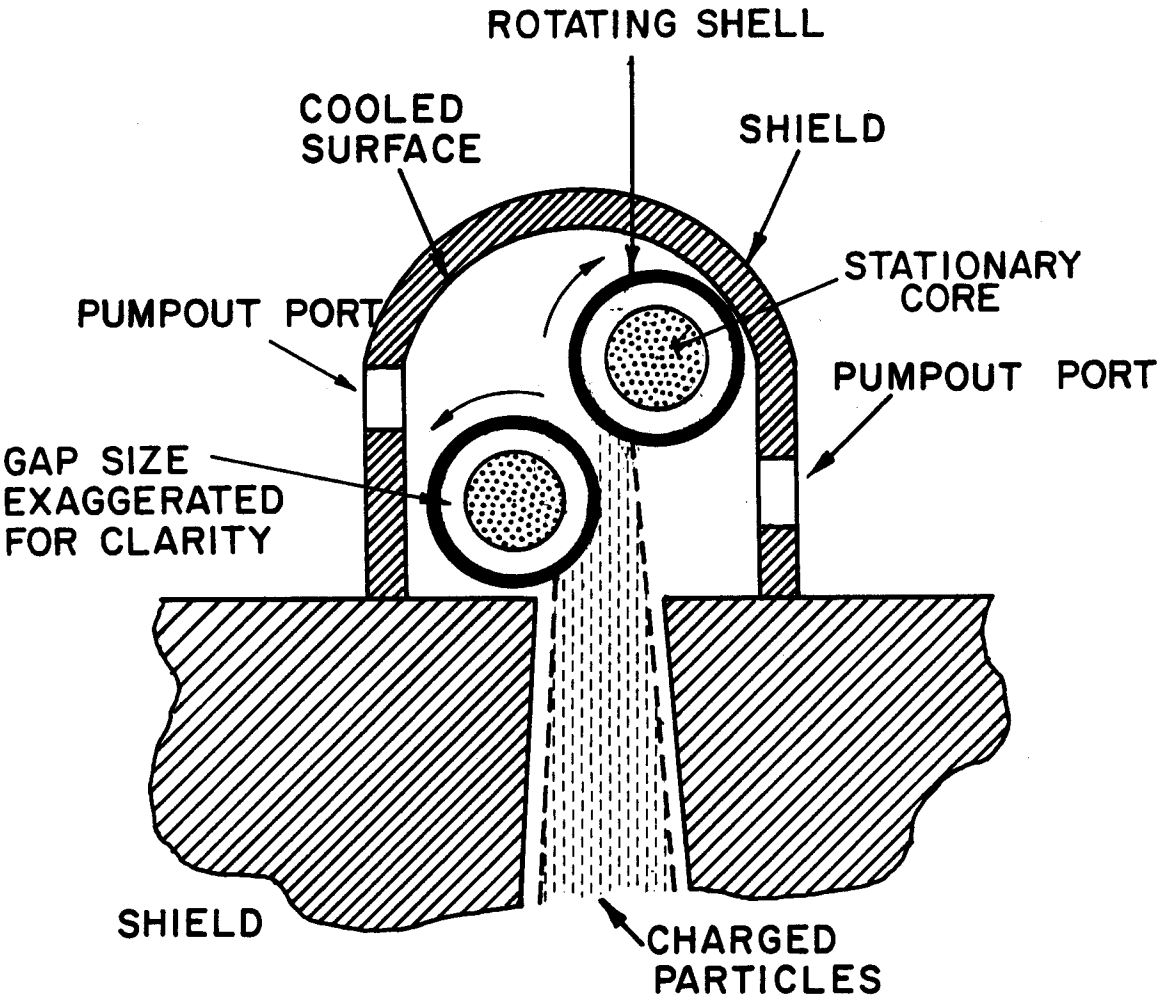

CROSS SECTION OF DIVERTOR TARGETS

Figure VIII.2-2

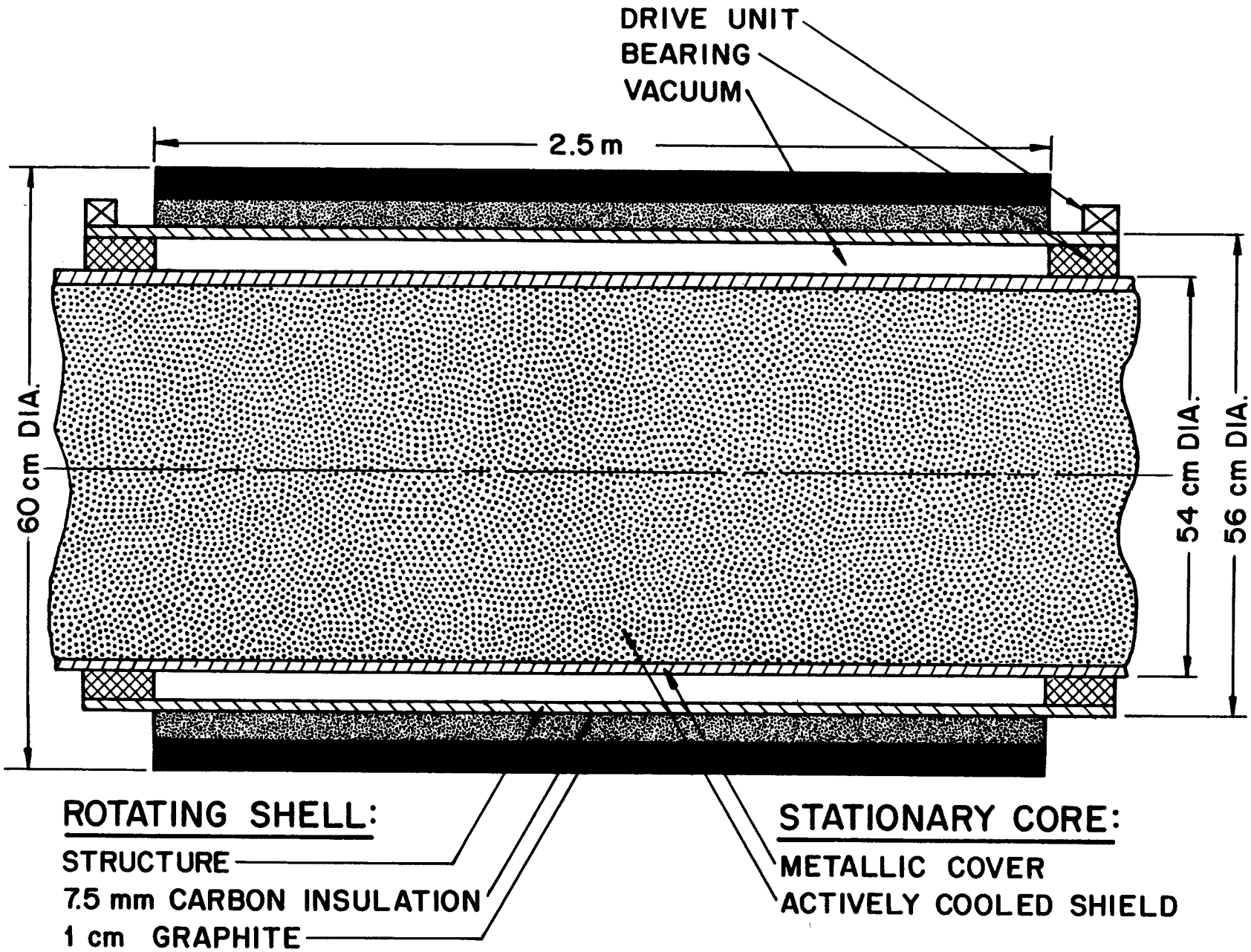

Figure VIII.2-3 Schematic of lengthwise cross section of a divertor target.

NOT TO SCALE

The shell was conceived as being constructed of three material layers. The outside layer is 2 mm thick graphite.* This material was chosen because of its ability to withstand the high temperature, high vacuum environment under prolonged neutron bombardment and its low atomic weight which makes it a less harmful plasma contaminant than other possible materials. The temperature limit is discussed in a later section.

The inner layer is a metallic structure which supports the graphite layer. The details and stress analysis of the structure are discussed in the next section.

The graphite and the structural regions are separated by a layer of carbon fiber insulation. This material makes use of the extreme anisotropy of graphite crystals to achieve (see Fig. VIII.2-4) a very low thermoconductivity. To achieve this property, the material must be in an inert atmosphere or a vacuum environment which is already the case in the UWTOR-M reactor. The effectiveness of this material is well documented and has been reported to have been marketed.[1,2]

The bearings and the drive for rotating the shell are not designed in any detail. However, they do not appear to pose a problem because of the very low weight (~ 30 kg) of the shield and low speed (~ 100 RPM) of the shell. It is anticipated that nonlubricated roller bearings with dissimilar metals could be used. The shell could possibly be driven electromagnetically, much like the rotor of an electric motor. To minimize torsion on the structure there should be a drive unit on each end of every divertor target.

---

*The calculations used 2 mm but the thickness could be increased to 1 cm or more without affecting the results.

Thermal Conductivity of Rigid Fibrous Carbon Insulation

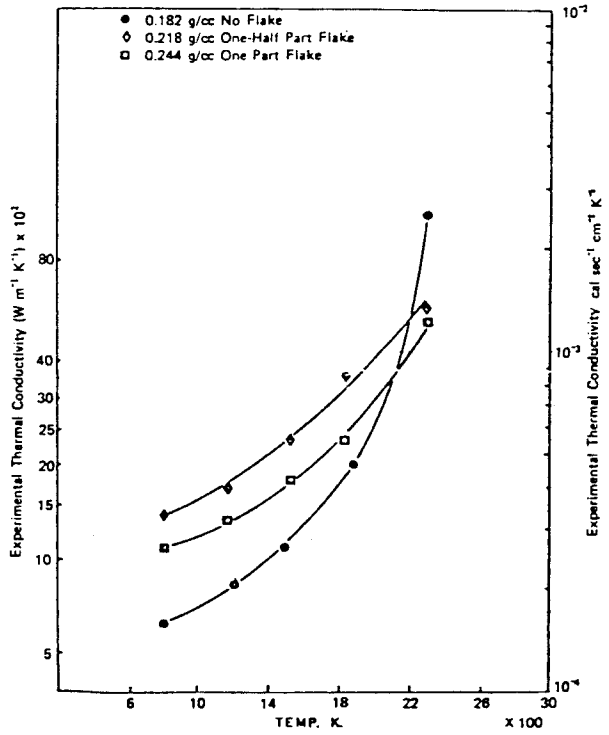

*This shows the effect of graphite flake additions on radiative and conductive heat transmission

Figure VIII.2-4 From reference 2.

VIII.2.2 Structural Considerations and Stress Analysis

The structural part of the rotating shield must be light and strong. Although the design presented in this report is not optimized, it shows that both criteria can be easily satisfied.

The design consists of a series of structural shells shown in Fig. VIII.2-5, which are joined together and make up the structure between the bearings. The part of the structure in contact with the bearings is not considered because it is not subjected to the bending forces of the shell's weight.

The structure is a cylindrical skeleton made of TZM resembling a radial vane for housing. It consists of 24 thin circumferential discs (see Fig. VIII.2-6) placed parallel to each other. Each adjacent pair of discs is connected together by 36 equally thin 10 cm long vanes which are oriented parallel to the axis of the divertor target.

The rotor housing was analyzed in a simple way. The structure was treated as a solid beam fixed at both ends and subject to a uniformly distributed load. Since it is driven from both ends, torsion was neglected. The stress in a beam is given by the formula

$$\sigma = Mc/I \qquad (1)$$

where M is the bending moment, c is the vertical distance from the neutral axis and I is the 2nd area moment of inertia about the neutral axis.

The maximum bending moment depends solely on the weight of the structure, the graphite and insulation. Allowing for all of the discs and vanes in the structure, the total volume between the bearings is about 715 cm^3. Using the

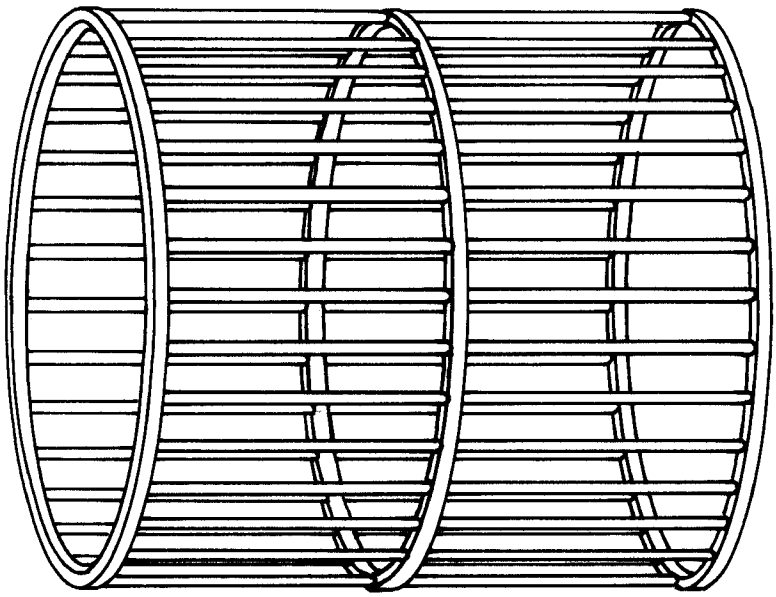

NOT TO SCALE

Figure VIII.2-5 Section of structure for rotating shell.

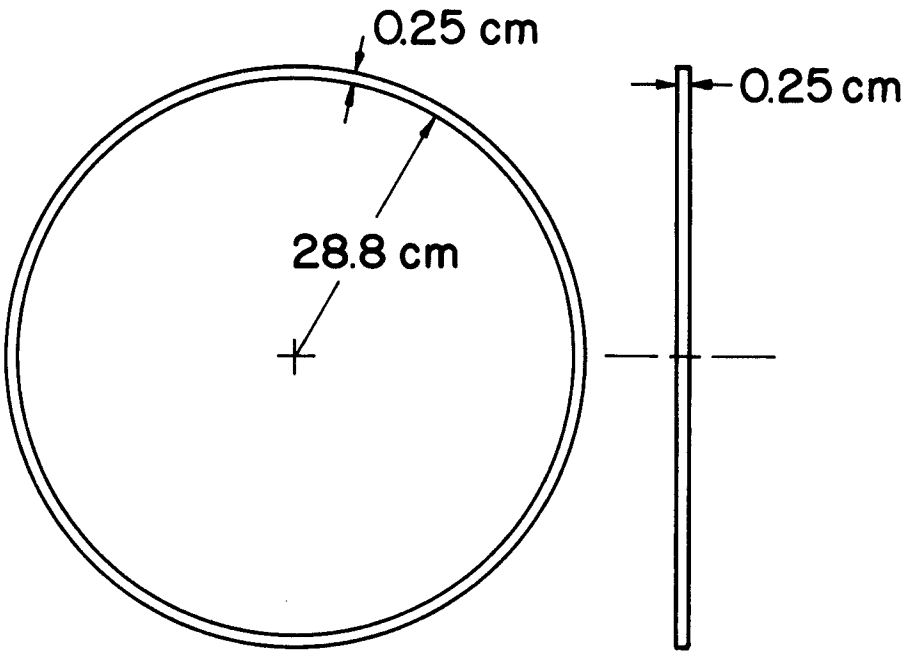

CIRCUMFERENTIAL DISC

AXIAL VANE

ORTHOGRAPHIC VIEW OF THE TWO BASIC STRUCTURAL PARTS

Figure VIII.2-6

material TZM (molybdenum alloyed with .5% Ti and .1% Zr) which has a density of 10.2 g/cm^3, the weight would be 7.3 kg. The weight of the 2 mm thick layer of graphite (density ~ 1.7 g/cm^3)[3,4] is 16 kg and the weight of the 7.5 mm thick layer of insulation (density ~ 0.18 g/cm^3)[1] is 6.4 kg. The total weight of 29.7 kg is assumed to be evenly distributed, producing the maximum bending moment M_{max} which can be estimated from[6]

$$M_{max} = \frac{WL}{12} \tag{2}$$

where L is the distance between the two bearings and W is the total weight.

The effective moment of inertia is calculated by Eq. (3):

$$I = A\, r_c^2 \left[2 + 4 \sum_{i=1}^{8} \sin^2 (\theta i)\right] \tag{3}$$

where A is the cross sectional area of a single strut, r_c is the distance from the centerline of the shell to the center of a vane and θ the angle between two adjacent vane which is taken as 10 degrees (see Fig. VIII.2-7). For the given configuration the moment of inertia is 740 cm^4.

Using Eq. (1) in the worst case, the maximum tensile stress would be 2.4 MPa (~ 345 psi(. For TZM the tensile strength at 870°C is given as ~ 570 MPa (83 ksi)[5] which is over two orders of magnitude higher than the calculated stress.

Towards the end of this study it was felt that graphite should be strongly considered as a possible candidate for the structural material. Graphite is surprisingly versatile.[3,4,9] It has been formed into very large electrodes for steel making, heat exchangers bigger than a man and even woven

CROSS SECTION OF STRUCTURE USED FOR CALCULATION OF I.

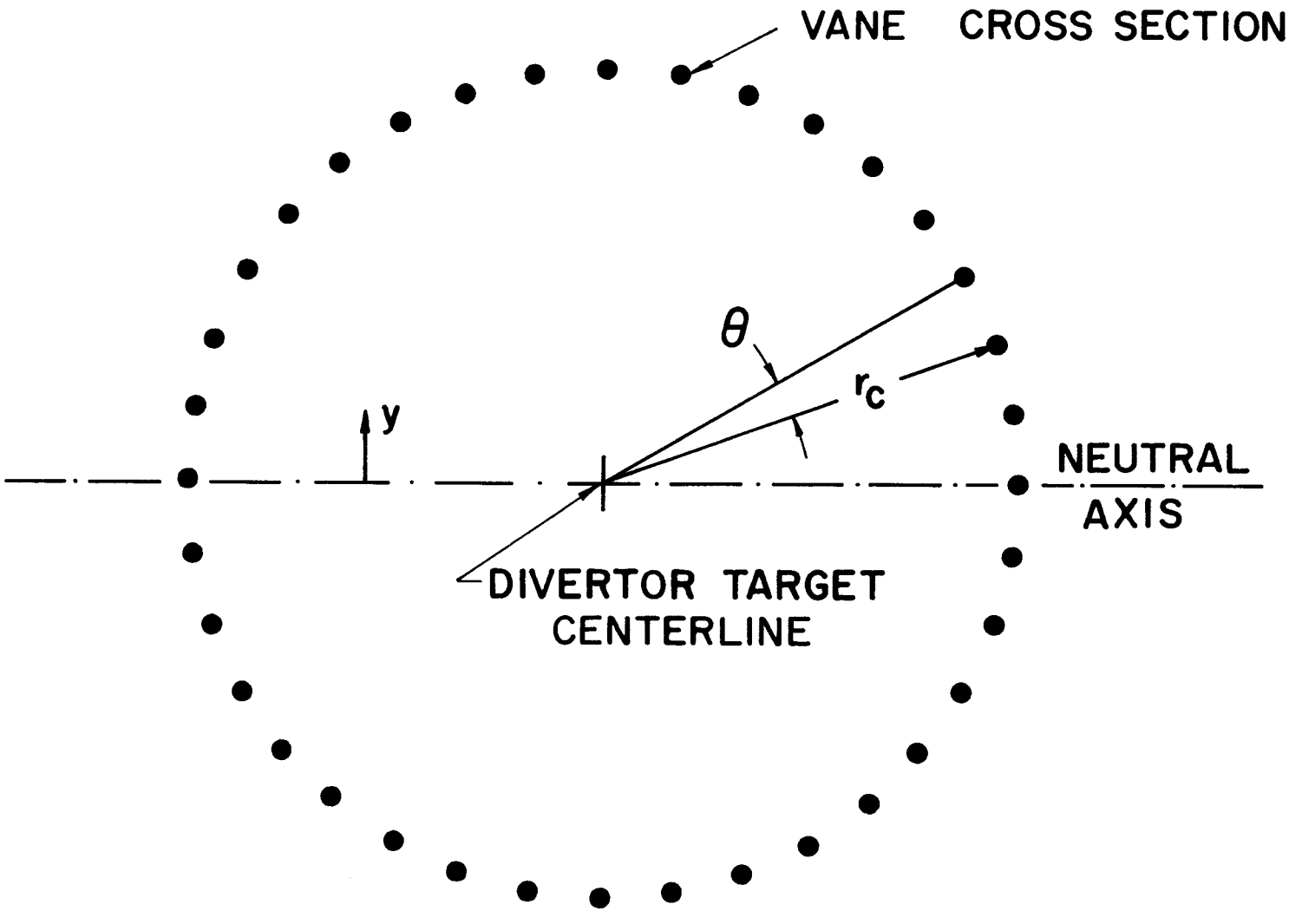

Figure VIII.2-7

into cloth. Its tensile strength at room temperature is on the order of 14 MPa (2 ksi) and increases with temperature. Though it is typically thought of as being brittle, it is remarkably insensitive to notches. It does not have any significant creep ductility below 1500°C[3,4] and has good thermal shock resistance. Compared to TZM, graphite is lighter, can withstand higher temperatures and has the added advantage of lower neutron heating. It appears that the rotating shell could be made almost entirely of carbon in one form or another.

Regardless of what the best material for the structure is, it appears that the shell will be very light and experience very low stresses.

VIII.2.3 Derivation of Heat Transfer Equations

To determine the feasibility of using a rotating shell divertor target, an idea of the steady-state temperature profile in the shell must be obtained. The transient behavior during startup is of little concern. In this section the derivation of the appropriate differential equations and boundary conditions is presented.

A number of simplifications were made. Figure VIII.2-8 shows a schematic of the resulting idealized model. The heat flow has been considered as being two-dimensional. Neutron and particle flux is treated as being equally and symmetrically distributed between the two divertor targets of a module. This implies that the temperature distribution of one target is the mirror image of the other. The cooled surface surrounding the rotating shells and the surface of the stationary core inside of each shell are assumed to have a uniform emissivity and temperature. Furthermore, the surrounding surface was assumed as circumventing both divertor targets even across the divertor slot.

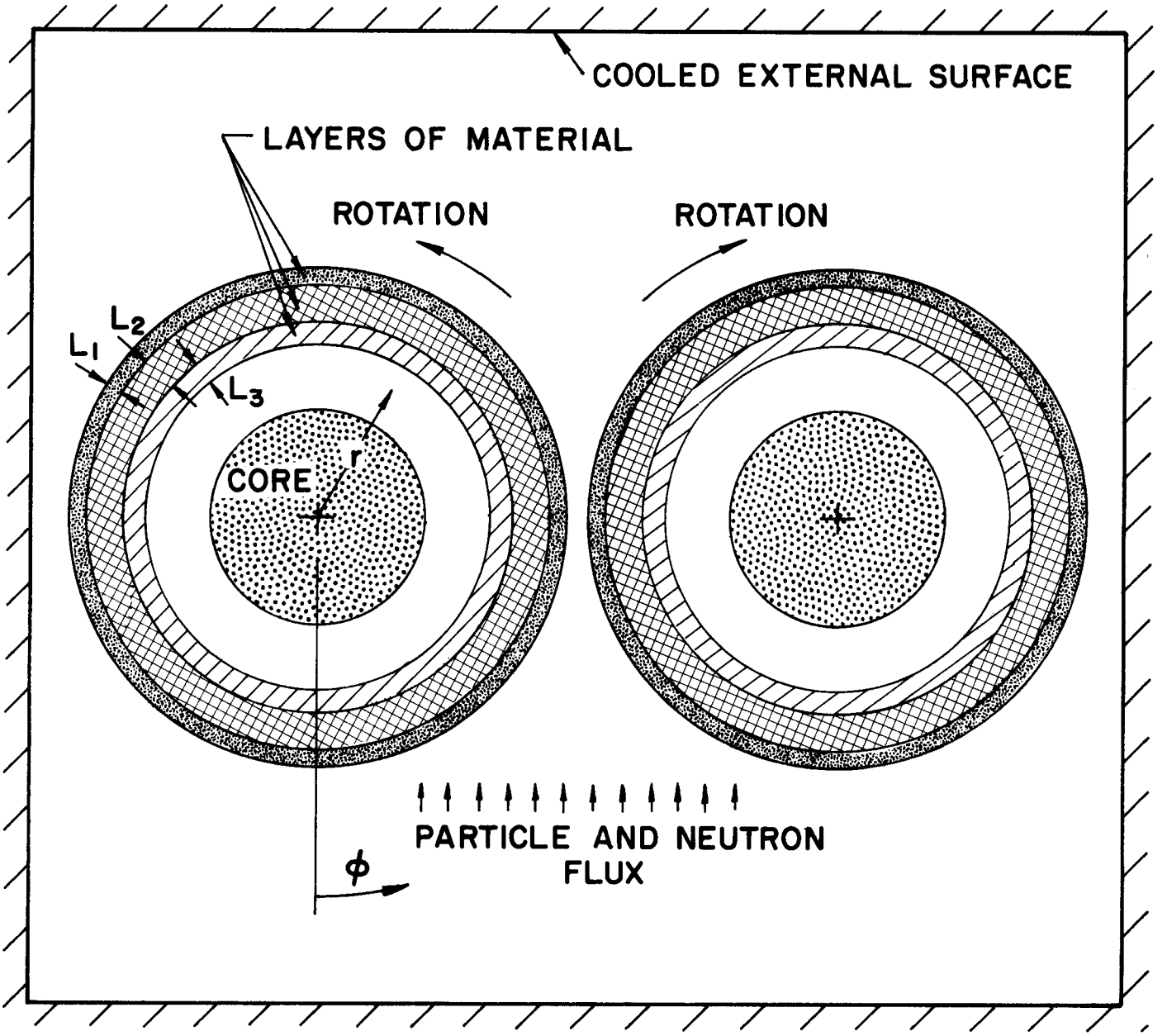

Figure VIII.2-8 Model used in heat transfer calculations.

Table VIII.2-1

Variables Useds in Heat Transfer Calculations

K_ℓ	Thermal conductivity of ℓth layer perpendicular to shell surface
$\tilde{K}_\ell$	Thermal conductivity of ℓth layer parallel to shell surface
C_ℓ	Specific heat of ℓth layer
ρ_ℓ	Density of ℓth layer
L_ℓ	Thickness of ℓth layer
r_ℓ	Radius of interface between ℓth and (ℓ+1)th layers
$\overline{x}_\ell$	Nondimensional depth of interface between ℓth and (ℓ+1)th layers
ℓ_{max}	Number of material layers
t	Temperature
r	Radial coordinate
ϕ	Angular coordinate
R	Outside radius of shell
ω	Rotational speed
g'''	Volumetric nuclear heating
s"	Surface heat flux
y	Distance around outside circumference
x	Depth into shell from outside surface
$\overline{x}$	Dimensionless distance
$\overline{t}$	Dimensionless temperature
ε_1	Emissivity of both the shell's external surface and the external heat sink
ε_2	Emissivity of shell's innermost layer and the stationary core's surface
t_1	Temperature of the external heat sink
t_2	Temperature of the stationary core's surface
V_F	Geometric view factor between two surface points on opposite shells
V_{F_1}	Geometric view factor between point on the shell surface and the external heat sink.

The radial coordinate system r,ϕ is shown in Fig. VIII.2-8 and the nomenclature used is listed in Table VIII.2-1. The coordinate system is stationary with respect to the ground and its origin is the center of one divertor target (the left one in Fig. VIII.2-8). The angle ϕ is measured counterclockwise from the line which points from the origin to the plasma. The shell of the left divertor target rotates counterclockwise with angular velocity ω with respect to the coordinate system. Figure VIII.2-8 shows 3 layers of material in each shell, but the derivation here is generalized for ℓ_{max} number of layers. To keep track of the layers they are numbered in order, starting at the outside of the shell going inwards, the ℓ_{max} layer being the innermost.

Although it may not be readily apparent, this is strictly a convection heat transfer problem. The solid shell acts as a fluid. It is analogous to fluid flow and the mechanical motion serves as a means of energy transport. The governing differential equation for a point in the ℓth layer is

$$K_\ell \frac{\partial^2 t}{\partial r^2} + \frac{1}{r} K_\ell \frac{\partial t}{\partial r} + \frac{1}{r^2} \tilde{K}_\ell \frac{\partial^2 t}{\partial \phi^2} + g''' = \rho_\ell c_\ell \omega \frac{\partial t}{\partial \phi} . \quad (4)$$

The first three terms on the left result from heat conduction and the fourth is due to heat generation from neutrons. The term on the right is a consequence of the convection mentioned earlier.

The third term on the left of Eq. (4) can be dropped. It represents conduction in the direction of motion and here, as with many convection problems, this is of little importance. Also the shell is very thin compared to its radius and as a result the second term on the left can also be dropped.

Equation (4) can now be rewritten as

$$K_\ell \frac{\partial^2 t}{\partial r^2} + g''' = \rho_\ell c_\ell \omega \frac{\partial t}{\partial \phi} . \tag{5}$$

At each interface between two layers there are two conditions that must be satisfied. Let (r_ℓ, ϕ_ℓ) be a boundary point for both the ℓth and the $(\ell+1)^{st}$ layers. First, the temperature profile at (r_ℓ, ϕ_ℓ) must be continuous. Taking an infinitesimally thin control volume containing the interface and applying the law of conservation of energy, the second condition is derived as

$$K_\ell \lim_{r \to r_\ell^+} \frac{\partial t}{\partial r}\Big|_{r,\phi_\ell} = K_{\ell+1} \lim_{r \to r_\ell^-} \frac{\partial t}{\partial r}\Big|_{r,\phi_\ell} . \tag{6}$$

The boundary conditions for the outside and inside external surfaces of the shell are respectively:

$$K_1 \frac{\partial t}{\partial r}\Big|_{r=R} = \frac{-\sigma\varepsilon_1}{(2-\varepsilon_1)} \left(t^4 - V_{F1}\, t_1^4 - \int_0^{2\pi} V_F\, t^4\, d\phi\right) + S'' \tag{7}$$

$$K_{\ell_{max}} \frac{\partial t}{\partial r} = \frac{\sigma\varepsilon_2}{(2-\varepsilon_2)} (t^4 - t_2^4) . \tag{8}$$

The last formula required is

$$t(0,r) = t(2\pi,r) \tag{9}$$

which is true for all values of r in the domain. This condition is necessary

in order to duplicate steady-state conditions. The domain of the temperature function can be restricted to $0 \leq \phi \leq 2\pi$.

Further simplification can be made by substituting the following into Eqs. (5)-(9):

$$X = R - r \ ,$$

$$\overline{X} = X/L_1 \ , \tag{10}$$

$$\overline{t} = t/t_1 .$$

The new variable X is the depth into the shell measured from its outside surface. The other two new variables $\overline{X}$ and $\overline{t}$ are dimensionless. The normalized form of Eq. (5) for each ℓth layer is

$$\frac{\partial^2 \overline{t}}{\partial \overline{X}^2} + \overline{G}_\ell = \frac{1}{\overline{A}_\ell} \frac{\partial \overline{t}}{\partial \phi} \ . \tag{11}$$

If applied to a point $(\phi_\ell, \overline{X}_\ell)$ on the mutual boundary between the ℓth and the $(\ell+1)^{st}$ layers, Eq. (6) becomes

$$\lim_{\overline{X} \to \overline{X}_\ell^-} \frac{\partial \overline{t}}{\partial \overline{X}} \Big|_{\overline{X}, \phi_\ell} = \overline{K}_\ell \lim_{\overline{X} \to \overline{X}_\ell^+} \frac{\partial \overline{t}}{\partial \overline{X}} \Big|_{\overline{X}, \phi_\ell} \ . \tag{12}$$

The boundary condition, Eqs. (7) and (8), become

$$\frac{\partial \overline{t}}{\partial \overline{X}} = - \overline{\sigma}_1 \left(\overline{t}^{\,"} - V_{F1} - \int_0^{2\pi} V_F \, \overline{t}^{\,4} \, d\phi \right) + \overline{S}^{"} \tag{13}$$

$$\frac{\partial \bar{t}}{\partial \bar{X}} = \bar{\sigma}_2 \left(\bar{t}^4 - \bar{t}_2^4\right) \tag{14}$$

where Eq. (13) is for the outside surface of $\bar{X}$=0 and Eq. (14) is for the maximum value of $\bar{X}$ at the inside surface of the shell. Equation (9), for all values of $\bar{X}$ in the domain, becomes

$$\bar{t}(\bar{X},0) = \bar{t}(\bar{X}, 2\pi) \ . \tag{15}$$

Equations (11) through (15) represent a normalized state of the boundary value problem. The dimensionless parameters and functions used in these equations are defined by

$$\bar{A}_\ell = K_\ell/(\rho_\ell c_\ell \omega L_1^2) \quad \ell = 1,2,\ldots, \ell_{max} \tag{16}$$

$$\bar{G}_\ell = g''' L_1^2/(t_1 K_\ell) \quad \ell = 1,2,\ldots, \ell_{max} \tag{17}$$

$$\bar{L}_\ell = L_\ell/L_1 \quad \ell = 2,\ldots, \ell_{max} \tag{18}$$

$$\bar{K}_\ell = K_{\ell+1}/K_\ell \quad \ell = 1,2,\ldots, (\ell_{max} - 1) \tag{19}$$

$$\bar{\sigma}_1 = \frac{\sigma \varepsilon_1 t_1^3 L_1}{K_1(2-\varepsilon_1)} \tag{20}$$

$$\bar{\sigma}_2 = \frac{\sigma \varepsilon_2 t_1^3 L_1}{K_{\ell max}(2-\varepsilon_2)} \tag{21}$$

$$\bar{S}'' = \frac{S'' L_1}{(t_1 K_1)} \ . \tag{22}$$

It should be pointed out that the dimensionless nuclear heating $\bar{G}_\ell$ and surface heating $\bar{S}''$ are functions of ϕ and $\bar{X}$. The form of these functions had to be assumed in the calculations. Any two designs with the same dimensionless parameters and variables, as defined by Eqs. (16)-(22), will have the same dimensionless temperature profile $\bar{t}$.

A computer program was written to approximate a solution to Eqs. (11)-(15). A finite difference method was used to derive a system of algebraic equations which were solved using a variation of the Gauss-Seidel iteration. View factors for small sections of the shell surface were calculated using the so-called crossed string method and were introduced into the main program. Using part of the calculations, Fig. VIII.2-9 shows a smooth curve through calculated values of view factors of surface nodes with respect to the heat sink surrounding the shell. The view factor for the whole shell with respect to this outside surface was determined to be 0.83.

As a check on the above derivation, there are two useful equations which give estimates of the average temperatures of the graphite surface and the structure. The first equation is

$$t_{ave} \approx \left(\frac{(2-\varepsilon_1)\ (S+G_1)}{\varepsilon_1\ A\sigma\ F} + t_1^4\right)^{1/4} \qquad (23)$$

where A = surface area of the shell

G_1 = total nuclear heating in graphite

S = total surface heat flux

F = view factor

t_{ave} = average temperature of the graphite surface.

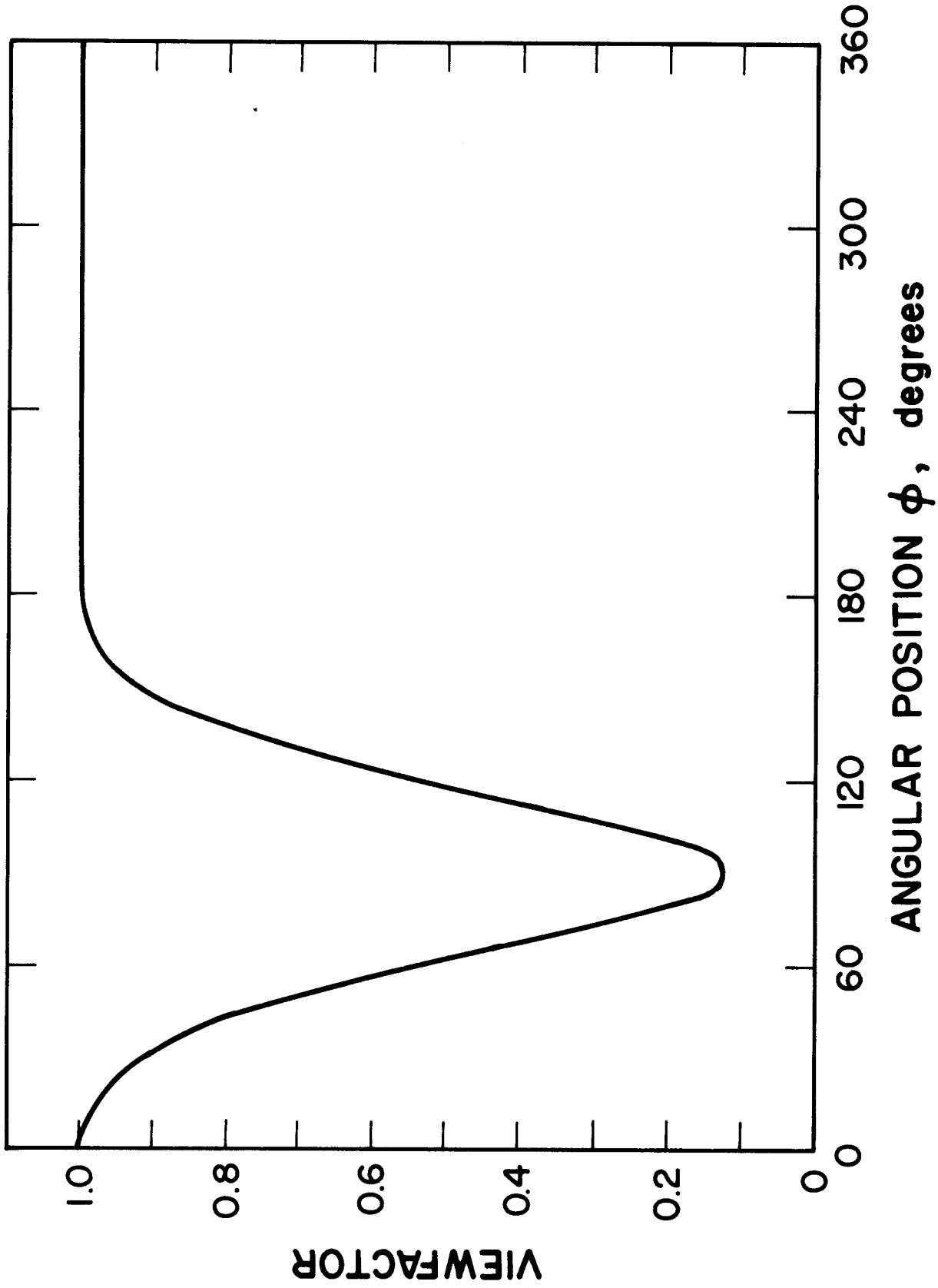

Figure VIII.2-9

This equation is derived by assuming that the graphite layer is of uniform temperature and that its boundary with the insulation is adiabatic.

The other equation, derived with similar assumptions, is:

$$\tilde{t}_{ave} \approx \left(\frac{(2-\varepsilon_2)G_2}{\varepsilon_2 A\sigma} + t_2^4\right)^{1/4} \qquad (24)$$

where G_2 = total nuclear heating in the structure

$\tilde{t}_{ave}$ = average temperature of the structure.

The usefulness of these equations will be discussed in the next section.

VIII.2.4 Results of Computations

Computer calculations were performed in which a single design case was analyzed where the nuclear heating in the graphite and insulation, the nuclear heating in the structure, the emissivity of the graphite and the external sink surfaces as well as the thermal conductivity of the graphite perpendicular to its surface were varied, one by one to see their effect upon the temperature.

In all of the calculations the structure was treated as though it were a complete layer instead of an array of disks and vanes. This is acceptable since heat conduction is only important in the radial direction. It is also clear from the upcoming discussion that the structure beneath a section of graphite has little effect on the temperature of the graphite.

The surface heat load due to the particle flux $S''(\phi)$ and the neutron induced volumetric heating $g''(\phi,\bar{X})$ were taken as simple step functions

$$S''(\phi) = \begin{cases} S''_{ave}, & 27^0 \leq \phi \leq 87^0 \\ 0, & \phi < 27^0 \\ 0, & \phi > 87^0 \end{cases}$$

$$g''(\phi,\overline{X}) = \begin{cases} g''_{\ell}, & 27^0 \leq \phi \leq 87^0 \\ 0, & \phi < 27^0 \\ 0, & \phi > 87^0 \end{cases}$$

where $(\phi,\overline{X})$ is in the ℓth layer. The quantity S''_{ave} is the total surface heat load divided by 1/6 of the shell's external surface area. The value of g''_{ℓ} is dependent on the material in the layer $(\phi,\overline{X})$. In effect, this assumes that nuclear heating within a single layer does not vary in the radial direction where in reality the heating declines exponentially with decreasing divertor target radius. The total neutron power dissipated in the divertor targets in the reactor is 159 MW. This is an average of 1.3 MW per target. If all of the energy were deposited in the graphite layer (which is most unlikely), g'''_1 would be 468 W/cm^3. Likewise if it all were absorbed by the structure g'''_3 would be 375 W/cm^3. These two numbers were used as extreme cases of nuclear heating in the graphite and the structure.

The data for the baseline case is given in Table VIII.2-2. The property values used are reasonably constant over the temperature ranges encountered. However, the emissivities and graphite thermal conductivity depend upon the manufacturing method.

Graphite crystals are extremely anisotropic.[4] As a result graphite materials can be very anisotropic and the thermal conductivity at 1200°C to 2000°C varies from .015 to over 2.0 W/cm^2[7] depending on the orientation and the manufacturing method.

In order to increase the emissivity all of the surfaces used for radiative heat transfer, could be covered with a thin layer of graphite. This would be worthwhile even if the layers had to be mechanically attached. If a surface were covered with a graphite layer 0.1 mm thick with the very low

Table VIII.2-2

Data for the Design Case

Shell length	250 cm
Outside radius	30 cm
Surface heat load per shell	1.475 MW
External surface area	47100 cm^2
Local surface heat load*	187.8 W/cm^2
Average surface heat load	31.3 W/cm^2
Emissivity of all surfaces	0.8

Material	Graphite	Carbon Fiber Insulation	TZM
Thickness, cm	0.2	0.75	0.25
Thermal conductivity, W/cm/°C	0.2	0.0015	1.1
Density, g/cm^3	1.7	0.18	10.2
Specific heat, J/gm/°C	2.0	2.0	0.272

*Total surface heat load divided by 1/6 of surface area

thermal conductivity of 0.015 W/cm^2 and subjected to a heat flux of 30 W/cm^2 the temperature rise across the graphite would only be 20°C. This is a small price to pay for increasing the emissivity of an otherwise metallic surface. Listed values for graphite emissivities range from 0.5 to 0.95.

These calculations lead us to three observations:

(1) The average temperature of the graphite surface is closely predicted by Eq. (23).

(2) If there is much nuclear heating, the structural temperature is near to that given by Eq. (24).

(3) Within limits, the magnitude of the graphite surface cyclic temperature fluctuations is a very strong function of the single dimensionless parameter $S''^2_{ave}/(t_1^2\, k_1\, \rho cw)$.

Before elaborating on these observations, Fig. VIII.2-10 will be presented showing a plot of the isotherms of the baseline case.

This figure illustrates some important features typical of the different cases studied. The structure is of almost uniform temperature. This is nearly true even at very high levels of nuclear heating in the structure. There is a very large temperature drop across the insulation. The largest temperature fluctuation, on the graphite surface, is 82°C, but further inward into the graphite the temperature rapidly becomes more and more uniform in the ϕ direction.

Support for the first two observations can be found in Figs. VIII.2-11 and VIII.2-12. Figure VIII.2-11 shows the effect of nuclear heating present only in the graphite and insulation and Fig. VIII.2-12 exhibits the occurrence of nuclear heating confined to the structure. Both plots have the maximum and minimum graphite surface temperatures and the average structural temperature

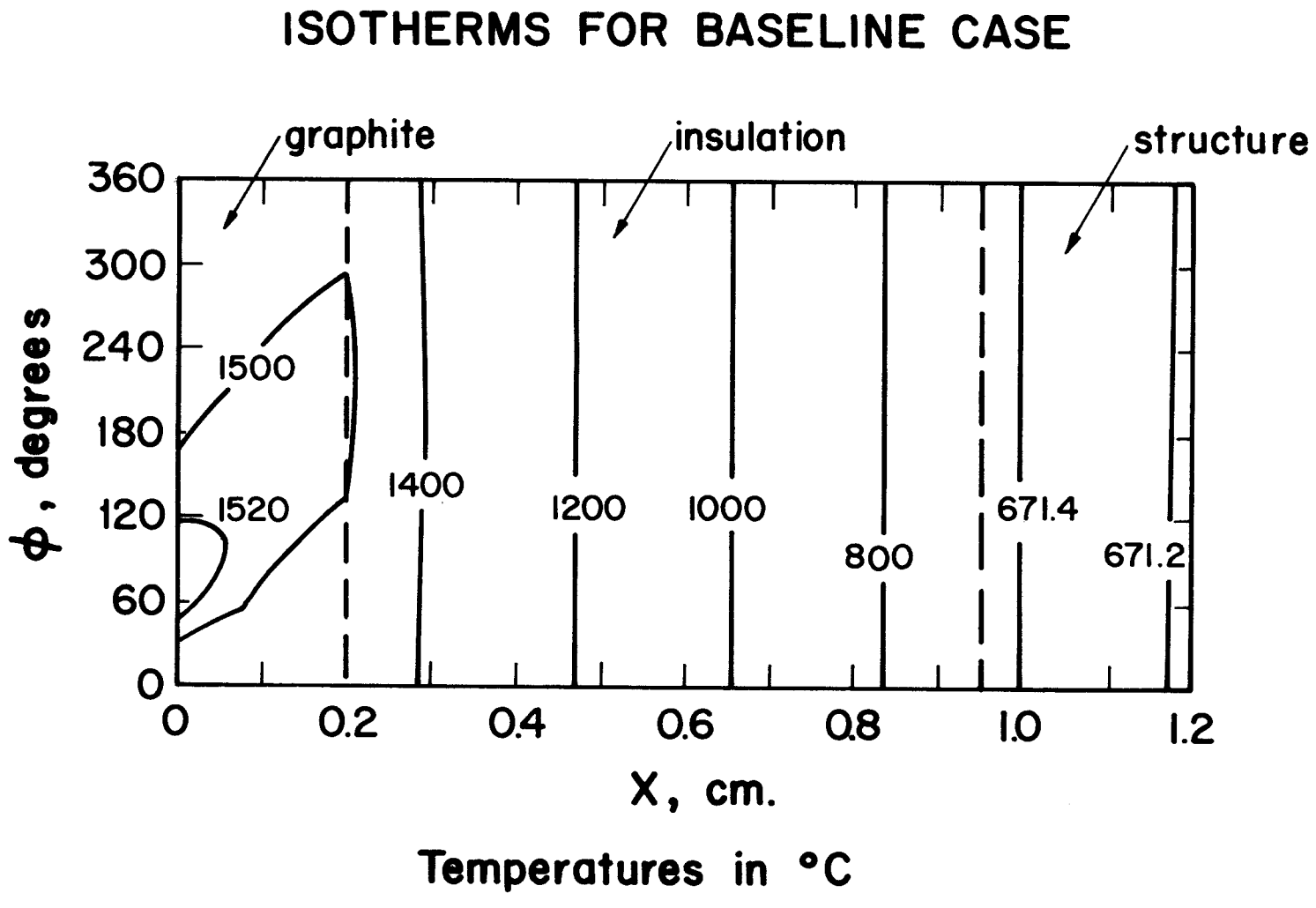

Figure VIII.2-10

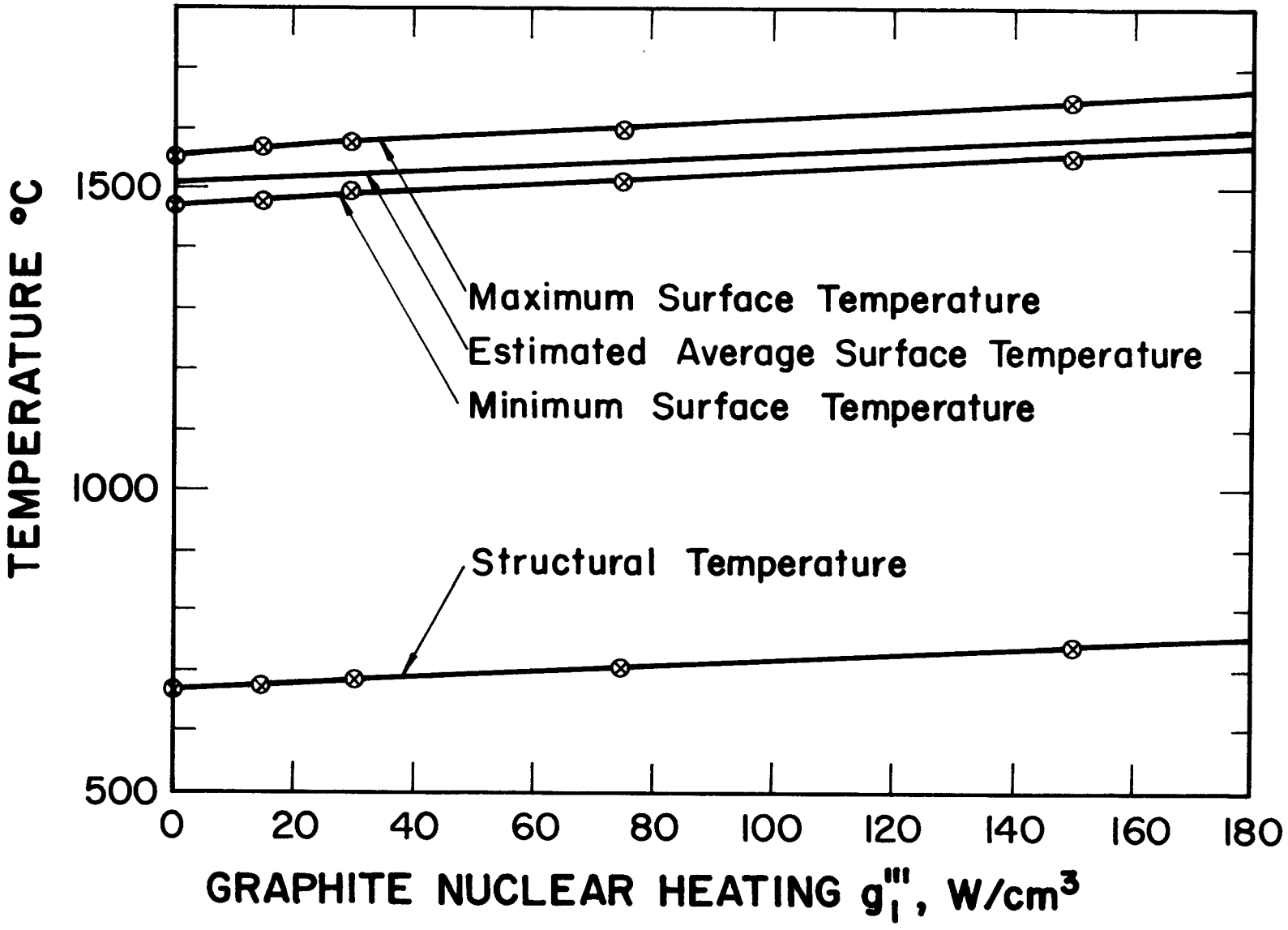

Figure VIII.2-11

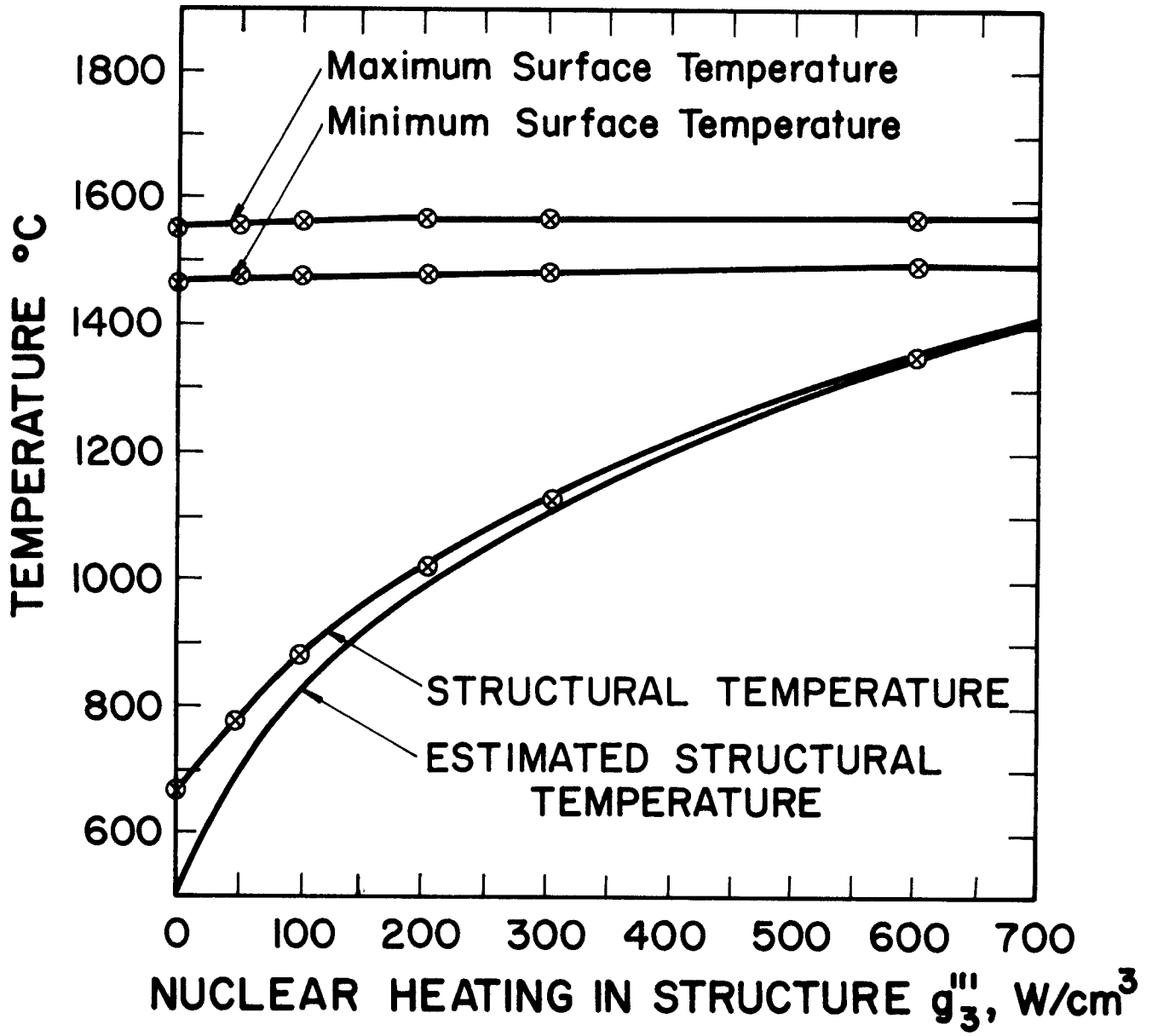

Figure VIII.2-12

plotted as a function of the appropriate nuclear heating. Included in Fig. VIII.2-11 is a graph of Eq. (23) while Eq. (24) is plotted in Fig. VIII.2-12. In Fig. VIII.2-11 the ratio of the volumetric heating of the insulation to that of the graphite was kept equal to the ratio ~ 1/10 of their densities. This is reasonable if the neutron flux in both materials was about the same.

The two figures show that due to the insulation, nuclear heating in either the graphite or structure has little effect on their mutual temperatures. Consequently, Eqs. (23) and (24) can be used to account for the effect of nuclear heating on the average temperature of the appropriate material layer. Figures VIII.2-13 and VIII.2-14 show plots of Eqs. (23) and (24) for different values of emissivity, respectively.

Appreciation for the third observation concerning the graphite surface temperature fluctuations can be obtained from Figs. VIII.2-15 and VIII.2-16. Figure VIII.2-15 shows the graphite surface temperature plotted as a function of ϕ for different levels of graphite nuclear heating and Fig. VIII.2-16 shows the same thing for different values of emissivity. It is remarkable that both variables change the average surface temperature with little effect on the profile shape. It should be noted, however, that if the nuclear heating was higher and sharply peaked at the graphite surface, the profile shape would be altered.

Changes in graphite thermal conductivity have a considerable effect on (see Fig. VIII.2-17) the shape of the temperature profile. The maximum temperature fluctuation varies from 30° to 300°C over the range of possible values of k_1.

The above observation has motivated an investigation of the effect different dimensionless variables (defined in Section VIII.2-3) have on the shape

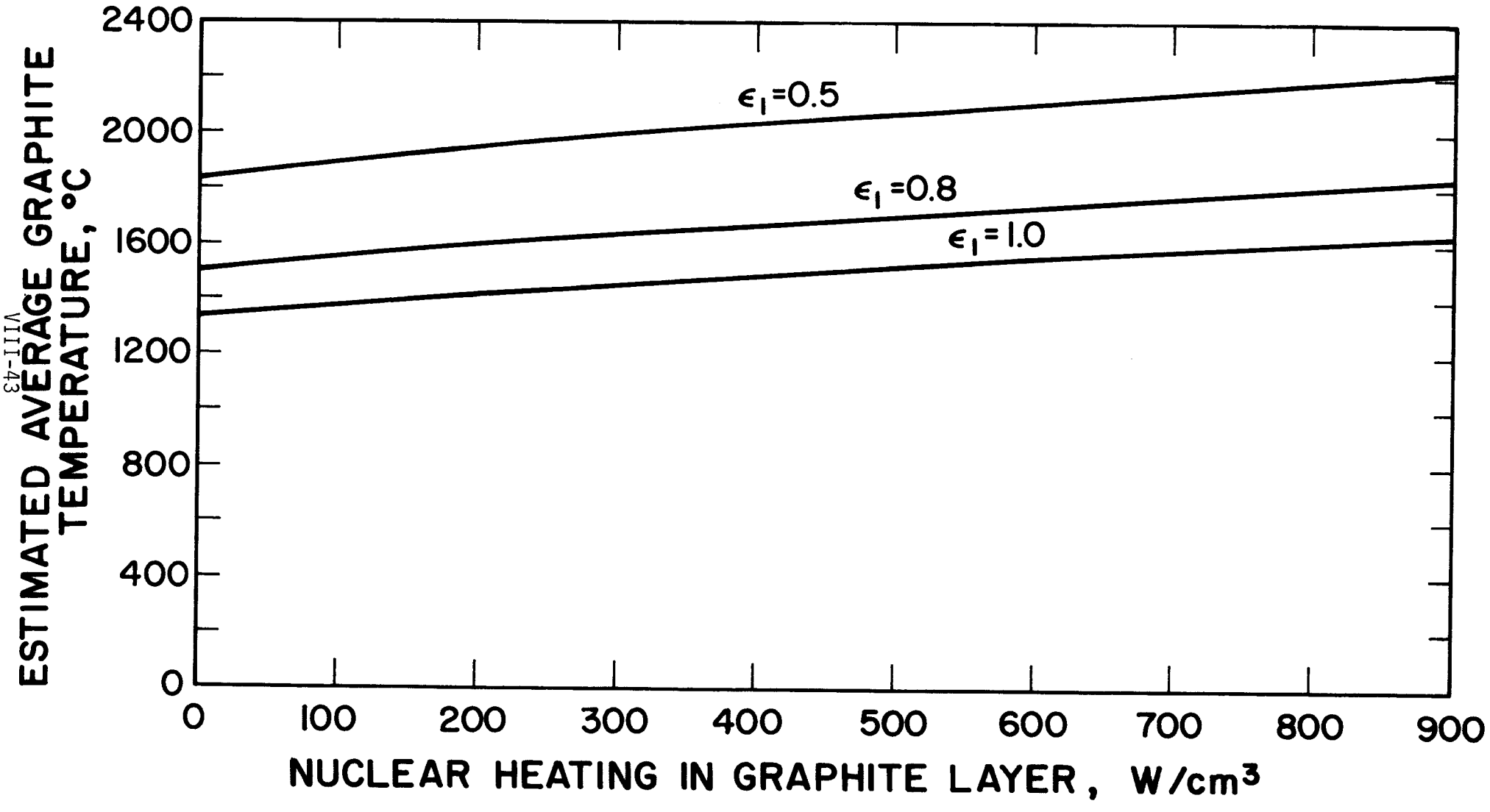

Figure VIII.2-13

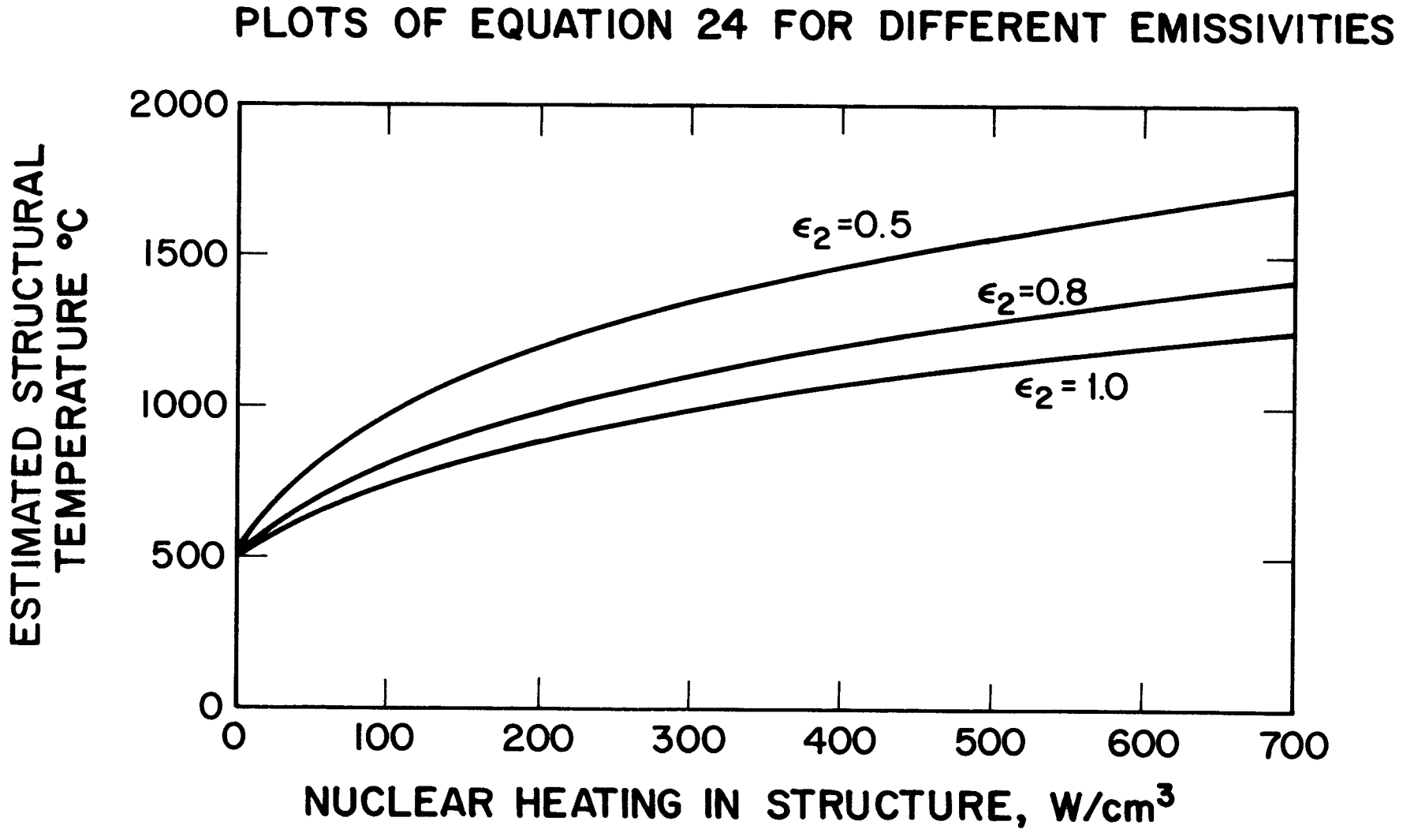

Figure VIII.2-14

SURFACE TEMPERATURE PROFILES AT DIFFERENT AMOUNTS OF NUCLEAR HEATING

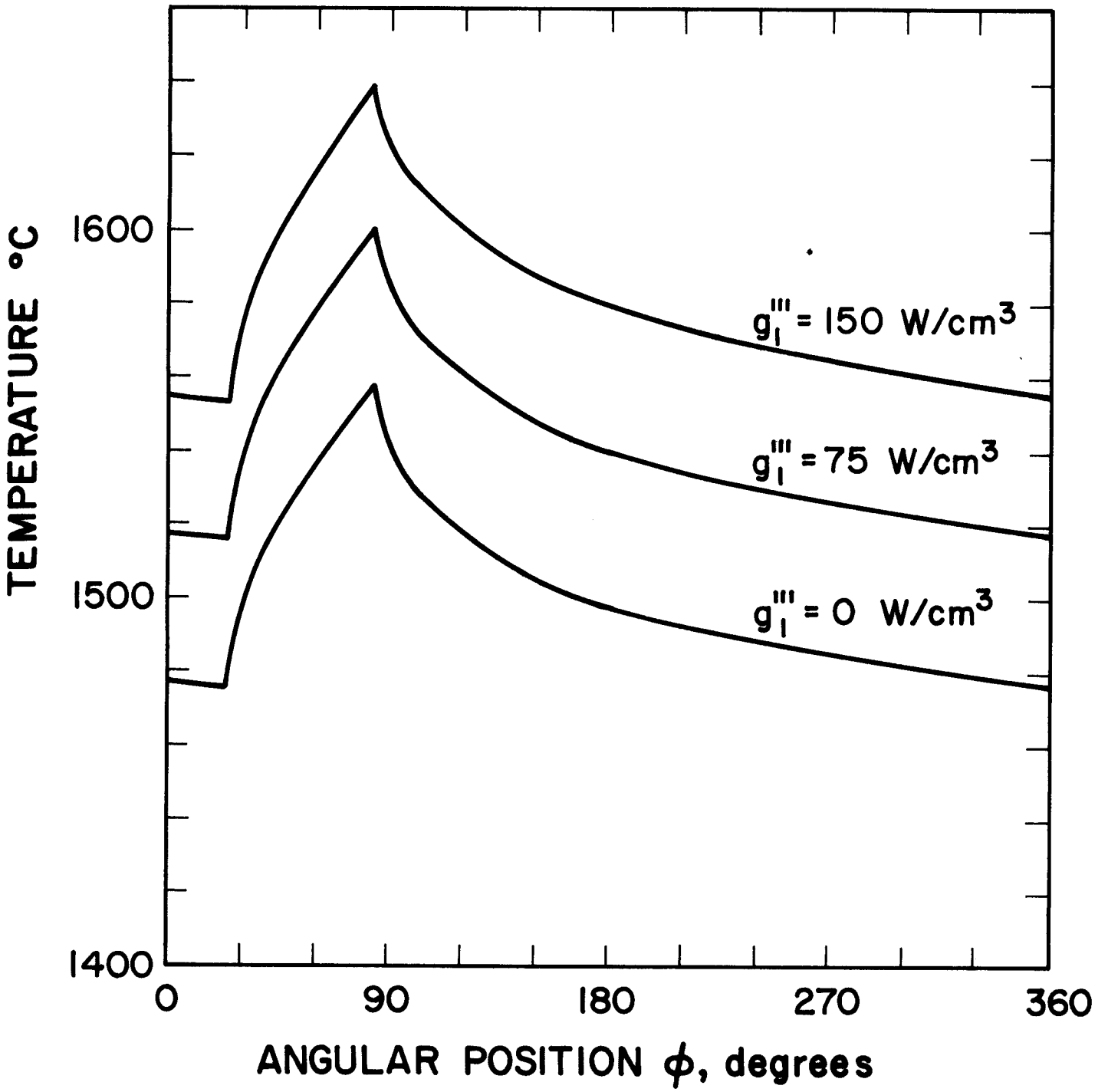

Figure VIII.2-15

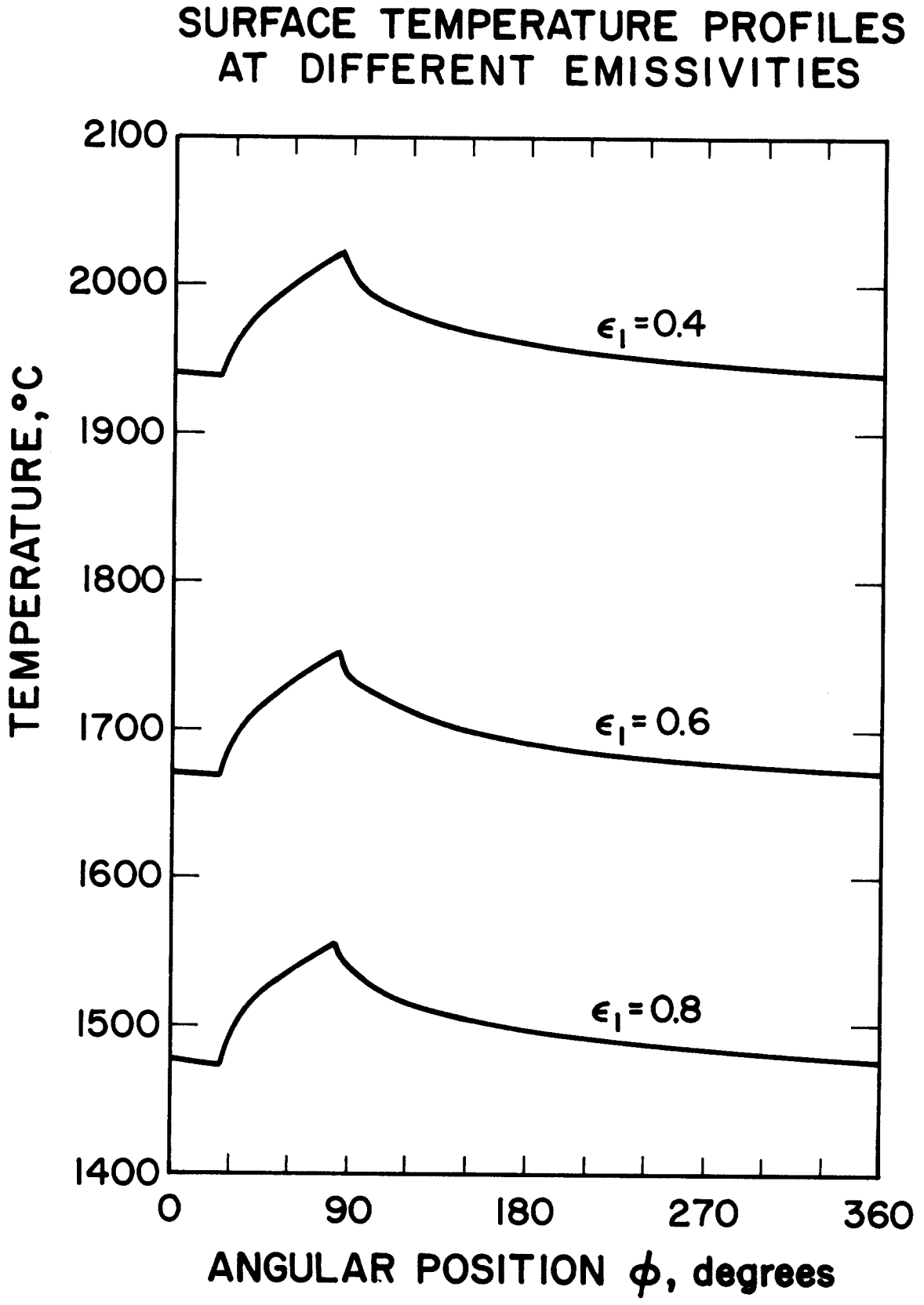

Figure VIII.2-16

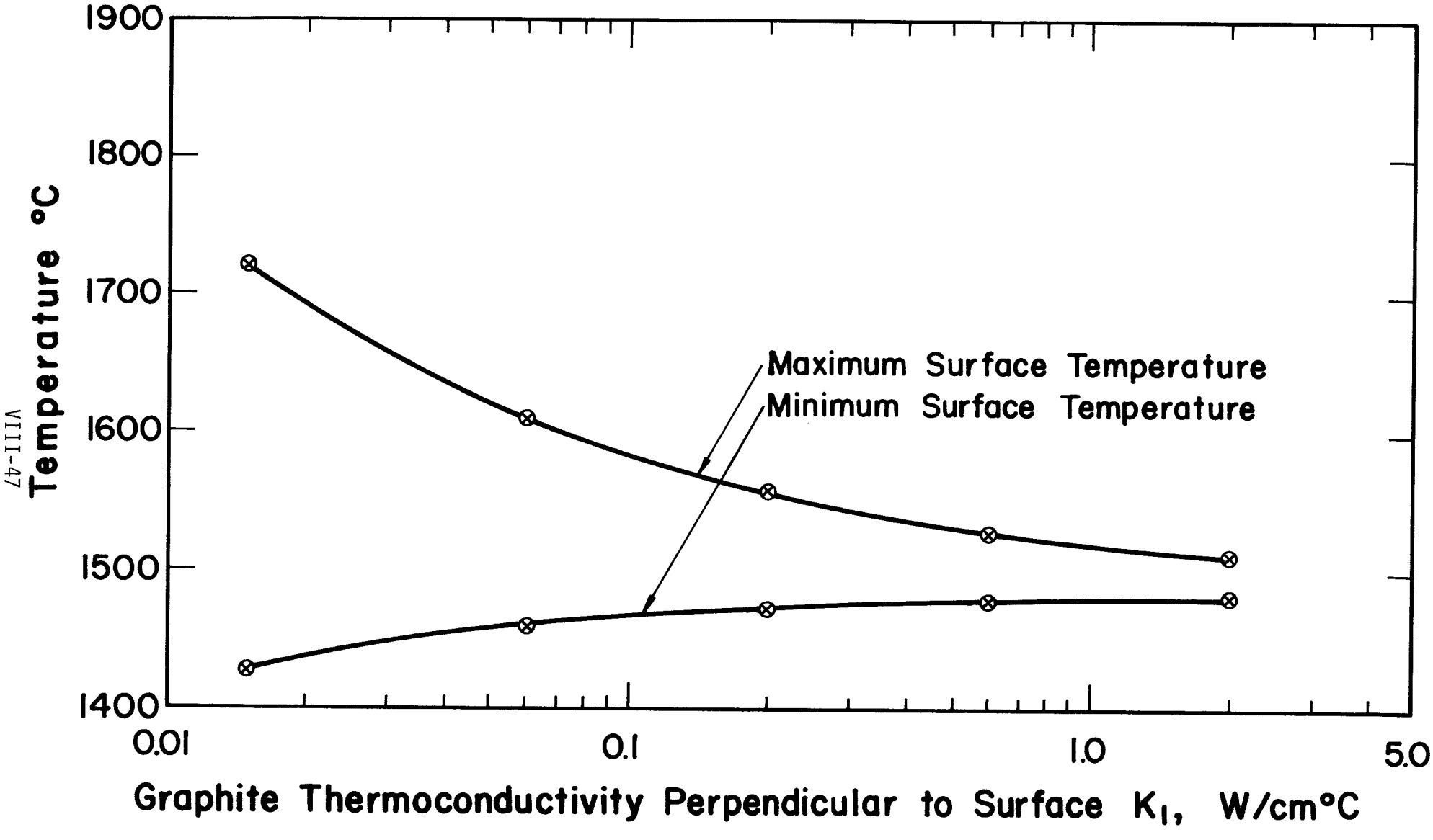

Figure VIII.2-17

of the surface temperature profile. It was discovered that the combination $\bar{A}_1 S''^2$ was of singular importance. A simplified form of this dimensionless term is $S''^2_{ave}/(t_1^2 k_1 w\rho_1 c_1)$. Let Δ be the difference between the highest and lowest graphite surface temperatures. Figure VIII.2-18 has Δ/t_1 plotted against $w k_1 \rho_1 c_1 t_1^2/S''^2_{ave}$. For every set of calculations performed, Fig. VIII.2-18 was accurate, within the numerical error, in predicting the value of Δ. We caution, however, that if a variable in the baseline case is substantially perturbed, Fig. VIII.2-18 could be erroneous. Though it should be used with some reservation, Fig. VIII.2-18 was found to predict Δ very closely for ~ 20% changes in S''_{ave} and t_1 from the baseline case.

There are two points to be made from Fig. VIII.2-18. First, changing w has the same effect as changing k_1 by the same factor. Second, Δ is not very sensitive to w. Doubling or reducing by half the revolution frequency will have a marginal effect.

VIII.2.5 Sputtering and Evaporation of the Graphite Surface

A major concern for the divertor targets is the sputtering of the graphite by the 8.8 keV He, D and T ions striking it. These ions erode away the graphite surface of the targets with the possibility that some of the expelled graphite, methane or acetylene byproducts may contaminate the plasma. The reactor exhaust rates for the different ion species are

D	3.23×10^{22}	atoms/sec
T	3.32×10^{22}	atoms/sec
He	1.5×10^{21}	atoms/sec,

giving a total reactor exhaust of 6.7×10^{22} atoms/sec.

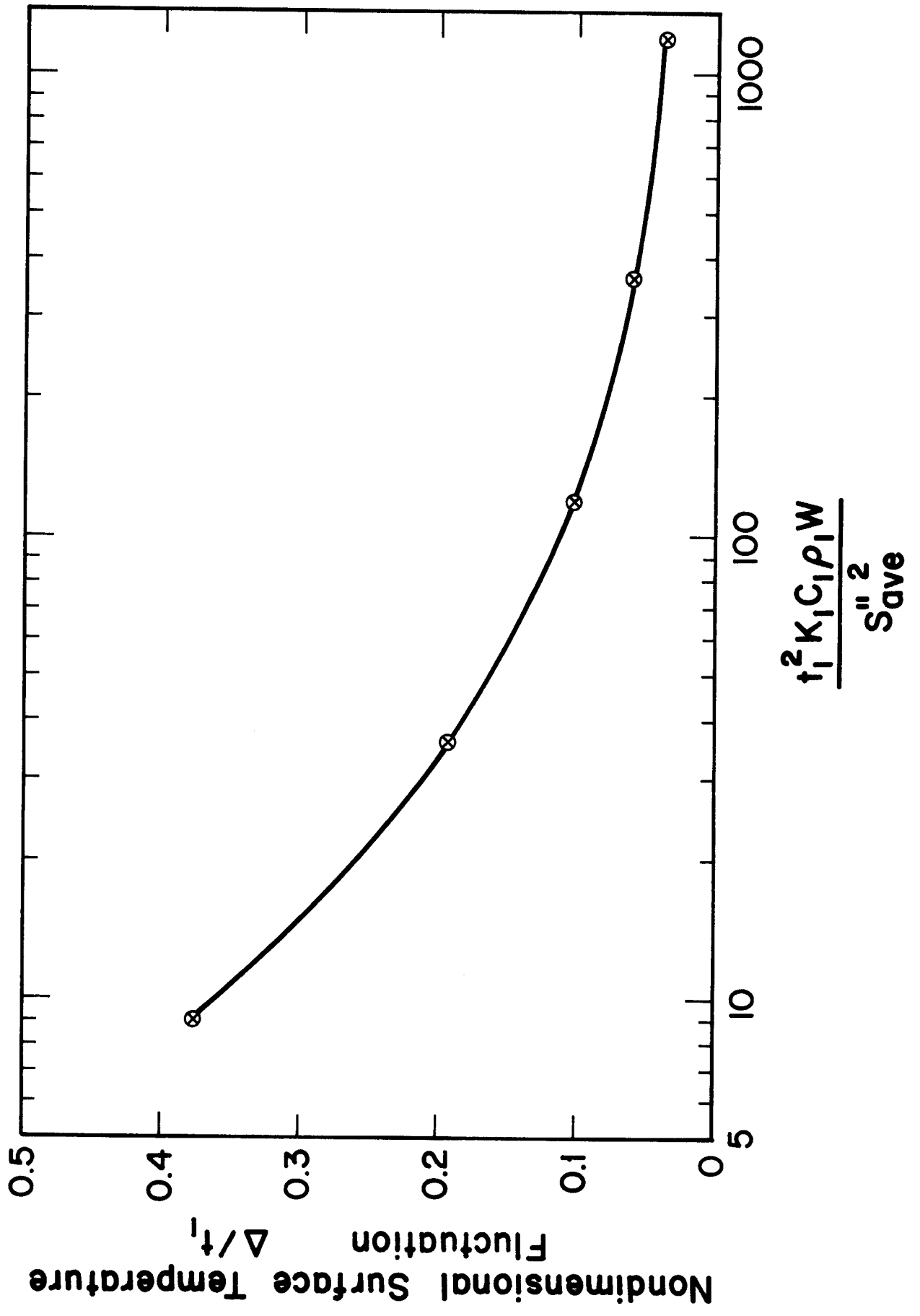

Figure VIII.2-18

There is not sufficient experimental data to accurately predict the sputtering coefficient* of the graphite surface. Until recently, experimental results were only available (see Fig. VIII.2-19) for graphite surfaces up to 1400°C under high energy ion bombardment. It had been often speculated that at higher temperatures hydrogen ions might form hydrocarbons with the graphite, thus accelerating the erosion process. Figure VIII.2-20 shows the relative probability of such reactions occurring as a function of temperature for the low energy ions.

Very recently, experiments have been performed at the higher temperatures for energetic ion bombardment. The experiments did not reveal any hydrocarbon production at temperatures from 1100 K to 2000 K for energetic H^+ bombardment. However, the sputtering coefficient did increase with temperature but this was solely due to physical sputtering. Figure VIII.2-22 has the results from this latest study for the sputtering of carbon by deuterium. From this a sputtering coefficient of ~ 0.1 appears possible for the UWTOR-M divertor target.

The erosion rate E(cm/FPY) can be calculated with the formula

$$E = \frac{S\dot{P}M}{2\pi RL N_A \rho N} \tag{25}$$

where: S is the sputtering coefficient

$\dot{P}$ is the reactor exhaust rate, particles/sec

R is the target radius

L is the target length

---

*The sputtering coefficient, also called sputtering yield, is defined as the number of surface molecules removed per incident particle.

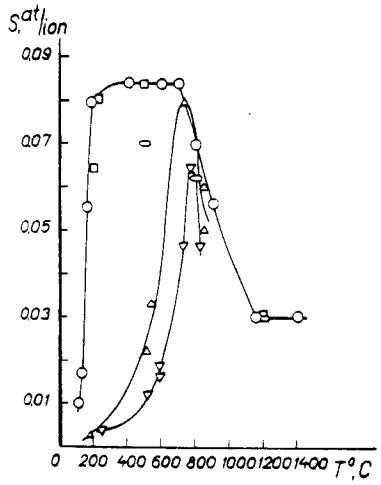

Temperature dependence of the graphite sputtering yield due to 10 keV H^+ ions. ○ - high purity graphite, □ - glass graphite, ⊖ - graphite WCA [1] Δ - pyrolite graphite, 1 keV (3 keV, H_3^+) [8], ▵ - pyrolytic graphite, 2 keV (6 keV, H_3^+) [8].

Figure VIII.2-19 From reference 9.

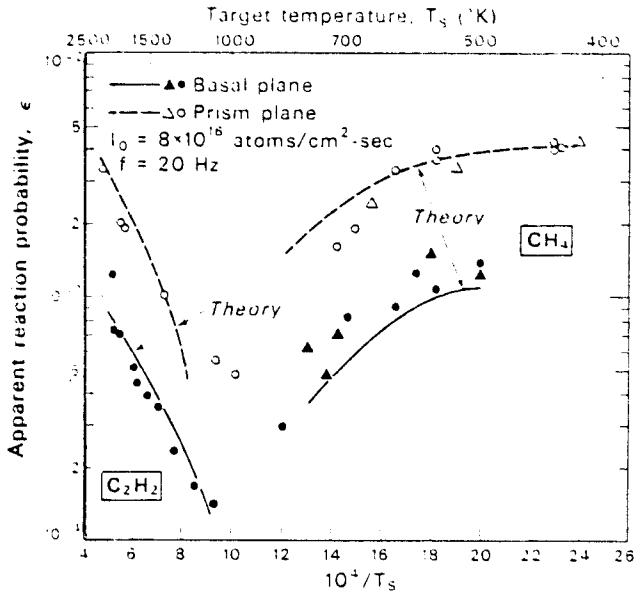

Figure VIII.2-20 Temperature dependence of the apparent reaction probabilities for methane and acetylene. Triangles and circles represent duplicate runs. From reference 10.

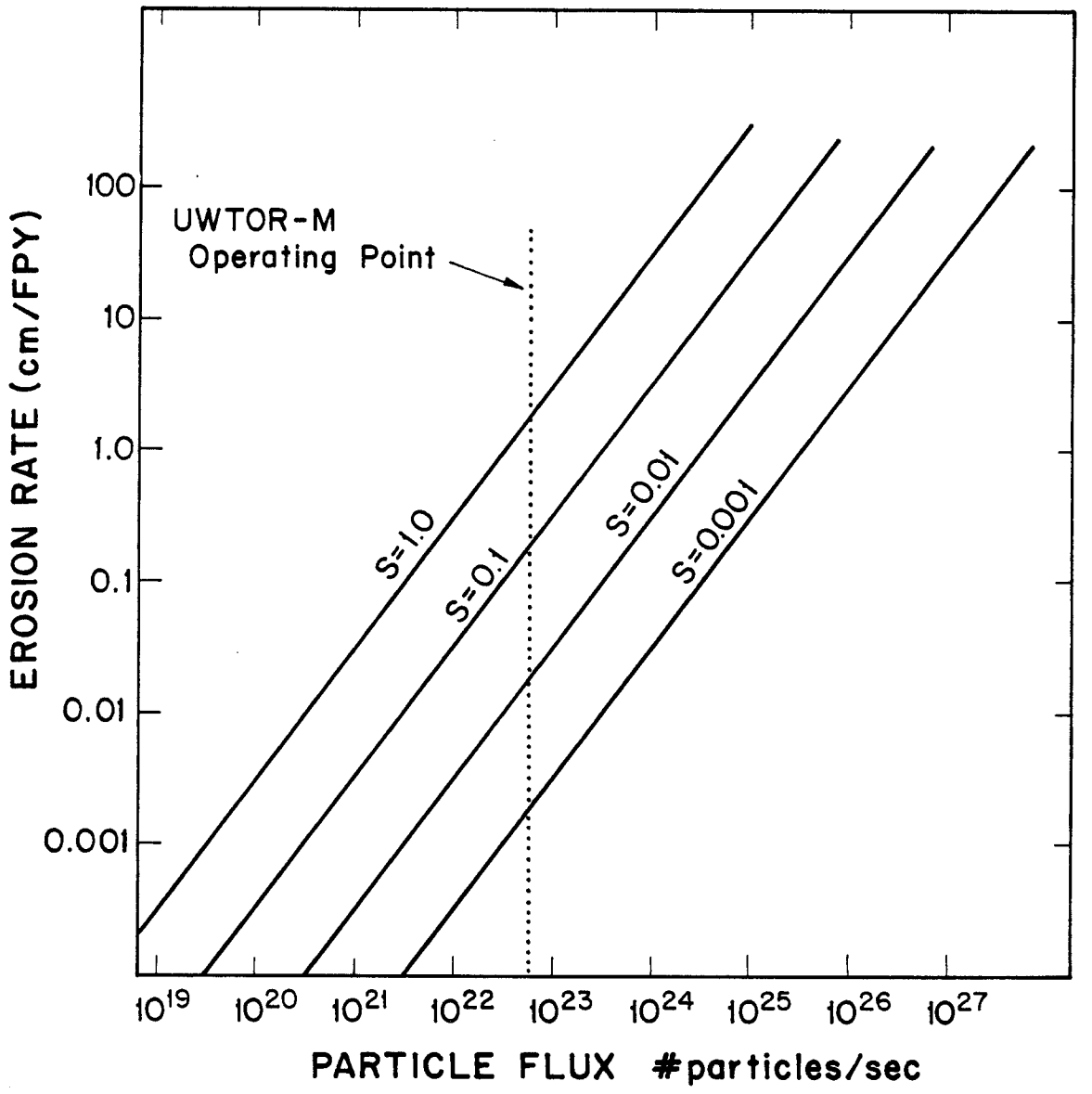

Figure VIII.2-21

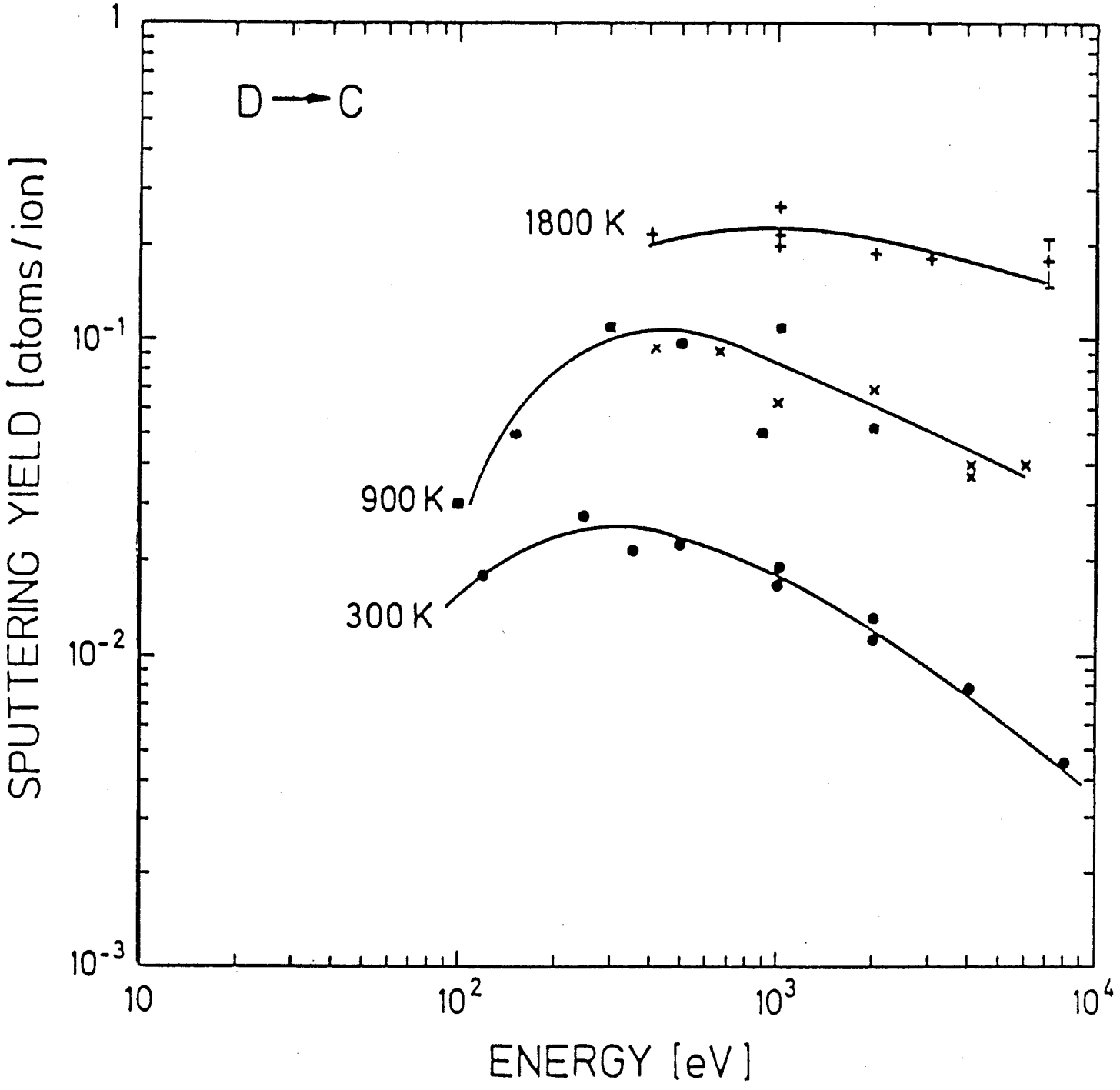

Figure VIII.2-22 From reference 9.

N_A is the Avogadro's number

ρ is the graphite density

N is the number of divertor targets

M is the molecular weight of carbon.

Erosion rate is plotted for different values of S in Fig. VIII.2-21. At the value S = 0.1 the erosion rate would amount to 0.2 cm every full power year. Since the graphite layer can be made 4 cm thick or more, even such a high erosion rate would not be detrimental. A 1 cm thickness would be sufficient to last between planned maintenance periods. Table VIII.2-3 shows estimates for the erosion rates of exposed graphite surface in the INTOR reactor design. Here too the erosion does not seem severe.

Although it is a different phenomenon, the evaporation rate of the graphite can be predicted from Eq. (25) and Fig. VIII.2-21 with slight modification. During steady state operations the carbon partial pressure in the target module will be almost equal to P_v, the graphite vapor pressure. Thus, the graphite will evaporate at the rate at which carbon is pumped out by the vacuum system which, assuming complete mixing, would be $\frac{P_v}{P_T} \dot{P}$, where P_T is the total pressure. Equation (25) and Fig. VIII.2-21 can be used if S is replaced with $\frac{P_v}{P_T}$ and E is taken as the evaporation rate. The expected P_T for the reactor is $\approx 10^{-4}$ torr, and at a temperature of 2200°C the vapor pressure of graphite is about 10^{-5} torr.[8] This gives $\frac{P_v}{P_T} = 0.1$ and the corresponding evaporation rate would be 0.2 cm per full power year. Thus, using this crude model, 2200°C would be a reasonable design limit for the graphite surface. Referring back to Fig. VIII.2-22 and using a conservative emissivity $\varepsilon = .5$, the average graphite temperature would be only 2100°C under the worst possible

Table VIII.2-3

Estimated Erosion Under Projected INTOR Conditions [11]

Source	Lifetime Erosion(cm)*	Yield**	T(K)	Assumption
Energetic hydrogen	1.5	3×10^{-2}	1500-1600	
Thermal Atomic hydrogen	0.008	2×10^{-3}	1500-1600	Edge sites, C_2H_2
Electron bombardment with thermal atomic hydrogen	0.009 2.9	5×10^{-2}	300	Only $E \geq 40$ eV All energies effective
Atomic oxygen	0.18	1.5×10^{-1}	1580	2% of neutral flux

* Assumed graphite density of $1.8 g/cm^3$

** Yield = product molecule removed per incident particle

condition where the graphite absorbs all of the neutron power. It therefore appears that graphite evaporation is not expected to be a problem.

References for Section VIII.2

1. T.G. Godfrey, D.L. McElroy and Z.L. Ardary, "Thermal Conductivity of Oriented Fibrous Carbon Insulation From 300 to 1300°K in Nitrogen and Argon at One Atmosphere", Nuclear Technology 22 (April 1974), 94.

2. R.G. Donnelly, et al., "Industrial Thermal Insulation: An Assessment", Oak Ridge National Laboratory Report TID-27120 (Aug. 1976).

3. L.C.F. Blackman, ed., "Modern Aspects of Graphite Technology", Academic Press, London and New York, 1970.

4. W.N. Reynolds, "Physical Properties of Graphite", Elsevier Publishing Co., Amsterdam, New York, 1968.

5. J.E. Hauck, ed., "1976 Materials Sector" (special issue), Materials Engineering 82-4 (Sept. 1975).

6. T. Baumeister, ed., E.A. Avallone, ed., T. Baumeister III, ed., "Marks' Standard Handbook for Mechanical Engineers", McGraw-Hill Book Compnay, 1978.

7. Y.S. Touloukian, ed., C.Y. Ho, ed., "Thermophysical Properties of Matter", Thermophysical Properties Research Center, Purdue University, IFI/Plenum, New York, Washington, 1970.

8. Y.S. Touloukian, ed., "Thermophysical Properties of High Temperature Solid Materials", Thermophysical Properties Research Center, Purdue University, Collier-MacMillian Limited, London, 1967.

9. J. Bohdansky, J. Roth and K.L. Wilson, "Chemical Erosion of Carbon Due to Bombardment With Energetic Hydrogen at Temperatures up to 2000 K", 5th Int. Conf. on Plasma Surface Interactions in Contr. Fusion Devices, Gatlinburg, Tenn., U.S.A., May 1982.

10. M. Balooch and D.R. Olander, "Reactions of Molecular Beams With Pyrolytic Graphite.III.Hydrogen", J. Chem. Phys. No. 11 (1 Dec. 1975).

11. C.I.H. Ashby, "Chemical Erosion of Graphite in a Plasma Environment", SAND81-0803, Sandia National Lab., Albuquerque, New Mexico (Aug. 1981).

12. N.P. Busharov, et al., "Chemical Sputtering of Graphite by H^+ Ions", J. of Nuclear Matls. 63 (Dec. 76).

VIII.3 Vacuum System

VIII.3.1 Introduction

As described in earlier sections, the reactor is contained in an evacuated building. Neutral gas from the divertor targets is exhausted into the building through ports in the divertor housing. The primary motivation for pursuing such a design concept is to avoid making seals between adjacent blanket segments and avoid extensive vacuum line plumbing between the divertor exhaust and the vacuum pumps.

Making seals between adjacent blanket modules has been one of the most challenging problems for fusion reactor designers. Some very early designs[1-3] proposed to have seals at the first wall as is customary in present plasma experiments. It should be recognized that plasma experiments operating with low densities are much more intolerant of impurity influx than reactor grade plasma will be. Reactor grade plasmas with densities several orders of magnitude higher can tolerate more impurities and will most likely have a higher pressure in the scrapeoff zone. On this premise, newer reactor designs[4-6] removed the seals to the back of the shield where they are more accessible. Further, because they are protected from neutrons by the shield, the seals could be elastomeric.

In UWTOR-M, several aspects of the design drove us into taking a yet further step, namely that of placing the main vacuum barrier at the wall of the containment building. This is by no means unprecedented. Almost all fusion reactor containment buildings are designed for evacuation into the millitorr range as a precaution against an accidental tritium release. Space simulation chambers much larger than the proposed UWTOR-M containment building have been built and evacuated down to the order of 10^{-7}-10^{-8} torr range.

These chambers were used to test space vehicles with complicated equipment not too dissimilar from fusion reactors.

The departure in the present design comes from the need for rather large access doors to be used for extracting coil modules from the reactor building. These doors are spaced behind every other coil. It is envisaged that these doors will be sealed with elastomer seals mounted on inflatable stainless steel bellows. Double seals with intermediate pumpouts can be used. Thus, although it will take some clever designing in how to maneuver, locate and support such large and heavy doors, it does not appear that there is anything fundamentally wrong in implementing such a concept. The many benefits which accrue from this concept, and the disadvantages are listed in Table VIII.3-1.

Something must be said about the tritium contaminated building. During reactor operation, assuming a 50/50% DT mixture, the radiation level at a pressure of 10^{-4} torr and 300 K is 11,200 Ci. After shutdown, the equilibrium pressure in the building will fall to $\sim 5 \times 10^{-7}$ torr and the DT partial pressure to $\sim 10^{-8}$ torr in about an hour. At this time the radiation level due to the T_2 in the atmosphere will be $\sim$ 1.0 Ci. It is difficult to determine the amount of T_2 trapped on the surfaces within the reactor building. An accurate definition of the type of surfaces and their temperature must be made before an estimate can be made. Tritium trapped on surfaces is a generic problem for fusion reactors which will have to be addressed in detail in the near future.

VIII.3.2 Required Pumping Capacity

Table VIII.3-2 gives the amounts of D_2, T_2 and He which will have to be handled by the vacuum pumps.

Table VIII.3-1

Advantages and Disadvantages of the UWTOR-M Evacuated Building Concept

ADVANTAGES

1. No seals required between adjacent blanket modules. Modules are simply butted against each other.

2. No complicated ducts required between divertor exhaust ports and the vacuum pumps.

3. Considerably reduced impedance due to the absence of ducts and thus, potential for higher pumping speed.

4. Readily accessible door seals.

5. A large space available for placement of pumping stations. Pumps are out of the way and, therefore, do not impede access to the reactor.

DISADVANTAGES

1. A tritium contaminated building. Most reactor containments are designed for evacuation in the case of an accidental tritium release and, therefore, must cope with the possibility of tritium contamination.

2. More difficult and costlier construction to allow evacuation down to $\sim 10^{-6}$ torr.

3. A difficult door sealing problem.

Table VIII.3-2

Mass Throughput in the Exhaust System

	T_2	D_2	He
Fraction burned (%)	4.4	4.5	---
Fuel injected (kg/d)	14.9	9.91	---
Fuel burned (kg/d)	0.656	0.437	---
Ash exhausted (kg/d)	---	---	0.875
Total exhaust (kg/d)	14.2	9.27	0.875

At room temperature the gas throughput is then:

$$\dot{Q}_{T_2} = 510 \text{ torr-liters/sec}$$

$$\dot{Q}_{D_2} = 497 \text{ torr-liters/sec}$$

$$\dot{Q}_{He} = 47 \text{ torr-liters/sec}$$

Using an equilibrium pressure of 5×10^{-5} torr in the building, the required pumping speed for D_2 and T_2 will have to be:

$$S_{D_2,T_2} = \frac{510 + 497 \text{ torr-liters}}{5 \times 10^{-5} \text{ torr sec}} = 2 \times 10^7 \text{ liters/sec}$$

Assuming a pumping speed of 6 $\ell/s \cdot cm^2$ for D_2 and T_2 the cryopanel area required is $\sim$ 333 m^2. To allow for a reserve margin the reactor will have 840 m^2 of cryopanels distributed among 12 pumping stations, with half of them on line and the other half being regenerated. Each pump station will be backed up with Roots blowers for regeneration. The vacuum system specifications are given in Table VIII.3-3.

Table VIII.3-3

Vacuum System Design Specifications

Number of pumping stations	12
Active cryopanel area per station (m^2)	35
Total cryopanel area per station (m^2)	70
D_2, T_2, DT throughput (torr-ℓ/s)	1007
He throughput (torr-ℓ/s)	47
D_2, T_2, DT pumping speed (ℓ/s)	2.5×10^7
He pumping speed (ℓ/s)	8.3×10^6
Equilibrium D_2, T_2 pressure (torr)	4×10^{-5}
Equilibrium He pressure (torr)	6×10^{-6}
Liquid He consumption (liters/day)	110×10^3
Liquid N_2 consumption (liters/day)	750×10^3

References for Section VIII.3

1. B. Badger, et al., "UWMAK-I, A Wisconsin Toroidal Fusion Reactor Design", UWFDM-68, University of Wisconsin, March 1974.

2. R.G. Mills, et al., "A Fusion Power Plant", MATT-1050, Plasma Physics Laboratory, Princeton, NJ, August 1974.

3. B. Badger, et al., "UWMAK-III, A Noncircular Tokamak Power Reactor Design", UWFDM-150, University of Wisconsin, July 1976.

4. B. Badger, et al., "NUWMAK, A Tokamak Reactor Design Study", UWFDM-330, University of Wisconsin, March 1979.

5. C.C. Baker, et al., "STARFIRE - A Commercial Tokamak Fusion Power Plant Study", ANL/FPP-80-1, Argonne National Laboratory, September 1980.

6. M. Abdou, et al., "A Demonstration Tokamak Power Plant Study", ANL/FPP/TM-154, Argonne National Laboratory, March 1982.

IX. Blanket Design

IX.1 Design Philosophy and General Considerations

The chief goals of a good fusion reactor blanket design, not necessarily in the order of importance are:

- Long life and reliability
- Adequate tritium breeding and low tritium leakage
- High blanket energy multiplication
- Safety
- Material compatibility
- Design and fabrication simplicity
- Maintainability
- Reasonable cost

Implicit in some of the above goals is the requirement that the blanket provide a proper environment for the initiation and perpetuation of the plasma burn. This is the most important requirement, since the plasma is the heart of a fusion reactor.

Obviously, any blanket design falls short of satisfying all the above goals to some degree, and what usually happens is that some goals are traded off against others. However, there are some requirements that cannot be compromised and those usually are safety, reliability, first wall/plasma compatibility and maintainability. Most of the time it is possible to exchange tritium breeding for energy multiplication. Long life, energy multiplication, good heat transfer, low pumping power, fabrication simplicity and maintainability all have economic implications and are, therefore, important considerations. The UWTOR-M blanket concept comes close to satisfying most of the above goals.

In many respects, the blanket for a stellarator reactor is very similar to that of a tokamak with several important differences. The similarities are that both blankets must operate in high magnetic fields, experience large surface wall heating and have the same kind of plasma/wall interaction problems. The differences lie in three main areas:

- Thermal stresses
- Plasma disruptions
- Configuration

Since the tokamak is inherently a pulsed machine, the first wall and blanket experience repeated thermal cycling and must be designed to withstand it. Furthermore, the first wall must be capable of withstanding a large instantaneous energy deposition from plasma disruptions. The stellarator, on the other hand, is a steady state device and thus the blanket will experience a much smaller number of thermal cycles. This would tend to prolong the blanket lifetime if it is limited by crack propagation due to thermal cycling. Perhaps more importantly, since the plasma in the stellarator will be current-less, there are no identifiable disruptions capable of large instantaneous energy deposition on the first wall. This obviates the need for protective armor to guard against such an eventuality. Some people may argue that stellarators could also have disruptions, precipitated, for example, by a coil failure or some other instability. However, these kinds of disruptions occur over longer time constants and are not nearly as detrimental.

The major difference between a tokamak and stellarator blanket design is the actual configuration. Except in the case of bundle divertor equipped tokamaks, the shape of the tokamak plasma is the same at any toroidal section. Furthermore, in most cases there is plasma symmetry about the midplane of the

tokamak. Tokamaks with single null poloidal divertors located at the upper or lower edge of the plasma are the only exception. Stellarators, however, have no planes of symmetry because of the helical nature of the flux surfaces. Additionally, the natural divertor of the stellarator must be accommodated with the blanket design. Stellarators with pumped limiters do not have to provide divertor slots but do need penetrations for pumpout ports. These aspects of the stellarator blanket add a degree of difficulty which are not present in the tokamak. The modular nature of the divertor in this case provides two mitigating factors. Twisting in a modular stellarator flux surface occurs in steps rather than continuously, and the magnetic divertor consists of discrete well defined flux bundles which are oriented toroidally. This provides a great simplification in the reaction chamber shape as will be evident from the section ahead.

A design decision which has tremendous impact on the reactor is the disposition of seals between blanket segments. In the past most designs provided a vacuum tight reaction chamber with the first wall as the vacuum barrier. More recent designs have recognized the difficulty of maintaining such blankets and have moved the vacuum barrier to the back of the shield.[1] In this design we have moved one step further and have assumed an evacuated reactor enclosure thus altogether obviating seals in the reactor itself. Although this idea seems unusual at first glance, the payoffs are significant design simplifications and relaxation of maintenance difficulty. Obviously, the consequences of a tritium contaminated reactor enclosure have to be evaluated.

In recent years it has become recognized that one of the better breeding materials is the eutectic alloy $Li_{17}Pb_{83}$. Neutron multiplication by lead

gives an excellent breeding performance while neutron attenuation provides good shielding. To avoid MHD effects on flow distribution on the irregular blanket geometry, it was decided to cool with steam forced through tubes immersed in the $Li_{17}Pb_{83}$. The tritium is allowed to diffuse into the steam and is recovered as HTO in the same way as heavy water is recovered in present heavy water plants. Since the total water inventory in the primary coolant loop is small, it appears that such a scheme is very attractive. The structural material for the FW/blanket was chosen and the ferritic steel HT-9 for its superior radiation damage characteristics and its compatibility with both steam and $Li_{17}Pb_{83}$.

To summarize, the major design points for the UWTOR-M blanket are:

- $Li_{17}Pb_{83}$ is used for its inertness toward water and air and good breeding and high energy multiplication.
- To avoid MHD effects, the molten $Li_{17}Pb_{83}$ is cooled in situ with steam going through pipes immersed in it.
- T_2 is allowed to diffuse into steam and is recovered in the same way as D_2 is recovered from water.
- HT-9 is used for FW/blanket structure due to its superior radiation damage characteristics.
- Two blanket segments, each divided into three regions, are used for each coil module.
- Blanket regions are interconnected to allow draining of segments for maintenance.
- Divertor slots are oriented toroidally.
- No seals are used between blanket segments; instead the reactor is within an evacuated enclosure.

Reference for Section IX.1

1. C.C. Baker et al., "STARFIRE - A Commercial Tokamak Fusion Power Plant," Argonne National Laboratory and others, ANL-FPP-80-1, Sept. 1980.

IX.2 Material Selection

IX.2.1 Structural Material

It is always difficult to chose a structural material. It is advantageous to have high temperature operation resulting in a high thermal efficiency. However, a high temperature blanket requires novel structural material with lack of experience and design code. It also requires a more complex blanket which will be more expensive and less reliable. Tritium confinement at high temperature is also difficult. For those reasons, the UWTOR-M design utilizes a high pressure, high temperature steam cycle. The blanket temperature is about 500°C. For this temperature, stainless steel and ferritic steels become primary candidates for structural materials.

There is certainly a wide data base for both alloys with respect to non-nuclear conditions. Areas such as mechanical strength, corrosion resistance, fabrication requirements and production capabilities are well known and there is a long history of design codes on which to base future projections. The irradiation data base is certainly extensive for the austenitic steels because of their role in the breeder reactor technology and there is a fair amount of relatively low temperature, low neutron fluence data for the ferritic steels. Furthermore, on the basis of irradiation test results from the National Clad/Duct Materials Development Program, the ferritic steels are being

actively investigated for service in the fast breeder cores and a large high temperature and high fluence data base will exist by the mid-1980's.

The main reasons UWTOR-M uses the martensitic (9 ~ 12% Cr) steel rather than the austenitic steel are:

A) Much greater resistance to neutron induced void formation and metal swelling.

B) A greater resistance to in-reactor creep below 600°C.

C) Better ductility retained after high temperature fission neutron irradiation.

D) Better thermal stress resistance, at least by a factor of two.

E) Better compatibility with the $Pb_{83}Li_{17}$ breeding material.

F) Considerably more experience in heat exchanger design and aqueous environments.

G) Lower material cost per unit weight.

H) Less demand on Cr (12 vs. 18%) and Ni (0.5 vs. ~ 8%) resources which generally have to be imported into the U.S.

Other factors which weighed heavily in our decision to use ferromagnetic steels over the austenitic alloys came from the analyses performed by scientists at General Atomic[1,2] on the effects of magnetic steels with respect to both plasma performance and magnetic forces. These studies concluded that for tokamaks, the effects were minimal. Magnetic perturbations should be even less of a factor during the steady state operation of a stellarator reactor.

Areas of concern that still need to be addressed before one could clearly support the ferritic steel system over the austenitic system include:

1) Effects of high helium content on the irradiation resistance exhibited by ferritic steels in fission reactors.

2) Demonstration that post welding heat treatment will not result in lower radiation damage resistance.

Finally, the specific choice of HT-9 over other ferritic steels should not be taken too seriously. This alloy system has been identified as one particularly attractive to the fast breeder and, as such, gives us a convenient data base from which to extrapolate its performance in a fusion environment. It is quite possible that other ferritic steels might be developed to give even better properties in a fusion environment and future studies ought to be open to new ideas in this aea.

IX.2.2 Breeding Material

Lithium-lead in various compositions has been proposed to fulfill the tritium breeding function in D-T fusion reactors. The form of LiPb can be a solid, as Li_7Pb_2; a liquid, as $Li_{17}Pb_{83}$; or even in a two phase mixture, as $Li_{62}Pb_{38}$. Most breeding compounds either have a high lithium atom density, or require a neutron multiplier to insure adequate breeding. The uniqueness of LiPb is the combination of breeding material and neutron multiplier. Thus, lithium inventory can be minimized while the blanket design will be less complicated.

The lead rich regime of this alloy is of particular interest. It is relatively inert when in contact with water and air, due to its high lead content and low lithium chemical activity. It has excellent neutronic properties, i.e., high breeding potential and excellent energy multiplication. It also has a very low tritium solubility, which will reduce blanket tritium inventory and minimize the problems associated with tritium recovery. For these reasons, a lead rich alloy of Li-Pb is used as the breeding material. $Li_{17}Pb_{83}$ is picked due to its low melting temperature of 235°C.

The very low tritium solubility in $Li_{17}Pb_{83}$ causes a difficult problem in tritium confinement. A typical tritium partial pressure in the $Li_{17}Pb_{83}$ system is 10^{-4} torr. The tritium leakage through the primary heat exchanger will be excessive. The corrosion problem and the associated transport of corrosion products between $Li_{17}Pb_{83}$ and ferrous alloys at a temperature of up to 500°C is potentially serious.

IX.2.3 Coolant

In a D-T fusion reactor, it is desirable to use the breeding material to serve the dual function of heat transport medium. Since 80% of the energy is generated in the breeding material, the heat transfer problems can be alleviated. In addition, the blanket design can be much simpler since there is no need for an internal heat exchanger in the blanket. For a stellarator reactor, liquid metal cooling is difficult due to the irregular blanket geometry. Liquid metal is a poor heat transfer medium in a magnetic field due to its tendency to suppress turbulence. Therefore, proper coolant distribution is required to elimiante potential hot spots. The irregular blanket geometry makes uniform coolant distribution very difficult. For this reason, it was decided that a static $Li_{17}Pb_{83}$ blanket will be used. A static $Li_{17}Pb_{83}$ blanket will also reduce problems associated with corrosion, corrosion product transport and tritium confinement problems.

There are four coolants to be considered:

1. A liquid metal, for example liquid sodium
2. A molten salt
3. Water
4. Gas

Any liquid metal will also have MHD problems which will be more severe than $Li_{17}Pb_{83}$ due to the limited space in the blanket for the coolant. A molten salt is usually a poor thermal conductor and, with a relatively high velocity, will have considerable corrosion problems. Water has been shown to be an economical and safe coolant in current fission reactors. However, the high tritium partial pressure in the $Li_{17}Pb_{83}$ will allow tritium to diffuse to the coolant. Tritium recovery from large amounts of water is expensive. High pressure helium has been proposed to be used as the coolant for HTGR. Helium has excellent heat transfer characteristics for a gas. However, its small volumetric heat capacity (ρc_p) calls for a larger pumping power. In this group, it appears that water and gas are the more attractive coolants. As a compromise, steam has been selected as a coolant for UWTOR-M.

A problem associated with using liquid water as the coolant is the amount of water in the primary coolant circuit. It will not be economically feasible to recover tritium from such large amounts of water. However, the mass inventory of water in the primary steam circuit is a factor of 100 less than in the water circuit. Therefore, it becomes feasible to let tritium concentrations in steam accumulate to a moderately high level and be recovered. As has already been stated, He gas has a small ρc_p, which requires larger pumping power. Steam, due to its much higher density, has almost twice as large a volumetric heat capacity as helium. Therefore, the pumping power required for steam is about half of that for helium.

To summarize, the blanket concept for UWTOR-M is comprised of HT-9 as the structure material, $Li_{17}Pb_{83}$ as the breeding material and steam as the coolant.

References for Section IX.2

1. W.Y. Chen et al., "Magnetic Aspects of Martensitic Stainless Steels as Structural Materials for Tokamak Reactors", to be published (see DOE/ET-0058/7, Sept. 1979).

2. S.N. Rosenwasser, et al., "Ferritic Stainless Steels for Fusion Applications," J. Nucl. Matl., 85 & 86, 177 (1979).

IX.3. Description and Mechanical Design

IX.3.1. Overall Configuration

The stellarator flux surface topology requires twisting in the toroidal direction. In continuous coil stellarators the twisting of the flux surfaces is continuous. Modular stellarators, however, are significantly different in that, although the general trend of the flux surfaces is helical, it is broken up by the discrete flux bundles which emerge between the coils constituting the modular magnetic divertor. Obviously, at the plasma edge the flux surfaces are helical but at larger radii from the plasma center they start breaking off into discrete, well focussed bundles which are oriented toroidally. This is well demonstrated in Fig. IX.3-1 which is a series of ϕ vs. θ plots for one toroidal field period at various radial cutoffs where ϕ is the poloidal and θ the toroidal angle. These figures are generated by launching magnetic field lines at various flux surfaces and following them until they emerge through a divertor slot. Close to the edge of the plasma (upper left figure) where the flux bundles have just started forming, the helical trend is quite evident. As the flux bundles progress further radially they become more toroidally oriented. Since the reaction chamber shape is dictated by the flux topology at the edge of the plasma, we find that by making the scrapeoff layer

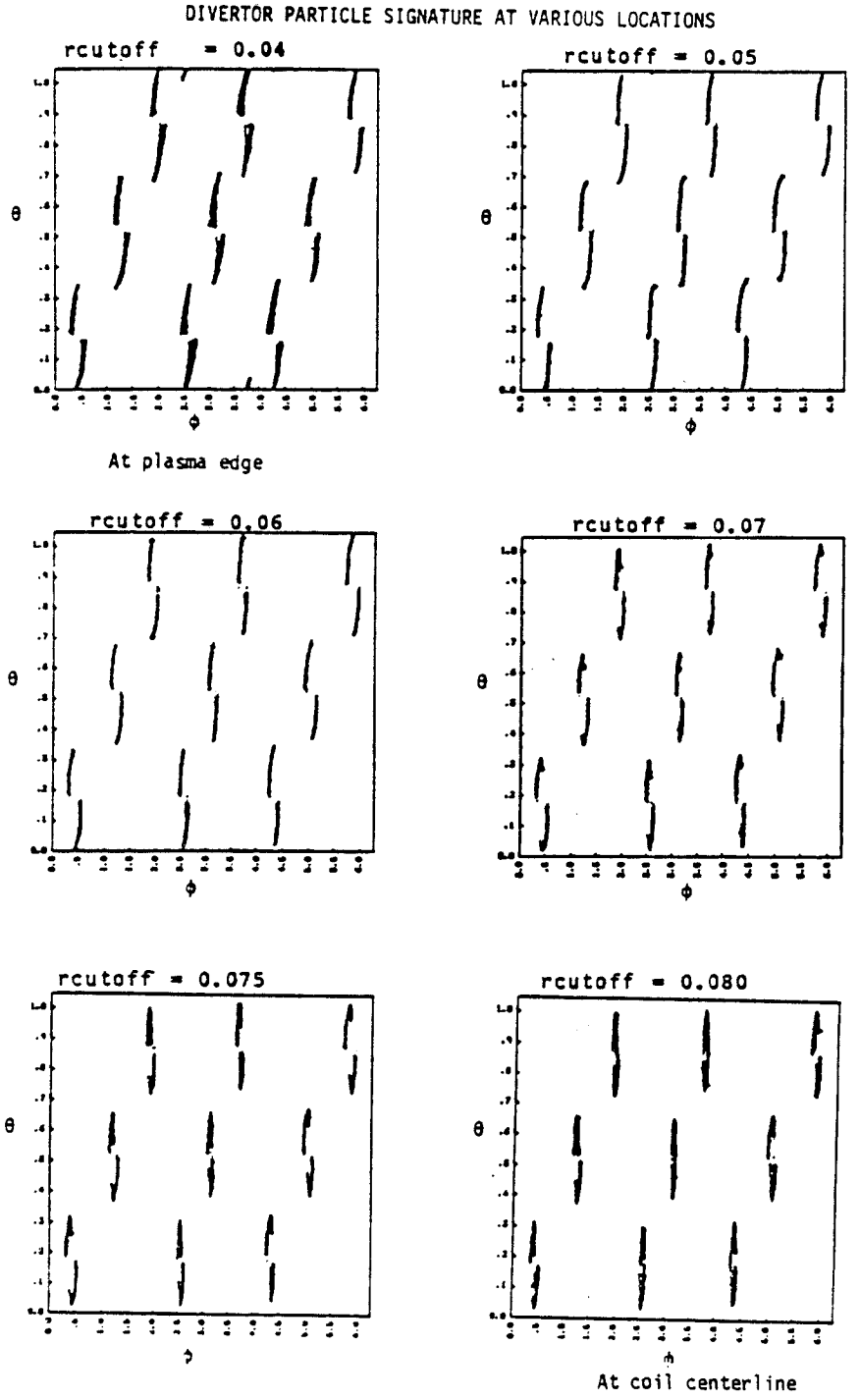

Figure IX.3-1 Particle signatures at different radial cutoff: 0.04 at plasma edge, 0.08 at coil centerline.

sufficiently large (two larmor radii) we can orient the chamber segments toroidally, rotating adjacent segments poloidally through an appropriate angle to accommodate the helical topology. A logical segmentation which seems consistent with the magnetic divertor is to have two blanket segments within each coil. Each segment is separately manifolded with coolant and is entirely independent of its neighboring segments. The design is such as to allow one segment to be removed from either side of a modular coil.

Figure IX.3-2 is a cross section through a modular coil showing the triangular plasma characteristic of an ℓ=3 stellarator. The blanket segment is divided into three regions filling out the space between the plasma and the inner surface of the reflector and separated by the divertor slots. The outer perimeter of the blanket segment is circular. The three blanket regions within a segment are interconnected to allow draining of breeding material through a line attached to the lowest point in the segment. Thus, the blanket segments are always empty of breeding material prior to initiation of any maintenance procedure. For protection against steam line leaks into the blanket, a blanket, a rupture disk will also be provided which will allow a quick routing of breeding material into a dump tank.

Each blanket region will have two supply and two return steam headers connected to common distribution manifolds. These manifolds are shown in Fig. IX.3-2 as circular with the headers radiating inwards to the blanket, resembling the spokes of a wagon wheel. The headers in turn supply manifolds within the segments to which the cooling tubes are attached.

Figure IX.3-3 shows a plan view and a cross-section of a blanket segment. The tubes are shown traversing the segment from supply to return manifolds and are spaced proportionately to the amount of nuclear heating. The first wall

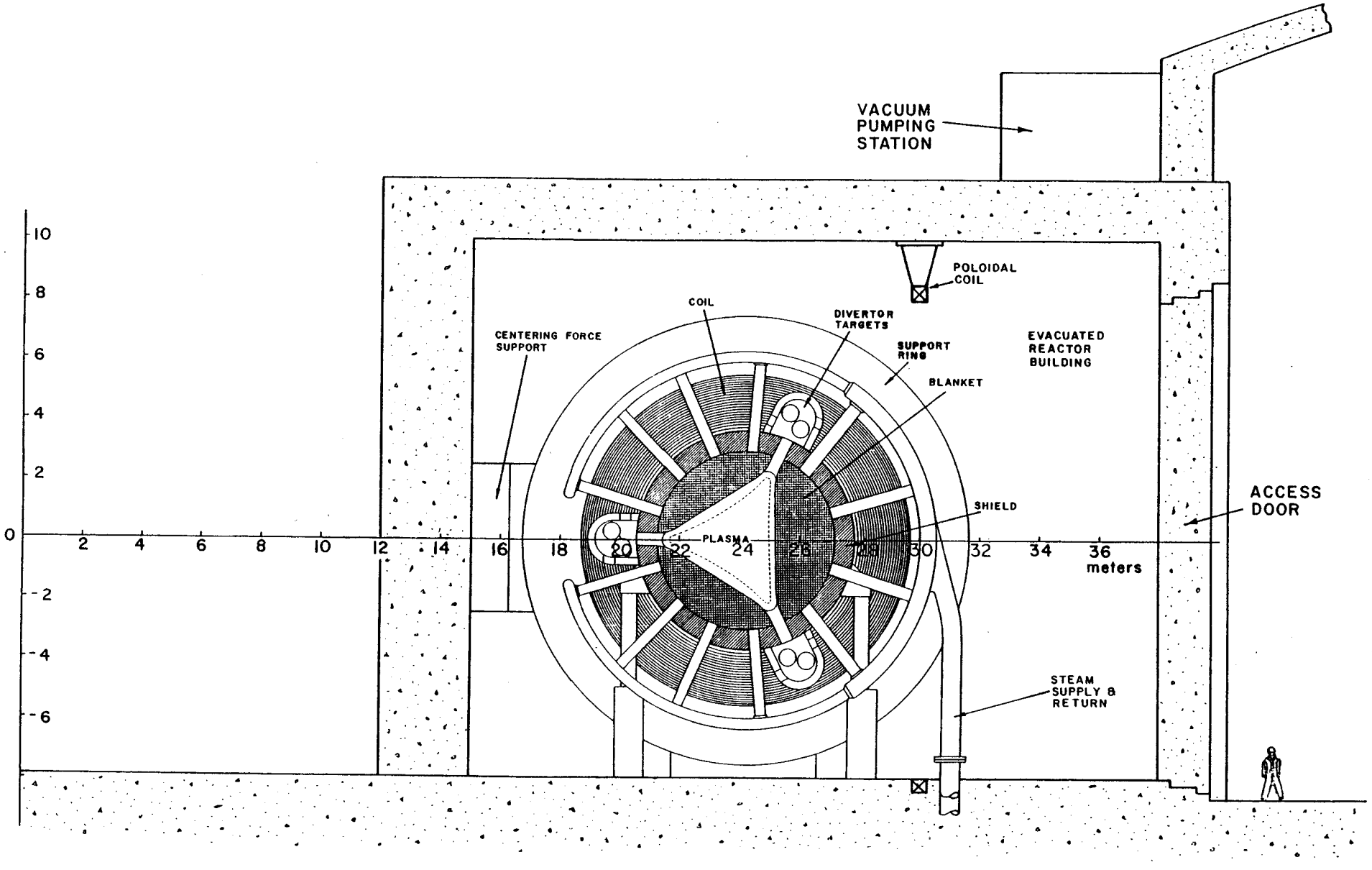

Figure IX.3-2 Cross section of the reactor.

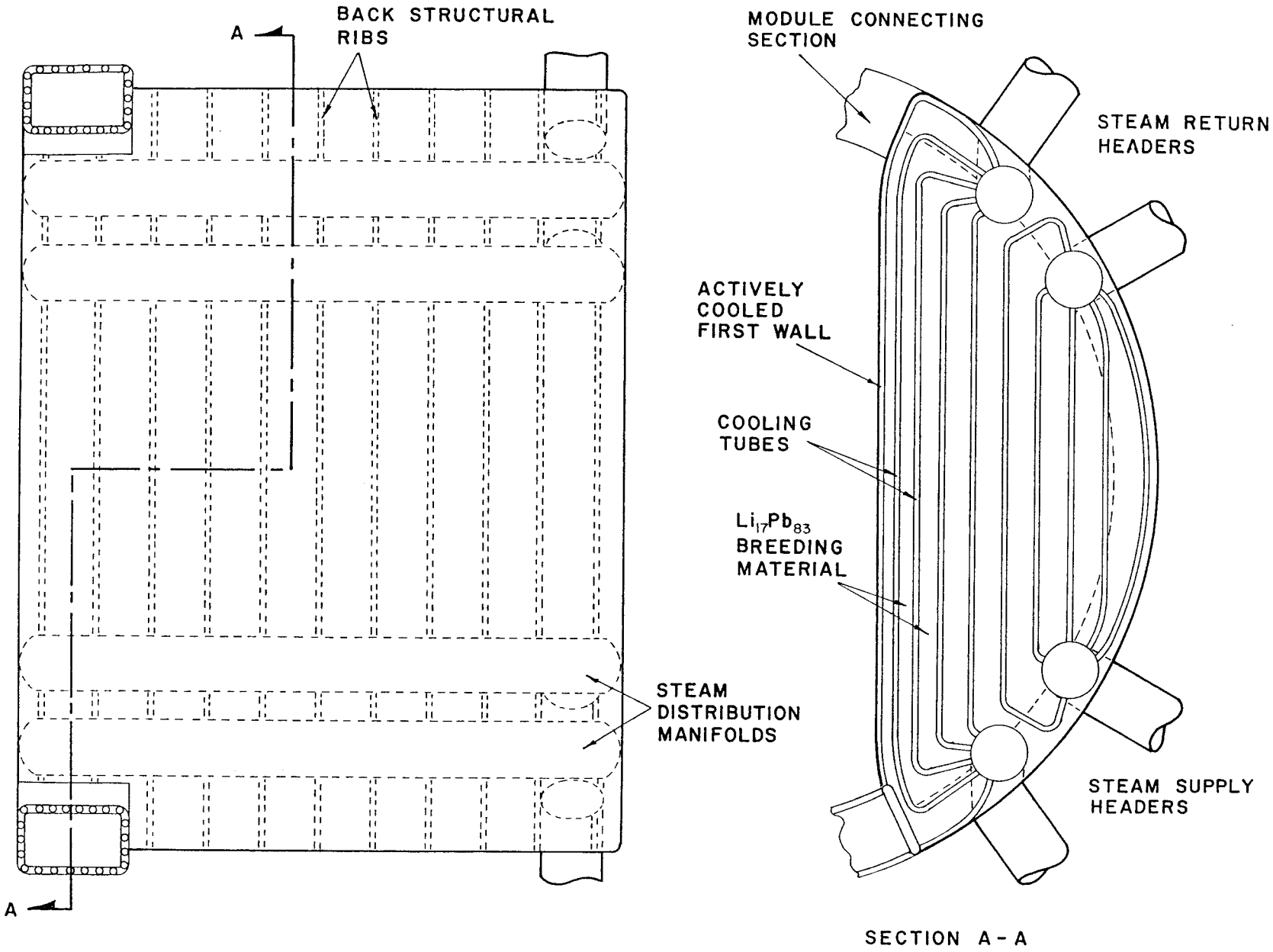

Figure IX.3-3 Plan view and a cross section of a part of a blanket segment.

and other areas exposed to surface heating are covered with close packed arrays of tubes supplied by the same manifolds.

Figure IX.3-4 is a perspective view of a blanket segment where the shaded area indicates the end plates of the three blanket regions. Note that the divertor slot is toroidal and that the inter-region connections are on the opposite side from the header penetrations. The inter-region connections actually fall in the middle of a modular coil, where there is no divertor action. The headers are thus connected on the opposite side to avoid making large slots in the reflector/shield. The second segment in the coil module will be a mirror image of the one shown but with the triangular shape of the reaction chamber and divertor slots rotated poloidally.

One of the most difficult problems in any blanket design is that of making seals between adjacent segments. Plasma experiments operating at base pressures on the order of 10^{-6}-10^{-7} torr have no choice but to provide vacuum tight first walls. Reactor grade plasmas, however, can operate at higher pressures, perhaps as high as 10^{-4} torr. This relaxation in pressure opens up design possibilities which are not available in current plasma experiments. Thus, recent designs have considered placing the vacuum barrier at the back of the shield where it is both accessible and protected from radiation damage. In principle such a design would be possible in UWTOR-M, but it would entail the use of large omega bellows at the shield interface between modules.

To avoid the complication of using bellows and mechanical or welded seals, we have decided to enclose the whole reactor in an evacuated building, thus avoiding seals between blanket segments altogether. This decison has enormous significance in the maintainability of the reactor. Making a vacuum tight building, however, is not easy, especially since it would have large

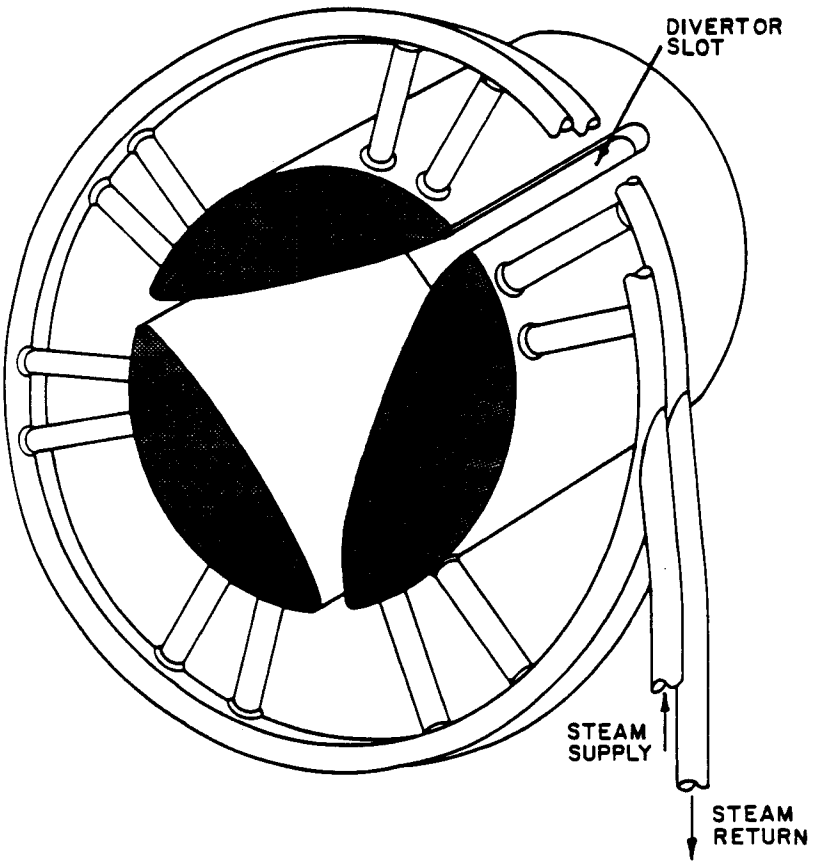

Figure IX.3-4 Perspective view of a blanket segment.

access ports. Experience with space simulation chambers, however, has shown that it is possible.

IX.3.2 Structural and Support Considerations

The design of the first wall in fusion reactors which have a moderate surface wall heating has always been a challenge. This is mainly due to several reasons, the most important of which are:

- The first wall is usually the vacuum barrier between the blanket zone and the reaction chamber.
- The first wall receives a surface heating which produces thermal stress due to the temperature drop across it.
- The first wall has to accommodate unusual shapes and provide for various penetrations, making it difficult to fabricate.

Aside from materials problems, such as compatibility with breeding and cooling media, and plasma contamination from sputtered wall material, the first wall in stellarators differs from tokamaks in two important aspects:

1 - It is not subjected to repeated thermal stress cycling because stellarators are truly steady state.

2 - It does not have to be protected against instantaneous concentrated energy dumps due to disruptions, because stellarators do not have free energy in the form of a net current in the plasma.

One of the problems in the UWTOR-M first wall is due to the blanket concept selected, namely the use of in situ cooled $Li_{17}Pb_{83}$ breeding material. Because $Li_{17}Pb_{83}$ is a very heavy material ($\rho \approx 9.4$ g/cm^3) and the blanket regions are interconnected for ease of draining, the static pressure at the lowest point in the blanket is 0.55 MPa ($\sim$ 80 psi). Normally, such a pressure is not excessive. However, because the areas in this blanket are large and it

is prudent to minimize the structure for neutronic reasons, it would be very difficult to design the first wall as free standing. It was, therefore, decided to attach the first wall to the back plate with stiffeners running parallel to the tubes.

Figure IX.3-5 is a cross section of the first wall. It shows a bank of tubes inserted between two corrugated sheets of HT-9 which are seam welded to each other. The back sheets are attached to the stiffener ribs, while the front sheet is continuous for the entire blanket region. The coolant tubes are loosely inserted into the spaces between the corrugated sheets and the voids are allowed to fill up with breeding material. This type of construction has several major advantages:

1 - The tubes are not as highly stressed by being decoupled from the first wall front sheet.

2 - Heat transfer is promoted by the fact that all the first wall parts are making good contact with the coolant tubes through the $Li_{17}Pb_{83}$.

3 - Thermal stresses both on the front sheet and the tubes are reduced by having the intervening layer of $Li_{17}Pb_{83}$ between them.

The first wall tubes are 1.0 cm in outer diameter and 1.0 mm wall thickness. The corrugated sheets are each 1.5 mm thick, making the effective thickness of the first wall 5 mm. However, only 3 mm are in hoop stress. Assuming a 20 cm spacing between the stiffener straps and a radius of curvature of 20 cm on the first wall, the membrane stress in it will be ~ 30 MPa. Surface wall heating of 15 W/cm^2 produces an additional thermal stress of ±16.5 MPa.

The stiffener straps are spaced at 20 cm intervals and are 2 mm thick. The maximum stress in the stiffener straps is ~ 46 MPa. Side plates of the

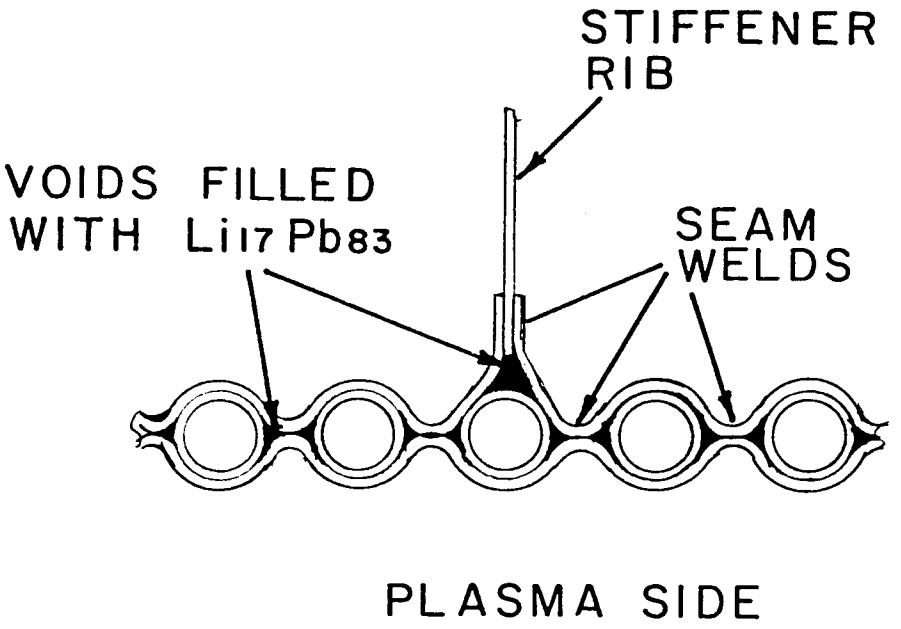

Figure IX.3-5 Cross section of first wall.

blanket regions will also be subjected to internal pressure and will have to be reinforced with ribs on the breeding material side. However, the side plates of adjacent segments will be in contact with each other and are, therefore, restrained from excessive distortion. Proper integration of the coolant tubes and the stiffener straps is critical since it is important that all internal support structures be adequately cooled while providing restraint against vibration and excessive deflection.

The backplate of the blanket will be sturdy enough to be able to transfer the static load of the $Li_{17}Pb_{83}$ to the reflector. In that sense, the back plate can be thought of as part of the reflector rather than the blanket. This eases the requirement of only 9% structure within the blanket. The connection between the blanket and the reflector will have to accommodate expansion from room to operating temperature. The reflector and shield are provided with adequate structure as to make them capable of supporting their own weight as well as the weight of the blanket when full of breeding material. Table IX.3-1 gives the important physical and structural parameters of the UWTOR-M blanket.

Table IX.3-1 Physical and Structural Parameters of UWTOR-M Blanket

Number of blanket segments	36
Outer radius (m)	3
Effective inner radius (m)	1.72
Toroidal length of segment (m)	4.2
Volumetric steam fraction (%)	9
Volumetric structural fraction (%)	9
Mass of structure/segment (tonnes)	45.2
Mass of $Li_{17}Pb_{83}$/segment (tonnes)	503
Effective first wall thickness (mm)	5
Cooling tube outer diam. (mm)	10
Cooling tube wall thickness (mm)	1
Thickness of corrugated FW sheets (mm)	1.5
Spacing of stiffener straps (mm)	20
Thickness of stiffener straps (mm)	2
Membrane stress in FW (MPa)	30
Thermal stress in FW (MPa)	±16.5
Stress in stiffener strap (MPa)	46

IX.4 Hydraulic and Heat Transfer

IX.4.1 Comparison of Steam and Helium

The pumping power required for circulating a gas is

$$P = V\Delta p \qquad \text{(IX.4.1)}$$

$$\text{and } V = Q/\rho c_p \Delta T \qquad \text{(IX.4.2)}$$

$$\Delta p = 2fv^2 L\rho/g_c D \qquad \text{(IX.4.3)}$$

$$\text{in which } v = q/A\rho c_p \Delta T \qquad \text{(IX.4.4)}$$

$$f = .0014 + 0.125\ (\frac{\mu}{Dv\rho})^{0.32} \qquad \text{(IX.4.5)}$$

where:

P = pumping power

Δp = coolant pressure drop

V = volumetric flow rate

Q = blanket power

ρ = density

c_p = specific heat

ΔT = coolant temperature rise

f = friction factor

v = velocity

L = coolant flow length

g_c = conversion factor

D = tube diameter

q = power to a single tube

A = tube cross-sectional area

μ = viscosity

The heat transfer coefficient, h, can be written by standard correlation

$$h = \frac{k}{D} \times 0.023 \left(\frac{Dv\rho}{\mu}\right)^{0.8} \left(\frac{c_p\mu}{k}\right)^{0.4} . \qquad \text{(IX.4.6)}$$

Therefore, the pumping power required for a gas coolant can be scaled as

$$P = f \left(\frac{1}{\rho^2 c_p^3}\right) \qquad \text{(IX.4.7)}$$

while heat transfer coefficient is

$$h = k^{0.6} c_p^{0.4} \rho^{0.8}/\mu^{0.4} . \qquad \text{(IX.4.8)}$$

The friction factor can be calculated by assuming a helium velocity of 30 m/sec and D = 1 cm. The corresponding steam velocity can be calculated by using Eq. IX.4.4 and is 16.3 m/sec. The material properties of helium and steam at 500°C and 50 atm are summarized in Table IX.4-1. The relative values of pumping power required and heat transfer coefficient are also listed. It appears that by using steam as the coolant instead of helium, the pumping power can be reduced by a factor of two and the heat transfer can gain by 12%. This advantage of steam is a result of it having a much larger density than that of helium.

Table IX.4-1 Thermal Properties of Helium and Steam at 500°C, 50 atm

	He	Steam
Density, g/cm^3	0.003	0.0136
Thermal conductivity, $\frac{watt}{cm-^oC}$	2.8×10^{-3}	6.7×10^{-4}
Specific heat, J/g-°C	5.18	2.13
Viscosity, g/sec-cm	3.9×10^{-4}	2.9×10^{-4}
Pumping power (relative)	9.2	5
Heat transfer coef. (relative)	1.2	1.4

Another advantage of using steam as the coolant is that H_2O is a good sink for tritium. As the tritium is diffusing toward the water, it is combined into HTO such that the mobility of tritium is much reduced. If helium is used as the coolant, it is necessary to add oxygen into the helium stream. The helium is thus in contact with an oxidizing atmosphere. This will enhance the formation of an oxide film on heat transfer surfaces and thus reduce the tritium permeation.

IX.4.2 Thermal Hydraulics

The thermal hydraulic design is carried out under the following guidelines:

1. Maximum pumping power does not exceed 5% of the power output of the reactor, or 220 MWt.
2. Maximum structural temperature $\leq$ 550°C.
3. Minimum $Li_{17}Pb_{83}$ temperature is 100°C above its melting temperature.
4. A coolant temperature rise of ~ 200°C.

The equations used for the thermal hydraulic design in this study are given in Table IX.4-2. The pumping power required to circulate a coolant around a loop is the product of the volumetric flow rate and the pressure drop of the coolant. The volumetric flow rate for a gas is very large due to the relatively small value of ρc_p. Therefore, a high pressure gas is desirable since the density of the gas, ρ, is directly proportional to the pressure. However, a higher pressure gas system requires a higher structural fraction, which will reduce the tritium breeding ratio. A 50 atm steam pressure is chosen as a compromise.

The coolant temperature rise through the reactor is chosen as 170°C. The neutron wall loading is 1.41 MW/m^2. The first wall surface heating from the

Table IX.4-2

Equations Used

1. $Q = VA\rho C_p(T_{out} - T_{in})$	Heat carried by coolant
2. $Q = hA(T_{coolant} - T_{wall})$	Heat transfer to coolant channel
3. $\frac{hD}{k} = 0.023\ (\frac{Dv\rho}{\mu})^{0.8}\ (\frac{c_p\mu}{k})^{0.4}$	Calculation of heat transfer coefficient
4. $\Delta p = \frac{2f\rho v^2 L}{g_c D}$	Pressure drop in coolant channel
5. $f = 0.0014 + 0.125\ (\frac{DV\rho}{\mu})^{-0.32}$	Friction factor calculation
6. $T_i' = T_i + [\sum_j C_{ij}\ (T_j - T_i)/V\rho C_p)_i + Q_i/\rho C_p]\Delta\theta$	Finite difference equation for temperature calculations
7. $\Delta\theta \leq (V\rho C_p)_i/\sum_j C_{ij}$	Maximum time step of iteration
8. $E = V\Delta p$	Pumping power required to circulate the coolant

Table IX.4-2 (continued)

Nomenclatures:

A	Area of coolant flow, or area of heat transfer
C_{ij}	Conductance between finite zones i and j
C_p	Specific heat
D	Diameter of coolant channel (= 4 R_H)
E	Pumping power required to circulate the coolant
f	Friction factor
h	Heat transfer coefficient
k	Thermal conductivity of coolant
L	Length of coolant channel
Δp	Coolant pressure drop
Q	Heat transferred into coolant
Q_i	Heat generated in finite zone i
T	Temperature
v	Coolant velocity
V	Coolant volumetric flow rate
V_i	Volume of finite zone i
ρ	Density
μ	Viscosity
R_H	Hydraulic radius

plasma is 23 W/cm^2. Combining these qualities together with the results from the neutronics calculations, the total coolant rate, as well as the flow rate through the coolant channel, can be calculated. The pressure drop can then be calculated through each section of the reactor by using Eq. 4 in Table IX.4-2. The total pressure drop is .07 MPa and the corresponding pumping power required is 75 MW. This is a high but acceptable value for the pumping requirement.

The temperature distribution in the blanket is of vital importance. It has effects on both the mechanical design of the blanket and radiation damage to the structural material. The coolant exit temperature is thus picked at 500°C so that the maximum structural temperature is within the design limit.

The coolant tube is 1 cm ID and 5 m long, as shown in Fig. IX.4-1. The tubes are arranged in triangular array with pitch inversely proportional to the local power generation rate. Thus, the tubes are closer packed near the first wall but further apart toward the back. The minimum center to center coolant tube distance is 1.4 cm. The pitch is arranged so that the heat flux on the coolant tube is constant at 8 W/cm^2. The flow rate of the coolant in the tube can then be calculated by energy balance, from which the heat transfer coefficient and tube wall temperature can be calculated. The maximum structural temperature is 530°C.

The temperature distribution in the blanket has to be calculated numerically to account for the nonuniform nuclear energy generation. A finite difference numerical computer program has been set up to perform those calculations. Using the heating rate obtained from the neutronic calculation as input, the temperature distribution in the blanket is calculated iteratively by using Eq. 6 in Table IX.4-2. The maximum allowable time step for the

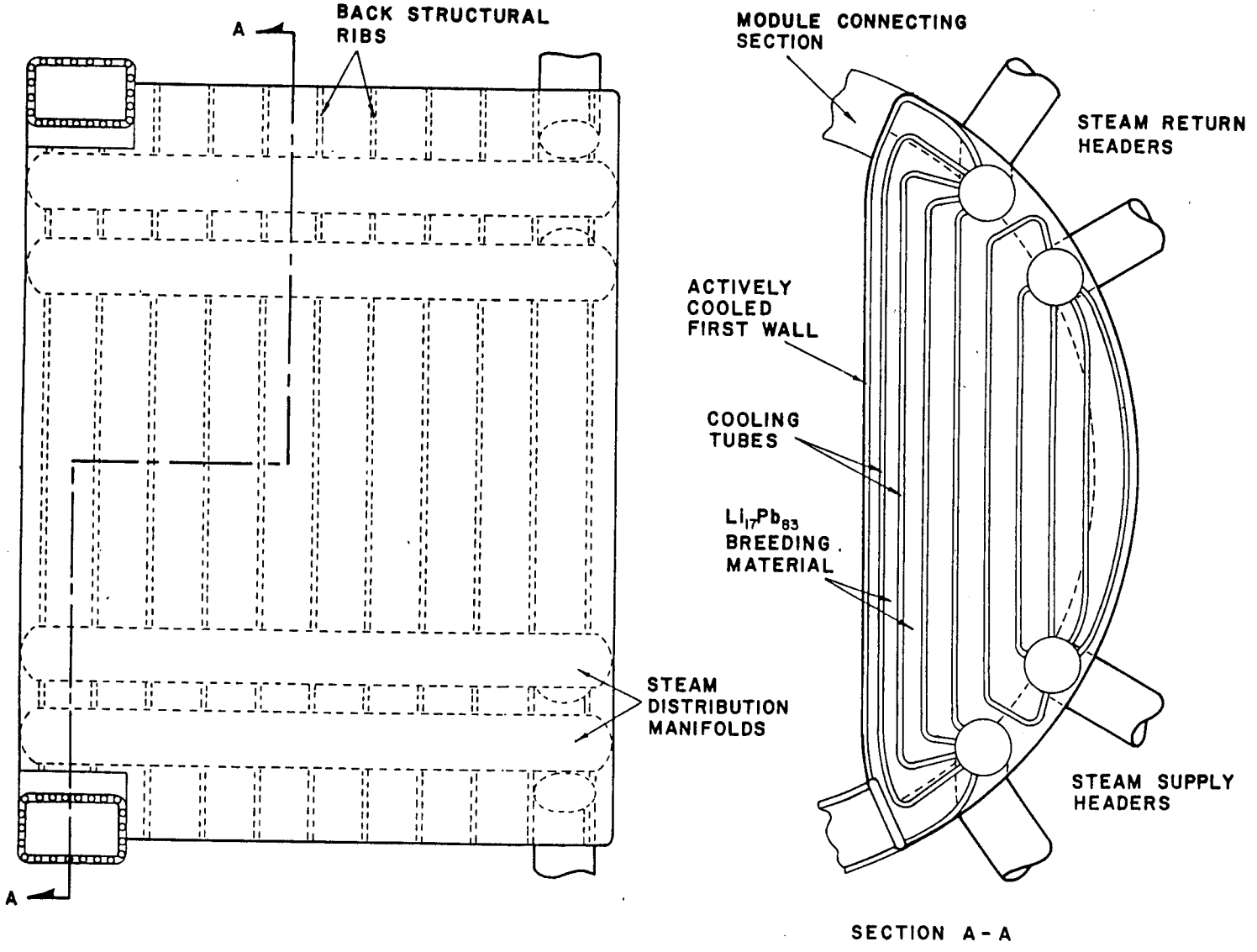

Figure IX.4-1 UWTOR-M blanket section.

iteration calculation is defined by Eq. 7 to insure testability of the iteration process. The maximum blanket temperature is thus calculated at 570°C.

The important blanket parameters are shown in Table IX.4-3. The thermal hydraulic parameters are summarized in Table IX.4-4.

Table IX.4-3 UWTOR-M Blanket Parameters

Fusion power	4300 MW
Blanket power	4340 MW
First wall area	2318 m^2
Neutron wall loading	1.41 MW/m^2
First wall surface heating	23 W/cm^2
Maximum nuclear heating	22.5 W/cm^3
Total heat transfer surface area	5.5×10^4 m^2
Nominal flux to coolant tube	8 W/cm^2
Structural material	HT-9
Breeding material	$Li_{17}Pb_{83}$
Coolant	Steam
Tritium breeding ratio	1.08
Tritium breeding rate	8.3×10^{-3} g/sec

Table IX.4-4 UWTOR-M Thermal Hydraulic Parameters

Blanket power	4340 MW
Divertor zone power	480 MW
Total thermal power	4820 MW
Coolant inlet temperature	330°C
Coolant outlet temperature	500°C
Coolant pressure	5 MPa
Coolant velocity in pipe	35 m/sec
Coolant heat transfer coefficient	0.23 W/cm^2-°C
Coolant flow length	5 m
Coolant pressure drop in pipe	0.07 MPa
Maximum structural temperature	530°C
Coolant tube arrangement	Triangular pitch
Minimum distance between two tubes (center to center)	1.40 cm
Coolant tube O.D.	1 cm
Coolant tube wall thickness	1 mm
Maximum $Li_{17}Pb_{83}$ temperature	570°C
Coolant flow rate	4.8×10^7 kg/hr
Coolant pumping power	75 MW

IX.4.3 Power Cycle

The primary steam coolant from the UWTOR-M blanket is heavily contaminated by tritium. Therefore, it cannot be fed directly to a steam turbine. A steam to steam heat exchanger is required. A simplified power cycle diagram is shown in Fig. IX.4-2. One major advantage of using steam as the primary coolant in the heat exchanger design is that H_2O acts as the sink for tritium by forming HTO. The permeation problem which causes tritium to escape to the downstream water side is much less severe. A conventional single wall steam generator is thus sufficient.

The primary cooling cycle consists of four steam loops. The principal components in each loop are the steam circulator, the steam to steam heat exchanger and the steam piping. The primary coolant circulators are driven by steam turbines with the steam being supplied from the steam generators, as shown in Fig. IX.4-2. 1.2×10^7 kg/hr of steam is circulated in each loop to remove 1205 MW.

The characteristics of the conceptual steam generator units are shown in Table IX.4-5. The total heat transfer area is 4.7×10^4 m^2. The temperature-enthalpy diagram of the steam generator is shown in Fig. IX.4-3. The pinch point temperature difference is 22°C, which is relatively large caused by the poor heat transfer on the primary coolant side. The steam temperature and pressure are 454°C and 13.8 MPa, respectively. The gross efficiency of such a cycle is 40%. The gross electric output is 1898 MW.

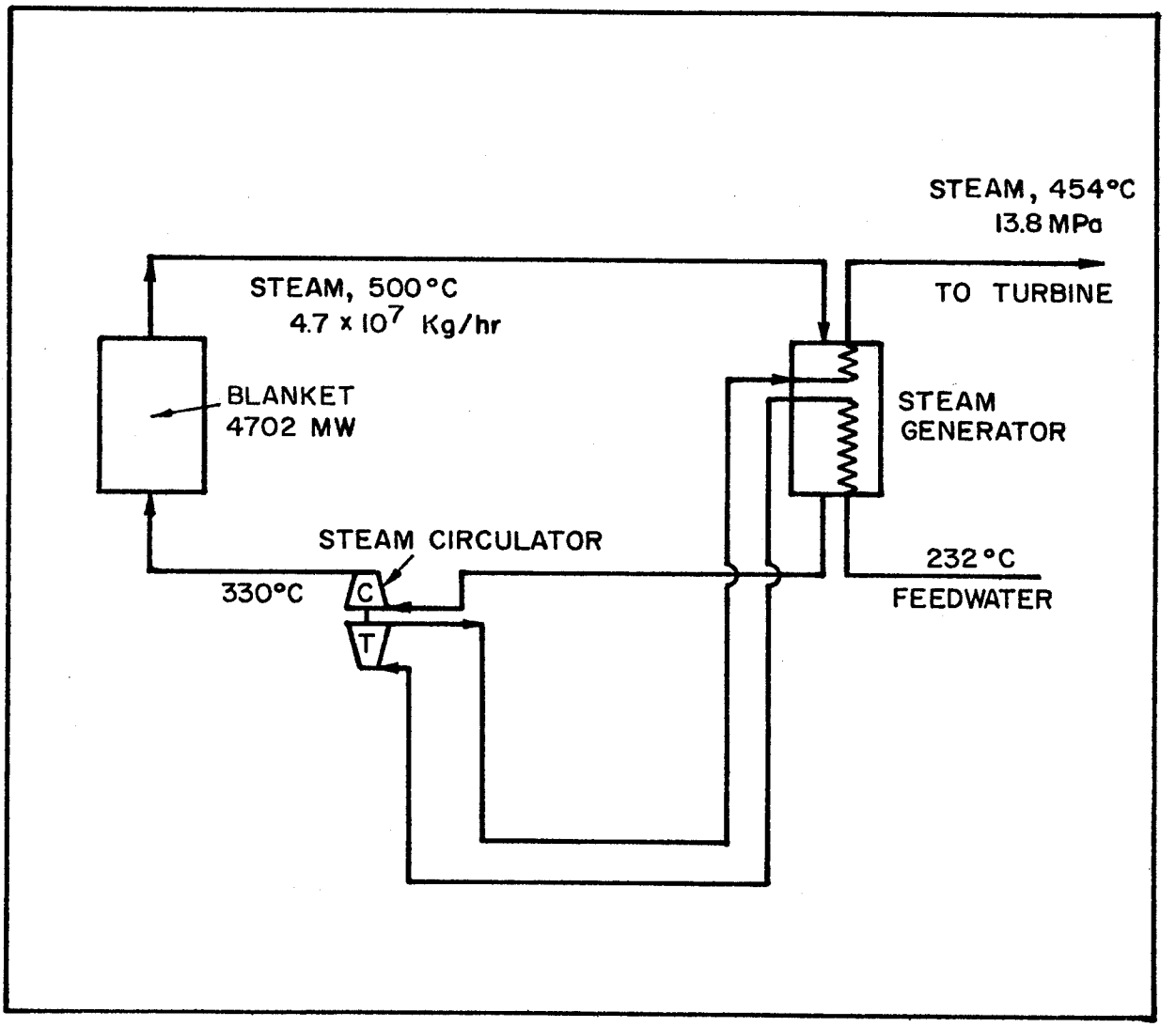

Figure IX.4-2 UWTOR-M power cycle

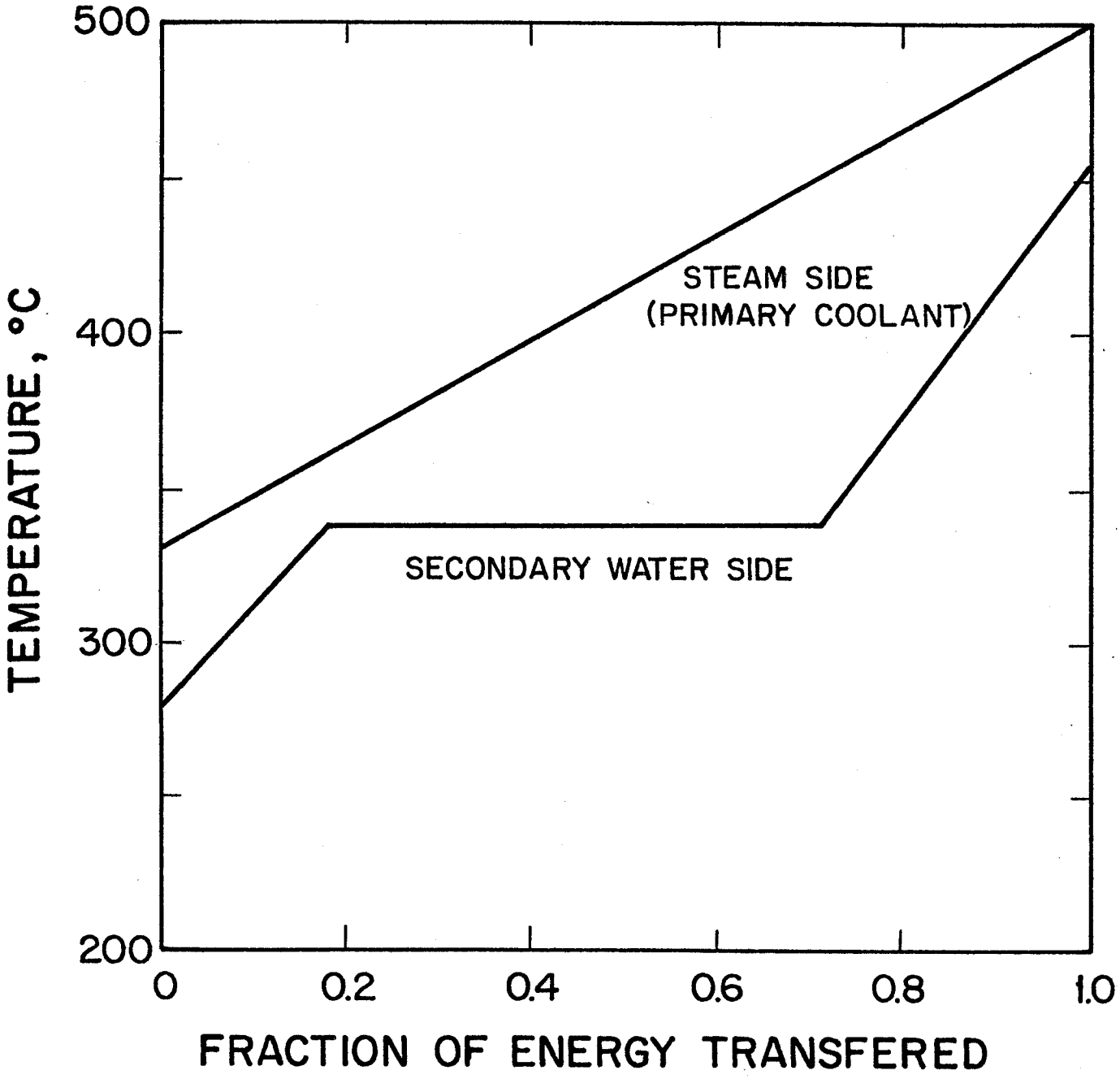

Figure IX.4-3 Temperature-enthalpy diagram for UWTOR-M.

Table IX.4-5 Power Conversion System

A single wall, once through steam to steam generator

Gross thermal power	4820 MW
Primary coolant inlet temperature	500°C
Primary coolant outlet temperature	330°C
Steam temperature	454°C
Steam pressure	13.8 MPa
Reheat temperature	454°C
Feedwater temperature	280°C
Pumping power requirement	75 MW
Net thermal power	4725 MW
Cycle efficiency	40%
Power output	1898 MW

IX.5 Tritium Considerations

IX.5.1 Hydrogen Solubility in $Li_{17}Pb_{83}$

There exists some controversy over the subject of hydrogen solubility in the lithium lead mixture. Ihle[1] first reported the solubility of deuterium in LiPb at two different temperatures. It appears that the result shows too large a temperature dependence such that extrapolation to lower temperatures is not possible.[2] Larsen, et al.[3] proposed the use of the activity of lithium in LiPb as the correction factor to estimate Sievert's constant of D in LiPb from D in pure lithium, or

$$K_s' = a_{Li(LiPb)} K_s \qquad \text{(IX.5-1)}$$

in which K_s' is Sievert's constant for D in LiPb

$a_{Li(LiPb)}$ is activity of lithium in LiPb

K_s is Sievert's constant of D in Li.

Recently, Veleckis measured Sievert's constant in $Li_{17}Pb_{83}$ and concluded that[4]

1. Within the experimental error, in the range from 400 to 600°C, the Sievert's constant for solutions of hydrogen in $Li_{17}Pb_{83}$ was found to be independent of temperature.
2. For the above temperature range, the Sievert's constant of hydrogen in liquid $Li_{17}Pb_{83}$ is given by

$$K_s = (5.1 \pm 1.3)\ (\text{appm})/[\text{torr}]^{1/2} . \qquad \text{(IX.5-2)}$$

Plots of the postulated Sievert's constant calculated from Eq. IX.5-1 and the

experimental data by Ihle, Veleckis and the data for pure lithium and lead are shown in Fig. IX.5-1. It appears that the range and temperature dependence of references 3 and 4 are reasonably consistent.

The Sievert's constant for tritium in $Li_{17}Pb_{83}$ is estimated to be ~ 2.9 appm/[Torr]$^{1/2}$.

$Li_{17}Pb_{83}$ has been used both as the breeding material and the primary coolant.(5) The breeding material process rate for tritium recovery can be estimated by

Breeding material process rate =

$$\frac{\text{tritium breeding rate}}{(\text{T conc. in breeding matl.}) \times (\text{frac. recovery})} .$$

To maintain a reasonable breeding material process rate, the tritium concentration in the breeding material cannot be too small. A reasonably small tritium concentration in the breeding material, due to the small Sievert's constant, will result in a very large tritium partial pressure over $Li_{17}Pb_{83}$. This large tritium partial pressure makes the tritium confinement problem in the primary heat exchanger particularly difficult. Therefore, the low tritium solubility, even though it results in low tritium inventory in the blanket, causes excessive problems in tritium confinement.

IX.5.2 Tritium Recovery Options

The most frequently suggested blanket breeding/coolant material combinations are of two basic types:

1. Gas or water cooled solid lithium compound breeding materials, with a helium purge gas for tritium recovery. In such a design, the tritium

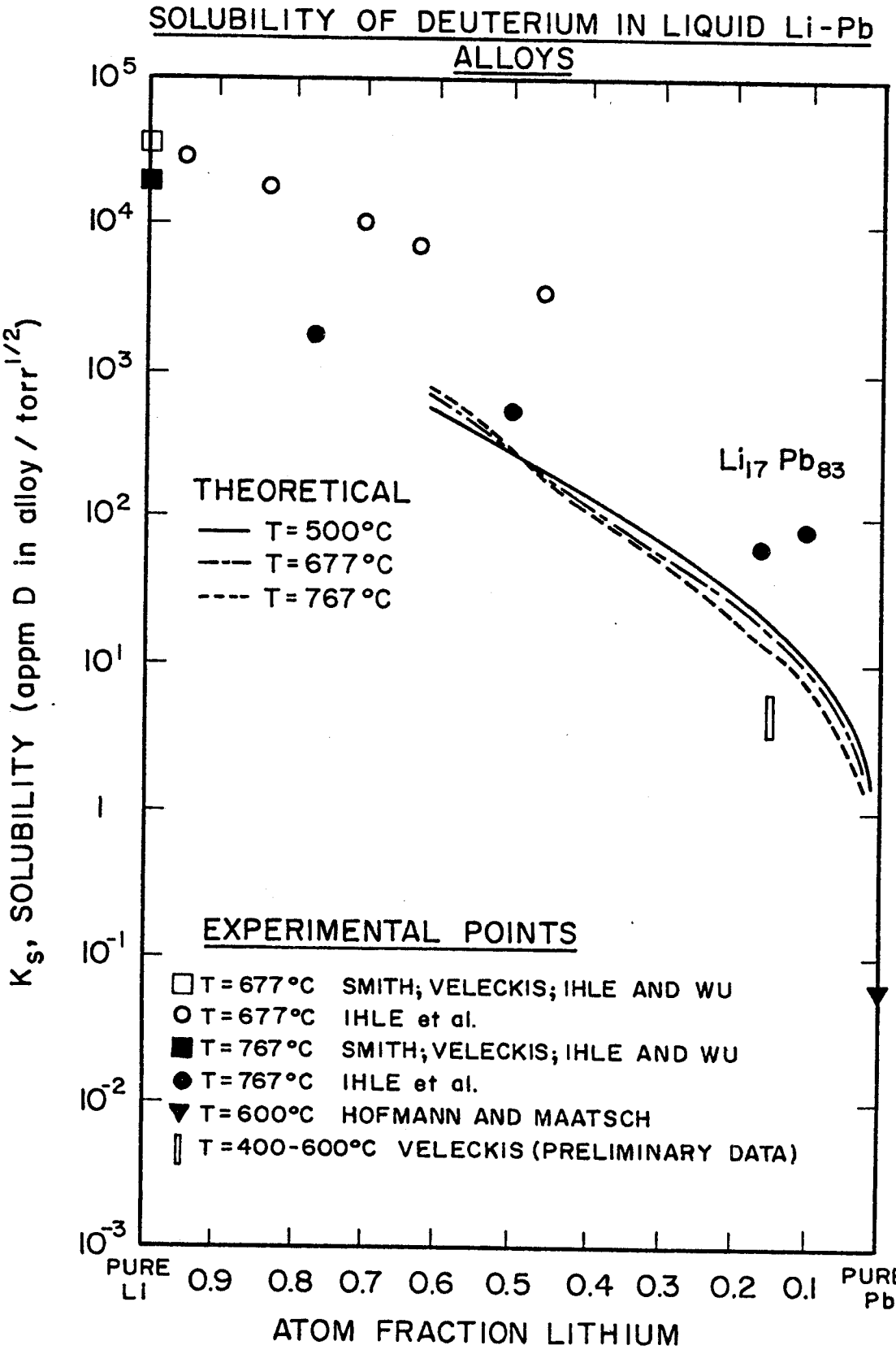
SOLUBILITY OF DEUTERIUM IN LIQUID Li-Pb ALLOYS
K_s, SOLUBILITY (appm D in alloy / torr$^{1/2}$)
10^5
10^4
10^3
10^2
10^1
1
10^{-1}
10^{-2}
10^{-3}
THEORETICAL
T = 500°C
T = 677°C
T = 767°C
$Li_{17}Pb_{83}$
EXPERIMENTAL POINTS
T = 677°C SMITH; VELECKIS; IHLE AND WU
T = 677°C IHLE et al.
T = 767°C SMITH; VELECKIS; IHLE AND WU
T = 767°C IHLE et al.
T = 600°C HOFMANN AND MAATSCH
T = 400-600°C VELECKIS (PRELIMINARY DATA)
PURE Li
0.9
0.8
0.7
0.6
0.5
0.4
0.3
0.2
0.1
PURE Pb
ATOM FRACTION LITHIUM

Figure IX.5-1

diffusion mechanism is not clear and the combination of rate limiting steps and radiation effects may lead to unacceptably large blanket tritium inventory. The "STARFIRE"[6] design, for example, estimated a blanket tritium inventory of 7.8 ~ 380 kg.

2. Circulating liquid lithium[7] or $Li_{17}Pb_{83}$.[5] The problems associated with such a design include corrosion, corrosion product transport, MHD and tritium confinement problems.

In the UWTOR-M blanket, we propose using a static volume of $Li_{17}Pb_{83}$ which is cooled by high pressure steam. High pressure steam is attractive due to its larger volumetric specific heat in comparison to helium at the same pressure so that pumping power required can be reduced by roughly half. The low tritium solubility, and consequently the high tritium partial pressure, will cause the tritium to diffuse through the HT-9 coolant tube walls to the steam coolant. The tritium diffusing into the steam will be oxidized to the form HTO. This coolant steam is circulated to a steam generator, but does not itself drive a turbine. Since T is tied up in HTO, the tritium permeation problem through the steam generator wall is very small. The tritium concentration in the primary steam can be allowed to reach a high level because total water inventory in the primary coolant is only 2000 kg. Conventional techniques for recovering deuterium from water can then be used to recover the tritium. A summary of the tritium permeation calculations is given in Table IX.5-1. The blanket tritium parameters are listed in Table IX.5-2.

IX.5.3 Some Problems Associated With Steam Coolant

1. Tritium recovery. One of the main objections against using water as the coolant in a DT fusion reactor is the problem associated with tritium recovery from water. In a steam cooled system, the water inventory in the

Table IX.5-1 T_2 Permeation Considerations

$$M = P_m \times (\text{time} \times \text{area} \times P_{T_2}^{1/2})/(\text{tube thickness})$$

$$P_m = .5 \text{ mole } T_2 \cdot \text{mm/d} \cdot m^2 \cdot atm^{1/2}$$

$$\dot{M} = 8.3 \times 10^{-3} \text{ g/sec}$$

$$\text{Thickness} = 1 \text{ mm}$$

$$\text{Area} = 5.5 \times 10^4 \text{ m}^2$$

The pressure required for tritium permeation to the coolant from $Li_{17}Pb_{83}$ is $P_{T_2} = 2 \times 10^{-2}$ torr.

Since Sievert's constant is 0.05/wppm T/torr$^{1/2}$ and total breeding material inventory is 10^7 kg,

$$\text{Tritium inventory} = 72 \text{ g}$$

Conclusion: Tritium diffusion toward the coolant appears feasible. The blanket tritium inventory can go up by x 10. The tritium permeation requirement can thus go down by x 10.

Table IX.5-2 Primary Loop Tritium Summaries

Tritium inventory in $Li_{17}Pb_{83}$	72 g
Tritium partial pressure	2×10^{-2} torr
Tritium inventory in coolant	100 g
Tritium dissolved in blanket structure	4 g
Tritium concentration in blanket	6 wppb
Tritium concentration in coolant	50 wppm
Tritium loss from primary coolant loop	< 10 curies/day
Total blanket system tritium inventory	176 g

primary circuit is only 2000 kg. With such a small water inventory, the tritium concentration can then be allowed to build up to a reasonably high level. This should considerably simplify the tritium recovery problem.

One possible tritium recovery process is shown in Fig. IX.5-2. A counter current liquid phase catalytic exchange process is used, in which a fraction of tritium in water is transferred to a hydrogen stream. The tritium in the hydrogen can then be recovered from a standard fractional distillation process. The recovery fraction, (1-x), from the catalytic exchange process, can be as low as 10%. The parameters of the tritium recovery system are listed in Table IX.5-3.

2. Safety. The potential chemical reactivity between water and breeding material is of major concern. However, by using $Li_{17}Pb_{83}$ as the breeding material and steam as coolant, the safety problem is not too critical. The blanket stored energy consists of thermal and chemical energy. Table IX.5-4 compares the stored energy in UWTOR-M and STARFIRE.[6] The stored energy per GW is very comparable.

3. Effect of oxide coating on tritium diffusion. For a steam coolant blanket, an oxide coating will develop on the inside surface of the coolant tube. The oxide coating may provide a tritium diffusion barrier as high as 500 times to that of the basic metal tube.[8] This will prevent the tritium from diffusing into the coolant. However, a hydrogen overpressure may be added to the steam circuit so that the steam will be in a reducing environment. If 1 torr of hydrogen is added to the steam the oxygen partial pressure will be reduced from 10^{-5} torr to 10^{-19} torr. The effect of reduction of oxygen partial pressure on the formation of the oxide coating has to be investigated.

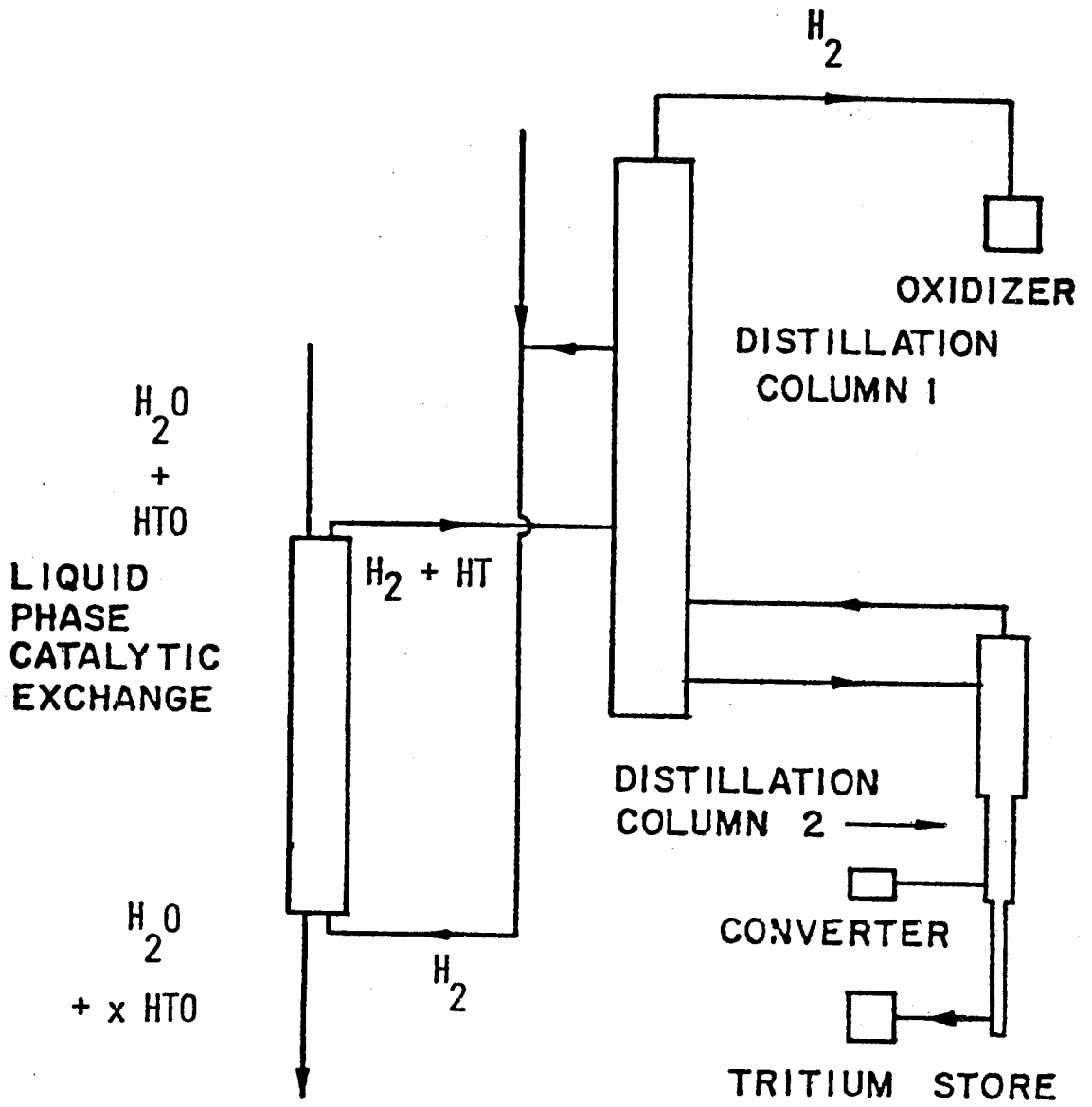

Figure IX.5-2 Tritium separation systems.

Table IX.5-3 Tritium Recovery Parameters

T concentration in H_2O to LPCE	300 appm (T/H_2O)
Fraction recovery (1-x)	20%
Water feed rate to LPCE	830 g/sec
T concentration in exit H_2 stream	30 appm (T/H_2)
T distribution factor	10
H_2 feed rate to LPCE	20 g/sec

The main difficulty of designing an LPCE is to reach $x \to 0$. For $x = 0.8$, the system becomes much simpler.

Table IX.5-4 Energy Stored in Blanket

	$Li_{17}Pb_{83}$/Steam	STARFIRE
Thermal	5.5×10^{10} J/GW	1.4×10^{11} J/GW
Chemical	4.9×10^{9} J/GW	~ 0

References for Section IX.5

1. H.R. Ihle, A. Neubert and C.H. Wu, "The Activity of Lithium and the Solubility of Deuterium in Lithium-Lead Alloys", Proc. Tenth Symp. Fusion Technology, Padova, Italy, September 4-9, 1978, Pergamon Press, New York, 639-644 (1979).

2. N.J. Hoffman, A. Darnell, J.A. Blink, "Properties of Lead-Lithium Solutions", Lawrence Livermore Laboratory, CA, October 1980, UCRL-84273.

3. E.M. Larsen et al., Comments on the Hydrogen Solubility Data for Liquid Lead, Lithium and Lithium-Lead Alloys and Review of a Tritium Solubility Model for Lithum-Lead Alloys, UWFDM-415, University of Wisconsin, Madison, WI, May 1981.

4. E. Veleckis, Argonne National Laboratory, private communication.

5. D.K. Sze et al., "Thermal and Mechanical Design of WITAMIR-I Blanket", Proceedings of the Fourth Topical Meeting on the Technology of Controlled Nuclear Fusion, October 14-17, 1980, King of Prussia, Pennsylvania.

6. C.C. Baker et al., "STARFIRE - A Commerical Tokamak Fusion Power Plant Study", ANL/FPP-80-1, Argonne National Laboratory, September 1980.

7. D.K. Sze et al., "Thermal and Mechanical Design Considerations for Lithium-Cooled Tokamak Reactor Blankets", 5th Symposium on Engineering Problems of Fusion Research, March 1973.

8. J.T. Bell et al., "Tritium Permeability of Structural Materials and Surface Effects on Permeation Rates", Proceedings of Tritium Technology in Fission, Fusion and Isotopic Applications, April 29 - May 1, 1980, Dayton, Ohio.

X. Neutronics

X.1. Introduction

The neutronics and photonics analysis of UWTOR-M was carried out using one- and three-dimensional calculations. The main blanket features are presented in Section X.2. A primary goal of the optimization study of the blanket and reflector discussed in Section X.3 is to achieve an overall tritium breeding ratio greater than one with the largest energy multiplication. The shield configuration was optimized as discussed in Section X.4 to reduce the radiation damage and heat loads on the superconducting magnet. Radiation streaming calculations through the divertor slots and pumpout ports are given in Section X.5. The biological shield required to surround the reactor is treated briefly in Section X.6.

X.2. Basic Blanket Features

The blanket of UWTOR-M consists of three segments having different cross-sectional areas as shown in the reactor vertical view of Fig. X.2-1. The first wall follows exactly the triangular plasma shape which has an equivalent radius of ~ 170 cm. The clearance between the first wall and the plasma boundary has an average value of 17 cm.

The radial neutron source density distribution is shown in Fig. X.2-2. This distribution can be approximated for the calculations by a uniform source in a triangular zone at the center of the plasma where ~ 76% of the neutrons are generated and another uniform source with lower density over the outer zone of the plasma. The total neutron source rate is 1.52×10^{21} n/sec which corresponds to a fusion power of 4297 MW (at 17.6 MeV/fusion). Some of these source neutrons will stream through the three divertor slots which occupy ~ 5% of the solid angle. A significant number of lower energy secondary neutrons

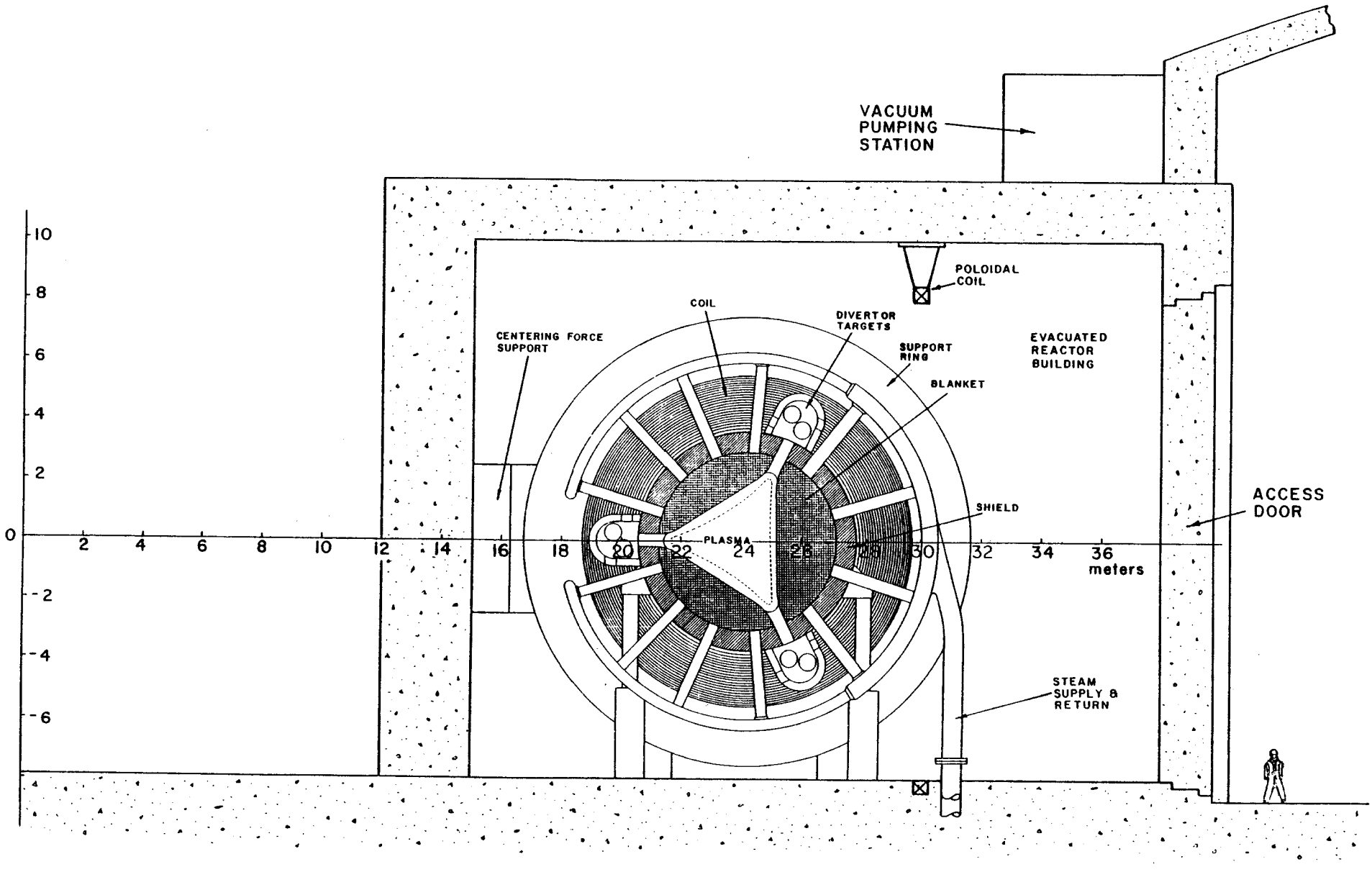

Figure X.2-1 Vertical cross section of blanket and coil within evacuated reactor containment.

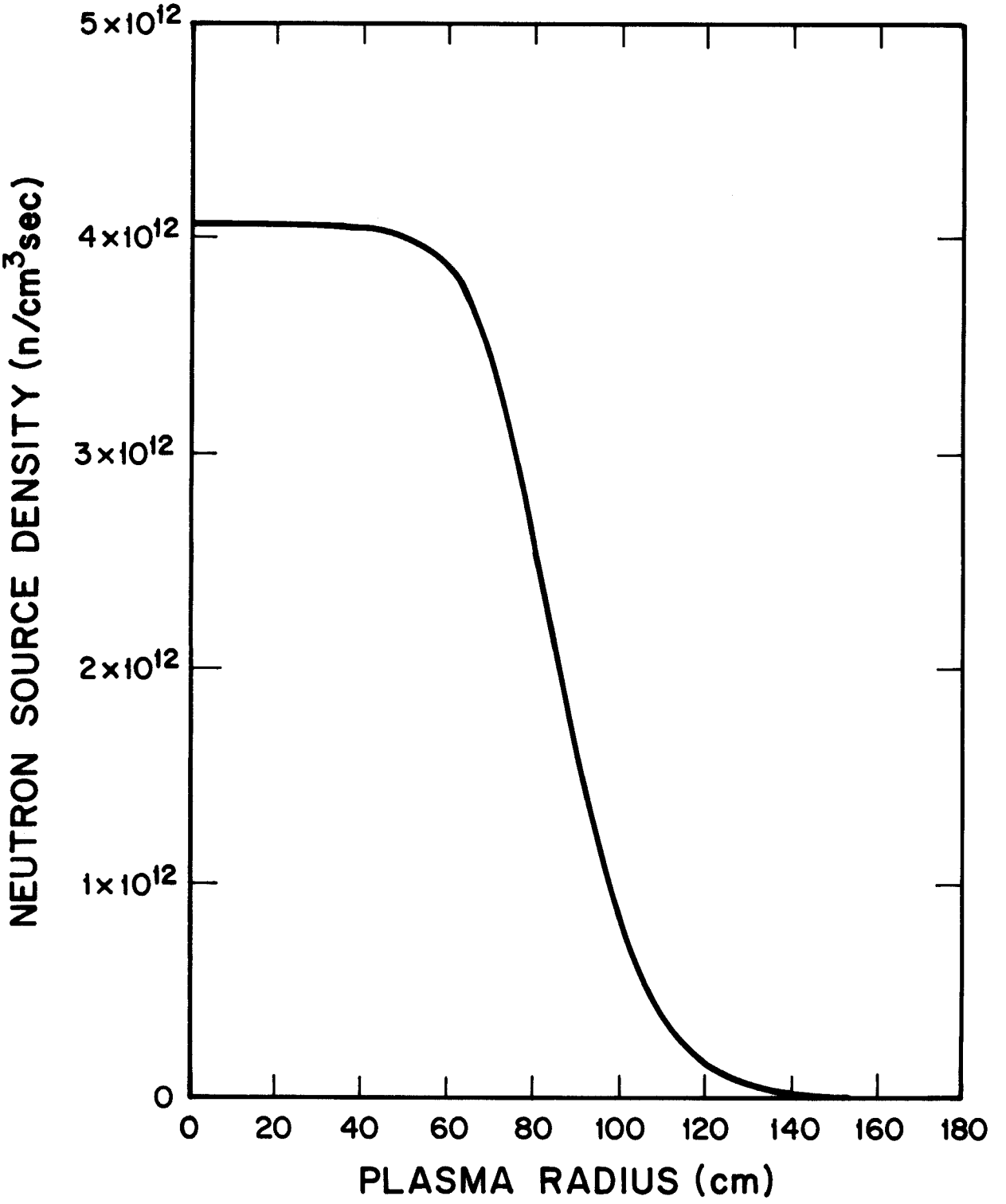

Figure X.2-2 Spatial variation of volumetric source strength.

that have been moderated in the blanket and reflector will also stream out from the slots along with some gamma photons that are produced in neutron interactions with different materials. Therefore, shielding materials are used in the divertor regions to protect the vital components in the toroidal hall against streaming radiation.

The blanket and its associated shield can be represented approximately by the schematic shown in Fig. X.2-3. The material composition of the different reactor zones is given in Table X.2-1. The blanket has an average thickness of 115.4 cm. The presence of the back structural ribs yields to an increase in the structural content in the last 30 cm of the blanket. The lithium in the $Li_{17}Pb_{83}$ breeder[1] is enriched to 90% and only 9 v/o HT-9 is used to achieve adequate breeding while meeting structural demands. A 20 cm thick metallic reflector made of HT-9 was used in the initial calculations to enhance the energy multiplication.[2] A 50 cm thick shield was considered to protect the superconducting magnet. In order to determine the overall tritium breeding ratio (BR) and the energy multiplication (M), an initial calculation was performed using the three-dimensional (3-D) Monte Carlo code MCNP.[3] The nuclear cross section sets used are based on ENDF/B-V evaluation and the problem was run on the MFE computer center at LLNL. The results for this initial blanket design gave an overall tritium breeding ratio of 1.25 and an energy multiplication of 1.115. This demonstrates the need for blanket and reflector optimization to lower the breeding ratio and maximize the energy multiplication.

X.3. Blanket and Reflector Optimization

The optimization study was carried out using the one-dimensional (1-D) discrete ordinates code ONEDANT,[4] the standard Los Alamos coupled 30 neutron

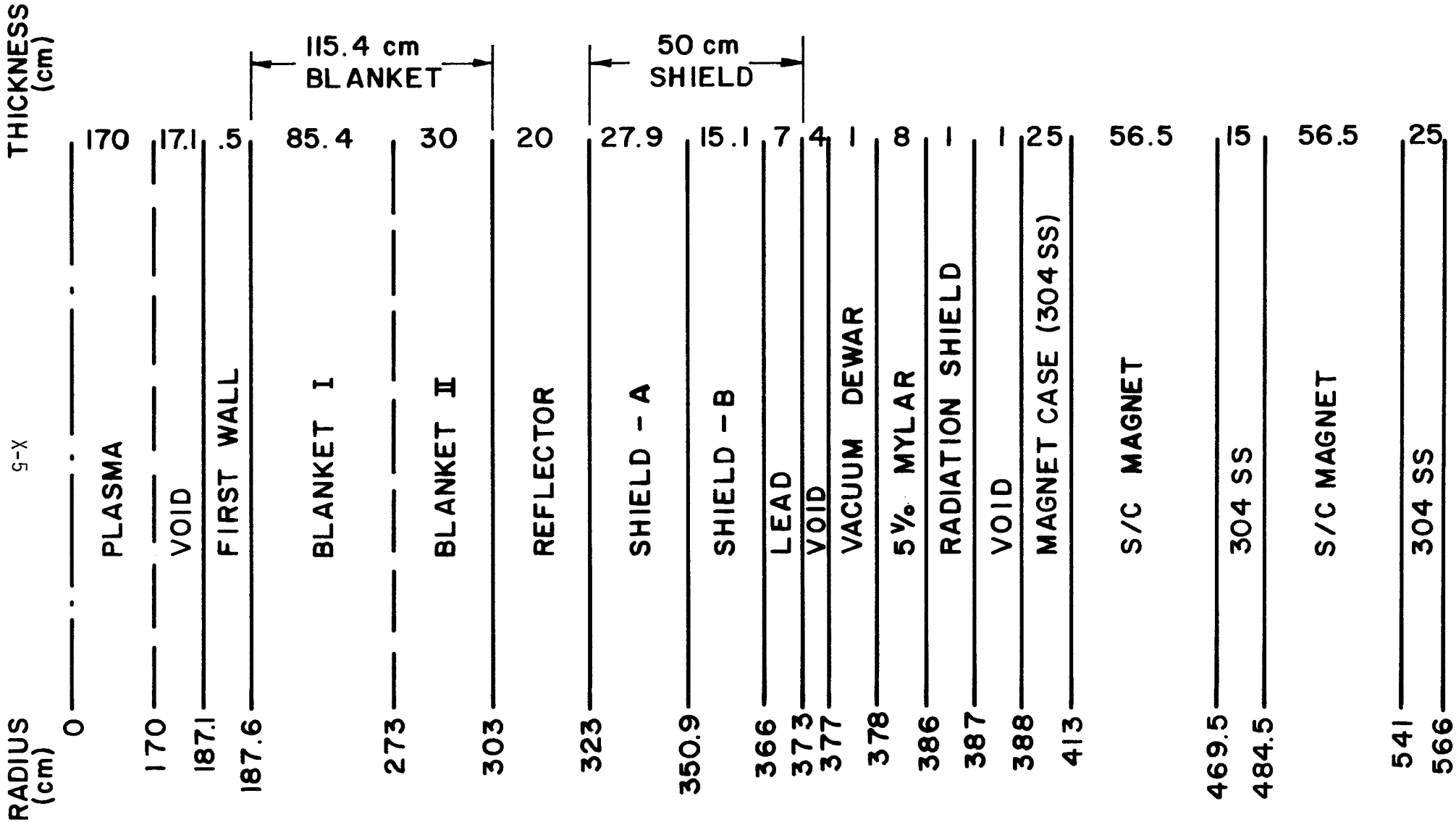

Figure X.2-3 Schematic of blanket, reflector, shield, and superconducting magnet.

Table X.2-1. Material Composition

First Wall	HT-9
Blanket I	82 v/o $Li_{17}Pb_{83}$ 9 v/o HT-9 9 v/o Steam
Blanket II	76 v/o $Li_{17}Pb_{83}$ 15 v/o HT-9 9 v/o Steam
Reflector	90 v/o Structure 10 v/o Steam
Shield-A	95 v/o Fe 1422 5 v/o H_2O
Shield-B	86 v/o B_4C (87% d.f.) 10 v/o Fe 1422 4 v/o H_2O
Superconducting Magnet	71.7 v/o Cu 3.3 v/o NbTi 16.7 v/o Epoxy 8.3 v/o He
Divertor Target Shield	95 v/o Fe 1422 5 v/o Steam
Biological Shield	87 v/o Ordinary Concrete 8 v/o C 1020 Steel Reinforcement 5 v/o H_2O

and 12 gamma energy groups, and P_3-S_8 approximation, in cylindrical geometry.

The schematic shown in Fig. X.2-3 was modeled in the 1-D calculations. Key results from these calculations are the local BR and M. These results are intended only to give a quantitative feel for any change in the enrichment or structural content on BR and M.

In order to lower the breeding ratio, the enrichment has to be decreased and/or the structural content has to be increased. Several 1-D calculations were carried out to determine the effects of lithium enrichment and the structural content on BR and M. In the first set of calculations, the enrichment was changed gradually from 90 to 20% for a 9 v/o structure. In the second set of calculations, the structural content was increased from 9 to 16 and then to 21 v/o, and the corresponding volume percent of $Li_{17}Pb_{83}$ was reduced to 75 and 70 v/o, respectively. Also the enrichment was decreased for each of the cases with different structural content from 90 to 20%.

A plot of the local BR versus M for the various cases is represented in Fig. X.3-1. An inspection of this figure shows that decreasing the enrichment results in decreasing the BR and increasing M. This is due to the fact that reducing the ^6Li percentage in the lithium gives more chance for neutrons to be parasitically absorbed in the structural material rather than producing tritium (a neutron parasitically absorbed releases ~ 7 MeV compared to 4.8 MeV released in a $^6Li(n,\alpha)T$ reaction). Also, decreasing the enrichment results in larger increases in M than does increasing the structural content. Furthermore, increasing the structural content results in an appreciable reduction in BR since an amount of the breeding material is replaced by structure. Figure X.3-1 reveals that the only way to increase M without having a drastic

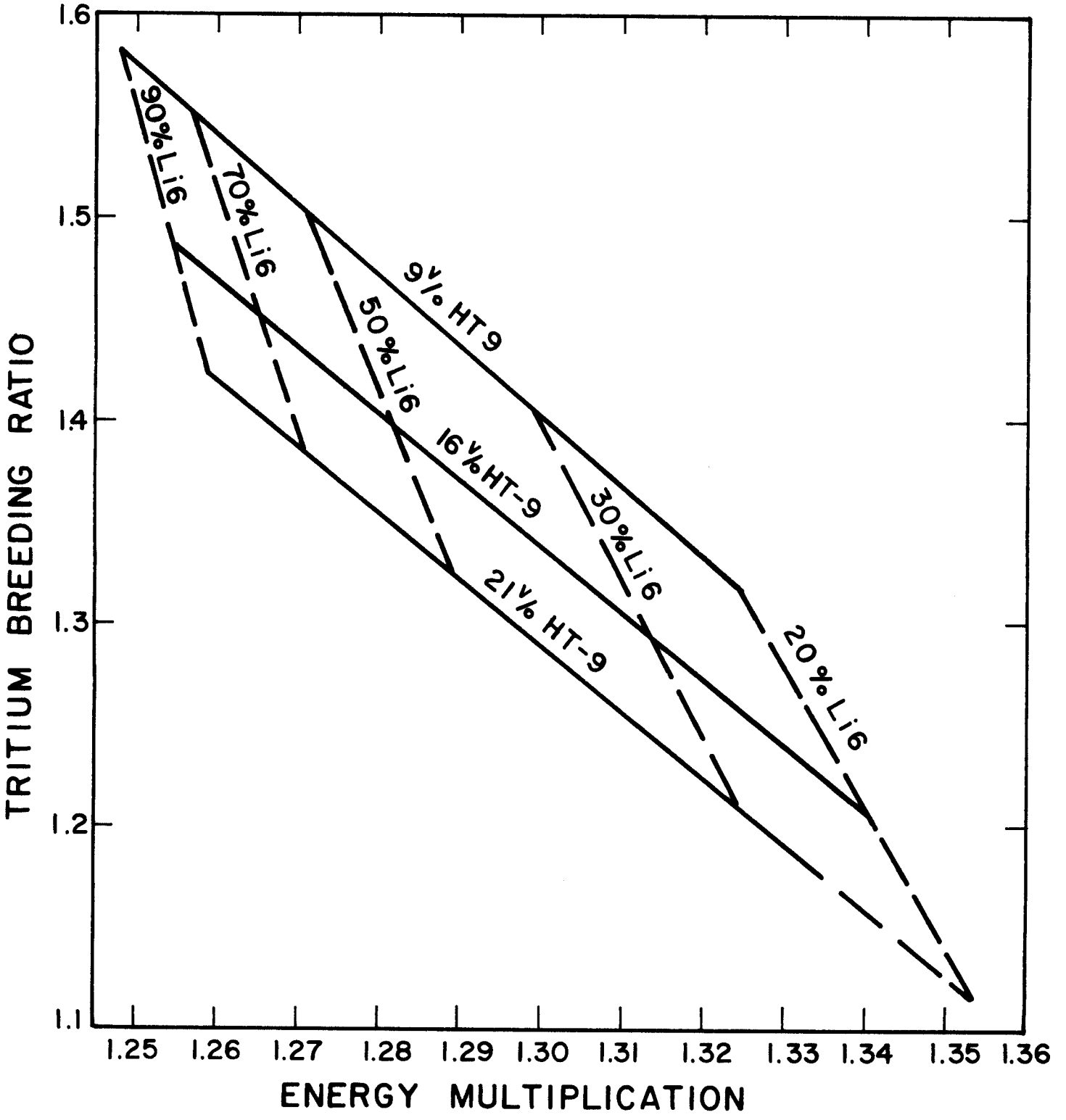

Figure X.3-1 Variation of tritium breeding ratio with energy multiplication for different ^{6}Li enrichment and structural contents.

reduction in BR is to lower the enrichment and keep the structural content to its minimal value.

To increase the fraction of energy recovered from the reflector, its thickness was doubled to intercept most of the neutron and gamma energies before leaking into the shield. In addition, the reflector structural material was changed to the low activation steel Fe 1422 (14 w/o Mn, 2 w/o Ni, 2 w/o Cr, and 82 w/o Fe). Since the manganese in Fe 1422 has a high (n,γ) cross section in the resonance range more nuclear heating will be produced in the reflector. The effect of these changes is expected to be more pronounced in the 3-D modeling of the blanket as more neutrons and gamma rays reach the reflector penetrating through the thin blanket regions which surround the divertor slots.

Preliminary 3-D calculations were performed using MCNP and results are based on 5,000 histories yielding relative standard deviations of less than 2% for the quantities of interest. A view emphasizing the blanket is shown in Fig. X.3-2 which is an output from the plotting routine of MCNP. The structural content in the blanket was kept at 9 v/o and the enrichment was varied gradually between 20% and 40%. The effect the enrichment has on radiation streaming is indicated in Fig. X.3-3. The high energy component of the streaming neutrons contains all neutrons in the energy range from 13.5 to 14.1 MeV. This includes the primary as well as some slightly lower energy neutrons which stream after colliding in the first few centimeters of the blanket. The fraction of primary neutrons streaming is less than that indicated by the solid angle fraction of the divertor slots (5%) because source neutrons are distributed in the triangular plasma zone. A fraction of 5% would have been obtained if all source neutrons were emitted at the plasma centerline.

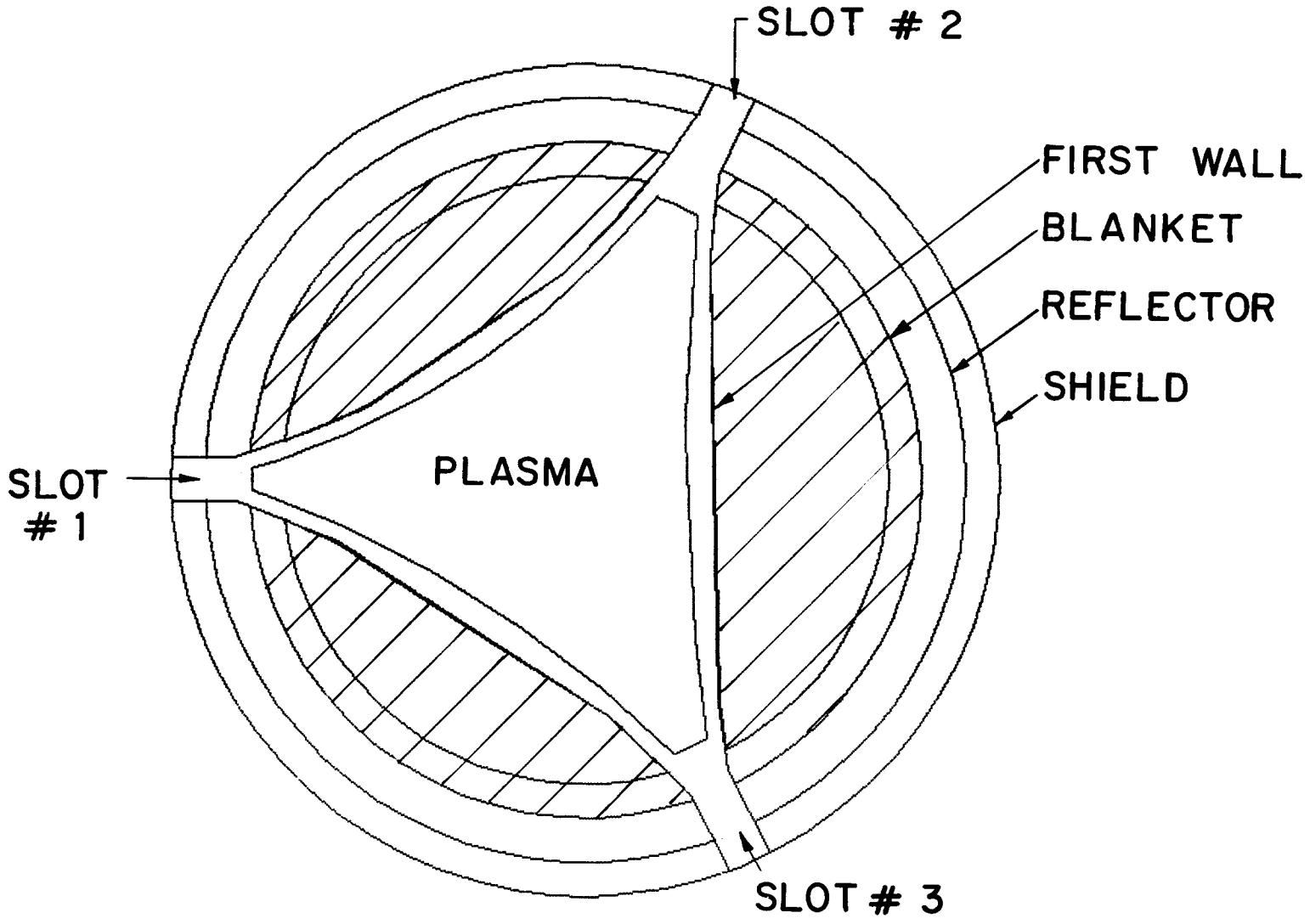

Figure X.3-2 Blanket and shield geometrical model used for 3-D calculations.

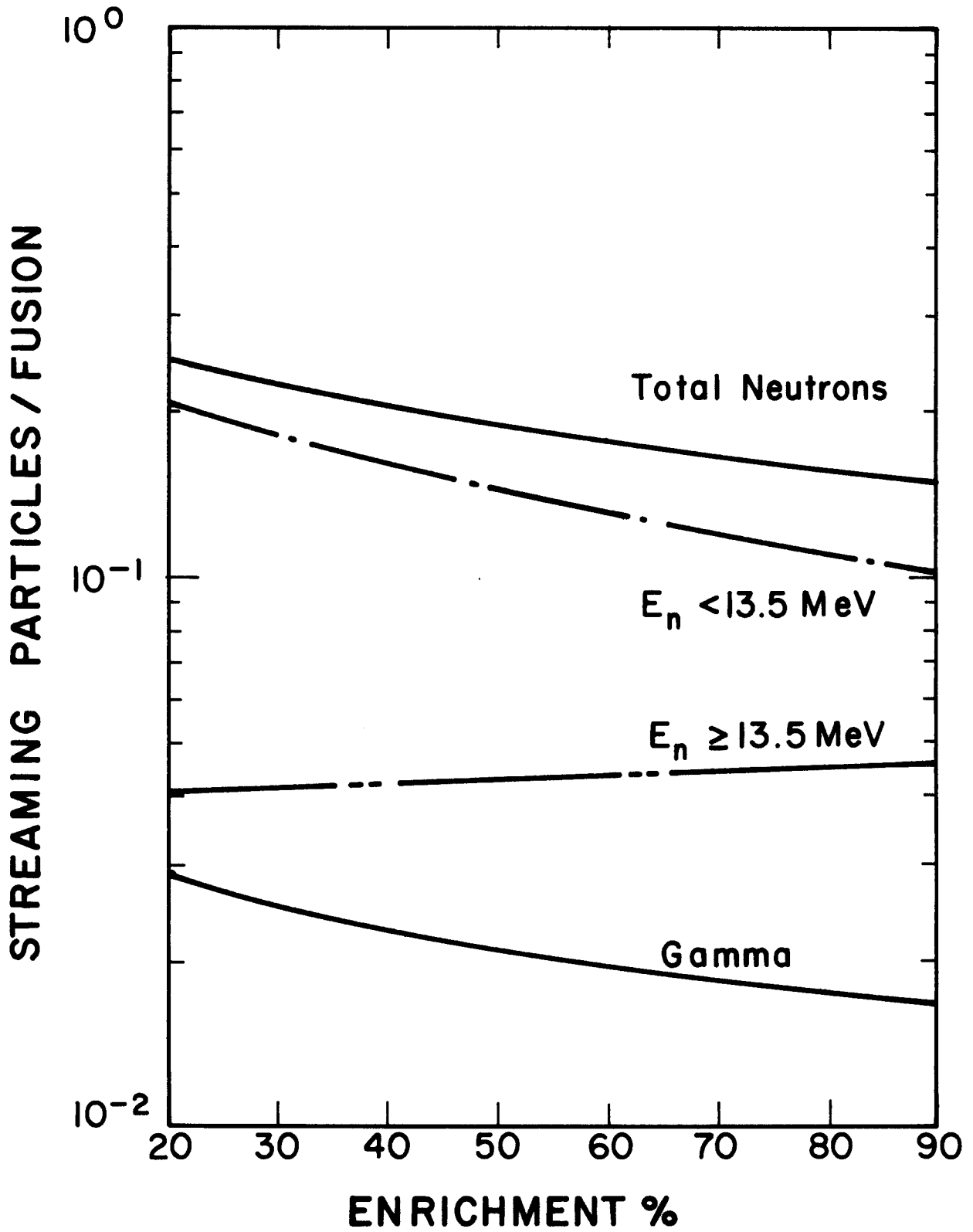

Figure X.3-3 Effect of ^{6}Li enrichment on radiation streaming.

The overall tritium production and total nuclear heating which are based on 3-D calculations are, as anticipated, lower than the local values for the following reasons:

1. Primary neutron streaming through the three divertor slots. These neutrons carry 14.1 MeV energy and their number is proportional to the solid angle occupied by the slots.
2. Streaming of the scattered neutrons and secondary gamma rays. This number increases as the enrichment decreases because of the decreased blanket attenuation as shown in Fig. X.3-3.
3. The thin blanket regions surrounding the divertor slots result in larger neutron and gamma ray leakage to the reflector and bulk shield.

The 3-D results show that an enrichment of 35% gives an adequate overall tritium breeding ratio of 1.08 and an energy multiplication of 1.153 (M is defined as the nuclear heating in the first wall, blanket, reflector, and the six divertor targets per 14.1 MeV source neutron). The region-wise details of the tritium production and the energy deposition are given in Tables X.3-1 and X.3-2, respectively. More than 98% of the breeding is contributed from ^{6}Li and, as expected, blanket I breeds most of the tritium. About 54% of the total nuclear heating results from gamma heating. It is interesting to compare the overall BR and M with the rather high local values of 1.44 and 1.295, respectively. The difference is mainly due to the reasons pointed out earlier.

The 1-D calculations provide some useful results for tritium, thermal hydraulics, and material analyses. The tritium production and the power density as a function of radius are shown in Fig. X.3-4 and Fig. X.3-5, respectively, for the 35% enrichment. The peak power density is 22 W/cm^3 and

Table X.3-1. Blanket Tritium Production

	Blanket I			Blanket II			Total Tritium Production
	Li-6	Li-7	Total	Li-6	Li-7	Total	
Segment 2-3*	0.358	4.964E-3	0.363	3.628E-2	2.114E-4	3.649E-2	0.400
Segment 1-3	0.289	4.453E-3	0.294	5.483E-2	3.470E-4	5.518E-2	0.349
Segment 1-2	0.279	4.348E-3	0.283	4.758E-2	3.262E-4	4.791E-2	0.331
Total	0.926	1.377E-2	0.940	0.139	8.846E-4	0.140	1.080

*2-3 means segment between slot #2 and 3 (see Fig. X.3-2).

Table X.3-2. Nuclear Heating (MeV/fusion)

	Neutron	Gamma	Total
First Wall	0.057	0.310	0.367
Blanket I	6.408	6.008	12.416
Blanket II	0.826	0.627	1.453
Reflector	0.088	1.279	1.367
Shield*	0.351	0.128	0.479
6 Divertor Targets†	0.122	0.533	0.655
Total Recoverable Energy	7.501	8.757	16.258

*Made of a homogenized mixture of the optimized shield shown in Fig. X.4-5.

†See Section X.5-2.

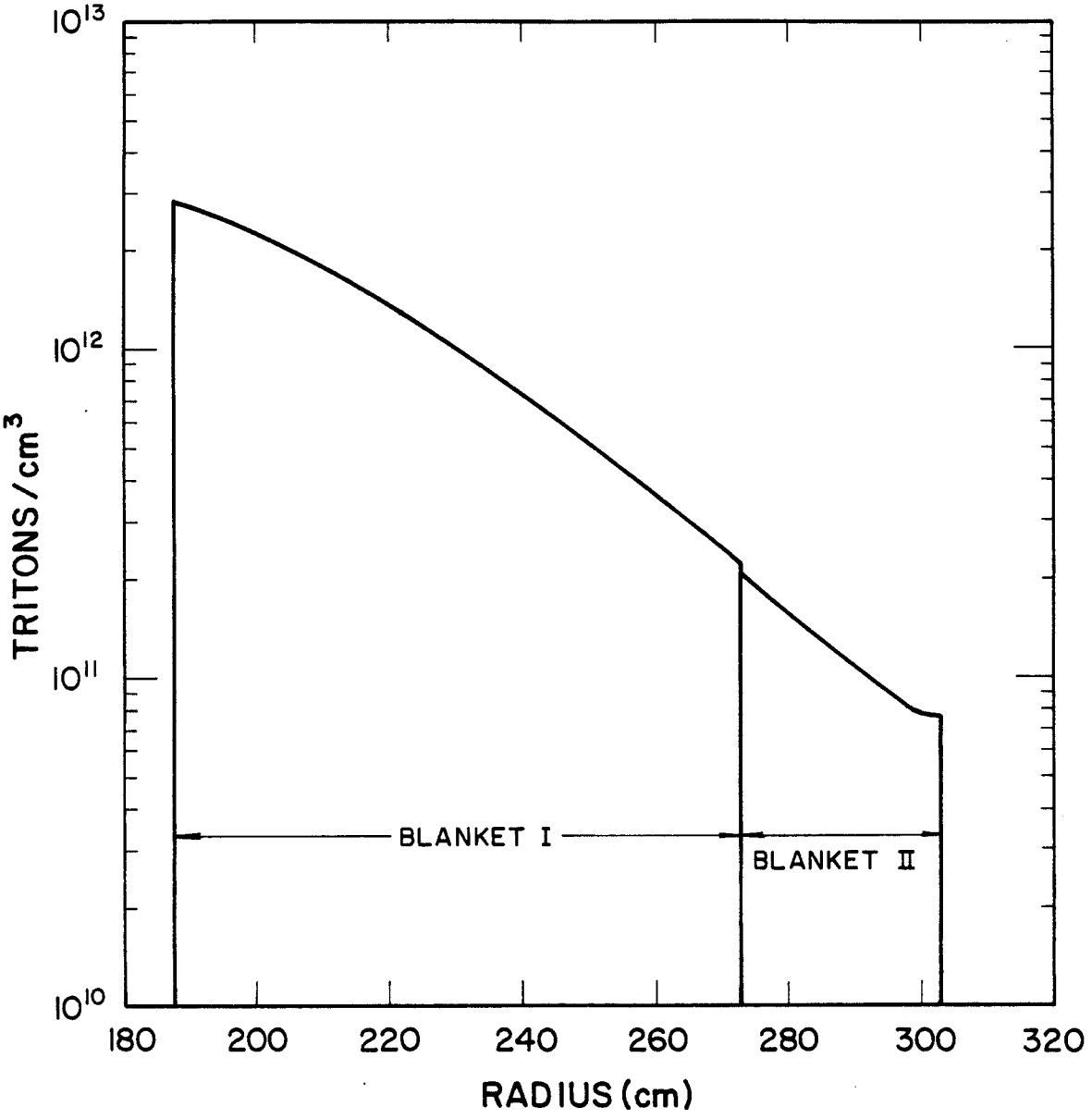

Figure X.3-4 Spatial variation of tritium production in blanket.

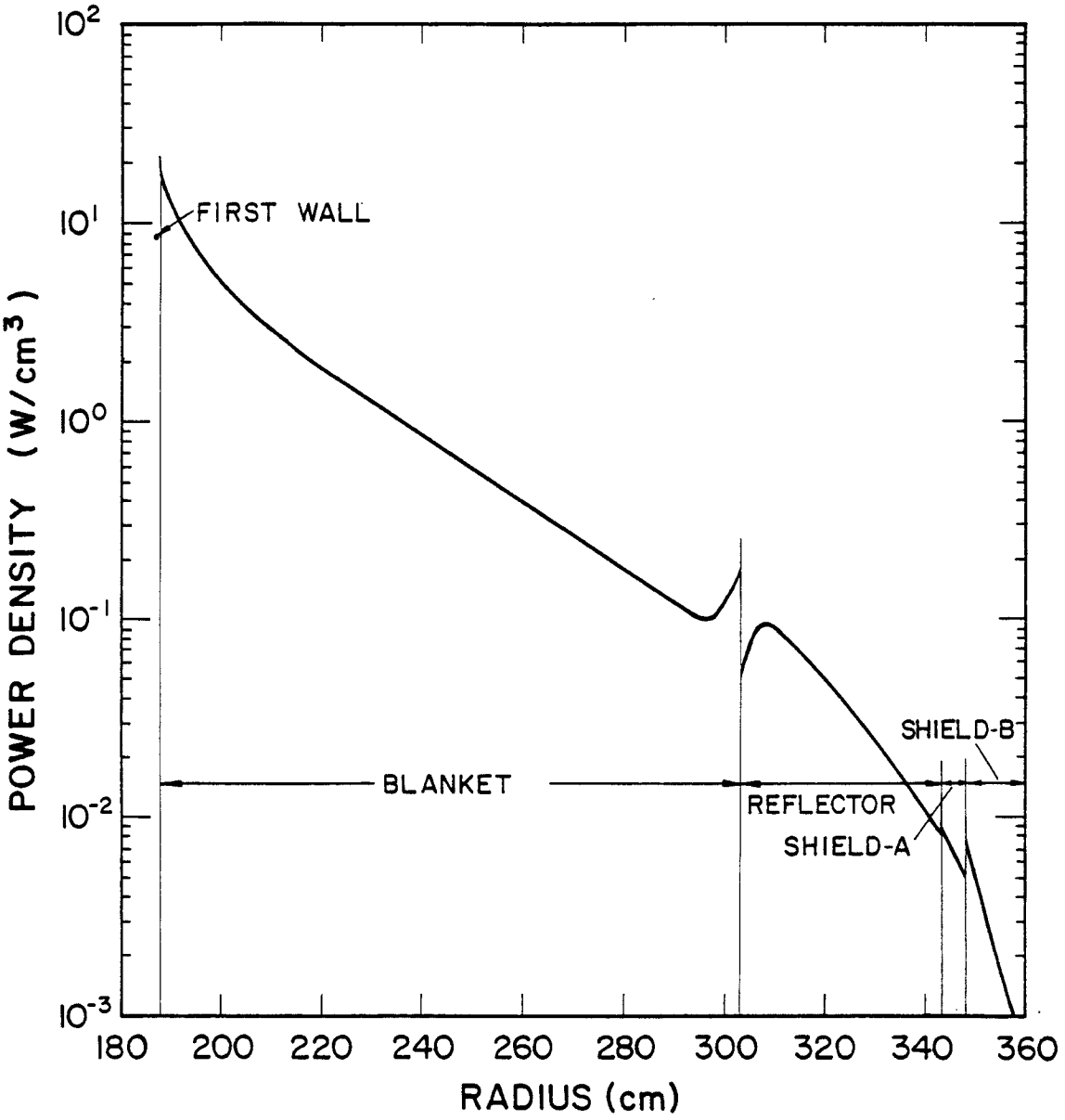

Figure X.3-5 Power density vs. radius in blanket, reflector, and shield.

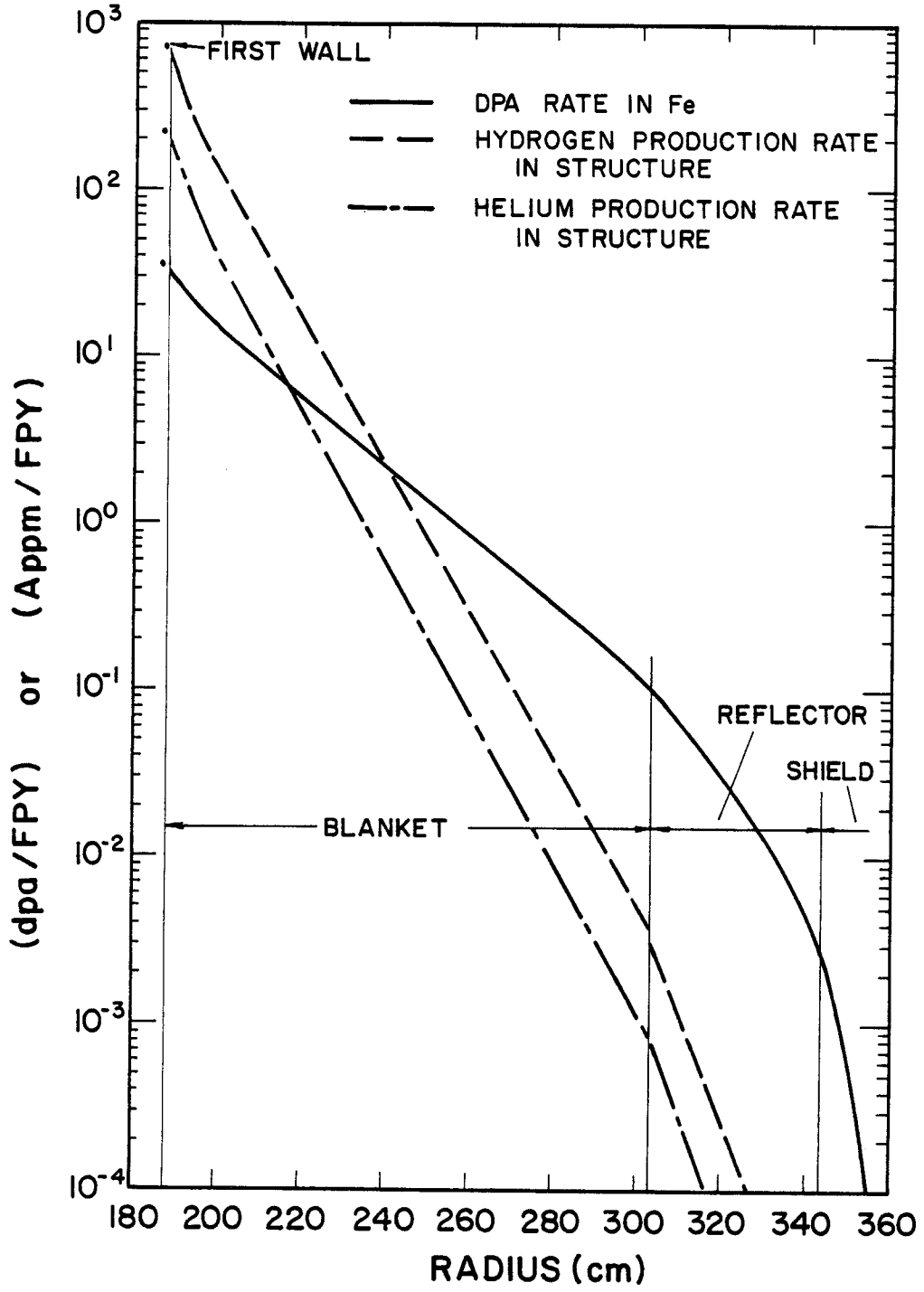

Figure X.3-6 DPA and gas production rates vs. radius in blanket, reflector, and shield.

falls rapidly into the blanket. The radiation damage rates as measured by the displacement per atom (dpa) of iron per full power year (FPY), and the gas production rates in atom parts per million (appm) in the structural material are shown in Fig. X.3-6 as a function of position. It should be noted that the threshold energies for helium and hydrogen production reactions are higher than that for dpa. This results in a faster fall of the gas production rates in the various regions.

X.4. Bulk Shield Optimization

Prior to the final 3-D calculation, several 1-D calculations were carried out to determine the optimum shield composition which provides adequate protection for the superconducting magnets. The magnet radiation limits are set by several criteria: deterioration of thermal and electrical superinsulators such as mylar and epoxy with dose, the cryogenic heat load, and the resistivity increase in the copper stabilizer. Dose limits for mylar and epoxy are taken as 10^{10} and 10^{9} rad, respectively. These insulators must last for the whole reactor lifetime estimated to be 24 FPY (based on 80% availability). The superconducting magnet design requires that the resistivity of the OFHC Cu stabilizer does not exceed 10^{-7} Ωcm. For Cu with a residual resistivity ratio of 107, this corresponds to a maximum allowable displacements per atom of 1.6×10^{-4} dpa (Ref. 5). Once this value of dpa is reached, the magnet must be annealed to ensure proper performance. Room temperature annealing is estimated to remove ~ 80% of the radiation induced resistivity.[6]

The space available for both reflector and shield is 70 cm. Since the reflector thickness was increased to 40 cm to enhance the energy multiplication, only 30 cm is left for the shield. To start the optimization study, a homogenized mixture of 65 v/o Fe 1422, 26 v/o B_4C, 14 v/o Pb, and 5 v/o cool-

ing water was considered for the shield. An attempt was made to heterogenize the shield to efficiently utilize the shielding capability of these materials. The steel layer, which is effective in slowing down the high energy neutrons, is placed in front of the B_4C layer, which moderates the neutrons further and acts as a good absorber for low energy neutrons. A thin layer of lead is placed at the back of the shield mainly to attenuate the generated gamma rays. The arrangement of the various layers for the shield optimization study is shown in Fig. X.4-1.

In the poloidal direction of the reactor, the position of the magnet varies behind the blanket segments. Parts of the magnet that are behind the middle of the segments are overprotected by the relatively thick blanket. The worst radiation effects occur in portions of the magnet behind the 40 cm diameter steam headers, shown in Fig. X.4-2, where only ~ 50 cm of blanket thickness is available in the smallest blanket segment. To assess the peak radiation damage in the magnet, the geometrical configuration at the steam headers was modeled in the 1-D calculations.

The radiation dose in the mylar superinsulator in front of the magnet was found to be the design driver for the shield as other magnet components are further protected by the 25 cm structural case. A series of 1-D neutron and gamma transport calculations were carried out in which the thicknesses of the three shield layers were varied one at a time to determine the optimum shield configuration. In the first set of calculations, the thickness of the lead layer was varied with the thicknesses of shield-A relative to shield-B being kept the same. Since lead is a good gamma absorber, reducing the lead thickness results in an increase in the peak gamma dose in mylar as shown in Fig. X.4-3. The corresponding decrease in neutron dose is mainly due to the in-

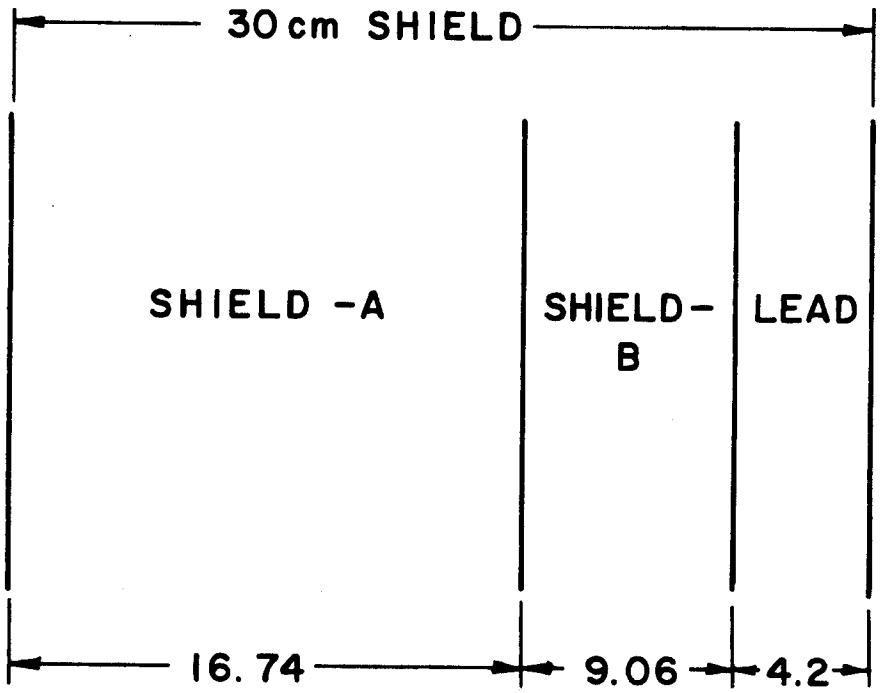

Figure X.4-1 Starting configuration for bulk shield optimization.

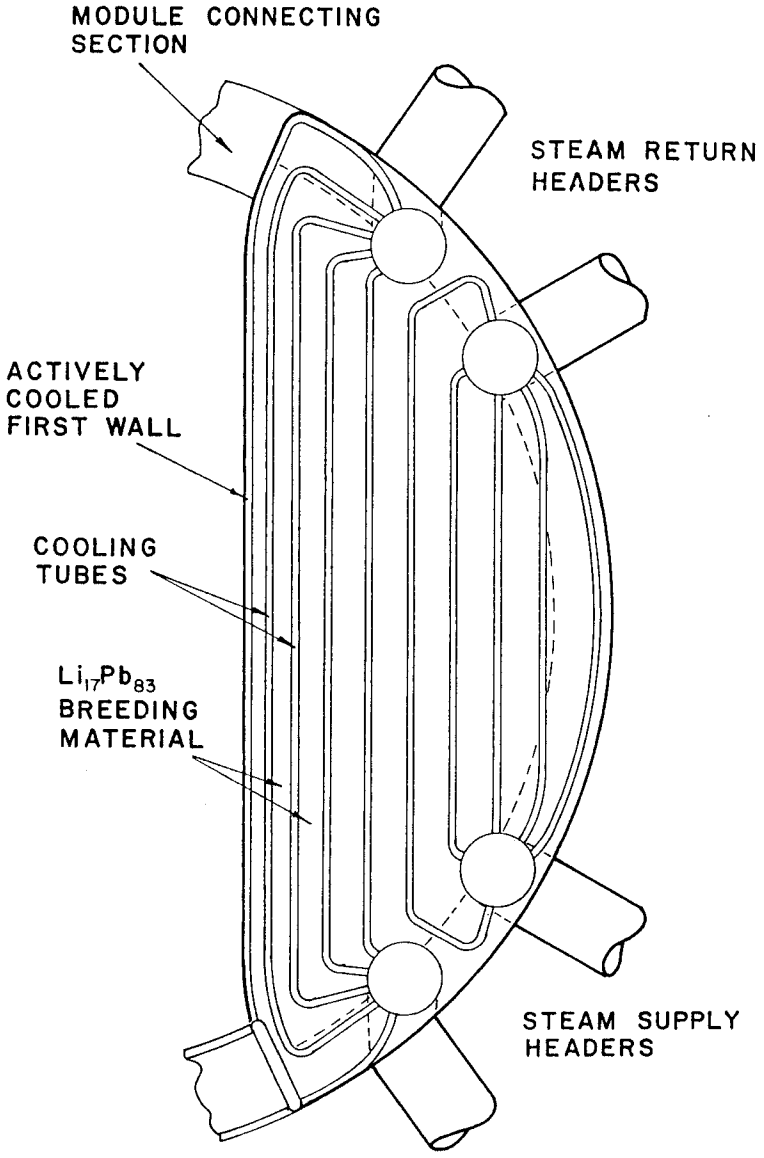

Figure X.4-2 Cross section of the largest blanket segment showing steam headers.

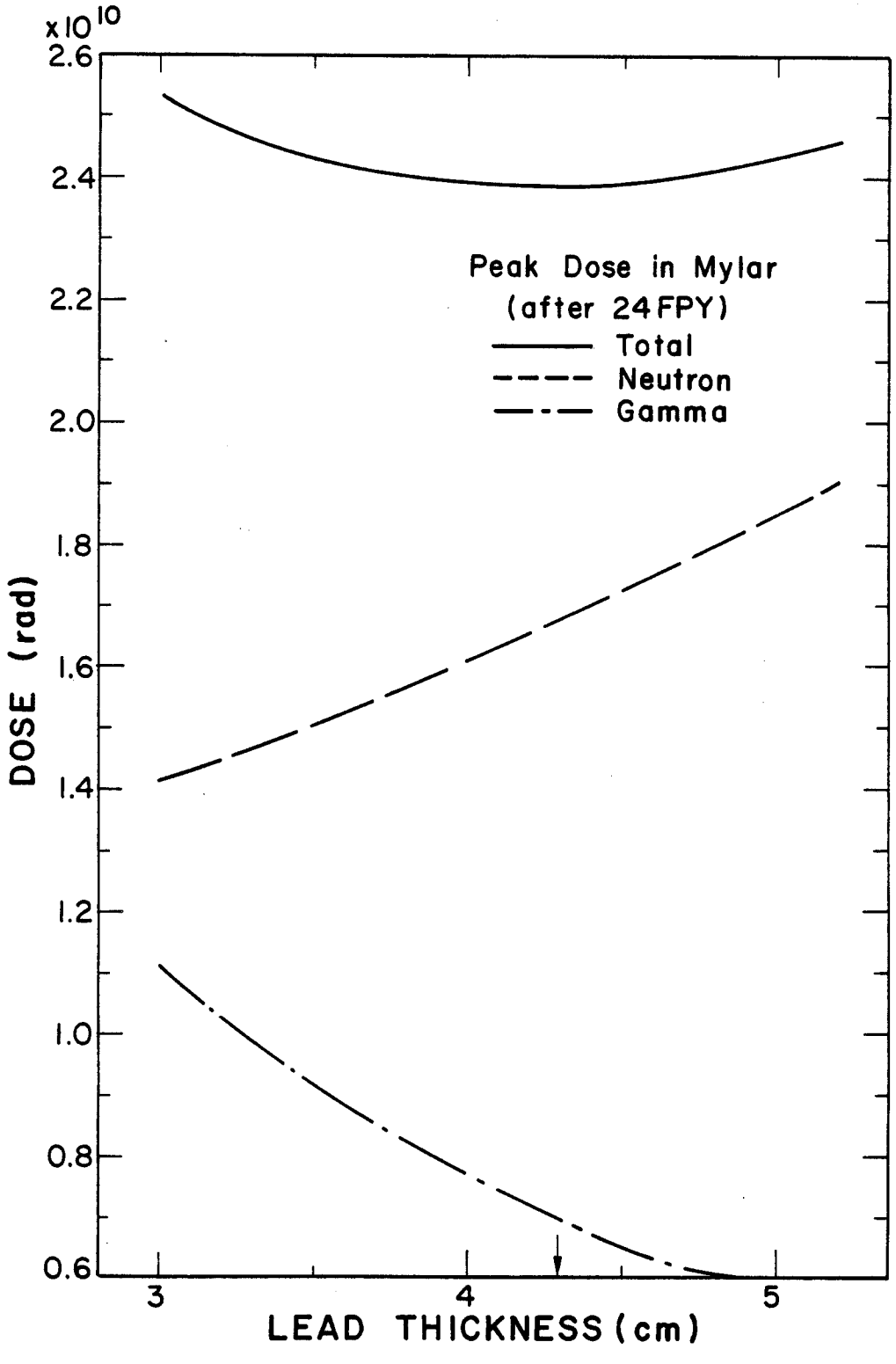

Figure X.4-3 Effect of lead shield thickness on dose in mylar.

creased thicknesses of shields A and B. These results indicate that 4.3 cm of lead is required to minimize the total dose in mylar.

In the second set of calculations, the lead thickness was kept fixed at 4.3 cm, while the B_4C layer was increased under the constraint that the total shield thickness remains 30 cm. Figure X.4-4 reveals that a substantial amount of B_4C is required for radiation attenuation. This is due to the fact that the energy spectrum behind the LiPb blanket and metallic reflector is relatively soft and B_4C is more suitable for attenuating such a spectrum than steel. To satisfy the design criteria for mylar, the thickness of shield-B was set at 20 cm which yields 8.757×10^9 rad in mylar after 24 FPY's, and the optimum shield configuration is shown in Fig. X.4-5. Other data of interest are the peak dpa in Cu stabilizer, the peak power density in the magnet, and the peak dose in epoxy after 24 FPY's. These are 6.476×10^{-6} dpa/FPY, 1.608×10^{-5} W/cm^3, and 4.163×10^8 rad, respectively. The dpa rate implies that magnet annealing is not required during the whole reactor lifetime.

X.5. Radiation Streaming Calculations

Radiation streaming through divertor slots and pumpout ports has large impact on the operation and maintenance of the reactor and its sensitive equipments. The effectiveness of the bulk shield is reduced by the streaming of radiation through the slots. Thus, the divertor region must also be shielded.

Three-dimensional neutronics and photonics calculations were performed using the MCNP code. The calculation procedure was divided into two parts by modeling the geometrical configuration of the reactor in two separate problems. The blanket and shield shown in Fig. X.3-2 is considered as one

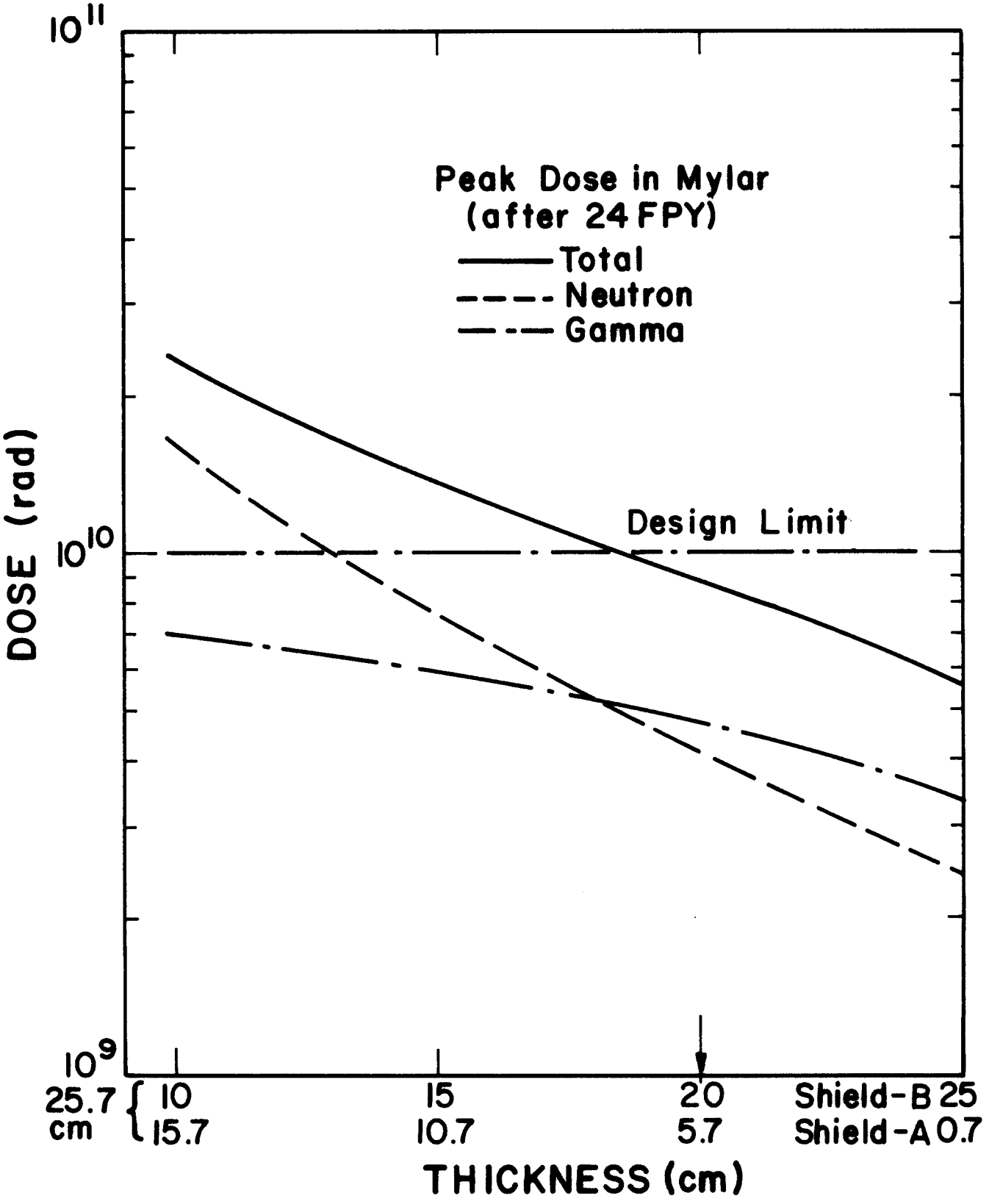

Figure X.4-4 Effect of relative thicknesses of shields-A and B on dose in mylar.

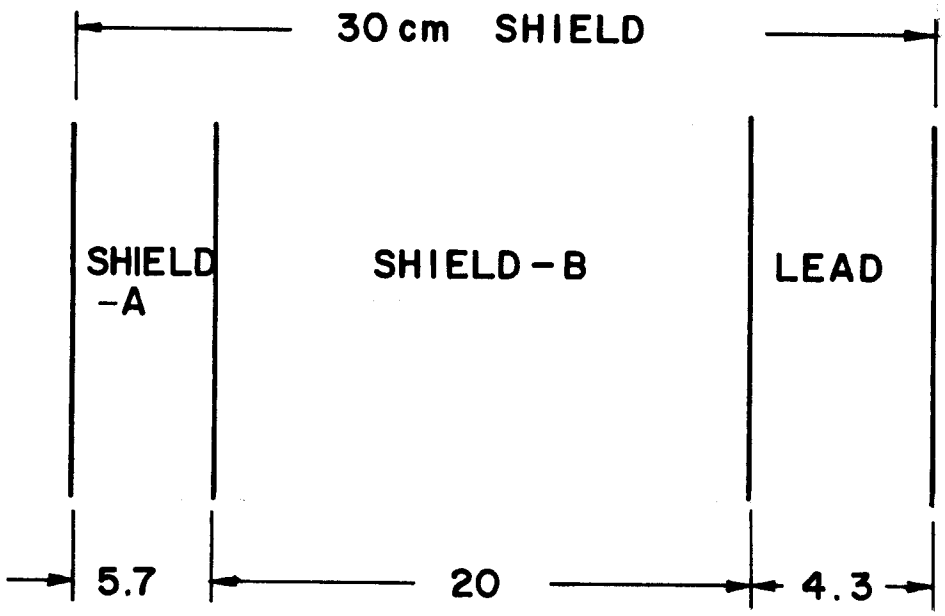

Figure X.4-5 Optimum shield configuration.

problem and the divertor targets and associated shield shown in Fig. X.5-1 is the other.

X.5.1. Radiation Streaming Through Divertor Slots

Trapping surfaces were located at the entrance of the three divertor slots of Fig. X.3-2. At these surfaces all particles entering the divertor regions are counted according to angle and energy bins. This information was then stored to serve as a surface source in later modeling of the divertor region itself. 5,000 histories in a run were sampled isotropically from the spatial variation of the source (shown in Fig. X.2-2) within the triangular plasma zone. The relative standard deviations were less than 6% for the quantities of interest.

The results show that for each D-T fusion event, the total neutrons and gamma photons streaming through the three divertor slots are 0.214 and 0.024, respectively, carrying a total energy of 0.723 MeV. The total power carried by streaming radiation is 176 MW which represents 5% of the neutron fusion power and fortunately most of it is recovered by the divertor targets as will be shown later. Detailed results of particles crossing the different trapping surfaces are given in Table X.5-1 on a per fusion and per second basis along with the energy carried by streaming radiation. Tabulated results show that the streaming radiation differs slightly for each slot depending on the size of the blanket segment surrounding it. Also, 83% of the energy is carried by the primary streaming neutrons.

The neutron and gamma energy spectra and their angular distributions averaged over the three slots are shown in Figs. X.5-2 and X.5-3. The average energies of the streaming neutrons and gamma photons are 3.229 and 1.332 MeV,

Table X.5-1. Radiation Streaming Through Divertor Slots

Slot #	Neutron						Gamma	
	Primary		Secondary		Total		Per Fusion	Per Sec
	Per Fusion	Per Sec	Per Fusion	Per Sec	Per Fusion	Per Sec		
1	1.530E-2	2.326E19	6.084E-2	9.248E19	7.614E-2	1.157E20	8.628E-3	1.312E19
2	1.435E-2	2.181E19	6.297E-2	9.571E19	7.732E-2	1.175E20	8.735E-3	1.328E19
3	1.199E-2	1.823E19	4.819E-2	7.325E19	6.018E-2	9.147E19	6.924E-3	1.052E19
Total into 3 slots	4.164E-2	6.330E19	0.172	2.614E20	0.214	3.247E20	2.429E-2	3.692E19
Streaming Energy Per Slot (MeV/Fusion)	0.192		0.038		0.230		0.011	

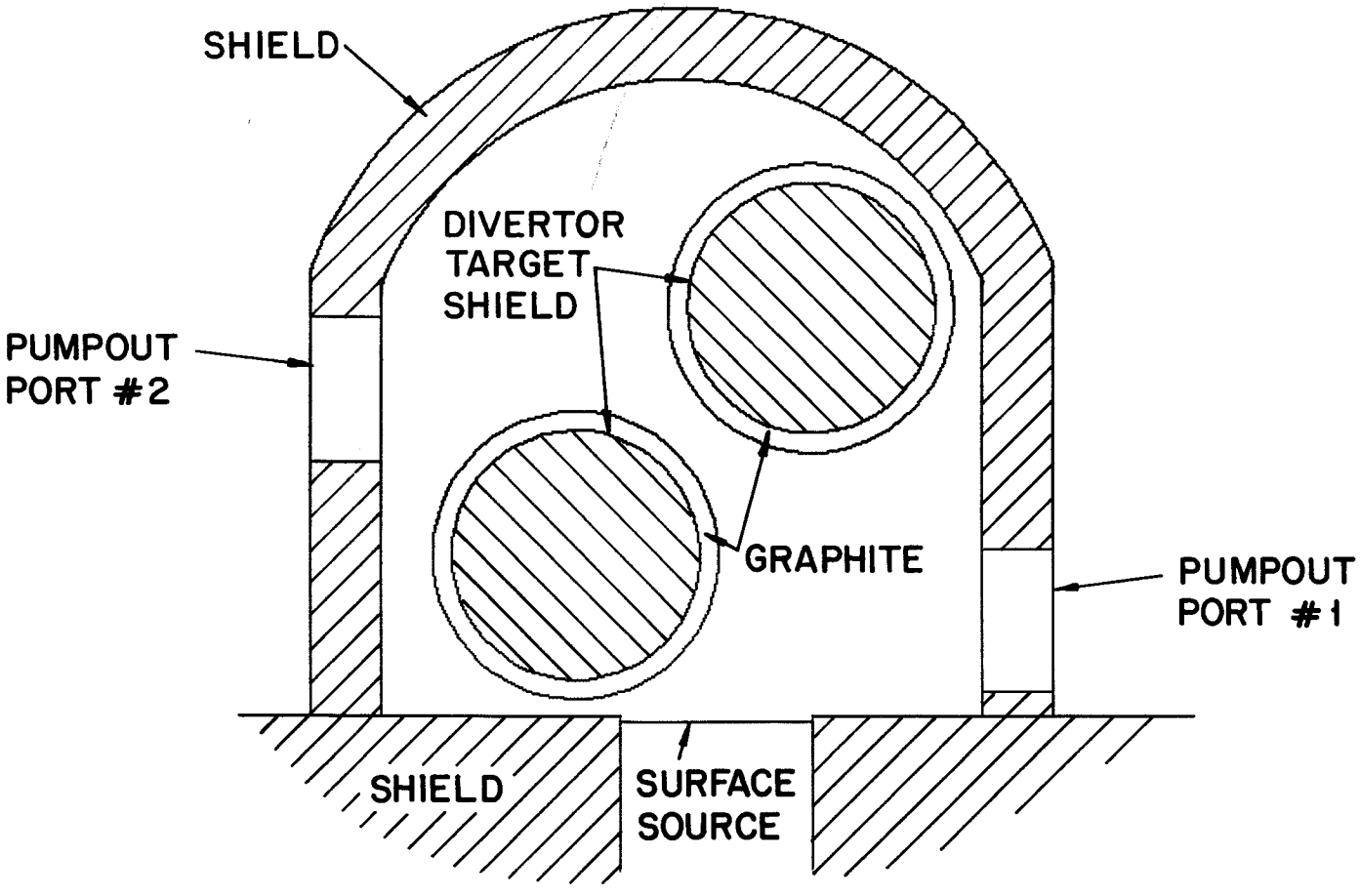

Figure X.5-1 Geometrical model of divertor region.

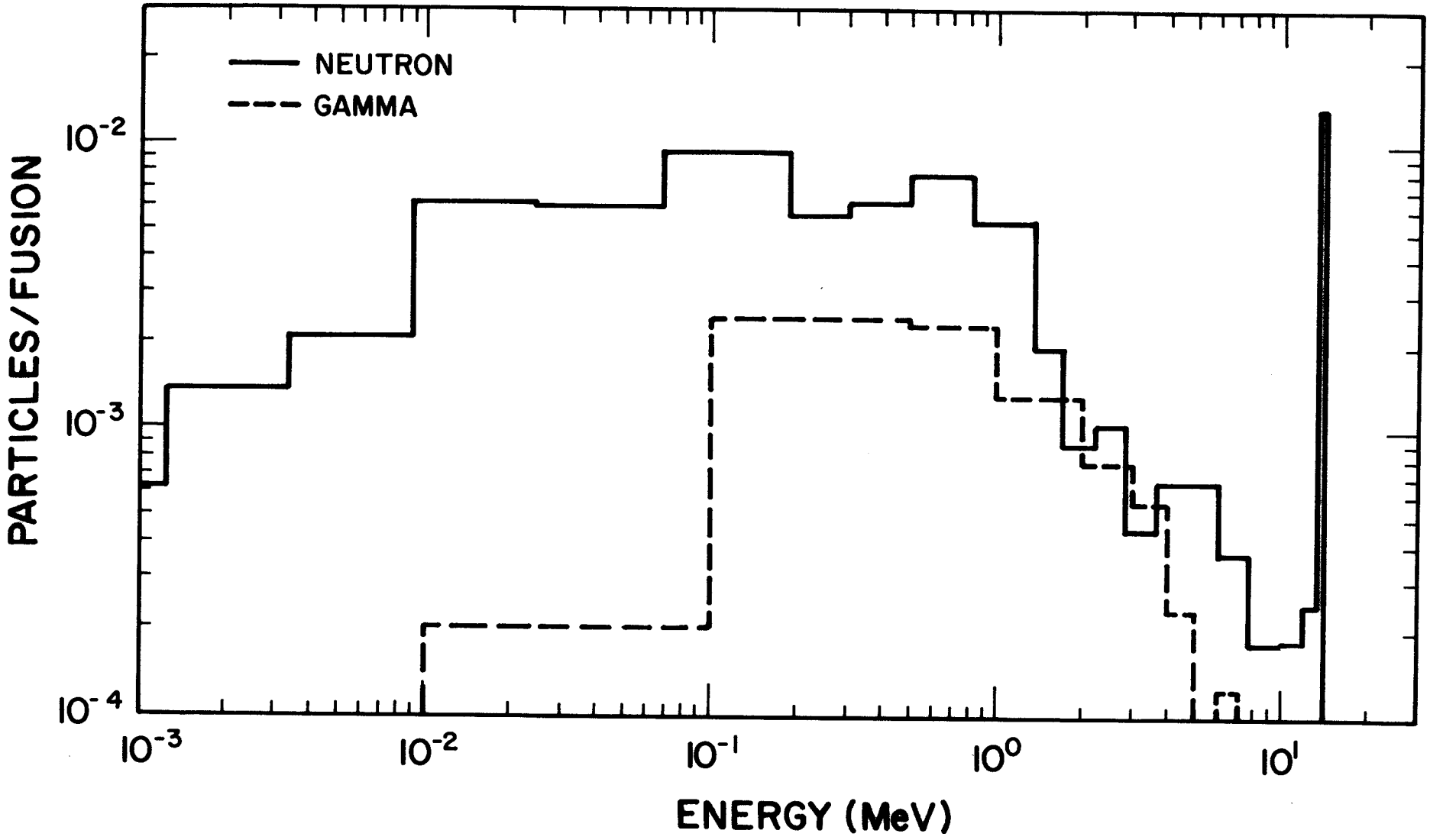

Figure X.5-2 Energy spectra of radiation streaming through divertor slot (averaged over the three slots).

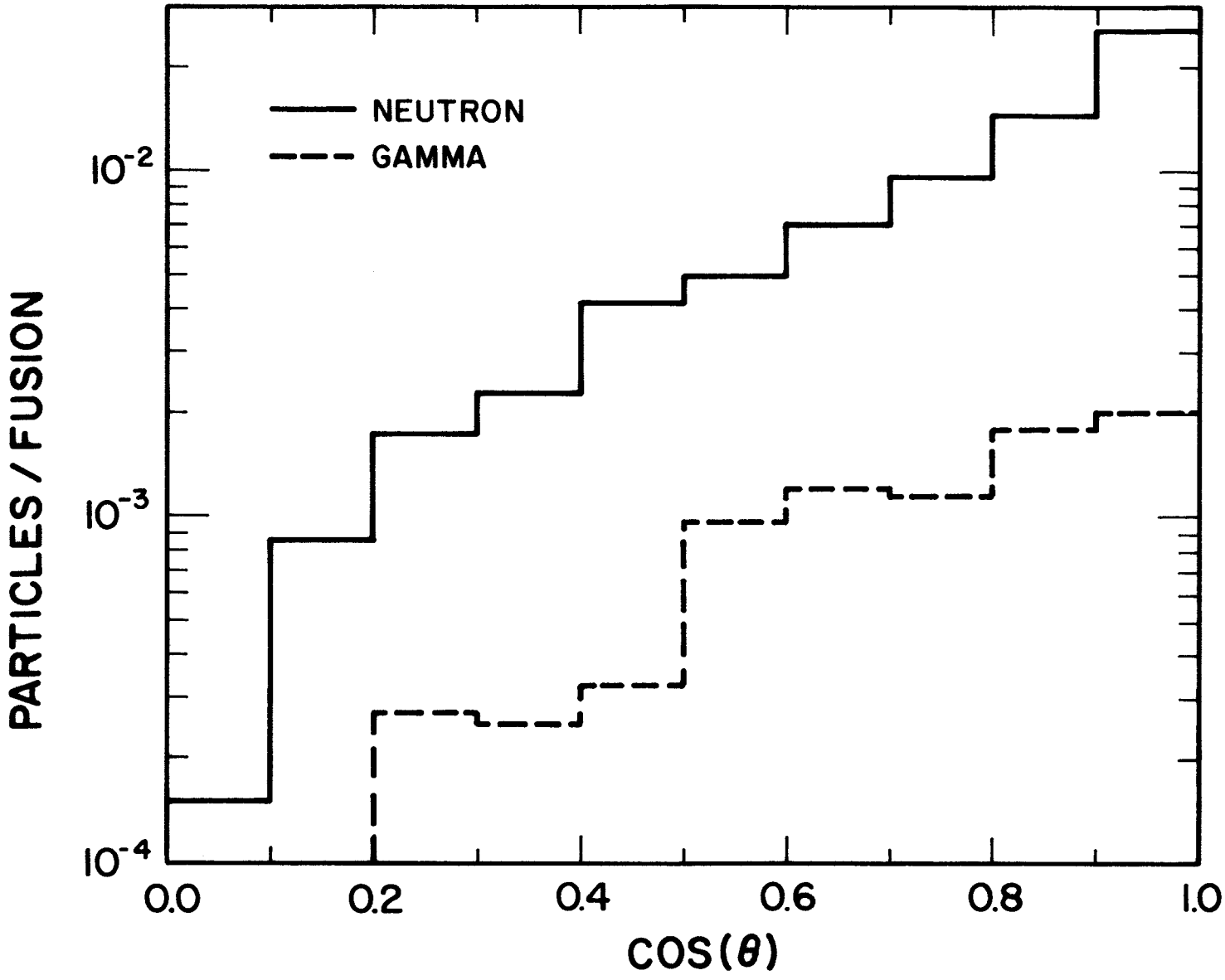

Figure X.5-3 Angular distributions of radiation streaming through divertor slot (averaged over the three slots); θ is measured from the normal to the surface.

respectively. The angular distributions peak at normal incidence and most particles will go into the divertor targets.

X.5.2. Divertor Region Model

A run of 30,000 histories was performed for the divertor region problem employing neutron and gamma surface sources at the entrance of 7.122×10^{-2} and 8.096×10^{-3} particles/fusion, respectively, as obtained from the previous run. The purpose of the calculations was twofold: (a) to obtain information about radiation exiting each pumpout port through the use of trapping surfaces, and (b) to estimate the amount of energy recovered by the divertor targets.

The divertor region was modeled for the Monte Carlo code MCNP and Fig. X.5-1 is an output from its plotting routine. The pair of rotating divertor targets are made of Fe 1422 steel, cooled with 10% steam by volume and covered with several centimeters of graphite. Charged particles striking these targets are neutralized and scattered into zones from which they are pumped out through the ports. The pumpout ports are appreciably off the direct line of sight of the flowing particles from the divertor entrance. This is of importance in reducing radiation streaming through the ports.

The numbers of particles streaming through ports #1 and 2 are given along with the streaming energy in Table X.5-2. Energy spectra of neutrons and gamma photons streaming through the two ports are provided in Figs. X.5-4 and X.5-5. The results indicate that considerable attenuation and spectrum softening result from neutron interactions with divertor targets. The average energies of streaming neutrons through ports #1 and 2 which are 0.913 and 0.362 MeV, respectively, are significantly softer than the corresponding 3.229 MeV of the streaming neutrons at the entrance to the divertor region. The

Table X.5-2. Streaming Radiation Through Pumpout Ports of a Divertor Region

Pumpout	Neutron		Gamma		Neutron Energy	Gamma Energy
Port #	Per Fusion	Per Sec	Per Fusion	Per Sec	MeV/Fusion	MeV/Fusion
1	7.290E-3	1.108E19	1.421E-3	2.160E18	6.653E-3	1.650E-3
2	9.671E-5	1.470E17	3.327E-5	5.057E16	3.496E-5	3.750E-5

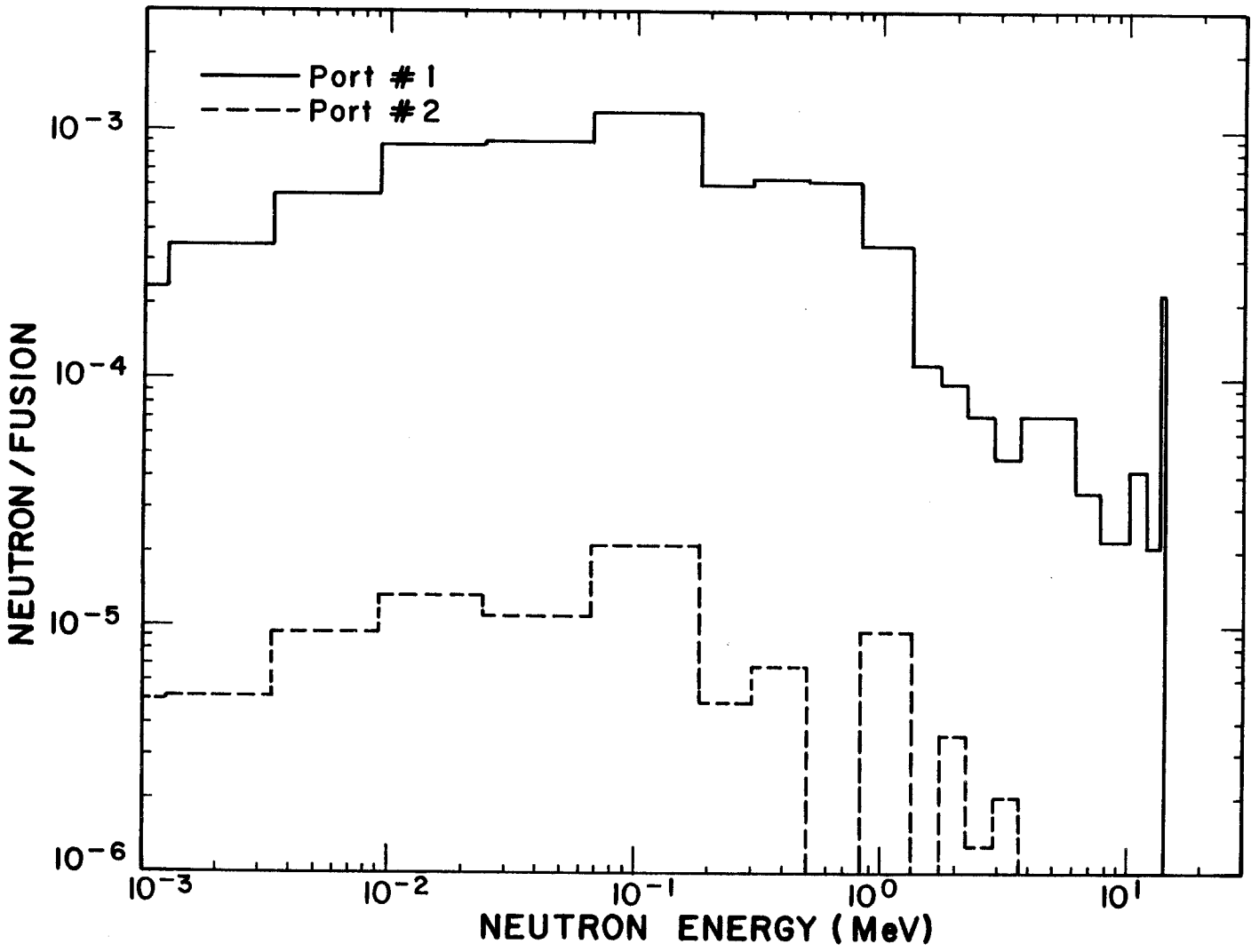

Figure X.5-4 Energy spectra of neutrons streaming through pumpout ports.

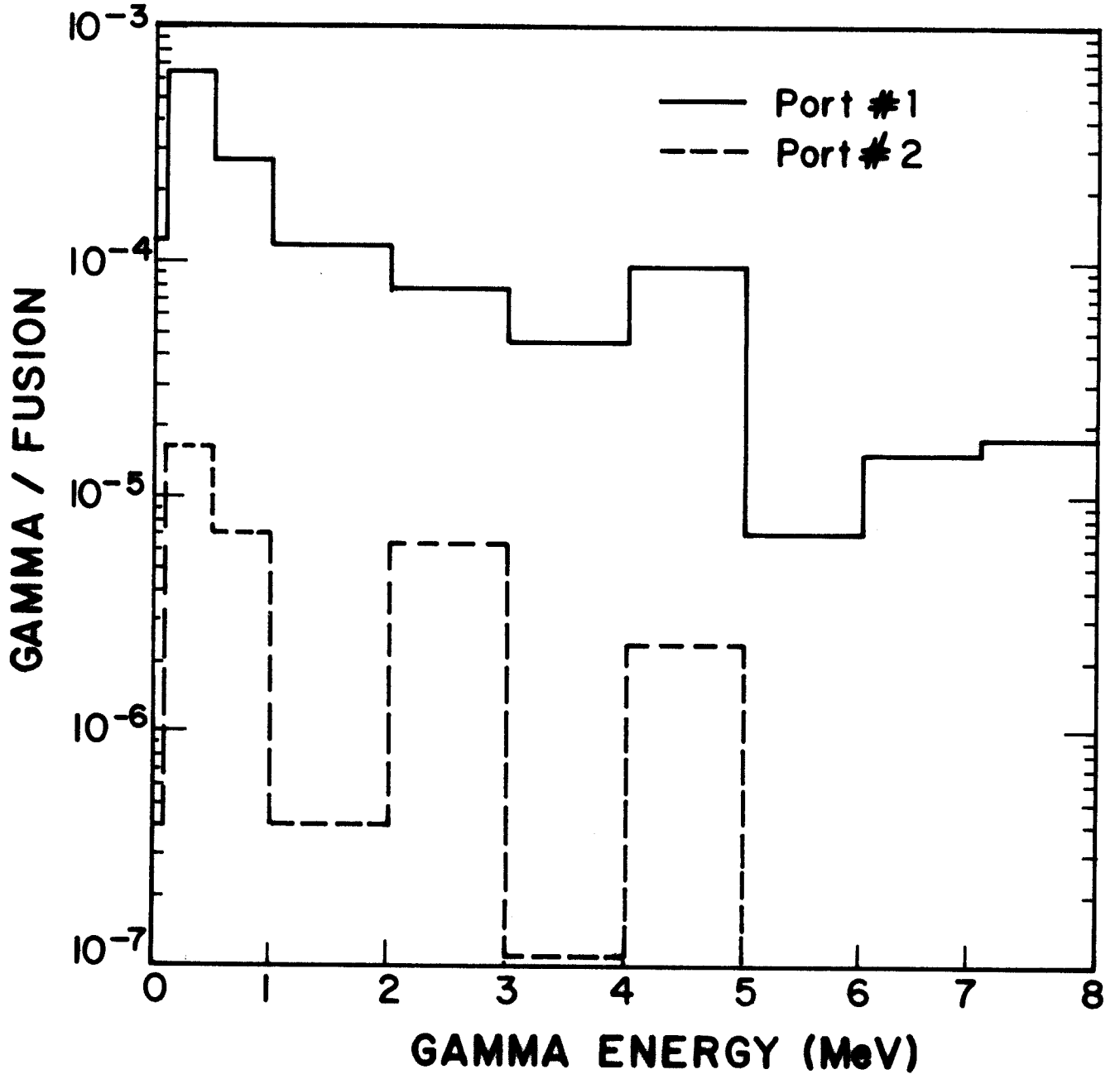

Figure X.5-5 Energy spectra of gammas streaming through pumpout ports.

neutron spectrum at port #1 contains few high energy neutrons, as expected, since the port is not directly in line with the plasma neutrons. Also, most of the neutrons can stream out of the port only through multiple scattering collisions with the divertor targets that degrade their energies considerably. These effects are more pronounced for streaming neutrons through port #2. About 80% of the streaming gamma rays are from those generated in the divertor targets resulting from parasitic neutron absorption in the steel. Their average energies are slightly smaller than those of gamma photons entering the divertor region.

The total power carried by radiation streaming through all ports of the three divertor regions is 6.12 MW representing only 0.178% of the neutron fusion power. Most of the particles entering the divertor region deposit their energy in the divertor targets as evidenced by the fact that the nuclear heating per each pair of targets is 0.218 MeV/fusion of which 81% is gamma heating. This corresponds to 91% of the energy carried by radiation streaming into the divertor region from the reaction chamber.

X.6. Biological Shielding

The bulk shield is mainly used to reduce the radiation damage and heat loads in the superconducting magnets and associated components. A biological shield usually made of concrete surrounds the toroidal reactor to reduce the biological dose to levels below the allowable 2.5 mrem/h during reactor operation.

Due to the necessity of penetrations in the shield, radiation streaming raises the dose levels. Comparison between the radiation current outside the bulk shield and that at the pumpout port #1 shows that the latter is at least factors of 50 and 100 higher for neutrons and gamma rays, respectively. On

this basis, the information obtained from the divertor model described in the previous section was used to define a plane source for the subsequent 1-D calculations to estimate the required concrete shield thickness.

The peak biological dose rate occurs at parts outside the inboard concrete shield closest to the divertor region. A 3.1 m thick biological shield was found to result in an acceptable dose of 2.35 mrem/h in the toroidal service hall during reactor operation.

X.7. Conclusion

The effects of radiation streaming through the divertor slots and pumpout ports have been evaluated using the 3-D Monte Carlo code MCNP. Although 21% of the source neutrons stream through the divertor slots, a tritium breeding ratio of 1.08 and energy multiplication of 1.153 were achieved using 35% enriched lithium in the $Li_{17}Pb_{83}$ breeder. The blanket and reflector were optimized to enhance the energy multiplication. The bulk shield composition was optimized to reduce the radiation damage and heat loads in the superconducting magnets. This results in an acceptable dose in mylar and epoxy insulators after the estimated 24 FPY's reactor lifetime. In addition, no magnet annealing is required during the reactor lifetime.

Only 20% of the radiation streaming through the divertor slots is primary neutrons and they carry 83% of the streaming energy. Considerable attenuation and spectrum softening result from neutron interactions with divertor targets which, as a result, recover 91% of the energy streaming into the divertor regions. A 3.1 m thick concrete shield is required to maintain an acceptable biological dose during operation in the toroidal service hall.

References for Chapter X

1. D.K. Sze et al., "LiPb, A Novel Material for Fusion Applications," Proc. Fourth ANS Topical Meeting on the Technology of Controlled Nuclear Fusion, King of Prussia, PA, 14-17 Oct. 1980.

2. E.T. Cheng, "The Reflector-Shield Concept for Fusion Reactor Designs," Trans. Am. Nucl. Soc. 34, 49 (1980).

3. Los Alamos Monte Carlo Group X-6, "MCNP - A General Monte Carlo Code for Neutron and Photon Transport, Version 2C," LA-7396-M, Revised (April 1981).

4. R.D. O'Dell et al., "User's Manual for ONEDANT: A Code Package for One-Dimensional, Diffusion-Accelerated, Neutral-Particle Transport," Los Alamos National Laboratory Report (to be issued).

5. M. Sawan, "Radiation Limits in Copper Stabilizer of Superconducting Magnets," MARS Project Memo, WIS-MARS-82-029, June 1982.

6. B. Brown et al., "Low Temperature Fast Neutron Radiation Damage Studies in Superconducing Materials," J. Nucl. Mat. 52, 215 (1974).

XI. Materials

XI.1 Introduction

There are 5 main classes of materials in the UWTOR-M reactor that must be considered with respect to radiation damage from neutrons:

1. Blanket Structure (HT-9)
2. Reflector Structure (Fe 1422)
3. Shield (Fe 1422, Pb, B_4C)
4. Divertor Drum Liner (C)
5. Superconducting Magnet Materials (Cu, NbTi, Polyimide)

We will first describe the environment in which these materials must operate and this will be followed by the anticipated response of these materials to neutron damage. Surface effects for the divertor drums are given in Chapter VIII.

Some non-nuclear materials aspects of UWTOR-M will be addressed in the latter part of this chapter. Corrosion of HT-9 in Pb-Li alloys will be discussed and an inventory of materials required for UWTOR-M operation will be included.

XI.2 Neutron Environment

XI.2.1 Displacement Damage

XI.2.1.1 Steel Structure

The overall descriptions and neutronic analysis of the blanket and shield regions are given in Chapter IX. We repeat here the schematic representation of the blanket region (Fig. XI.2-1) and identify the critical locations for damage considerations. It can be seen from Fig. XI.2-1 that there are four main points to be concerned about for the various blanket-reflector-shield configurations. Point A represents the region where the highest neutron wall

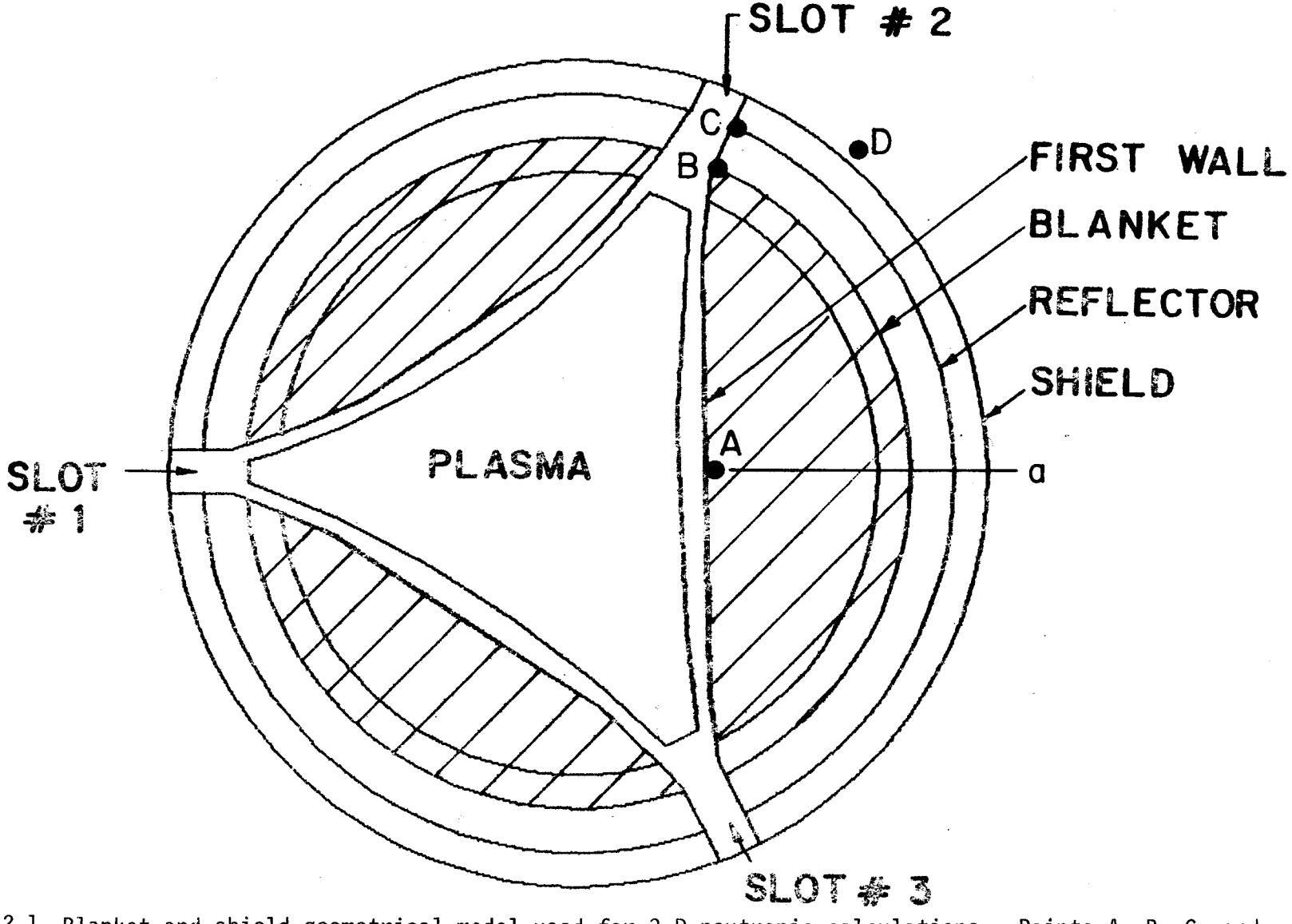

Fig. XI.2-1 Blanket and shield geometrical model used for 3-D neutronic calculations. Points A, B, C, and D represent the maximum neutron damage position for the blanket, reflector shield and S/C magnet respectively.

loading will occur in the first wall. Point B is the point at which the maximum displacement damage occurs down the divertor slot. Note that this region is more vulnerable than that immediately behind the blanket region. Similarly, point C represents the maximum damage level in the shield region. Finally, point D is the position of maximum neutron damage to the Cu stabilizer and NbTi superconductor.

More quantitative numbers can be obtained for Point A from a 1-D calculation of the displacement damage as one proceeds midway through the blanket, reflector and shield region (line Aa). Figure XI.2-2 gives the radial damage profile and there are three important conclusions that can be drawn:

i) The maximum dpa rate in the first wall is 53 dpa/FPY. (This corresponds to ~ 5 MW-y/m^2 of displacement damage per FPY.)

ii) The damage rate quickly falls to 0.02 dpa/FPY at the front of the Blanket II region, and to 0.004 dpa/FPY at the beginning of the reflector region.

iii) The maximum damage rate in the shield is 10^{-4} dpa/FPY.

However, the maximum damage values in the reflector and shield regions along the divertor slots are 17.3 dpa/FPY (position B) and 0.44 dpa/FPY (position C). These lower damage rates in the reflector and shield (as compared to the first wall) are still very high considering the much lower temperatures in these regions.

XI.2.1.2 Graphite in Divertor Drum

The neutrons which stream down the divertor slots can do substantial damage to the graphite on the divertor drum. (The surface effects and erosion of the graphite are covered in Chapter VIII.) Three-dimensional calculations reveal that the damage in the drums varies between the left drum (see Fig.

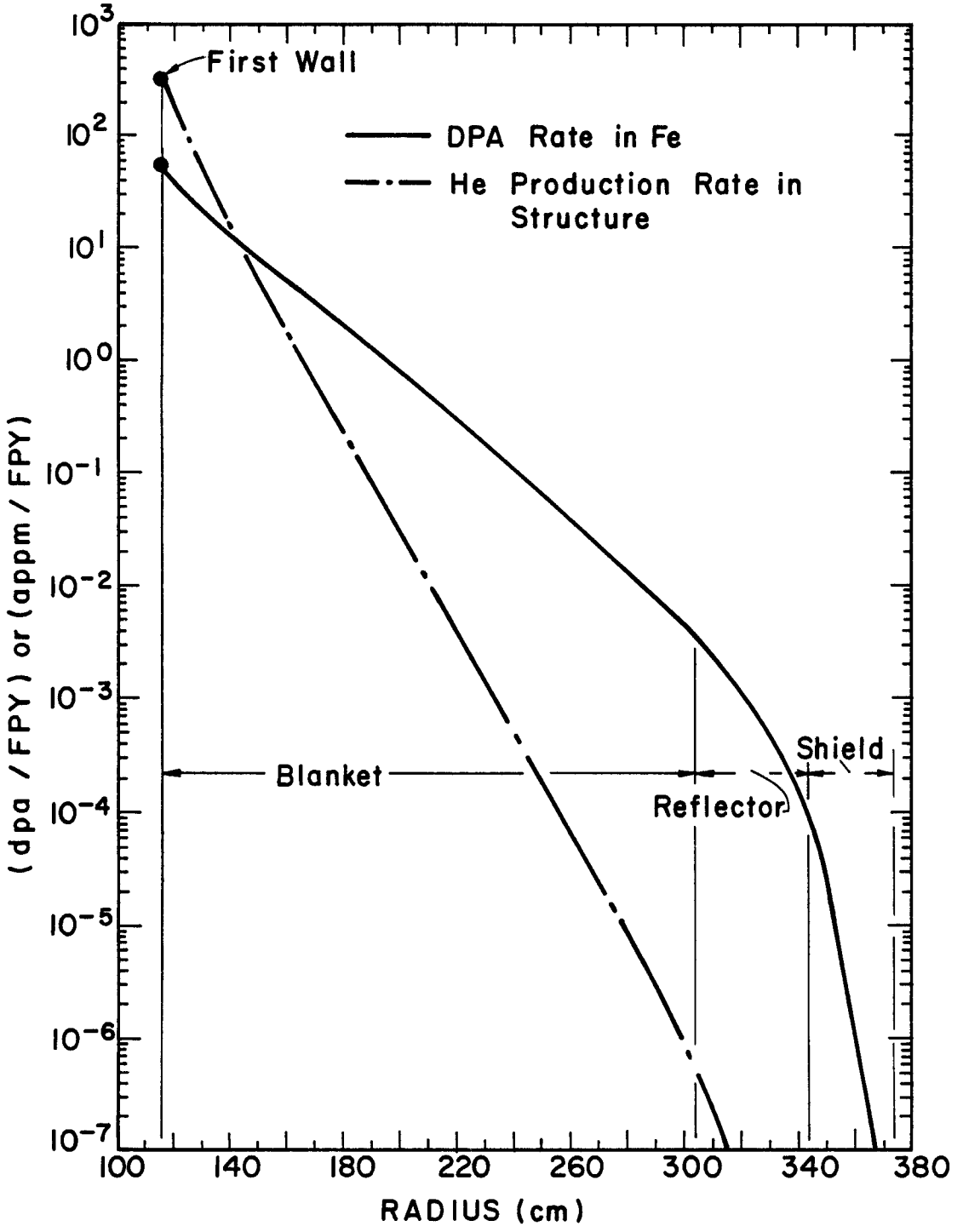

Fig. XI.2-2

Radiation damage in steel components along line Aa in Fig. XI.2-1.

X.5-1) and the right drum. It was found that, accounting for the rotation of the drums, the maximum damage rate in the left drum is 1.4 dpa/FPY and in the right drum it is 2.1 dpa/FPY.

XI.2.1.3 Copper Stabilizer Material

The displacement damage rate in the stabilizer and superconductor immediately behind the shield at point D has also been calculated. We find that the maximum damage rate is 6.5×10^{-6} dpa/FPY in the Cu (and approximately the same in the NbTi). The peak dose to the epoxy insluators from both gammas and neutrons is $\sim 8 \times 10^{6}$ Rads/FPY.

XI.2.1.4 Summary

We have shown in Fig. XI.2-3 the damage-temperature relationship for the materials of interest in UWTOR-M. The damage rate is normalized to 1 FPY and one can get a feeling for the total damage by multiplying the numbers in Fig. XI.2-3 by 24 FPY's.

XI.2.2 Gas Production Rates

XI.2.2.1 Structural Steels

Since the most important gas production rates apply to helium, we will only quote those values in this chapter. The reason that helium production is so important has to do with the embrittlement of metals and alloys at high temperatures (i.e., greater than 0.4 of the absolute melting point) when the concentration exceeds a few ppm. Therefore the helium production is of most importance in the blanket regions and perhaps parts of the reflector.

Figure XI.2-2 shows how the gas production varies along the line Aa in Fig. XI.2-1. The peak helium production rate is 341 appm/FPY and this drops to $\sim 10^{-6}$ appm/FPY at the beginning of the reflector. The maximum helium

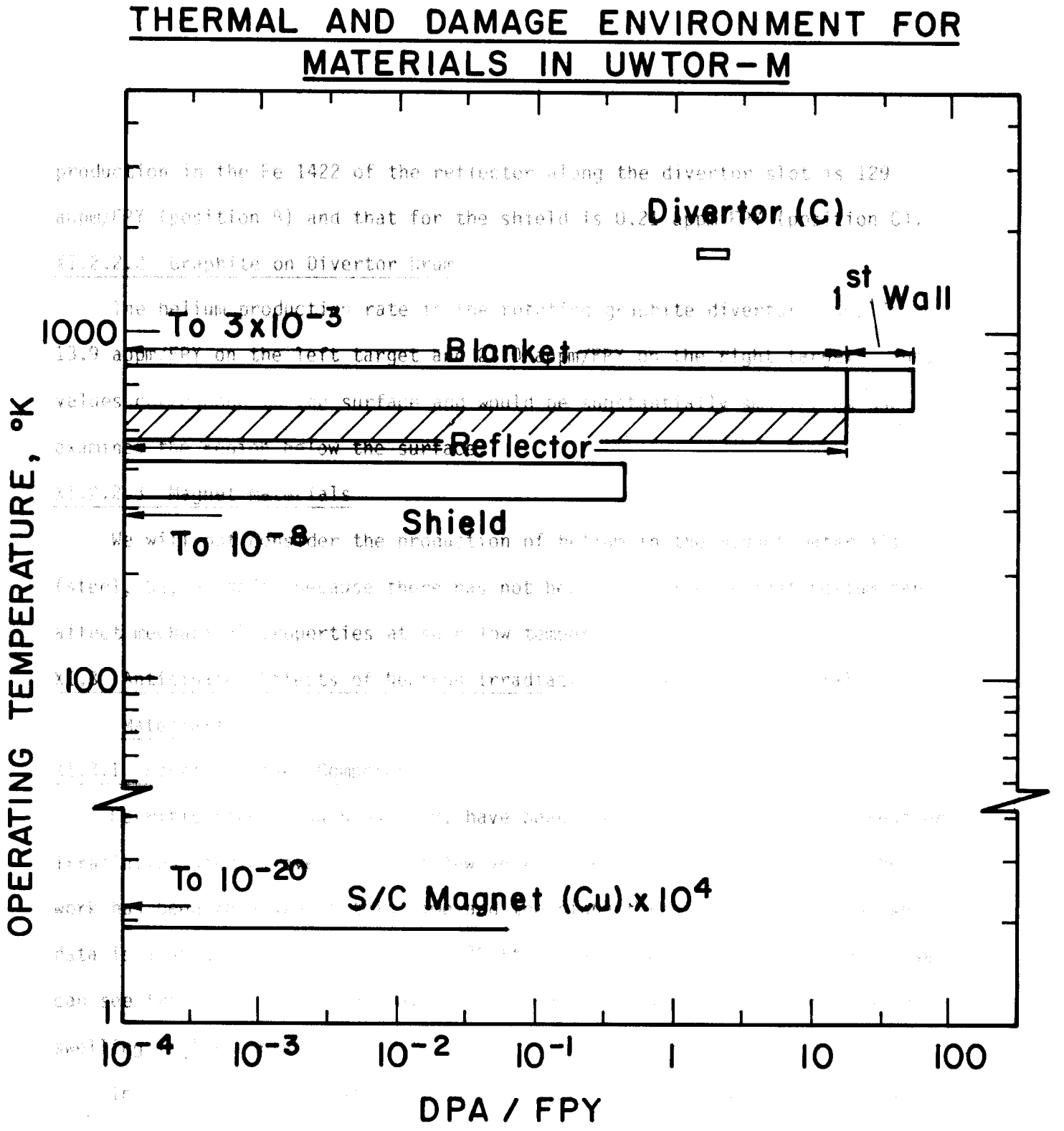
THERMAL AND DAMAGE ENVIRONMENT FOR MATERIALS IN UWTOR-M
Divertor (C)
1st Wall
1000
To 3x10-3
Blanket
Reflector
Shield
To 10-8
100
To 10-20
S/C Magnet (Cu) x 10^4
OPERATING TEMPERATURE, °K
1
10-4
10-3
10-2
10-1
1
10
100
DPA / FPY

Figure XI.2-3.

production in the Fe 1422 of the reflector along the divertor slot is 129 appm/FPY (position B) and that for the shield is 0.21 appm/FPY (position C).

XI.2.2.2 Graphite on Divertor Drum

The helium production rate in the rotating graphite divertor drums is 13.9 appm/FPY on the left target and 23.0 appm/FPY on the right target. These values correspond to the surface and would be substantially smaller as one examines the region below the surface.

XI.2.2.3 Magnet Materials

We will not consider the production of helium in the magnet materials (steel, Cu, or NbTi) because there has not been any evidence that helium can affect mechanical properties at such low temperatures.

XI.3 Anticipated Effects of Neutron Irradiation on UWTOR-M Structural Materials

XI.3.1 Ferritic Steel Components

Ferritic steels, such as HT-9, have been the subject of extensive neutron irradiation studies over the past few years. Unfortunately not all of the work has been released at this time and the highest neutron exposure for which data is available is ~ 75 dpa at 500°C (this corresponds to ~ 6 MW-y/m^2). We can see from Fig. XI.3-1 that even at this damage level the neutron induced swelling is less than 1%.

In order to extrapolate this data to higher exposures we need to know whether or not we have passed the incubation stage for the nucleation of voids in HT-9. Once the incubation stage is passed in austenitic steels, scientists at HEDL (F. Garner et al.[1]) have shown that the austenitic steels swell at the rate of ~ 10% per MW-y/m^2. In contrast to that high swelling rate, ion bombardment experiments on ferritic steels show that the swelling rate, after

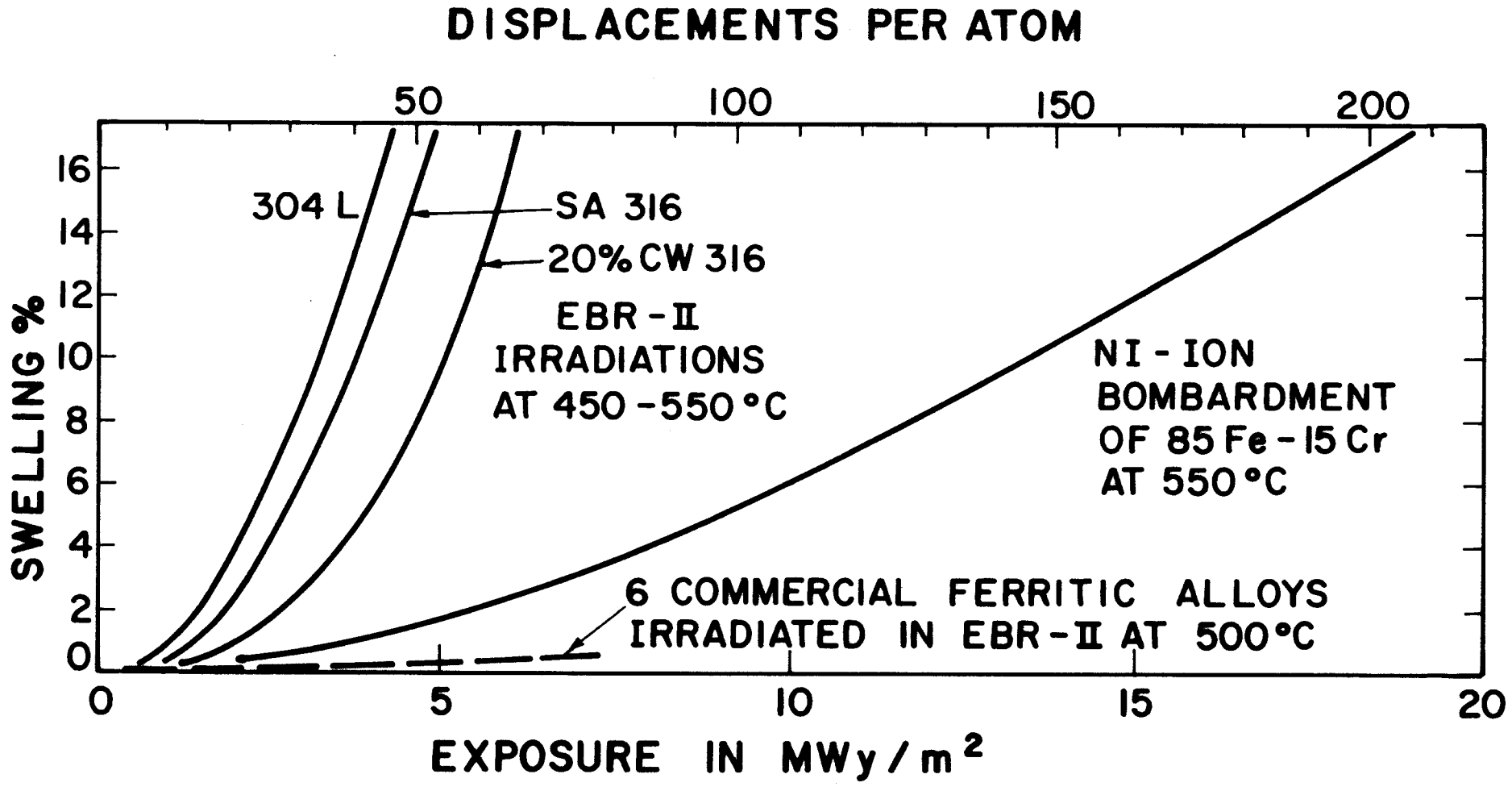

Fig. XI.3-1

Comparison of swelling in stainless steels after high damage exposures.[1]

the incubation period, is ~ 1% per MW-y/m^2 at 550°C. If this is also true of the neutron irradiated material at 500°C, then we would not anticipate a 5% swelling value until ~ 10 MW-y/m^2. Until further data is released we will use that as a design limit for the first wall materials.

The second area of concern for UWTOR-M is the increase in the ductile to brittle transition temperature (DBTT) of the HT-9. While it is difficult to obtain clear data on this property (because of the lower limit of irradiation temperature in most fast fission test reactors) Ghoniem[2] has tried to predict this DBTT shift with the following expression:

$$\Delta DBTT = \frac{1.87 \times 10^4}{T - 238} \{1 - \exp[-(\frac{4T - 350}{T}) (dpa)^{1/2}]\}$$

where: T = irradiation temperature in °C,

ΔDBTT = shift in °C.

This equation predicts the following DBTT shift at points A and B in Fig. XI.2-1 (assume that the initial DBTT ≅ 0°C):

	A	B
Operating Temperature, °C	450	330
ΔDBTT, °C - 0.1 MW-y/m^2	85	193
- 1 MW-y/m^2	88	203
- 10 MW-y/m^2	88	203

We can see from the data above that:

a) The shift in the DBTT is less at the higher temperature (Point A) than at the lower temperature (Point B).

b) The absolute shift of ~ 200°C is still below the melting temperature of 254°C for $Pb_{83}Li_{17}$.

The third area of concern is the creep-rupture life of the HT-9 blanket structure. Again, Ghoniem[2] has proposed the following design equation for HT-9,

$$t_R = \frac{\exp[K(T) \cdot M(T)]}{\sigma[M(T)]}$$

where: $K(T) = A_1 + A_2T + A_3T^2$

$M(T) = B_1 + B_2/T + B_3/T^2$

$T = °K$

$A_1 = 4.35$

$A_2 = A_3 = 0$

$B_1 = -367.277$

$B_2 = 5.573 \times 10^5$

$B_3 = -2.024 \times 10^8$

σ = ksi = 15 x design stress

t_R = hours.

The maximum allowable design stress for 3 full power years (2.6×10^4 hr) at 550°C is 15 ksi (~ 104 MPa). In fact, if the design stress was below 11.3 ksi (~ 80 MPa) the stress rupture life would exceed 30 years at the maximum UWTOR-M temperature. Since the maximum thermal and load stresses are less than ~ 5 ksi, we conclude that the stress rupture life is not a limiting feature of the UWTOR-M blanket.

Fig. XI.3-2

Incubation parameter vs. temperature for Core 1 steel using a three parameter model (R and α constant).[3]

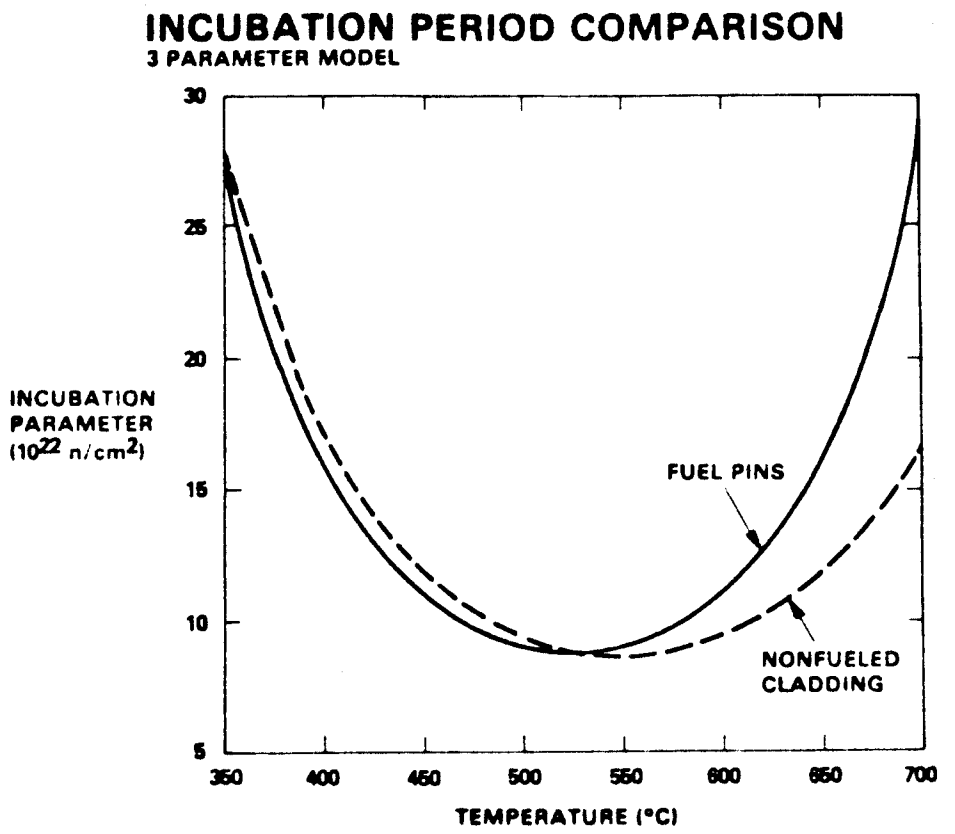

XI.3.2 Radiation Damage in the Austenitic Reflector Material

The area of most concern here is the swelling of the Fe-1422 at point B in Fig. XI.2-1. The damage level at this point is 17.3 dpa/FPY and the maximum temperature is ~ 300°C. The damage rate is severe but the operating temperature may be low enough to suppress the nucleation and growth of voids. Since there is no specific irradiation data on Fe-1422, we can only infer the level of swelling for this alloy from other austenitic systems. Makenas et al.[3] have studied the incubation dose as a function of irradiation temperature. They show (Fig. XI.3-2) that at 350°C the incubation dose is greater than 25 x 10^{22} ncm^{-2} (~ 125 dpa). At 300°C the incubation dose may be even greater than 200 dpa which indicates that we could achieve ~ 10 FPY of irradiation before the swelling might begin in position B at 300°C. The swelling could be suppressed even more if we lowered the temperature another 25 to 50°C. Therefore we feel it is reasonable to expect ~ 20 FPY of operation before serious swelling would require replacement of the reflector.

References for Section XI.3

1. F. Garner, HEDL, to be published.
2. N. Ghoniem, UCLA, to be published.
3. B.J. Makenas, J.F. Bates, and J.W. Jost, p. 17 in Effects of Radiation on Materials, Special Tech. Publ., 782, ASTM, Philadelphia, 1982.

XI.4 Corrosion of HT-9 by Pb-Li Alloys

There is a scarcity of corrosion data concerning $Li_{17}Pb_{83}$ and structural materials like HT-9. The only available data is for a static system,[1] as

shown in Fig. XI.4-1. Two conclusions can be drawn from the experimental results.

1. The static corrosion rate of HT-9 by $Li_{17}Pb_{83}$ is one order of magnitude less than the allowable corrosion limit set by J. DeVan.[2]
2. The static corrosion rate is only weakly dependent on temperature between 300 and 500°C.

It is important to remember that the $Li_{17}Pb_{83}$ in the UWTOR-M blanket is not circulated as the coolant. Although there are temperature gradients in the blanket, consequences of natural convection should be small due to the MHD effects. Therefore, static data should be applicable in this case. Preliminary results as shown in Fig. XI.4-1 shows that effect of corrosion is small.

The corrosion mechanism in Pb will probably resemble the corrosion of $Li_{17}Pb_{83}$ because of the small Li concentration (0.7% by weight). Therefore, observations of Pb corrosion in steel will provide some indication of $Li_{17}Pb_{83}$/steel compatibility. The corrosion by liquid lead is primarily due to straightforward solution. In commenting upon such corrosion, it is essential to be specific not only with respect to temperature, but also to temperature gradient, coolant velocity and coolant impurity level. At 1000°C, rapid intergranular attack of various steels has been reported,[3] but only a slight attack on 304 SS was found in another study.[4]

At temperatures around 600°C, however, the alloys are far more corrosion resistant as the following table shows:[5]

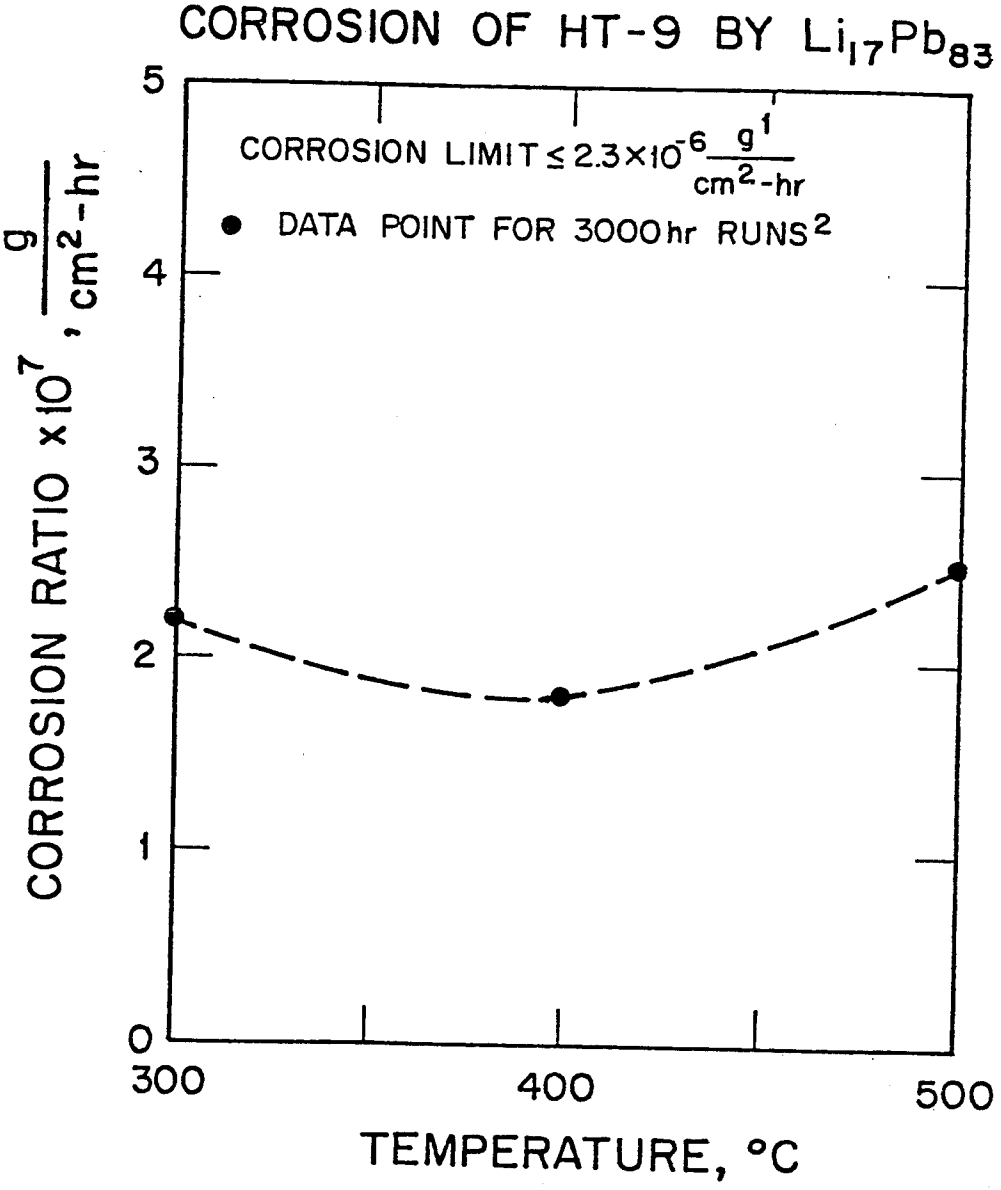
CORROSION OF HT-9 BY $Li_{17}Pb_{83}$
CORROSION LIMIT ≤ $2.3\times10^{-6}\frac{g^1}{cm^2\text{-}hr}$
DATA POINT FOR 3000hr RUNS[2]
CORROSION RATIO $\times10^7$, $\frac{g}{cm^2\text{-}hr}$
0
1
2
3
4
5
300
400
500
TEMPERATURE, °C

Figure XI.4-1.

Alloy	Max T°C	ΔT°C	Exposure hr	Calculated Corrosion Rate mils/yr
ASTM A106	573	111	5064	12
Croloy 2-1/4	593	111	5156	10
410 SS	655	167	1346	15

For comparison, corrosion of 316 SS by lithium at 600°C is estimated to be 23 mils/yr.[6] If the temperature is reduced to 400°C, 304 SS showed no attack at all after 500 h.[7] On the basis of these data, we conclude that at temperatures below 500°C, dissolution attack by lead will probably be reasonably slow even for stainless steels in pure lead.

Since nickel and nickel base alloys are much more soluble than iron, it is not surprising that the austenitic stainless steels with their higher nickel content are somewhat more easily corroded. Chromium also has a higher solubility than iron, but it is lower than for nickel. At 600°C, the solubility of iron in Pb was reported[8] to be only 2.3×10^{-4} wt.%, while for nickel at 635°C[9] the solubility was 0.85 wt.%. For this reason we would favor the use of stainless iron alloys (ferritic or martensitic) rather than the higher nickel austenitic alloys.

Finally, it is noted that little effort has yet been extended to further reduce the corrosion rate by inhibiting techniques. Addition of trace amounts of Zr and Mg have been shown[10,11] to provide complete protection of a 2-1/4 croloy alloy over three years with temperatures up to 550°C in spite of strong thermal gradients in the test loop.

It can be concluded that there are reasonable grounds for optimism for the use of steels as structural materials in liquid lead (and hence PbLi) up to 500°C. This initial conclusion, however, should not be used as an argument to neglect corrosion studies for these systems. The data we have used, while they are encouraging, are far from definitive and it is important to conduct simple coupon tests to validate the alloys proposed for first wall materials in liquid lead lithium alloys.

References for Section XI.4

1. J. DeVan, "Compatibility of Structural Materials with Fusion Reactor Coolant and Breeder Fluid."

2. P. Tortorelli and J. DeVan, "Compatibility of S.S. with Pb-17 at % Li."

3. W.D. Wilkinson, E.W. Hoyt and H.V. Rhude, "Attack on Materials by Lead at 1000°C," USAEC Report ANL-5449 (Oct. 1955).

4. R. Parkman and O.C. Cutler, "Investigation of Materials for Use in a Heat Transfer Loop Containing Liquid Lead Alloys," Report XII, USAEC Report ORO-45 (June 1951).

5. G.M. Tolson and A. Taboda, "A Study of Lead and Lead Salt Corrosion in Thermal-Convection Loops," USAEC Report ORNL-TM-1437 (April 1966).

6. W.N. Gill et al., "Mass Transfer in Liquid-Lithium Systems," AIChE J. 6, 139 (1960).

7. J.H. Frye, W.D. Manly and J.E. Cunningham, "Metallurgy Division Annual Progress Report for Period Ending September 1, 1959," USAEC Report ORNL-2839 (Dec. 16, 1959).

8. J.R. Weeks, NASA Special Publication SP-41 (1963).

9. M. Hanson, "Constitution of Binary Alloys," McGraw-Hill (1958).

10. R.C. Asher, D. Davids and S.A. Beetham, "Some Observation on the Compatibility of Structural Materials with Molten Lead," Corrosion Science 17, 545 (1977).

11. A.J. Romano, C.J. Klamut and D.H. Gurinski, "The Investigation of Container Materials for Bi and Pb Alloys, Part 1, Thermal Convection Loops," USAEC Report BNL-811 (July 1963).

XI.5 Materials Inventory for UWTOR-M

A materials inventory has been tabulated for both nuclear island and the balance of plant. Table XI.5-1 gives the materials in the nuclear island both in the elemental breakdown and as an aggregate. Table XI.5-2 does the same thing for the balance of plant.

Table XI.5-1. Materials in UWTOR-M Nuclear Island

Elemental Breakdown

	Blanket Initial	Blanket 30 Yr. Replacem.	Reflector	Shield	Modular Coils	Control Coils	Divertor Target	ICRH Launchers	Cryopumps	Support Structure	Total (tonnes)	Tonnes MWe
Al												
B				880							880	0.479
C				244							244	0.133
Cr	187	1,309	162.5	37.2	2,447	71.4	47		34.6	7.8	4,303.5	2.344
Cu					6,462	101		8	150	3.1	6,724.1	3.662
Fe	1,394.5	9,761.5	6,664	1,526.8	10,641	309	1,919.		138.2	602.7	32,956.7	17.950
He*					24.3	0.5					24.8	0.014
Li	127										127	0.069
Mn	8.1	56.7	1,138	260.7	303.4	8.8	328		3.8	7.8	2,115.6	1.152
Mo	16.3	114			284.4	7.8	1.6				424.1	0.231
Nb					125	2.7					127.7	0.070
Ni	8.1	56.7	162.5	37.2	1,498.3	43	47		15.4		1,868.5	1.018
Pb	17,973			1,582							19,555	10.651
Ta					38						38	0.021
Ti					162	2.7		0.3			165	0.090
V	4.9	34.3						6.2			45.5	0.025
W	8.1	56.7									65.1	0.035
Zr										0.6	0.6	---
									TOTAL		69,655.2	37.9
									Total Less He		69,640.4	

Material Breakdown

HT-9	1,627	11,389									13,016	
$Li_{17}Pb_{83}$	18,100										18,100	
B_4C				1,124							1,124	
Pb				1,582							1,582	
316 SS					14,220	390					14,610	
304 SS					954	50			192		1,196	
Cu					6,462	101		8	150		6,721	
NbTi					174	5.3					179.3	
NbTiTa					150						150	
Fe-1422			8,127	1,862			2,341				12,330	
A-242										622	622	
TZM							1.6				1.6	
G-10**					126	3.5					129.5	
VTi								6.5			6.5	
TOTAL	19,727	11,389	8,127	4,568	22,086	549.8	2,342.6	14.5	342	622	69,767.9	
									Total Less G-10		69,638.4	

*He was not included in lower table.

**G-10 was not included in elemental breakdown.

Table XI.5-2. Materials in UWTOR-M Balance of Plant

Elemental Breakdown

Element	Pipes, Valves & Pipe Hangers	Steam Gen. & Feedwtr. Heaters	Dump Tanks	Steam Circulators & LiPb Pumps	Cryo Generators	Liq. He Storage Distrib.	Building Liners	Buildings	Turbines	Generators	Total (Tonnes)	Tonnes MWe
Al				1.6					9.1		10.7	0.006
C	0.8			0.40				120	4.0	0.82	126.02	0.069
Cr	116.1	20.7	13.8	17.2	22.8	4.8			70.7	2.76	268.86	0.146
Cu					22.5	7.5				57	87.0	0.047
Fe	5,758.2	885.5	102.9	177.8	144.6	109.8	3,948	59,640	1,689	850.6	73,306.4	39.927
Co				2					11.4		13.4	0.007
Mn	33.3	4.6	0.5	1.5	3.00	1.77	52	240	6.6	2.27	345.54	0.188
Mo	51.6	9.2	1.2	5.0	2.85	0.6			22.8	1.25	94.5	0.051
Ni			0.6	52.5	14.25	3			284		354.35	0.193
Pb												
Si										8.30	8.3	0.005
Ti				2					11.4		13.4	0.007
V			0.4								0.4	---
W			0.6								0.6	---
										TOTAL	74,629.5	40.65

Material Breakdown

HT-9			120								120	
Croloy.	5,160	920								125	6,205	
A-242	380					90	4,000				4,470	
1020	420			150	45			60,000	1,653	410	62,678	
316 SS				30	142.5	30					202.5	
Cu					22.5	7.5				57	87	
Hastelloy R-235				80					456		536	
Silicon Steel										331	331	
TOTAL	5,960	920	120	260	210	127.5	4,000	60,000	2,109	923	74,629.5	

XII. Tritium Systems

XII.1 Overview

The tritium systems in UWTOR-M are designed to purify and recycle the tritium and deuterium fuel for the reactor. Tritium production and recovery from the blanket are discussed in Chapter IX. The tritium systems are patterned after information available from the Tritium Systems Test Assembly at Los Alamos National Laboratory.

The UWTOR-M reactor is fueled by injection of 14.9 kg-T/d and 9.71 kg-D/d as cryogenic DT pellets. The inventory in the pellet injection system is 23 g. The reactor produces 4300 MW of fusion power by burning 0.656 kg-T/d and 0.437 kg-D/d which corresponds to a tritium and deuterium burn fraction of 4.40% and 4.50%, respectively. The exhaust gases exit through divertor slots, strike rotating graphite targets and scatter into the evacuated reactor building. The exhaust and impurity gases are pumped by cryopumps and the tritium inventory in the pumps is 1.2 kg for a 2 hr on-line time. Helium ash (0.875 kg/d) is separated from the fuel during regeneration of the cryopumps.

The graphite divertor targets are operated under conditions where hydrocarbon production is minimal, although physical sputtering of graphite is anticipated. Other impurities in the exhaust will include hydrogen, which permeates from the steam cooling tubes, xenon, which is added to the plasma and oxygen and nitrogen, which outgas at low levels from construction materials. These impurities are separated from the hydrogen isotope stream by the fuel cleanup unit (FCU). This unit consists of molecular sieve beds at 75°K which condense impurities. The inventory on the sieve beds is estimated as 120 g for a 12 hr operation cycle. The beds are regenerated by heating and the impurities then pass through an oxidizing unit which forms HTO and tritium

free compounds. The HTO is electrolyzed and the hydrogen isotopes are sent to the Isotopic Separation System (ISS).

The ISS consists of a 2 column unit with one equilibration cell. It produces a waste hydrogen stream with less than 1 Ci/d vented to the atmosphere and a purified DT fuel stream. The tritium inventory in the columns is estimated as 270 g.

The total estimated inventory in the fuel recycling system is 1.6 kg of tritium. There is also a 1 day fuel supply of 14.9 kg of tritium kept in storage on uranium beds.

The reactor building serves as a primary containment vessel and must be designed to maintain a tritium release rate of $\lesssim$ 10 Ci/d.

XII.2 Fueling and Exhaust System

UWTOR-M is a steady state stellarator reactor which produces 4300 MW of fusion power. The reactor is fueled by DT pellet injection. The tritium and deuterium burn fractions are 4.40% and 4.50%, respectively. The fueling and exhaust parameters are listed in Table XII.2-1. Heating is accomplished with the use of about 100 MW of ICRH power and no neutral beams are used during steady state operation. Several start-up scenarios with and without the use of deuterium neutral beams have been considered. The design of a fuel handling system adapted for conditions particular to a neutral beam start-up scenario has not been addressed. The fuel processing system described is designed for steady state operation.

The exhaust gases and impurities exit the reactor through divertor slots. Rotating graphite drums are used as divertor targets. The charged particles striking the divertor targets are neutralized and scatter into an evacuated reactor building which surrounds the stellarator. The gases are pumped by a system of compound cryopumps with turbomolecular backing pumps located in pumping stations placed at strategic points in the reactor building. The gases are then sent to the tritium facility for reprocessing.

XII.2.1 Fueling

The reactor is fueled by injection of cryogenic pellets with a deuterium: tritium mole ratio of 1:1.03. Pellets are injected at a frequency of 35 every ten seconds and a velocity on the order of 10 km/s is required. The pellet radius is 4.2 mm and each pellet contains 82 mg of DT fuel which corresponds to 10% of the particles that are in the plasma.

A pellet injection system capable of obtaining the high velocity required has not been developed at this time. Pneumatic and centrifugal fuel injectors

Table XII.2-1. Fueling and Exhaust Parameters

	Tritium	Deuterium	Helium
Fraction Burned (%)	4.40	4.50	---
Fuel Injected (kg/d)	14.9	9.91	---
Fuel Burned (kg/d)	0.656	0.437	---
Ash Produced (kg/d)	---	---	0.875
Exhaust Pumped (kg/d)	14.2	9.27	0.875

have been developed for injection velocities on the order of 1 km/s. Laser injection systems may be capable of producing higher velocities. Further development of pellet injection systems is needed.

Two different types of pellet sources have been studied. Droplet generators form spherical pellets by applying a perturbation of a given frequency to a jet of liquid fuel. The liquid drops are solidified by keeping the pressure in the droplet chamber below the triple point of the fuel mixture.[1] The other pellet production method is an extrusion technique where the frozen fuel mixture is forced through an orifice and the resulting rod is cut with a heated wire into cylindrical pellets.[2,3]

Both production systems are capable of producing pellets rapidly. For example, hydrogen spheres > 200 μm have been produced at a rate of 10^5/s using a droplet generator.[4] After the pellet is produced, it is analyzed for mass and size, transported to the injector, loaded and fired. Each step in this process would be automized and would require on the order of seconds for completion. Since each step is considered to be rapid, there is no rate controlling step and the inventory can be related to the total time of the process. If a process time of two minutes is assumed and the process is 90% efficient, then ~ 470 pellets would have to be made in this time period in order to inject the pellets at a rate of 3.5 per sec. The tritium inventory would be 23 g. To minimize tritium handling, development of a continuous process that produces and injects pellets rapidly and efficiently is required. Pellet systems are expected to be enclosed in a secondary containment structure to prevent leakage.

XII.2.2 Reactor Exhaust

The reactor exhaust consists mainly of the unburned deuterium and tritium fuel and the helium ash as shown in Table XII.2-1. Impurities will also be present. Xenon is an impurity which is added to the plasma to provide some added power loss by radiation. The density of xenon in the plasma is 3.27×10^{10} atoms/cm^3 which is 0.021% of the plasma density. The xenon exhaust rate is 0.021% of the total plasma exhaust rate of 6.7×10^{22} atoms/s. This corresponds to an impurity flow of 1.4×10^{19} Xe atoms/s or 2.0 mol Xe/d. Hydrogen will be present as a result of nuclear reactions, outgassing from materials and permeation from the steam used to cool the blanket modules. The hydrogen permeation rate through 2 mm thick HT-9 tubing at 450°C is 1.4×10^{-2} mol H_2-d^{-1}torr$^{-1/2}$m^{-2}.(5) For a tube area of 2.2×10^3 m^2 and H_2 pressure of 0.1 torr the hydrogen impurity flow rate is 10 mol H_2/d or 20 mol HD,HT/d which enters the exhaust system.

Other impurities such as oxygen, nitrogen and carbon are also expected to be present. A list of impurities that are anticipated for fusion reactors is given in Table XII.2-2. This level of impurities will be used in testing the fuel recycling system in the Tritium Systems Test Assembly (TSTA).(6) The graphite divertor targets may increase the amount of tritiated hydrocarbon impurities. This is discussed below.

XII.2.2.1 Graphite Divertor Targets

The graphite drums used as divertor targets (Chapter VIII) will be operating under the following conditions:

D(T) ion flux	6.5×10^{15} atoms-cm^{-2}s^{-1}
Average ion energy	9 keV
Graphite temperature	1400°C (1673°K)

Table XII.2-2. Maximum Inlet Quantities for TSTA Fuel Cleanup Unit

Component	Ratio to (D_2 + DT + T_2)	Mols/Day
Q_2^* (= D_2 + DT + T_2)	1.0	356.4
HQ (= HD + HT)	0.02	7.20
C (= $\underline{CQ_4}$ + CO)	0.001	0.36
O (= $\underline{Q_2O}$ + CO + NO + 1/2 O_2)	0.005	1.80
N (= $\underline{NQ_3}$ + NO + 1/2 N_2)	0.001	0.36
Ar	0.05	18.00
TOTAL FLOW		384.12

---

*Q = any mix of D and T atoms

Principal species underlined

There have been numerous studies on the interactions of graphite and hydrogen and several reviews have been written summarizing the data.[7-9] Key studies relating to the chemical erosion of graphite under conditions similar to the UWTOR divertor targets are mentioned here. The bulk of the studies on hydrogen bombardment of graphite have been done in the temperature range 25°C - 1000°C. There are three studies which have been done at temperatures greater than 1000°C.

One of the studies used a thermal atomic hydrogen beam (~ 0.2 eV) and observed acetylene as the primary product at temperatures greater than 1000°C.[10] At 1400°C they report the C_2H_2 reaction probability to be 2×10^{-3} for graphite composed of edge sites (prism plane) and 6×10^{-4} for basal plane graphite samples. For high energy ion beams (~ 10 keV), the ions can penetrate the graphite as deep as 10^3 Å.[11] At this depth all of the valence bonds of a carbon atom are occupied and formation of hydrocarbons is less likely to occur than for thermal hydrogen atoms which interact primarily on the surface. Therefore, this study using low energy hydrogen is not applicable to the UWTOR divertor targets which will experience an ion flux with an average energy of 9 keV.

The two other high temperature studies have used high energy incident beams. Busharov et al.[11] observed sputtering of 3×10^{-2} atoms/ion with 10 keV H^+ ions at 1400°C and an average flux of 1.9×10^{15} atoms-$cm^{-2}s^{-1}$. The results of this study are shown in Fig. XII.2-1. The sputtering peak for 10 keV ions occurs between 150-750°C and is due mainly to the formation of methane. At temperatures greater than 1100°C physical sputtering is dominant and no hydrocarbon production was reported.

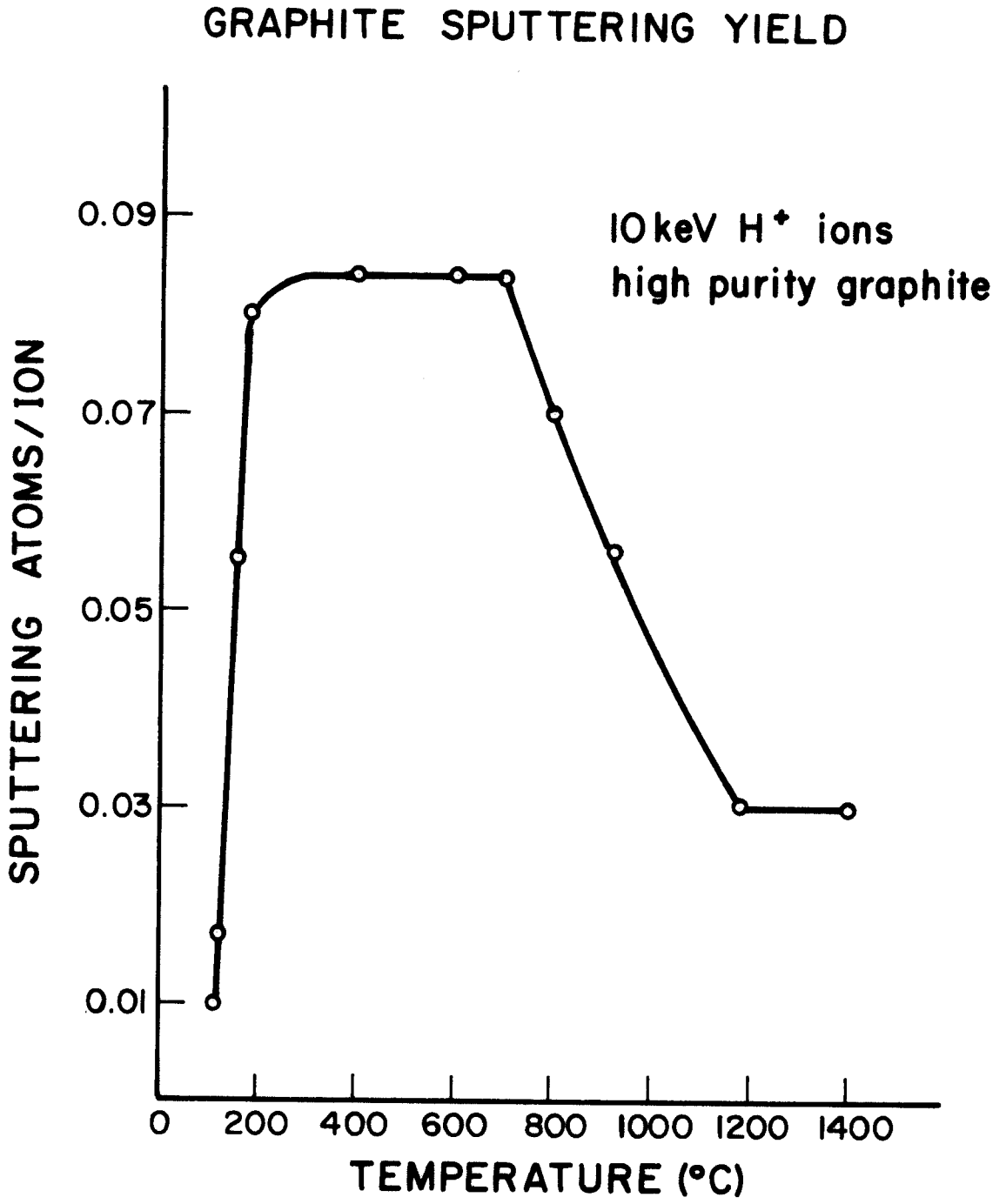

Figure XII.2-1 Temperature dependence of the graphite sputtering yield due to 10 keV H^+ ions on high purity graphite. Busharov et al.(11)

The third study by Roth et al.[12] used 0.4 to 7 keV ions between room temperature and 2000°K. Both weight loss measurements and residual gas analysis were applied to determine chemical sputtering and reaction products. At temperatures around 630°C (~ 900°K) an erosion peak corresponding to methane production is observed in general agreement with Busharov's data. At temperatures above 830°C (~ 1100°K) erosion occurred due to graphite sputtering and again no hydrocarbon formation was observed. The data is illustrated in Fig. XII.2-2. For 10 keV deuterium ions at 1527°C (1800°K) with a current density of 10^5 D $cm^{-2}s^{-1}$, the sputtering yield is 0.13 atoms/ion. This value was shown to be dependent on ion mass and independent of ion flux and angle of incidence.

The conclusion from these studies indicates that at the temperatures and ion energies expected for the graphite divertor targets, sputtering on the order of 0.1 atom/ion will consist of graphite particles and hydrocarbon formation is expected to be small. The hydrocarbon impurities produced by the interactions of the fuel exhaust and graphite are expected to scale with the estimates for the TSTA fuel cleanup design. Synergistic effects of simultaneous ion and electron bombardment for high energy ions have yet to be investigated.[9]

XII.2.2.2 Vacuum System

The fuel exhaust enters the evacuated reactor building and is pumped by compound cryopumps located in stations around the reactor building. Separation of hydrogen from helium can be accomplished at this step by first regenerating the helium panel, and then the cryocondensation panel is warmed to remove hydrogen isotopes from the pump.[13] This pumping system is being tested by TSTA. If hydrogen/helium separation is not accomplished at this

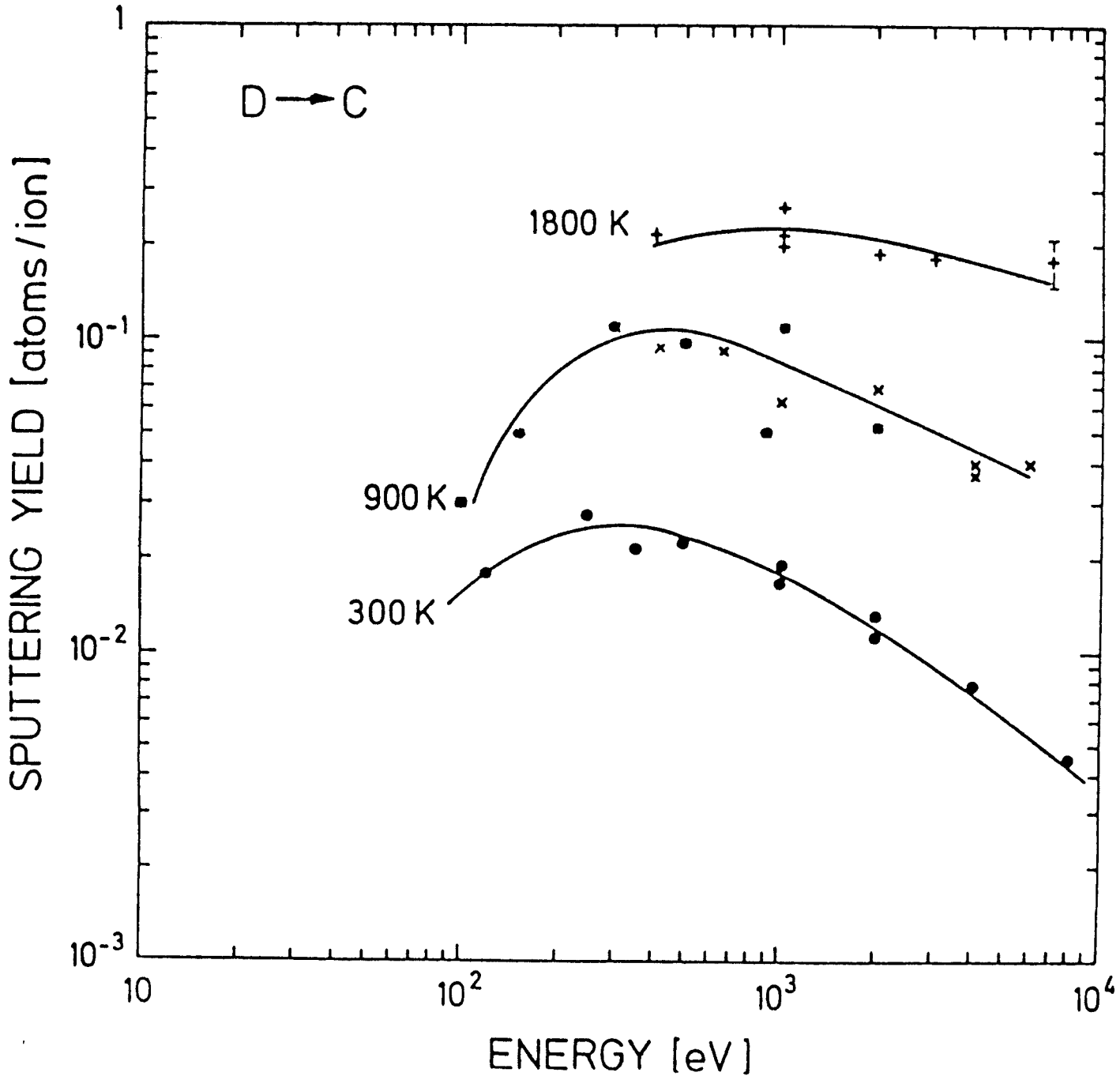

Figure XII.2-2 Energy dependence of the sputtering yield of carbon by deuterium ions at 300, 900, and 1800°K. Roth et al.[12]

step a falling film He/hydrogen isotope separator[14] may be required. The on-line time for the pumps is 2 hours and the tritium inventory tied up in the vacuum pumps is 1.2 kg.

References for Section XII.2

1. C.A. Foster, K. Kim, R.J. Turnbull, and C.D. Hendricks, "Apparatus for Producing Uniform Solid Spheres of Hydrogen," Rev. Sci. Instrum. 48(6), 625-631 (June 1977).

2. T.R. Jarboe and W.R. Baker, "Apparatus for Producing Laser Targets of 50 μ Deuterium Pellets," Rev. Sci. Instrum. 45(3), 431-433 (March 1974).

3. W. Amenda, K. Büchl, R. Lang, L.L. Lengyel, W. Riedmüller, "Pellet Ablation Studies at Garching," Proc. of the Fusion Fueling Workshop, CONF-771129, pp. 110-113, Princeton University, Princeton, NJ, Nov. 1-3, 1977.

4. C.D. Hendricks, W.L. Johnson, "Power Plant Production of Inertial Confinement Fusion Targets," Lawrence Livermore Laboratory, UCRL-52539, February 15, 1979.

5. A summary of the permeation data for Cr-Mo ferritic steels is given in: B. Badger et al., "WITAMIR-I - A Tandem Mirror Reactor Study," University of Wisconsin Fusion Engineering Program Report UWFDM-400 (Dec. 1979), Chapter XI, pp. XI-16 - XI-24.

6. E.C. Kerr, J.R. Bartlit, and R.H. Sherman, "Fuel Cleanup System for the Tritium Systems Test Assembly: Design and Experiments," Proc. Tritium Technology in Fission, Fusion and Isotopic Applications, Dayton, OH, April 29 - May 1, 1980, CONF-800427, American Nuclear Society (1980), pp. 115-118.

7. R. Behrisch, "Surface Erosion from Plasma Materials Interaction," J. Nucl. Mater. 85 & 86, 1047-1061 (1979).

8. C.I.H. Ashby, "Chemical Erosion of Graphite in a Plasma Environment," Sandia National Laboratory, SAND81-0803, Aug. 1981.

9. J.A. Borders, "A Critical Review of Carbon and Carbide Erosion Data by Hydrogen for Fusion Reactor Applications," Sandia National Laboratory, SAND82-0601, March 1982.

10. M. Balooch and D.R. Olander, "Reactions of Modulated Molecular Beams with Pyrolytic Graphite. III. Hydrogen," J. Chem. Phys. 63(11), 4772-4786 (Dec. 1, 1975).

11. N.P. Busharov, E.A. Gorbatov, V.M. Gusev, M.I. Guseva, Yu.V. Martynenko, "Chemical Sputtering of Graphite by H^+ ions," J. Nucl. Mater. 63, 230-234 (1976).

12. J. Roth, J. Bohdansky, K.L. Wilson, "Chemical Erosion of Carbon Due to Bombardment with Energetic Hydrogen at Temperatures up to 2000°K," Proc. 5th Int. Conference on Plasma Surface Interactions in Controlled Fusion Devices, Gatlinburg, TN, May 1982.

13. J.L. Anderson, "Design and Construction of the Tritium Systems Test Assembly," Proc. Tritium Technology in Fission, Fusion and Isotopic Applications, Dayton, OH, April 29 - May 1, 1980, CONF-800427, American Nuclear Society (1980), pp. 341-346.

14. J.L. Anderson and R.H. Sherman, "Tritium System Test Assembly Design for Major Device Fabrication Review," LA-6855-P, Los Alamos Scientific Lab. (June 1977).

XII.3 Fuel Purification and Storage

The reactor exhaust is pumped and transferred to the tritium facility. It then passes first through a fuel cleanup unit (FCU) which removes nonhydrogen isotope impurities, followed by the isotopic separation system (ISS) which purifies the DT fuel. The DT fuel is mixed in the appropriate composition and the pellets are then produced and injected. Tritium that is bred in the blanket is purified in a separate system which is discussed in Chapter IX. The purified blanket tritium can re-enter the fuel cycle in the fuel blending process. The tritium building will also contain facilities for tritium and deuterium storage and a tritiated waste treatment unit (TWT). Tritium that is accidentally released into the reactor building or tritium facility would be recovered by an emergency atmospheric tritium recovery system (ETR). This unit would also be used to scrub tritium from the reactor building if an air leakage into the building should occur.

The tritium systems for UWTOR-M are patterned after the Tritium Systems Test Assembly, TSTA.[1-3] This facility is expected to have demonstrated the technology required for the tritium purification and containment in a fusion reactor by 1990. The tritium inventory in the fuel processing system for UWTOR-M is summarized in Table XII.3-1.

XII.3.1 Fuel Cleanup

The fuel cleanup unit (FCU) serves to purify the hydrogen isotopes from tritiated water, hydrocarbons, xenon, nitrogen compounds or any other impurities that would condense at the liquid hydrogen temperatures employed in the isotope separation system (ISS). Impurity levels must be maintained below 1 ppm (except for He) to ensure safe, long-term operation of the ISS.[3]

Table XII.3-1. Summary of Tritium Inventories in Fuel Processing Systems for UWTOR-M

Subtotals (kg):	
Pellet Injector	0.023
Cryopumps	1.2
Fuel Cleanup	0.120
Distillation Columns	0.270
Fuel and Exhaust Systems Total (kg):	1.6
Storage (1 Day Fuel Supply) (kg):	14.9

The tritiated water and ammonia are condensed out of the hydrogen isotope stream, after which the low melting impurities are separated from the hydrogen molecules by adsorption on molecular sieve beds at 75°K. Tritium impurities are recovered by periodic regeneration of the adsorption beds by heating. These impurities are catalytically oxidized to form tritiated water and tritium free compounds. The water is condensed and eletrolyzed to recover the tritium.[1] The xenon impurity (boiling point = 165°K, melting point = 161°K) will essentially follow the same path as CO_2 impurities (sublimation point = 195°K) and should not complicate the fuel cleanup process.

The present TSTA process will test two purification systems; the cryogenic molecular sieves discussed above and hot uranium metal beds which react with C, N and O impurities forming stable uranium compounds with these elements.[3] The cryogenic process is felt to be superior as it operates at low temperatures and since the beds are regenerable, solid wastes are minimized. The uranium beds operating at 1140°K create permeation problems and replacement of the poisoned uranium beds is costly. At present, a reliable electrolysis cell necessary for the cryogenic based FCU has not been developed. It is anticipated that such a cell will be available for a commercial fusion reactor.

The tritium inventory in the FCU is estimated from the anticipated flow of tritium impurities listed in Table XII.3-2. The C, N and O impurity levels are derived by scaling the anticipated impurity levels for TSTA (Table XII.2-2) with the DT flow rate. The maximum flow rate of condensible tritium compounds is estimated assuming the C, N and O compounds are saturated with tritium. The impurity flow rate is 81 mol-T/d and if the adsorption beds are regenerated every 12 hours, the tritium inventory is 120 g. The inventory associated with the oxidizing unit is assumed to be small and the inventory in

Table XII.3-2. Tritium and Impurity Flow Rates in UWTOR-M Reactor Exhaust

Species	Flow Rate (mol/d)
Q_2^* (D_2, DT, T_2)	4700
HQ (HD, HT)	20.
C (CQ_4, CO)	4.7
O (Q_2O, CO, NO, 1/2 O_2)	24.
N (NQ_3, NO, 1/2 N_2)	4.7
Xe	2.0

*Q = any mix of D and T atoms.

the electrolysis cell is unknown. Increased impurity levels would impact the inventory. A tritiated hydrocarbon production larger than anticipated from the graphite divertor would create more condensible tritium compounds. Tritium which interacts with oxygen impurities present in the reactor building will form HTO. This effect must be minimized to control the amount of HTO that is condensed in the FCU and to reduce the concentration of the more toxic oxide form of tritium in the reactor building atmosphere. If necessary the FCU could be modified to handle increased loads of HTO and tritiated hydrocarbons. Larger molecular sieve beds would be required to absorb more impurities and more frequent regenerations would be used to reduce tritium inventories.

XII.3.2 Isotopic Separation System

The percentages of the hydrogen isotopes which enter the ISS are 50.5% T, 49.3% D and 0.214% H. The primary goals of the separation system are to remove hydrogen impurites from the fuel stream, to form a hydrogen waste stream containing $\leq$ 1 Ci/d and to produce the fuel mixture with the appropriate DT ratio. This can be accomplished by a system of 2 cryogenic distillation columns and one equilibrator as illustrated in Fig. XII.3-1. Column I achieves a high deuterium:tritium separation. The deuterium rich stream at the top of Column I is sent to an equilibrator to convert HT species primarily to HD. Column II separates the H_2, HD components from the DT stream which exits at the bottom of Column II. The design of the columns is based on those in the literature.[2,4] The inventory in the distillation unit is estimated as 270 g.

XII.3.3 Storage

A certain quantity of tritium must be maintained in storage in the event of a temporary malfunction of any of the tritium handling equipment, such as

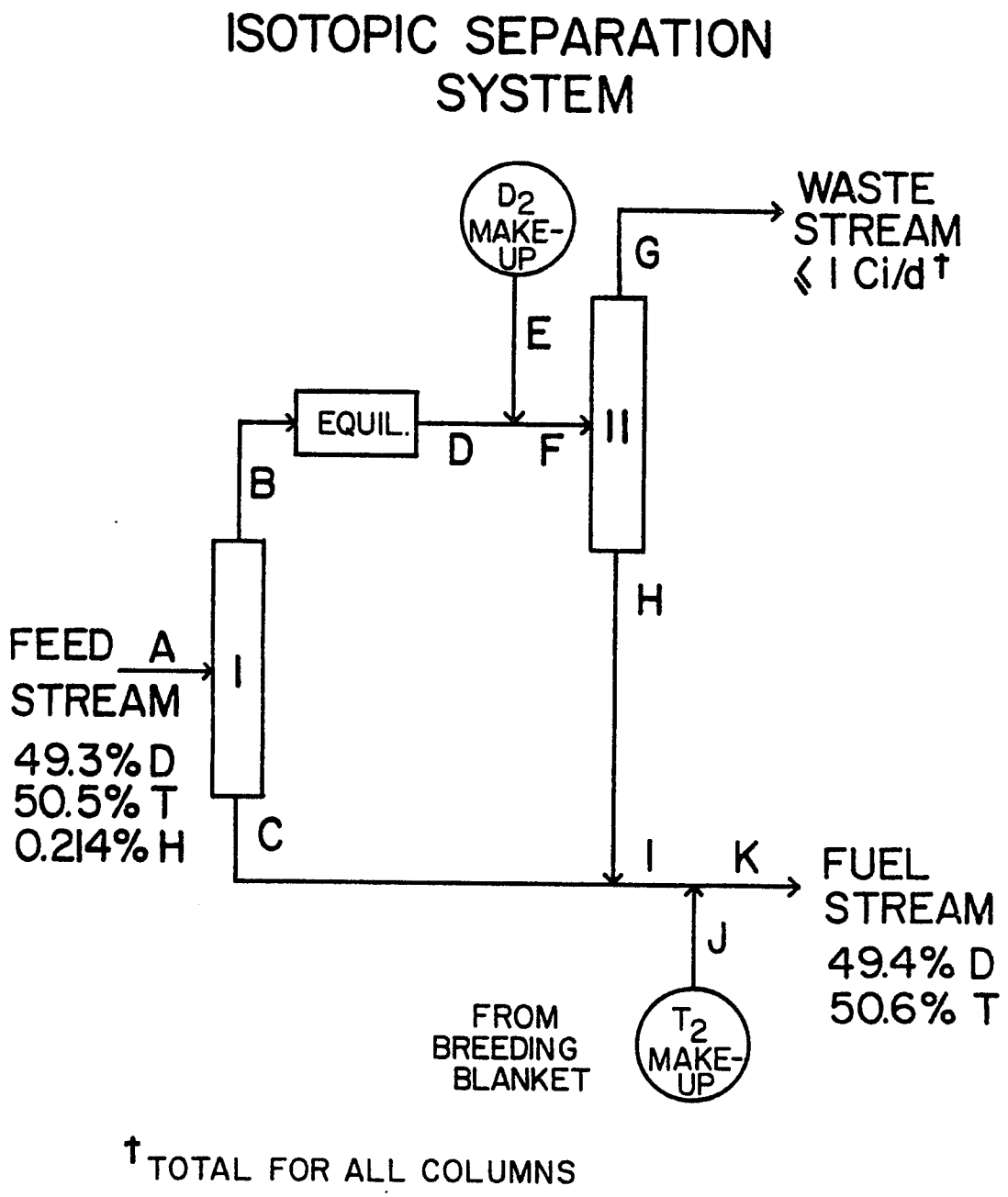

Figure XII.3-1 Cryogenic distillation system for UWTOR-M.

the fuel cleanup unit, the isotope separation system or the blanket tritium extraction system. This tritium should be in a purified state with only a minimal time required to release it from storage and bring it to the cryogenic temperatures of the pellet maker.

The tritium is stored on uranium beds in UWTOR-M. A problem exists with the formation of helium-3 if the tritium is stored for extended periods of time[5] and a falling film T_2/He separator[1] may be required to remove helium from the tritium before insertion into the reactor chamber. Tritium equivalent to one day's pellet injection rate (14.9 kg) is stored on the uranium beds.

XII.3.4 Containment Systems

The UWTOR reactor building serves as a primary containment structure. The building volume is 70,000 m^3 and the pressure is kept at about 5×10^{-5} torr. Assuming the building pressure consists mainly of a 50:50 DT mixture, the building will contain 0.56 g of tritium and the tritium concentration in the building is 0.081 Ci/m^3. The building must be kept as free of oxygen as possible to prevent HTO formation. Surface area within the building should be minimized and cryogenic equipment must be well-insulated to prevent "pumping" of tritium onto cold surfaces. The existence of oil, water, water vapor or other tritium sinks on surfaces or in the atmosphere must be excluded. Since the cryopumps contain a large fraction of the tritium inventory, the vacuum equipment can be housed in secondary containment enclosures and large gate valves would be necessary to isolate the vacuum system from the reactor building. The building is constructed of thick steel walls and must be kept leak-tight. Containment systems for the tritium facility will be patterned after TSTA.[1]

References for Section XII.3

1. J.L. Anderson and R.H. Sherman, "Tritium Systems Test Assembly Design for Major Device Fabrication Review," LA-6855-P, Los Alamos Scientific Lab., (June 1977).

2. J.L. Anderson, "Design and Construction of the Tritium Systems Test Assembly," Proc. Tritium Technology in Fission, Fusion and Isotopic Applications, Dayton, OH, April 29 - May 1, 1980, CONF-800427, American Nuclear Society (1980), pp. 341-346.

3. E.C. Kerr, J.R. Bartlit, and R.H. Sherman, "Fuel Cleanup System for the Tritium Systems Test Assembly: Design and Experiments," Proc. Tritium Technology in Fission, Fusion, and Isotopic Applications, Dayton, OH, April 29 - May 1, 1980, CONF-800427, American Nuclear Society (1980), pp. 115-118.

4. B. Badger et al., "TETR - A Tokamak Engineering Test Reactor to Qualify Materials and Blanket Components for Early DT Fusion Power Reactors," University of Wisconsin Fusion Engineering Program Report UWFDM-191 (June 1977), Chapter XII.

5. R.S. Carlson, "The Uranium-Tritium System - The Storage of Tritium," Proc. Int. Conf. Radiation Effects and Tritium Technology for Fusion Reactors, Gatlinburg, TN, October 1-3, 1975, CONF-750989, U.S. Energy Research and Development Administration (1975) IV-36-52.

XIII. Assembly and Maintenance

XIII.1 Introduction

One of the most important engineering requirements of a fusion power reactor is that it be maintainable. Regardless of how much reliability and redundancy can be built into a component, it is worthless unless it can be replaced, or at the very least, repaired in place, should an unforeseen or off normal failure occur.

Aside from some early setbacks in stellarator experiments,[1] an aspect which has impeded the development of this concept as a viable power reactor has been concern over its maintainability. In large measure, this was due to the fact that all the variations of this concept, namely stellarators, torsatrons and heliotrons required continuous helical coils to generate the required twisting flux surfaces. In addition, the heliotron has toroidal field coils which surround the helices in the poloidal direction. Later improvements resulted in the so called ultimate stellarators and torsatrons, in which the toroidal field components were generated by varying the pitch of the helices on the outer and inner edges of the toroid. Nevertheless, continuous helices were still necessary ingredients of those designs.

Over the years there have been attempts at making continuous helices maintainable and reactor designs with demountable superconducting coils have been proposed.[2] Making demountable joints in a superconducting coil is extremely difficult. The conventional method for splicing superconductors is to overlap long segments, clamp them together and maintain them under constant pressure. Although soldered connections would not be useful for a demountable joint, experiments have shown that they are not as effective as clamped connections. It is obvious that a clamped connection would be much thicker than

the original conductor. Furthermore, such a joint is resistive, because the current is shunted through the stabilizer at the point of contact. Adequate provision has to be made for cooling the joint to dissipate the ohmic heating. Such a demountable superconducting coil joint may have several hundred (Bitter coil) to several thousand (conventional coil) connections, all in the same general vicinity.

There are at least two other problems that a demountable superconducting joint must deal with. The first is that the energized coils carry enormous radial and lateral forces which must be transmitted across the joint. This implies more structure that further increases the bulk. The second problem has to do with the cryogen container and the vacuum dewar that must necessarily surround any superconductor. Breeching and reconsructing the liquid helium and vacuum vessels is very difficult because it requires leak checking which would be almost impossible to perform in situ. The difficulty of implementing such a joint is greatly amplified in the realization that the whole task has to be performed by remote control.

Based on these considerations it appears, from present understanding of demountable superconducting joints, that they may not be practical because they will be difficult to implement and may compromise the performance of the coil and the dewar. This does not mean that future developments may not change this viewpoint.

The appearance of several versions of modular coils have changed maintainability aspects of stellarators. Discrete twisted coils can now be removed from the coil set for repair in a hot cell. Spare coils can be used to minimize the downtime needed for such repair.

Because the coils in stellarators are steady state, it is very unlikely that they would be subjected to frequent failure. Nevertheless, problems such as vacuum leaks or leaks in the cryogen barrier will necessitate repairs. Modular coils now make it possible with good assurance that such repairs can be carried out under controlled conditions in a hot cell.

Modular coils have also opened up possibilities for maintaining the blanket which must necessarily be replaced several times during the 30-40 year lifetime of the reactor. In the next several sections the philosophy and the procedures for maintaining the blanket, divertor targets and the coils will be discussed.

XIII.2 Maintenance Philosophy

The philosophy for maintaining the blanket in UWTOR-M entails the radial extraction of nine of the eighteen modular coils. This has been necessitated by two aspects of the design:

1. The use of grossly twisted modular coils for maximizing rotational transform, thus requiring external support structure.
2. The decision to utilize the magnetic divertor for impurity control.

The reasons for adopting these design aspects have been elaborated on earlier in the report. The consequences are a somewhat more difficult maintenance requirement entailing the moving of heavy and rather cumbersome modules consisting of the coil itself, the shield, blanket and divertor targets.

It should be pointed out that there are modular coil stellarator reactor designs which do not require the extraction of coils for blanket maintenance.[3] These designs have a much smaller coil distortion in which the coil case itself is sufficient to react the radial forces. They also propose the use of pumped limiters for impurity control. Blanket modules are maintained

through spaces between the coils. If the pumped limiter proves to be effective as an impurity control mechanism, it will most likely need frequent attention as compared to externally located divertor targets. This will necessitate frequent breeching of the vacuum space within the reaction chamber, taking up valuable time and impacting availability. It is not clear at this stage whether extraction of a fraction of the coils (such as proposed in UWTOR-M) will necessarily mean a lower reactor availability if such an operation is performed every 4-6 years.

One major advantage of this maintenance scheme is that it automatically provides for the capability of servicing the magnets. There is a danger that coil maintainability can be compromised on the theory that nothing will ever go wrong with them. Thus, a carefully laid out maintenance of the blanket is proposed, but little or no provision is made for servicing the coils. At least this danger does not exist in UWTOR-M.

It should be mentioned that modular stellarators in general and UWTOR-M in particular are not unique in proposing maintenance requirements of this nature. The TRW team designing a blanket for MARS (Mirror Advanced Reactor Study) has proposed maintaining the central cell blanket modules by moving two coils with integral blanket/shield weighing on the order of 1500 tonnes.[4] There are 24 such modules in the 150 m long central cell. Further, the end plug coils will also have to be maintained by translating them out of the reactor and they too, will be heavy and bulky.

Questions have been raised as to the feasibility of moving loads of ~ 2050 tonnes and whether the relatively tight tolerances of locating the coils upon replacement can be maintained. These are not trivial problems which must be carefully addressed. However, given that these loads will be moved on guide

rails and will be equipped with stops and locaters in the form of guide dowels, it would seem such problems are solvable. Further, once a coil is located in place, locking mechanisms will be activated to fix the support ring to the centering support column and to the floor of the reactor containment building. Such locking mechanisms will be remotely activated with provision for manual override.

In UWTOR-M, radial extraction of the coil modules is, therefore, central to the maintenance scheme. It provides for:

1) Maintenance of the blanket segments with the extraction of one-half of the coil modules.
2) Maintenance of the coils by either straight radial extraction or initial circumferential, then radial extraction (in the case of coils not moved for blanket maintenance).
3) Maintenance of divertor targets in the same way as the blanket.

The mass of a coil module is about 2045 tonnes with the breakdown given in Table XIII.2-1. Transporter units with electric drives operating on rails with a working capacity of 250 tonnes are available from Western Gear. Ten such units will be needed for each module. Once a module is locked in its place in the reactor, the load is shared between the transporters and permanent supports, such that the added mass of the breeding material would not overload the units. Alternatively, fourteen units can be employed for a total capacity of 3500 tonnes.

Figure XIII.2-1 is a top view of the reactor inside the reactor hall, showing access doors located behind every other coil. A complete coil module, as viewed from the back, is shown in Fig. XIII.2-2 without the transporters and rails. Blanket segments with the steam manifolds attached come out of

Table XIII.2-1 Breakdown of Masses in a Single Coil Module

	Tonnes
Coil and support ring	1175
Blanket structure	90.5
Reflector	451
Shield	254
Divertor targets (6 sets)	52
Steam manifolds	3.5
Support structure	19
Total	2045

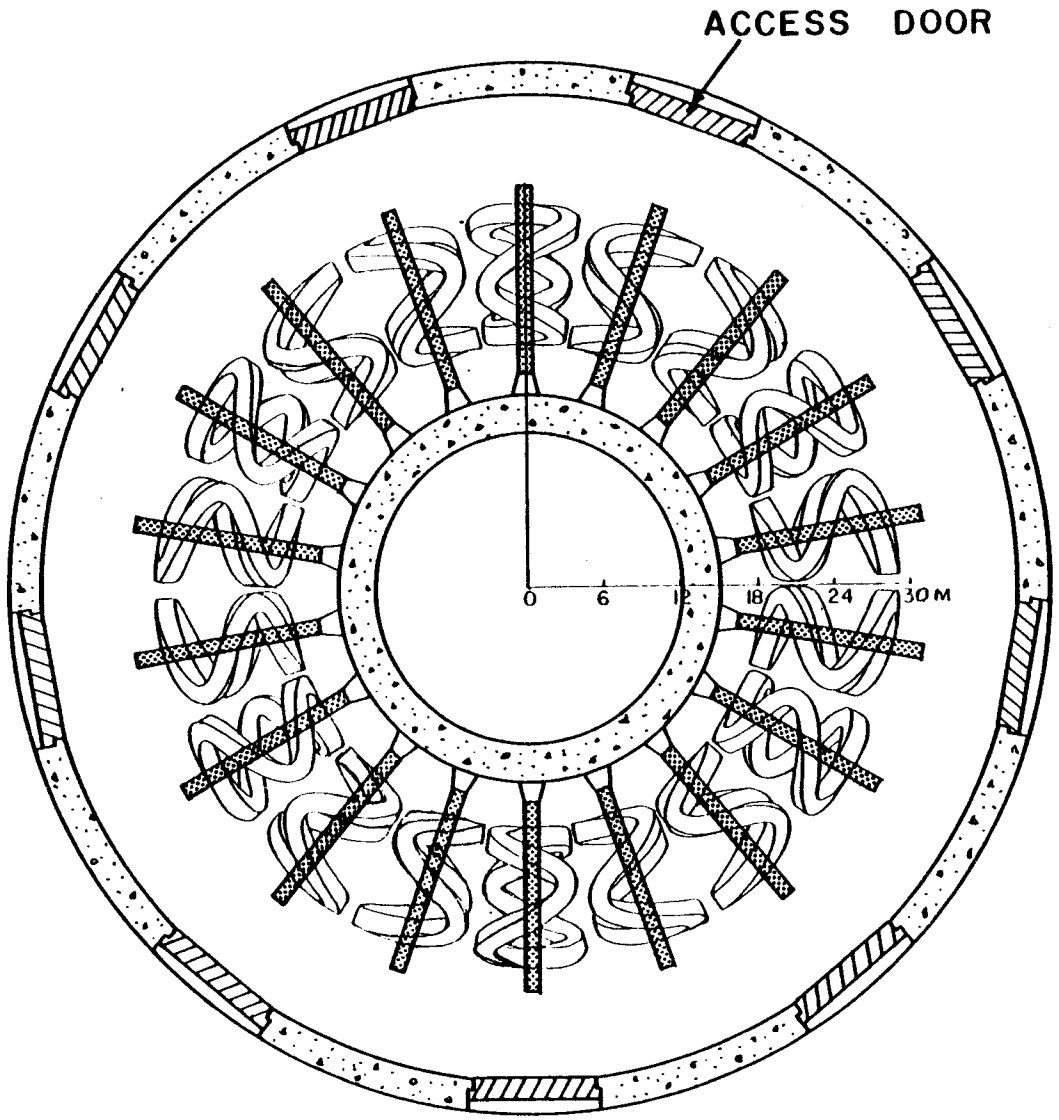

TOP VIEW OF UWTOR-M WITHIN EVACUATED REACTOR BUILDING

Figure XIII.2-1

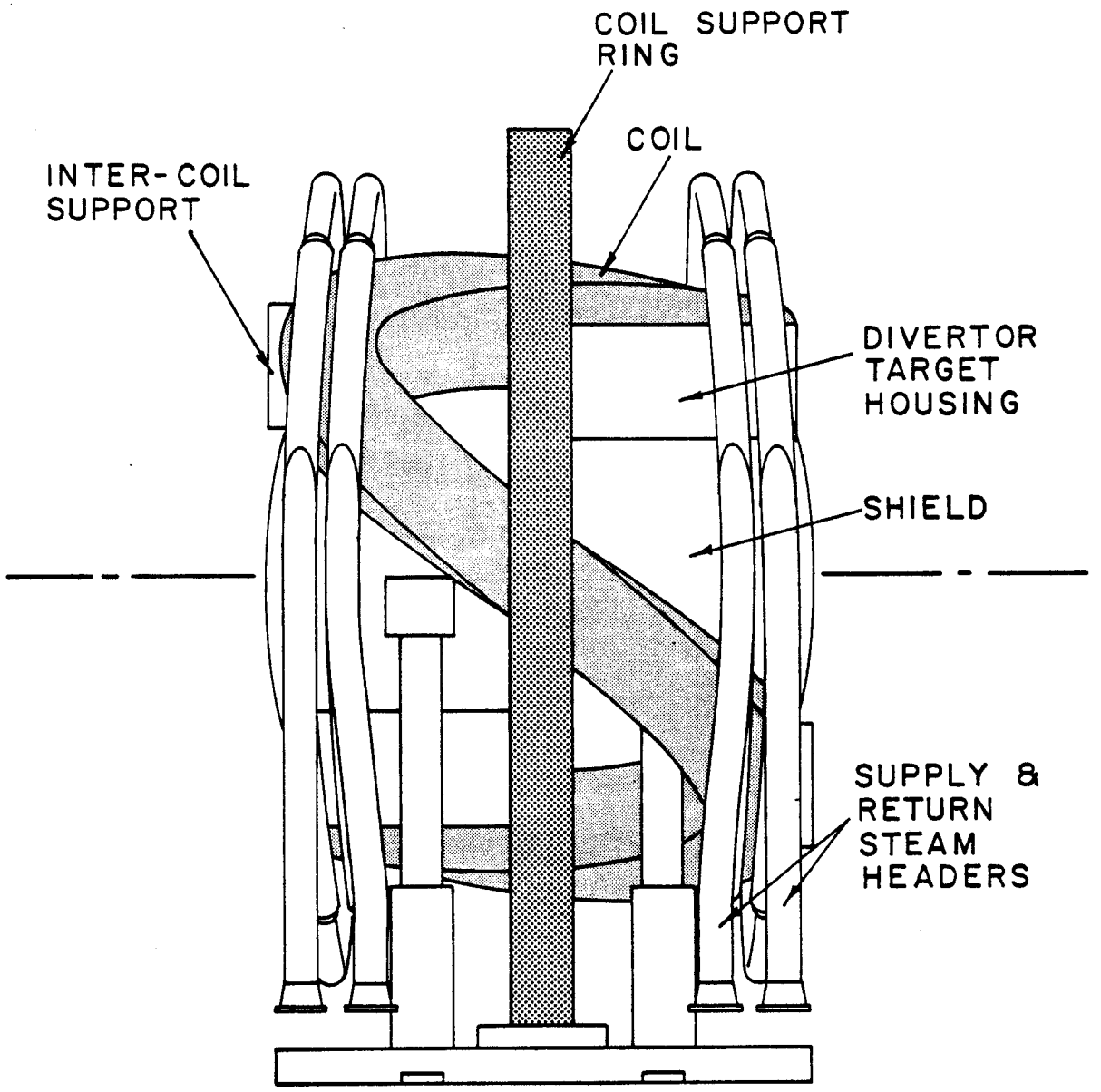

REACTOR MODULE AS VIEWED FROM THE BACK

Figure XIII.2-2

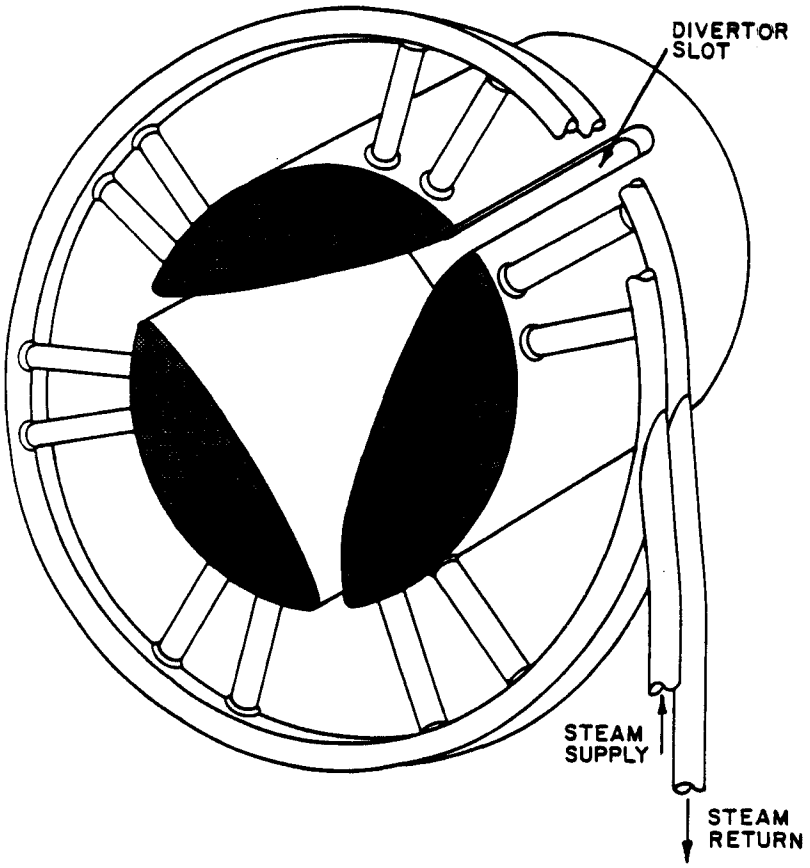

Figure XIII.2-3 Perspective view of a blanket segment.

each side of the module. Such a blanket segment, shown in Fig. XIII.2-3, weighs ~ 45 tonnes and can be easily handled with an overhead crane.

Specially designed carriages will enter the space vacated by a coil module. They will have the capability of removing the blanket segments within the stationary modules. In this way, only 50% of the modules need to be moved for routine blanket and divertor target maintenance. Obviously, coil maintenance of the stationary modules will necessitate circumferential translation first, then radial extraction as in the case of the movable modules.

XIII.3 Maintenance Procedure

In the next section an attempt will be made to lay out a sequence of events/tasks in the order of occurence needed to carry out the extraction of a coil module.

During the first 24 hours after shutdown:

- Coils are gradually deenergized.
- Vacuum pumps are left on in order to reduce the T_2 partial pressure to an acceptable level.
- Coolant is circulated in the blanket to carry away decay heat.
- Breeding material is drained out of the blanket.

During the next 48 hours:

- The vacuum pumps are valved off.
- The coil support ring locking mechanism is activated to release the locks. A slight backward motion will open up gaps at the intercoil supports to provide insulation at the interface between the cold and the warm structure.
- Reactor hall is brought up to dry air.

- The proper access door is opened up. These doors will be designed to open in the same way as airplane doors, but will be supported on transporters running on rails.
- The helium is drained out of the coil and the supply and vent lines disconnected and sealed.
- The breeding material, shield coolant and steam lines are disconnected and sealed.

The coil module is now ready to be transported radially from the reactor hall into the service hall and taken to a service station where the blanket segments are unbolted from the reflector and removed. New segments are installed in their place. Similarly, the divertor targets are inspected and replaced if needed. Simultaneously, the blanket segments and divertor targets in the stationary coils adjacent to the extracted module are also replaced.

The reverse of this sequence will be needed to return a coil module back into the reactor set. After leak checking all the coolant connections and the access door seal, the reactor hall is evacuated. The coil is then cooled back from whatever temperature it had attained during the maintenance operation. As the coils are energized, the centering force will close the insulating gaps in the intercoil structure completing the load path which reacts the toroidal forces. At the same time, the coil structural ring locking mechanisms are activated, attaching the coil supports to their surroundings and to the central reaction column.

XIII.4 Maintenance Schedule

A maximum neutron wall loading of 3.12 MW/m^2 will allow a wall lifetime of at least three full power years, assuming that HT-9 can withstand ~ 15 MW

years/m^2. This is equivalent to 3.75 actual years at an availability of 80% and 4 actual years at an availability of 75%.

Routine blanket changeout can be carried out every 16 months when 1/3 of the blanket segments can be replaced. Thus, during a routine blanket changeout shutdown, three coil modules will have to be moved. Since many of the operations can be carried out in parallel, it would seem that a 4-week shutdown may be adequate to perform this type of maintenance.

XIII.5 Summary and Conclusions

In summary, the following points can be made about the maintenance of UWTOR-M.

- The reactor is enclosed within an evacuated reactor hall.
- No seals are employed between blanket segments.
- Coolant connections are minimized.
- One-half of the coil set (9 coils) can be extracted radially out of the reactor hall providing access for maintaining all the blanket segments and divertor targets.
- In the event of a coil failure, the remaining coils can be extracted by initial circumferential, then radial movement.

The design issues which must be evaluated and verified for this maintenance scheme to succeed are:

- The implications of a T_2 contaminated reactor hall.
- The ability to make leak tight joints in coolant and other connections.
- The ability to seal large access doors.
- The capability of performing fairly complicated tasks by remotely controlled equipment.

Most of these issues are generic to all fusion systems, but they take an added importance in a design which requires an evacuated building. Some indepth investigations are needed to determine the viability of such a scheme.

References for Chapter XIII

1. J.L. Johnson, G. Grieger, D.J. Lees, M.S. Rabinovich, J.L. Shohet and K. Uo, "The Stellarator Program", IEEE Transactions on Plasma Science, Dec. 1981, p. 142.

2. L.M. Lidsky, et al., "The T-1 Self-Consistent Point Design", Stellarators - Status and Future Directions", Joint U.S. Euratom Report, July 1981.

3. R.L. Miller, R.A. Krakowski and C.G. Bathke, "MSR-Modular Stellarator Reactor", Los Alamos National Laboratory - Los Alamos, NM, to be published.

4. J.D. Gordon, "TRW/GD High Temperature Blanket Design for MARS", August 1982, to be published in interim MARS report.

XIV. System Economics

XIV.1 Introduction

The economic analysis for UWTOR-M conforms to the guidelines provided in the DOE "Fusion Reactor Design Studies - Standard Accounts for Cost Estimates".(1)

The two modes of analysis used are the constant dollar and the current dollar. The constant dollar mode defines general inflation rates and component escalation rates equal to zero. All costs, regardless of the time of incurrence, will be reported in present year price levels. In the current dollar mode, cost escalation on the estimated capital is assumed to exist and is taken as a single escalation during construction account.

It should be kept in mind that comparing constant dollar mode power costs obtained for UWTOR-M with present power costs from existing power plants is not really fair, because the present year price levels used are not de-escalated back to the year when construction will have been started (eight to ten years, depending on the construction period), and interest during construction is based on present year prices. Therefore, these cost estimates should be used only for comparison with other conceptual designs using the same guidelines.

XIV.1.1 Level of Technology

A design of a fusion reactor must necessarily cover many levels of technology ranging from current to advanced. The definition of advanced technology is one that has not been demonstrated on a commercial scale.

Clearly, almost all the nuclear island technology is advanced since much of it has not even been demonstrated experimentally, let alone on a commercial scale. However, the level of technology in the balance of plant, with some

possible exceptions, is current. This is particularly true since a conventional superheated steam cycle is envisaged as the power conversion system for UWTOR-M. Thus, steam generators, turbine and electric plant equipment, condensing and heat rejection equipment and almost all the miscellaneous plant equipment is of current PWR and BWR technology.

It should be clearly stated, however, that UWTOR-M, as most other conceptual design studies, is assumed to be a 10th of a kind modular stellarator power reactor. That is to say, all of the advanced tecnology will have been thoroughly tested and demonstrated. Further, no R & D costs are included in the estimates.

XIV.2 Design Allowance, Contingency and Spare Parts

A design allowance is a sum of money included to account for the difference between a technically immature design (at the time the reactor is designed) and the final mature design. It, therefore, takes care of some uncertainties that may be present at the time of the design. This account varies with the degree of maturity. Thus, no design allowance was allocated for Act. No. 21, Structures and Site Facilities. The remaining accounts have design allowances of 5% to 15%, depending on the maturity of the technology invoked.

Contingency is an allowance for unforeseen or unpredictable expenses that will be incurred during facility construction and startup. It should reflect cost uncertainty resulting from potential acts of nature (weather conditions, natural disasters, etc.) and non-design related construction problems (labor problems, supplier delays, etc.) and not from uncertainty resulting from lack of design definition. Experience has shown that contingency funds are almost

always completely spent. Thus all the accounts have a 10% contingency allowance.

The spare parts allowance is the purchase cost and inventory cost prior to facility operation of the initial inventory of spare parts required onsite. Reactor parts rotated into service as part of a scheduled maintenance are not considered as spare parts.

The following spare parts allowances were used in UWTOR-M:

21	Structures and Site Facilities	0.5%
22	Reactor Plant Equipment	2%
23	Turbine Plant Equipment	1%
24	Electric Plant Equipment	0.5%
25	Miscellaneous Plant Equipment	0.5%

XIV.3. Reactor Plant Equipment Costs (Act. 22)

XIV.3.1 Blanket and First Wall (22.01.01)

The unit cost for the HT-9 first wall and blanket structure including the attached distribution manifolds was taken as $40/kg. This reflects the somewhat complex blanket shape required with a unit cost of about a factor of two higher than simpler construction. A design allowance of 10% was used on the blanket structure. The $Li_{17}Pb_{83}$ material which uses 35% enriched ^{6}Li has a unit cost of $6.35/kg. Figure XIV.3-1 shows the cost of $Li_{17}Pb_{83}$ as a function of ^{6}Li enrichment.

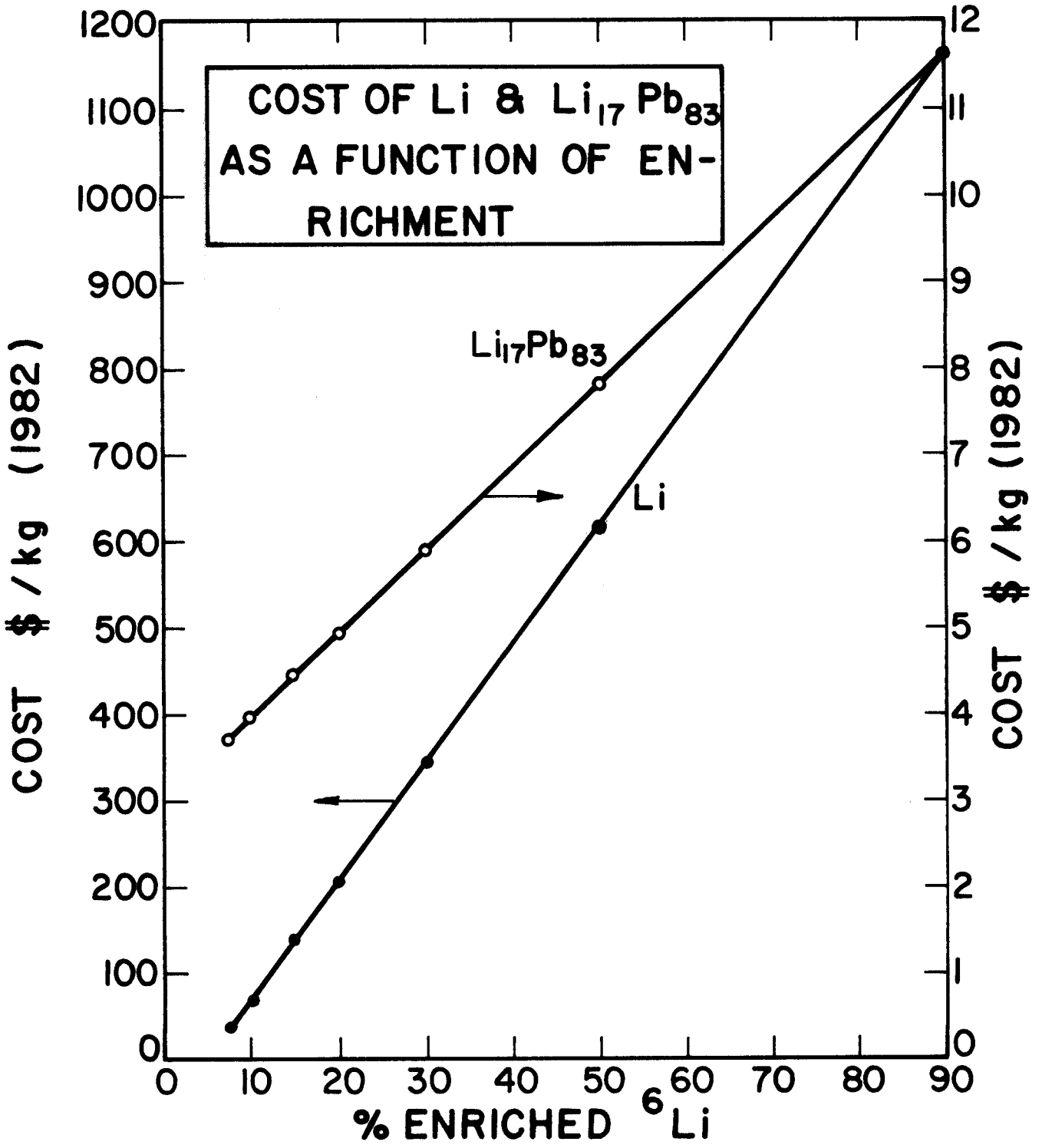

Figure XIV.3-1

XIV.3.2 Shield and Reflector (22.01.02)

The following unit costs were used for the reflector and shield:

		$/kg
Reflector	(1422) ferritic steel	9.0
Shield	(1422) ferritic steel	9.0
	B_4C - 80% density	30.0
	Pb	3.0

A design allowance of 5% was used.

XIV.3.3 Magnets (22.01.03)

Table XIV.3-1 gives the breakdown of the materials and unit costs for a single magnet. The unit costs used are 70% of the MFTF-B first yin yang coil costs to reflect the 10th of a kind criterion. The second yin yang coil for MFTF-B is being wound faster and at a lower cost. The overall unit cost for UWTOR-M is $41/kg as compared to $53/kg for the first MFTF-B yin yang. In contrast, the "STARFIRE"[2] TF coils had an overall unit cost of $24/kg.

XIV.3.4 Supplemental Heating (22.01.04)

UWTOR-M will require ~ 100 MW of ICRH for ignition. Although this heating lasts for only 11 sec at startup, unfortunately, all the required hardware must be provided. However, since the system can be protected from neutrons after ignition, it should be somewhat more reliable. The unit cost of $1.25/W used here takes a 30% cost advantage over the usual unit cost of $1.80/W for ICRH which is continuously exposed to neutrons. The design allowance taken is 5%.

Table XIV.3-1. Material Quantities for Each Coil and Unit Costs (22.01.03)

	Mass (10^3 kg)	Unit Cost ($/kg)	Total ($ x 10^6)
NbTiTa + Cu / NbTi + Cu Conductor	377	75.0	28.275
Coil form (also LHe container) (316 SS)	481	10.25	4.930
Structural ring (316 SS)	309	10.25	3.167
4.2°K thermal shield (Cu)	12.4	15.0	1.864
Vacuum dewar (304 SS)	52.8	20.0	1.056
G-10 CR insulation	7.0	20.0	0.140
Superinsulation	853 m^2	$100/$m^2$	0.085
Above total			39.517
Design allowance 15%			5.928
Total cost/coil			$45.4x10^6$

Table XIV.3-2. Material Quantities in Each Control Coil (22.01.03)

	Mass (10^3 kg)	Unit Cost ($/kg)	Total ($ x 10^6)
NbTi + Cu	53	75.0	3.975
Coil form	195	10.25	2.000
Vacuum dewar	25	20.00	0.500
Superinsulation	335 m^2	100/m^2	0.034
Above total			6.509
Design allowance 15%			0.976
Total cost/coil			7.485

XIV.3.5 Primary Support Structure (22.01.05)

This account includes the following items broken down in cost:

	$ x 10^6
1. Central support struts	5.00
2. Ground support structure	3.42
3. Intercoil support structure	2.70
4. Transport rails (in situ)	2.68
5. Transporters (for use during maint.)	16.2
Above total	30.00
Design allowance 8%	2.40
Total	32.40×10^6

XIV.3.6 Reactor Vacuum (22.01.06)

The magnet vacuum system is estimated at $\$0.22 \times 10^6$ per coil. The cryo-pumps for the evacuation of the reactor building are priced at $\$22 \times 10^3/m^2$ and the roots blowers for the regeneration system for each station (12 pump stations) are $\$60 \times 10^3$. Roughing down of the building is accomplished with the regeneration pumps. The design allowance is 5%.

XIV.3.7 Power Supplies (22.01.07)

The supplemental heating power supplies are included in the ICRH costing in Act. 22.01.04.

The modular coil power supplies of ~ 5 MVA cost $\$450 \times 10^3$ and the plasma breakdown and control coils of 2 MVA, about $\$180 \times 10^3$. Protective circuitry for both systems is included in Act. 22.01.03. The design allowance is 5%.

XVI.3.8 Impurity Control (22.01.08)

The modular magnetic divertor is employed for impurity control and the energy is recovered with high performance divertor targets. Materials in a

single divertor target cylinder are as follows:

	Mass (kg)	Unit Cost ($/kg)	Total ($)
Rotating surface:			
1 - Molybdenum superstructure	7.3	300	2,190
2 - Graphite surface	22.4	500	11,200
Stationary core:			
1422 ferritic steel	4,340	9	36,060
Drive system			
Bearing and 100 RPM drive	2 ea.	10,000	20,000
Design allowance 10%			7,245
Total/target			79,695
Shield enclosure for each 2 targets			
1422 ferritic steel	13,000	9	117,000
Design allowance	5%	5%	5,850
Total/housing			122,850

The total cost of the impurity control system is:

	$ x 10^6
Divertor targets (216)	17.21
Shielded housings (108)	13.26
Total cost (22.01.08)	$30.47x10^6$

XIV.3.9 Main Heat Transfer System (22.02.01)

The primary steam cycle carries away the thermal energy in the blanket, the reflector, the divertor targets and the target shield housing. Steam pressure is low, only 5 MPa (730 psi), entering at 330°C and exiting at 500°C. There are 36 blanket segments in the reactor. Nine segments are manifolded into a single steam generator. Thus, there will be four steam generators of ~ 1150 MWth capacity with the associated plumbing, valves and pumps. The estimated costs are:

	$ x 10^6
Steam generators (4 ea.)	20.00
Distribution manifolds	10.20
Major piping	7.00
Small piping	5.50
Valves, elbows, etc.	6.00
Water purification and makeup	3.80
Pressurizer	4.20
Pumps	4.0
Tritium extraction system	5.0
Design allowance 5%	3.28
Total (22.02.01)	$69.98 x 10^6$

The tritium extracton system is based on experience with heavy water, involving a liquid phase catalytic exchange followed by two distillation columns, an oxidizer, a converter and T_2 storage.

XIV.3.10 Auxiliary Cooling Systems (22.03)

The magnet heat load at 1.8 K is estimated at ~ 4 kW (see Chapter VII) and an additional 10 kW at 4.2 K. This amounts to a refrigeration load at 300 K of 6 MW. The heat load on the cryopumps is estimated at ~ 20 kW at 4.2 K, giving an added 6.0 MW. Assuming a 12 MW cryogenerator and using the following algorithm which gives the cost of the refrigerator, distribution system, storage vessels, gas bags, etc.,

$$C = 31{,}460\ (kW_{300\ K})^{0.7}$$

the cost of the system is $22.55 x 10^6. Assuming a design allowance of 10% we

get \$23.68 x 10^6. The liquid N_2 system with a capacity of ~ 2000 liters/h is estimated at \$1.2 x 10^6.

The shield cooling system which dissipates 116 MW is estimated at \$1.5 x 10^6 MW.

XIV.3.11 Radwaste Treatment and Disposal (22.04)

The unit costs have been taken from PNL-2987[3] which give the following for radwaste treatment:

Liquid waste	\$150/MWth
Gaseous waste	\$400/MWth
Solid waste	\$300/MWth

On this basis, assuming a design allowance of 10%, we get \$4.68 x 10^6.

XIV.3.12 Fuel Handling and Storage

In the fuel handling and storage, following the sequence given in PNL-648, we have estimated these quantities:

	\$ x 10^6
Fuel purification including isotopic separation, cleanup, pumps, valves, etc.	10.00
Pellet preparation, mixing and freezing	1.00
Pellet injection	3.50
Fuel storage	2.50
Tritium recovery (included in 22.02.01)	
Emergency air detritiation:	
Reactor hall (included in 22.01.06)	
Service hall and fuel handling and storage building	12.00

Assuming a design allowance of 8%, the total is \$31.32 x 10^6.

XIV.3.13 Other Reactor Plant Equipment (22.06)

Although the transporters and transport rails were included in Act. 22.01.05, other remote maintenance equipment for the different areas within the reactor complex are estimated as follows:

	$ x 10^6
Reactor building	9.5
Reactor service building	6.2
Two hot cells	12.00
Steam generator building	8.30
Fuel handling building	2.5
Radwaste	1.5
Design allowance 10%	4.0
Total	44.00

XIV.3.14 Instrumentation and Control

It is presumed that instrumentation in a stellarator may be simpler than in tokamaks because of the steady-state magnetic fields and the absence of disruptions. Thus a sum of $20 x 10^6 was allocated with a design allowance of 10%.

XIV.4 Structures and Site Facilities

XIV.4.1 Reactor Building

The reactor building is toroidal with a major radius of 38 m, a minor radius of 15 m and a height of 18 m. The volume is ~ 69,000 m^3 contrasted with the "STARFIRE"[2] reactor building which was 255,000 m^3 in volume. The building provides the primary vacuum enclosure for the reactor and must be capable of evacuation down to ~ 10^{-6} torr. This is consistent with space simulation chambers used in aerospace research. The building will be steel lined and appropriately reinforced to withstand 1.5 atm of overpressure. For

maintaining the reactor, there are nine access doors, large enough to allow a coil module through. They will be sealed with multi-elastomer seals mounted on inflatable stainless steel gaskets. The seals will have intermediate pump-outs to reduce leakage and to intercept any tritium. Such doors are used on airlocks on the space simulation chambers.

Because of its rather unconventional nature, we have used a unit cost of $\$1000/m^3$ for the reactor building giving a total of $\$69 \times 10^6$.

XVI.4.2 Reactor Service Building

The reactor service building is also toroidal, surrounding the reactor building on all sides. It has a major radius of 62 m, a minor radius of 40 m and is 24 m high. This building will also be steel lined and equipped with a detritiation system, although during operation it will not be evacuated. The unit cost is the same as in the "STARFIRE" reactor building, $\$615/m^3$. Thus, the total cost is $\$104.05 \times 10^6$.

XIV.4.3 Turbine Plant Building

The turbine building is similar to current power plants and is of a conventional construction. It houses two turbine generators and is 120 m long, 60 m wide and 38 m high with a volume of 273,600 m^3. Using a unit cost of $\$150/m^3$ the cost is $\$41.04 \times 10^6$.

XIV.4.4 Hot Cells

There are two hot cells each ~ 50,000 m^3. The construction is similar to the reactor service building with a steel liner and thick concrete walls. At $\$615/m^3$ the cost is $\$61.5 \times 10^6$.

XIV.4.5 Fuel Handling and Storage Building

The fuel handling and storage building contains all the tritium processing equipment and will be located on the inside of the reactor building using

the inner reactor wall as its outer wall. It will also be steel lined and have a volume of 10,000 m^3. Since it shares the outer wall with the reactor building its unit cost is taken as \$400/m^3 and will thus cost \$4 x 10^6.

XIV.4.6 Other Buildings

The remaining buildings such as the power supply, cryogenic and gas storage, control room, administration, auxiliary systems, security and other services are estimated collectively at ~ \$30 x 10^6.

XIV.5. Balance of Plant Costs

The Turbine Plant, Electric Plant and Miscellaneous Plant equipment were estimated from "Fusion Reactor Design Studies: Standard Cost Estimating Rules", PNL-2987 with a few minor adjustments. This document gives the unit costs for a 1000 MWe gross superheated steam cycle power plant with appropriate scaling to higher power output. The estimates made for UWTOR-M are for a 2000 MWe gross power plant. A design allowance of 5% was used for the Balance of Plant.

			\$ x 10^6
XIV.6 Direct Cost Accounts			
20	Land & Land Rights	3.30	
20.01	Land and privilege acquisition		3.00
20.02	Building relocation, etc.		0.30
21	Structures & Site Facilities	355.36	
21.01	Site improvement and facilities		10.00
21.02	Reactor building		69.00
21.03	Reactor service building		104.05
21.04	Turbine plant building		41.04
21.05	Hot cells		61.50
21.06	Fuel handling and storage		4.00
21.07	Other buildings		30.00
21.08	Ventilation stack		2.00

21.98	Spare parts allowance			1.61	
21.99	Contingency			32.16	
22	Reactor Plant Equipment		1764.99		
22.01	Reactor equipment				
	22.01.01	Blanket and first wall		186.53	
		Breeding material			114.93
		Blanket structure			71.60
	22.01.02	Reflector and shield		134.79	
		Reflector			76.80
		Shield			57.99
	22.01.03	Magnets		832.17	
		Twisted coils			817.2
		Control coils			14.97
	22.01.04	Supplemental heating		131.25	
	22.01.05	Primary support structure		34.20	
		Reactor supports			12.01
		Transport rails			2.89
		Transporters			17.50
	22.01.06	Reactor vacuum		22.24	
	22.01.07	Power supplies		0.66	
	22.01.08	Impurity control		30.47	
		Divertor targets			17.21
		Shielded housings			13.26
22.02	Main heat transfer system			68.98	
	Steam genertors				21.00
	Distribution manifolds				10.71
	Large and small piping				13.12
	Valves and fitting				6.30
	Pumps				4.20
	Water purification and makeup				3.99
	Pressurizers				4.41
	Tritium extraction system				5.25

22.03	Auxiliary cooling system		26.65	
	22.03.01	LHe supply system		23.68
	22.03.02	LN_2 supply system		1.32
	22.03.03	Shield cooling		1.65
22.04	Radwaste treatment and disposal		4.68	
	22.04.01	Liquid waste		0.83
	22.04.02	Gaseous waste		2.20
	22.04.03	Solid waste		1.65
22.05	Fuel handling and storage		31.32	
	22.05.01	Fuel purification and separation		10.80
	22.05.02	Pellet preparation		1.08
	22.05.03	Pellet injectors system		3.78
	22.05.04	Fuel sotrage		2.70
	22.05.05	Emergency air detritiation		12.96
22.06	Other reactor plant equipment		49.94	
	22.06.01	Reactor maintenance		44.00
	22.06.02	Breeding material dump tanks		1.50
	22.06.03	Breeding material pumps		1.25
	22.06.04	Gas system		0.09
	22.06.05	Leak detection		1.80
	22.06.06	Standby cooling		1.30
22.07	Instrumentation and control		22.00	
22.98	Spare parts allowance		31.52	
22.99	Contingency allowance		157.59	
23	Turbine Plant Equipment	301.62		
23.01	Turbine generators		115.75	
	23.01.01	Turbine generators & accessories		113.25
	23.01.02	Foundations		2.50
23.02	Main steam system		12.39	
23.03	Heat rejection systems		47.25	
23.04	Condensing systems		25.67	
23.05	Feed heating system		17.85	
23.06	Other turbine plant equipment		31.50	
23.07	Instrumentation and control		21.32	

23.98	Spare parts allowance		2.72
23.99	Contingency allowance		27.17
24	Electric Plant Equipment	137.03	
24.01	Switch gear		16.80
24.02	Station service equipment		21.00
24.03	Switchboards (trace heating)		0.53
24.04	Protective equipment		2.73
24.05	Electrical structures and wiring		34.65
24.06	Power and control wiring		44.10
24.07	Electrical lighting		4.20
24.98	Spare parts allowance		0.62
24.99	Contingency allowance		12.40
25	Miscellaneous Plant Equipment	45.48	
25.01	Transportation and lifting eq.		18.90
25.02	Air and water service		13.65
25.03	Communication equipment		7.35
25.04	Furnishing and fixtures		1.26
25.98	Spare parts allowance		0.20
25.99	Contingency allowance		4.12
26	Special Materials	3.50	
26.01	Helium gas		3.50
TOTAL DIRECT COSTS		2611.28	

XIV.7 Indirect Costs

XIV.7.1 Construction Facilities, Equipment and Services (91)

Included in this account are all the facilities which are temporary aids during the construction phase. Although for a 1000 MWe plant, this account runs ~ 15% of the direct costs, it tends to rise exponentially with capacity. Following the example of other studies (STARFIRE[2] and others) we have assumed 10% of direct costs for this account.

XIV.7.2 Engineering and Construction Management (92)

The engineering and construction management account is taken as 8% of the direct costs following the example of other studies.[2]

XIV.7.3 Other Costs (93)

This account includes taxes, insurance, staff training and plant startup, and owners' G&A costs. A 5% of direct costs are used.

XIV.8 Time Related Costs

The time related costs consist of interest and escalation during construction. As mentioned at the start of this chapter, the cost analysis is performed in both constant dollars and current dollars. In the constant dollar mode interest on capital is taken at 5%, and escalation is assumed to be zero. This estimate reflects the cost of energy comparable with current costs, and in this sense, a zero escalation is justified since the costing is done in present day dollar values. Similarly, the interest on capital is taken as what it may have been eight or ten years ago, when the construction was begun.

In the current dollar mode, a 10% interest on capital is assumed and escalation is taken at 5%.

An eight year construction period has been assumed for UWTOR-M. It is figured that with an established industry, a coil winding facility can be put into operation within six months at the reactor site. Thereafter, the winding schedule can go on at the rate of four coils per year, with all the coils ready at the end of the fifth year of construction.

The cost flow profile used to determine the F_{IDC} (interest during construction factor and F_{EDC} (escalation during construction factor) is the classic s-curve biased about 20% to the right. This kind of profile seems to fit major fissile and nuclear power plants constructed thus far. The F_{IDC} and F_{EDC} factors have been taken from Table 2, page 21 of PNL-2648.

XIV.9 Total Capital Cost Summary

Acct. No.	Description	Cost ($\$x10^6$)	
20	Land and land rights	3.30	
21	Structures and site facilities	355.36	
22	Reactor plant equipment	1764.99	
23	Turbine plant equipment	301.62	
24	Electric plant equipment	137.03	
25	Miscellaneous plant equipment	45.48	
26	Special materials	3.50	
	TOTAL DIRECT COSTS		2611.28
91	Construction facilities	261.13	
92	Engineering and construction management	208.90	
93	Other costs	130.56	
TOTAL INDIRECT COSTS			600.59
TOTAL DIRECT AND INDIRECT COSTS			3211.87

		Constant Dollar	Current Dollar
94	Interest during construction		
	F_{IDC} (constant dollar) = 0.170	546.02	
	F_{IDC} (current dollar) = 0.466		1496.73
95	Escalation during construction		
	F_{EDC} (constant dollar) = 0	0.00	
	F_{EDC} (current dollar) = 0.261		838.30
	TOTAL CAPITAL COSTS	3757.89	5546.90

The net power output of the plant is 1836 MWe. Thus the unit plant costs are:

	Constant Dollar (1982)	Current Dollar (1982)
Unit Plant Cost, $/kWe	2047.00	3021.00

XIV.10 Busbar Energy Cost

The busbar energy cost in mills/kWh is the expense which a utility incurs in generating a kilowatt-hour of electricity. When the utility sells this electricity to the customer it adds a quantity to account for profit.

The expenses which make up the busbar energy costs are:

1. Fixed charge rate.
2. Annual operating and maintenance.
3. Scheduled component replacement.
4. Annual fuel costs.

Other elements needed to determine busbar costs are plant capacity and plant availability. Each of these items will be discussed separately.

XIV.10.1 Fixed Charge Rate

A major part of the fixed charge rate is the cost of capital which consists of the annual expense resulting from having to borrow the money to construct and start up the power plant. The cost of procuring the required capital is equivalent to the rate of return on the investment allowed by regulatory agencies. The capital structure of the utility and the rate of return required for each component of the capital structure determines this cost of capital. Other elements which are a part of the fixed charge rate are:

1. Depreciation.
2. Interim Replacement.
3. Property Insurance.
4. Federal Income Tax.
5. State and Local Taxes.

The fixed charge rates used are 10% for the constant dollar mode and 15% for the current dollar mode.

XIV.10.2 Annual Operation and Maintenance

The recommended[1] guideline for operation and maintenance is 2% of direct and indirect costs. In the STARFIRE study[2] in which a farily comprehensive determination of this account was made, it was found that somewhat less than 1% of the total direct and indirect costs can be taken when nuclear liability insurance, license and inspection fees and major retrofits are excluded. The O&M is then taken as 1% of the total direct and indirect costs for UWTOR-M.

XIV.10.3 Scheduled Component Replacement

The predicted lifetime of the first wall and blanket in UWTOR-M is three full power years. This is based on a maximum dpa in the first wall of 52.5

per full power year. At an availability of 75% this amounts to 4 years or 48 months. The total cost of replacing the blanket and the rotating graphite surfaces of the divertor targets including bearings and drives:

	$ x 10^6
Blanket Structure	71.60
Divertor Targets	8.37
	$79.97x$10^6$

The annual cost of scheduled blanket and divertor target replacement is $20 x 10^6. An additional $3 x 10^6 is allocated for other reactor components. The labor of replacement is included in the annual O&M.

XIV.10.4 Annual Fuel Cost

It is assumed that a fusion reactor which has a T_2 breeding ratio in excess of 1.05 is self-sufficient with respect to T_2. The only other fuel needed is D_2 and a small amount of makeup for burned lithium.

The daily D_2 burnup is 0.44 kg/day (see Chapter XII). At an availability of 75% and a unit cost of $2200/kg[3] this amounts to $275,000.

The Li burnup rate at 75% availability is 440 kg/year. From Fig. XIV.3-1 we see the unit cost of 35% ^{6}Li enriched lithium is $410/kg and thus the annual cost of replacing the lithium is $0.18 x 10^6.

The total annual fuel cost is $0.46 x 10^6.

XIV.10.5 Plant Availability

It was estimated that 4 weeks of scheduled downtime will be needed to replace 30% of the blanket. Since the lifetime of the blanket is taken as 3 full power years (4 operating years at a 75% availability), we will assume a 4 week shutdown every 16 months of operation. To maintain an availability of

75%, the unscheduled downtime must not exceed 67 days per year. This amounts to ~ 31 hours every week. Since UWTOR-M is an ignited reactor which does not require any plasma recirculating power fraction, it does not have any critical components which are continuously exposed to neutrons. It is assumed that the RF startup launching structures can be protected during the burn and will therefore have a long life and a high reliability.

On the basis of such reasoning, a 75% availability appears plausible.

XIV.10.6 Overall Plant Capacity

The gross electric power output of UWTOR-M is 1898 MWe (see Chapter IX). The estimated power requirements are as follows:

Cryogenerators	12 MW
Magnets	5 MW
Heat Transp. & Cond.	30 MW
B.O.P. Auxiliary	15 MW
	62 MWe

The net power output is therefore 1836 MWe. It should be kept in mind that the pumping power of 75 MW was taken off the turbine shaft as thermal power.

A 75% availability thus makes the saleable plant capacity equal to:

$$\text{Plant Capacity} = 1836 \times 10^3 \text{ kW} \times \frac{8760 \text{ hr}}{\text{yr}} \times 0.75 \text{ avail.}$$

$$= 1.206 \times 10^{10} \text{ kWh/yr.}$$

XIV.10.7 Busbar Unit Costs

XIV.10.7.1 Constant Dollar Mode

The fixed charge rate in this mode was taken at 10%. The busbar costs are:

$$\text{Busbar Costs} = \frac{[(\text{Total Capital Costs})(\text{Fixed Charge Rate}) + (\text{O\&M}) + (\text{Comp. Replacement}) + (\text{Fuel Costs})]1000 \text{ mills}}{\text{Plant Capacity kWh}}$$

$$= \frac{[(3757.89 \times 10^6)0.1 + (37.58 \times 10^6) + (23.0 \times 10^6) + (0.46 \times 10^6)]1000 \text{ mills}}{1.206 \times 10^{10} \text{ kWh}}$$

$$= 36.2 \text{ mills/kWh} .$$

XIV.10.7.2 Current Dollar Mode

In the current dollar mode the fixed charge rate is taken as 15% and O&M, scheduled component replacement and fuel costs are escalated at 5% per year for 8 years, the construction period for the reactor.

$$\text{Busbar Costs} = \frac{\{[(5546.90 \times 10^6)(0.15)] + (55.47 \times 10^6 + 23.0 \times 10^6 + 0.46 \times 10^6)(1.05)^8\} 1000 \text{ mills}}{1.206 \times 10^{10} \text{ kWh}}$$

$$= 78.7 \text{ mills/kWh (in 1990 dollars)} .$$

XIV.11 Results and Discussion

It is interesting to compare the UWTOR-M results with STARFIRE, the most comprehensive tokamak study to date. Costing guidelines are almost the same for the two studies but STARFIRE is a great deal more detailed. The results show that the plant costs and busbar costs are comparable for the two systems in the constant dollar mode. The difference in the current dollar mode comes

from the construction period which is 8 years for UWTOR-M and 6 years for STARFIRE. Table XIV.11-1 compares the results of the two systems.

Figure XIV.11-1 shows a breakdown of the reactor plant equipment (RPE) for UWTOR-M. The magnets dominate the picture accounting for 52.4% of the RPE costs. In constrast, the magnets in STARFIRE claimed only 17.7%, and in WITAMIR,[4] a tandem mirror with thermal barriers, the magnets comprised 25% of the RPE costs. The other major accounts are the first wall and blanket (12%), reflector and shield (8.6%) and supplemental heating (8.4%).

It is also interesting to note that the RPE costs for UWTOR-M make up a larger fraction of the total direct costs than in STARFIRE. The various direct cost accounts are compared in Table XIV.11-2.

XIV.12 Conclusions

- A reasonably detailed cost analysis indicates that modular stellarators are competitive with other magnetic fusion systems.
- To be competitive, indications are that modular stellarators must be in the 4000-5000 MWth range.
- Risks associated with the magnets are higher for modular stellarators because they comprise a higher fraction of the reactor plant equipment.

Table XIV.11-1. Comparison of Plant Costs and Busbar Costs Between UWTOR-M and STARFIRE

	Constant Dollars	Current Dollars
Plant Costs		
UWTOR-M ($/kWe)	2034 (1982)	3001 (1900)
STARFIRE ($/kWe)	2000 (1980)	2665 (1986)
Busbar Costs		
UWTOR-M (mills/kWh)	36 (1982)	76 (1990)
STARFIRE (mills/kWh)	35.1 (1980)	67.1 (1986)

Table XIV.11-2. Comparison of Direct Cost Accounts Between UWTOR-M and STARFIRE

Acct. No.	Description	UWTOR-M	STARFIRE
20	Land and Load Rights (%)	0.1	0.2
21	Structures and Site Facilities (%)	13.7	20.
22	Reactor Plant Equipment (%)	67.4	56.1
23	Turbine Plant Equipment (%)	11.6	14.5
24	Electric Plant Equipment (%)	5.3	6.8
25	Miscellaneous Plant Equipment (%)	1.8	2.4
26	Special Materials (%)	0.1	---

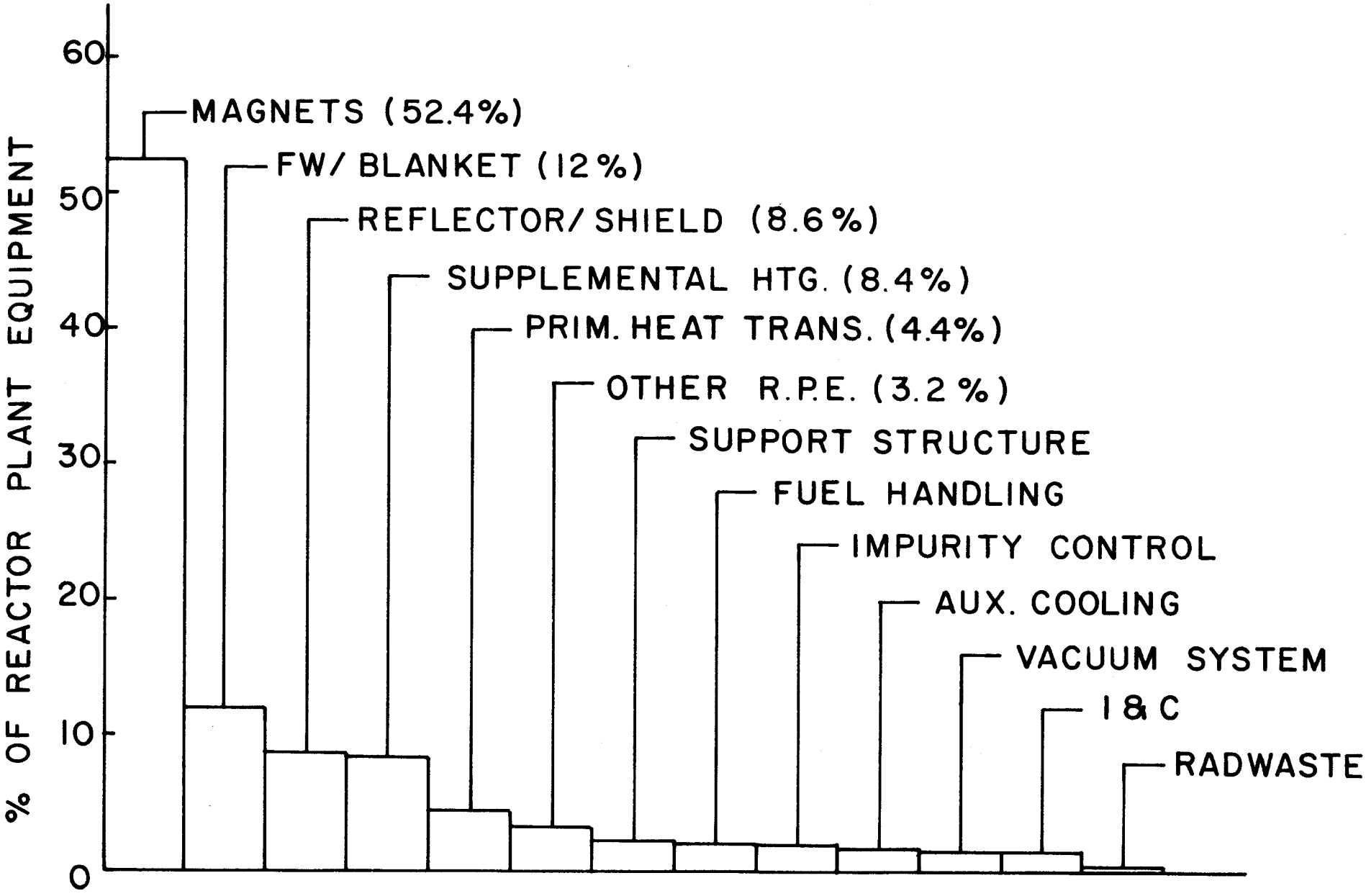

Figure XIV.11-1 Percentage breakdown of reactor plant equipment.

References for Chapter XIV

1. S.C. Schulte, T.L. Willke, and J.R. Young, "Fusion Reactor Design Studies - Standard Accounts for Cost Estimates," PNL-2648, Richmond, Washington, May 1978.

2. C.C. Baker et al., "STARFIRE - A Commercial Tokamak Fusion Power Plant Study," Argonne National Laboratory and others, ANL-FPP-80-1, Sept. 1980.

3. S.C. Schulte et al., "Fusion Reactor Design Studies - Standard Unit Costs and Cost Scaling Rules," PNL-2987, Sept. 1979.

4. B. Badger et al., "WITAMIR-I, A University of Wisconsin Tandem Mirror Reactor Design," UWFDM-400, Sept. 1980.

UWTOR-M PARAMETER LIST

GENERAL REACTOR PARAMETERS

1.	Thermal Power - MW_{th}	4820
2.	DT fusion power - MW_{th}	4300
3.	Plasma Q - value	∞
4.	Gross electric power - MW_e	1898
5.	Net electric power - MW_e	1836
6.	Recirculating power fraction - %*	3.3
7.	Net elect. efficiency - %	38
8.	Major radius - m	24.09
9.	Minor radius - m	4.77
10.	Coil aspect ratio	5.05
11.	Plasma aspect ratio	14
12.	Average β - %	6
13.	Magnetic field on axis - T	4.5
14.	Max. field on conductor - T	11.6
15.	Multipolarity	3
16.	No. of field periods	6
17.	Coils per period	3
18.	Reactor structural material	HT-9
19.	Breeding material	$Li_{17}Pb_{83}$
20.	Reactor coolant	Steam
21.	Breeding ratio (global)	1.08
22.	Ave. neutron wall loading - MW/m^2	1.41
23.	Peak neutron wall loading - MW/m^2	3.10
24.	Total T_2 inventory (kg)	1.8
25.	No. of divertor slots	108
26.	No. of divertor targets	216
27.	Total power to divertor - MW_{th}	480

*Pumping power of 75 MW_{th} is taken off the turbine shaft and thus is not included in recir. power fraction

PLASMA

1.	Plasma major radius - m	24.1
2.	Plasma minor radius - m	1.72
3.	Multipolarity (ℓ)	3
4.	Plasma aspect ratio	14
5.	n_o - centerline density - m^{-3}	3.82×10^{20}
6.	$\bar{n}$ average density (ion) - m^{-3}	1.46×10^{20}
7.	τ_{E_i}, ion energy conf. time - s	3.7
8.	τ_E, electron energy conf. time - s	0.9
9.	τ_p, particle conf. time - s	4.0
10.	$n\tau_{E_i}$ (averaged through plasma) - sm^{-3}	5.4×10^{20}
11.	β_o centerline toroidal beta - %	18.3
12.	$\langle\beta\rangle$ average toroidal beta - %	6
13.	T_{io} centerline ion temp. - keV	10.4
14.	$\bar{T}_i$ average ion temp. - keV	9.8
15.	$\bar{T}_e$ average electron temp. - keV	9.5
16.	Centerline z_{eff}	1.28
17.	Rotational transform - edge	1.13
18.	Rotational transform - center	0.16
19.	Duty cycle	St. state
20.	Fuel cycle	DT
21.	Plasma heating method	ICRF
22.	Plasma heating power - MW	100
23.	Heating frequency - Hz	69×10^6
24.	Fueling method	Pellets
25.	Pellet velocity (m/s)	1.7×10^4

BLANKET AND SHIELD

1.	Blanket structural material	HT-9
2.	Blanket coolant	Steam
3.	Effective first wall thickness, mm	5
4.	First wall coolant	Steam
5.	Breeding material	$Li_{17}Pb_{83}$
6.	^{6}Li enrichment %	35
7.	Blanket fractional composition	
	a. Structure %	9-15
	b. Coolant %	9
	c. Breeding material %	82-76
8.	Blanket dimensions	
	a. Avg. inside radius, m	1.88
	b. Outside radius, m	3.03
	c. Avg. thickness, m	1.15
9.	Global breeding ratio	1.08
10.	Blanket energy multiplication	1.15
11.	Reflector material	1422 steel
12.	Reflector thickness, m	0.40
13.	Shield thickness, m	0.30
14.	Shield composition	
	a. 1422 steel %	25
	b. B_4C %	57
	c. Pb %	14
	d. H_2O %	4
15.	Avg. neutron wall loading, MW/m^2	1.41
16.	Max. neutron wall loading, MW/m^2	3.1
17.	Blanket power, MW_{th}	4340
18.	Avg. surface heating, W/cm^2	23
19.	Max. surface heating, W/cm^2	57
20.	Coolant inlet temp., C	330
21.	Coolant outlet temp., C	500
22.	Max. blanket struc. temp., C	530

23.	Coolant pressure MPa	5
24.	Coolant mass flow, kg/hr	4.8×10^7
25.	Coolant pumping power, MW_{th}	75
26.	Shield coolant	H_2O
27.	Shield coolant temp., C	60-100
28.	Power in the shield, MW	116
29.	First wall area, m^2	2318
30.	Volume of blanket, m^3	2348
31.	Volume of reflector, m^3	1173
33.	Volume of shield, m^3	979
34.	Max. stress in first wall, MPa	46.5
35.	Max. stress in blanket, MPa	46
36.	Mass of a blanket module tonnes	45.2
37.	Total mass of blanket str., tonnes	1627
38.	Total mass of breeding mat., tonnes	18,100
39.	Total mass of reflector, tonnes	8,127
40.	Total mass of shield, tonnes	4,568

DIVERTOR

1.	Power to divertor	
	a. Surface heat MW	320
	b. Nuclear heat MW	160
2.	Number of div. slots	108
3.	Number of div. targets	216
4.	Shape of div. targets	Cylindrical
5.	Divertor target dim.	
	a. Outer diameter, m	0.6
	b. Length, m	2.5
6.	Materials in div. targets	
	a. Rotating surface	Graphite
	b. Stationary shield	1422 steel
	c. Coolant	Steam
7.	Avg. heat load, W/m^2	31.3
8.	Max. heat load, W/m^2	189
9.	Coolant inlet temp., C	330
10.	Coolant outlet temp., C	550
11.	Max. surface temp., C	> 1000
12.	Surface revolution rate, RPM	100
13.	Graphite sputtering rate, mm/FPY	2
14.	Surface replacement rate, years	4
15.	Mass of diverter target, tonnes	4.3

MAGNET

1.	Major radius - m	24.1
2.	Minor radius - m	4.77
3.	Total coil current - MA	31.2
4.	Field on axis - T	4.5
5.	Max. field on cond. - T	11.6
6.	Multipolarity	3
7.	No. of field periods	6
8.	Coils per period	3
9.	Total no. coils	18
10.	Max. field ripple components - %	23
11.	Total stored energy (GJ)	171
12.	Coil inductance (H)	48
13.	Discharge time - s	100
14.	Overall current density - MA/m^2	11.7
15.	Type of conductor	Monolythic
16.	Type of supercond.	NbTi/NbTiTa
17.	Conductor current - kA	20
18.	Conductor current density - MA/m^2	33.3
19.	No. of turns	1560
20.	Mode of cooling	HeII pool
21.	Stabilizing material	3/4 hard Cu
22.	Structural material	304 LN-SS
23.	Elect. insulating material	G10-CR
24.	Thickness of casing - mm	150-250
25.	Vacuum dewar - mm	10
26.	Thickness of superinsulation zone - mm	80
27.	Cross section of conductor bundle - mxm	1.1x1.3
28.	Overall outer dim. of dewar - mxm	1.68 1.96
29.	Radius to first surface of dewar - m	3.77
30.	Mass of each coil and dewar - tonnes	918
31.	Max. radial force - MN/m	74
32.	Max. stress in cond. - MPa	120

33.	Max. stress in coil case - MPa	533
34.	Max. strain in cond. - %	0.12
35.	Total refrigeration power - MW	5
36.	Helium volume/magnet - ℓ	9300

TRITIUM

1.	Mode of fueling	Pellets
2.	T_2 fractional burnup - %	4.4
3.	Rate of T_2 fueling - g/sec	0.172
4.	Mode of T_2 recovery	LPCE/CD*
5.	Type of vacuum pumps	Cryopumps
6.	Vacuum pumping speed - ℓ/s	2×10^7
7.	T_2 inventory in blanket - g	180
8.	T_2 inventory in pumps - g	1200
9.	T_2 inventory in recovery and fueling system - g	400
10.	Total active plant T_2 inventory - g	1800
11.	T_2 inventory for 1 day fueling - kg	14.9
12.	Total plant T_2 inventory - kg	16.7
13.	T_2 permeation into primary coolant - Ci/day	7.1×10^6

*Liquid phase catalytic exchange/cryogenic distillation

NEUTRONICS

1. General

(3-D results except where indicated by an asterisk)

a.	Neutron fusion power, MW	3442.5
b.	Max. neutron wall loading, MW/m^2	3.121
c.	Av. neutron wall loading, MW/m^2	1.41
d.	Overall tritium breeding ratio	1.080
e.	Overall energy multiplication	1.153
f.	Total neutron streaming through divertor slots, n/fusion	0.214
g.	Total gamma streaming through divertor slots, γ/fusion	2.43 E-2
h.	Power in first wall, MW	89.366
i.	Power in breeding blanket, MW	3377.157
j.	Power in reflector, MW	332.870
k.	Power in shield, MW	116.638
l.	Power in 6 divertor targets, MW	159.495
m.	Max. first wall power density*, W/cm^3	8.346
n.	Max. blanket power density*, W/cm^3	22.440
o.	Max. reflector power density*, W/cm^3	13.076
p.	Peak dose outside biological shield*, mrem/hr	2.35

2. Composition

a.	First wall	HT-9
b.	Blanket I	82 v/o $Li_{17}Pb_{83}$ (35% ^6Li)
		9 v/o HT-9
		9 v/o steam
c.	Blanket II	76 v/o $Li_{17}Pb_{83}$ (35% ^6Li)
		15 v/o HT-9
		9 v/o steam
d.	Reflector	90 v/o Fe 1422
		10 v/o steam
e.	Bulk shield	25 v/o Fe 1422
		57 v/o B_4C (87% d.f.)

*1-D results

		4 v/o H_2O
		14 v/o Pb
f.	Divertor target shield	95 v/o Fe 1422
		5 v/o steam
g.	Biological shield	87 v/o ordinary concrete
		8 v/o C1020 steel reinforcement
		5 v/o H_2O
3.	Dimensions	
a.	First wall equivalent thickness, cm	0.5
b.	First wall area, m^2	2318
c.	Av. blanket thickness, m	1.154
d.	Reflector I.D., m	6.06
e.	Reflector thickness, m	0.4
f.	Bulk shield thickness, m	0.3
g.	Divertor target radius, m	0.3
h.	Divertor region shield thickness, m	0.15
i.	Biological shield thickness, m	3.1
4.	First Wall	
a.	Avg. inside radius, m	1.871
b.	Volume, m^3	11.592
c.	Nuclear heating per 14.1 MeV neutron, MeV/fusion	
	Neutron	0.057
	Gamma	0.310
	Total	0.367
d.	Av. power density, W/cm^3	
	Neutron	1.197
	Gamma	6.512
	Total	7.709
e.	Max. DPA* in Fe, dpa/FPY	52.539
f.	Max. H production* in HT-9, appm/FPY	1111.03
g.	Max. He production* in HT-9, appm/FPY	341.334
5.	Breeding Blanket	
a.	Avg. inside radius, m	1.876

b.	Volume, m^3	2348
c.	Overall breeding ratio	
	^6Li	1.065
	^7Li	0.015
	Total	1.08
d.	Local breeding ratio	1.44
e.	Nuclear heating per 14.1 MeV neutron, MeV/fusion	
	Neutron	7.234
	Gamma	6.635
	Total	13.869
f.	Av. power density, W/cm^3	
	Neutron	0.698
	Gamma	0.640
	Total	1.338
g.	Max. DPA* in Fe, dpa/FPY	49.241
h.	Max. H production* in HT-9, appm/FPY	979.395
i.	Max. He production* in HT-9, appm/FPY	299.184
6.	Reflector	
a.	Inside radius, m	3.03
b.	Volume, m^3	1.157E3
c.	Nuclear heating per 14.1 MeV neutron, MeV/fusion	
	Neutron	0.088
	Gamma	1.279
	Total	1.367
d.	Av. power density, W/cm^3	
	Neutron	0.019
	Gamma	0.269
	Total	0.288
e.	Max. DPA* in Fe, dpa/FPY	17.283
f.	Max. H production* in Fe 1422, appm/FPY	417.223
g.	Max. He production* in Fe 1422, appm/FPY	128.740

*1-D results

7.	Bulk Shield	
a.	Inside radius, m	3.43
	Volume, m^3	967.323
b.	Nuclear heating per 14.1 MeV neutron, MeV/fusion	
	Neutron	0.351
	Gamma	0.128
	Total	0.479
c.	Av. power density, W/cm^3	
	Neutron	0.088
	Gamma	0.032
	Total	0.120
d.	Percentage of energy deposited in shield	3%
e.	Max. DPA* in Fe, dpa/FPY	0.440
f.	Max. H production* in Fe 1422, appm/FPY	0.747
g.	Max. He production* in Fe 1422, appm/FPY	0.207
8.	Divertor Region	
a.	Av. dpa in graphite layer of left divertor target, dpa/FPY	1.411
b.	Av. dpa in graphite layer of right divertor target, dpa/FPY	2.141
c.	Av. He production in graphite layer of left divertor target, appm/FPY	13.850
d.	Av. He production in graphite layer of right divertor target, appm	23.015
e.	Neutron streaming through divertor Slot #1, n/fusion	7.614E-2
	Slot #2	7.732E-2
	Slot #3	6.018E-2
	Total	0.214

*1-D results

f.	Gamma streaming through divertor	Slot #1 γ/fusion	8.628E-3
		Slot #2	8.735E-3
		Slot #3	6.924E-3
		Total	.0243
g.	Total energy carried by streaming radiation, MeV/fusion		
		Neutron	0.690
		Gamma	0.032
		Total	0.722
h.	Energy deposited in a pair of divertor targets, MeV/fusion		
		Neutron	0.041
		Gamma	0.178
		Total	0.219
i.	Percentage of streaming energy deposited in the targets		91%
	Nuclear heating in shield, MeV/fusion		
		Neutron	0.067
		Gamma	0.027
		Total	0.094
j.	Radiation streaming through pumpout port #1		
		Neutron/fusion	7.290E-3
		Gamma/fusion	1.421E-3
k.	Energy carried by radiation streaming through port #1, MeV/fusion		
		Neutron	6.653E-3
		Gamma	1.650E-3
		Total	8.303E-3
l.	Radiation streaming through port #2		
		Neutron/fusion	9.671E-5
		Gamma/fusion	3.327E-5
m.	Energy carried by radiation streaming through port #2, MeV/fusion		
		Neutron	3.496E-5
		Gamma	3.750E-5
		Total	7.246E-5
9.	Superconducting Magnet		
a.	Coil Inside radius, m		4.13
b.	Peak dose in mylar* (after 24 FPY), rad		8.757E9

c.	Peak dose in epoxy* (after 24 FPY), rad	4.163E8
d.	Peak DPA in Cu stabilizer*, dpa/FPY	6.476E-6
e.	Peak power density*, mW/cm^3	
	Neutron	0.006
	Gamma	0.010
	Total	0.016

*1-D results

MATERIALS

First Wall		
1.	Material	HT-9
2.	Operating temp. range, °C	330-530
3.	Max. stress, MPa	46.5
4.	Avg. neutron wall load, MW/m^2	1.41
5.	Max. neutron wall load, MW/m^2	3.1
6.	Max. surface heat flux	57
7.	Max. dpa/FPY	52.5
8.	Max. He/FPY, appm/FPY	341.3
9.	Max. H_2/FPY, appm/FPY	1111
10.	% swelling/FPY	> 1
11.	Shift in DBTT, C/FPY	85
12.	Estimated life, y	4
Blanket Structure		
13.	Material	HT-9
14.	Operating temp. range, °C	330-530
15.	Max. stress, MPa	46
16.	Avg. power density, W/cm^3	1.34
17.	Max. dpa/FPY	49.24
18.	Max. He/FPY, appm/FPY	299.2
19.	Max. H_2/FPY, appm/FPY	979.4
20.	% swelling/FPY	> 1
21.	Shift in DBTT C/FPY	200
22.	Estimated life, y	4
Breeding Material		
23.	Material	$Li_{17}Pb_{83}$
24.	^6Li enrichment %	35
25.	Temp. range - °C	330-550
26.	Velocity	Static
27.	Pressure, MPa	0.55
Reflector		
28.	Material	1422 steel

29.	Coolant	Steam
30.	Temp. range	330-550
31.	Avg. power density, W/cm^3	0.288
32.	Max. dpa/FPY	17.28
33.	Max. He/FPY, appm/FPY	128.7
34.	Max. H/FPY, appm/FPY	417.2
Shield		
35.	Materials	
	a	1422 steel
	b	B_4C
	c	Pb
36.	Coolant	H_2O
37.	Temp. range, °C	60-100
38.	Avg. power density, W/cm^3	0.120
39.	Percent of energy in the shield, %	3
40.	Max. dpa in Fe, dpa/FPY	0.44
41.	Max. He/FPY, appm/FPY	0.207
42.	Max. H/FPY, appm/FPY	0.747

POWER CYCLE

1.	Thermal energy, MW	4820
2.	Steam temperature, °C	454
3.	Steam pressure, MPa	138
4.	Reheat temperature, °C	454
5.	Feedwater temperature, °C	280
6.	Pumping power, MW_{th}	75
7.	Net thermal power, MW_{th}	474.5
8.	Cycle efficiency, %	40
9.	Power output, MW	1898

DOE Parameter List

The following parameter list format was prepared by DOE (DOE letter RS & A:CRH:#478, March 7, 1979) with a request that all reactor design studies fill it out for comparison. The list is amended slightly to conform to modular stellarators. "Not applicable" is designated as N.A. whereas "not available" as N/A.

The nuclear island is defined as all that encompassed in Acct. 22 in PNL-2648 "Fusion Reactor Design Studies - Standard Accounts for Cost Estimates".

1. Characteristic Machine Dimensions		Unit	Value
1.1	Reactor envelope		
1.1.1	Height	m	16.2
1.1.2	Width	m	64 dia.
1.1.3	Length	m	N.A.
1.2	First wall		
1.2.1	Major radius	m	24.09
1.2.2	Minor radius (effective)	m	1.87
1.2.3	Volume	m^3	1930
1.2.4	Inner surface area	m^2	2318

2. Plasma Parameters			
2.1	Plasma dimensions		
2.1.1	Major radius, R	m	24.1
2.1.2	Minor radius, a	m	1.72
2.1.3	Plasma elongation		Triangular
2.2	Centerline fuel density (n_{DTO})	m^{-3}	3.82×10^{20}
2.3	Average density ($\bar{n}_{DT}$)	m^{-3}	1.46×10^{20}
2.4	τ_E, electron energy confinement time	s	0.9
2.5	τ_e, ion energy confinement time	s	3.7
2.6	τ_i, particle confinement time	s	4.0
2.7	$n_{\tau E}$ (averaged through plasma)	s/m^3	5.4×10^{20}
2.8	β_o, peak toroidal beta	%	18.3
2.9	$\langle\beta\rangle$, average toroidal beta	%	6
2.10	β_{PO}, centerline poloidal beta		N.A.
2.11	$\langle\beta_p\rangle$, average poloidal beta		N.A.
2.12	I_p, plasma current	MA	0
2.13	T_{io}, centerline ion temperature	keV	10.4
2.14	$\bar{T}_i$, average ion temperature	keV	9.8
2.15	T_{eo}, centerline electron temperature	keV	N.A.
2.16	$\bar{T}_e$, average electron temperature	keV	9.5
2.17	Z_{eff}, effective plasma ion charge		1.28
2.18	q, plasma safety factor		N.A.
2.19	Volt-seconds	Volt-s	N.A.

		Unit	Value
2.20	Reactor cycle		Steady-state
2.20.1	Burn pulse length	s	N.A.
2.20.2	Total pulse length	s	N.A.
2.21	Fuel cycle (i.e., D-T, D-D, etc.)		D-T
2.22	Plasma heating method		ICRF
2.23	Plasma heating power	MW	100
2.24	Plasma heating energy or freq.	Hz	69×10^6
2.25	Plasma energy gain, Q_p (plasma fusion power/plasma heating power)		∞
3. Power Output			
3.1	Plasma fusion power (peak)	MWth	4300
3.2	Plasma fusion power (total cycle time average)	MWth	4300
3.2.1	Thermal power	MWth	4820
3.3	Power to first wall/blanket (peak neutron)	MWth	3442
3.4	Power to first wall/blanket (total cycle time average) (fusion neutron power)	MWth	3442
3.4.1	Nuclear heating in first-wall/ blanket	MW	3466
3.5	Blanket power amplification factor		1.15
3.6	Power to direct convertor (peak)	MWth	N.A.
3.7	Power to direct convertor (total cycle time average)	MWth	N.A.
3.8	Power to divertor (peak)	MWth	159.5
3.9	Power to divertor (total cycle time average)	MWth	159.5
3.10	Plasma chamber power density (total cycle time average)	MW/m^3	2.2
3.10.1	Plasma power density	MW/m^3	3.1

		Unit	Value
3.11	Nuclear island power density (total cycle time average)	MW/m^3	0.14
3.11.1	Engineering power density	MW/m^3	0.32
3.12	Plant gross electrical output	MWe	1898
3.13	Plant net electrical output	MWe	1836
3.14	Thermal cycle efficiency	%	40
3.15	Direct convertor efficiency	%	N.A.
3.16	Net plant efficiency	%	38
4. Reactor Coolant System			
4.1	Blanket coolant type		H_2O
4.2	Blanket outlet temperature (hot leg) - peak/average	°C	500/500
4.3	Blanket inlet temperature (cold leg) - peak/average	°C	330/330
4.4	Blanket outlet pressure - peak/average	MPa	5/5
4.5	Blanket inlet pressure - peak/average	MPa	5.1/5.1
4.6	Blanket coolant flow rate	kg/s	13,333
4.7	Blanket coolant pipe material		HT-9
4.8	First wall coolant type		H_2O
4.9	First wall outlet temperature - peak/average	°C	500/500
4.10	First wall inlet temperature - peak/average	°C	330/330
4.11	First wall outlet pressure - peak/average	MPa	5/5
4.12	First wall inlet pressure - peak/average	MPa	5.1/5.1
4.13	First wall coolant flow rate	kg/s	2066
4.14	Total number of first wall/blanket coolant loops		4

		Unit	Value
4.15	Type of blanket coolant circulator		From turbine shaft
4.16	Power input to each circulator	MWth	20
4.17	Peak first-wall/blanket temperature in case of loss of coolant flow		
4.17.1	First wall	°C	N/A
4.17.2	Multiplier	°C	N/A
4.17.3	Breeder	°C	N/A
4.17.4	First wall structure	°C	N/A
4.18	Energy storage	J	N/A
5. Intermediate Coolant System			
6. Steam Generation System			
6.1	Steam outlet temperature	°C(°F)	454 (850)
6.2	Steam outlet pressure	MPa (psia)	13.8 (2000)
6.3	Steam flow rate	kg/s (lb/hr)	2464 (19.6×10^6)
6.4	Feedwater temperature	°C(°F)	280 (536)
6.5	Number of steam generators per loop		1
6.6	Number of sectors per steam generator		9
6.7	Steam generator materials, shell/tube		Low carbon stl/inconel 600
7. Shield Coolant System			
7.1	Total energy deposited in the shield	MWth	116.6
7.2	Shield coolant type		H_2O
7.3	Shield outlet temperature - peak/ average	°C	100/100
7.4	Shield inlet temperature - peak/ average	°C	60/60
7.5	Coolant outlet pressure - peak/ average	MPa	0.35/0.35

		Unit	Value
7.6	Coolant inlet pressure - peak/ average	MPa	0.6/0.6
7.7	Coolant flow rate	kg/s	992
8. Reactor Auxiliary Systems			
8.1	Vacuum pumping system		
8.1.1	Plasma chamber pressure (base)	Pa	1.3×10^{-6}
8.1.2	Plasma chamber volume	m^3	1930
8.1.2.1	Plasma volume	m^3	1400
8.1.3	Number of pumps		120 (60 on line, 60 regenerating)
8.1.4	Capacity of each pump	$Pa\text{-}m^3$	5×10^5
8.1.5	Helium pumping speed of each pump	m^3/s	8600
8.2	Magnet cooling system		
8.2.1	Cooling load	MW (300 K)	6
8.3	Plasma heating system		
8.3.1	Heat removal from rf system	MW	N.A.
8.4	Plasma fueling system		
8.4.1	Type		Pellets
8.4.2	Fuel composition (i.e., %D, %T, etc.)		50%D, 50%T
8.4.3	Fueling rate	kg/s	1.7×10^{-4} (T) 1.1×10^{-4} (D)
8.4.4	Pellet size (if used)	m	3.6×10^{-3}
8.4.5	Pellet injection frequency (if used)	s	50
8.5	Tritium processing and recovery system		
8.5.1	Total tritium inventory (active)	kg	1.8
8.6	Impurity control system		
8.6.1	Type		Divertor
9. Reactor Components			
9.1	First wall/blanket		
9.1.1	Structural material		HT-9

		Unit	Value
9.1.2	Breeding material/neutron multiplier		$Li_{17}Pb_{83}$ Fe 1422
9.1.3	Breeding ratio		1.08
9.1.4	Number of sectors		18
9.1.5	Weight of sector	Tonnes	90.5
9.1.6	Weight of largest single component	Tonnes	90.5
9.1.7	Dimensions of largest component	DxL	6x4.3
9.1.8	First wall loading (peak/average)		
9.1.8.1	14.1 MeV neutrons	MW/m^2	3.1/1.4
9.1.8.2	Alpha particle flux	MW/m^2	(Very small)
9.1.8.3	Electromagnetic radiation plus charge exchange neutrals (peak/average)	MW/m^2	0.51/0.23
9.1.8.4	Plasma thermal conduction (particle transport)	MW/m^2	0.1
9.1.8.5	Wall life	$MW-yr/m^2$	15
9.2	Shielding		
9.2.1	Material		
9.2.1.1	Inboard		Steel, B_4C, Pb, H_2O
9.2.1.2	Outboard		Pb, B_4C, steel, H_2O
9.2.2	Number of sectors		18
9.2.3	Weight of each sector	Tonnes	306
9.2.4	Weight of largest single component	Tonnes	254
9.2.5	Dimensions of largest component	DXL	7.46 x 8.6
9.3	Magnets		
9.3.1	Modular magnets		
9.3.1.1	Superconducting	Yes/no	Yes
9.3.1.2	Conductor/stabilizer material		NbTiTa/NbTi/Cu
9.3.1.3	Structural material		304 LN-SS
9.3.1.4	Operating temperature	K	1.8
9.3.1.5	Coolant		He-II, bath cooling
9.3.1.6	Maximum stress in coil	MPa	533
9.3.1.7	Maximum force transmitted to building	N/m^2	N.A.

		Unit	Value
9.3.1.8	Maximum field	T	11.6
9.3.1.9	Field on plasma axis	T	4.5
9.3.1.10	Number of magnets		18
9.3.1.11	Field ripple-plasma edge/plasma axis	%	23
9.3.1.12	Stored energy	GJ	171
9.3.2	Poloidal coils		
9.3.2.1	Superconducting	Yes/no	Yes
9.3.2.2	Conductor/stabilizer material		NbTi/Cu
9.3.2.3	Structural material		304 LN-SS
9.3.2.4	Operating temperature	K	4.2
9.3.2.5	Coolant	K	Liquid He, bath cooling
9.3.2.6	Maximum stress in coil	N/m^2	$530x10^6$
9.3.2.7	Maximum force transmitted to building	N/m^2	N.A.
9.3.2.8	Maximum field	T	7
9.3.2.9	Field on axis	T	> 1
9.3.2.10	Number of magnets		2
9.3.2.11	Field ripple-edge/center	%	0/0
9.3.2.12	Stored energy	J	N.A.
9.4	Energy transfer and storage for startup		N/A
9.4.1	Plasma preparation		
9.4.1.1	Type		ICRF
9.4.1.2	Energy per unit	MJ	110
9.4.1.3	Total energy	MJ	990
9.4.1.4	Peak power transfer rate	MW	90
9.4.1.5	Transfer time	s	11
9.4.1.6	Power required from grid	MWe	150
9.4.1.7	Recharge time	s	N.A.
9.4.1.8	Pulse frequency	MHz	69
9.4.1.9	Switching requirements		
9.4.1.9.1	Current, power supply output	A	125

		Unit	Value
9.4.1.9.2	Volts, power supply output	kV	40
9.4.1.9.3	Number of power supplies		30
9.4.2	Power supplies		N.A.
9.4.3	Magnet power supply		
9.4.3.1	Type		Solid state
9.4.3.2	Peak power rating	MVA	5
9.4.3.3	On time	s	Continuous
9.4.4	Poloidal coil supplies		
9.4.4.1	Main equilibrium coil supply		
9.4.4.1.1			Solid state rectifier, inverter
9.4.4.1.2	Peak power rating	MVA	2
9.4.4.1.3	On time	s	N.A.
9.4.4	Poloidal coil supplies		
9.4.4.1	Main equilibrium coil supply		
9.4.4.1.1	Type		Solid state rectifier, inverter
9.4.4.1.2	Peak power rating	MVA	2
9.4.4.1.3	On time	s	N.A.
10. Electrical Power Requirements			
10.1	Cold start power from grid	MWe vs. s	212 vs. 11
10.2	Auxiliary power requirements (normal operation)	MWe	62
10.2.1	Electrical energy storage (EF coils)	MWe	None
10.2.2	Magnet power supply (other than energy storage)	MWe	5
10.2.3	First-Wall/Blanket Circulators	MWe	Turbine driven
10.2.4	Divertor coolant circulators	MWe	Included in 10.2.5
10.2.5	Shield coolant circulators	MWe	2.5
10.2.6	Refrigeration system	MWe	12

		Unit	Value
10.2.7	Vacuum system (roughing)	MWe	0.15
10.2.8	Plasma heating system	MWe	N.A.
10.2.9	Miscellaneous reactor plant auxiliaries	MWe	(Incl. in 10.2.13)
10.2.10	Feed pump system	MWe	N.A. (turbine driven)
10.2.11	Condensing system	MWe	4.5
10.2.12	Heat rejection system	MWe	23
10.2.13	Misc. BOP auxiliaries (transformer cable)	MWe	15
11. Buildings			
11.1	Reactor building		
11.1.1	Characteristic dimensions (IRxORxh)	mxmxm	15x38x18
11.1.2	Enclosed volume	m^3	$69x10^3$
11.1.3	Minimum wall thickness for shielding	m	3.1
11.1.4	Internal pressure, normal/accident (gage)	MPa	$5x10^{-9}$/+0.165
11.1.5	Containment atmosphere		Vacuum
11.2	Electrical energy storage building		N.A.
11.3	Reactor service building		
11.3.1	Characteristic dimensions (IRxORxh)	mxmxm	40x62x24
11.3.2	Turbine building	mxmxm	60x120x38
11.3.3	Hot cells		
11.3.3.1	Number		2
11.3.3.2	Characteristic volume m^3		$100x10^3$
11.3.4	Fuel handling and storage building		
11.3.4.1	Characteristic volume m^3		$10x10^3$

		Unit	Value
12. Reactor Maintenance			
12.1	Blanket/first wall replacement	% surface area/16 months	30 450
		tonnes/yr	
12.2	Radioactive material storage requirement, years/volume	Yr/m^3	N/A